BEILSTEIN JOURNAL OF NANOTECHNOLOGY

Topological materials

Edited by Juan Jose Palacios, Elsa Prada and Alfredo Levy Yeyati

Imprint

Beilstein Journal of Nanotechnology
www.bjnano.org
ISSN 2190-4286
Email: journals-support@beilstein-institut.de

The *Beilstein Journal of Nanotechnology* is published by the Beilstein-Institut zur Förderung der Chemischen Wissenschaften.

Beilstein-Institut zur Förderung der Chemischen Wissenschaften
Trakehner Straße 7–9
60487 Frankfurt am Main
Germany
www.beilstein-institut.de

BEILSTEIN JOURNAL OF NANOTECHNOLOGY

Revealing the interference effect of Majorana fermions in a topological Josephson junction

Jie Liu*[1], Tiantian Yu[1] and Juntao Song[2]

Full Research Paper

Open Access

Address:
[1]Department of Applied Physics, School of Science, Xi'an Jiaotong University, Xi'an 710049, China and [2]Department of Physics and Hebei Advanced Thin Film Laboratory, Hebei Normal University, Shijiazhuang 050024, China

Email:
Jie Liu* - jieliuphy@xjtu.edu.cn

* Corresponding author

Keywords:
density of states; fractional Josephson effect; Majorana fermion

Beilstein J. Nanotechnol. **2018,** *9,* 520–529.
doi:10.3762/bjnano.9.50

Received: 04 September 2017
Accepted: 12 January 2018
Published: 12 February 2018

This article is part of the Thematic Series "Topological materials".

Guest Editor: J. J. Palacios

Abstract

We study theoretically the local density of states (DOS) in a topological Josephson junction. We show that the well-known 4π Josephson effect originates from the interference effect between two Majorana fermions (MFs) that are localized at the Josephson junction. In addition, the DOS for electrons (holes) shows the 4π interference information along each parity conserved energy spectrum. The DOS displays a 2π period oscillation when two trivial states interfere with each other. This means that the DOS information may be used to distinguish the MFs from trivial localized states. We suggest that the interference effect and the DOS can be detected by using two STM leads or two normal leads. A single side lead can only detect the Andreev reflection tunneling process in the junction, which cannot reveal information about the interference effect in general. However, using two side leads, we can reveal information about the interference effect of the MFs as well as the DOS by combining Andreev reflection with the electron transmission process.

Introduction

After Kitaev reported that Majorana fermions (MFs) can appear as quasi-particle states at the ends of a one-dimensional (1D) p-wave superconductor [1], the generation of MFs became a popular goal in condensed matter physics [2]. Several methods were suggested to fabricate and detect MFs in effective 1D p-wave superconductor systems [3-11]. The use of a semiconductor wire with Rashba spin–orbit coupling and proximity-induced superconductivity appear to be the most promising method [4]. Indeed, a semiconductor–superconductor nanowire was manufactured to confirm the prediction of the theory [12-14]. The second topological superconducting system that was realized experimentally is related to ferromagnetic atomic chains, which are put on a trivial superconductor [15]. It is believed that MFs can generate a zero-bias conductance peak (ZBP) in the conductance spectrum [16-19], and indeed the signature of ZBPs has been observed in both systems in tunneling experiments. These advances accelerate the development of nanotechnology [20-27]. Recently, a breakthrough was

achieved in research groups led by Kouwenhoven and Marcus. Both groups observed the integer ZBPs in a nanowire system [28]. These are the most persuading results so far. However, all these achievements relied on the observation of ZBPs, which means that many other unique properties of MFs still require further verification and investigation.

Apart from the ZBP, another significant feature of MFs is the 4π Josephson current. When two topological superconducting wires are combined to form a topological Josephson junction (Top-JJ), the period of the supercurrent is 4π if MFs exist at the ends of both wires. This is different from the trivial case without MFs. In the trivial case in which only Cooper pairs can tunnel, the period is 2π. Since MFs have only half a degree of usual fermions, half a degree of Cooper pairs can tunnel in the Top-JJ when the two MFs combine. In this situation, the period is doubled. Because the 4π Josephson effect is a unique transport property of MFs, many groups attempt to observe it. Indeed, Kouwenhoven's and Marcus' groups fabricated such a junction and obtained some preliminary results. However, the expected 4π period was not observed [23-25]. The 4π Josephson effect needs a stringent condition that is known as the parity conservation [29]. The evolution of the states is expected to follow one fixed branch of the energy spectrum. It is particularly susceptible at the degenerate point when the even and the odd parity states intersect at zero energy for $\phi = (2n + 1)\pi$. The state then changes from one parity to another because of quasiparticle poisoning, the background and the thermal effect [30-34]. In this case, the 4π period will return to the conventional 2π. Thus, to reveal the 4π nature of the MFs, it may be necessary to observe more than just a supercurrent. Interestingly, several groups have studied superconductor-topological insulator–superconductor junctions that also display a 4π Josephson current. However, the behavior of the 4π Josephson current is not consistent with the theoretical prediction [35-41]. To distinguish the 4π information of MFs, it is necessary to reveal additional characteristic properties of such a Josephson junction.

In this paper, we study a Top-JJ composed of two topological superconductors as shown in Figure 1a. Unlike previous studies, we focus on the density of states (DOS) for both the electron part and the hole part. The essential property of the MFs is that the wave function of the electron part must be conjugated with the wave function of the hole part, which is known as the self-Hermitian property of the MFs. More specifically, the self-Hermitian property of the MFs can be demonstrated directly from the DOS of the electron and of the hole part, which is a basic assumption used in this paper. Since the DOS only shows the steady information of the whole energy spectrum, it does not relate to the parity-conserving problem, which is a problem of dynamic evolution. Therefore, compared to the supercurrent,

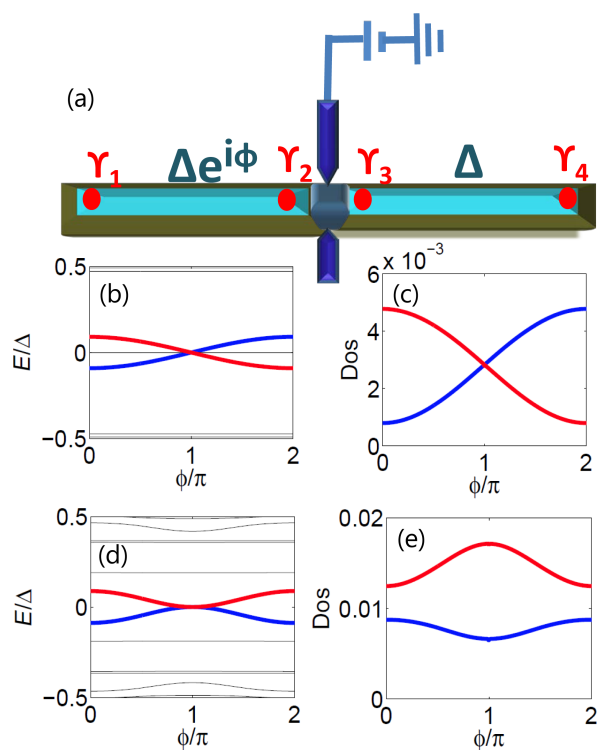

Figure 1: (a) Schematic setup of an experiment in which two STM leads or normal leads are connected to a Top-JJ that supports the MFs. (b) Energy spectrum of the Top-JJ with chemical potential $\mu = -2t$, which lies in the topological region. The two MFs, which are localized at the junction, interfere with each other and display a 4π oscillation. (c) DOS for electron part of the coupled MFs in the Top-JJ. Both even parity state and odd parity state show a parity-correlated 4π oscillation. (d) Energy spectrum of the Top-JJ with chemical potential $\mu = -2t + 5.7\Delta$, which lies in the trivial region, and the disorder strength $\mathbf{w} = 0.13t$. In this case, there does not exist any MF that is localized at the junction. However, the trivial Andreev bound states occasionally touch with each other in the presence of disorder. In such situation, the trivial Andreev bound states behave like the Andreev bound states formed by the two MFs in panel (b). (e) DOS of the trivial Andreev bound states for the electron part. It is totally different from the DOS of the nontrivial Andreev bound states in panel (c). The period of the trivial state is 2π.

the DOS are easier to detect. We show that the two Andreev bound states formed by the MFs exhibit a 4π period due to the interference effect between the two MFs. Furthermore, the DOS of both the electron and the hole part can also reveal the 4π period. The electron (hole) DOS of the two Andreev bound states are related: One is destructive, while the other is constructive. However, the DOS of the trivial Andreev bound states contains different information. In general, the interference effects in the trivial Andreev bound states are unrelated, and their period is 2π. Thus, it may be a way to distinguish them using information contained in the DOS. We suggest that the interference effect can be detected using two STM leads or two normal leads. We show that a single side lead can only detect the Andreev reflection tunneling process in the junction, which cannot reveal information about the interference effect in

general. However, using the two side leads, we can display information about the interference effect of the MFs by combining Andreev reflection and the electron-transmission process.

Model Hamiltonian and formula

A typical Top-JJ is composed of two topological superconducting wires that have different superconducting phases. According to [9,18], the tight-binding model of a superconducting wire is:

$$\begin{aligned} H_{s,q1D} &= \sum_{\mathbf{i},\mathbf{d},\alpha} -t\left(\psi^{\dagger}_{\mathbf{i}+\mathbf{d},\alpha}\psi_{\mathbf{i},\alpha} + h.c.\right) - \mu\psi^{\dagger}_{\mathbf{i},\alpha}\psi_{\mathbf{i},\alpha} \\ &\quad - \sum_{\mathbf{i},\mathbf{d},\alpha,\beta} iU_{\mathbf{R}}\psi^{\dagger}_{\mathbf{i}+\mathbf{d},\alpha}\hat{z}\cdot(\vec{\sigma}\times\mathbf{d})_{\alpha\beta}\,\psi_{\mathbf{i},\beta} \\ &\quad + \sum_{\mathbf{i},\alpha,\beta}\psi^{\dagger}_{\mathbf{i},\alpha}\left[(V_x\sigma_x)_{\alpha\beta} + V_{\mathrm{imp}}(\mathbf{i})\delta_{\alpha\beta}\right]\psi_{\mathbf{i},\beta} \quad (1) \\ &\quad + \sum_{\mathbf{i},\alpha}\Delta e^{i\phi_s}\psi^{\dagger}_{\mathbf{i},\alpha}\psi^{\dagger}_{\mathbf{i},-\alpha} + h.c. \\ H_c &= \sum_{\mathbf{i}_\mathbf{y},\alpha}\left(t_c\psi^{\dagger}_{LN,\mathbf{i}_\mathbf{y},\alpha}\psi_{R1,\mathbf{i}_\mathbf{y},\alpha} + h.c.\right). \end{aligned}$$

Here, $H_{s,q1D}$ is the Hamiltonian of the left (right) wire with $s = L$ (R). The only difference between the two wires is the phase of the superconducting order $\Delta e^{i\phi_s}$ (here we set $\phi_L = \phi$ and $\phi_R = 0$). Furthermore, **i** denotes the lattice site, and **d** denotes the two unit vectors $\mathbf{d_x}$ and $\mathbf{d_y}$, which connect the nearest neighbor sites in the x and y directions, respectively. Moreover, α, β are the spin indices, t is the hopping amplitude, μ is the chemical potential, U_R is the Rashba coupling strength, and V_x is the Zeeman energy caused by magnetic field along the wire direction. Δ is the superconducting pairing amplitude and $V_{\mathrm{imp}}(\mathbf{i})$ is the Gaussian impurity. H_c describes the coupling between the left and the right topological superconducting wires.

To obtain the tunneling coefficient at the junction, we use the recursive Green function method. We can then calculate the scattering matrix of the system. The scattering matrix is related to the Green functions via

$$S^{\alpha\beta}_{ij} = -\delta_{i,j}\delta_{\alpha,\beta} + i\left[\Gamma^{\alpha}_{i}\right]^{1/2}\cdot G^{r}\cdot\left[\Gamma^{\beta}_{j}\right]^{1/2}. \quad (2)$$

Here, $S^{\alpha,\beta}_{ij}$ is an element of the scattering matrix that denotes the scattering amplitude of a β particle from the j-th lead to an α particle in the i-th lead. Furthermore, $i,j = 1$ or 2, where 1 and 2 denote, respectively, the first and the second normal lead as shown in Figure 1a. $\alpha,\beta \in \{e,h\}$ denote the electron (e) or hole (h) channels. In addition,

$$G^{r} = \left[E - H_{L,q1D} - H_{R,q1D} - H_c - \sum_{i,\alpha}\left(\Sigma^{\alpha}_{i}\right)^{r}\right]^{-1}$$

is the retarded Green function of the Josephson junction, and $\Gamma^{\alpha}_{i} = i[(\Sigma^{\alpha}_{i})^{r} - (\Sigma^{\alpha}_{i})^{a}]$ is the linewidth function of an α particle in the i-th lead, where $(\Sigma^{\alpha}_{i})^{r(a)}$ is the retarded (advanced) self-energy of the α particle for the i-th lead. In the following calculation we set $\Gamma^{\alpha}_{i} = 0.1\Delta$ through wide-band approximation. The physical meaning of the scattering matrix is: $S^{e,h}_{ii}$ means the Andreev reflection coefficient T_A in the i-th lead, and $S^{e,e}_{ij}$ means the electron transmission coefficient T_e from the i-th lead to the j-th lead.

To match the experiment in [12], the parameters in the tight-binding model were chosen as follows: Δ = 250 μeV, $t = 25\Delta$, $U_R = 2\Delta$, and the superconductor coherence length is $\xi = t/\Delta a = 500$ nm with a being the lattice constant. In addition, we set $V_x = 2\Delta$ such that the superconducting wire can support the MF end states by tuning the chemical potential.

Results and Discussion

The following section is divided into three subsections. In the first subsection, the 4π oscillation of the DOS is shown. In the second subsection, the same oscillation information in a ring structure is shown and in the third subsection, we discuss how the information about the DOS is detected.

4π oscillation of the density of states

In this subsection, we consider the origin of the 4π Josephson effect. Then, we show that the DOS for the electron (hole) part can also exhibit the 4π interference effect. The well-known 4π Josephson effect is directly related to the fractional nature of the MFs. Because a single MF has only half a degree of a conventional fermion, we can define a conventional fermion using $\psi_j = (\gamma_{2j-1} + i\gamma_{2j})$. For the Top-JJ in Figure 1a, there are two pairs of the MFs, which are localized at the ends of the superconductor. We assume that the length of the wire is sufficient so that γ_1 and γ_2 (γ_3 and γ_4) are not coupled to each other. In this case, only γ_2 and γ_3 can couple to each other at the junction, which is described in Equation 1. Because the phase of the left wire is ϕ and the phase of the right wire is 0, the Hamiltonian of the left wire can be transformed into the right one using a unitary transformation $U = \mathrm{diag}(e^{-i\phi/2}, e^{i\phi/2})$. The phase difference between γ_2 and γ_3 is $\phi/2$. These two MFs will interfere with each other and form two Andreev bound states because of this phase difference. The effective Hamiltonian can be obtained by projecting the coupling of Equation 1 onto the subspace of the MFs using $\psi_{LN,\mathbf{i}_\mathbf{y},\alpha} \to ie^{-i\phi/2}\gamma_2$ and $\psi_{R1,\mathbf{i}_\mathbf{y},\alpha} \to \gamma_3$[6]. Then, the low-energy effective Hamiltonian is

$$\begin{aligned} H_{\mathrm{eff}} &= -\Gamma_{\mathrm{eff}}\cos(\phi/2)i\gamma_2\gamma_3 \\ &= -\Gamma_{\mathrm{eff}}\cos(\phi/2)(\hat{N} - 1/2). \end{aligned} \quad (3)$$

Here, $\hat{N} = \psi^{\dagger}\psi$ is the number operator and $\psi = \gamma_3 + i\gamma_2$. Then, the occupation number has two values: $N_v = 0,1$, with $N_v = 0$ corresponding to the even parity state, and $N_v = 1$ corresponding to the odd parity state. The Josephson current mediated by the MFs can be given by $I_J = \partial E(\phi)/\partial\phi \propto (-1)^{N_v} sin(\phi/2)$, which displays the 4π oscillation. This is very different from the case without the MFs. In such case, only Cooper pairs can tunnel from one superconductor to another, and the period is 2π.

We show that the fractional Josephson effect can be attributed to the interference effect between the two MFs. Next, we show that the DOS of the electron and the hole part of the Andreev bound states, which are formed by the MFs, also display the 4π period. The MF is a particle that is its own antiparticle. For such a particle, the wave function of the electron part must be conjugated with the wave function of the hole part, which is the self-Hermitian property of the MF. Thus, the general wave function of the MFs should be [42]:

$$\tilde{\gamma}_n = \left[e^{-i\phi_n/2}\tilde{\psi}(x), e^{i\phi_n/2}\tilde{\psi}^*(x)\right]^T.$$

Here, $\tilde{\psi}(x)$ is the wave function of the electron part, when the phase of the superconducting order parameter is 0. In the Top-JJ shown in Figure 1(a),

$$\tilde{\gamma}_2 = \left(e^{-i\phi/2}\tilde{\psi}(x), e^{i\phi/2}\tilde{\psi}^*(x)\right)^T$$

and

$$\tilde{\gamma}_3 = \left(i\tilde{\psi}(x), -i\tilde{\psi}^*(x)\right)^T.$$

These two degenerate MFs will couple with each other to form an Andreev bound state via $\psi = (\gamma_3 + i\gamma_2)$, and the excited wave function should be combined using the same rule:

$$\tilde{\psi}_{\pm} = \tilde{\gamma}_3 + i(-1)^{N_v}\tilde{\gamma}_2 = \begin{pmatrix} (1 \pm e^{-i\phi/2})\tilde{\psi}(x) \\ (1 \mp e^{i\phi/2})\tilde{\psi}^*(x) \end{pmatrix} = \begin{pmatrix} u_{\pm} \\ \upsilon_{\pm} \end{pmatrix}. \quad (4)$$

From Equation 4 we can see that the DOS for the electron part is $|u_{\pm}|^2 \propto 1 \pm \cos(\phi/2)$, while the DOS for the hole is $|\upsilon_{\pm}|^2 \propto 1 \mp \cos(\phi/2)$. There are several unique properties of the DOS for the Andreev bound states formed by the MFs: First, the period along each energy spectrum is 4π. Second, it is parity correlated. The DOS is $1 + \cos(\phi/2)$ for the even parity state, and the DOS is $1 - \cos(\phi/2)$ for the odd parity state. Third, the DOS of the hole part for the even parity state is the same as that of the electron part for the odd parity state due to the self-Hermitian property of the MFs. Because of these unique properties of the DOS, we may differentiate the 4π information using the DOS of the electron (hole) part, which should provide clearer distinctions than the trivial states.

Our numerical results provide direct evidence for this conclusion. We use the tight-binding model in Equation 1. The length of each wire is $N_x a = 4\mu m$ and $t_c = 0.4t$. Figure 1b shows the energy spectrum as a function of the flux ϕ with the chemical potential $\mu = -2t$, which lies in the topological region. The red solid line is the energy spectrum for the odd parity state, while the blue solid line is the energy spectrum for the even parity state. We can see that both of them oscillate with a period of 4π. Next, we study the information of the DOS more closely. Figure 1(c) shows the information of the local DOS for the electron part $|\psi_J^e|^2$ along the fixed even parity state (blue solid line) and the odd parity state (red solid line). Here, ψ_J^e is the electron part wave-function localized at the junction, which can be extracted through diagonalization of the lattice Hamiltonian in Equation 1. The DOS of the electron oscillates with a period of 4π and the interference pattern is correlated with the parity. Furthermore, this relation is still valid in the presence of moderate disorder. Figure 1b and Figure 1c are calculated for the Gaussian disorder of $w = 0.06t$. We can see that the relation still holds.

Interestingly, when the two trivial fermion states interfere with each other, the situation is very different. Though an analytic result cannot be obtained, our numerical simulation suggest that the general formula for the DOS for the electron (hole) part should be $a \pm b\cos(\phi)$, with a and b being real constants. This can be understood as follows: For the trivial case, only Cooper pairs can tunnel through the junction. Thus, the DOS must be a function of $\cos(\phi)$ instead of $\cos(\phi/2)$. From our numerical results, we know there are several differences to the nontrivial case. First, the period is 2π. Second, there is no corresponding parity-correlated interference effect for the trivial case. Third, the maximum (minimum) value of the DOS is at $\phi = (2n + 1)\pi$ for the trivial case and at $2n\pi$ for the nontrivial case. In Figure 1d, we show the energy spectrum as a function of the flux under strong disorder, $w = 0.13t$ with $\mu = -2t + 5.7\Delta$. It is typical that the two trivial Andreev bound states are accidentally in contact with each other for the strong disorder. From Figure 1b and Figure 1d, we can see that the energy spectra are very similar between the trivial case without the MFs and the nontrivial case with the MFs. In this situation, it is difficult to distinguish the trivial Andreev bound states from the Andreev bound states formed by the MFs. Even though the period of the Josephson current is still 2π, it may be changed into 4π via a Landau–Zener transition [43]. Thus, the Josephson current cannot distinguish the trivial Andreev bound states and the

nontrivial Andreev bound states formed by the MFs. Figure 1e displays the information of the DOS for the electron part for the two trivial Andreev bound states. We can see that the DOS is described by $a \pm b\cos(\phi)$, which is distinct from the nontrivial case shown in Figure 1(c). Therefore, the DOS are clearly distinct.

Interference effect in a ring structure

Another typical Josephson junction is the ring structure shown in Figure 2a. In such a ring structure, when a magnetic flux threads the ring, the two MFs interfere with each other due to the phase difference. In Figure 2b, we show the energy spectrum as a function of the flux. The Andreev bound states formed by the two MFs show the same behavior as for the Top-JJ shown in Figure 2b. Furthermore, the DOS of the electron part in Figure 2c also contains the same interference information as the one shown in Figure 2c. They are parity correlated with a 4π period. Thus, we can see that the fractional Josephson effect originates from the interference effect between the two MFs.

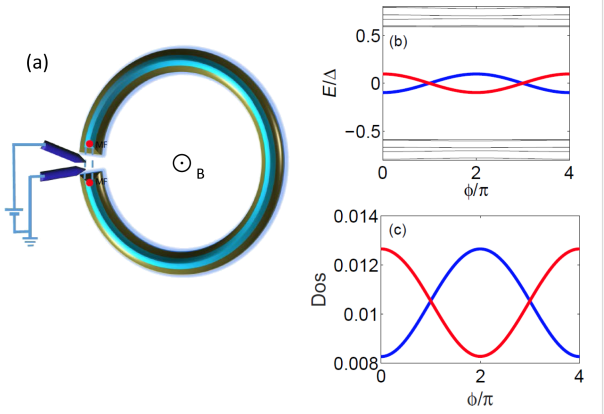

Figure 2: Interference effect in a typical Top-JJ of a ring structure. (a) Schematic setup of the experiment. (b) Energy spectrum of the Top-JJ with the chemical potential μ = −2*t* which lies at the topological region. The two MFs which are localized at the junction interfere with each other and display the 4π oscillation. (c) DOS for the electron part of the coupled MFs in the Top-JJ. Both the even parity and the odd parity states show parity correlated 4π oscillation.

Although the two different structures show the same information for the interference effect, we can say that they are qualitatively different. The parity in the ring structure will not be destroyed when the parity of the whole system is conserved. However, the parity in the junction, as shown in Figure 1a, will be destroyed even if the total parity is conserved. This is attributed to the fact that there are two pairs of MFs in the system of Figure 1a, while there is only one pair of MFs in the ring structure shown in Figure 2a. If there are two pairs of MFs, the effect from the other MFs must be considered. For example, in the Josephson junction shown in Figure 1a, γ_1 will couple with γ_2,

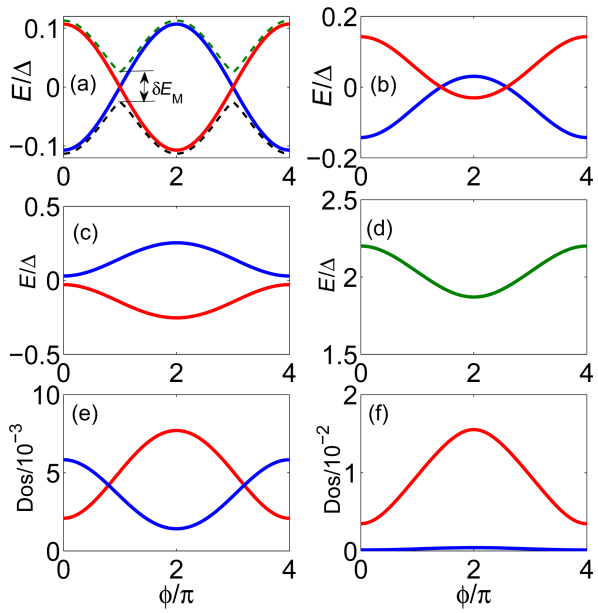

Figure 3: (a) For the Top-JJ shown in Figure 1a, when we consider the energy splitting induced by the finite length of the wire, the parity will be destroyed. The dashed line shows the energy spectrum versus the phase difference with $L_1 = L_2 = 100a$. A small gap δE_M can be observed due to the finite-length effect. (b) Energy spectrum as a function of the flux in the ring structure with μ = −2*t* + 0.4Δ and $N_x = 50a$. Here, $E_M = 0.05\Delta$ and $\Gamma_{eff} = 0.1\Delta$. We can see that the gap is not opened and the 4π period persists. (c) Energy spectrum as a function of the flux in the ring structure with μ = −2*t* + 0.8Δ and $N_x = 50a$. Here, $E_M = -0.12\Delta > \Gamma_{eff}$. We can see that the two states of different parity are separated in energy space. (d) An energy spectrum that is beyond the superconducting gap in the ring structure and also oscillates with the 4π period. (e) Flux-dependent DOS of the electron part (red solid line) and the hole part (blue solid line) along the odd parity state energy spectrum in panel (c). They are correlated with each other. (f) Flux-dependent DOS of the electron part (red solid line) and the hole part (blue solid line) along the energy spectrum in panel (d). They are not correlated with each other.

and γ_3 will couple with γ_4. The effective coupling Hamiltonian should be $H_M = E_{M1}i\gamma_1\gamma_2 + E_{M2}i\gamma_3\gamma_4$, where $E_{M1(2)}$ represents the energy splitting between the two MFs in the left (right) superconducting wire. $E_{M1(2)}$ decreases exponentially with the length $L_{1(2)}$ of the left (right) wire: $E_{M1(2)} \propto \exp(-L_{1(2)}/\xi)$ with ξ being the coherence length of the superconducting wire [42,44,45]. When effective coupling is considered in the Hamiltonian in Equation 3, the Andreev bound states would not intersect at $\phi = \pi$. In Figure 3a the red (blue) solid line shows the energy spectrum for the even (odd) parity state of the Andreev bound states formed by the MFs. Here, the wire length is infinite. Therefore, γ_1 and γ_4 will not destroy the parity of the Andreev bound states. When the wire length is finite (e.g., $L_1 = L_2 = 100a$), we can see from the dashed line that a band gap δE_M exists at $\phi = \pi$. Thus, the parity is destroyed, and the Josephson current has a 2π period. There is no 4π fractional Josephson Effect in the junction shown in Figure 1a.

While there are only two MFs, the parity of states will not be destroyed even if we consider the effective coupling induced by the finite length of the wire. In this case, the total low-energy effective Hamiltonian can be described as follows:

$$H_{T\text{eff}} = \left[\Gamma_{\text{eff}} \cos\left(\phi/2\right) + E_M\right] i\gamma_1\gamma_2. \quad (5)$$

Here, Γ_{eff} is the effective coupling between the two MFs at the junction and E_M is the energy splitting between the two MFs due to the finite length of the ring shown in Figure 2a. We can see that E_M only shifts the energy of the even (odd) parity state but does not destroy the parity. In Figure 3b, we show the energy spectrum for a varying flux with $\mu = -2t + 0.4\Delta$ and $t_c = 0.4t$. Here, $E_M = 0.05\Delta$ and $\Gamma_{\text{eff}} = 0.1\Delta$. The two energy spectra cross over without destroying the parity of the Andreev bound states. When we consider the case of $E_M > \Gamma_{\text{eff}}$, the two states are separated. The energy spectra of the Andreev bound states shown in Figure 3c are separated and show the 4π oscillation for the ground state. In this case, we can ignore the parity conservation problem. Here, $E_M = -0.12\Delta$ when the parameters are $L = 50a$, $t_c = 0.4t$ and $\mu = -2t + 0.8\Delta$. The analysis above indicates there are qualitative differences between one pair of MFs and two pairs of MFs. If there are two pairs of MFs, the parity of the Andreev bound states formed by the two MFs can be affected by coupling with the other MFs. However, if there is only one pair of MFs, coupling only affects the effective coupling between the two MFs but it does not destroy the parity of states. In fact, coupling induced by the finite-length effect can cause the same interference effect as in the Top-JJ of the ring structure. Both of them originate from the interference effect between the MFs.

We have shown that the 4π Josephson Effect can appear in the mesoscopic ring structure without the need to consider the parity-conserving problem. However, in this case, an unexpected coherent single electron tunneling process would occur in the mesoscopic ring structure, which is similar to the persistent current in the mesoscopic ring. It will occur in the conduction band, which lies above the superconducting gap. Figure 3d shows the energy spectrum that lies above the superconducting gap. It also oscillates with a 4π period. It is difficult to derive these two cases from the period. Here, we show that the DOS can distinguish the two different cases. The DOS caused by the MFs is parity related and has a 4π period, whereas the DOS caused by the coherent tunneling does not exhibit a parity-related oscillation. Figure 3e shows the DOS of the electron part (red solid line) and the hole part (blue solid line) of the odd parity state, respectively. We can see that they show the parity related interference pattern, where one is constructive and the other is destructive. Although the total DOS is not conserved due to the splitting of the MFs, it is qualitatively different from the DOS of the energy spectrum above the superconducting gap (Figure 3f). The DOS in Figure 3f is not parity related and shows very different oscillation behavior between the DOS of the electron part and the hole part. Thus, they can be well distinguished by considering the DOS.

Detecting the 4π oscillation through two STM leads

In the last section, we have shown that the main features of the DOS for the nontrivial Andreev bound states are parity-correlated with a 4π period, which is very different from the trivial case. Next, we describe how the parity-correlated 4π period of the DOS can be detected. The intuitive approach would be to put a STM lead (normal lead) to detect the local DOS. However, this does not work. In our previous paper [46], we studied the conductance at the junction with a single STM lead. A butterfly-pattern conductance caused by nontrivial Andreev bound states would be observed as we vary the flux, which is distinct from the conductance of a single impurity state localized at the junction. Hence, the butterfly pattern can be regarded as a unique property of the nontrivial Andreev bound states. Figure 4a shows the same butterfly-pattern conductance. However, the peak value of the butterfly for each parity-conserved energy spectrum has a 2π period instead of a 4π period. The reason for this is that a single STM lead can only read the information of the local DOS via Andreev reflection. Although the numerical results in Figure 4 and Figure 5 are calculated using recursive Greens function methods, the relation between Andreev reflection and DOS can be obtained using a simplified effective model. These two methods are consistent with each other. The calculation of the Andreev reflection coefficient through the effective model can be found in the appendix or in [47], and can be expressed simply as

$$T_A = \frac{\Gamma_{e,\text{eff}}\Gamma_{h,\text{eff}}}{\left(\omega - E_M\right)^2 + \left(\Gamma_{e,\text{eff}} + \Gamma_{h,\text{eff}}\right)^2}.$$

Here, $\Gamma_{e,\text{eff}}$ is the effective self-energy of the electron part of the leads, $\Gamma_{h,\text{eff}}$ is the effective self-energy of the hole part of the leads, and E_M is the coupling energy of the two MFs. $\Gamma_{e,\text{eff}} \propto |u_\pm|^2 = 1 \pm \cos(\phi/2)$ is proportional to the DOS of the electron part, and $\Gamma_{h,\text{eff}} \propto |\upsilon_\pm|^2 = 1 \mp \cos(\phi/2)$ is proportional to the DOS of the hole part. Thus, the Andreev reflection reveals the combined DOS of the electron and the hole parts, which is a 2π period. It cannot reveal the DOS of the electron (hole) part separately. In addition, we can see that if the two MFs are decoupled from each other, $|u_\pm|^2 = |\upsilon_\pm|^2$ and T_A shows the well-known resonant Andreev reflection caused by the MFs.

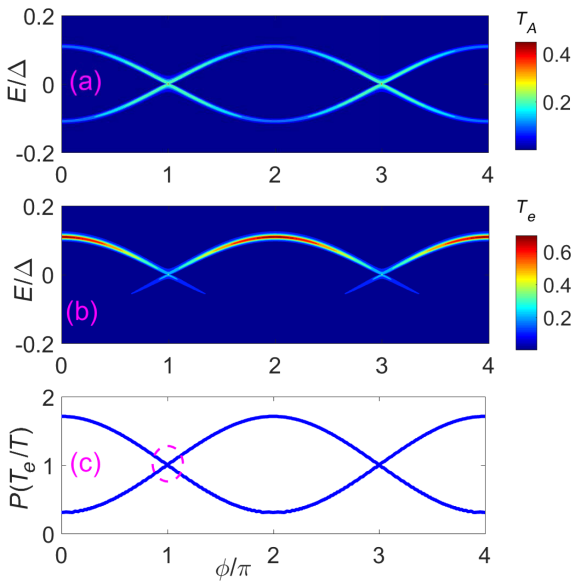

Figure 4: Two STM leads (or weak coupled normal leads) localized at the junction can read the putative 4π period through the differential conductance. (a) Contour plot of the Andreev reflection coefficient T_A of a STM lead as a function of the flux ϕ and the incident energy E. (b) Contour plot of the electron tunneling coefficient T_e from the STM lead 1 to the STM lead 2 as funciton of the flux ϕ and the incident energy E. (c) The ratio between the peak value of T_e and the peak value of T, here $T = (T_e + T_A)/2$. They show similar information of the DOS (see Figure 1c). The DOS of one energy spectrum exhibits a 4π period. However, when both spectra are considered, the period returns to 2π. In this situation, we can distinguish by the even–odd cross point as indicated by dashed circle. The parameters are $N_x = 200a$, μ = −2t, and $V_x = 2\Delta$.

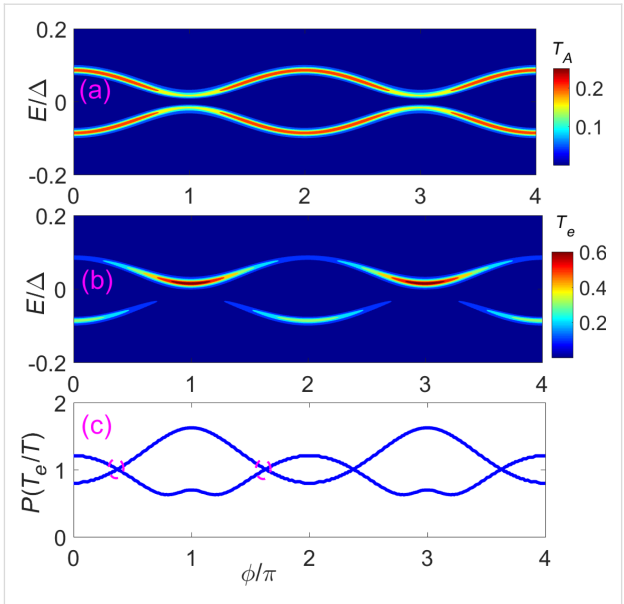

Figure 5: The case for two accidentally touching Andreev bound states. (a) Contour plot of the Andreev Reflection coefficient T_A as a function of flux ϕ and the incident energy E. (b) Contour plot of the electron tunneling coefficient T_e from the STM lead 1 to the STM lead 2 as funciton of the flux ϕ and the incident energy E. For both cases, the period is 2π. (c) The ratio between the peak value of T_e and the peak value of T, here $T = (T_e + T_A)/2$. They yield similar information as the DOS for the trivial states. The obvious characteristic is that they will intersect an even number of times or not at all in a 2π period as indicated by dashed circles. The parameters are $N_x = 200a$, μ = −2t + 5.7Δ, and $V_x = 2\Delta$.

To detect the local DOS of the electron part or the hole part, we need additional information beyond the Andreev reflection process. Thus, it is necessary to add another STM lead to detect the electron transmission or the crossed Andreev reflection between the two leads [47,48]. This can directly reveal the information of the DOS. During this process, the electron tunneling coefficient between the two leads is

$$T_e = \frac{\Gamma_{Le,\mathrm{eff}}\Gamma_{Re,\mathrm{eff}}}{\left(\omega - E_M\right)^2 + \left(\Gamma_{Le,\mathrm{eff}} + \Gamma_{Lh,\mathrm{eff}} + \Gamma_{Re,\mathrm{eff}} + \Gamma_{Rh,\mathrm{eff}}\right)^2}.$$

Here, $\Gamma_{L(R)e,\mathrm{eff}} \propto |u_\pm|^2 = 1 \pm \cos(\phi/2)$ is the effective electron part self-energy of the STM lead L(R), which is proportional to the local DOS for the electron part. In Figure 4b, we show the contour plot of T_e as a function of the flux ϕ and the incident energy E. We can see that the peak value of the tunneling coefficient T_e is proportional to $(1 - \cos(\phi/2))^2$, i.e., the square of the DOS of the electron part. In addition, there is a sharp peak located at $\phi = (2n + 1)\pi$. The peak appears due to the overlap between the two energy spectra at the position $\phi = (2n + 1)\pi$. This is a main feature of nontrivial Andreev bound states: The two energy spectra intersect with each other. A better way to distinguish the information of DOS is to combine both the Andreev reflection and the electron transmission. In Figure 4c, we plot the ratio between the peak value of T_e and the peak value of T. Here $T = (T_e + T_A)/2$ is the average tunneling coefficient of the Andreev reflection and electron transmission. We can see that this ratio is very similar to the DOS. One spectrum is proportional to $1 + \cos(\phi/2)$, while the other one is proportional to $1 - \cos(\phi/2)$. Thus, combining the electron transmission and the Andreev reflection process can reveal the parity-correlated 4π oscillation of the DOS.

The tunneling coefficients show a very different behavior when we use two normal leads to detect the trivial Andreev bound states. Figure 5a shows the Andreev reflection coefficient as a function of the flux ϕ, while Figure 5b displays the evolution of the electron transmission coefficient with varying ϕ. The obvious 2π period can be easily distinguished using the tunneling coefficient of electron transmission. However, the trivial Andreev bound states are susceptible to the external circumstance. When the two leads are attached to the junction, the two accidently touched trivial states will not overlap. In addition, the DOS will also be affected by the lead contact. The DOS will show a small variance when the coupling strength of the leads

changes. As shown in Figure 5c, the ratio T_e/T changes a little compared to the DOS of trivial Andreev bound states. However, two properties are preserved: First, the period is still 2π and can be described as $a + b\cos(\phi)$; second, both electron DOS and hole DOS are generally unrelated, which strongly indicates that the two Andreev bound states are not clearly correlated with each other. Thus, the nontrivial Andreev bound states can be distinguished from the trivial Andreev bound states by combining both the electron transmission process and the Andreev reflection process.

Finally, we want to point out that the actual period in Figure 4c returns to 2π when both parity states are considered. However, we can still distinguish the trivial Andreev bound states and the nontrivial Andreev bound states by the DOS. As shown in Figure 4c, the DOS of nontrivial Andreev bound states is $1-\cos(\phi/2)$ for an even parity state and $1+\cos(\phi/2)$ for an odd parity state. The plots of the DOS for different parity states would overlap once (see the dashed circle in Figure 4c). While the DOS of the trivial Andreev bound states is $a + b\cos(\phi)$, the plot of the DOS for trivial states would overlap with zero or even times in a 2π period as indicated by dashed circle in Figure 5(c). This is decided by the functional properties of $\cos(\phi)$ and $\cos(\phi/2)$. This kind of even–odd crossing would not be affected by a small variance of the DOS. Thus, in general, we can still distinguish the trivial states and nontrivial states through the even–odd crossing of the DOS in a 2π period.

Conclusion

We have studied the interference effect of two MFs in a topological Josephson junction and a ring structure system. We show that the 4π Josephson effect originates from the interference between the two MFs, and so does the DOS of the nontrivial Andreev bound states. Thus, detecting the behavior of the DOS can directly reveal the nature of the fractional Josephson effect. The trivial states, which behave like the nontrivial Andreev bound states, are considered in the paper. Although it is difficult to distinguish the two cases through the supercurrent and the energy spectrum, it can be well separated through the DOS. We suggest that the DOS can be detected using two normal leads, i.e., STM leads. With the two leads, we can obtain the electron transmission process beyond the Andreev tunneling process. Then, the information of the DOS can be derived by combining the two processes.

Appendix

Effective Hamiltonian and effective current formula

In the main text we calculate the tunneling coefficients using the recursive Green function method. To better understanding the numerical results, we obtain the analytical results using the effective Hamiltonian and scattering matrices. The effective Hamiltonian $H_{\text{eff}} = H_N + H_M + H_T$ can be formulated as follows:

$$\begin{aligned} H_N &= -iv_f \sum_{\alpha\in L/R} \int_{-\infty}^{+\infty} \psi_\alpha^\dagger(x)\partial_x\psi_\alpha(x)\,\mathrm{d}x, \\ H_M &= iE_M\gamma_1\gamma_2, \\ H_T &= \sum_\alpha -i\Big[\gamma_1\left(\tilde{t}_{\alpha,1}\psi_\alpha^\dagger(0)+\tilde{t}_{\alpha,1}\psi_\alpha(0)\right) \\ &\quad +\gamma_2\left(\tilde{t}_{\alpha,2}e^{-i\phi/2}\psi_\alpha^\dagger(0)+\tilde{t}_{\alpha,2}e^{-i\phi/2}\psi_\alpha(0)\right)\Big] \end{aligned} \tag{6}$$

Here, H_N is the Hamiltonian of the left and right normal leads; $\psi_{L(R)}$ denotes a fermion operator of the left (right) normal lead, and v_f is the corresponding Fermi velocity of the leads. H_M describes the two coupled MFs, where E_M is the coupling strength between the two MF end states γ_1 and γ_2. The coupling between the leads and the MFs is described by H_T, where the coupling strengths are represented by $\tilde{t}_{\alpha,1}$ and $\tilde{t}_{\alpha,2}$, respectively.

To calculate the scattering matrix of the system, we perform a transformation first. Considering that a single MF is just half of an ordinary fermion state, we can change the MF representation into the fermion representation $\gamma_1 = d + d^\dagger$, $\gamma_2 = i(d - d^\dagger)$. Then, H_M and H_T are changed to:

$$\begin{aligned} \tilde{H}_M &= E_M d^\dagger d \\ \tilde{H}_T &= \sum_\alpha\left(\tilde{t}_{\alpha,e}\psi_\alpha^\dagger(0)\,d+\tilde{t}_{\alpha,h}\psi_\alpha^\dagger(0)\,d^\dagger+h.c.\right) \\ &\quad \text{with} \\ \tilde{t}_{\alpha,e} &= -i\left(\tilde{t}_{\alpha,1}+i\tilde{t}_{\alpha,2}e^{-i\phi/2}\right), \\ \tilde{t}_{\alpha,h} &= -i\left(\tilde{t}_{\alpha,1}+i\tilde{t}_{\alpha,2}e^{i\phi/2}\right). \end{aligned} \tag{7}$$

Next, we can formulate the scattering matrix in a model-independent form,

$$S(E) = 1 - 2\pi i W^\dagger\left(E-\tilde{H}_M+i\pi WW^\dagger\right)^{-1}W, \tag{8}$$

with W the matrix that describes the coupling between the scattering region and the leads:

$$W = \begin{pmatrix} \tilde{t}_{L,e} & \tilde{t}_{R,e} & \tilde{t}_{L,h} & \tilde{t}_{R,h} \\ -\tilde{t}'_{L,h} & -\tilde{t}'_{R,h} & -\tilde{t}'_{R,e} & -\tilde{t}'_{R,e} \end{pmatrix}.$$

In general, we can write the approximation as:

$$S_{lk}^{\alpha\beta} = -\delta_{l,k}\delta_{\alpha,\beta} + i\sqrt{\Gamma_{l,\alpha}\Gamma_{k,\beta}}\Big/\left(E - E_M + i\Gamma\right).$$

Here, $\Gamma_{l,\alpha}$ is the self-energy of the α part of the lead l, which is renormalized by the local DOS of the two coupled MFs. Furthermore, it is proportional to the local DOS of the α part of the two coupled MFs. Thus, using the scattering matrix we can find the information of the local DOS. However, only a single tunneling process cannot provide all information. We need more tunneling processes, and the two leads are necessary here. There are three tunneling processes in such a two-lead setup: the Andreev reflection, the crossed Andreev reflection, and the electron transmission. We consider a symmetric connection case and simplify the result. For this condition, the coefficient of the Andreev reflection is the same as the coefficient of the crossed Andreev reflection. Then, the current for lead 1 is $I_1 = (2T_A \times V_1 + (T_A + T_e)(V_1 - V_2))e/h$ and the current for lead 2 is $I_2 = (-2T_A \times V_2 + (T_e - T_A)(V_1 - V_2))e/h$. Thus, T_e and T_A can be obtained using the current relation.

Acknowledgements

We gratefully acknowledge the support from NSF-China under Grant Nos.11574245 (J.L.), 11474085 (J.T.S.). Jie is also supported by the China Post-doctoral Science Foundation Grant Under Grant No. 2015M580828 and the China Fundamental Research Funds for central University with Grant No. xjj2015059. We would like to thank Ai-Min Guo, Qing-Feng Sun and X.C. Xie for many helpful discussions. This work is a revised version of arXiv preprint 1603.03582.

References

1. Kitaev, A. Yu. *Phys.-Usp.* **2001,** *44,* 131. doi:10.1070/1063-7869/44/10S/S29
2. Nayak, C.; Simon, S. H.; Stern, A.; Freedman, M.; Das Sarma, S. *Rev. Mod. Phys.* **2008,** *80,* 1083–1159. doi:10.1103/RevModPhys.80.1083
3. Fujimoto, S. *Phys. Rev. B* **2008,** *77,* 220501. doi:10.1103/PhysRevB.77.220501
4. Sau, J. D.; Lutchyn, R. M.; Tewari, S.; Das Sarma, S. *Phys. Rev. Lett.* **2010,** *104,* 040502. doi:10.1103/PhysRevLett.104.040502
5. Sato, M.; Takahashi, Y.; Fujimoto, S. *Phys. Rev. B* **2010,** *82,* 134521. doi:10.1103/PhysRevB.82.134521
6. Alicea, J. *Phys. Rev. B* **2010,** *81,* 125318. doi:10.1103/PhysRevB.81.125318
7. Lutchyn, R. M.; Sau, J. D.; Das Sarma, S. *Phys. Rev. Lett.* **2010,** *105,* 077001. doi:10.1103/PhysRevLett.105.077001
8. Oreg, Y.; Refael, G.; von Oppen, F. *Phys. Rev. Lett.* **2010,** *105,* 177002. doi:10.1103/PhysRevLett.105.177002
9. Potter, A. C.; Lee, P. A. *Phys. Rev. B* **2011,** *83,* 094525. doi:10.1103/PhysRevB.83.094525
10. Nadj-Perge, S.; Drozdov, I. K.; Bernevig, B. A.; Yazdani, A. *Phys. Rev. B* **2013,** *88,* 020407. doi:10.1103/PhysRevB.88.020407
11. Klinovaja, J.; Stano, P.; Yazdani, A.; Loss, D. *Phys. Rev. Lett.* **2013,** *111,* 186805. doi:10.1103/PhysRevLett.111.186805
12. Mourik, V.; Zuo, K.; Frolov, S. M.; Plissard, S. R.; Bakkers, E. P. A. M.; Kouwenhoven, L. P. *Science* **2012,** *336,* 1003–1007. doi:10.1126/science.1222360
13. Deng, M. T.; Yu, C. L.; Huang, G. Y.; Larsson, M.; Caroff, P.; Xu, H. Q. *Nano Lett.* **2012,** *12,* 6414–6419. doi:10.1021/nl303758w
14. Das, A.; Ronen, Y.; Most, Y.; Oreg, Y.; Heiblum, M.; Shtrikman, H. *Nat. Phys.* **2012,** *8,* 887–895. doi:10.1038/nphys2479
15. Nadj-Perge, S.; Drozdov, I. K.; Li, J.; Chen, H.; Jeon, S.; Seo, J.; MacDonald, A. H.; Bernevig, B. A.; Yazdani, A. *Science* **2014,** *346,* 602–607. doi:10.1126/science.1259327
16. Law, K. T.; Lee, P. A.; Ng, T. K. *Phys. Rev. Lett.* **2009,** *103,* 237001. doi:10.1103/PhysRevLett.103.237001
17. Wimmer, M.; Akhmerov, A. R.; Dahlhaus, J. P.; Beenakker, C. W. J. *New J. Phys.* **2011,** *13,* 053016. doi:10.1088/1367-2630/13/5/053016
18. Liu, J.; Potter, A. C.; Law, K. T.; Lee, P. A. *Phys. Rev. Lett.* **2012,** *109,* 267002. doi:10.1103/PhysRevLett.109.267002
19. Bagrets, D.; Altland, A. *Phys. Rev. Lett.* **2012,** *109,* 227005. doi:10.1103/PhysRevLett.109.227005
20. Zhang, H.; Gül, Ö.; Conesa-Boj, S.; Nowak, M. P.; Wimmer, M.; Zuo, K.; Mourik, V.; de Vries, F. K.; van Veen, J.; de Moor, M. W. A.; Bommer, J. D. S.; van Woerkom, D. J.; Car, D.; Plissard, S. R.; Bakkers, E. P. A. M.; Quintero-Pérez, M.; Cassidy, M. C.; Koelling, S.; Goswami, S.; Watanabe, K.; Taniguchi, T.; Kouwenhoven, L. P. *Nat. Commun.* **2017,** *8,* 16025. doi:10.1038/ncomms16025
21. Albrecht, S. M.; Higginbotham, A. P.; Madsen, M.; Kuemmeth, F.; Jespersen, T. S.; Nygård, J.; Krogstrup, P.; Marcus, C. M. *Nature* **2016,** *531,* 206. doi:10.1038/nature17162
22. Deng, M. T.; Vaitiekėnas, S.; Hansen, E. B.; Danon, J.; Leijnse, M.; Flensberg, K.; Nygård, J.; Krogstrup, P.; Marcus, C. M. *Science* **2016,** *354,* 1557–1562. doi:10.1126/science.aaf3961
23. van Woerkom, D. J.; Proutski, A.; van Heck, B.; Bouman, D.; Väyrynen, J. I.; Glazman, L. I.; Krogstrup, P.; Nygård, J.; Kouwenhoven, L. P.; Geresdi, A. *Nat. Phys.* **2017,** *13,* 876–881. doi:10.1038/nphys4150
24. Zuo, K.; Mourik, V.; Szombati, D. B.; Nijholt, B.; van Woerkom, D. J.; Geresdi, A.; Chen, J.; Ostroukh, V. P.; Akhmerov, A. R.; Plissard, S. R.; Car, D.; Bakkers, E. P. A. M.; Pikulin, D. I.; Kouwenhoven, L. P.; Frolov, S. M. *arXiv* **2017,** No. 1706.
25. Goffman, M. F.; Urbina, C.; Pothier, H.; Nygård, J.; Marcus, C. M.; Krogstrup, P. *New J. Phys.* **2017,** *19,* 092002. doi:10.1088/1367-2630/aa7641
26. Albrecht, S. M.; Hansen, E. B.; Higginbotham, A. P.; Kuemmeth, F.; Jespersen, T. S.; Nygård, J.; Krogstrup, P.; Danon, J.; Flensberg, K.; Marcus, C. M. *Phys. Rev. Lett.* **2017,** *118,* 137701. doi:10.1103/PhysRevLett.118.137701
27. Feldman, B. E.; Randeria, M. T.; Li, J.; Jeon, S.; Xie, Y.; Wang, Z.; Drozdov, I. K.; Andrei Bernevig, B.; Yazdani, A. *Nat. Phys.* **2017,** *13,* 286–291. doi:10.1038/nphys3947
28. Zhang, H.; Liu, C.-X.; Gazibegovic, S.; Xu, D.; Logan, J. A.; Wang, G.; van Loo, N.; Bommer, J. D. S.; de Moor, M. W. A.; Car, D.; het Veld, R. L. M. O.; van Veldhoven, P. J.; Koelling, S.; Verheijen, M. A.; Pendharkar, M.; Pennachio, D. J.; Shojaei, B.; Lee, J. S.; Palmstrom, C. J.; Bakkers, E. P. A. M.; Das Sarma, S.; Kouwenhoven, L. P. *arXiv* **2017,** No. 1710.
29. Law, K. T.; Lee, P. A. *Phys. Rev. B* **2011,** *84,* 081304. doi:10.1103/PhysRevB.84.081304
30. San-Jose, P.; Prada, E.; Aguado, R. *Phys. Rev. Lett.* **2012,** *108,* 257001. doi:10.1103/PhysRevLett.108.257001

31. Domínguez, F.; Hassler, F.; Platero, G. *Phys. Rev. B* **2012,** *86,* 140503. doi:10.1103/PhysRevB.86.140503
32. Crépin, F.; Trauzettel, B. *Phys. Rev. Lett.* **2014,** *112,* 077002. doi:10.1103/PhysRevLett.112.077002
33. Houzet, M.; Meyer, J. S.; Badiane, D. M.; Glazman, L. I. *Phys. Rev. Lett.* **2013,** *111,* 046401. doi:10.1103/PhysRevLett.111.046401
34. Lee, S.-P.; Michaeli, K.; Alicea, J.; Yacoby, A. *Phys. Rev. Lett.* **2014,** *113,* 197001. doi:10.1103/PhysRevLett.113.197001
35. Ren, H.; Hart, S.; Wagner, T.; Leubner, P.; Mühlbauer, M.; Brüne, C.; Buhmann, H.; Molenkamp, L. W.; Yacoby, A. *Nat. Phys.* **2014,** *10,* 638–643. doi:10.1038/NPHYS3036
36. Pribiag, V. S.; Beukman, A. J. A.; Qu, F.; Cassidy, M. C.; Charpentier, C.; Wegscheider, W.; Kouwenhoven, L. P. *Nat. Nanotechnol.* **2015,** *10,* 593. doi:10.1038/nnano.2015.86
37. Pang, Y.; Shen, J.; Wang, J.; Feng, J.; Qu, F.; Lyu, Z.; Fan, J.; Liu, G.; Ji, Z.; Jing, X.; Yang, C.; Sun, Q.; Xie, X. C.; Fu, L.; Lu, L. *arXiv* **2015,** No. 1503.
38. Wiedenmann, J.; Bocquillon, E.; Deacon, R. S.; Hartinger, S.; Herrmann, O.; Klapwijk, T. M.; Maier, L.; Ames, C.; Brüne, C.; Gould, C.; Oiwa, A.; Ishibashi, K.; Tarucha, S.; Buhmann, H.; Molenkamp, L. W. *Nat. Commun.* **2016,** *7,* 10303. doi:10.1038/ncomms10303
39. Bocquillon, E.; Deacon, R. S.; Wiedenmann, J.; Leubner, P.; Klapwijk, T. M.; Brüne, C.; Ishibashi, K.; Buhmann, H.; Molenkamp, L. W. *Nat. Nanotechnol.* **2017,** *12,* 137–143. doi:10.1038/nnano.2016.159
40. Deacon, R. S.; Wiedenmann, J.; Bocquillon, E.; Domínguez, F.; Klapwijk, T. M.; Leubner, P.; Brüne, C.; Hankiewicz, E. M.; Tarucha, S.; Ishibashi, K.; Buhmann, H.; Molenkamp, L. W. *Phys. Rev. X* **2017,** *7,* 021011. doi:10.1103/PhysRevX.7.021011
41. Picó-Cortés, J.; Domínguez, F.; Platero, G. *Phys. Rev. B* **2017,** *96,* 125438. doi:10.1103/PhysRevB.96.125438
42. Peltonen, J. T.; Astafiev, O. V.; Korneeva, Yu. P.; Voronov, B. M.; Korneev, A. A.; Charaev, I. M.; Semenov, A. V.; Golt'sman, G. N.; Ioffe, L. B.; Klapwijk, T. M.; Tsai, J. S. *Phys. Rev. B* **2013,** *88,* 220506. doi:10.1103/PhysRevB.88.220506
43. Sau, J. D.; Setiawan, F. *Phys. Rev. B* **2017,** *95,* 060501. doi:10.1103/PhysRevB.95.060501
44. Prada, E.; San-Jose, P.; Aguado, R. *Phys. Rev. B* **2012,** *86,* 180503. doi:10.1103/PhysRevB.86.180503
45. Rainis, D.; Trifunovic, L.; Klinovaja, J.; Loss, D. *Phys. Rev. B* **2013,** *87,* 024515. doi:10.1103/PhysRevB.87.024515
46. Wang, P.; Liu, J.; Sun, Q.-f.; Xie, X. C. *Phys. Rev. B* **2015,** *91,* 224512. doi:10.1103/PhysRevB.91.224512
47. Liu, J.; Zhang, F.-C.; Law, K. T. *Phys. Rev. B* **2013,** *88,* 064509. doi:10.1103/PhysRevB.88.064509
48. Nilsson, J.; Akhmerov, A. R.; Beenakker, C. W. J. *Phys. Rev. Lett.* **2008,** *101,* 120403. doi:10.1103/PhysRevLett.101.120403

License and Terms

The definitive version of this article is the electronic one which can be found at:
doi:10.3762/bjnano.9.50

BEILSTEIN JOURNAL OF NANOTECHNOLOGY

An implementation of spin–orbit coupling for band structure calculations with Gaussian basis sets: Two-dimensional topological crystals of Sb and Bi

Sahar Pakdel[1,2], Mahdi Pourfath[*1,3,4] and J. J. Palacios[*2,5]

Full Research Paper

Open Access

Address:
[1]School of Electrical and Computer Engineering, University College of Engineering, University of Tehran, Tehran 14395-515, Iran, [2]Departamento de Física de la Materia Condensada, Universidad Autónoma de Madrid, 28049 Madrid, Spain, [3]School of Nano Science, Institute for Research in Fundamental Sciences (IPM), Tehran 19395-5531, Iran, [4]Institute for Microelectronics, TU Wien, Gusshausstrasse 27–29/E360, 1040 Vienna, Austria and [5]Instituto Nicolás Cabrera (INC), and Condensed Matter Physics Institute (IFIMAC), Universidad Autónoma de Madrid, 28049 Madrid, Spain.

Email:
Mahdi Pourfath[*] - pourfath@ut.ac.ir;
J. J. Palacios[*] - juanjose.palacios@uam.es

* Corresponding author

Keywords:
antimonene; electronic structure; Sb few-layers; spin–orbit coupling (SOC); topological material

Beilstein J. Nanotechnol. **2018,** *9,* 1015–1023.
doi:10.3762/bjnano.9.94

Received: 14 December 2017
Accepted: 28 February 2018
Published: 28 March 2018

This article is part of the Thematic Series "Topological materials".

Associate Editor: P. Leiderer

Abstract

We present an implementation of spin–orbit coupling (SOC) for density functional theory band structure calculations that makes use of Gaussian basis sets. It is based on the explicit evaluation of SOC matrix elements, both the radial and angular parts. For all-electron basis sets, where the full nodal structure is present in the basis elements, the results are in good agreement with well-established implementations such as VASP. For more practical pseudopotential basis sets, which lack nodal structure, an ad-hoc increase of the effective nuclear potential helps to capture all relevant band structure variations induced by SOC. In this work, the non-relativistic or scalar-relativistic Kohn–Sham Hamiltonian is obtained from the CRYSTAL code and the SOC term is added a posteriori. As an example, we apply this method to the Bi(111) monolayer, a paradigmatic 2D topological insulator, and to mono- and multilayer Sb(111) (also known as antimonene), the former being a trivial semiconductor and the latter a topological semimetal featuring topologically protected surface states.

Introduction

The topological character of topological materials (mostly insulators but also non-insulators) in most relevant cases originates from relativistic corrections that cannot be neglected in the Hamiltonian of heavy elements, more specifically from spin–orbit coupling (SOC). Such materials are usually characterized by non-zero topological invariants that can be either

computed simply from the parity of the Bloch wave functions in centrosymmetric crystals or from other more involved implementations in non-centrosymmetric systems [1-6]. Topological materials typically feature a band inversion. In a gedanken experiment, one can imagine tuning the SOC at will. As the SOC is increased from zero towards its nominal value, it pushes up the valence band while bringing down the conduction band of the imaginary SOC-free material. In this process, the gap closes and reopens again, giving rise to the non-zero topological invariant.

The essential features of the band structure of topological materials (at least the elemental ones) can be obtained from the tight-binding (TB) model where the Hamiltonian is built through a Slater–Koster [7] atomic parametrization. These models, however, are usually restricted to the description of valence electrons, implicitly by assuming a minimal basis set of spd orbitals. The SOC is included by adding the matrix elements of the $\lambda\hat{\vec{L}}\cdot\hat{\vec{S}}$ operator where λ is taken as an atomic parameter [8]. Although the simplicity of TB modeling is appealing, this method is obviously restricted to a limited set of problems. TB parameters are available for most elemental materials [9], but not in general for all compound materials (which is the case of most topological insulators). The versatility of this model is also limited by the sensitivity of the TB parameters to the specific structural variations which also needs to be parametrized [10].

On the opposite side of sophistication, the electronic structure of topological materials can be evaluated through density functional theory (DFT). According to the type of basis sets, DFT codes fall into two broad categories: those making use of plane-waves and those using localized orbitals. Arguably, the most reliable implementations of SOC can be found in the code FLEUR [11] and also in codes such as Vienna Ab initio Simulation Package [12] (VASP) or QuantumEspresso [13,14] (QE), all of them employing plane-waves for the interstitial or valence electrons, while approaching the core electrons differently. Since localized orbitals are convenient for a number of reasons, for instance for quantum transport calculations [15,16], a Kohn–Sham Hamiltonian obtained from plane-wave DFT codes may be transformed into a TB-like Hamiltonian by changing to a basis of Wannier functions [17,18]. While the results of this transformation can be accurate, they are not straightforward to carry out. On the other hand, self-consistent implementations of SOC for codes using localized orbitals for valence electrons are, however, much less common [19,20].

In most currently available implementations, including those using localized orbitals basis sets, the SOC is effectively introduced through pseudopotentials [19,20]. Here, we propose a different route, employing the actual shape of the basis functions. In particular we present an implementation of SOC for DFT calculations based on Gaussian-type localized basis sets, attempting to bridge the gap between the simplicity of TB Hamiltonians with their one-parameter implementation of SOC and the accuracy and transferability of a DFT-level description of the band structure. We make use of the non-relativistic (or scalar relativistic) Kohn–Sham Hamiltonian, here obtained using the CRYSTAL code [21-23], to which we add the SOC a posteriori. The matrix elements are explicitly evaluated for both radial and angular parts of the basis elements, by using the screened nuclear potential. For the radial part, we rely on the actual analytical expressions of the Gaussian-type basis elements, as employed in codes such as CRYSTAL, Gaussian [24], Nwchem [25], etc. Among the available basis sets, all-electron (AE) basis sets [26], featuring the full nodal structure of the orbitals and able to properly capture SOC effects, might not be well designed for band structure calculation of solids in general or appear inefficient due to their computational cost. Here we show that when AE basis sets work properly at the band structure level in calculations without SOC, accurate results can be obtained from our proposed implementation. Alternatively, basis sets using effective core potentials or pseudopotentials, which reproduce better band structures and are computationally less demanding, lack nodal structure near the nucleus. This has prompted us to modify the nuclear potential through a fitting multiplicative factor to effectively model the SOC effect. Importantly, despite the fact that we are dealing with different types of orbitals of different shells, only a single parameter is needed since the relative values of the matrix elements are properly captured.

As possibly relevant examples, we have chosen to apply our implementation to Sb and Bi, which are prototypical topological materials where SOC plays a crucial role. Despite being elemental, they present a broad range of behaviors. While bulk Bi is a trivial semimetal, a Bi(111) monolayer is a 2D topological insulator (TI) [27]. Sb few-layers in the (111) direction, typically for more than ≈7 layers, behave as a 3D topological semimetal, while the Sb(111) monolayer is a trivial indirect-gap semiconductor. In order for our SOC implementation to be of practical use, it should capture these trivial/non-trivial topological transitions and give the most faithful representation of the electronic band structure for any number of layers. This includes the presence of helical and topologically protected edge or surface states. For comparison, and as a reliable reference, we make use of the band structures obtained from the well-established plane-wave code VASP. In general, we find a very satisfactory agreement between the band structures calculated by our approach for both AE (without parameters), pseudopotential (single parameter) basis sets, and the VASP results, proving ours to be a practical a posteriori implementa-

tion of SOC once a standard non-relativistic or scalar relativistic DFT calculation based on localized orbitals has been performed.

Methodology

Gaussian basis sets

The accuracy of electronic structure calculations is limited, not only by functional, but also by the basis set used to expand the wave functions. When working with localized basis sets, it is crucial to choose a large enough number of elements or a set of properly chosen ones. Typically, the basis functions are centered on atoms, and are so called "atomic orbitals". Two types of atomic orbital functions are typically employed in molecular orbital calculations, namely, Slater type orbitals (STOs) and Gaussian type orbitals (GTOs). Slater [7] introduced STOs as basis functions due to their similarity with the eigenfunctions of the hydrogen atom. They possess an exponential decay at long range and Kato's cusp [28] condition at short range. Their general definition is

$$\Psi^{\mathrm{STO}}_{nlm,\zeta}\left(r,\vartheta,\varphi\right)=Nr^{n-1}e^{-\zeta r}Y_{lm}\left(\vartheta,\varphi\right), \tag{1}$$

where N is the normalization constant. The radial part is characterized by the principal quantum number n and the exponent ζ while the angular part is given by the spherical harmonics which are orthogonal to the radial part and characterized by l and m, the azimuthal and magnetic quantum numbers, respectively. The ζ parameter, is variationally optimized with respect to the total energy of each atom. STOs have the advantage of a direct physical interpretation and are thus naturally good basis for molecular orbitals. However, from a computational point of view, STOs are not competitive. In practice, the radial part of STOs is approximated by a linear combination of GTOs (or primitives). Spherical GTOs were proposed by Boys [29] with a radial part defined as

$$R^{\mathrm{GTO}}\left(r\right)=Nr^{n-1}e^{-\alpha r^2}, \tag{2}$$

where the exponent α determines the extension of the function. Huzinaga [30] has illustrated that it is adequate to consider $n = l + 1$ and hence optimized GTO basis sets use 1s functions to represent all s-type orbitals, 2p functions for p-type, etc. Despite the computational benefits, GTOs have two major disadvantages, namely, they do not have a cusp at the nucleus and they fall off to zero too rapidly for large radius. However, these shortcomings can be overcome by considering linear combinations of GTOs to form contracted Gaussian-type orbitals (CGTOs):

$$R^{\mathrm{CGTO}}\left(r\right)=N_0\left\{\sum_{\mathrm{i}}d_{\mathrm{i}}\left(N_{\mathrm{i}}r^{n-1}e^{-\alpha_{\mathrm{i}}r^2}\right)\right\}. \tag{3}$$

Here each primitive, as defined in Equation 2, is normalized on its own (N_{i}) and the whole contracted function has an overall normalization constant (N_0). The coefficients d_{i} and exponents α_{i} determine the radial shape of the CGTO. A large enough number of primitives with coefficients d_{i} of different signs can reproduce the expected atomic nodal behavior of wave functions near the nucleus. Introducing the nodal structure in the basis sets turns out to be irrelevant for most band structure calculations and increases the computational effort, significantly. However, as we will show in the next section, for the calculation of SOC, the exact behavior of the wave functions near the core is required.

Evaluation of SOC matrix elements

The output Hamiltonian and overlap matrices of the CRYSTAL code, ignoring broken spin-symmetry solutions, are the same for up and down spin electrons. SOC is considered to be a purely intra-atomic interaction. Rigorous approximations to the full relativistic Dirac–Kohn–Sham Hamiltonian, which decouple the electronic part from the positronic part, yield to lowest order a SOC correction of the form $\xi\left(r\right)\vec{L}\cdot\vec{S}$ (see, e.g., [31] for a nice overview of a fairly extensive topic) which mixes orbital angular momentum (m) and spin (σ) quantum numbers. Since the angular and radial parts of the wave functions are orthogonal, SOC matrix elements between different CGTOs can be straightforwardly evaluated as

$$\xi_{\mathrm{ij}}\left\langle l_{\mathrm{i}};m_{l_{\mathrm{i}}};s\left|\vec{L}\cdot\vec{S}\right|l_{\mathrm{j}};m_{l_{\mathrm{j}}};s'\right\rangle, \tag{4}$$

where $\vec{L}\cdot\vec{S}$ acts on the spin degree of freedom and the spherical harmonics, while the radial contribution can be obtained from

$$\xi_{\mathrm{ij}}=\frac{e^2}{2m_ec^2}\int_0^\infty\frac{1}{r}\frac{\mathrm{d}V_{\mathrm{eff}}\left(r\right)}{\mathrm{d}r}R_{\mathrm{i}}\left(r\right)R^*_{\mathrm{j}}\left(r\right)r^2\mathrm{d}r\,. \tag{5}$$

Here $R_{\mathrm{i}}(r)$ is the radial part of the i-th atomic CGTO (built as described in the previous section) and $V_{\mathrm{eff}}(r)$ is the effective screened nuclear potential that electrons actually feel. Here we are not concerned with the rigorous discussion concerning the approximations that lead to Equation 5 and the origin of V_{eff} (for details see [31]). It suffices to say that, intuitively, the potential must be of the form Z/r very close to the core and behave as $1/r$ far apart. For the case of an isolated atom, it has

been shown that making use of the unscreened nuclear potential will result in an over estimation of SOC splittings. A simple model has also been suggested for screened nuclear potential, which includes the screening by adding an orbital dependent charge term (placed at the origin) to the bare nuclear potential [32]. The effective potential can also be extracted from an atomic DFT calculation. Here, we explored both possibilities and found no significant differences.

A correct electronic band structure in solids requires an accurate description of chemical bondings and hence, enough variational flexibility in the valence region. On the other hand, since the main contribution to the SOC matrix elements stems from the vicinity of the nucleus, a correct description of orbitals is also essential near the core. AE basis sets specifically designed for the latter purpose are common in atomic physics and molecular chemistry. While they can capture the full nodal structure of the orbitals, it is, however, unclear how well they perform when it comes to the band structure of solids, which is our main concern here. Our results indicate that, when AE basis sets band structures are in good agreement with those of plane-wave calculations before including SOC (which might not be always the case), fairly accurate results can be obtained after including SOC. We have also found out that a proper renormalization of the effective potential makes even pseudopotential basis sets (without nodal structure) suitable for band structure calculations where SOC plays an important role.

Results and Discussion: Elemental topological Materials, Sb and Bi 2D Crystals

Antimonene

Antimonene, a term generically used for Sb(111) in 2D form, has been recently added to the growing library of 2D crystals. Its recent isolation and characterization [33], is bringing this material into the focus of the research community. Several DFT studies on this material have predicted a number of exciting physico-chemical properties, including a tunable band gap with potential applications in optoelectronics [34-37], low thermal conductance with low electrical resistivity for energy generation through thermoelectricity [38], and exotic topological features under strain [39-41]. However, it was not until last year that few experimental works brought all those expectations closer to reality [33]. It was demonstrated that it is possible to isolate few or even single stable layers of antimonene, in ambient conditions. Moreover, new procedures such as liquid exfoliation and epitaxial growth methods were reported.

Theoretical works on antimonene can be divided into two categories. The most recent publications refer to monolayer antimonene (or occasionally bilayer antimonene) and can be found in the context of new 2D crystals. Other works, which go a few years back in time, refer to few-layered (FL) antimonene (or Sb(111) thin films), and can be found in the context of 3D TIs [1]. The physical properties of antimonene evolve quite drastically from mono- to few-layer cases, and each deserves a separate discussion.

Monolayer antimonene

Figure 1 presents the DFT band structure of a single layer of antimonene without SOC, in the framework of the Perdew–Burke–Ernzerhof local density approximation [42] to the functional for different basis sets. Panel (a) shows the results using the VASP [12] package. Calculations are performed with a plane-wave cutoff of 400 eV on a 15 × 15 × 1 Monkhorst–Pack *k*-point mesh. For structural relaxation, all atoms are allowed to relax until atomic forces are smaller than 0.01 eV/Å.

In agreement with previous studies for free standing antimonene [43], we obtain an in plane lattice constant of the relaxed structure $a = 4.12$ Å and a buckling height $h = 1.64$ Å. Panels (b) and (c) show the band structure obtained with CRYSTAL using two standard AE basis sets properly converged in the number of elements. The former is based on relativistically contracted atomic natural orbitals [44,45] (ANO) and the latter belongs to the family of well-tempered basis sets [46] (WTBS). Examples of (the radial part of) basis elements from these two basis sets are shown in Figure 2a. For the sake of simplicity in the discussions and since no significant differences have been found, the same lattice structure (relaxed with VASP in presence of SOC) and same functional has been used in all band structure calculations. When compared to the VASP results, ANO bands turn out not too satisfactory at the high symmetry Γ point where the ordering of degenerate and non-degenerate bands is not reproduced. For other *k*-points across the Brillouin zone the results are comparatively better. The WTBS results shown in (c) manifest a significant improvement, particularly for the conduction bands, although the ordering of the valence bands is still not the correct one at the Γ point. Interestingly, we have found out that a combination of both ANO and WTBS basis sets [panel (d)] improves the band structure to the point of making it essentially similar to the VASP result. Here we have complemented the WTBS basis with additional valence orbitals from the ANO basis set. Adding this flexibility to the basis, even the flat valence band falls below the degenerate ones at the Γ point. This band structure corresponds to that of a semiconductor with an indirect gap, as previously reported [34]. The use of a hybrid functional such as HSE06 [37] will certainly increase the value of the gap, but we are not concerned with this issue here.

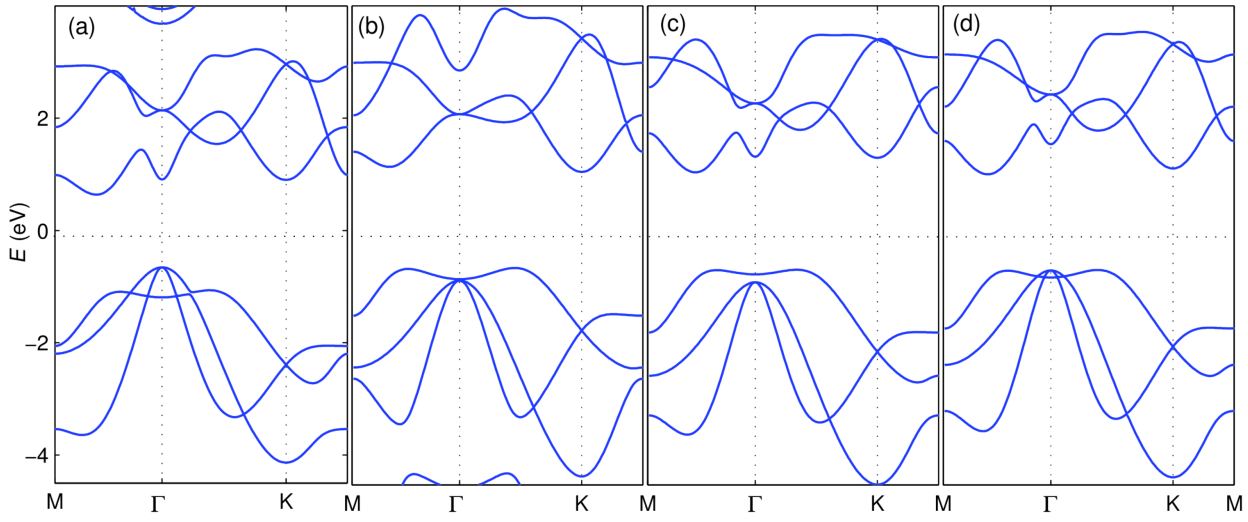

Figure 1: Comparison between different calculations of the band structure of monolayer antimonene as obtained from (a) VASP and CRYSTAL with different basis sets: (b) ANO, (c) WTBS, and (d) WTBS+ANO (see text for details). The lattice structure relaxed with VASP has been considered for all cases and SOC has not been included in the calculations.

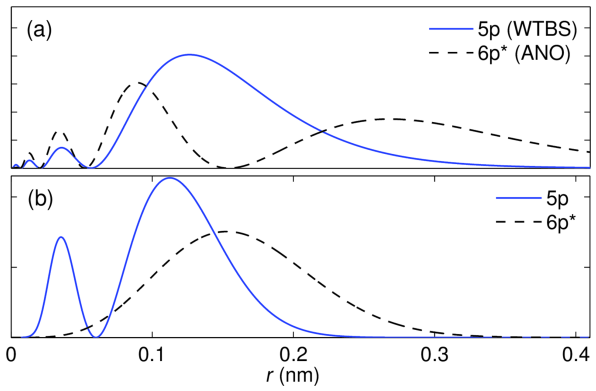

Figure 2: Radial probability density of two selected elements of the AE and small-core basis sets used in the calculations. (a) Solid blue curve corresponds to the 5p shell of the WTBS while the dashed black represents the 6p (virtual) shell in the ANO basis set (see text). (b) Same as in (a), the last partially occupied and the first empty (virtual) shell of the small-core pseudopontential basis set (see text), showing the lack of nodal structure required, in principle, for an appropriate SOC calculation.

Figure 3 shows the band structure obtained with CRYSTAL using three different pseudopotential basis sets. From (a) to (c) the quality of the basis set is improved. Starting from the bands obtained with a large effective core (46 electrons) and a minimal 4 element basis set [sp^3] [47,48] [shown in panel (a)], we first increase the number of valence basis elements to 8 [$2s2p^3$] [49] [see panel (b)], and then decrease the number of effective core electrons down to 28, while keeping a large 23 element basis set for the valence electrons [$4s3p^32d^5$] [50] [panel (c)]. Figure 2b shows the radial part of the last two p-orbitals (or p-type CGTOs) in this third basis set. As can be observed, the nodal structure near the origin is absent. The shorter radial extension when compared to the corresponding orbital-like AE CGTOs (in particular for the one labeled 6p) is due to the fact that one cannot naively make a one-to-one correspondence between atomic orbitals and these basis elements. Except for the results using the minimal basis set, where the ordering of the bands is not the correct one (keeping in mind that the lattice parameters are the same for all calculations), the

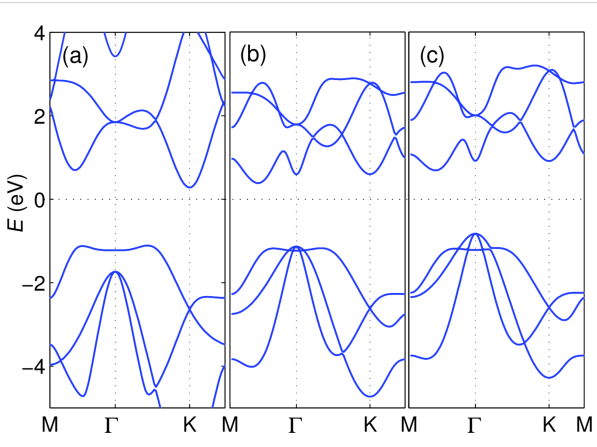

Figure 3: Comparison between different calculations of the band structure of monolayer antimonene as obtained from CRYSTAL with different pseudopotential basis sets: (a) large-core (46 electrons) and minimal basis set, (b) large- core as in (a) but a larger basis set, and (c) small-core and large basis set (see text for details). The lattice structure relaxed with VASP has been used for all cases and SOC was not included in the calculations.

results of the other two calculations are fairly satisfactory. In particular, the small-core basis set bands in Figure 3c match nicely those obtained with VASP in Figure 1a. The slight discrepancies between the bands in Figure 1a and Figure 3c on one hand and the bands in Figure 1d on the other can be due to the use of pseudopotentials in the former two or to an inaccurate closure relation of the AE basis set in the latter. We will not address this issue any further here. Finally, we stress that our proposed implementation is not restricted to any specific Gaussian-type basis set. As an advantage when compared to, e.g., TB calculations, it can capture the SOC effect for more flexible and larger basis sets when a minimal basis does not give satisfactory results in a band structure calculation, as is the case shown in Figure 3a.

Now that we have verified that we can obtain essentially the same band structure with two different DFT codes and three different basis sets (plane waves, AE, and pseudopotential ones), we add SOC. Figure 4 shows the band structure obtained with VASP [panel (a)] and with our proposed implementation, applied to the WTBS+ANO basis set [panel (b)] and to the small core pseudopotential basis set [panel (c)]. The AE basis set bands share all the features of the VASP bands, except a slightly larger gap which originates from the calculations without SOC. For the pseudopotential basis set, as discussed above, we have increased the effective nuclear potential by a factor of ≃65 (for this specific basis set) that makes the bands look as similar as possible to those in panel (a). As can be seen, these last bands, tuned by a single parameter, are essentially indistinguishable from the VASP bands. As can be observed, the sizable SOC of Sb changes the previous band structure calculated without SOC considerably, removing degeneracies, but not in a qualitative manner. The changes are, however, not so trivial for few-layered antimonene as shown in the next section.

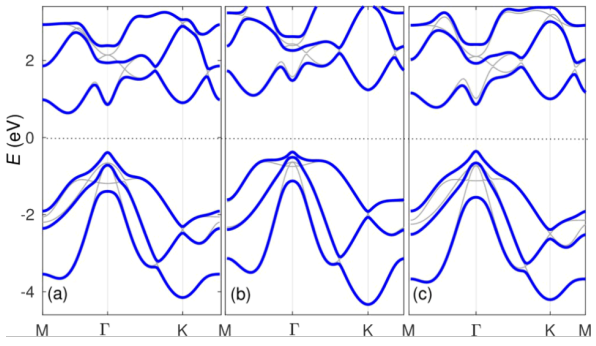

Figure 4: Comparison between different calculations of the band structure of monolayer antimonene including SOC: (a) VASP code, (b) AE basis set (WTBS+ANO), and (c) small-core pseudopotential basis set. As a reference, thin gray curves indicate the bands before adding SOC. The same lattice structure relaxed with VASP has been used for all cases.

Multilayer antimonene

As an elemental bulk material, Sb appears to be a topological semi-metal due to an inversion of the ”natural” bulk band order [1]. Despite the absence of a bulk gap, its non-zero topological invariant guarantees that antimony features protected topological surface states (TSS), although coexisting with bulk bands at the Fermi energy [51-54]. Sb(111) in thin film form could become, in principle, a 3D (TI) if quantum confinement opened a gap in the bulk bands. However, for sufficiently thin films, the TSS situated on opposite surfaces can get coupled which degrades or even destroys the TSS exotic properties such as their expected protection against backscattering. Ultimately, a single Sb(111) layer or monolayer antimonene even becomes a trivial semiconductor, as discussed in the previous section. Previous calculations have shown that the decoupling of the TSS requires a minimum of ≃7 layers [54,55]. In between the semiconductor monolayer and the 7-layered antimonene a crossover occurs, where claims of the existence of a 2D topological insulator have also been reported, but we do not pursue the investigation of this issue here [55]. When TSS are decoupled and the gap at the Dirac point closes down, the Fermi energy crosses the Dirac cone above the Dirac point, but also crosses 6 surface state pockets and 3 bulk pockets (see, e.g., [51]).

It has been shown that multilayer antimonene with hexagonal structure, prefers ABC stacking and is more stable than other allotropes for thicknesses larger than 3 layers [43]. In the relaxed structure of 9 layer antimonene, the lattice constant is $a = 4.27$ Å and the intra- and interlayer distances are $h = 1.52$ Å and $d = 3.68$ Å, respectively. In Figure 5 we show the band structure of 9 layers of antimonene including SOC, as obtained with the small-core pseudopotential basis set and the same enhancement factor as in the previous section. The results compare rather well down to any practical detail with those reported in the literature. In the inset of Figure 5 we show that the spin texture of the surface Dirac cone states around the Γ point and of the states in the nearby pockets, comes out as expected [51,56]. This provides further evidence that not only the band structure is reproduced at first glance, but also the wave functions are properly evaluated. This non-trivial example illustrates the practicality of our proposed single-parameter implementation, when AE basis sets are computationally demanding.

Bi(111) monolayers

A monolayer of Bi(111) was one of the first 2D crystals predicted to be a 2D TI [27] and with actual chances to be experimentally isolated and characterized. However, only a few reports have confirmed the non-trivial topological character of this material [57-60]. Having seen the trivial bands of antimonene monolayer changing to nontrivial in multilayers, the

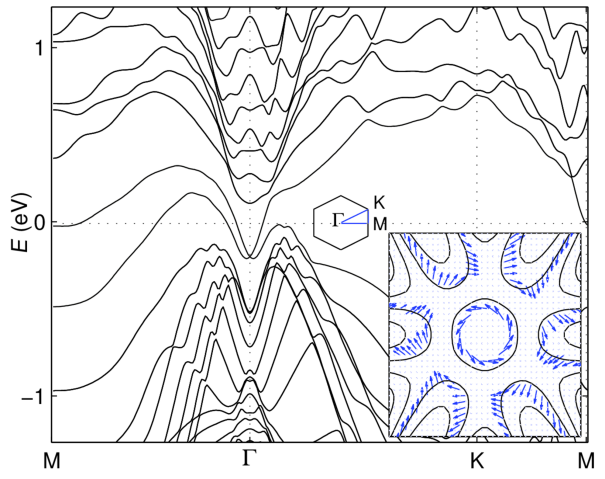

Figure 5: Band structure of 9 layers, ABC stacking Sb(111) films as obtained from small core pseudopotential basis. The spin texture around the Γ point is presented in the inset.

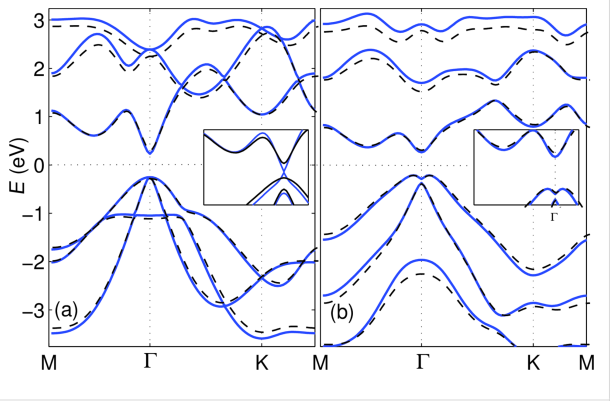

Figure 6: Band structure of a Bi(111) monolayer, obtained from VASP (dashed black) and small core pseudopotential basis set (solid blue) (a) without and (b) with SOC. Inset of panel (a) shows closing (blue) and reopening (black) of the gap with two parameter values of 70 and 100, respectively. Inset of panel (b), using the final parameter value of 120, is the same bands zoomed in near the Γ point showing the similarity of the inverted bands compared to the VASP result.

band inversion of Bi(111) is addressed in this section. Using different DFT packages, a wide range of structural parameters have been reported for Bi(111). Being aware of the sensitivity of the band structure to the exact atomic structure and for the sake of comparison we use a lattice constant $a = 4.33$ Å and a buckling height $h = 1.74$ Å as reported in a similar VASP calculation [61]. Figure 6 shows the band structure of Bi(111) monolayer, as obtained from VASP (dashed black), and that calculated with a small-core pseudopotential basis set (solid blue), as obtained with our implementation. Starting from very similar band structures without SOC (a), the proposed implementation of SOC gives a band structure in close resemblance with the one obtained from VASP (b) (the multiplicative factor needed to increase the nuclear potential is $\simeq$120 in case of this specific basis set). Increasing the multiplicative factor of our implementation from zero to two intermediate values (for example 70 and 100), as shown in the inset of Figure 6a, one can follow the evolution of the band structure from trivial to nontrivial bands and the ”Mexican hat” shaped valence band in Figure 6b. The band inversion at the Γ point is evident. However, this visual evidence is not sufficient to prove that this system is a topological insulator and a calculation of the Z2 number demonstrates that this is case.

Regardless of the shortcomings of tight binding method which led us towards this implementation of SOC, here, we want to compare the order of magnitude of tight binding SOC parameters with our SOC correction. In TB implementation, only one multiplicative parameter serves as the radial correction of SOC and this factor is much smaller than our multiplicative factors. The TB parameter entirely replaces the actual evaluation of the radial integral in Equation 5. However, our multiplicative factor is used to correct the radial integral which we actually perform for all matrix elements. The large numbers that we report come about because the radial matrix elements can be very small due to the lack of nodal structure of the basis elements, but, in the end, the correction parameter that accompanies the angular part for the valence orbitals will be in the same order of magnitude as what is reported for similar tight binding models.

Conclusion

We have presented an implementation of SOC suitable for DFT band structure calculations based on CGTOs basis sets. We evaluate both angular and radial part of the SOC relativistic correction to the Hamiltonian, considering the spherical harmonics and CGTOs as the angular and radial part of the basis functions, respectively. The evaluated SOC term is then added after a standard non-relativistic (or scalar relativistic) self-consistent calculation. We have shown that if the AE band structure is in good agreement with plane-wave bands without SOC, when our implementation is applied, it can reproduce the band structure obtained from the VASP code (used as a reference) to our satisfaction. Although we have only tested it in the cases of antimonene and Bi(111), we see no reason why it should not work for other elemental and compound materials, since it is essentially first-principles and SOC is an intra-atomic correction. We have also shown that a simple modification (by a multiplicative factor) of the effective nuclear potential makes this implementation applicable for pseudopotential basis sets which lack nodal structure. Remarkably, the results obtained in this last manner fit even better those obtained with plane-waves and the VASP code. In contrast to standard TB implementations where the SOC parameter acts on the valence orbitals of a minimal basis set, our method does not consider any pre-

assumptions for the basis elements. Note that using GTOs as basis elements, the so-called valence orbital might be split into two or more basis elements to improve the quality of the band structure. Our proposed approach is a practical way of including SOC to standard DFT non-relativistic band structure calculations based on localized basis sets.

Acknowledgements

We thank W. S. Paz for help with the DFT calculations. J.J.P. acknowledges MINECO (Spain) for financial support under grant FIS2016-80434-P and the "María de Maeztu" program for Units of Excellence in R&D (MDM-2014-0377); the European Union structural funds and the Comunidad de Madrid under grants nos. P2013/MIT-3007 and P2013/MIT-2850; the Generalitat Valenciana under grant no. PROMETEO/2012/011; the Fundación Ramón Areces; and the computer resources and assistance provided by the Centro de Computación Científica of the Universidad Autónoma de Madrid and the RES.

ORCID® iDs

Sahar Pakdel - https://orcid.org/0000-0002-4676-0780

References

1. Fu, L.; Kane, C. L. *Phys. Rev. B* **2007,** *76,* 045302. doi:10.1103/PhysRevB.76.045302
2. Hasan, M. Z.; Kane, C. L. *Rev. Mod. Phys.* **2010,** *82,* 3045. doi:10.1103/RevModPhys.82.3045
3. Qi, X.-L.; Zhang, S.-C. *Rev. Mod. Phys.* **2011,** *83,* 1057. doi:10.1103/RevModPhys.83.1057
4. Ren, Y.; Qiao, Z.; Niu, Q. *Rep. Prog. Phys.* **2016,** *79,* 066501. doi:10.1088/0034-4885/79/6/066501
5. Shen, S.-Q. *Topological insulators: Dirac equation in condensed matters;* Springer Science & Business Media, 2013; Vol. 174.
6. Bernevig, B. A.; Hughes, T. L. *Topological insulators and topological superconductors;* Princeton University Press, 2013.
7. Slater, J. C. *Phys. Rev.* **1930,** *36,* 57. doi:10.1103/PhysRev.36.57
8. Liu, Y.; Allen, R. E. *Phys. Rev. B* **1995,** *52,* 1566. doi:10.1103/PhysRevB.52.1566
9. Papaconstantopoulos, D. A. *Handbook of the Band Structure of Elemental Solids From Z = 1 To Z = 112;* Springer US: Boston, MA, 2015.
10. Papaconstantopoulos, D.; Mehl, M. *J. Phys.: Condens. Matter* **2003,** *15,* R413. doi:10.1088/0953-8984/15/10/201
11. For program description, see. http://www.flapw.de (accessed Dec 12, 2017).
12. Kresse, G.; Furthmüller, J. *Comput. Mater. Sci.* **1996,** *6,* 15. doi:10.1016/0927-0256(96)00008-0
13. Giannozzi, P.; Baroni, S.; Bonini, N.; Calandra, M.; Car, R.; Cavazzoni, C.; Ceresoli, D.; Chiarotti, G. L.; Cococcioni, M.; Dabo, I.; Corso, A. D.; de Gironcoli, S.; Fabris, S.; Fratesi, G.; Gebauer, R.; Gerstmann, U.; Gougoussis, C.; Kokalj, A.; Lazzeri, M.; Martin-Samos, L.; Marzari, N.; Mauri, F.; Mazzarello, R.; Paolini, S.; Pasquarello, A.; Paulatto, L.; Sbraccia, C.; Scandolo, S.; Sclauzero, G.; Seitsonen, A. P.; Smogunov, A.; Umari, P.; Wentzcovitch, R. M. *J. Phys.: Condens. Matter* **2009,** *21,* 395502. doi:10.1088/0953-8984/21/39/395502
14. For program description, see. http://www.quantum-espresso.org/ (accessed Dec 12, 2017).
15. Jacob, D.; Palacios, J. J. *J. Chem. Phys.* **2011,** *134,* 044118. doi:10.1063/1.3526044
16. Palacios, J. J.; Pérez-Jiménez, A. J.; Louis, E.; Vergés, J. A. *Nanotechnology* **2001,** *12,* 160. doi:10.1088/0957-4484/12/2/318
17. Mostofi, A. A.; Yates, J. R.; Pizzi, G.; Lee, Y.-S.; Souza, I.; Vanderbilt, D.; Marzari, N. *Comput. Phys. Commun.* **2014,** *185,* 2309. doi:10.1016/j.cpc.2014.05.003
18. For program description, see. http://wannier.org/ (accessed Dec 12, 2017).
19. Fernández-Seivane, L.; Oliveira, M. A.; Sanvito, S.; Ferrer, J. *J. Phys.: Condens. Matter* **2006,** *18,* 7999. doi:10.1088/0953-8984/18/34/012
20. Crowley, J. M.; Tahir-Kheli, J.; Goddard, W. A., III. *J. Phys. Chem. Lett.* **2015,** *6,* 3792. doi:10.1021/acs.jpclett.5b01586
21. Dovesi, R.; Orlando, R.; Erba, A.; Zicovich-Wilson, C. M.; Civalleri, B.; Casassa, S.; Maschio, L.; Ferrabone, M.; De La Pierre, M.; D'Arco, P.; Noël, Y.; Causà, M.; Rérat, M.; Kirtman, B. *Int. J. Quantum Chem.* **2014,** *114,* 1287. doi:10.1002/qua.24658
22. Dovesi, R.; Saunders, V.; Roetti, C.; Orlando, R.; Zicovich-Wilson, C.; Pascale, F.; Civalleri, B.; Doll, K.; Harrison, N.; Bush, I.; D'Arco, P.; Llunell, M.; Causá, M.; Noël, Y. CRYSTAL14 User's Manual. http://www.crystal.unito.it/Manuals/crystal14.pdf (accessed Dec 12, 2017).
23. For program description, see. http://www.crystal.unito.it/ (accessed Dec 12, 2017).
24. For program description, see. http://gaussian.com/ (accessed Dec 12, 2017).
25. For program description, see. http://www.nwchem-sw.org/ (accessed Dec 12, 2017).
26. Pantazis, D. A.; Neese, F. *Wiley Interdiscip. Rev.: Comput. Mol. Sci.* **2014,** *4,* 363. doi:10.1002/wcms.1177
27. Murakami, S. *Phys. Rev. Lett.* **2006,** *97,* 236805. doi:10.1103/PhysRevLett.97.236805
28. Kato, T. *Commun. Pure Appl. Math.* **1957,** *10,* 151. doi:10.1002/cpa.3160100201
29. Boys, S. F. *Proc. R. Soc. London, Ser. A* **1950,** *200,* 542. doi:10.1098/rspa.1950.0036
30. Huzinaga, S. *J. Chem. Phys.* **1965,** *42,* 1293. doi:10.1063/1.1696113
31. Reiher, M. *Theor. Chem. Acc.* **2006,** *116,* 241. doi:10.1007/s00214-005-0003-2
32. Boettger, J. C. *Phys. Rev. B* **2000,** *62,* 7809. doi:10.1103/PhysRevB.62.7809
33. Ares, P.; Aguilar-Galindo, F.; Rodríguez-San-Miguel, D.; Aldave, D. A.; Díaz-Tendero, S.; Alcamí, M.; Martín, F.; Gómez-Herrero, J.; Zamora, F. *Adv. Mater.* **2016,** *28,* 6332. doi:10.1002/adma.201602128
34. Zhang, S.; Yan, Z.; Li, Y.; Chen, Z.; Zeng, H. *Angew. Chem., Int. Ed.* **2015,** *54,* 3112. doi:10.1002/anie.201411246
35. Zhang, S.; Xie, M.; Li, F.; Yan, Z.; Li, Y.; Kan, E.; Liu, W.; Chen, Z.; Zeng, H. *Angew. Chem., Int. Ed.* **2016,** *55,* 1666. doi:10.1002/anie.201507568
36. Chen, X.; Yang, Q.; Meng, R.; Jiang, J.; Liang, Q.; Tan, C.; Sun, X. *J. Mater. Chem. C* **2016,** *4,* 5434. doi:10.1039/C6TC01141A
37. Xu, Y.; Peng, B.; Zhang, H.; Shao, H.; Zhang, R.; Zhu, H. *Ann. Phys. (Berlin, Ger.)* **2017,** *529,* 1600152. doi:10.1002/andp.201600152
38. Peng, B.; Zhang, D.; Zhang, H.; Shao, H.; Ni, G.; Zhu, Y.; Zhu, H. *Nanoscale* **2017,** *9,* 7397. doi:10.1039/C7NR00838D

39. Wu, X.; Zhang, X.; Wang, X.; Zeng, Z. *AIP Adv.* **2016,** *6,* 045318. doi:10.1063/1.4948537
40. Huang, Z.-Q.; Hsu, C.-H.; Chuang, F.-C.; Liu, Y.-T.; Lin, H.; Su, W.-S.; Ozolins, V.; Bansil, A. *New J. Phys.* **2014,** *16,* 105018. doi:10.1088/1367-2630/16/10/105018
41. Zhao, M.; Zhang, X.; Li, L. *Sci. Rep.* **2015,** *5,* 16108. doi:10.1038/srep16108
42. Kresse, G.; Joubert, D. *Phys. Rev. B* **1999,** *59,* 1758. doi:10.1103/PhysRevB.59.1758
43. Wang, G.; Pandey, R.; Karna, S. P. *ACS Appl. Mater. Interfaces* **2015,** *7,* 11490. doi:10.1021/acsami.5b02441
44. Almlöf, J.; Taylor, P. R. *Adv. Quantum Chem.* **1991,** *22,* 301. doi:10.1016/S0065-3276(08)60366-4
45. Roos, B. O.; Lindh, R.; Malmqvist, P.-Å.; Veryazov, V.; Widmark, P.-O. *Chem. Phys. Lett.* **2005,** *409,* 295. doi:10.1016/j.cplett.2005.05.011
46. Huzinaga, S.; Miguel, B. *Chem. Phys. Lett.* **1990,** *175,* 289. doi:10.1016/0009-2614(90)80112-Q
47. Hurley, M. M.; Pacios, L. F.; Christiansen, P. A.; Ross, R. B.; Ermler, W. C. *J. Chem. Phys.* **1986,** *84,* 6840. doi:10.1063/1.450689
48. LaJohn, L. A.; Christiansen, P. A.; Ross, R. B.; Atashroo, T.; Ermler, W. C. *J. Chem. Phys.* **1987,** *87,* 2812. doi:10.1063/1.453069
49. Causà, M.; Dovesi, R.; Roetti, C. *Phys. Rev. B* **1991,** *43,* 11937. doi:10.1103/PhysRevB.43.11937
50. Peterson, K. A.; Figgen, D.; Goll, E.; Stoll, H.; Dolg, M. *J. Chem. Phys.* **2003,** *119,* 11113. doi:10.1063/1.1622924
51. Hsieh, D.; Xia, Y.; Wray, L.; Qian, D.; Pal, A.; Dil, J. H.; Osterwalder, J.; Meier, F.; Bihlmayer, G.; Kane, C. L.; Hor, Y. S.; Cava, R. J.; Hasan, M. Z. *Science* **2009,** *323,* 919. doi:10.1126/science.1167733
52. Bian, G.; Miller, T.; Chiang, T.-C. *Phys. Rev. Lett.* **2011,** *107,* 036802. doi:10.1103/PhysRevLett.107.036802
53. Benia, H. M.; Straßer, C.; Kern, K.; Ast, C. R. *Phys. Rev. B* **2015,** *91,* 161406. doi:10.1103/PhysRevB.91.161406
54. Bian, G.; Wang, X.; Liu, Y.; Miller, T.; Chiang, T.-C. *Phys. Rev. Lett.* **2012,** *108,* 176401. doi:10.1103/PhysRevLett.108.176401
55. Zhang, P.; Liu, Z.; Duan, W.; Liu, F.; Wu, J. *Phys. Rev. B* **2012,** *85,* 201410. doi:10.1103/PhysRevB.85.201410
56. Yao, G.; Luo, Z.; Pan, F.; Xu, W.; Feng, Y. P.; Wang, X.-s. *Sci. Rep.* **2013,** *3,* 2010. doi:10.1038/srep02010
57. Sabater, C.; Gosálbez-Martínez, D.; Fernández-Rossier, J.; Rodrigo, J. G.; Untiedt, C.; Palacios, J. J. *Phys. Rev. Lett.* **2013,** *110,* 176802. doi:10.1103/PhysRevLett.110.176802
58. Drozdov, I. K.; Alexandradinata, A.; Jeon, S.; Nadj-Perge, S.; Ji, H.; Cava, R. J.; Andrei Bernevig, B.; Yazdani, A. *Nat. Phys.* **2014,** *10,* 664. doi:10.1038/nphys3048
59. Kawakami, N.; Lin, C.-L.; Kawai, M.; Arafune, R.; Takagi, N. *Appl. Phys. Lett.* **2015,** *107,* 031602. doi:10.1063/1.4927206
60. Liu, X.; Du, H.; Wang, J.; Tian, M.; Sun, X.; Wang, B. *J. Phys.: Condens. Matter* **2017,** *29,* 185002. doi:10.1088/1361-648X/aa655a
61. Huang, Z.-Q.; Chuang, F.-C.; Hsu, C.-H.; Liu, Y.-T.; Chang, H.-R.; Lin, H.; Bansil, A. *Phys. Rev. B* **2013,** *88,* 165301. doi:10.1103/PhysRevB.88.165301

License and Terms

BEILSTEIN JOURNAL OF NANOTECHNOLOGY

Non-equilibrium electron transport induced by terahertz radiation in the topological and trivial phases of $Hg_{1-x}Cd_xTe$

Alexandra V. Galeeva[1], Alexey I. Artamkin[1], Alexey S. Kazakov[1], Sergey N. Danilov[2], Sergey A. Dvoretskiy[3], Nikolay N. Mikhailov[3], Ludmila I. Ryabova[4] and Dmitry R. Khokhlov[*1,5]

Letter

Open Access

Address:
[1]Physics Department, M.V. Lomonosov Moscow State University, Leninskie Gory 1 bld.2, 119991 Moscow, Russia, [2]Faculty of Physics, University of Regensburg, Universitaetstr. 31, D-93053 Regensburg, Germany, [3]Rzhanov Institute of Semiconductor Physics, pr. Lavrentieva 13, 630090 Novosibirsk, Russia, [4]Chemistry Department, M.V. Lomonosov Moscow State University, Leninskie Gory 1 bld.3, 119991 Moscow, Russia and [5]P.N. Lebedev Physical Institute, Leninskiy prosp. 53, 119991 Moscow, Russia

Email:
Dmitry R. Khokhlov[*] - khokhlov@mig.phys.msu.ru

* Corresponding author

Keywords:
terahertz radiation; topological insulator; photoconductivity

Beilstein J. Nanotechnol. **2018,** *9,* 1035–1039.
doi:10.3762/bjnano.9.96

Received: 08 December 2017
Accepted: 02 March 2018
Published: 29 March 2018

This article is part of the Thematic Series "Topological materials".

Guest Editor: J. J. Palacios

Abstract

Terahertz photoconductivity in heterostructures based on n-type $Hg_{1-x}Cd_xTe$ epitaxial films both in the topological phase ($x < 0.16$, inverted band structure, zero band gap) and the trivial state ($x > 0.16$, normal band structure) has been studied. We show that both the positive photoresponse in films with $x < 0.16$ and the negative photoconductivity in samples with $x > 0.16$ have no low-energy threshold. The observed non-threshold positive photoconductivity is discussed in terms of a qualitative model that takes into account a 3D potential well and 2D topological Dirac states coexisting in a smooth topological heterojunction.

Findings

Discovery of theoretically predicted quantum spin Hall effect states in HgTe quantum wells [1,2] has initiated extensive studies of topological insulator materials [3,4]. Noteworthy, the ARPES technique, being a well-developed method to probe topological surface states, is a challenge in the case of HgTe-based topological insulators due to its zero-gap energy spectrum in the bulk. Nevertheless, formation of topological surface states in 3D HgTe has been convincingly proved by ARPES experiments in several detailed studies [5-7].

$Hg_{1-x}Cd_xTe$ solid solutions demonstrate a composition-driven transition from the topological phase with inverted band structure to the trivial phase with normal band structure ordering at $x \approx 0.16$ [8]. In contrast to most of the 3D topological insulators, $Hg_{1-x}Cd_xTe$ solid solutions are characterized by relatively low free carrier concentration values in the bulk, and may be therefore considered as good candidates for a case study focused on determination of the topological state contribution to the charge carrier transport. Laser terahertz probing is known to

be a powerful tool that may provide an insight into the electron dynamics in semiconductors, particularly, in topological insulators [9-11]. Study of non-equilibrium processes in $Hg_{1-x}Cd_xTe$ in the terahertz spectral range is additionally motivated by the application aspects related to the terahertz photodetector development [12].

In our recent paper [13], we have shown that photoconductivity in $Hg_{1-x}Cd_xTe$ solid solutions at 280 μm wavelength changes its sign across the topological transition from the inverted to the normal band structure. It was assumed that the negative photoresponse in the samples with the normal band structure is most likely related to the electron gas heating, while the positive photoconductivity in the zero band gap mercury cadmium telluride was reasonable to associate with interband transitions.

In this work, we focus on the study of terahertz photoconductivity in the spectral range of 90–496 μm of $Hg_{1-x}Cd_xTe$ solid solutions in close vicinity of the band inversion point. This is done to determine possible effects of the topological states on the non-equilibrium transport.

The $Hg_{1-x}Cd_xTe$ heterostructures were synthesized by MBE. ZnTe and CdTe buffer layers, a CdTe-rich mercury cadmium telluride relaxed layer, a 3D $Hg_{1-x}Cd_xTe$ layer, and a CdTe-rich cap layer were successively grown on a GaAs (013) semi-insulating substrate (see the inset in upper right corner of the Figure 1). The active 3D $Hg_{1-x}Cd_xTe$ layer thickness was about 4 μm. Composition of the films was controlled by ellipsometry. The synthesis is described in detail in [14].

We have chosen samples with $x = 0.13$; 0.15; 0.17 for our study. The latter corresponds to the trivial phase with the normal band structure. The two others are characterized by the inverted band structure (topological phase). Hall effect measurements have shown that all the samples are of the n-type. Free electron concentration values determined in magnetic field of 0.05 T at $T = 4.2$ K are in the range from 3.7×10^{14} cm^{-3} to 5.2×10^{14} cm^{-3}. Within the two-band Kane model, the given concentrations correspond to the Fermi level position not lower than at 3 meV, 5 meV, and 7 meV above the conduction band edge for the samples with $x = 0.13$, 0.15, 0.17, respectively. The energy distance between the conduction band and the light-hole

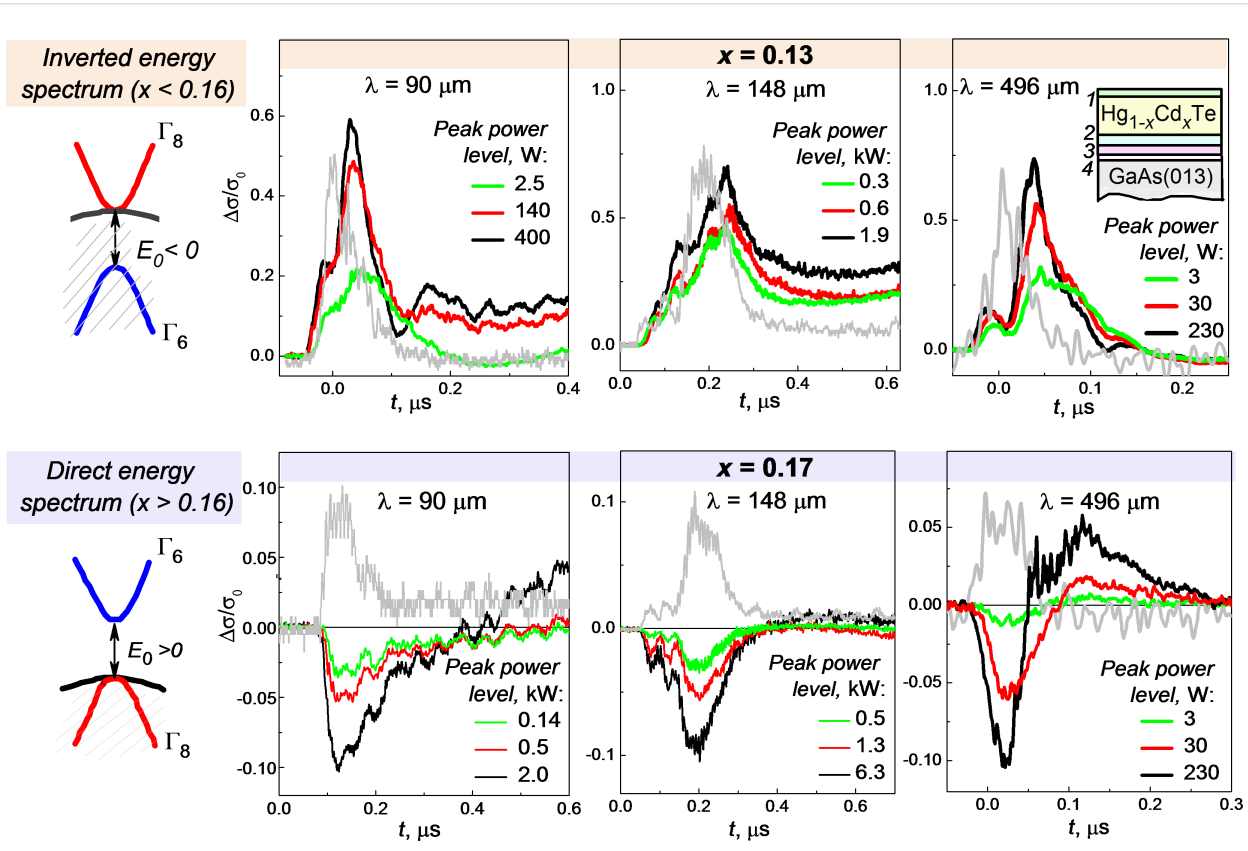

Figure 1: Photoconductivity kinetics $\Delta\sigma/\sigma_0$ in $Hg_{1-x}Cd_xTe$ films with $x = 0.13$ (the upper panel) and $x = 0.17$ (the lower panel) at the wavelengths λ = 90; 148; 496 μm for various radiation peak power levels. The laser pulse time profiles are shown by grey lines. The energy band structure for both solid solutions is shown schematically to the left of the plots. The heterostructure layers are outlined in the right upper corner. The cap and relaxed $Hg_{1-y}Cd_yTe$, buffer CdTe and ZnTe layers are indicated by the numbers from 1 to 4, respectively.

valence subband used in the Kane model calculations was estimated using the empirical relations [15-20].

Photoconductivity kinetics has been studied under 90, 148, 280, and 496 μm wavelength pulse laser radiation at the temperature 4.2 K. The measurements have been done in the Hall bar geometry using the 4-probe method. The incident radiation was normal to the sample surface. Duration of the pulse was ≈100 ns. The radiation power was up to 7 kW and could be varied by calibrated attenuators. The use of the incident radiation power as a variable parameter can help to figure out mechanisms of the photoelectric phenomena in some cases [21,22]. The experimental details can be found elsewhere [23-27].

The photoconductivity kinetics $\Delta\sigma/\sigma_0$ for the samples with x = 0.13 (the upper panel) and x = 0.17 (the lower panel) is shown in the Figure 1. Here $\Delta\sigma$ is the change in conductivity under pulse irradiation, σ_0 is the conductivity value before the laser pulse. The data for the structures with x = 0.13 and x = 0.15 (inverted band structure) are quite similar, therefore only data for the sample with x = 0.13 are presented in the Figure 1. The observed kinetics are rather complicated and can be described by several superimposed processes characterized by different relaxation time parameters. We will address here only to relatively fast processes with the characteristic times of 100–200 ns. The long-term photoconductivity observed at longer times after the laser pulse end may be due to photoinduced transitions to or from the local electron states in the barriers. This long-term photoconductivity is not discussed in this paper. It is important that the signs of the fast photoresponse for the normal and inverted band structure samples are opposite. For the latter, the photoconductivity is positive. Beside that, it demonstrates certain time delay with respect to the excitation laser pulse. The negative photoconductivity in the normal band structure case is much smaller in amplitude, and its kinetics repeats the laser pulse time profile.

Photoconductivity kinetics keeps the features mentioned above at lower radiation power levels (Figure 1). The absolute value of photoresponse amplitude $|\Delta\sigma/\sigma_0|_{peak}$ versus the number of the incident quanta N per unit time is shown in the Figure 2 for all wavelengths used and all samples studied. The photoconductivity amplitude dependence on the photon flux N for the samples with x = 0.13 and x = 0.15 is nonlinear and may be well fitted by the power dependence $|\Delta\sigma/\sigma_0| \sim N^{\alpha}$, where α is close to 1/4. It is important that the experimental data corresponding to the samples with x = 0.13 and x = 0.15 are close for all wavelengths used. It means that the photoconductivity value is defined only by the incident photon flux N irrespectively of the wavelength. It is reasonable to assume therefore that the positive photoconductivity in these samples results from an increase in the free carrier concentration due to the photogeneration process with the constant quantum efficiency independently on the wavelength. It should be stressed that the positive photoconductivity is still observed even for the sample with x = 0.15 for which the Fermi energy (>5 meV) well exceeds the quantum energy of the 496 μm wavelength laser radiation (2.5 meV).

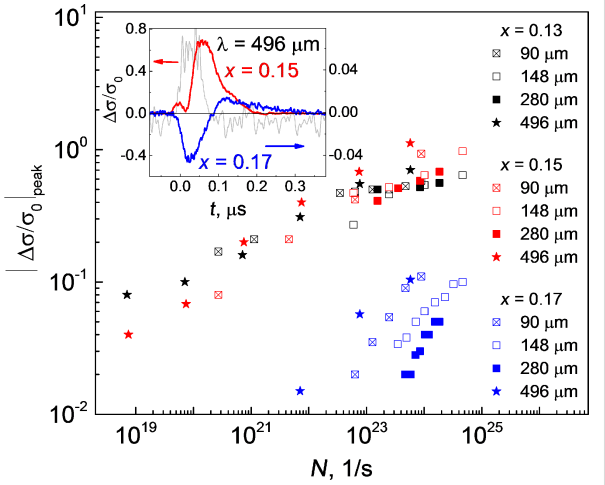

Figure 2: Dependence of the absolute value of the peak photoresponse amplitude $|\Delta\sigma/\sigma_0|_{peak}$ (σ_0 is the conductivity before a laser pulse, $\Delta\sigma$ is the conductivity change under illumination) on the photon flux density N for $Hg_{1-x}Cd_xTe$ films with x = 0.13 (black symbols), x = 0.15 (red symbols), and x = 0.17 (blue symbols) at various wavelengths. The photoconductivity kinetics at 496 μm for the samples with x = 0.15 and x = 0.17 are shown in the inset. A typical pulse time profile is shown by the grey line.

In contrast to that, the negative photoconductivity (sample with x = 0.17) depends strongly on the radiation wavelength. The electron gas heating by the incident radiation followed by an electron mobility drop is most likely responsible for this effect. This mobility drop is due to a scattering time drop with increasing energy, as well as to a substantial increase in the electron effective mass of hot electrons. This process obviously has no energy threshold. In such a case, the photoconductivity is negative and depends on the power absorbed. Therefore, the data calculated as a function of the incident quantum flux (see Figure 2) differ for different wavelengths. An additional discrepancy may come out as a result of carrier trapping by acceptor resonant states [28,29].

Let us discuss now in more detail the experimental results obtained for the $Hg_{1-x}Cd_xTe$ topological phase (x < 0.16). The most unusual result is the absence of a threshold energy in the strong generation-related positive photoconductivity. The photoresponse is observed even if the Fermi energy exceeds the energy of the incident radiation quantum. Existence of the topological heterojunction may be a key factor that determines the non-threshold photoexcitation in the structures studied.

Indeed, the buffer and cap layers of the heterostructure are formed of $Hg_{1-x}Cd_xTe$ solid solutions with a relatively high CdTe content providing normal band structure ordering. The film under study is in the topological phase with the inverted relative positions of the conduction and light hole bands. The CdTe content x varies quite smoothly on the characteristic length of about 1 μm along the heterojunctions between the buffer and the film, as well as between the film and the cap layer. Previously, it was theoretically demonstrated that in such a situation, there should appear a 3D potential well in the heterojunction area [30-32]. Beside that, 2D topological Dirac states are formed at the position z_0 corresponding to the gap absence between the conduction and light hole bands (Figure 3). To the right of z_0, the bulk semiconductor energy spectrum is gapless. The Fermi level position in such a structure varies with respect to the potential well bottom along the heterostructure profile. Therefore, for any given energy of a terahertz quantum, there should exist a position in the heterojunction area for which photogeneration from the heavy hole band to the conduction band becomes possible. It is important that this generation process has no threshold in energy, and its intensity is defined by the number of incident radiation quanta. Therefore, it may give rise to the positive photoconductivity observed experimentally.

There is one more possible mechanism providing appearance of the positive photoconductivity in heterostructures under study. As it was mentioned earlier, 2D Dirac states are formed at the position z_0 corresponding to the bottom of the 3D heterojunction potential well. Heating of electrons by the incident terahertz radiation in the 3D well leads to two competing effects. The first one is the mobility drop that should result in the negative photoconductivity. The second effect corresponds to the spatial diffusion of excited electrons to the 2D area. Indeed, it is located at the bottom of the well. Beside that, the density of the 2D Dirac states depends linearly on energy E, whereas it is proportional to $E^{1/2}$ for the bulk conduction band states. It means that for the heated electrons, there is an increased probability to diffuse to the z_0 position. Mobility of 2D Dirac electrons is much higher than it is for the bulk electrons, therefore this diffusion process results in the positive photoconductivity. The amplitude of this effect is much higher than the mobility drop due to the electron gas heating, so the positive photoconductivity prevails. Moreover, the diffusion process is delayed with respect to the photoexcitation which is observed experimentally. This is due to the fact that the spin direction of 2D Dirac electrons is locked to their momentum vector direction, whereas the 3D electrons in the well do not possess this feature. The suggested mechanism for the positive photoconductivity is non-threshold in energy. As a final argument, the 3D potential wells, as well as 2D Dirac states should not be formed for the

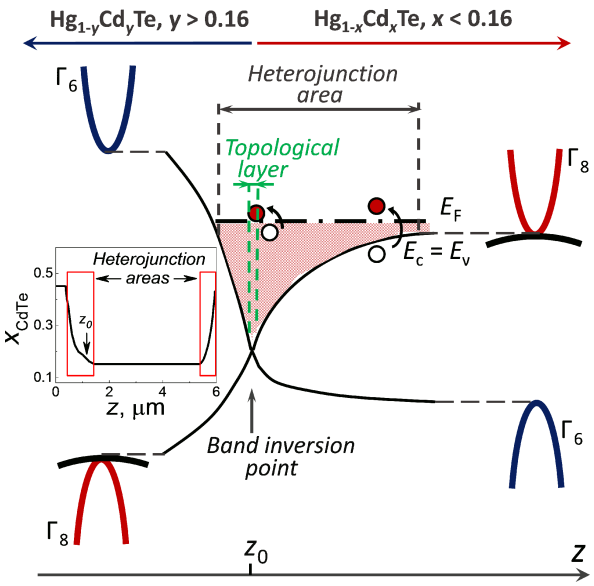

Figure 3: Sketch of the smooth heteroboundary between the $Hg_{1-x}Cd_xTe$ active layer (with the inverted band structure) and the $Hg_{1-y}Cd_yTe$ barrier layer (with the normal band structure) in the samples with $x < 0.16$. Variable position edges of the conduction (E_c) band, the heavy hole valence (E_v) subband, and the light hole subband in the heterojunction are schematically shown by black solid lines. The Fermi level is shown by the dash-dot line. The topological layer located in the close vicinity to the z_0 position is sketched up by green dashed lines. The red and the blank circles shown above and below the Fermi level, respectively, correspond to the suggested mechanisms of the positive photoconductivity effect. The CdTe content along the heterostrocture profile is presented in the inset. The red rectangles correspond to the heterojunction areas, the left one of which is zoomed in the main part of the figure.

$Hg_{1-x}Cd_xTe$ films with the composition corresponding to the trivial phase, and the positive delayed photoconductivity is not observed for these structures.

The two mechanisms for the positive photoconductivity suggested above may coexist in the same structure.

In summary, we have observed a non-threshold positive photoconductivity in heterostructures based on $Hg_{1-x}Cd_xTe$ thick films being in the topological phase. We suggest possible mechanisms responsible for the effect that takes into account diffusion of photoexcited electrons in the heterojunction area to the 2D Dirac state.

Acknowledgements

The authors are grateful to Prof. S.D. Ganichev. Prof. V.V. Bel'kov, Dr. D.A. Kozlov, and to G.M. Min'kov for fruitful discussions and technical assistance. The research described in this paper was supported by the grant of the Russian Science Foundation #17-72-10064.

ORCID® iDs

Sergey A. Dvoretskiy - https://orcid.org/0000-0002-1295-5598
Dmitry R. Khokhlov - https://orcid.org/0000-0003-2292-117X

References

1. Bernevig, B. A.; Hughes, T. A.; Zhang, S.-C. *Science* **2006,** *314,* 1757–1761. doi:10.1126/science.1133734
2. König, M.; Wiedmann, S.; Brüne, C.; Roth, A.; Buhmann, H.; Molenkamp, L. W.; Qi, X.-L.; Zhang, S.-C. *Science* **2007,** *318,* 766–770. doi:10.1126/science.1148047
3. Hasan, M. Z.; Kane, C. L. *Rev. Mod. Phys.* **2010,** *82,* 3045–3067. doi:10.1103/RevModPhys.82.3045
4. Bansil, A.; Lin, H.; Das, T. *Rev. Mod. Phys.* **2016,** *88,* 021004. doi:10.1103/RevModPhys.88.021004
5. Brüne, C.; Liu, C. X.; Novik, E. G.; Hankiewicz, E. M.; Buhmann, H.; Chen, Y. L.; Qi, X. L.; Shen, Z. X.; Zhang, S. C.; Molenkamp, L. W. *Phys. Rev. Lett.* **2011,** *106,* 126803. doi:10.1103/physrevlett.106.126803
6. Crauste, O.; Ohtsubo, Y.; Ballet, P.; Delplace, P.; Carpentier, D.; Bouvier, C.; Meunier, T.; Taleb-Ibrahimi, A.; Levy, L. P. *arXiv* **2013,** No. 1307.2008.
7. Liu, C.; Bian, G.; Chang, T.-R.; Wang, K.; Xu, S.-Y.; Belopolski, I.; Miotkowski, I.; Cao, H.; Miyamoto, K.; Xu, C.; Matt, C. E.; Schmitt, T.; Alidoust, N.; Neupane, M.; Jeng, H.-T.; Lin, H.; Bansil, A.; Strocov, V. N.; Bissen, M.; Fedorov, A. V.; Xiao, X.; Okuda, T.; Chen, Y. P.; Hasan, M. Z. *Phys. Rev. B* **2015,** *92,* 115436. doi:10.1103/physrevb.92.115436
8. Orlita, M.; Basko, D. M.; Zholudev, M. S.; Teppe, F.; Knap, W.; Gavrilenko, V. I.; Mikhailov, N. N.; Dvoretskii, S. A.; Neugebauer, P.; Faugeras, C.; Barra, A.-L.; Martinez, G.; Potemski, M. *Nat. Phys.* **2014,** *10,* 233–238. doi:10.1038/nphys2857
9. Valdés Aguilar, R.; Stier, A. V.; Liu, W.; Bilbro, L. S.; George, D. K.; Bansal, N.; Wu, L.; Cerne, J.; Markelz, A. G.; Oh, S.; Armitage, N. P. *Phys. Rev. Lett.* **2012,** *108,* 087403. doi:10.1103/PhysRevLett.108.087403
10. Wu, L.; Brahlek, M.; Valdés Aguilar, R.; Stier, A. V.; Morris, C. M.; Lubashevsky, Y.; Bilbro, L. S.; Bansal, N.; Oh, S.; Armitage, N. P. *Nat. Phys.* **2013,** *9,* 410–414. doi:10.1038/nphys2647
11. Luo, C. W.; Chen, H.-J.; Tu, C. M.; Lee, C. C.; Ku, S. A.; Tzeng, W. Y.; Yeh, T. T.; Chiang, M. C.; Wang, H. J.; Chu, W. C.; Lin, J.-Y.; Wu, K. H.; Juang, J. Y.; Kobayashi, T.; Cheng, C.-M.; Chen, C.-H.; Tsuei, K.-D.; Berger, H.; Sankar, R.; Chou, F. C.; Yang, H. D. *Adv. Opt. Mater.* **2013,** *1,* 804–808. doi:10.1002/adom.201300221
12. Rogalski, A. *Rep. Prog. Phys.* **2005,** *68,* 2267–2336. doi:10.1088/0034-4885/68/10/R01
13. Galeeva, A. V.; Artamkin, A. I.; Mikhailov, N. N.; Dvoretskii, S. A.; Danilov, S. N.; Ryabova, L. I.; Khokhlov, D. R. *JETP Lett.* **2017,** *106,* 162–166. doi:10.1134/S0021364017150061
14. Dvoretsky, S.; Mikhailov, N.; Sidorov, Yu.; Shvets, V.; Danilov, S.; Wittman, B.; Ganichev, S. *J. Electron. Mater.* **2010,** *39,* 918–923. doi:10.1007/s11664-010-1191-7
15. Hansen, G. L.; Schmidt, J. L.; Casselman, T. N. *J. Appl. Phys.* **1982,** *53,* 7099–7101. doi:10.1063/1.330018
16. Chu, J.; Xu, S.; Tang, D. *Appl. Phys. Lett.* **1983,** *43,* 1064–1066. doi:10.1063/1.94237
17. Schmit, J. L.; Stelzer, E. L. *J. Appl. Phys.* **1969,** *40,* 4865. doi:10.1063/1.1657304
18. Scott, M. W. *J. Appl. Phys.* **1969,** *40,* 4077. doi:10.1063/1.1657147
19. Finkman, E.; Nemirovsky, Y. *J. Appl. Phys.* **1979,** *50,* 4356. doi:10.1063/1.326421
20. Wiley, I. D.; Dexter, R. N. *Phys. Rev.* **1969,** *181,* 1181.
21. Galeeva, A. V.; Egorova, S. G.; Chernichkin, V. I.; Tamm, M. E.; Yashina, L. V.; Rumyantsev, V. V.; Morozov, S. V.; Plank, H.; Danilov, S. N.; Ryabova, L. I.; Khokhlov, D. R. *Semicond. Sci. Technol.* **2016,** *31,* 095010. doi:10.1088/0268-1242/31/9/095010
22. Galeeva, A. V.; Krylov, I. V.; Drozdov, K. A.; Knjazev, A. F.; Kochura, A. V.; Kuzmenko, A. P.; Zakhvalinskii, V. S.; Danilov, S. N.; Ryabova, L. I.; Khokhlov, D. R. *Beilstein J. Nanotechnol.* **2017,** *8,* 167–171. doi:10.3762/bjnano.8.17
23. Ganichev, S. D.; Ziemann, E.; Gleim, T.; Prettl, W.; Yassievich, I. N.; Perel, V. I.; Wilke, I.; Haller, E. E. *Phys. Rev. Lett.* **1998,** *80,* 2409–2412. doi:10.1103/PhysRevLett.80.2409
24. Ganichev, S. D.; Yassievich, I. N.; Prettl, W.; Diener, J.; Meyer, B. K.; Benz, K. W. *Phys. Rev. Lett.* **1995,** *75,* 1590–1593. doi:10.1103/PhysRevLett.75.1590
25. Ganichev, S. D.; Terent'ev, Y. V.; Yaroshetskii, I. D. *Sov. Tech. Phys. Lett.* **1985,** *11,* 20.
26. Ganichev, S. D.; Yassievich, I. N.; Prettl, W. *J. Phys.: Condens. Matter* **2002,** *14,* R1263–R1295. doi:10.1088/0953-8984/14/50/201
27. Egorova, S. G.; Chernichkin, V. I.; Ryabova, L. I.; Skipetrov, E. P.; Yashina, L. V.; Danilov, S. N.; Ganichev, S. D.; Khokhlov, D. R. *Sci. Rep.* **2015,** *5,* 11540. doi:10.1038/srep11540
28. Rumyantsev, V. V.; Kozlov, D. V.; Morozov, S. V.; Fadeev, M. A.; Kadykov, A. M.; Teppe, F.; Varavin, V. S.; Yakushev, M. V.; Mikhailov, N. N.; Dvoretskii, S. A.; Gavrilenko, V. I. *Semicond. Sci. Technol.* **2017,** *32,* 095007. doi:10.1088/1361-6641/aa76a0
29. Rumyantsev, V. V.; Morozov, S. V.; Antonov, A. V.; Zholudev, M. S.; Kudryavtsev, K. E.; Gavrilenko, V. I.; Dvoretskii, S. A.; Mikhailov, N. N. *Semicond. Sci. Technol.* **2013,** *28,* 125007. doi:10.1088/0268-1242/28/12/125007
30. Volkov, B. A.; Idlis, B. G.; Usmanov, M. S. *Phys.-Usp.* **1995,** *38,* 761–771. doi:10.1070/PU1995v038n07ABEH000097
31. Volkov, V. A.; Enaldiev, V. V. *J. Exp. Theor. Phys.* **2016,** *122,* 608–620. doi:10.1134/S1063776116030213
32. Tchoumakov, S.; Jouffrey, V.; Inhofer, A.; Bocquillon, E.; Plaçais, B.; Carpentier, D.; Goerbig, M. O. *Phys. Rev. B* **2017,** *96,* 201302. doi:10.1103/PhysRevB.96.201302

License and Terms

BEILSTEIN JOURNAL OF NANOTECHNOLOGY

Thermoelectric current in topological insulator nanowires with impurities

Sigurdur I. Erlingsson[1], Jens H. Bardarson[2] and Andrei Manolescu[*1]

Full Research Paper

Open Access

Address:
[1]School of Science and Engineering, Reykjavik University, Menntavegur 1, IS-101 Reykjavik, Iceland and [2]Department of Physics, KTH Royal Institute of Technology, Stockholm, SE-106 91 Sweden

Email:
Andrei Manolescu[*] - manoles@ru.is

* Corresponding author

Keywords:
topological insulators, nanowires, thermoelectric current

Beilstein J. Nanotechnol. **2018,** *9,* 1156–1161.
doi:10.3762/bjnano.9.107

Received: 04 December 2017
Accepted: 09 March 2018
Published: 12 April 2018

This article is part of the Thematic Series "Topological materials".

Guest Editor: J. J. Palacios

Abstract

In this paper we consider charge current generated by maintaining a temperature difference over a nanowire at zero voltage bias. For topological insulator nanowires in a perpendicular magnetic field the current can change sign as the temperature of one end is increased. Here we study how this thermoelectric current sign reversal depends on the magnetic field and how impurities affect the size of the thermoelectric current. We consider both scalar and magnetic impurities and show that their influence on the current are quite similar, although the magnetic impurities seem to be more effective in reducing the effect. For moderate impurity concentration the sign reversal persists.

Introduction

It has been known for quite some time now that the efficiency of thermoelectric devices can be increased by reducing the system size. The size reduction can improve electronic transport properties and also reduce the phonon scattering which then leads to increased efficiency [1]. Interestingly, often the materials that show the best thermoelectric properties on the nanoscale can also exhibit topological insulator properties [2], although the connection between the two properties is not always straightforward [3]. Even though few experimental studies exist on thermoelectric properties in topological insulator nanowires (TIN), many studies have reported magnetoresistance oscillations, both in longitudinal and transversal fields for TINs [4-10].

In its simplest form, thermoelectric current is generated when a temperature gradient is maintained across a conducting material. In the hotter end (reservoir) the particles have higher kinetic energy and thus velocity compared to the colder reservoir. This leads to a flow of energy from the hot to cold end of the system. Under normal circumstances this will lead to particles flowing in the same direction as the energy flow. The charge current can of course be positive or negative depending on the charge of the carriers, i.e., whether they are electrons or holes. Recently, it was shown that in systems showing non-monotonic transmission properties the particle current can change sign as a function of the temperature difference [11]. Sign changes of the thermoelectric current are well-known in quantum dots [12-15]

when the chemical potential crosses a resonant state. A sign change of the thermoelectric current can be obtained when the temperature gradient is increased, which affects the population of the resonant level in the quantum dot [16-19].

For topological insulator nanowires one can expect reversed, or anomalous, currents measured in tens of nanoamperes [11], well within experimental reach. Also, since the transport is over long systems, it is much simpler to maintain a large temperature difference of tens of kelvins, compared to the case of quantum dots. In this paper we extend our previous work on thermoelectric currents in TIN [11], by including the effects of impurities, both scalar and magnetic ones. The impurities deteriorate the ballistic quantum transport properties, but as long there are still remnants of the quantized levels, the predicted sign reversal of the thermoelectric current remains visible.

Results and Discussion

Clean nanowires

When a topological insulator material, such as BiSe, is formed into a nanowire, topological states can appear on its surface. Recently, such wires in a magnetic field have been studied extensively both theoretically [20-24] and experimentally [5-10,25]. When the nanowires are of circular cross section the electrons move on a cylindrical surface with radius R. The surface states of the topological insulator are Dirac fermions, described by the Hamiltonian [20,21,26]

$$H_{\mathrm{TI}} = -i\hbar v_{\mathrm{F}}\left[\sigma_z\left(\partial_z + i\frac{eB}{\hbar}R\sin\varphi\right) + \sigma_y\frac{1}{R}\partial_\varphi\right], \quad (1)$$

where v_{F} is the Fermi velocity, and the spinors satisfy antiperiodic boundary conditions $\hat{\psi}(\varphi) = -\hat{\psi}(\varphi + 2\pi)$ because of a Berry phase [20,21]. We chose the coordinate system such that the magnetic field is along the x-axis, $\mathbf{B}$ = (B,0,0), the vector potential being $\mathbf{A}$ = (0,0,By) = (0,0,BRsinφ). For B = 0 the angular part of the Hamiltonian has eigenfunctions $e^{i\varphi n}/\sqrt{2\pi}$ where n are half-integers to fulfill the boundary condition. It is convenient to diagonalize Equation 1 in the angular basis, which are exact eigenstates when B = 0.

An example of the energy spectrum is shown in Figure 1 for B = 0 (Figure 1a) and for B = 4.0 T (Figure 1b). The model parameters are comparable to experimental values [10]. For zero magnetic field the energy spectrum has a gap at k = 0 resulting from the antiperiodic boundary conditions [20,21]. For the case of non-zero magnetic fields, precursors of Landau levels around k = 0 are seen, both at negative and positive energy. The local minima away from k = 0 are precursors of snaking states. Such sates have been studies for quadratic dispersion (Schrödinger) where the Lorentz force always bends the electron trajectory towards the line of vanishing radial component of the magnetic field [27-30]. In fact, this is a classical effect known in the two-dimensional electron gas in inhomogeneous magnetic fields with sign change [31-34]. For Dirac electrons it has been reported in graphene p–n junctions in a homogeneous magnetic field, since in this case the charge carriers change sign [35].

In order to calculate the current in multi-channel one-dimensional systems one needs to calculate the product of the velocity $v_n(E)$ and density of states $\rho_n(E)$ of a given mode n at energy E [36]. This product is a constant $v_n(E)\rho_n(E) = 1/h$, irrespective of the form of $\varepsilon_n(k)$, which leads to the well-known conductance quantum e^2/h. For infinitely long, ballistic systems all channels are perfectly transmitted T_n = 1, so one can simply count the number of propagating modes to obtain the conductance.

If the curvature of the dispersion is negative (here we consider positive energy states) at k = 0, then the mode can contribute twice to the conductance since there are two values of k that fulfill $\varepsilon_n(k) = E$ and have the same sign of $v_n(E)$ (see Figure 1b).

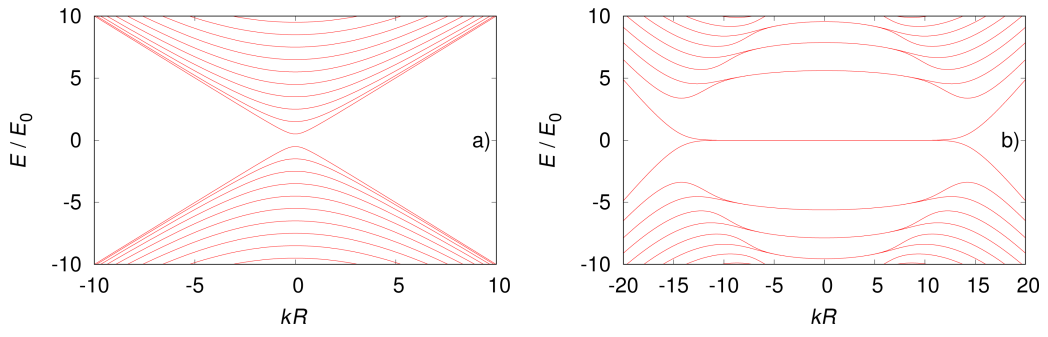

Figure 1: Energy spectra for a) B = 0 and b) B = 4.0 T. Note that the system is gapped at B = 0 but not at B = 4.0 T. We used $v_{\mathrm{F}} = 10^5$ m/s and R = 50 nm for the current calculations, which gives $E_0 = (\hbar v_{\mathrm{F}})/R \approx 1.3$ meV.

The transmission, which in this case is simply the number of propagating modes, can jump up by two unit values and then again fall by one unit value as a function of the energy. As was pointed out recently, the presence of such non-monotonic behavior in the transmission function $T(E)$ can give rise to anomalous thermoelectric currents [11].

In order clarify the origin of the sign reversal of the thermoelectric current, and how its affected by magnetic field, we will briefly outline how the current is calculated using the Landauer formula. The charge current I_c is given by

$$I_c = \frac{e}{h}\int T(E)\left[f_R(E) - f_L(E)\right]\mathrm{d}E. \tag{2}$$

Here $f_{L/R}(E)$ are the Fermi functions for the left/right reservoir with chemical potentials $\mu_{L/R}$ and temperatures $T_{L/R}$. We will consider $\mu_L = \mu_R = \mu$. If the transmission function $T(E)$ increases with energy over the integration interval (and the chemical potential is situated somewhere in the interval) the thermoelectric current is positive. This is the normal situation. An anomalous negative current can instead occur if the transmission function decreases with energy. The curve for $B = 2.0$ T in Figure 2a shows the normal situation where the chemical potential is positioned at an upward step at $\mu = 6.8$ meV. The vertical line indicates the position of μ. The resulting charge current is shown in Figure 2b) where the normal situation is evident for $B = 2.0$ T. If the magnetic field is increased to $B = 2.8$ T, the energy spectrum changes (not shown) and so will the transmission function $T(E)$. Now a downward step occurs at μ, which leads to an anomalous current, as can be seen in Figure 2b. Note that the current sign an be changes by either varying the temperature of the right reservoir or the magnetic field. The anomalous current can be in the range of tens of nanoamperes, which is well within experimental reach.

Modeling of impurities

The anomalous current introduced above relies on non-monotonic steps in the transmission function. For ballistic nanowires the steps are sharp, but in the presence of impurities the steps will get distorted. In order to simulate transport in a realistic nanowires, we will assume short-range impurities. These are described by

$$V_{\mathrm{imp}}(z,\varphi) = \sum_i W\delta(z - z_i)\delta(\varphi - \varphi_i), \tag{3}$$

where W is the impurity strength. Due to fermion doubling, the Hamiltonian in Equation 1 can not be directly discretized [37]. However, adding a fictitious quadratic term

$$H_\lambda = -\frac{v_F\hbar}{R}\lambda^2\sigma_x\left(R^2\partial_z^2\right) \tag{4}$$

solves the issue of fermion doubling [38]. To fix the value of λ, we will first look at the longitudinal part of Equation 1 in the absence of a magnetic field

$$H_{\mathrm{TI},z} = -i\hbar v_F\sigma_z\partial_z - \frac{v_F\hbar}{R}\lambda^2\sigma_x\left(R^2\partial_z^2\right). \tag{5}$$

If this Hamiltonian is discretized on a lattice with the lattice parameter a the spectrum will be

$$\varepsilon_\pm(k) = \pm\frac{\hbar v_F}{R}\sqrt{\frac{R^2}{a^2}\sin^2(ka) + (2\lambda)^4\frac{R^4}{a^4}\sin^4\left(\frac{ka}{2}\right)}, \tag{6}$$

where $ka \in [-\pi, \pi]$. The value of λ can be set by the condition that the Taylor expansion of $(\varepsilon_\pm(k))^2$ contains no quartic term, which maximizes the region showing linear dispersion. This condition is fulfilled when

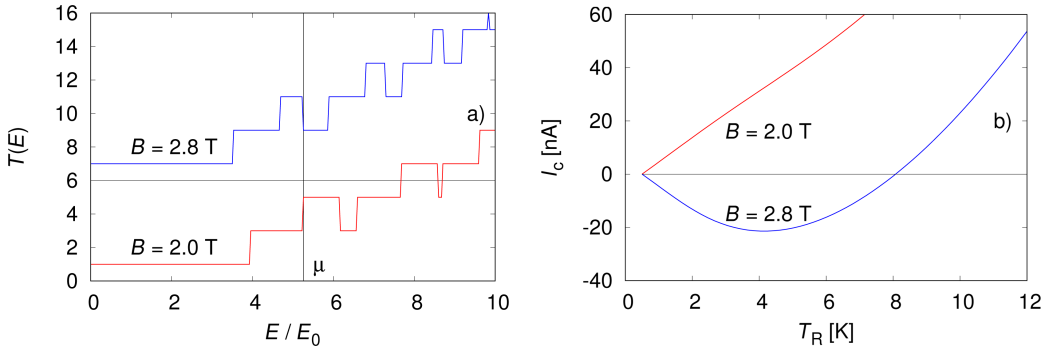

Figure 2: a) Transmission function and b) thermoelectric current for two different magnetic fields. In a), the transmission function $T(E)$ for $B = 2.8$ T is offset by 6 for clarity. We used $v_F = 10^5$ m/s and $R = 50$ nm for the current calculations, which gives $E_0 = (\hbar v_F)/R \approx 1.3$ meV.

$$\lambda = \frac{1}{3^{1/4}}\sqrt{\frac{a}{R}}. \tag{7}$$

For zero magnetic field we choose the lattice parameter $a = 0.02\ R$, which ensures that the first ten states calculated via the lattice model with the λ^2 term deviate by less than 1% from those obtained with the continuum model (Figure 1a). For a non-zero magnetic field we use $a = 0.01\ R$, because more states contribute to the flat bands at $E = 0$. At this point we are free to use standard discretization schemes and the transmission function in the case when impurities are included is obtained using the recursive Green's function method [39].

Experiments on normal (not topological) nanowires show a conductance that can be complicated, but reproducible trace for a given nanowire. This means that the measurement can be repeated on the same nanowire and it will give the same conductance trace as long as the sample is kept under unchanged conditions. But a different nanowire would show a different, but reproducible, conductance trace [40]. This motivates us to consider a fixed impurity configuration, i.e., no ensemble average.

In Figure 3 we show the transmission functions and the thermoelectric currents for a magnetic field of $B = 4.0$ T, for a nanowire of length $L = 1000$ nm. The disorder strength is set to $W = 4.8\ (\hbar v_F)/R$ and the density of impurities is varied: $n_i = 3.0\ \text{nm}^{-1}$, $6.0\ \text{nm}^{-1}$ and $12\ \text{nm}^{-1}$. For comparison, we consider two types of impurities: scalar impurities described by Equation 3 (red traces), and magnetic impurities described by $V_{\text{imp}}\sigma_x$ (blue traces).

When the transmission function in Figure 3a in the presence of impurities is studied, a definite trend towards reduced non-monotonic intervals is visible as the density of impurities is increased from 3.0 to 6.0 and 12 nm^{-1}. This applies both to scalar (red) and magnetic impurities (blue), even though the magnetic impurities seem to cause a quicker reduction in the transmission peaks. Both scalar and magnetic impurities open up a gap around $E = 0$. This is due to scattering between counter-propagating states on the same side of the nanowire [24]. When looking at the calculated charge current in Figure 3b, the difference between the scalar and magnetic impurities becomes more clear. In both cases the strength and density of impurities is the same but magnetic impurities are substantially more effective in reducing the anomalous current. Note that due to the different impurity configurations between the magnetic and scalar cases we adjusted the chemical potential to $\mu = 7.15$ meV to maximize the anomalous current. The values of W_{imp} and n_i used here were chosen such that we could observe an evolution in Figure 3a from resolving the quantized steps to not seeing any. For experiments, this would mean that samples that show some indication of quantized conductance steps should suffice to observe the anomalous current.

In our calculations we neglected the Coulomb interactions between electrons that, in the nonlinear regime of transport, may alter the current, at least in non-topological materials [41-43]. To our knowledge, the present experimental data in TI nanowires can be explained without considering the Coulomb interaction. But, nevertheless, this issue can be an open question for future research.

Conclusion

We studied the reversal of the thermoelectric current in topological insulator nanowires and how it evolves with changing magnetic fields. Using lattice models we simulated realistic nanowires with both scalar and magnetic impurities. Even though both scalar and magnetic impurities reduce the size of the

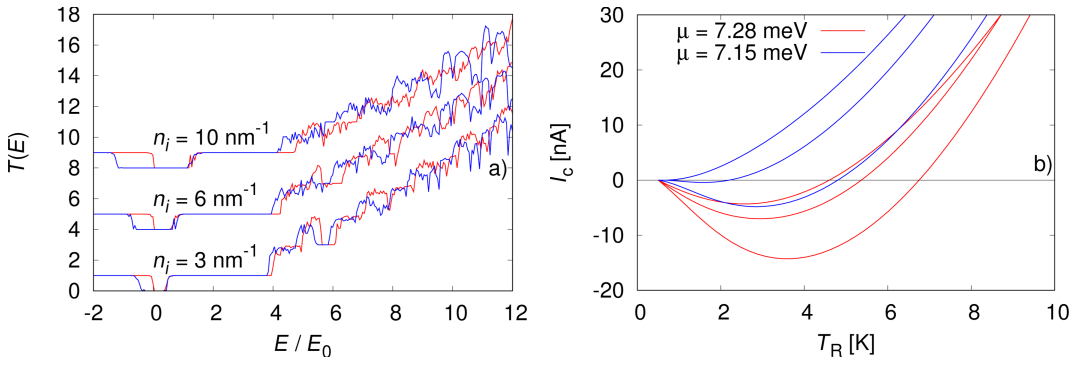

Figure 3: a) Transmission function and b) thermoelectric current calculated in the presence of impurities at $B = 4.0$ T. The nanowire length is $L = 1000$ nm and the impurity densities are $n_i = 3.0\ \text{nm}^{-1}$, $6.0\ \text{nm}^{-1}$ and $12\ \text{nm}^{-1}$. The red curves are for scalar impurities with chemical potential $\mu = 7.28$ meV and the blue curves are for magnetic impurities with $\mu = 7.15$ meV.

anomalous current we expect that in quasiballistic samples the effect should be observable. Interestingly, magnetic impurities seem to be more effective than scalar impurities when it comes to reducing the anomalous thermoelectric current. For hollow nanowires described by the Schrödinger equation the backscattering is the same for magnetic and scalar impurities, in the absence of spin–orbit interactions. This is in contrast to the TI nanowires studies here, which are more susceptible to scattering by magnetic impurities due to spin–momentum locking of the surface states [23].

Acknowledgements

This work was supported by: RU Fund 815051 TVD and ERC Starting Grant 679722.

ORCID® iDs

Andrei Manolescu - https://orcid.org/0000-0002-0713-4664

References

1. Caballero-Calero, O.; Martín-González, M. *Scr. Mater.* **2016,** *111,* 54. doi:10.1016/j.scriptamat.2015.04.020
2. Pennelli, G. *Beilstein J. Nanotechnol.* **2014,** *5,* 1268. doi:10.3762/bjnano.5.141
3. Gooth, J.; Gluschke, J. G.; Zierold, R.; Leijnse, M.; Linke, H.; Nielsch, K. *Semicond. Sci. Technol.* **2015,** *30,* 015015. doi:10.1088/0268-1242/30/1/015015
4. Bäßler, S.; Hamdou, B.; Sergelius, P.; Michel, A.-K.; Zierold, R.; Reith, H.; Gooth, J.; Nielsch, K. *Appl. Phys. Lett.* **2015,** *107,* 181602. doi:10.1063/1.4935244
5. Peng, H.; Lai, K.; Kong, D.; Meister, S.; Chen, Y.; Qi, X.-L.; Zhang, S.-C.; Shen, Z.-X.; Cui, Y. *Nat. Mater.* **2010,** *9,* 225. doi:10.1038/nmat2609
6. Xiu, F.; He, L.; Wang, Y.; Cheng, L.; Chang, L.-T.; Lang, M.; Huang, G.; Kou, X.; Zhou, Y.; Jiang, X.; Chen, Z.; Zou, J.; Shailos, A.; Wang, K. L. *Nat. Nanotechnol.* **2011,** *6,* 216. doi:10.1038/nnano.2011.19
7. Dufouleur, J.; Veyrat, L.; Teichgräber, A.; Neuhaus, S.; Nowka, C.; Hampel, S.; Cayssol, J.; Schumann, J.; Eichler, B.; Schmidt, O. G.; Büchner, B.; Giraud, R. *Phys. Rev. Lett.* **2013,** *110,* 186806. doi:10.1103/PhysRevLett.110.186806
8. Cho, S.; Dellabetta, B.; Zhong, R.; Schneeloch, J.; Liu, T.; Gu, G.; Gilbert, M. J.; Mason, N. *Nat. Commun.* **2015,** *6,* 7634. doi:10.1038/ncomms8634
9. Jauregui, L. A.; Pettes, M. T.; Rokhinson, L. P.; Shi, L.; Chen, Y. P. *Nat. Nanotechnol.* **2016,** *11,* 345. doi:10.1038/nnano.2015.293
10. Dufouleur, J.; Veyrat, L.; Dassonneville, B.; Xypakis, E.; Bardarson, J. H.; Nowka, C.; Hampel, S.; Schumann, J.; Eichler, B.; Schmidt, O. G.; Büchner, B.; Giraud, R. *Sci. Rep.* **2017,** *7,* 45276. doi:10.1038/srep45276
11. Erlingsson, S. I.; Manolescu, A.; Nemnes, G. A.; Bardarson, J. H.; Sanchez, D. *Phys. Rev. Lett.* **2017,** *119,* 036804. doi:10.1103/PhysRevLett.119.036804
12. Beenakker, C. W. J.; Staring, A. A. M. *Phys. Rev. B* **1992,** *46,* 9667. doi:10.1103/PhysRevB.46.9667
13. Staring, A. A. M.; Molenkamp, L. W.; Alphenaar, B. W.; van Houten, H.; Buyk, O. J. A.; Mabesoone, M. A. A.; Beenakker, C. W. J.; Foxon, C. T. *Europhys. Lett.* **1993,** *22,* 57. doi:10.1209/0295-5075/22/1/011
14. Dzurak, A. S.; Smith, C. G.; Pepper, M.; Ritchie, D. A.; Frost, J. E. F.; Jones, G. A. C.; Hasko, D. G. *Solid State Commun.* **1993,** *87,* 1145. doi:10.1016/0038-1098(93)90819-9
15. Svensson, S. F.; Persson, A. I.; Hoffmann, E. A.; Nakpathomkun, N.; Nilsson, H. A.; Xu, H. Q.; Samuelson, L.; Linke, H. *New J. Phys.* **2012,** *14,* 033041. doi:10.1088/1367-2630/14/3/033041
16. Svensson, S. F.; Hoffmann, E. A.; Nakpathomkun, N.; Wu, P. M.; Xu, H. Q.; Nilsson, H. A.; Sánchez, D.; Kashcheyevs, V.; Linke, H. *New J. Phys.* **2013,** *15,* 105011. doi:10.1088/1367-2630/15/10/105011
17. Sierra, M. A.; Sánchez, D. *Phys. Rev. B* **2014,** *90,* 115313. doi:10.1103/PhysRevB.90.115313
18. Stanciu, A. E.; Nemnes, G. A.; Manolescu, A. *Rom. J. Phys.* **2015,** *60,* 716.
19. Zimbovskaya, N. A. *J. Chem. Phys.* **2015,** *142,* 244310. doi:10.1063/1.4922907
20. Bardarson, J. H.; Brouwer, P. W.; Moore, J. E. *Phys. Rev. Lett.* **2010,** *105,* 156803. doi:10.1103/PhysRevLett.105.156803
21. Zhang, Y.; Vishwanath, A. *Phys. Rev. Lett.* **2010,** *105,* 206601. doi:10.1103/PhysRevLett.105.206601
22. Zhang, Y.-Y.; Wang, X.-R.; Xie, X. C. *J. Phys.: Condens. Matter* **2012,** *24,* 015004. doi:10.1088/0953-8984/24/1/015004
23. Ilan, R.; de Juan, F.; Moore, J. E. *Phys. Rev. Lett.* **2015,** *115,* 096802. doi:10.1103/PhysRevLett.115.096802
24. Xypakis, E.; Bardarson, J. H. *Phys. Rev. B* **2017,** *95,* 035415. doi:10.1103/PhysRevB.95.035415
25. Arango, Y. C.; Huang, L.; Chen, C.; Avila, J.; Asensio, M. C.; Grützmacher, D.; Lüth, H.; Lu, J. G.; Schäpers, T. *Sci. Rep.* **2016,** *6,* No. 29493. doi:10.1038/srep29493
26. Bardarson, J. H.; Moore, J. E. *Rep. Prog. Phys.* **2013,** *76,* 056501. doi:10.1088/0034-4885/76/5/056501
27. Tserkovnyak, Y.; Halperin, B. I. *Phys. Rev. B* **2006,** *74,* 245327. doi:10.1103/PhysRevB.74.245327
28. Ferrari, G.; Goldoni, G.; Bertoni, A.; Cuoghi, G.; Molinari, E. *Nano Lett.* **2009,** *9,* 1631. doi:10.1021/nl803942p
29. Manolescu, A.; Rosdahl, T. O.; Erlingsson, S. I.; Serra, L.; Gudmundsson, V. *Eur. Phys. J. B* **2013,** *86,* 445. doi:10.1140/epjb/e2013-40735-5
30. Chang, C.-H.; Ortix, C. *Int. J. Mod. Phys. B* **2017,** *31,* 1630016. doi:10.1142/S0217979216300164
31. Müller, J. E. *Phys. Rev. Lett.* **1992,** *68,* 385. doi:10.1103/PhysRevLett.68.385
32. Ibrahim, I. S.; Peeters, F. M. *Phys. Rev. B* **1995,** *52,* 17321. doi:10.1103/PhysRevB.52.17321
33. Ye, P. D.; Weiss, D.; Gerhardts, R. R.; Seeger, M.; von Klitzing, K.; Eberl, K.; Nickel, H. *Phys. Rev. Lett.* **1995,** *74,* 3013. doi:10.1103/PhysRevLett.74.3013
34. Zwerschke, S. D. M.; Manolescu, A.; Gerhardts, R. R. *Phys. Rev. B* **1999,** *60,* 5536. doi:10.1103/PhysRevB.60.5536
35. Rickhaus, P.; Makk, P.; Liu, M.-H.; Tóvári, E.; Weiss, M.; Murand, R.; Richter, K.; Schönenberger, C. *Nat. Commun.* **2015,** *6,* 6470. doi:10.1038/ncomms7470
36. Nazarov, Y. V. Quantum transport and circuit theory. In *Handbook of Theoretical and Computational Nanotechnology;* Rieth, M.; Schommers, W., Eds.; American Scientific Publishers, 2005; Vol. 1.
37. Stacey, R. *Phys. Rev. D* **1982,** *26,* 468. doi:10.1103/PhysRevD.26.468
38. Masum Habib, K.; Sajjad, R. N.; Ghosh, A. W. *Appl. Phys. Lett.* **2016,** *108,* 113105. doi:10.1063/1.4943790
39. Ferry, D. K.; Goodnick, S. M. *Transport in Nanostructures;* Cambridge University Press: Cambridge, United Kingdom, 1997.

40. Wu, P. M.; Gooth, J.; Zianni, X.; Svensson, S. F.; Gluschke, J. G.; Dick, K. A.; Thelander, C.; Nielsch, K.; Linke, H. *Nano Lett.* **2013,** *13,* 4080. doi:10.1021/nl401501j
41. Sánchez, D.; López, R. *C. R. Phys.* **2016,** *17,* 1060. doi:10.1016/j.crhy.2016.08.005
42. Sierra, M. A.; Saiz-Bretín, M.; Domínguez-Adame, F.; Sánchez, D. *Phys. Rev. B* **2016,** *93,* 235452. doi:10.1103/PhysRevB.93.235452
43. Torfason, K.; Manolescu, A.; Erlingsson, S. I.; Gudmundsson, V. *Phys. E (Amsterdam, Neth.)* **2013,** *53,* 178. doi:10.1016/j.physe.2013.05.005

License and Terms

BEILSTEIN JOURNAL OF NANOTECHNOLOGY

Inverse proximity effect in semiconductor Majorana nanowires

Alexander A. Kopasov*[1], Ivan M. Khaymovich[1,2] and Alexander S. Mel'nikov[1,3]

Full Research Paper

Open Access

Address:
[1]Institute for Physics of Microstructures, Russian Academy of Sciences, 603950 Nizhny Novgorod, GSP-105, Russia, [2]Max Planck Institute for the Physics of Complex Systems, 01187 Dresden, Germany and [3]Lobachevsky State University of Nizhny Novgorod, 23 Gagarina, 603950 Nizhny Novgorod, Russia

Email:
Alexander A. Kopasov* - kopasov@ipmras.ru

* Corresponding author

Keywords:
inverse proximity effect; Majorana fermions; semiconducting nanowires

Beilstein J. Nanotechnol. **2018,** *9,* 1184–1193.
doi:10.3762/bjnano.9.109

Received: 30 November 2017
Accepted: 09 March 2018
Published: 16 April 2018

This article is part of the Thematic Series "Topological materials".

Guest Editor: J. J. Palacios

Abstract

We study the influence of the inverse proximity effect on the superconductivity nucleation in hybrid structures consisting of semiconducting nanowires placed in contact with a thin superconducting film and discuss the resulting restrictions on the operation of Majorana-based devices. A strong paramagnetic effect for electrons entering the semiconductor together with spin–orbit coupling and van Hove singularities in the electronic density of states in the wire are responsible for the suppression of superconducting correlations in the low-field domain and for the reentrant superconductivity at high magnetic fields in the topologically nontrivial regime. The growth of the critical temperature in the latter case continues up to the upper critical field destroying the pairing inside the superconducting film due to either orbital or paramagnetic mechanism. The suppression of the homogeneous superconducting state near the boundary between the topological and non-topological regimes provides the conditions favorable for the Fulde–Ferrel–Larkin–Ovchinnikov instability.

Introduction

The transport phenomena in semiconducting wires with induced superconducting ordering and strong spin–orbit interaction are in the focus of current experimental and theoretical research in field of nanophysics and quantum computing [1-10]. The interest in these systems is stimulated by the perspectives of their use for design of topologically protected quantum bits. The key idea is based on the observation that for a certain range of parameters and rather strong applied magnetic fields H the induced superconducting order parameter reveals so called p-wave symmetry realizing, thus, a model of Kitaev's chain [1]. The edges of such wires can host the subgap quasiparticle states that are considered as a realization of Majorana particles in condensed matter systems [11-16].

In most cases, theoretical studies of these Majorana wires are based on a simplified model of the superconducting correlations described by a phenomenological gap potential inside the wire [3,4] placed in contact with a standard s-wave superconductor (Figure 1). This model, while being useful in many cases for a qualitative understanding of the induced superconduc-

tivity, is known to possess still a number of important shortcomings. An obvious way to overcome these shortcomings is to use the microscopic theory of the proximity effect [17-24], i.e., Gor'kov equations. The microscopic approach allows one to get the effective gap operator analogous to the one used in the phenomenological model. On top of that it gives the gap dependence on the transparency of the interface between the wire and the s-wave superconductor and chemical potential via density of states (DOS). Another important point is that the exchange of electrons between the wire and superconductor can cause a so-called inverse proximity effect, i.e., the suppression of the gap function at the superconductor surface. For a rather thin superconducting shell covering the wire this gap suppression can result in the change of the superconducting critical temperature of the whole system. The analysis of this inverse proximity phenomenon is important to find out the optimal range of parameters that allows one to realize the switching between the topologically trivial and nontrivial states of the semiconducting wire used in various braiding protocols.

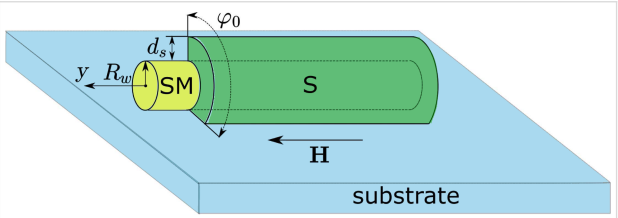

Figure 1: Schematic picture of the semiconducting wire (yellow) covered by the superconducting layer (green) placed on a substrate (light blue). R_w, d_s and φ_0 show linear and azimuthal dimensions. The magnetic field H is applied along the wire axis Oy while the Rashba spin–orbit vector is perpendicular to the substrate (not shown).

The goal of this work is the self-consistent analysis of the critical-temperature behavior of the wires while considering the influence of the inverse proximity effect on the induced superconducting ordering. For this purpose we start from the full set of microscopic equations for the Green functions taking into account both scattering rates describing the quasiparticle transfer between the superconducting film and the wire [17]. The first rate, γ_s, characterizes the electron leakage from the wire to the superconductor and is responsible for the energy-level broadening in the wire. The second rate, γ_w, corresponds to the reverse process. These rates are determined both by the probability of electron tunneling through the barrier at the superconductor/semiconductor (S/SM) interface and the corresponding densities of states. In particular, it is important that the rate γ_w is proportional to the DOS in the SM nanowire resulting in its non-trivial energy dependence. Indeed, considering, e.g., a single-channel nanowire we get the DOS diverging as a square root function of the energy relative to the bottom of the conduction band. This van Hove singularity in the DOS should cause a strong energy dependence of the scattering rate γ_w and, as a consequence, the superconducting critical temperature should depend on the position of the Fermi level with respect to the bottom of the one-dimensional conduction band in the SM wire. The influence of the van Hove singularity on superconductivity should be also accompanied by the strengthening of the paramagnetic effect. Indeed, one can naturally expect that the scattering rate γ_w could result in an additional effective Zeeman field induced in the superconductor due to the electron exchange with the SM wire. Due to the divergence in the DOS together with the large g-factor in the wire this induced Zeeman field can even exceed the value of the usual Zeeman field. Under such conditions the field dependence of the critical temperature would have a minimum near the fields $H \approx |\mu_w|/g\beta$, where μ_w is the Fermi energy of the wire relative to the bottom of its conduction band at $H = 0$ and β is the Bohr magneton. Strictly speaking, the spin–orbit interaction may cause the emergence of the third van Hove singularity below $-g\beta H/2$, but it appears only at rather large spin–orbit interaction strengths. Note that for a vanishing induced superconducting gap Δ_{ind} this field separates the regimes with trivial and nontrivial topological properties of the system [3,4,18]. Further increase in the magnetic field is known to suppress the proximity effect since in the absence of the spin–orbit coupling the Fermi level crosses the only energy branch with a complete spin polarization along the magnetic field direction. The nonzero spin–orbit coupling destroys this spin polarization mixing different spin projections and resulting in a nonzero induced superconducting gap in the wire of approximately $\alpha\Delta_{\text{ind}}/g\beta H$, where Δ_{ind} is the induced superconducting order parameter in the wire, and α is the spin–orbit coupling constant. Still, even in the presence of the spin–orbit coupling the increasing magnetic field suppresses the induced superconductivity, which definitely restores the superconducting order parameter in the S film. This reentrant superconductivity stimulated by the magnetic field can only be maintained up to the upper critical field associated with either orbital or intrinsic paramagnetic effect in the S shell.

The suppression of the superconducting order parameter near the line of transition between the topologically trivial and nontrivial phases can result in one more interesting phenomenon: Similarly to the standard paramagnetic effect this suppression can cause the transition into the analogue of the so-called Fulde–Ferrel–Larkin–Ovchinnikov (FFLO) [25,26] state with the spatially modulated superconducting order parameter.

The paper is organized as follows: In section “Basic equations” we give the main equation of our model. Section “Results and Discussion” is devoted to the description of the solution and the analysis of the phase diagrams. In the Conclusion section we summarize our results and the suggestions for the experiment.

Basic Equations

Hereafter we consider a long 1D semiconducting wire partially covered by a thin superconducting shell with the thickness $d_s \ll \xi_s$, where ξ_s is the superconducting coherence length. In the cross section of the wire the superconducting film covers the angular sector φ_0. The model system is schematically shown in Figure 1. Hereafter we use the units with $k_B = \hbar = 1$, where k_B is the Boltzmann constant, and $\hbar$ is the Planck constant. The Hamiltonian of the system reads:

$$\mathcal{H} = \mathcal{H}_s + \mathcal{H}_w + \mathcal{H}_t \,, \tag{1}$$

with the first term

$$\mathcal{H}_s = d_s R_w \int \mathrm{d}y\, \mathrm{d}\varphi \Big[\psi^\dagger_\sigma(\mathbf{r})\varepsilon_s(\mathbf{r})\psi_\sigma(\mathbf{r}) + \Delta_s(\mathbf{r})\psi^\dagger_\uparrow(\mathbf{r})\psi^\dagger_\downarrow(\mathbf{r}) + \Delta^*_s(\mathbf{r})\psi_\downarrow(\mathbf{r})\psi_\uparrow(\mathbf{r})\Big], \tag{2}$$

describing the s-wave superconducting shell.

$$\mathcal{H}_w = S_w \int \mathrm{d}y\, a^\dagger_\sigma(y)\Big[\varepsilon_w(y) - i\alpha\hat{\sigma}_x\partial_y + h\hat{\sigma}_y\Big]_{\sigma\sigma'} a_{\sigma'}(y) \tag{3}$$

corresponds to the Hamiltonian of the nanowire, and the tunnel Hamiltonian takes the form

$$\mathcal{H}_t = \sqrt{d_s R_w S_w} \int \mathrm{d}y\, \mathrm{d}\varphi \Big[\psi^\dagger_\sigma(\varphi, y)\mathcal{T}(\varphi, y)a_\sigma(y) + a^\dagger_\sigma(y)\mathcal{T}^\dagger(\varphi, y)\psi_\sigma(\varphi, y)\Big]. \tag{4}$$

Here σ = ↑, ↓ denotes spin degrees of freedom (summation over repeated spin indices is always assumed throughout the paper), while $\hat{\sigma}_m$ ($m = x, y, z$) are the Pauli matrices in the spin space. R_w is the radius and $S_w = \pi R_w^2$ is the cross-sectional area of the wire, $(\mathbf{r}) = (R_w, \varphi, y)$, φ is the polar angle in the plane perpendicular to the wire axis, which changes in the interval $0 < \varphi < \varphi_0$. y denotes the coordinate along the wire, $\varepsilon_s(\mathbf{r}) = -\nabla^2_{\mathbf{r}}/2m_s - \mu_s$ and $\varepsilon_w(y) = -\partial^2_y/2m_w - \mu_w$ stand for the quasiparticle kinetic energies in the shell and in the wire with respect to the corresponding chemical potentials μ_s and μ_w. m_s and m_w are the effective masses of the electrons in the subsystems, $\Delta_s(\mathbf{r})$ is the superconducting order parameter, α is the spin–orbit coupling constant, $h = g\beta H/2$ is the Zeeman energy, and H is the applied magnetic field.

We consider the incoherent tunneling model, which does not conserve the momentum, e.g., due to the presence of the disorder at the interface. Thus, the ensemble average of the tunneling amplitudes has the form:

$$\overline{\mathcal{T}(\mathbf{r})\mathcal{T}(\mathbf{r}')} = t^2 \ell_c \delta(y - y')\delta(\varphi - \varphi'), \tag{5}$$

where ℓ_c is the length of the order of the atomic scale. The tunneling is also assumed to be independent of energy and spin and occurs locally in time and in space, i.e., from a point **r** on the superconducting shell into the point y in the wire and back with the amplitude $\mathcal{T}(\mathbf{r})$.

It is important to note that here we do not consider the orbital effects in the superconducting shell. This approximation imposes some restrictions on the value of magnetic fields under consideration, which are nevertheless quite realistic for the experiments aimed at the manipulation with Majorana states in such systems. It is the large g-factor in the SM wire that allows to have the magnetic field values affecting the electronic states in the wire and barely affecting the ones in the superconducting cover. Note that omitting the orbital effects we cannot describe possible Little–Parks effect arising in the wires fully covered by the S shell [27,28].

Neglecting the order parameter inhomogeneity in the shell for $d_s \ll \xi_s$, we derive the following system of Gor'kov equations written in the frequency–momentum representation (see Supporting Information File 1 for the details of the derivation):

$$\big(i\omega_n - \varepsilon_s\check{\tau}_z + \check{\Delta} - \check{\Sigma}_s\big)\check{G}_s = \check{1}, \tag{6}$$

$$\big(i\omega_n - \varepsilon_w\check{\tau}_z - \alpha p_y\hat{\sigma}_x - h\hat{\sigma}_y - \check{\Sigma}_w\big)\check{G}_w = \check{1}, \tag{7}$$

where $\omega_n = 2\pi T(n + 1/2)$ is the Matsubara frequency, T is the temperature, p_y is the momentum along the wire, $\check{\tau}_m$ ($m = x, y, z$) are the Pauli matrices acting in the Nambu space, $\check{\Delta} = (\hat{\Delta}\check{\tau}_+ + \hat{\Delta}^\dagger\check{\tau}_-)$, $\hat{\Delta} = \Delta_s(i\hat{\sigma}_y)$, Δ_s is the superconducting order parameter, which we assume to be constant in space and real-valued, $\check{\tau}_\pm = (\check{\tau}_x \pm i\check{\tau}_y)/2$, and $\varepsilon_w = p_y^2/2m_w - \mu_w$. The tunneling self-energy parts are given by the following expression:

$$\check{\Sigma}_{s(w)} = \Gamma_{w(s)}\,\check{\tau}_z\,\check{g}_{w(s)}\,\check{\tau}_z \,, \tag{8}$$

where $\Gamma_s = t^2\ell_c R_w m_s \varphi_0/2$ and $\Gamma_w = t^2\ell_c/2\upsilon_0$. The functions $\check{g}_{s(w)}$ are the quasiclassical Green's functions:

$$\check{g}_s = \frac{1}{\pi}\int \mathrm{d}\varepsilon_s\, \check{G}_s(\omega_n, \varepsilon_s), \tag{9}$$

$$\check{g}_w = \frac{\upsilon_0}{\pi}\int \mathrm{d}p_y\, \check{G}_w\left(\omega_n, p_y\right). \tag{10}$$

The precise definitions of the Green's functions $\check{G}_{w,s}$ of the wire and of the shell, respectively, together with the derivation of Equation 6 and Equation 7 are given in Supporting Information File 1.

Note that we neglect here the possible dependence of these quasiclassical Green's functions on the coordinate along the wire. That is, we assume the limit of an infinitely long wire without edge effects. The velocity υ_0 is introduced just for the purpose of unification of dimensionality of the tunneling rates Γ_w and Γ_s and does not appear in the product $\Gamma_w \check{g}_w$ that enters the measurable quantities. One can choose this velocity, e.g., as $\upsilon_0 = \sqrt{2\mu_w / m_w}$ so that the rate Γ_w includes the divergent DOS in the 1D wire.

Tunneling rates for the quasiparticles from the shell into the wire, Γ_w, and from the wire into the shell, Γ_s, can be expressed in terms of the normal-state tunnel resistance $\mathcal{R}$ in the following manner [20]:

$$\Gamma_w = \frac{1}{4\pi\mathcal{R}SG_0\nu_s} \propto \mu_s \frac{\mathcal{R}_0}{\mathcal{R}}\frac{k_{Fw}}{k_{Fs}}\frac{1}{\left(k_{Fs}R_w\right)}, \tag{11}$$

$$\Gamma_s = \frac{1}{4\pi\mathcal{R}\ell_w G_0\nu_w} \propto \mu_w \frac{\mathcal{R}_0}{\mathcal{R}}, \tag{12}$$

where $S = 2\pi R_w \ell_w$ is the contact area, ℓ_w is the wire length, $G_0 = e^2/\pi$ is the conductance quantum, $\nu_s = m_s/2\pi$ and $\nu_w = (2m_w/\mu_w)^{1/2}$ are the normal DOS in the shell and in the wire, respectively, $\mathcal{R}_0 = (NG_0)^{-1}$, $N = k_{Fw}\ell_w$, and $k_{Fs(w)}$ is the Fermi momentum in the shell (wire). The expressions for the tunneling rates can be conveniently written through the numbers of transverse modes in the superconducting shell ($N_s \approx k_{Fs}^2 d_s R_w \varphi_0$) and in the wire ($N_w$):

$$\Gamma_s \approx t^2 \ell_c \frac{N_s}{\upsilon_{F_s}}, \tag{13}$$

$$\Gamma_w \approx t^2 \ell_c \frac{N_w}{\upsilon_0}, \tag{14}$$

where $\upsilon_{F_s} = k_{F_s}/m_s$. Here we use the simplest generalization [17] of the expression for Γ_w for the case of an arbitrary number of transverse modes in the nanowire assuming also the value $1/\upsilon_0$ to be averaged over these modes. The resulting ratio of the tunneling rates takes the form:

$$\frac{\Gamma_w}{\Gamma_s} \approx \frac{N_w}{N_s}\frac{\upsilon_{F_s}}{\upsilon_0}. \tag{15}$$

Due to the growth of N_s with the shell thinkness d_s in the multimode regime of the superconductor this ratio may become rather small weakening the inverse proximity effect (the details of experimental relevance are considered in the next section).

Equation 6 and Equation 7 must be solved together with the self-consistency equation for the superconducting gap function:

$$\Delta_s^* = \frac{\lambda\pi T}{2}\sum_{\omega_n}\mathrm{Tr}\left[\left(\check{g}_s\right)_{21}\left(i\hat{\sigma}_y\right)\right], \tag{16}$$

where λ is the dimensionless pairing constant and the trace is taken over the spin indices. The next section is devoted to the perturbative solution of the Gor'kov equations (Equation 6 and Equation 7) and the self-consistency equation (Equation 16) in the gap potential which allows one to find the critical temperature of superconducting transition as a function of magnetic field and materials parameters.

Results and Discussion

Considering the perturbation theory in the superconducting gap function Δ_s it is natural to start with the equations for the normal Green's functions

$$\left(i\omega_n - \varepsilon_s - \Gamma_w\hat{g}_w\right)\hat{G}_s = \hat{1}, \tag{17}$$

$$\left(i\omega_n + \varepsilon_s - \Gamma_w\hat{\tilde{g}}_w\right)\hat{\tilde{G}}_s = \hat{1}, \tag{18}$$

$$\left(i\omega_n - \varepsilon_w - \alpha p_y\hat{\sigma}_x - h\hat{\sigma}_y - \Gamma_s\hat{g}_s\right)\hat{G}_w = \hat{1}, \tag{19}$$

$$\left(i\omega_n + \varepsilon_w - \alpha p_y\hat{\sigma}_x - h\hat{\sigma}_y - \Gamma_s\hat{\tilde{g}}_s\right)\hat{\tilde{G}}_w = \hat{1}, \tag{20}$$

which give us the zero-order solution of the Gor'kov equations

$$\hat{G}_s = \frac{i\omega_n - \varepsilon_s - \Gamma_w g_{w0} + \Gamma_w \mathbf{g}_w\hat{\boldsymbol{\sigma}}}{\left(i\omega_n - \varepsilon_s - \Gamma_w g_{w0}\right)^2 - \left(\Gamma_w\mathbf{g}_w\right)^2}, \tag{21}$$

$$\hat{G}_w = \frac{i\omega_n - \varepsilon_w - \Gamma_s g_{s0} + \mathbf{U}_w\hat{\boldsymbol{\sigma}}}{\left(i\omega_n - \varepsilon_w - \Gamma_s g_{s0}\right)^2 - \mathbf{U}_w^2}. \tag{22}$$

Here, $\mathbf{U}_w = [(\alpha p_y + \Gamma_s g_{sx}), (h + \Gamma_s g_{sy}), \Gamma_s g_{sz}]$ and the quasiclassical Green's functions are written in the spin form

$$\hat{g}_k = g_{k0} + \mathbf{g}_k \hat{\boldsymbol{\sigma}}, \tag{23}$$

with $k = s(w)$ for the shell (wire). The solutions for spin matrix functions $\hat{\bar{G}}_k$ are given by Equation 21 and Equation 22 with the replacements $\varepsilon_k \to -\varepsilon_k$ and $\hat{g}_k \to \hat{\bar{g}}_k$.

According to the definitions for the quasiclassical Green's functions (Equation 9 and Equation 10) and due to a specific spin structure of the Zeeman term and spin–orbit coupling term in Equation 17–Equation 20, one can easily get that only g_{k0} and g_{ky} are nonzero. It is convenient to rewrite the normal Green's function in the wire as a sum of singular contributions $G_w^{p\pm}$:

$$\begin{aligned}\hat{G}_w = &\frac{(\varepsilon_{so}+\varepsilon_0)G_w^{p+} - (\varepsilon_{so}-\varepsilon_0)G_w^{p-}}{2\varepsilon_0} \\ &- \frac{\left(G_w^{p+} - G_w^{p-}\right)}{2\varepsilon_0}\left(\alpha p_y \hat{\sigma}_x + h\hat{\sigma}_y\right),\end{aligned} \tag{24}$$

$$\begin{aligned}\hat{\bar{G}}_w = &\frac{-\left(\varepsilon_{so}-\varepsilon_0^*\right)\bar{G}_w^{p+} + \left(\varepsilon_{so}+\varepsilon_0^*\right)\bar{G}_w^{p-}}{2\varepsilon_0^*} \\ &- \frac{\left(\bar{G}_w^{p+} - \bar{G}_w^{p-}\right)}{2\varepsilon_0^*}\left(\alpha p_y \hat{\sigma}_x + h\hat{\sigma}_y\right),\end{aligned} \tag{25}$$

where

$$\begin{aligned}G_w^{p\pm} &= \left(i\bar{\omega}_n - \varepsilon_w + \varepsilon_{so} \pm \varepsilon_0\right)^{-1}, \\ \bar{G}_w^{p\pm} &= -\left(G_w^{p\mp}\right)^*, \\ \varepsilon_0 &= \sqrt{2\varepsilon_{so}\left(\mu_w + i\bar{\omega}_n\right) + \varepsilon_{so}^2 + h^2}, \\ \varepsilon_{so} &= m_w\alpha^2 \quad \text{and} \\ \bar{\omega}_n &= \omega_n + \Gamma_s \operatorname{sign}(\omega_n).\end{aligned}$$

The equations for the anomalous Green's functions read:

$$\left(i\omega_n + \varepsilon_s - \Gamma_w \hat{\bar{g}}_w\right)\hat{F}_s^\dagger = -\left(\hat{\Delta}^\dagger + \Gamma_w \hat{f}_w^\dagger\right)\hat{G}_s, \tag{26}$$

$$\left(i\omega_n + \varepsilon_w - \alpha p_y \hat{\sigma}_x - h\hat{\sigma}_y - \Gamma_s \hat{\bar{g}}_s\right)\hat{F}_w^\dagger = -\Gamma_s \hat{f}_s^\dagger \hat{G}_w, \tag{27}$$

and give the solution for the anomalous Green's functions $\hat{F}_k^\dagger$ within the first-order perturbation theory in the superconducting gap:

$$\hat{F}_s^\dagger = -\hat{\bar{G}}_s\left(\hat{\Delta}^\dagger + \Gamma_w \hat{f}_w^\dagger\right)\hat{G}_s, \tag{28}$$

$$\hat{F}_w^\dagger = -\hat{\bar{G}}_w \Gamma_s \hat{f}_s^\dagger \hat{G}_w\,. \tag{29}$$

Introducing a general presentation for the components of the quasiclassical anomalous Green's functions

$$\hat{f}_k^\dagger = -i\hat{\sigma}_y\left(f_{k0}^\dagger + \mathbf{f}_k^\dagger \hat{\boldsymbol{\sigma}}\right), \tag{30}$$

we get the set of equations in Equation 31 for them with $f_{sx}^\dagger = f_{sz}^\dagger = 0$.

The solutions of Equation 31 take the form given in Equation 32 and Equation 33.

We use the following notations:

$$\begin{aligned}I_{\nu\eta}^w &= \int \frac{\mathrm{d}p_y}{\pi}\bar{G}_w^{p\nu}G_w^{p\eta} \\ &= \frac{\bar{g}_w^{p\nu} + g_w^{p\eta}}{2i\bar{\omega}_n + \nu\varepsilon_0^* + \eta\varepsilon_0},\end{aligned} \tag{34}$$

$$\begin{pmatrix} -1+\gamma\left[I_{sy}I_{wy} + I_{s0}(I_{w0} - I_{wx})\right] & \gamma\left[I_{s0}I_{wy} + I_{sy}(I_{w0} + I_{wx})\right] \\ \gamma\left[I_{s0}I_{wy} + I_{sy}(I_{w0} - I_{wx})\right] & -1+\gamma\left[I_{sy}I_{wy} + I_{s0}(I_{w0} + I_{wx})\right] \end{pmatrix}\begin{pmatrix} f_{s0}^\dagger \\ f_{sy}^\dagger \end{pmatrix} = \Delta_s \begin{pmatrix} I_{s0} \\ I_{sy} \end{pmatrix}. \tag{31}$$

$$f_{s0}^\dagger = -\Delta_s \frac{\left[I_{s0} - \gamma\left(I_{w0} + I_{wx}\right)\left(I_{s0}^2 - I_{sy}^2\right)\right]}{\left[1 - 2\gamma\left(I_{s0}I_{w0} + I_{sy}I_{wy}\right) + \gamma^2\left(I_{s0}^2 - I_{sy}^2\right)\left(I_{w0}^2 - I_{wx}^2 - I_{wy}^2\right)\right]} \tag{32}$$

$$f_{sy}^{\dagger} = -\Delta_s \frac{\left[I_{sy} + \gamma I_{wy}\left(I_{s0}^2 - I_{sy}^2\right)\right]}{\left[1 - 2\gamma\left(I_{s0}I_{w0} + I_{sy}I_{wy}\right) + \gamma^2\left(I_{s0}^2 - I_{sy}^2\right)\left(I_{w0}^2 - I_{wx}^2 - I_{wy}^2\right)\right]} \tag{33}$$

$$I_{\nu\eta}^{wx} = \int \frac{dp_y}{\pi}\frac{p_y^2}{2m_w}\bar{G}_w^{p\nu}G_w^{p\eta} = \frac{\bar{g}_w^{p\nu}\left(-i\bar{\omega}_n - \nu\varepsilon_0^* + \mu_w + \varepsilon_{so}\right)}{\left(2i\bar{\omega}_n + \eta\varepsilon_0 + \nu\varepsilon_0^*\right)} + \frac{+g_w^{p\eta}\left(i\bar{\omega}_n + \eta\varepsilon_0 + \mu_w + \varepsilon_{so}\right)}{\left(2i\bar{\omega}_n + \eta\varepsilon_0 + \nu\varepsilon_0^*\right)}, \tag{35}$$

$$I_{wx} = \sum_{\nu,\eta=\pm1}\nu\eta\frac{\varepsilon_{so}I_{\nu\eta}^{wx}}{2\left|\varepsilon_0\right|^2}, \tag{36}$$

$$I_{w0} = \sum_{\nu,\eta=\pm1}\left[\left(\varepsilon_0^* - \nu\varepsilon_{so}\right)\left(\varepsilon_0 + \eta\varepsilon_{so}\right) + h^2\nu\eta\right]\frac{I_{\nu\eta}^{w}}{4\left|\varepsilon_0\right|^2}, \tag{37}$$

$$I_{wy} = \sum_{\nu,\eta=\pm1}\left(\eta\varepsilon_0^* + \nu\varepsilon_0\right)\frac{(-h)I_{\nu\eta}^{w}}{4\left|\varepsilon_0\right|^2}. \tag{38}$$

In addition, ν, η = ±1. The expressions for the integrals involving the products of the normal Green's functions in the shell can be written as follows:

$$I_{s0} = I_{s+} + I_{s-}, \tag{39}$$

$$I_{sy} = I_{s+} - I_{s-}, \tag{40}$$

$$I_{s\eta} = \int \frac{\mathrm{d}\varepsilon_s}{(2\pi)}\bar{G}_{s\eta}G_{s\eta} = \frac{1}{2}\frac{\left(\bar{g}_{s\eta} + g_{s\eta}\right)}{\left[2i\omega_n - \Gamma_w\left(\bar{g}_{w\eta} + g_{w\eta}\right)\right]}. \tag{41}$$

In the definitions in Equation 34 and Equation 35 and Equation 39–Equation 41, we have introduced the following functions:

$$\bar{g}_{s\eta} = g_{s\eta} = g_{s0} = -i\,\mathrm{sign}\left(\omega_n\right), \quad g_{sy} = 0, \tag{42}$$

$$g_w^{p\eta} = -2i\sqrt{\frac{m_w}{2}}\frac{\mathrm{sign}\left(\bar{\omega}_n + \eta\varepsilon_I\right)}{\sqrt{\eta\varepsilon_0 + \mu_w + \varepsilon_{so} + i\bar{\omega}_n}}. \tag{43}$$

Here, $g_{k\eta} = (g_{k0} + \eta g_{ky})$, $\bar{g}_w^{p\eta} = -[g_w^{p(-\eta)}]^*$, and $\varepsilon_I = \mathrm{Im}(\varepsilon_0)$. Finally, we explicitly show the expressions for the normal Green's functions in the wire:

$$g_{w0} = -i\sqrt{\frac{m_w}{2}}\sum_{\eta=\pm1}\frac{\left(\varepsilon_0 + \eta\varepsilon_{so}\right)\mathrm{sign}\left(\bar{\omega}_n + \eta\varepsilon_I\right)}{\varepsilon_0\sqrt{\eta\varepsilon_0 + \mu_w + \varepsilon_{so} + i\bar{\omega}_n}}, \tag{44}$$

$$g_{wy} = ih\sqrt{\frac{m_w}{2}}\sum_{\eta=\pm1}\frac{\eta\,\mathrm{sign}\left(\bar{\omega}_n + \eta\varepsilon_I\right)}{\varepsilon_0\sqrt{\eta\varepsilon_0 + \mu_w + \varepsilon_{so} + i\bar{\omega}_n}}. \tag{45}$$

Note that in the absence of spin–orbit coupling, zero magnetic field and for energy-independent DOS in the wire the self-consistency equation formally coincides with the one obtained in the seminal work by McMillan [17].

Turning now to the case of nonzero Zeeman energy and spin–orbit coupling we use a numerical approach to analyze the solution of the self-consistency Equation 16 with the Equation 32 and Equation 33 for the anomalous Green function. Typical dependencies of the critical superconducting temperature on the magnetic field and chemical potential μ_w are shown in Figure 2. Note that here we choose the strength of the spin–orbit coupling consistent with the properties of InAs [22]: $\varepsilon_{so} = m_w\alpha^2 = 52$ μeV, which corresponds to approximately 600 mK. Taking the critical temperature of Al $T_{c0} \approx 1.3$ K, we find $\varepsilon_{so} = m_w\alpha^2 = 0.46T_{c0}$.

The color plots in Figure 2 show the critical temperature T_c both in topologically trivial ($|\mu_w| > h$) and nontrivial ($|\mu_w| < h$) regimes. The border lines $\mu_w = \pm h$ (shown by white dashed lines) coincide with the locations of van Hove singularities in the SM nanowire. One can clearly see that the suppression of the critical temperature appears to be the strongest close to these lines. The magnetic field dependence of T_c appears to be drastically different in topologically trivial and nontrivial regimes. Indeed, in the nontopological regime the critical temperature decays as we increase the magnetic field due to a standard paramagnetic effect. In contast, in the topologically nontrivial regime T_c increases (with or without initial decay at small fields). This increase in the critical temperature originates from the reduction of the proximity effect due to almost pure spin polarization of quasiparticles in the wire. The above mentioned increase in the critical temperature is limited from above by either orbital or intrinsic paramagnetic effects in the S shell and

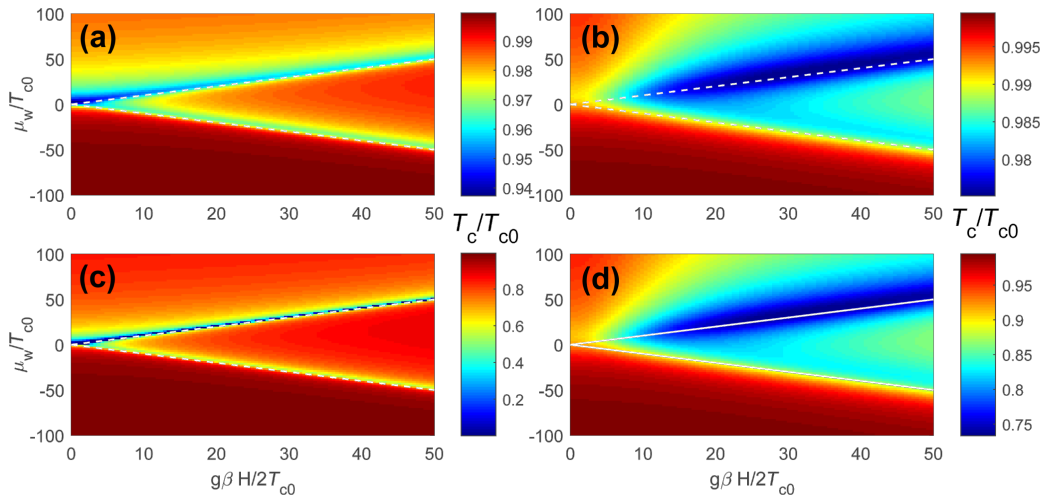

Figure 2: Color plot of the critical temperature of the system as a function of the chemical potential μ_w and the Zeeman energy $h = g\beta H/2$ for $\varepsilon_{so} = m_w\alpha^2 = 0.46T_{c0}$ and several values of $\Gamma_s = t^2\ell_c R_w m_s \varphi_0 / 2$ and $\Gamma_w = t^2\ell_c / 2\upsilon_0$ with $\upsilon_0 = \sqrt{2T_{c0} / m_w}$. In panels (a) and (b) $\Gamma_w = 0.1T_{c0}$, while in panels (c) and (d) we take $\Gamma_w = T_{c0}$. In panels (a) and (c) $\Gamma_s = 0.1T_{c0}$, in panels (b) and (d) $\Gamma_s = 10T_{c0}$. In all panels the white dashed lines denote the boundaries between nontopological and topological regimes $\mu_w = \pm h$.

continues up to the upper critical field in the superconductor. One can see that the scattering rates Γ_w and Γ_s have a strong quantitative effect on the above physical picture because of smearing and shifting of the peculiarities of the DOS and the resulting smoothing of T_c variations. The nonmonotonic behavior of T_c is illustrated by the plots in Figure 3. Using the above expressions in Equation 13–Equation 15 for the tunneling rates, we estimate the ratio of mode numbers as $N_w/N_s \approx 10^{-5}$–10^{-4} for typical Majorana nanowires [11-16]. Taking into account the decrease of the υ_0 value close to the van Hove singularity ($\upsilon_{F_s}/\upsilon_0 \approx 10^2$–$10^3$), we get $\Gamma_w/\Gamma_s \approx 10^{-3}$–$10^{-1}$. Assuming strong coupling between the nanowire and superconducting shell with $\Gamma_s \geq T_{c0}$, we get $\Gamma_w \approx (10^{-3}$–$10^{-1})T_{c0}$. Note that under realistic experimental conditions the number of modes in the wire (N_w) can increase due to the formation of the accumulation layer near the superconductor–semiconductor interface [29-31]. However, the increase of the shell thickness d_s may weaken the effect in the multimode regime of the superconductor. Overall, such estimate allows us to expect that the consequences of the inverse proximity effect analyzed in our paper can be observed experimentally.

It is worth noting that the $T_c(h)$ plot in the Figure 3a clearly demonstrates the appearance of h regions where the linearized self-consistency equation has three solutions instead of one. In other words, there can exist three critical temperatures corresponding to a given magnetic field. This is evidence for the fact that although the superconducting shell has a small g-factor, the indirectly superconducting region is affected by effective Zeeman field through tunneling. The presence of several solu-

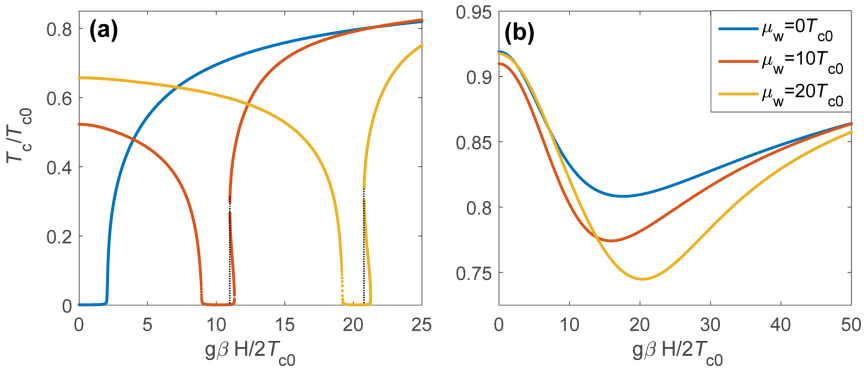

Figure 3: The critical temperature of the system as a function of the Zeeman field h for different values of the chemical potential in the wire μ_w (shown in the legend). Here, $\varepsilon_{so} = 0.46T_{c0}$ and $\Gamma_w = T_{c0}$. (a) $\Gamma_s = 0.1T_{c0}$ and (b) $\Gamma_s = 10T_{c0}$.

tions for T_c is typical for the standard paramagnetic effect in superconductors and usually this behavior results in the FFLO instability of the homogeneous solution for the gap function [32]. To verify this scenario in our system we have solved a self-consistency equation for the modulated order parameter $\Delta_s \propto e^{iqy}$ and found that the regions with several solutions for T_c for the homogeneous gap can, indeed, host an energetically more favorable inhomogeneous FFLO gap function. The critical temperature $T_c(q)$ for different q values can be seen in Figure 4. As we increase the h value from $h = 10.8$ to $h = 11.05$ the q value corresponding to the maximal T_c changes from $k_{Fs}q/m_s = T_{c0}$ to $k_{Fs}q/m_s = 0.44T_{c0}$. It is important to note that as we solve the linearized equation for the superconducting gap, we find, of course, only the critical temperatures corresponding to the second-order phase transitions. Changing the period of the gap modulation of the FFLO-type we also find only the temperatures corresponding to the second-order phase transition. The physical picture can become more complicated if one takes into account possible first-order transitions corresponding to the interplay between different local minima of the thermodynamic potential in the nonlinear regime. However, the solution of nonlinear gap equations is beyond the scope of the current work and needs further investigations. Note also that the possible FFLO phase appears on either side of topological transition ($h^2 = \mu_w^2 + \Delta_{\text{ind}}^2$) depending on the sign of the chemical potential μ_w. Indeed, in general the temperature as a formal solution of the self-consistency Equation 16 is not a single-valued function of the magnetic field in the regions $h \geq \pm\mu_w$ slightly above the positions of van Hove singularities, being inside the topological (trivial) regime for the upper (lower) sign. In experimentally feasible cases of considered $\Gamma_{s,w}$ (Figure 2) the upper singularity at $\mu_w = h$ is more pronounced (Figure 3). Additionally, an accurate analysis of the FFLO state should include careful consideration of the modulation of the superconducting order parameter both along the wire and in the azimuthal direction [27,28].

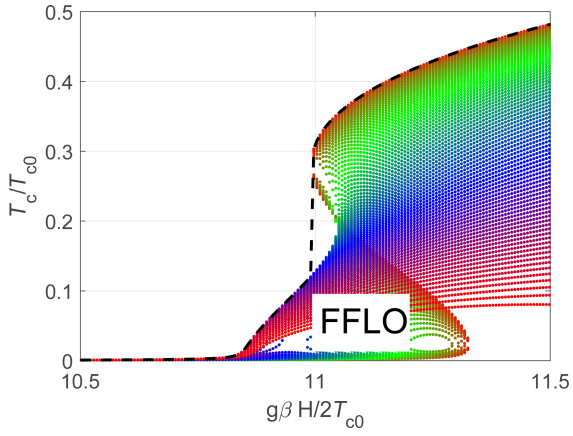

Figure 4: Critical temperature of the system as a function of the Zeeman field h for $\varepsilon_{so} = 0.46T_{c0}$, $\Gamma_s \to 0$ and $\Gamma_w = T_{c0}$ for the superconducting states with different modulation vectors q ranging from $q = 0.44m_sT_{c0}/k_{Fs}$ at $h = 11.05T_{c0}$ to $q = m_sT_{c0}/k_{Fs}$ at $h = 10.8T_{c0}$.

Before we conclude, we discuss briefly the influence of the inverse proximity effect on the effective induced gap operator Δ_{top} in the topological regime, $h^2 > \mu_w^2 + \Delta_{\text{ind}}^2$, which is of crucial importance for topological superconducting electronics and topologically protected fault-tolerant quantum computing. In our estimates we take the standard limit of $\mu_w = 0$ for the sake of simplicity. First, the increase of Γ_w reduces the parameter range of the topological insulator regime $\alpha p \gg h$ as the magnetic field should well exceed Γ_w to avoid the suppression of the critical temperature due to the van Hove singularities (see Figure 2a,c for small Γ_s values). As soon as Γ_w becomes comparable with αp with the typical quasiparticle momentum $p \simeq \sqrt{2m_w h}$ this regime completely disappears. Further increase of the scattering rate should suppress the gap $\Delta_{top} \propto \alpha p \Delta_{\text{ind}} / h$ in the Kitaev limit. Indeed, for $\Gamma_w > m_w\alpha^2 = \varepsilon_{so}$ its value is limited from above by the quantity $\Delta_{top} \approx \Delta_{\text{ind}}(\varepsilon_{so}/\Gamma_w)^{1/2} < \Delta_{\text{ind}}$. Such decrease in the attainable induced gap values imposes more strict conditions on working temperatures for Majorana-based devices, due to quasiparticle poisoning as the residual quasiparticle density is exponentially sensitive to the gap values [33-36]. Of course, at large values of Γ_s (see Figure 2b,d) the van Hove singularities are smeared and the critical temperature (together with the gap value) is suppressed only partially. However, even the partial suppression up to tens of percents may drastically increase the effect of quasiparticle poisoning mentioned above.

Conclusion

We have studied the distinctive features of the inverse proximity effect arising in the presence of a large Zeeman energy and strong spin–orbit coupling in the hybrid systems consisting of the SM nanowires covered by thin superconducting films. Assuming a strong difference in g-factors between the wire and superconducting metal we find the range of parameters and fields corresponding to the FFLO instability and the regime of reentrant superconductivity. We focus on the topologically nontrivial regime of relatively large magnetic fields and analyze consequences of the inverse proximity effect on the quasiparticle poisoning in Majorana-based devices.

Supporting Information

Supporting Information File 1

Derivation of the model Equation 6 and Equation 7.
[https://www.beilstein-journals.org/bjnano/content/supplementary/2190-4286-9-109-S1.pdf]

Acknowledgements

We are pleased to thank J. P. Pekola for valuable and stimulating discussions. This work has been supported in part by the Russian Foundation for Basic Research Grant Nos. 17-52-12044, 18-02-00390 (A. A. K.), German Research Foundation (DFG) Grant No. KH 425/1-1 (I. M. K.), by the Russian Science Foundation, Grant No. 17-12-01383 (A. S. M.), Foundation for the advancement of theoretical physics "BASIS", and the Academy of Finland Grant No. 298451.

ORCID® iDs

Ivan M. Khaymovich - https://orcid.org/0000-0003-2160-5984

References

1. Kitaev, A. Yu. *Phys.-Usp.* **2001,** *44,* 131. doi:10.1070/1063-7869/44/10S/S29
2. Alicea, J. *Phys. Rev. B* **2010,** *81,* 125318. doi:10.1103/PhysRevB.81.125318
3. Lutchyn, R. M.; Sau, J. D.; Das Sarma, S. *Phys. Rev. Lett.* **2010,** *105,* 077001. doi:10.1103/PhysRevLett.105.077001
4. Oreg, Y.; Refael, G.; von Oppen, F. *Phys. Rev. Lett.* **2010,** *105,* 177002. doi:10.1103/PhysRevLett.105.177002
5. Nayak, C.; Simon, S. H.; Stern, A.; Freedman, M.; Das Sarma, S. *Rev. Mod. Phys.* **2008,** *80,* 1083–1159. doi:10.1103/RevModPhys.80.1083
6. Alicea, J.; Oreg, Y.; Refael, G.; von Oppen, F.; Fisher, M. P. A. *Nat. Phys.* **2011,** *7,* 412. doi:10.1038/nphys1915
7. Aasen, D.; Hell, M.; Mishmash, R. V.; Higginbotham, A.; Danon, J.; Leijnse, M.; Jespersen, T. S.; Folk, J. A.; Marcus, C. M.; Flensberg, K.; Alicea, J. *Phys. Rev. X* **2016,** *6,* 031016. doi:10.1103/PhysRevX.6.031016
8. Alicea, J. *Rep. Prog. Phys.* **2012,** *75,* 076501. doi:10.1088/0034-4885/75/7/076501
9. Elliott, S. R.; Franz, M. *Rev. Mod. Phys.* **2015,** *87,* 137–163. doi:10.1103/RevModPhys.87.137
10. Aguado, R. *Riv. Nuovo Cimento Soc. Ital. Fis.* **2017,** *40,* 523. doi:10.1393/ncr/i2017-10141-9
11. Mourik, V.; Zuo, K.; Frolov, S. M.; Plissard, S. R.; Bakkers, E. P. A. M.; Kouwenhoven, L. P. *Science* **2012,** *336,* 1003–1007. doi:10.1126/science.1222360
12. Chang, W.; Albrecht, S. M.; Jespersen, T. S.; Kuemmeth, F.; Krogstrup, P.; Nygård, J.; Marcus, C. M. *Nat. Nanotechnol.* **2015,** *10,* 232. doi:10.1038/nnano.2014.306
13. Higginbotham, A. P.; Albrecht, S. M.; Kiršanskas, G.; Chang, W.; Kuemmeth, F.; Krogstrup, P.; Jespersen, T. S.; Nygård, J.; Flensberg, K.; Marcus, C. M. *Nat. Phys.* **2015,** *11,* 1017. doi:10.1038/nphys3461
14. Krogstrup, P.; Ziino, N. L. B.; Chang, W.; Albrecht, S. M.; Madsen, M. H.; Johnson, E.; Nygård, J.; Marcus, C. M.; Jespersen, T. S. *Nat. Mater.* **2015,** *14,* 400. doi:10.1038/nmat4176
15. Albrecht, S. M.; Higginbotham, A. P.; Madsen, M.; Kuemmeth, F.; Jespersen, T. S.; Nygård, J.; Krogstrup, P.; Marcus, C. M. *Nature* **2016,** *531,* 206. doi:10.1038/nature17162
16. Zhang, H.; Gül, Ö.; Conesa-Boj, S.; Nowak, M. P.; Wimmer, M.; Zuo, K.; Mourik, V.; de Vries, F. K.; van Veen, J.; de Moor, M. W. A.; Bommer, J. D. S.; van Woerkom, D. J.; Car, D.; Plissard, S. R.; Bakkers, E. P. A. M.; Quintero-Pérez, M.; Cassidy, M. C.; Koelling, S.; Goswami, S.; Watanabe, K.; Taniguchi, T.; Kouwenhoven, L. P. *Nat. Commun.* **2017,** *8,* 16025. doi:10.1038/ncomms16025
17. McMillan, W. L. *Phys. Rev.* **1968,** *175,* 537–542. doi:10.1103/PhysRev.175.537
18. Sau, J. D.; Tewari, S.; Lutchyn, R. M.; Stanescu, T. D.; Das Sarma, S. *Phys. Rev. B* **2010,** *82,* 214509. doi:10.1103/PhysRevB.82.214509
19. Kopnin, N. B.; Melnikov, A. S. *Phys. Rev. B* **2011,** *84,* 064524. doi:10.1103/PhysRevB.84.064524
20. Kopnin, N. B.; Khaymovich, I. M.; Mel'nikov, A. S. *Phys. Rev. Lett.* **2013,** *110,* 027003. doi:10.1103/PhysRevLett.110.027003
21. Kopnin, N. B.; Khaymovich, I. M.; Mel'nikov, A. S. *J. Exp. Theor. Phys.* **2013,** *117,* 418. doi:10.1134/S1063776113110113
22. Stanescu, T. D.; Lutchyn, R. M.; Das Sarma, S. *Phys. Rev. B* **2011,** *84,* 144522. doi:10.1103/PhysRevB.84.144522
23. Reeg, C.; Loss, D.; Klinovaja, J. *Phys. Rev. B* **2017,** *96,* 125426. doi:10.1103/PhysRevB.96.125426
24. Reeg, C.; Loss, D.; Klinovaja, J. *arXiv* **2018,** No. 1801.06509.
25. Larkin, A. I.; Ovchinnikov, Yu. N. *Sov. Phys. - JETP* **1965,** *20,* 762.
26. Fulde, P.; Ferrell, R. A. *Phys. Rev.* **1964,** *135,* A550. doi:10.1103/PhysRev.135.A550
27. Samokhvalov, A. V.; Mel'nikov, A. S.; Ader, J.-P.; Buzdin, A. I. *Phys. Rev. B* **2009,** *79,* 174502. doi:10.1103/PhysRevB.79.174502
28. Samokhvalov, A. V. *J. Exp. Theor. Phys.* **2017,** *125,* 298–309. doi:10.1134/S106377611707010X
29. Antipov, A. E.; Bargerbos, A.; Winkler, G. W.; Bauer, B.; Rossi, E.; Lutchyn, R. M. *arXiv* **2018,** 1801.02616.
30. Mikkelsen, A. E. G.; Kotetes, P.; Krogstrup, P.; Flensberg, K. *arXiv* **2018,** 1801.03439.
31. Woods, B. D.; Stanescu, T. D.; Das Sarma, S. *arXiv* **2018,** 1801.02630.
32. Saint-James, D.; Sarma, G.; Thomas, E. *Type II Superconductivity;* Pergamon Press: Oxford, United Kingdom, 1969.
33. Saira, O.-P.; Kemppinen, A.; Maisi, V. F.; Pekola, J. P. *Phys. Rev. B* **2012,** *85,* 012504. doi:10.1103/PhysRevB.85.012504
34. Knowles, H. S.; Maisi, V. F.; Pekola, J. P. *Appl. Phys. Lett.* **2012,** *100,* 262601. doi:10.1063/1.4730407
35. Maisi, V. F.; Lotkhov, S. V.; Kemppinen, A.; Heimes, A.; Muhonen, J. T.; Pekola, J. P. *Phys. Rev. Lett.* **2013,** *111,* 147001. doi:10.1103/PhysRevLett.111.147001
36. van Woerkom, D. J.; Geresdi, A.; Kouwenhoven, L. P. *Nat. Phys.* **2015,** *11,* 547. doi:10.1038/nphys3342

BEILSTEIN JOURNAL OF NANOTECHNOLOGY

Circular dichroism of chiral Majorana states

Javier Osca[1] and Llorenç Serra[*1,2]

Full Research Paper

Open Access

Address:
[1]Institut de Física Interdisciplinària i de Sistemes Complexos IFISC (CSIC-UIB), E-07122 Palma de Mallorca, Spain and [2]Departament de Física, Universitat de les Illes Balears, E-07122 Palma de Mallorca, Spain

Email:
Llorenç Serra[*] - llorens.serra@uib.es

* Corresponding author

Keywords:
chiral states; circular dichroism; Majorana modes; optical absorption; topological matter

Beilstein J. Nanotechnol. **2018,** *9,* 1194–1199.
doi:10.3762/bjnano.9.110

Received: 11 December 2017
Accepted: 13 March 2018
Published: 16 April 2018

This article is part of the Thematic Series "Topological materials".

Guest Editor: J. J. Palacios

Abstract

Background: Majorana states in condensed matter devices may be of a localized nature, such as in hybrid semiconductor/superconductor nanowires, or chirally propagating along the edges such as in hybrid 2D quantum-anomalous Hall/superconductor structures.

Results: We calculate the circular dichroism due to chiral Majorana states in a hybrid structure made of a quantum-anomalous Hall insulator and a superconductor. The optical absorption of chiral Majorana states is characterized by equally spaced absorption peaks of both positive and negative dichroism. In the limit of a very long structure (a 2D ribbon) peaks of a single sign are favored.

Conclusion: Circular-dichroism spectroscopy of chiral Majorana states is suggested as a relevant probe for these peculiar states of topological matter.

Introduction

The physics of Majorana states in condensed matter devices is attracting strong interest for a few years now [1-8]. The measured zero-bias conductance peaks in hybrid semiconductor/superconductor nanowires have been attributed to the presence of localized Majorana modes on the two ends of the nanowires [9-14]. A Majorana mode enhances the zero-bias conductance by allowing a perfect Andreev backscattering at zero excitation energy when the nanowire is attached to a normal lead. These peculiar pairs of states may be seen as nonlocal split fermions, protected by an energy gap that separates them from other normal states lying at finite energies. Besides the zero energy of the Majorana state, also the conductance peak height was recently seen to coincide with the expected value $2e^2/h$ [15].

Majorana end states in (quasi) 1D nanowires are inherently localized, i.e., their wave function decays exponentially with the distance to the nanowire end. By contrast, propagating Majorana states with sustained spatial oscillations can be present at the edges and along the perimeter of 2D-like hybrid structures.

This is the situation in presence of $p + ip$ superconductivity for spinless quasiparticles, a class of hybrid systems where Majorana states appear around 2D vortex cores in the bulk and on the external edges of the sample [16]. Another class of 2D materials with propagating Majorana modes are the topological insulators based on the quantum-anomalous Hall effect. We refer, specifically, to the hybrid devices of [17], consisting of a quantum-anomalous Hall insulator and a superconductor material. In such systems, chiral Majorana modes propagating along the edges in a clockwise or anticlockwise manner, depending on the orientation of a perpendicular magnetic field, are formed at the 2D interfaces between the quantum-anomalous Hall and the superconductor materials [18-22]. Each chiral Majorana state contributes $0.5e^2/h$ to the linear conductance of the device, such that by tuning the number of Majorana states the conductance takes values $0.5e^2/h$ and $1e^2/h$ for the topological phases with one and two chiral Majorana states, respectively. It is remarkable that the intrinsic magnetization of the material in the anomalous Hall effect allows for the tuning of the phase transitions using much weaker magnetic fields than with the standard Hall effect.

In this work we discuss the connection between chiral Majorana states and optical absorption. We expect that in presence of chiral Majorana states, the optical absorption of circularly polarized light will differ for clockwise and anti-clockwise polarizations. The difference, known as circular dichroism (CD) [23,24], can thus be seen as a measure of the existence of such chiral states. We want to investigate how this behavior is actually realized by explicit calculations of the optical aborption. In previous works we analyzed the optical absorption of localized Majorana states in nanowires [25,26]. In those systems the CD vanishes and the presence of the Majorana state is signaled by a plateau with lower absorption, starting at mid-gap energy, of the y-polarized signal with respect to the x-polarized signal. It is also worth mentioning that alternative techniques for detecting Majorana fermions, based on microwave photoassisted tunneling in Majorana nanocircuits have been suggested in [27].

For chiral Majorana states in a 2D square or rectangular geometry the CD at low energies is characterized by a sequence of equally spaced peaks, corresponding to transitions of Bogoliubov–deGennes quasiparticles from negative to positive energy. In the usual energy ordering of quasiparticle states ($n = \pm1, \pm2, \ldots$), the selection rules are: a) transitions between conjugate states $-n \rightarrow n$ are forbidden by electron–hole symmetry, b) transitions $-n \rightarrow m$ are allowed only when n and m are both even or both odd. The rationale behind rule b) is the constructive interference of the corresponding quasiparticle states connected by the excitation operator on the edges of the system. Furthermore, it will be shown below that the CD peaks corresponding to those even–even or odd–odd quasiparticle transitions may be either positive or negative. In the limit of a long 2D ribbon there is a preferred CD sign, depending on the magnetic field orientation. For a disc geometry the generalized angular momentum J_z becomes a good quantum number. Then, the combination of circular and particle–hole symmetries in a disc causes a vanishing absorption for $p_x \pm ip_y$ fields and, obviously, also a vanishing CD.

Model

We use the model of [17] for a quantum-anomalous Hall (3D) thin film in contact with two different superconductors. This model represents the device as two surfaces with a certain interaction between them, with Majorana states being located at their edges. In a Nambu spinorial representation that groups the field operators in the top (t) and bottom (b) layers,

$$\left[\left(\Psi^t_{k\uparrow}, \Psi^t_{k\downarrow}, \Psi^{t\dagger}_{-k\downarrow}, -\Psi^{t\dagger}_{-k\uparrow}\right), \left(\Psi^b_{k\uparrow}, \Psi^b_{k\downarrow}, \Psi^{b\dagger}_{-k\downarrow}, -\Psi^{b\dagger}_{-k\uparrow}\right)\right]^T,$$

the Hamiltonian is reformulated in the notation of Pauli matrices (with t and b surfaces corresponding to the Pauli indices 1 and 2, respectively):

$$\begin{aligned}\mathcal{H} = &\left[m_0 + m_1\left(p_x^2 + p_y^2\right)\right]\tau_z\lambda_x + \Delta_B\sigma_z - \mu\tau_z \\ &-\alpha\left(p_x\sigma_y - p_y\sigma_x\right)\tau_z\lambda_z \\ &+\Delta_p\tau_x + \Delta_m\tau_x\lambda_z.\end{aligned} \tag{1}$$

This Hamiltonian is acting in the combined position–spin–isospin–pseudospin space. Spatial positions are treated as a 2D continuum ($x, y \in L_x \times L_y$) and a discrete two-valued pseudospin (z). The two-valued spin, isospin and pseudospin degrees of freedom are represented by σ, τ and λ Pauli matrices, respectively. As mentioned, the pseudospin (λ) is modeling a coupled bilayer system in which quasiparticles move. The set of Hamiltonian parameters is m_0, m_1, Δ_B, μ, α, Δ_p and Δ_m. The latter two are given in terms of the pairing interaction in the two layers, Δ_t and Δ_b, by

$$\Delta_{p,m} = \frac{\Delta_t \pm \Delta_b}{2}. \tag{2}$$

Hybridization of the two surfaces is represented by parameters m_0 and m_1. Δ_B is an effective Zeeman-like parameter including the exchange field associated with the intrinsic magnetization of the material. The chemical potential is given by μ while α represents a Rashba-type spin–orbit interaction.

Below we numerically determine the eigenvalues and eigenstates of $\mathcal{H}$ using a 2D grid for x and y. When Δ_B is increased, the spectrum of low-energy eigenvalues evolves from a gapped (void) spectrum around zero energy at low values of Δ_B, to the emergence of chiral near-zero-energy modes for sufficiently large values of Δ_B. When the pairing parameters for each layer are equal ($\Delta_m = 0$) chiral Majorana states appear in pairs (0–2–…), while for sufficiently different parameters it is $\Delta_m \neq 0$ and there may be phases with odd numbers of chiral Majorana states as well.

The numerical results shown below are given in an effective unit system, characterized by the choice of $\hbar \equiv 1$, mass $m \equiv 1/2m_1 \equiv 1$ and a chosen length unit L_U, typically $L_\mathrm{U} \approx 1$ μm. The corresponding energy unit is then $E_\mathrm{U} = \hbar^2 / mL_\mathrm{U}^2$.

Circular dichroism

We compute the optical absorption cross section for right (+) and left (−) circularly-polarized light from

$$\mathcal{S}_\pm(\omega) = 4m_1^2 \sum_{k>0,s<0} \frac{1}{\omega_{ks}} \left| \langle k \mid p_x \pm \mathrm{i}p_y \mid s \rangle \right|^2 \delta(\omega - \omega_{ks}), \quad (3)$$

where $\hbar\omega_{ks} = \varepsilon_k - \varepsilon_s$ is the energy difference between particle (unoccupied) and hole (occupied) states. The prefactor $4m_1^2$ gives the squared inverse effective mass ($1/m_\mathrm{eff}^2$) of the Hamiltonian and fixes the dimensions of $\mathcal{S}$ as an area. The circular dichroism at a given frequency $\mathcal{S}_\mathrm{CD}(\omega)$ is then defined as the difference between the absorptions for the two circular polarizations,

$$\mathcal{S}_\mathrm{CD}(\omega) = \mathcal{S}_+(\omega) - \mathcal{S}_-(\omega). \quad (4)$$

Obviously, in absence of any chirality preference $\mathcal{S}_\mathrm{CD}$ exactly vanishes.

Results and Discussion

Chiral bands

Figure 1 shows the evolution of the eigenvalue spectrum as a function of the magnetic field parameter Δ_B. The results reproduce already known results [17]. At vanishing Δ_B the spectrum around zero energy is gapped, a gap that tends to close with increasing Δ_B by the appearance of a quasi-continuum distribution of eigenvalues. These low-energy states are indicating the presence of propagating Majorana states, energy-discretized due to the finite size of the system. When $\Delta_t = \Delta_b$ (Figure 1a,c) the degeneracy is such that the Majorana branches appear in pairs. Directly determining the degeneracy of the energy eigenstates close to zero energy is an alternative way to characterize the topological invariant or Chern number discussed in [20]. We also notice that there is no qualitative difference in the eigenvalue distribution between a square and a rectangle (upper vs lower panels). It is remarkable that when a Majorana phase is well developed the low-energy states are equally spaced in energy. This is particularly clear for $2 < \Delta_B/E_\mathrm{U} < 4$ in Figure 1a and Figure 1c, corresponding to the phases with two Majorana states. It can also be seen in Figure 1b and Figure 1d for the phases with one Majorana state while that the equally spaced distribution also hints to the beginning of the phase with two Majorana states.

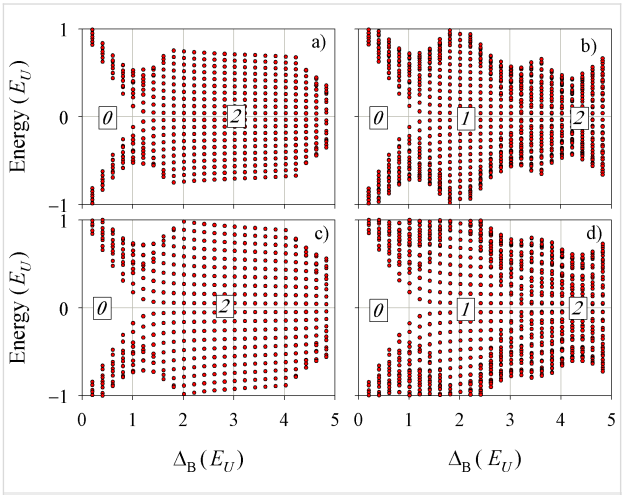

Figure 1: Energy eigenvalues close to zero energy as a function of Δ_B. Panels a) and b) are for a square of dimensions $L_x = L_y = 10L_\mathrm{U}$, while c) and d) correspond to a rectangle of $L_x = 2L_y = 20L_\mathrm{U}$. In a) and c) the same pairing energy is assumed in each layer $\Delta_t = \Delta_b = E_\mathrm{U}$ while in b) and d) it is $\Delta_t = \Delta_b/3 = E_\mathrm{U}$. The framed labels indicate the degeneracy of the near-zero energy states, which indicates the topological phase. Other parameters: $m_0 = 0$, $\mu = 0$, $\alpha = E_\mathrm{U}L_\mathrm{U}$.

The chiral character of the gap-closing Majorana states is clearly seen in Figure 2. The equally spaced states at low energy arrange themselves on a line (a chiral band) when plotted as a function of the z-component of the angular momentum. For positive Δ_B the angular momentum decreases with increasing energy, causing empty (particle) states to have negative values of $\langle J_z \rangle$, while occupied (hole) states have positive values of $\langle J_z \rangle$. The results of Figure 2a,b correspond to the rectangle with different pairing energies in each layer shown in Figure 1d. For $\Delta_B = 2E_\mathrm{U}$ (Figure 2a) there is a single chiral band, while for $\Delta_B = 4.75E_\mathrm{U}$ (Figure 2b) there are two overlapping bands. Notice that the overlap of states in Figure 2b degrades as the energy deviates from zero, indicating that the second Majorana band is not yet fully settled for this particular Δ_B. Additionally, Figure 2c explicitly shows the edge character of the states of a chiral Majorana band. A similar distribution is obtained for all the states in a chiral band. On the contrary, states that are not

aligned along the chiral band in Figure 2a,b are bulk states separated by a gap from zero energy.

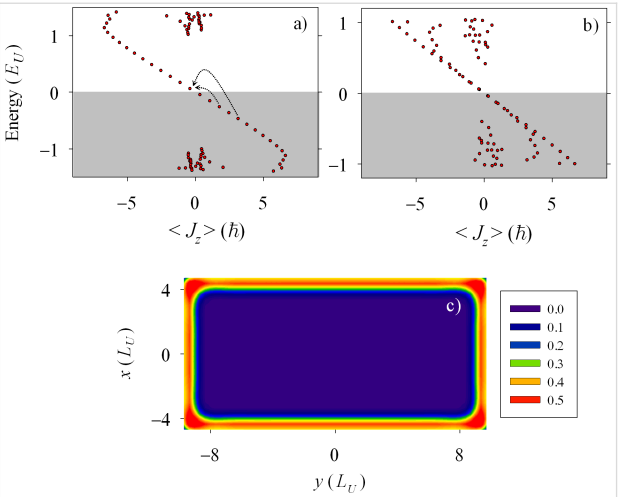

Figure 2: Energy eigenvalues as a function of $\langle J_z \rangle$. Panels a) and b) correspond to the phases in Figure 1d with one ($\Delta_B = 2E_U$) and two ($\Delta_B = 4.75E_U$) Majorana states, respectively. The grey shaded zones indicate the occupied (hole) states while the arrows in panel a) show the two lowest allowed transitions to the first particle state. Panel c) shows the probability density corresponding to the lowest positive-energy state in panel a), adding all spin, isospin and pseudospin contributions.

Absorption and CD

Absorption cross-sections and CD for the spectra of the rectangle with different pairing energies in the two layers (Figure 1d) are shown in Figure 3 for selected values of Δ_B. They correspond to zero (Figure 3a), one (Figure 3b) and two (Figure 3c) chiral bands. As anticipated, in presence of the chiral states the system develops a clear CD. For the sake of a better comparison, identical scales have been used in the three panels of Figure 3. In these scales, the two absorptions and the CD essentially vanish in the absence of chiral modes (Figure 3a). The rightmost inset in panel Figure 3a shows that for energies exceeding the quasiparticle gap a small absorption eventually appears due to transitions between bulk states (cf. Figure 1d). However, the CD still vanishes within numerical precision. The negative CD peaks dominate in Figure 3b,c due to the negative slope of the chiral bands (Figure 2a,b). It is remarkable, however, that a few positive peaks are also present. We attribute them to the fact that in a rectangular geometry J_z is not a good quantum number and, therefore, there are states with mixed angular momentum. We have performed calculations in a circular geometry confirming this interpretation. Therefore, quasiparticle scattering by the corners plays a nontrivial role on the absorption by chiral edge states.

The most conspicuous feature of Figure 3b is the regular energy spacing of the first few CD peaks. Analysing them in terms of

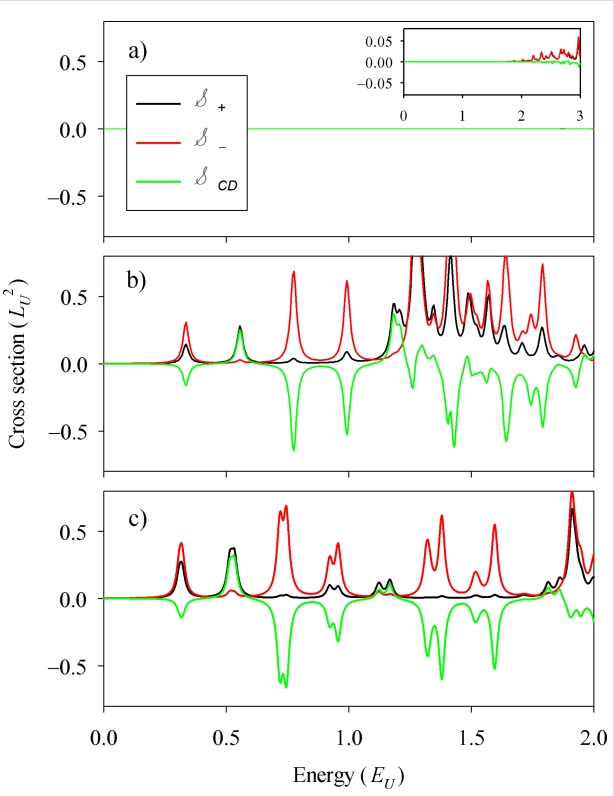

Figure 3: Absorption cross-sections $\mathcal{S}_+$, $\mathcal{S}_-$ and $\mathcal{S}_{CD}$ defined in the main text. The shown results correspond to the spectra of Figure 1d for Zeeman parameters of (a) $\Delta_B = 0.3E_U$, (b) $2E_U$), and (c) $4.75E_U$. The rightmost inset in Figure 3a corresponds to an extended energy range and a zoomed vertical scale for the data of this panel.

energy transitions of the chiral band it is easily noticed that they correspond to jumps of 3, 5, 7,… steps (see arrows in Figure 2a). We explain this selection rule noticing the following restrictions for transitions from the negative n-th state to the positive m-th state ($-n \rightarrow m$): (a) Transitions between conjugate states $-n \rightarrow n$ are forbidden by particle–hole symmetry [25], and (b) n even to m odd transitions (or vice versa) are forbidden because of destructive interference along the nanostructure perimeter with the excitation operator. This rule is far less obvious than rule (a) and results from the approximately 1D character of the chiral edge modes and the interference induced by the propagation through corners. Indeed, we have seen that for active transitions within the chiral bands the regions around the corners are those contributing the most to the matrix element in Equation 3.

For a disc, J_z becomes a good symmetry and, by angular momentum conservation with a dipole operator only the transition $-1 \rightarrow 1$ is possible. However, this transition is blocked by rule (a) and, therefore, no dipole absorption is possible and the CD exactly vanishes. We have also checked this behavior by explicit calculation for a device with circular geometry. For a

square and rectangle, quasiparticle scattering by the corners plays a nontrivial role yielding the mentioned deviations with respect to the disc.

The pattern of equally spaced peaks is fulfilled only when one or several chiral bands are fully developed and they exactly overlap. In Figure 3c we see that the slight degradation of the two-band overlaps of Figure 2b manifests in a small twofold splitting of the CD peaks. It is also worth stressing that once the chiral bands are fully formed, the energy positions of the first few CD peaks become independent on Δ_B (cf. Figure 2b and Figure 2c).

Figure 4 shows the absorption results for different geometries, a square (Figure 4a) and a long rectangle resembling a 2D ribbon (Figure 4b). For the square, the first CD peaks alter sign in a remarkable way. For the ribbon the alternation is of a longer period, the positive peaks having a much lower intensity than the negative ones and there are groups of a few consecutive negative peaks. The 2D ribbon shape thus favors the observation of CD peaks of the same sign. Nevertheless, the presence of the corners is still essential since for a strictly infinite ribbon the CD exactly vanishes. This is clear when realizing that with fully translational invariant states the p_x operator in Equation 3 is not yielding any excitation and, therefore, the sign of the p_y operator becomes irrelevant, yielding $\mathcal{S}_+ = \mathcal{S}_-$.

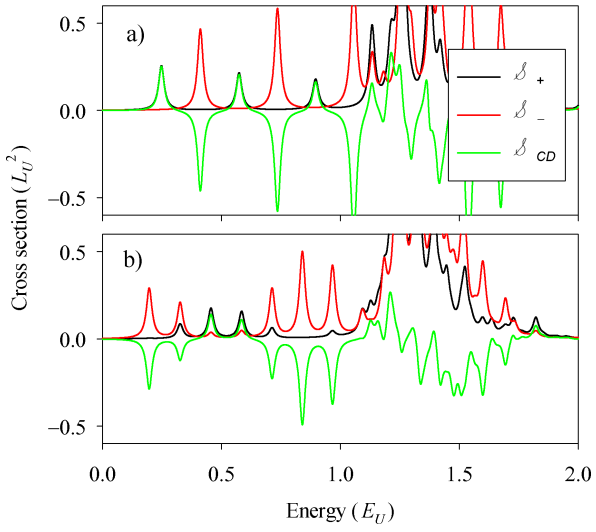

Figure 4: Absorption cross-sections $\mathcal{S}_+$, $\mathcal{S}_-$ and $\mathcal{S}_{CD}$ for (a) a square of $L_x = L_y = 20\,L_U$), and for (b) a rectangle of $L_x = 6L_y = 60L_U$ (b). In both cases we used $\Delta_B = 2E_U$ and $\Delta_t = \Delta_b/3 = E_U$.

Conclusion

In this work we have investigated the manifestation of chiral Majorana modes in the CD of the dipole absorption. The chiral bands formed at the edges of a hybrid system made of a quantum-anomalous Hall insulator and a superconductor yield equally spaced peaks in the CD signal. We identified the particle–hole selection rules responsible for this behavior from the analysis in terms of chiral bands. In a disc there is no CD signal due to the incompatibility of the selection rules with the angular momentum restriction; a square or rectangular geometry (or, more generally, a system with straight edges or breaking circular symmetry) is needed. The presence of two chiral bands can be inferred from the small splitting of the CD peaks. Finally, both positive and negative CD peaks can be seen, with a perfect alternation in a square and a favored sign in a long 2D ribbon geometry.

Our results suggest the use of CD spectroscopy as a valuable probe of chiral Majorana states, complementing the evidences obtained with electrical conductance measurements [17]. This may require the use of an array of absorbing devices, in order to achieve a combined signal of sufficient intensity. Alternatively, techniques such as those developed for single plasmonic nanoparticle sensing [28] might be applied to an isolated chiral Majorana device. Particularly, among the latter we stress the techniques for single-particle absorption that have allowed measuring the extinction spectrum of a single silica shell-coated silver nanoparticle excited with varying polarizations [29].

Acknowledgements

This work was funded by MINECO (Spain), grants FIS2014-52564 and MAT2017-82639.

ORCID® iDs

Llorenç Serra - https://orcid.org/0000-0001-8496-7873

References

1. Nayak, C.; Simon, S. H.; Stern, A.; Freedman, M.; Das Sarma, S. *Rev. Mod. Phys.* **2008,** *80,* 1083–1159. doi:10.1103/RevModPhys.80.1083
2. Alicea, J.; Oreg, Y.; Refael, G.; von Oppen, F.; Fisher, M. P. A. *Nat. Phys.* **2011,** *7,* 412–417. doi:10.1038/nphys1915
3. Stanescu, T. D.; Tewari, S. *J. Phys.: Condens. Matter* **2013,** *25,* 233201. doi:10.1088/0953-8984/25/23/233201
4. Beenakker, C. W. J. *Annu. Rev. Condens. Matter Phys.* **2013,** *4,* 113–136. doi:10.1146/annurev-conmatphys-030212-184337
5. Franz, M. *Nat. Nanotechnol.* **2013,** *8,* 149–152. doi:10.1038/nnano.2013.33
6. Elliott, S. R.; Franz, M. *Rev. Mod. Phys.* **2015,** *87,* 137–163. doi:10.1103/RevModPhys.87.137
7. Aguado, R. *Riv. Nuovo Cimento Soc. Ital. Fis.* **2017,** *40,* 523–593. doi:10.1393/ncr/i2017-10141-9
8. Lutchyn, R. M.; Bakkers, E. P. A. M.; Kouwenhoven, L. P.; Krogstrup, P.; Marcus, C. M.; Oreg, Y. *ArXiv* **2017,** No. 1707.04899.
9. Lutchyn, R. M.; Sau, J. D.; Das Sarma, S. *Phys. Rev. Lett.* **2010,** *105,* 077001. doi:10.1103/PhysRevLett.105.077001

10. Oreg, Y.; Refael, G.; von Oppen, F. *Phys. Rev. Lett.* **2010,** *105,* 177002. doi:10.1103/PhysRevLett.105.177002
11. Mourik, V.; Zuo, K.; Frolov, S. M.; Plissard, S. R.; Bakkers, E. P. A. M.; Kouwenhoven, L. P. *Science* **2012,** *336,* 1003–1007. doi:10.1126/science.1222360
12. Gül, Ö.; Zhang, H.; Bommer, J. D. S.; de Moor, M. W. A.; Car, D.; Plissard, S. R.; Bakkers, E. P. A. M.; Geresdi, A.; Watanabe, K.; Taniguchi, T.; Kouwenhoven, L. P. *Nat. Nanotechnol.* **2018,** *13,* 192–197. doi:10.1038/s41565-017-0032-8
13. Deng, M. T.; Yu, C. L.; Huang, G. Y.; Larsson, M.; Caroff, P.; Xu, H. Q. *Nano Lett.* **2012,** *12,* 6414–6419. doi:10.1021/nl303758w
14. Das, A.; Ronen, Y.; Most, Y.; Oreg, Y.; Heiblum, M.; Shtrikman, H. *Nat. Phys.* **2012,** *8,* 887–895. doi:10.1038/nphys2479
15. Zhang, H.; Liu, C.-X.; Gazibegovic, S.; Xu, D.; Logan, J. A.; Wang, G.; van Loo, N.; Bommer, J. D. S.; de Moor, M. W. A.; Car, D.; het Veld, R. L. M. O.; van Veldhoven, P. J.; Koelling, S.; Verheijen, M. A.; Pendharkar, M.; Pennachio, D. J.; Shojaei, B.; Lee, J. S.; Palmstrom, C. J.; Bakkers, E. P. A. M.; Das Sarma, S.; Kouwenhoven, L. P. *ArXiv* **2017,** No. 1710.10701.
16. Alicea, J. *Rep. Prog. Phys.* **2012,** *75,* 076501. doi:10.1088/0034-4885/75/7/076501
17. He, Q. L.; Pan, L.; Stern, A. L.; Burks, E. C.; Che, X.; Yin, G.; Wang, J.; Lian, B.; Zhou, Q.; Choi, E. S.; Murata, K.; Kou, X.; Chen, Z.; Nie, T.; Shao, Q.; Fan, Y.; Zhang, S.-C.; Liu, K.; Xia, J.; Wang, K. L. *Science* **2017,** *357,* 294–299. doi:10.1126/science.aag2792
18. Qi, X.-L.; Hughes, T. L.; Zhang, S.-C. *Phys. Rev. B* **2010,** *82,* 184516. doi:10.1103/PhysRevB.82.184516
19. Chung, S. B.; Qi, X.-L.; Maciejko, J.; Zhang, S.-C. *Phys. Rev. B* **2011,** *83,* 100512. doi:10.1103/PhysRevB.83.100512
20. Wang, J.; Zhou, Q.; Lian, B.; Zhang, S.-C. *Phys. Rev. B* **2015,** *92,* 064520. doi:10.1103/PhysRevB.92.064520
21. Lian, B.; Wang, J.; Zhang, S.-C. *Phys. Rev. B* **2016,** *93,* 161401. doi:10.1103/PhysRevB.93.161401
22. Kaladzhyan, V.; Despres, J.; Mandal, I.; Bena, C. *Eur. Phys. J. B* **2017,** *90,* 211. doi:10.1140/epjb/e2017-80103-y
23. Eisfeld, A.; Kniprath, R.; Briggs, J. S. *J. Chem. Phys.* **2007,** *126,* 104904. doi:10.1063/1.2464097
24. Longhi, G.; Castiglioni, E.; Koshoubu, J.; Mazzeo, G.; Abbate, S. *Chirality* **2016,** *28,* 696–707. doi:10.1002/chir.22647
25. Ruiz, D.; Osca, J.; Serra, L. *J. Phys.: Condens. Matter* **2015,** *27,* 125302. doi:10.1088/0953-8984/27/12/125302
26. Osca, J.; Serra, L. *Phys. Status Solidi C* **2015,** *12,* 1409–1411. doi:10.1002/pssc.201510131
27. Dartiailh, M. C.; Kontos, T.; Douçot, B.; Cottet, A. *Phys. Rev. Lett.* **2017,** *118,* 126803. doi:10.1103/PhysRevLett.118.126803
28. Olson, J.; Dominguez-Medina, S.; Hoggard, A.; Wang, L.-Y.; Chang, W.-S.; Link, S. *Chem. Soc. Rev.* **2015,** *44,* 40–57. doi:10.1039/C4CS00131A
29. Baida, H.; Billaud, P.; Marhaba, S.; Christofilos, D.; Cottancin, E.; Crut, A.; Lermé, J.; Maioli, P.; Pellarin, M.; Broyer, M.; Del Fatti, N.; Vallée, F.; Sánchez-Iglesias, A.; Pastoriza-Santos, I.; Liz-Marzán, L. M. *Nano Lett.* **2009,** *9,* 3463–3469. doi:10.1021/nl901672b

License and Terms

BEILSTEIN JOURNAL OF NANOTECHNOLOGY

Proximity effect in a two-dimensional electron gas coupled to a thin superconducting layer

Christopher Reeg*, Daniel Loss and Jelena Klinovaja

Full Research Paper

Open Access

Address:
Department of Physics, University of Basel, Klingelbergstrasse 82, CH-4056 Basel, Switzerland

Email:
Christopher Reeg* - christopher.reeg@unibas.ch

* Corresponding author

Keywords:
Majorana fermions; mesoscopic physics; proximity effect; quantum computing; topological superconductivity

Beilstein J. Nanotechnol. **2018,** *9,* 1263–1271.
doi:10.3762/bjnano.9.118

Received: 27 January 2018
Accepted: 23 March 2018
Published: 23 April 2018

This article is part of the Thematic Series "Topological materials".

Guest Editor: J. J. Palacios

Abstract

There have recently been several experiments studying induced superconductivity in semiconducting two-dimensional electron gases that are strongly coupled to thin superconducting layers, as well as probing possible topological phases supporting Majorana bound states in such setups. We show that a large band shift is induced in the semiconductor by the superconductor in this geometry, thus making it challenging to realize a topological phase. Additionally, we show that while increasing the thickness of the superconducting layer reduces the magnitude of the band shift, it also leads to a more significant renormalization of the semiconducting material parameters and does not reduce the challenge of tuning into a topological phase.

Introduction

Topological superconductors host zero-energy Majorana bound states at their edges that are highly sought for applications in topological quantum computing [1-3]. The two proposals to realize topological superconductivity that have received the most attention to date involve engineering Majorana bound states in either low-dimensional semiconducting systems [4-23] or in ferromagnetic atomic chains [24-32]. After the first signatures of topological superconductivity were observed [33-37], much of the experimental focus was placed on developing more suitable devices for realizing robust topological superconducting phases. One of the most significant experimental advances of the past few years was the successful epitaxial growth of thin layers of superconducting Al on InAs and InSb nanowires [38-42]. The intimate contact between the semiconductor and superconductor in these devices ensures a hard induced superconducting gap. Recently, this epitaxial growth technique has been applied also to InAs two-dimensional electron gases (2DEGs) [43-47].

The proximity effect has been theoretically studied recently in both strictly one-dimensional (1D) [48] and quasi-1D [49] wires coupled to thin superconducting layers. In both instances, a

strong proximity coupling induces a large band shift on the semiconducting wire. This band shift is comparable to the level spacing in the superconductor, $\delta E_s = \pi\hbar v_F / d$ (which is $\delta E_s \sim$ 400 meV for a superconductor thickness of $d \sim 10$ nm and a Fermi velocity of Al of $v_F \sim 2 \times 10^6$ m/s). In both cases, this large band shift makes it very challenging to realize a topological phase when utilizing thin superconducting layers.

In this paper, we extend the works of [48,49] to the 2D limit. We show that the large band shift that plagues the 1D case persists also in two dimensions. First, we show that the self-energy induced in an infinite 2DEG coupled to a superconductor of finite thickness is equivalent to that induced in an infinite wire coupled to a 2D superconductor of finite width (corresponding to the theoretical model of [48]), with the simple replacement of a 1D momentum by the magnitude of a 2D momentum. Analyzing the self-energy, we find that the induced gap in the presence of only Rashba spin–orbit coupling can be made comparable to the bulk gap of the superconductor only if the tunneling energy scale exceeds the large level spacing of the superconducting layer. As in the 1D case, the large tunneling energy scale induces a large band shift on the 2DEG and makes it very challenging to realize a topological phase. We also show that while the band shift can be significantly reduced by increasing the thickness of the superconducting layer, the topological phase is still difficult to realize if the 2DEG/superconductor interface remains very transparent.

Model of the Proximity Effect

The system we consider consists of a 2DEG with strong Rashba spin–orbit interaction (SOI) proximity-coupled to an *s*-wave superconductor of thickness d, as shown in Figure 1. The 2DEG-superconductor heterostructure is described by the action

$$S = S_{2D} + S_s + S_t. \tag{1}$$

The action of the 2DEG in Nambu space is given by

$$S_{2D} = \frac{1}{2}\int_{\mathbf{k},\omega} c^\dagger_{\mathbf{k},\omega}\left(\mathrm{i}\omega - \mathcal{H}^{2D}_{\mathbf{k}}\right)c_{\mathbf{k},\omega}, \tag{2}$$

where ω is a Matsubara frequency, $\mathbf{k} = (k_x,k_y)$ is the momentum,

$$\int_{\mathbf{k},\omega} \equiv \int \mathrm{d}\omega/2\pi \int \mathrm{d}\mathbf{k}/(2\pi)^2,$$

and

$$c_{\mathbf{k},\omega} = \left(c_{\mathbf{k},\omega,\uparrow}, c_{\mathbf{k},\omega,\downarrow}, c^\dagger_{-\mathbf{k},-\omega,\uparrow}, c^\dagger_{-\mathbf{k},-\omega,\downarrow}\right)^T$$

is a spinor of Heisenberg operators describing states in the 2DEG. The Hamiltonian density is

$$\mathcal{H}^{2D}_{\mathbf{k}} = \xi_k \tau_z + \alpha\left(k_y\sigma_x - k_x\tau_z\sigma_y\right), \tag{3}$$

where $\xi_k = k^2/2m_{2D} - \mu_{2D}$ (m_{2D} and μ_{2D} are the effective mass and chemical potential of the 2DEG, respectively, and $k^2 = k_x^2 + k_y^2$), α is the Rashba SOI constant, and $\sigma_{x,y,z}$ ($\tau_{x,y,z}$) are Pauli matrices acting in spin (Nambu) space. The superconductor is described by the BCS action,

$$S_s = \frac{1}{2}\int_{\mathbf{k},\omega}\int_0^d \mathrm{d}z\,\eta^\dagger_{\mathbf{k},\omega}(z)\left[\mathrm{i}\omega - \mathcal{H}^s_k(z)\right]\eta_{\mathbf{k},\omega}(z), \tag{4}$$

where

$$\eta_{\mathbf{k},\omega} = \left[\eta_{\mathbf{k},\omega,\uparrow}, \eta_{\mathbf{k},\omega,\downarrow}, \eta^\dagger_{-\mathbf{k},-\omega,\uparrow}, \eta^\dagger_{-\mathbf{k},-\omega,\downarrow}\right]^T$$

is a spinor of Heisenberg operators describing states in the superconductor and the Hamiltonian density is

$$\mathcal{H}^s_k(z) = \left(-\frac{\partial_z^2}{2m_s} + \frac{k^2}{2m_s} - \mu_s\right)\tau_z - \Delta\sigma_y\tau_y, \tag{5}$$

with m_s, μ_s, and Δ the effective mass, chemical potential, and pairing potential of the superconductor, respectively. Local tunneling at the interface between the two materials is assumed to conserve both spin and momentum,

$$S_t = -\frac{t}{2}\int_{\mathbf{k},\omega}\left[\eta^\dagger_{\mathbf{k},\omega}(z_{2D})\tau_z c_{\mathbf{k},\omega} + H.c.\right], \tag{6}$$

where t is the tunneling amplitude. We must take the 2DEG to be located at some finite z_{2D} ($0 < z_{2D} < d$) due to the breakdown of the tunneling Hamiltonian approach for the case where the 2DEG is located at the boundary of the superconductor. The breakdown of the tunneling Hamiltonian results from our

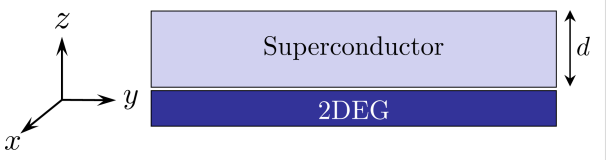

Figure 1: A 2DEG is proximity-coupled to an *s*-wave superconductor with finite thickness *d*. Both systems are taken to be infinite in the *xy*-plane.

neglect of the thickness of the 2DEG (for related calculations in which the finite thickness is taken into account, see [50-53]). However, as shown in [48], choosing $k_F z_{2D} \ll 1$ (where $k_F = \sqrt{2m_s\mu_s}$ is the Fermi momentum of the superconductor) yields good agreement with numerical calculations in which there is no issue with placing the 2DEG strictly at the boundary.

In the absence of tunneling, the spectrum of the 2DEG consists of two spin–orbit-split subbands described by

$$E_{\pm}^2(k) = \left(\xi_k \pm \alpha k\right)^2. \tag{7}$$

When the finite-size quantization scale of the superconductor greatly exceeds the gap, $1/m_s d^2 \gg \Delta$, the first few subbands of the superconductor follow a linearized form given by ($\hbar = 1$)

$$E_n^2(k) = \left(\left[k_F d/\pi - n\right]\delta E_s - \frac{k^2}{2m_s}\right)^2 + \Delta^2, \tag{8}$$

where $\delta E_s = \pi v_F/d$ is the level spacing in the superconductor ($v_F = k_F/m_s$ is the Fermi velocity) and $n \in \mathbb{Z}^+$. When the thickness of the superconducting layer is much smaller than its coherence length, $d \ll \xi_s = \pi v_F/\Delta$, the level spacing of the layer greatly exceeds its gap, $\delta E_s \gg \Delta$.

The spectra of the 2DEG and the superconductor are plotted in Figure 2. Provided that $\min(|k_F d/\pi - n|) \gg \Delta/\delta E_s$, the bands of the 2DEG and superconductor intersect at high energies $E \sim \delta E_s \gg \Delta$. Since we impose momentum conservation (in addition to energy conservation) in Equation 6, the subbands are coupled only at the intersection points. Thus, a weak tunnel coupling induces anticrossings in the spectrum, as indicated in Figure 2, which leads to a shift in the subbands of the 2DEG. Additionally, the tunnel coupling opens a superconducting gap at the Fermi momenta of the 2DEG; however, due to the intersection points lying at very large energies, the gap opened in the 2DEG is very small. A large gap can only be induced if tunneling is strong enough to overcome the large energy mismatch similar to δE_s.

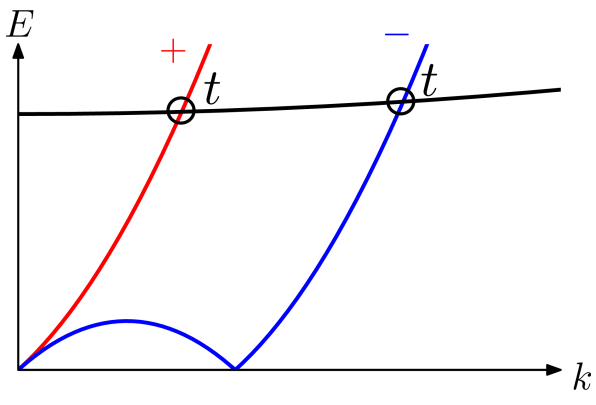

Figure 2: Sketch of Bogoliubov excitation spectra as a function of $k = (k_x^2 + k_y^2)^{1/2}$ in the absence of tunneling, assuming $\delta E_s \gg E_{so}$ and $\mu_{2D} = 0$. The red and blue curves correspond to ± subbands of the 2DEG (Equation 7), respectively, which result from the spin-splitting Rashba SOI. The black curve corresponds to the lowest-energy subband of the superconductor (Equation 8). A weak tunneling amplitude t induces anticrossings in the spectrum where indicated and induces a superconducting gap in the 2DEG at the Fermi momenta (corresponding to those momenta for which $E_{\pm}(k)$=0). Due to the large energy mismatch between the superconducting subband and the Fermi points of the 2DEG, the induced gap is very small.

To determine the self-energy of the 2DEG induced by the superconductor, we integrate out the superconducting degrees of freedom. After integrating out, the 2DEG can be described by the effective action

$$S_{\text{eff}} = \int_{\mathbf{k},\omega} c^{\dagger}_{\mathbf{k},\omega}\left(\mathrm{i}\omega - \mathcal{H}^{\text{2D}}_{\mathbf{k}} - \Sigma_{k,\omega}\right)c_{\mathbf{k},\omega}, \tag{9}$$

with the self-energy given by

$$\Sigma_{k,\omega} = t^2 \tau_z G^{\text{s}}_{k,\omega}\left(z_{\text{2D}}, z_{\text{2D}}\right)\tau_z. \tag{10}$$

In Equation 10, $G^{\text{s}}_{k,\omega}(z,z')$ is the Green's function of the bare superconductor (in the absence of tunneling), which satisfies

$$\left[\mathrm{i}\omega - \mathcal{H}^{\text{s}}_k(z)\right]G^{\text{s}}_{k,\omega}(z,z') = \delta(z-z'). \tag{11}$$

Imposing a vanishing boundary condition at $z = 0$ and $z = d$, we find a solution to Equation 11 given by

$$\begin{aligned} G^{\text{s}}_{k,\omega}(z,z') = {} & \frac{1}{2v_F\Omega}\left(\mathrm{i}\omega - \Delta\tau_y\sigma_y + \mathrm{i}\Omega\tau_z\right) \\ & \times\left\{\frac{\sin\left[k_+(d-z')\right]}{\sin(k_+ d)}e^{\mathrm{i}k_+ z}\right. \\ & \left.+\left[\mathrm{i}+\cot(k_+ d)\right]\sin(k_+ z')e^{-\mathrm{i}k_+ z}\right\} \\ & +\frac{1}{2v_F\Omega}\left(\mathrm{i}\omega - \Delta\tau_y\sigma_y - \mathrm{i}\Omega\tau_z\right) \\ & \times\left\{\left[-\mathrm{i}+\cot(k_- d)\right]\sin(k_- z')e^{\mathrm{i}k_- z}\right. \\ & \left.+\frac{\sin\left[k_-(d-z')\right]}{\sin(k_- d)}e^{-\mathrm{i}k_- z}\right\} \\ & +G^{\text{bulk}}_{k,\omega}(z-z'), \end{aligned} \tag{12}$$

where $k_\pm^2 = 2m_s(\mu_s \pm i\Omega) - k^2$ and $\Omega^2 = \Delta^2 + \omega^2$ [48,54]. The Green's function of a bulk superconductor, expressed in real space, is

$$\begin{aligned} G^{\text{bulk}}_{k,\omega}(z-z') &= -\int \frac{dk_z}{2\pi} \frac{i\omega + \left(\xi_k + k_z^2/2m_s\right)\tau_z - \Delta\tau_y\sigma_y}{\omega^2 + \left(\xi_k + k_z^2/2m_s\right)^2 + \Delta^2} e^{ik_z(z-z')} \\ &= -\frac{1}{v_F\Omega\varphi}\Big[\left(i\omega - \Delta\tau_y\sigma_y\right)\cos\left(\zeta\,|\,z-z'\,|\right) \\ &\quad -\Omega\tau_z \sin\left(\zeta\,|\,z-z'\,|\right)\Big] e^{-\chi|z-z'|}, \end{aligned} \tag{13}$$

where, in evaluating the integral, we make a semiclassical expansion $k_\pm = k_F\varphi \pm i\Omega/(v_F\varphi) \equiv \zeta \pm i\chi$ (valid in the limit $\mu_s \gg \Omega$) and define a quantity $\varphi^2 = 1 - k^2/k_F^2$ that parametrizes the trajectories of states in the superconductor. Substituting the Green's function (Equation 12) into the self-energy (Equation 10), we find

$$\Sigma_{k,\omega} = \left(i\omega + \Delta\tau_y\sigma_y\right)\left(1 - 1/\Gamma_{k,\omega}\right) - \delta\mu_{k,\omega}\tau_z, \tag{14}$$

where we define

$$\begin{aligned} \Gamma_{k,\omega} &= \Bigg(1 + \frac{\gamma}{\Omega\varphi\left[\cosh\left(2\chi d\right) - \cos\left(2\zeta d\right)\right]} \\ &\quad \times\Big\{\sinh\left(2\chi d\right) - \cos\left(2\zeta z_{2D}\right)\sinh\left[2\chi\left(d - z_{2D}\right)\right] \\ &\quad -\cos\left[2\zeta\left(d - z_{2D}\right)\right]\sinh\left(2\chi z_{2D}\right)\Big\}\Bigg)^{-1}, \\ \delta\mu_{k,\omega} &= -\frac{\gamma}{\varphi[\cosh(2\chi d) - \cos(2\zeta d)]} \\ &\quad \times\Big\{\sin(2\zeta d) - \sin(2\zeta z_{2D})\cosh\left[2\chi\left(d - z_{2D}\right)\right], \\ &\quad -\sin\left[2\zeta\left(d - z_{2D}\right)\right]\cosh\left(2\chi z_{2D}\right)\Big\}, \end{aligned} \tag{15}$$

with $\gamma = t^2/v_F$, an energy scale determined by the tunneling strength. The quantity $\Gamma_{k,\omega}$ can be interpreted as an effective quasiparticle weight, as it takes values of $0 < \Gamma < 1$, and is responsible for inducing superconductivity in the 2DEG, while $\delta\mu_{k,\omega}$ corresponds to a tunneling-induced shift in the effective chemical potential of the 2DEG. Quite surprisingly, the self-energy in Equation 14 and Equation 15 coincides with that of a nanowire coupled to a two-dimensional superconductor with finite width as found in [48], with the simple replacement of a 1D momentum by the magnitude of a 2D momentum.

Results and Discussion

Induced gap and band shift

Using the self-energy derived in the previous section, we first calculate the size of the proximity-induced gap in the 2DEG. Once we find an expression for the gap, we estimate the tunneling strength needed in order for the gap in the 2DEG to be comparable to that in the superconductor. We then add a Zeeman term to the Hamiltonian of the 2DEG and estimate the Zeeman energy needed to reach the topological phase in such a setup.

It is convenient to work in the chiral basis in which the normal Green's function of the 2DEG is diagonal. To this end, we introduce a unitary transformation

$$U_{\mathbf{k}} = \frac{1}{\sqrt{2}}\begin{pmatrix} 1 & 1 & 0 & 0 \\ -ie^{i\phi_{\mathbf{k}}} & ie^{i\phi_{\mathbf{k}}} & 0 & 0 \\ 0 & 0 & 1 & 1 \\ 0 & 0 & -ie^{-i\phi_{\mathbf{k}}} & ie^{-i\phi_{\mathbf{k}}} \end{pmatrix}, \tag{16}$$

with $\phi_{\mathbf{k}} = \tan^{-1}(k_y/k_x)$, which can be used to convert between the spin (σ) and chiral (λ) bases, $G^{\lambda}_{\mathbf{k},\omega} = U^{\dagger}_{\mathbf{k}} G^{\sigma}_{\mathbf{k},\omega} U_{\mathbf{k}}$. The Green's function in the spin basis is given by $G^{\sigma}_{\mathbf{k},\omega} = (i\omega - \mathcal{H}^{2D}_{\mathbf{k}} - \Sigma_{k,\omega})^{-1}$. Rotating to the chiral basis, we find a Green's function given by

$$G^{\lambda}_{\mathbf{k},\omega} = \begin{pmatrix} \frac{-i\tilde{\omega} - \tilde{\xi}_+}{\tilde{\omega}^2 + \tilde{\xi}_+^2 + \tilde{\Delta}^2} & 0 & \frac{i\tilde{\Delta}e^{-i\phi_{\mathbf{k}}}}{\tilde{\omega}^2 + \tilde{\xi}_+^2 + \tilde{\Delta}^2} & 0 \\ 0 & \frac{-i\tilde{\omega} - \tilde{\xi}_-}{\tilde{\omega}^2 + \tilde{\xi}_-^2 + \tilde{\Delta}^2} & 0 & \frac{-i\tilde{\Delta}e^{-i\phi_{\mathbf{k}}}}{\tilde{\omega}^2 + \tilde{\xi}_-^2 + \tilde{\Delta}^2} \\ \frac{-i\tilde{\Delta}e^{i\phi_{\mathbf{k}}}}{\tilde{\omega}^2 + \tilde{\xi}_+^2 + \tilde{\Delta}^2} & 0 & \frac{-i\tilde{\omega} + \tilde{\xi}_+}{\tilde{\omega}^2 + \tilde{\xi}_+^2 + \tilde{\Delta}^2} & 0 \\ 0 & \frac{i\tilde{\Delta}e^{i\phi_{\mathbf{k}}}}{\tilde{\omega}^2 + \tilde{\xi}_-^2 + \tilde{\Delta}^2} & 0 & \frac{-i\tilde{\omega} + \tilde{\xi}_-}{\tilde{\omega}^2 + \tilde{\xi}_-^2 + \tilde{\Delta}^2} \end{pmatrix}, \tag{17}$$

where $\tilde{\omega} = \omega/\Gamma_{k,\omega}$, $\tilde{\xi}_\pm = \xi_k - \delta\mu_{k,\omega} \pm \alpha k$ and $\tilde{\Delta} = \Delta(1/\Gamma_{k,\omega} - 1)$. The spin–singlet pairing induced by the superconductor appears as intraband chiral p-wave pairing (of the form $p_x \pm ip_y$) when expressed in the chiral basis.

Before continuing, let us simplify the parameters $\Gamma_{k,\omega}$ and $\delta\mu_{k,\omega}$. We will focus on the limit where the thickness of the superconducting layer is much smaller than its coherence length, $d \ll \xi_s$ (equivalently, $\Delta \ll \delta E_s$), and where the normal layer is located close to the edge of the superconductor, $k_F z_{2D} \ll 1$. Because of the large Fermi surface mismatch between the 2DEG and superconductor, we must have $k \ll k_F$ (or, equivalently, $\varphi \approx 1$); in the following, we neglect the momentum dependence by setting $\varphi = 1$ (which is justified as long as we only consider momenta $k \ll 1/\sqrt{k_F d}$). In the limit $\omega \ll \delta E_s$, the parameters simplify to

$$\Gamma = \left(1+\frac{2\pi\gamma\left(k_{\mathrm{F}}z_{2\mathrm{D}}\right)^2}{\delta E_{\mathrm{s}}\sin^2\left(k_{\mathrm{F}}d\right)}\right)^{-1}, \qquad (18)$$
$$\delta\mu = 2\gamma\left(k_{\mathrm{F}}z_{2\mathrm{D}}\right)\left[1-\left(k_{\mathrm{F}}z_{2\mathrm{D}}\right)\cot\left(k_{\mathrm{F}}d\right)\right],$$

where we drop the subscript (k,ω) because both Γ and $\delta\mu$ are now independent of frequency and momentum. In expanding Equation 15 to arrive at Equation 18, we assumed that $|\sin(k_{\mathrm{F}}d)| \gg \Delta/\delta E_{\mathrm{s}}$ (therefore, these expressions break down when $k_{\mathrm{F}}d/\pi \to n$, with $n \in \mathbb{Z}^+$).

The spectrum of the proximitized 2DEG is determined by the poles of the retarded Green's function. After analytic continuation $i\omega \to E + i0^+$, we find two branches of the spectrum from Equation 17 given by

$$E_{\pm}^2(k) = \Gamma^2\left(\frac{k^2}{2m_{2\mathrm{D}}} - \mu_{\mathrm{eff}} \pm \alpha k\right)^2 + \Delta^2(1-\Gamma)^2, \qquad (19)$$

where $\mu_{\mathrm{eff}} = \mu_{2\mathrm{D}} + \delta\mu$ is an effective chemical potential of the 2DEG. The spectrum describes an *s*-wave superconductor with Rashba-split bands and an excitation gap

$$E_{\mathrm{g}} = \Delta(1-\Gamma). \qquad (20)$$

We see that the size of the excitation gap is determined by the parameter Γ. When $\Gamma \ll 1$, the full bulk gap of the superconductor is induced in the 2DEG, while for $(1-\Gamma) \ll 1$, a very small gap is induced. In order to have an induced gap comparable (but not equal) to the bulk gap, we require that neither $\Gamma \ll 1$ nor $(1-\Gamma) \ll 1$ is satisfied. However, to realize this situation requires a tunneling strength

$$\gamma \sim \delta E_{\mathrm{s}}, \qquad (21)$$

where we have assumed that $(k_{\mathrm{F}}z_{2\mathrm{D}})^2/\sin^2(k_{\mathrm{F}}d) \sim 1$. If the tunneling strength is chosen as in Equation 21, the band shift measured at $k = 0$, $E_{\pm}(0)$, is

$$E_{\pm}(0) \sim \Gamma\delta\mu \sim \delta E_{\mathrm{s}}. \qquad (22)$$

Therefore, the scale of the band shift is also set by the level spacing in the thin superconducting layer. We note that while the quantity $\delta\mu$ is bounded only by the chemical potential of the superconductor μ_{s} (as the tunneling Hamiltonian approach itself should break down for $\gamma \sim \mu_{\mathrm{s}}$), the band shift saturates to $E_{\pm}(0) \sim \delta E_{\mathrm{s}}$ in the limit $\gamma \gg \delta E_{\mathrm{s}}$ (where $\Gamma \ll 1$).

We plot the spectrum of the 2DEG (see Equation 19) in Figure 3. In the weak-coupling limit (Figure 3a), there is a rather small band shift but a negligible superconducting gap is opened in the 2DEG. In the strong-coupling limit (Figure 3b), we show that while a larger gap is induced, the band shift is very large.

Topological transition

We now add a Zeeman splitting Δ_{Z} to the Hamiltonian of the 2DEG such that

$$\mathcal{H}_{\mathbf{k}}^{2\mathrm{D}} = \xi_k\tau_z + \alpha\left(k_y\sigma_x - k_x\tau_z\sigma_y\right) - \Delta_{\mathrm{Z}}\tau_z\sigma_z. \qquad (23)$$

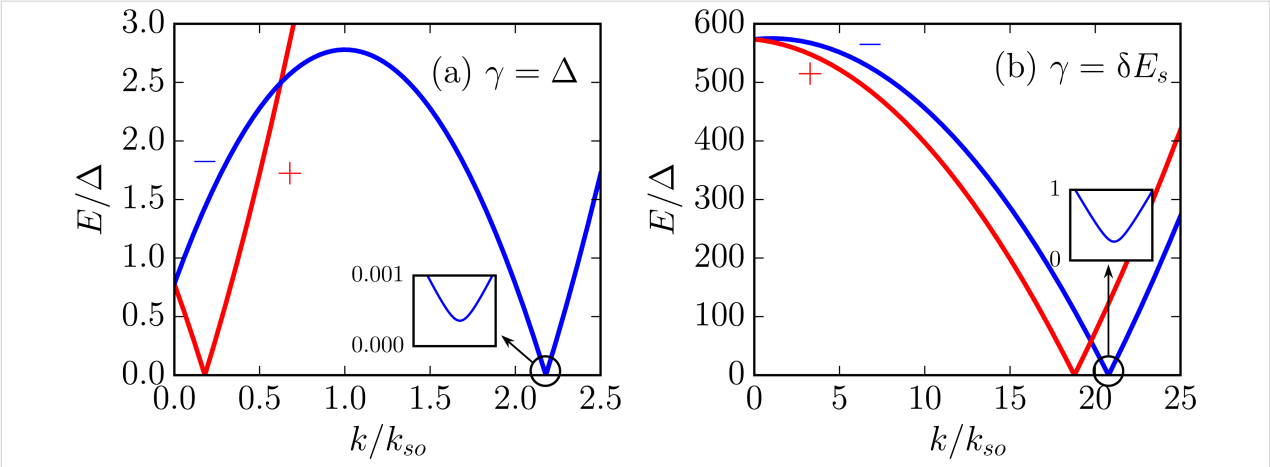

Figure 3: Spectrum of a 2DEG coupled to a thin superconducting layer (see Equation 19) for (a) $\gamma = \Delta$ (corresponding to $\Gamma = 0.9996$ and $\delta\mu = 0.78\Delta$) and (b) $\gamma = \delta E_{\mathrm{s}}$ (corresponding to $\Gamma = 0.735$ and $\delta\mu = 780\Delta$). When tunneling is weak (as in panel a), the band shift is rather small but the induced gap is negligible. If tunneling is strong enough to open a sizable gap (as in panel b), the band shift is very large (note that the band shift is given by $E_{\pm}(0) \sim \Gamma\delta\mu$ rather than $\delta\mu$). In both plots, $E_{\mathrm{so}} = 2\Delta$, $\delta E_{\mathrm{s}} = 1000\Delta$, $\mu_{2\mathrm{D}} = 0$, $k_{\mathrm{F}}d/\pi = 48.75$, and $k_{\mathrm{F}}z_{2\mathrm{D}} = 0.3$. Here $k_{\mathrm{so}} = m\alpha$ is the spin–orbit momentum. Note that although, in the insets, we show only the induced gap on the "−"-subband, there is an equally large gap induced on the "+"-subband.

Such a Zeeman splitting can arise due to the application of an out-of-plane magnetic field [4,5] (though orbital effects are not incorporated here) or due to the proximity of a magnetic insulator [8]. Also, it is possible to apply an in-plane magnetic field (to avoid unwanted orbital effects) to reach the topological phase if the 2DEG has a finite Dresselhaus SOI, as shown in [9]. An in-plane magnetic field in the presence of only Rashba SOI is not sufficient to reach the topological phase because it does not open a gap in the Rashba spectrum. The spectrum in the presence of the Zeeman splitting, which again is determined by poles in the retarded Green's function $G^R_{\mathbf{k},E} = (E - \mathcal{H}^{2D}_{\mathbf{k}} - \Sigma + i0^+)^{-1}$, is given by

$$E^2 = \Gamma^2\left[\Delta_Z^2 + \left(\xi_k - \delta\mu\right)^2 + \alpha^2 k^2\right] + E_g^2 \pm 2\Gamma\sqrt{\Delta_Z^2 E_g^2 + \Gamma^2\left(\xi_k - \delta\mu\right)^2\left(\Delta_Z^2 + \alpha^2 k^2\right)}, \tag{24}$$

where we have used $E_g = \Delta(1 - \Gamma)$ as in Equation 20. Therefore, we find a gap-closing topological transition at $k = 0$ for the critical Zeeman splitting

$$\Gamma\Delta_Z^c = \sqrt{\Gamma^2\left(\mu_{2D} + \delta\mu\right)^2 + E_g^2}. \tag{25}$$

In the case of a very large band shift, $\Gamma\delta\mu \gg E_g$ and $\delta\mu \gg \mu_{2D}$, the topological transition is given by $\Delta_Z^c = \delta\mu$ [note that Γ drops out of Equation 25 in this limit].

We now provide an estimate of the Zeeman splitting at which we expect the $k = 0$ gap-closing transition to occur experimentally in an Al/InAs 2DEG heterostructure. Given the thickness of the superconducting Al layer of $d = 10$ nm [44], we estimate a level spacing of $\delta E_s = \pi\hbar v_F / d = 413$ meV (taking $v_F = 2 \times 10^6$ m/s). Therefore, if a sizable gap is induced in the 2DEG, as observed experimentally, typical values for the band shift are of the same order of magnitude as the level spacing, $\Gamma\delta\mu \sim 400$ meV. Then, provided that the chemical potential cannot be controlled over such a large scale by external gates, the critical Zeeman splitting needed to reach the topological phase is $\Delta_Z^c = \delta\mu \sim 400$ meV. Such a large Zeeman splitting cannot be achieved in the 2DEG without destroying superconductivity in the thin layer. We also note the possibility that, by coincidence, the band shift vanishes (or becomes small); from Equation 18, we see that $\delta\mu = 0$ if $k_F d = \cot^{-1}(1/k_F z_{2D}) + n\pi$ (for $n \in \mathbb{Z}$). In this special case, which requires the thickness of the superconducting layer to be finely tuned on the scale of its Fermi wavelength, there is no band shift to prevent one from tuning into a topological phase. However, for most devices, the large band shift makes it very challenging to realize a topological phase.

Increasing thickness of superconducting layer

The self-energy appearing most frequently in the literature to describe proximitized nanowires and 2DEGs [55-60], which also has been used often in interpreting experimental results [40,42], is that induced by a bulk superconductor,

$$\Gamma_{bulk} = \left(1 + \gamma/\Omega\right)^{-1}, \quad \delta\mu_{bulk} = 0. \tag{26}$$

Equation 26 can be obtained by setting $z_{2D} = d/2$ and taking the limit $d \to \infty$ in Equation 15 (or, as it is usually done, by substituting the bulk Green's function in Equation 13 when evaluating the self-energy in Equation 10). Hence, this self-energy describes a 2DEG embedded within a bulk superconductor, as shown in Figure 4a. To describe the case where a 2DEG is placed at the surface of a bulk superconductor (as shown in Figure 4b), the limit $d \to \infty$ should be taken in Equation 15 while keeping z_{2D} finite (or, equivalently, substituting the Green's function of a semi-infinite (SI) superconductor when evaluating the self-energy in Equation 10). For this case, we obtain

$$\Gamma_{SI} = \left(1 + \frac{\gamma}{\Omega}\left\{1 - \cos\left(2\zeta z_{2D}\right)e^{-2\chi z_{2D}}\right\}\right)^{-1}, \quad \delta\mu_{SI} = \gamma\sin\left(2\zeta z_{2D}\right)e^{-2\chi z_{2D}}. \tag{27}$$

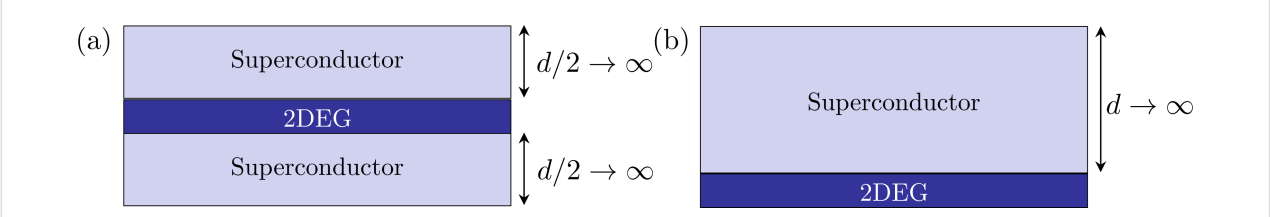

Figure 4: (a) Evaluating the self-energy with the Green's function of a bulk superconductor (see Equation 26) corresponds to a 2DEG embedded within an infinitely large superconductor. (b) Evaluating the self-energy with the Green's function of a semi-infinite superconductor (see Equation 27) corresponds to a 2DEG placed on the surface of an infinitely large superconductor.

The most notable difference is the presence of a nonzero band shift in the semi-infinite case. However, this band shift is significantly reduced compared to the case of a thin superconducting layer, as it saturates to $E_{\pm}(0) \sim \Gamma_{SI}\delta\mu_{SI} \sim \Delta$ in the limit $\gamma \gg \Delta$.

Although it may seem that a topological phase can be much more easily realized by simply increasing the thickness of the superconducting layer in order to reduce the band shift induced on the 2DEG, this is not the case. Crucially, both the bulk and the semi-infinite self-energies give the ratio γ/Δ as the relevant parameter determining whether the system is in the weak-coupling [$(1-\Gamma) \ll 1$, or equivalently $E_g \ll \Delta$] or strong-coupling [$(1 - \Gamma) \sim 1$, or equivalently $E_g \sim \Delta$] limit. This is in stark contrast to the limit of a thin superconducting layer, where a tunneling energy $\gamma \sim \delta E_s \gg \Delta$ is required to open a gap $E_g \sim \Delta$ in the 2DEG. Therefore, because the tunneling energy γ is a property of the interface and should not be expected to change as the thickness of the superconducting layer is increased, this energy is fixed to $\gamma \sim \delta E_s$ provided that the interface is transparent enough to induce a gap in the thin-layer limit (as seen in the experiments). If the thickness of the superconductor is increased, such that $d \gg \xi_s$, the system will be deep within the strong-coupling limit; from Equation 26 and Equation 27, we find $\Gamma \sim \Delta / \gamma \ll 1$. The critical Zeeman splitting needed to induce a topological phase (see Equation 25) is therefore given by $\Delta_Z^c \sim \Delta/\Gamma \sim \gamma \sim 400$ meV. We note that in the case of a thin superconducting layer, the topological transition is pushed to large Zeeman splitting by very large $\delta\mu$, which could possibly be compensated for if the chemical potential μ_{2D} has a large range of tunability. In the case of a bulk system, the topological transition is pushed to large Zeeman splitting by very small Γ, which cannot be affected by tuning μ_{2D}. Hence, even if the thickness d of the superconducting layer is made infinite, the topological phase transition is determined by the interfacial tunneling energy. In order to induce a topological phase more reliably, a much weaker coupling between a 2DEG and a bulk superconductor (such that $\gamma \leq \Delta$) should be sought. We also note that this result applies to the 1D model considered in [48] as well.)

Conclusion

We have studied the proximity effect in a two-dimensional electron gas (2DEG) strongly coupled to a thin superconducting layer, showing that the detrimental band shift shown in [48,49] to dominate the proximity effect in wires is also crucial in 2DEGs. In order to induce a sizable gap in the 2DEG, the tunneling energy scale must overcome the large level spacing within the superconductor. However, introducing such a large energy scale to the semiconductor induces a large band shift that makes it challenging to realize a topological phase. This challenge cannot be alleviated by simply increasing the thickness of the superconducting layer but requires a significant weakening of the proximity coupling afforded by the epitaxial interface.

Acknowledgements

This work was supported by the Swiss National Science Foundation and the NCCR QSIT.

ORCID® iDs

Christopher Reeg - https://orcid.org/0000-0002-2357-4766
Daniel Loss - https://orcid.org/0000-0001-5176-3073

References

1. Kitaev, A. Y. *Phys.-Usp.* **2001,** *44,* 131. doi:10.1070/1063-7869/44/10S/S29
2. Nayak, C.; Simon, S. H.; Stern, A.; Freedman, M.; Das Sarma, S. *Rev. Mod. Phys.* **2008,** *80,* 1083. doi:10.1103/RevModPhys.80.1083
3. Alicea, J. *Rep. Prog. Phys.* **2012,** *75,* 076501. doi:10.1088/0034-4885/75/7/076501
4. Sato, M.; Fujimoto, S. *Phys. Rev. B* **2009,** *79,* 094504. doi:10.1103/PhysRevB.79.094504
5. Sato, M.; Takahashi, Y.; Fujimoto, S. *Phys. Rev. Lett.* **2009,** *103,* 020401. doi:10.1103/PhysRevLett.103.020401
6. Lutchyn, R. M.; Sau, J. D.; Das Sarma, S. *Phys. Rev. Lett.* **2010,** *105,* 077001. doi:10.1103/PhysRevLett.105.077001
7. Oreg, Y.; Refael, G.; von Oppen, F. *Phys. Rev. Lett.* **2010,** *105,* 177002. doi:10.1103/PhysRevLett.105.177002
8. Sau, J. D.; Lutchyn, R. M.; Tewari, S.; Das Sarma, S. *Phys. Rev. Lett.* **2010,** *104,* 040502. doi:10.1103/PhysRevLett.104.040502
9. Alicea, J. *Phys. Rev. B* **2010,** *81,* 125318. doi:10.1103/PhysRevB.81.125318
10. Chevallier, D.; Sticlet, D.; Simon, P.; Bena, C. *Phys. Rev. B* **2012,** *85,* 235307. doi:10.1103/PhysRevB.85.235307
11. Halperin, B. I.; Oreg, Y.; Stern, A.; Refael, G.; Alicea, J.; von Oppen, F. *Phys. Rev. B* **2012,** *85,* 144501. doi:10.1103/PhysRevB.85.144501
12. Sticlet, D.; Bena, C.; Simon, P. *Phys. Rev. Lett.* **2012,** *108,* 096802. doi:10.1103/PhysRevLett.108.096802
13. Klinovaja, J.; Stano, P.; Loss, D. *Phys. Rev. Lett.* **2012,** *109,* 236801. doi:10.1103/PhysRevLett.109.236801
14. Klinovaja, J.; Gangadharaiah, S.; Loss, D. *Phys. Rev. Lett.* **2012,** *108,* 196804. doi:10.1103/PhysRevLett.108.196804
15. Prada, E.; San-Jose, P.; Aguado, R. *Phys. Rev. B* **2012,** *86,* 180503. doi:10.1103/PhysRevB.86.180503
16. Domínguez, F.; Hassler, F.; Platero, G. *Phys. Rev. B* **2012,** *86,* 140503. doi:10.1103/PhysRevB.86.140503
17. Klinovaja, J.; Loss, D. *Phys. Rev. X* **2013,** *3,* 011008. doi:10.1103/PhysRevX.3.011008
18. DeGottardi, W.; Thakurathi, M.; Vishveshwara, S.; Sen, D. *Phys. Rev. B* **2013,** *88,* 165111. doi:10.1103/PhysRevB.88.165111
19. Maier, F.; Klinovaja, J.; Loss, D. *Phys. Rev. B* **2014,** *90,* 195421. doi:10.1103/PhysRevB.90.195421
20. Vernek, E.; Penteado, P. H.; Seridonio, A. C.; Egues, J. C. *Phys. Rev. B* **2014,** *89,* 165314. doi:10.1103/PhysRevB.89.165314
21. Weithofer, L.; Recher, P.; Schmidt, T. L. *Phys. Rev. B* **2014,** *90,* 205416. doi:10.1103/PhysRevB.90.205416
22. Thakurathi, M.; Deb, O.; Sen, D. *J. Phys.: Condens. Matter* **2015,** *27,* 275702. doi:10.1088/0953-8984/27/27/275702

23. Dmytruk, O.; Trif, M.; Simon, P. *Phys. Rev. B* **2015,** *92,* 245432. doi:10.1103/PhysRevB.92.245432
24. Nadj-Perge, S.; Drozdov, I. K.; Li, J.; Chen, H.; Jeon, S.; Seo, J.; MacDonald, A. H.; Bernevig, B. A.; Yazdani, A. *Science* **2014,** *346,* 602. doi:10.1126/science.1259327
25. Ruby, M.; Pientka, F.; Peng, Y.; von Oppen, F.; Heinrich, B. W.; Franke, K. J. *Phys. Rev. Lett.* **2015,** *115,* 197204. doi:10.1103/PhysRevLett.115.197204
26. Pawlak, R.; Kisiel, M.; Klinovaja, J.; Meier, T.; Kawai, S.; Glatzel, T.; Loss, D.; Meyer, E. *npj Quantum Inf.* **2016,** *2,* 16035. doi:10.1038/npjqi.2016.35
27. Klinovaja, J.; Stano, P.; Yazdani, A.; Loss, D. *Phys. Rev. Lett.* **2013,** *111,* 186805. doi:10.1103/PhysRevLett.111.186805
28. Vazifeh, M. M.; Franz, M. *Phys. Rev. Lett.* **2013,** *111,* 206802. doi:10.1103/PhysRevLett.111.206802
29. Braunecker, B.; Simon, P. *Phys. Rev. Lett.* **2013,** *111,* 147202. doi:10.1103/PhysRevLett.111.147202
30. Nadj-Perge, S.; Drozdov, I. K.; Bernevig, B. A.; Yazdani, A. *Phys. Rev. B* **2013,** *88,* 020407. doi:10.1103/PhysRevB.88.020407
31. Pientka, F.; Glazman, L. I.; von Oppen, F. *Phys. Rev. B* **2013,** *88,* 155420. doi:10.1103/PhysRevB.88.155420
32. Awoga, O. A.; Björnson, K.; Black-Schaffer, A. M. *Phys. Rev. B* **2017,** *95,* 184511. doi:10.1103/PhysRevB.95.184511
33. Mourik, V.; Zuo, K.; Frolov, S. M.; Plissard, S. R.; Bakkers, E. P. A. M.; Kouwenhoven, L. P. *Science* **2012,** *336,* 1003. doi:10.1126/science.1222360
34. Deng, M. T.; Yu, C. L.; Huang, G. Y.; Larsson, M.; Caroff, P.; Xu, H. Q. *Nano Lett.* **2012,** *12,* 6414. doi:10.1021/nl303758w
35. Das, A.; Ronen, Y.; Most, Y.; Oreg, Y.; Heiblum, M.; Shtrikman, H. *Nat. Phys.* **2012,** *8,* 887. doi:10.1038/nphys2479
36. Churchill, H. O. H.; Fatemi, V.; Grove-Rasmussen, K.; Deng, M. T.; Caroff, P.; Xu, H. Q.; Marcus, C. M. *Phys. Rev. B* **2013,** *87,* 241401. doi:10.1103/PhysRevB.87.241401
37. Finck, A. D. K.; Van Harlingen, D. J.; Mohseni, P. K.; Jung, K.; Li, X. *Phys. Rev. Lett.* **2013,** *110,* 126406. doi:10.1103/PhysRevLett.110.126406
38. Chang, W.; Albrecht, S. M.; Jespersen, T. S.; Kuemmeth, F.; Krogstrup, P.; Nygård, J.; Marcus, C. M. *Nat. Nanotechnol.* **2015,** *10,* 232. doi:10.1038/nnano.2014.306
39. Albrecht, S. M.; Higginbotham, A. P.; Madsen, M.; Kuemmeth, F.; Jespersen, T. S.; Nygård, J.; Krogstrup, P.; Marcus, C. M. *Nature* **2016,** *531,* 206–209. doi:10.1038/nature17162
40. Deng, M. T.; Vaitiekėnas, S.; Hansen, E. B.; Danon, J.; Leijnse, M.; Flensberg, K.; Nygård, J.; Krogstrup, P.; Marcus, C. M. *Science* **2016,** *354,* 1557. doi:10.1126/science.aaf3961
41. Gazibegovic, S.; Car, D.; Zhang, H.; Balk, S. C.; Logan, J. A.; de Moor, M. W. A.; Cassidy, M. C.; Schmits, R.; Xu, D.; Wang, G.; Krogstrup, P.; Op het Veld, R. L. M.; Zuo, K.; Vos, Y.; Shen, J.; Bouman, D.; Shojaei, B.; Pennachio, D.; Lee, J. S.; van Veldhoven, P. J.; Koelling, S.; Verheijen, M. A.; Kouwenhoven, L. P.; Palmstrøm, C. J.; Bakkers, E. P. A. M. *Nature* **2017,** *548,* 434. doi:10.1038/nature23468
42. Zhang, H.; Liu, C.-X.; Gazibegovic, S.; Xu, D.; Logan, J. A.; Wang, G.; van Loo, N.; Bommer, J. D. S.; de Moor, M. W. A.; Car, D.; het Veld, R. L. M. O.; van Veldhoven, P. J.; Koelling, S.; Verheijen, M. A.; Pendharkar, M.; Pennachio, D. J.; Shojaei, B.; Lee, J. S.; Palmstrom, C. J.; Bakkers, E. P. A. M.; Das Sarma, S.; Kouwenhoven, L. P. *arXiv* **2017,** No. 1710.10701.
43. Kjaergaard, M.; Nichele, F.; Suominen, H. J.; Nowak, M. P.; Wimmer, M.; Akhmerov, A. R.; Folk, J. A.; Flensberg, K.; Shabani, J.; Palmstrøm, C. J.; Marcus, C. M. *Nat. Commun.* **2016,** *7,* 12841. doi:10.1038/ncomms12841
44. Shabani, J.; Kjaergaard, M.; Suominen, H. J.; Kim, Y.; Nichele, F.; Pakrouski, K.; Stankevic, T.; Lutchyn, R. M.; Krogstrup, P.; Feidenhans'l, R.; Kraemer, S.; Nayak, C.; Troyer, M.; Marcus, C. M.; Palmstrøm, C. J. *Phys. Rev. B* **2016,** *93,* 155402. doi:10.1103/PhysRevB.93.155402
45. Kjaergaard, M.; Suominen, H. J.; Nowak, M. P.; Akhmerov, A. R.; Shabani, J.; Palmstrøm, C. J.; Nichele, F.; Marcus, C. M. *Phys. Rev. Appl.* **2017,** *7,* 034029. doi:10.1103/PhysRevApplied.7.034029
46. Suominen, H. J.; Kjaergaard, M.; Hamilton, A. R.; Shabani, J.; Palmstrøm, C. J.; Marcus, C. M.; Nichele, F. *Phys. Rev. Lett.* **2017,** *119,* 176805. doi:10.1103/PhysRevLett.119.176805
47. Nichele, F.; Drachmann, A. C. C.; Whiticar, A. M.; O'Farrell, E. C. T.; Suominen, H. J.; Fornieri, A.; Wang, T.; Gardner, G. C.; Thomas, C.; Hatke, A. T.; Krogstrup, P.; Manfra, M. J.; Flensberg, K.; Marcus, C. M. *Phys. Rev. Lett.* **2017,** *119,* 136803. doi:10.1103/PhysRevLett.119.136803
48. Reeg, C.; Loss, D.; Klinovaja, J. *Phys. Rev. B* **2017,** *96,* 125426. doi:10.1103/PhysRevB.96.125426
49. Reeg, C.; Loss, D.; Klinovaja, J. *arXiv* **2018,** No. 1801.06509.
50. Volkov, A. F.; Magnée, P. H. C.; van Wees, B. J.; Klapwijk, T. M. *Physica C* **1995,** *242,* 261. doi:10.1016/0921-4534(94)02429-4
51. Fagas, G.; Tkachov, G.; Pfund, A.; Richter, K. *Phys. Rev. B* **2005,** *71,* 224510. doi:10.1103/PhysRevB.71.224510
52. Tkachov, G. *Physica C* **2005,** *417,* 127. doi:10.1016/j.physc.2004.10.015
53. Reeg, C. R.; Maslov, D. L. *Phys. Rev. B* **2016,** *94,* 020501. doi:10.1103/PhysRevB.94.020501
54. Reeg, C.; Klinovaja, J.; Loss, D. *Phys. Rev. B* **2017,** *96,* 081301. doi:10.1103/PhysRevB.96.081301
55. Sau, J. D.; Lutchyn, R. M.; Tewari, S.; Das Sarma, S. *Phys. Rev. B* **2010,** *82,* 094522. doi:10.1103/PhysRevB.82.094522
56. Potter, A. C.; Lee, P. A. *Phys. Rev. B* **2011,** *83,* 184520. doi:10.1103/PhysRevB.83.184520
57. Kopnin, N. B.; Melnikov, A. S. *Phys. Rev. B* **2011,** *84,* 064524. doi:10.1103/PhysRevB.84.064524
58. Zyuzin, A. A.; Rainis, D.; Klinovaja, J.; Loss, D. *Phys. Rev. Lett.* **2013,** *111,* 056802. doi:10.1103/PhysRevLett.111.056802
59. van Heck, B.; Lutchyn, R. M.; Glazman, L. I. *Phys. Rev. B* **2016,** *93,* 235431. doi:10.1103/PhysRevB.93.235431
60. Reeg, C.; Maslov, D. L. *Phys. Rev. B* **2017,** *95,* 205439. doi:10.1103/PhysRevB.95.205439

BEILSTEIN JOURNAL OF NANOTECHNOLOGY

Andreev spectrum and supercurrents in nanowire-based SNS junctions containing Majorana bound states

Jorge Cayao[1], Annica M. Black-Schaffer[1], Elsa Prada[2] and Ramón Aguado[*3]

Full Research Paper

Open Access

Address:
[1]Department of Physics and Astronomy, Uppsala University, Box 516, S-751 20 Uppsala, Sweden, [2]Departamento de Física de la Materia Condensada, Condensed Matter Physics Center (IFIMAC) & Instituto Nicolás Cabrera, Universidad Autónoma de Madrid, E-28049 Madrid, Spain and [3]Instituto de Ciencia de Materiales de Madrid (ICMM-CSIC), Cantoblanco, 28049 Madrid, Spain

Email:
Ramón Aguado[*] - raguado@icmm.csic.es

* Corresponding author

Keywords:
hybrid superconductor–semiconductor nanowire–superconductor junctions; Josephson effect; Majorana bound states; nanowires; spin–orbit coupling; Zeeman interaction

Beilstein J. Nanotechnol. **2018,** *9,* 1339–1357.
doi:10.3762/bjnano.9.127

Received: 03 January 2018
Accepted: 04 April 2018
Published: 03 May 2018

This article is part of the Thematic Series "Topological materials".

Associate Editor: J. M. van Ruitenbeek

Abstract

Hybrid superconductor–semiconductor nanowires with Rashba spin–orbit coupling are arguably becoming the leading platform for the search of Majorana bound states (MBSs) in engineered topological superconductors. We perform a systematic numerical study of the low-energy Andreev spectrum and supercurrents in short and long superconductor–normal–superconductor junctions made of nanowires with strong Rashba spin–orbit coupling, where an external Zeeman field is applied perpendicular to the spin–orbit axis. In particular, we investigate the detailed evolution of the Andreev bound states from the trivial into the topological phase and their relation with the emergence of MBSs. Due to the finite length, the system hosts four MBSs, two at the inner part of the junction and two at the outer one. They hybridize and give rise to a finite energy splitting at a superconducting phase difference of π, a well-visible effect that can be traced back to the evolution of the energy spectrum with the Zeeman field: from the trivial phase with Andreev bound states into the topological phase with MBSs. Similarly, we carry out a detailed study of supercurrents for short and long junctions from the trivial to the topological phases. The supercurrent, calculated from the Andreev spectrum, is 2π-periodic in the trivial and topological phases. In the latter it exhibits a clear sawtooth profile at a phase difference of π when the energy splitting is negligible, signalling a strong dependence of current–phase curves on the length of the superconducting regions. Effects of temperature, scalar disorder and reduction of normal transmission on supercurrents are also discussed. Further, we identify the individual contribution of MBSs. In short junctions the MBSs determine the current–phase curves, while in long junctions the spectrum above the gap (quasi-continuum) introduces an important contribution.

Introduction

A semiconducting nanowire with strong Rashba spin–orbit coupling (SOC) with proximity-induced *s*-wave superconducting correlations can be tuned into a topological superconductor by means of an external Zeeman field [1-3]. This topological phase is characterized by the emergence of zero-energy quasiparticles with Majorana character localized at the nanowire ends. These Majorana bound states (MBSs) are attracting a great deal of attention owing to their potential for topological, fault-tolerant quantum computation [4-6]. Tunneling into such zero-energy MBSs results in a zero-bias peak of high $2e^2/h$ in the tunnelling conductance in normal–superconductor (NS) junctions due to perfect Andreev reflection into a particle–hole symmetric state [7]. Early tunnelling experiments in NS junctions [8-12] reported zero-bias peak values much smaller than the predicted $2e^2/h$. This deviation from the ideal prediction, together with alternative explanations of the zero-bias peak, resulted in controversy regarding the interpretation. Recent experiments have reported significant fabrication improvements and high-quality semiconductor–superconductor interfaces [13-16] with an overall improvement on tunnelling data that strongly supports the observation of MBS [17-21].

Given this experimental state-of-the-art [22], new geometries and signatures beyond zero-bias peaks in NS junctions will likely be explored in the near future. Among them, nanowire-based superconductor–normal–superconductor (SNS) junctions are very promising since they are expected to host an exotic fractional 4π-periodic Josephson effect [4,23,24], signalling the presence of MBSs in the junction. While this prediction has spurred a great deal of theoretical activity [25-32], experiments are still scarce [33], arguably due to the lack of good junctions until recently. The situation is now different and, since achieving high-quality interfaces is no longer an issue, Andreev-level spectroscopy and phase-biased supercurrents should provide additional signatures for the unambiguous detection of MBSs in nanowire SNS junctions. Similarly, multiple Andreev reflection transport in voltage-biased SNS junctions [34,35] is another promising tool to provide further evidence of MBSs [36].

Motivated by this, we here present a detailed numerical investigation of the formation of Andreev bound states (ABSs) and their evolution into MBSs in nanowire-based short and long SNS junctions biased by a superconducting phase difference ϕ. Armed with this information, we also perform a systematic study of the phase-dependent supercurrents in the short- and long-junction limits. Due to finite length, the junction always hosts four MBSs in the topological regime. Apart from the MBSs located at the junction (inner MBSs), two extra MBSs are located at the nanowire ends (outer MBSs). Despite the early predictions [4,23,24] of a 4π-periodic Josephson effect in superconducting junctions containing MBSs, in general we demonstrate that the unavoidable overlap of these MBSs renders the equilibrium Josephson effect 2π-periodic [26,27] in short and long junctions, since they hybridize either through the normal region or through the superconducting regions giving rise to a finite energy splitting at phase difference $\phi = \pi$. As an example, our calculations show that, for typical InSb parameters, one needs to consider junctions with long superconducting segments of the order of $L_S \geq 4\mu m$, where L_S is the length of the S regions, in order to have negligible energy splittings.

In particular, we show that in short junctions with $L_N \ll \xi$, where L_N is the normal region length and ξ is the superconducting coherence length, the four MBSs (inner and outer) are the only levels within the induced gap. On the contrary, the four MBSs coexist with additional levels in long junctions with $L_N \gg \xi$, which affect their phase dependence. Despite this difference, we demonstrate that the supercurrents in both limits exhibits a clear sawtooth profile when the energy splitting near $\phi = \pi$ is small, therefore signalling the presence of weakly overlapping MBSs. We find that while this sawtooth profile is robust against variations in the normal transmission and scalar disorder, it smooths out when temperature effects are included, making it a fragile, yet useful, signature of MBSs.

We identify that in short junctions the current–phase curves are mainly determined by the levels within the gap and by the four MBSs, with only very little quasi-continuum contribution. In long junctions, however, all the levels within the gap, the MBSs and the additional levels due to longer normal region together with the quasi-continuum determine the current–phase curves. In this situation, the additional levels that arise within the gap disperse almost linearly with ϕ and therefore affect the features of the supercurrents carried by MBSs only.

Another important feature we find is that the current–phase curves do not depend on L_S in the trivial phase (for both short and long junctions), while they strongly depend on L_S in the topological phase. Our results demonstrate that this effect is purely connected to the splitting of MBSs at $\phi = \pi$, indicating another unique feature connected with the presence of MBSs in the junction. The maximum of such current–phase curves in the topological phase increases as the splitting is reduced, saturating when the splitting is completely suppressed. This and the sawtooth profile in current–phase curves are the main findings of this work. Results presented here therefore strongly complement our previous study on critical currents [37] and should provide useful insight for future experiments looking for Majorana-based signatures in nanowire-based SNS junctions.

The paper is organized as follows. In section "Nanowire model" we describe the model for semiconducting nanowires with SOC, where we show that only the right combination of Rashba SOC, a Zeeman field perpendicular to the spin–orbit axis and *s*-wave superconductivity leads to the emergence of MBSs. Similar results have been presented elsewhere but we include them here for the sake of readability of the next sections. In section "Results and Discussion" we discuss how nanowire-based SNS junctions can be readily modeled using the tools of section "Nanowire model". Then, we describe the low-energy Andreev spectrum and its evolution from the trivial into the topological phase with the emergence of MBSs. In the same section, we report results on the supercurrent, which exhibits a sawtooth profile at $\phi = \pi$ as a signature of the emergence of MBSs. In section "Conclusion" we present our conclusions. For the sake of completeness, we also show wavefunction localization and exponential decay as well as homogeneous charge oscillations of the MBSs in wires and SNS junctions in Supporting Information File 1.

Nanowire model

The aim of this part is to properly describe the emergence of MBSs in semiconducting nanowires with SOC. We consider a single-channel nanowire in one-dimension with SOC and Zeeman interactions, the model Hamiltonian of which is given by [38-43]

$$H_0 = \frac{p_x^2}{2m} - \mu - \frac{\alpha_R}{\hbar}\sigma_y p_x + B\sigma_x, \tag{1}$$

where $p_x = -i\hbar\partial_x$ is the momentum operator, μ the chemical potential that determines the filling of the nanowire, α_R represents the strength of Rashba spin–orbit coupling, $B = g\mu_B\mathcal{B}/2$ is the Zeeman energy as a result of the applied magnetic field $\mathcal{B}$ in the x-direction along the wire, g is the g-factor of teh wire and μ_B the Bohr magneton. Parameters for InSb nanowires include [8]: the effective mass of the electron, $m = 0.015m_e$, with m_e being the mass of the electron, and the spin–orbit strength $\alpha_R = 20$ meV·nm.

We consider a semiconducting nanowire placed in contact with an *s*-wave superconductor with pairing potential $\Delta_{S'}$ (which is in general complex) as schematically shown in Figure 1. Electrons in such a nanowire experience an effective superconducting pairing potential as a result of the so-called proximity effect [44,45]. In order to have a good proximity effect, a highly transmissive interface between the nanowire and the superconductor is required, so that electrons can tunnel between these two systems [13-16]. This results in a superconducting nanowire, with a well-defined induced hard gap (namely, without residual quasiparticle density of states inside the induced superconducting gap). The model describing such a proximitized nanowire can be written in the basis $(\psi_\uparrow, \psi_\downarrow, \psi_\uparrow^\dagger, \psi_\downarrow^\dagger)$ as

$$H = \begin{pmatrix} H_0 & \Delta_S(x) \\ \Delta_S^\dagger(x) & -H_0^* \end{pmatrix}, \tag{2}$$

where $\Delta_S < \Delta_{S'}$. Since the superconducting correlations are of *s*-wave type, the pairing potential is given by

$$\Delta_S(x) = i\sigma_y \Delta e^{i\phi}, \tag{3}$$

where ϕ is the superconducting phase. We set $\phi = 0$ when discussing superconducting nanowires, while the SNS geometry of course allows a finite phase difference $\phi \neq 0$ across the junction.

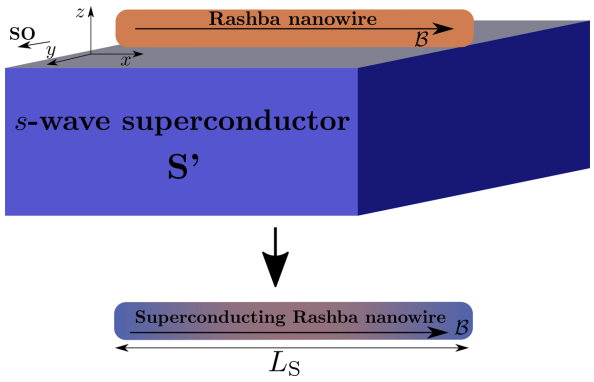

Figure 1: A semiconducting nanowire with Rashba SOC is placed on a *s*-wave superconductor (S') with pairing potential $\Delta_{S'}$ and it is subjected to an external magnetic field $\mathcal{B}$ (denoted by the black arrow). Superconducting correlations are induced into the nanowire via proximity effect, thus becoming superconducting with the induced pairing potential $\Delta_S < \Delta_{S'}$.

It was shown [1,2,46] that the nanowire with Rashba SOC and in proximity to an *s*-wave superconductor, described by Equation 2, contains a topological phase characterized by the emergence of MBSs localized at the ends of the wire. This can be understood as follows: The interplay of all these ingredients generates two intraband *p*-wave pairing order parameters

$$\Delta_{--,++}(k) = \left(\pm\alpha_R k\Delta\right)\Big/\sqrt{B^2 + \alpha_R^2 k^2}$$

and one interband *s*-wave

$$\Delta_{+-} = (B\Delta)\Big/\sqrt{B^2 + \alpha_R^2 k^2}$$

where + and − denote the Rashba bands of H_0. The gaps associated with the ± Bogoliubov–de Gennes (BdG) spectrum are different and correspond to the inner and outer part of the spectrum, denoted by $\Delta_{1,2}$ at low and high momentum, respectively. These gaps depend in a different way on the Zeeman field. Indeed, as the Zeeman field B increases, the gap Δ_1, referred to as the inner gap, is reduced while Δ_2, referred to as the outer gap, is slightly reduced although for strong SOC it remains roughly constant. The inner gap Δ_1 closes at $B = B_c$ and reopens for $B > B_c$ giving rise to the topological phase, while the outer gap remains finite. The topological phase is effectively reached due to the generation of an effective p-wave superconductor, which is the result of projecting the system Hamiltonian onto the lower band (−) keeping only the intraband p-wave pairing Δ_{--} [1,2]. Deep in the topological phase $B > B_c$, the lowest gap is Δ_2.

In order to elucidate and visualize the topological transition, we first analyze the low-energy spectrum of the superconducting nanowire. This spectrum can be numerically obtained by discretising the Hamiltonian given by Equation 1 into a tight-binding lattice:

$$H_0 = \sum_i c_i^\dagger h c_i + \sum_{\langle ij \rangle} c_i^\dagger v c_j + \text{h.c.}, \tag{4}$$

where the symbol $\langle ij \rangle$ means that v couples the nearest-neighbor sites i, j; $h = (2t - \mu)\sigma_0 + B\sigma_x$ and $v = -t\sigma_0 + it_{SO}\sigma_y$ are matrices in spin space, $t = \hbar^2 / (2m^* a^2)$ is the hopping parameter and $t_{SOC} = \alpha_R/(2a)$ is the SOC hopping. The dimension of H_0 is set by the number of sites of the wire. Then, it is written in Nambu space as given by Equation 2. Such a Hamiltonian is then diagonalized numerically with its dimensions given by the number of sites N_S of the wire. Since this description accounts for wires of finite length, it is appropriate for investigating the overlap of MBSs. The length of the superconducting wire is $L_S = N_S a$, where N_S is the number of sites and a is the lattice spacing. As mentioned before, the superconducting phase in the order parameter is assumed to be zero as it is only relevant when investigating Andreev bound states in SNS junctions.

In Figure 2 we present the low-energy spectrum for a superconducting nanowire as a function of the Zeeman field at a fixed wire length L_S. Figure 2a shows the case of zero superconducting pairing and finite SOC ($\Delta = 0$, $\alpha_R \neq 0$), while Figure 2b

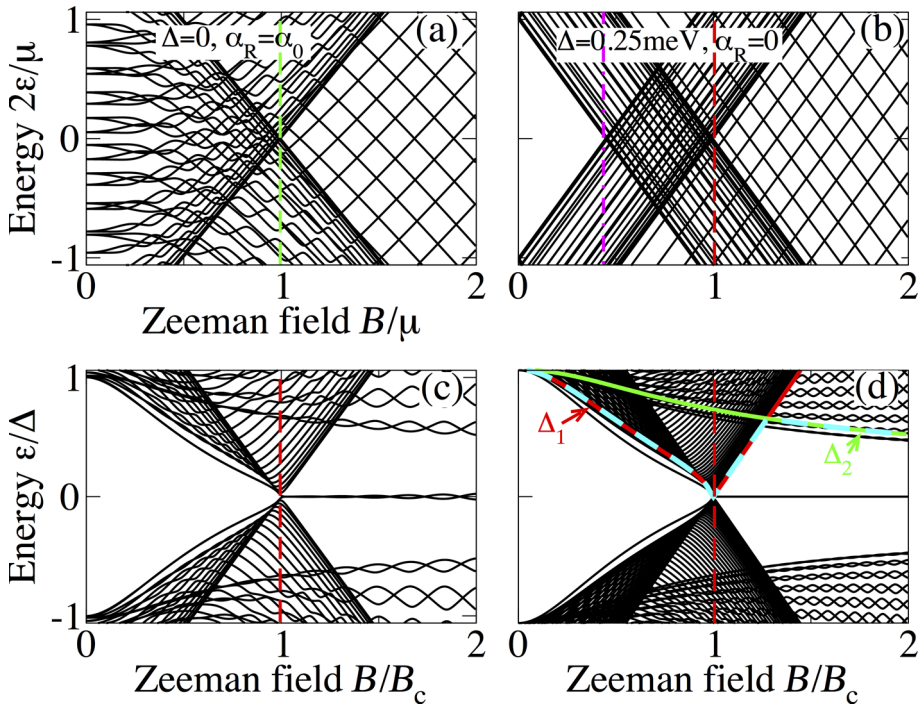

Figure 2: Low-energy spectrum of a superconducting nanowire as function of the Zeeman field B. At zero superconducting pairing with finite SOC the spectrum is gapless and becomes spin-polarized at $B = \mu$ as indicated by the green dashed line (a), while a finite superconducting pairing with zero SOC induces a gap for low values of B (b). As B increases, the induced gap is reduced and closed at $B = \Delta$ (vertical magenta dash-dot line). The bottom panels correspond to both finite superconducting pairing and SOC for L_S = 4000 nm (c) and L_S = 10000 nm (d). Note that as the Zeeman field increases the spectrum exhibits the closing of the gap at $B = B_c$. While in the trivial phase, $B < B_c$, there are no levels within the induced gap (c,d), in the topological phase for $B > B_c$, the two lowest levels develop an oscillatory behaviour around zero energy (c). These lowest levels are the sought-for MBSs. For sufficiently long wires the amplitude of the oscillations is reduced (d) and these levels acquire zero energy. Solid red, green and dashed cyan curves indicate the induced gaps $\Delta_{1,2}$ and $\min(\Delta_1, \Delta_2)$. Parameters: α_0 = 20 meV·nm, μ = 0.5 meV, Δ = 0.25 meV and L_S = 4000 nm (a,b).

shows a situation of finite pairing but with zero SOC ($\Delta \neq 0$, $\alpha_R = 0$). These two extreme cases are very helpful in order to understand how a topological transition occurs when the missing ingredient (either superconducting pairing of finite SO) is included. This is illustrated in the bottom panels, which correspond to both finite SOC and superconducting pairing for $L_S < 2\xi_M$ and $L_S > 2\xi_M$, respectively. Here, ξ_M represents the Majorana localization length, which can be calculated from Equation 2[1,31],

$$k^2 + 4\left(\mu + C\alpha_R^2\right)Ck^2 + 8\lambda C^2\Delta\alpha_R k + 4C_0C^2 = 0,$$

where $C = m/\hbar^2$ and $C_0 = \mu^2 + \Delta^2 - B^2$. The Majorana localization length is defined as $\xi_M = \max[-1/k_{sol}]$.

For the sake of the explanation, we plot the spectrum in the normal state ($\Delta = 0$), Figure 2a, which is, of course, gapless. As the Zeeman field increases, the energy levels split and, within the weak Zeeman phase, $B < \mu$, the spectrum contains energy levels with both spin components. In the strong Zeeman phase, $B > \mu$, one spin sector is completely removed giving rise to a spin-polarized spectrum at low energies as one can indeed observe in Figure 2a. The transition point from weak to strong Zeeman phases is marked by the chemical potential $B = \mu$ (green dashed line). Figure 2b shows the low-energy spectrum at finite superconducting pairing, $\Delta \neq 0$, and zero SOC, $\alpha_R = 0$. Firstly, we notice, in comparison with Figure 2a, that the superconducting pairing induces a gap with no levels for energies below Δ at $B = 0$, being in agreement with Anderson's theorem [47]. A finite magnetic field induces a so-called Zeeman depairing, which results in a complete closing of the induced superconducting gap when B exceeds Δ. This is indeed observed in Figure 2b (magenta dash-dot line). Further increasing of the Zeeman field in this normal state gives rise to a region for $\Delta < B < B_c$, which depends on the finite value of the chemical potential (between red and magenta lines) where the energy levels contain both spin components (for $\mu = 0$ the magenta dash-dot and the red dashed line coincide, not shown). Note that $B_c = \sqrt{\Delta^2 + \mu^2}$. For $B > B_c$, one spin sector is removed and the energy levels are spin-polarized, giving rise to a set of Zeeman crossings that are not protected. Remarkably, when $\alpha_R \neq 0$, the low-energy spectrum undergoes a number of important changes, Figure 2c,d. First, the gap closing changes from Δ, Figure 2b, to $B_c = \sqrt{\Delta^2 + \mu^2}$ (bottom panels). Second, a clear closing of the induced gap at $B = B_c$ and reopening for $B > B_c$ is observed as the Zeeman field increases. This can be seen by plotting the induced gaps $\Delta_{1,2}$, which are finite only at finite Zeeman fields. In Figure 2d, the red, green and dashed cyan curves correspond to Δ_1, Δ_2 and $\min(\Delta_1, \Delta_2)$. Remarkably, the closing and reopening of the induced gap in the spectrum follows exactly the gaps $\Delta_{1,2}$ derived from the continuum (up to some finite-size corrections). Third, the spin-polarized energy spectrum shown in Figure 2b at zero SOC for $B > B_c$ is washed out, keeping only the crossings around zero energy of the two lowest levels. This kind of closing and reopening of the spectrum at the critical field B_c indicates a topological transition where the two remaining lowest-energy levels for $B > B_c$ are the well-known MBSs. Owing to the finite length L_S, the MBSs exhibit the expected oscillatory behaviour due to their finite spatial overlap [48-51]. For sufficiently long wires $L_S \gg 2\xi_M$, the amplitude of the oscillations is considerably reduced (even negligible), which pins the MBSs to zero energy. Fourth, the SOC introduces a finite energy separation between the two lowest levels (crossings around zero) and the rest of the low-energy spectrum denoted here as "topological minigap". Note that the value of this minigap, related to the high momentum gap Δ_2, remains finite and roughly constant for strong SOC. In the case of weak SOC the minigap is reduced and for high Zeeman field it might acquire very small values, affecting the topological protection of the MBSs.

To complement this introductory part, calculations of the wavefunctions and charge density associated with the lowest levels of the topological superconducting nanowire spectrum are presented in the Supporting Information File 1.

Results and Discussion

Nanowire SNS junctions

In this part, we concentrate on SNS junctions based on the proximitized nanowires that we discussed in the previous section. The basic geometry contains left (S_L) and right (S_R) superconducting regions of length L_S separated by a central normal (N) region of length L_N, as shown in Figure 3. The regions N and

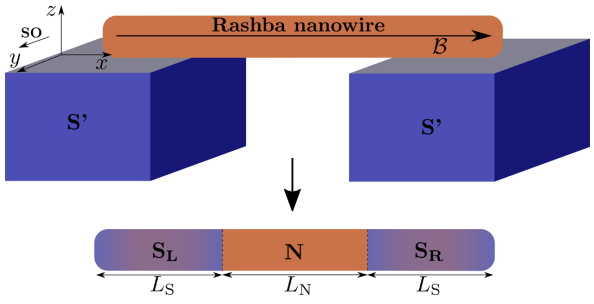

Figure 3: Schematic of SNS junctions based on Rashba nanowires. Top: A nanowire with Rashba SOC of length $L = L_S + L_N + L_S$ placed on top of two *s*-wave superconductors (S') with pairing potentials $\Delta_{S'}$ and subjected to an external magnetic field $\mathcal{B}$ (denoted by the black arrow). Superconducting correlations are induced into the nanowire through the proximity effect. Bottom: Left and right regions of the nanowire become superconducting, denoted by S_L and S_R, with induced pairing potentials $\Delta_{S_{L(R)}} < \Delta_{S'}$ and chemical potentials $\mu_{S_{L(R)}}$, while the central region remains in the normal state with $\Delta_N = 0$ and chemical potential μ_N. This results in a superconductor–normal–superconductor (SNS) junction.

$S_{L(R)}$ are described by the tight-binding Hamiltonian H_0 given by Equation 4 with their respective chemical potentials, μ_N and $\mu_{S_{L(R)}}$. The Hamiltonian describing the SNS junction without superconductivity is then given by

$$h_{\rm SNS} = \begin{pmatrix} H_{\rm S_L} & H_{\rm S_L N} & 0 \\ H^{\dagger}_{\rm S_L N} & H_{\rm N} & H_{\rm NS_R} \\ 0 & H^{\dagger}_{\rm NS_R} & H_{\rm S_R} \end{pmatrix}, \qquad (5)$$

where H_{S_i} with i = L/R and H_N are the Hamiltonians of the superconducting and normal regions, respectively, H_{S_iN} and H_{NS_i} are the ones that couple S_i to the normal region N. The elements of these coupling matrices are non-zero only for adjacent sites that lie at the interfaces of the S regions and of the N region, while zero everywhere else. This coupling is parametrized between the interface sites by a hopping matrix $v_0 = \tau v$, where $\tau \in [0,1]$, providing a good control of the normal transmission T_N. The parameter τ controls the normal transmission that ranges from fully transparent ($\tau = 1$) to tunnel ($\tau \leq 0.6$), as discussed in [37] for short junctions, being also valid for long junctions.

The superconducting regions of the nanowire are characterized by chemical potential $\mu_{S_{L(R)}}$ and the uniform superconducting pairing potentials [52,53] $\Delta_{S_L} = \overline{\Delta} e^{-i\phi/2}$ and $\Delta_{S_R} = \overline{\Delta} e^{i\phi/2}$, where $\Delta < \Delta_{S'}$ and $\overline{\Delta} = i\sigma_y \Delta$. The central region of the nanowire is in the normal state without superconductivity, $\Delta_N = 0$, and with chemical potential μ_N. Thus, the pairing potential matrix in the junction space reads

$$\Delta_{\rm SNS} = \begin{pmatrix} \Delta_{\rm S_L} & 0 & 0 \\ 0 & \Delta_{\rm N} & 0 \\ 0 & 0 & \Delta_{\rm S_R} \end{pmatrix} = \begin{pmatrix} \Delta_{0,S} e^{i\phi_L} & 0 & 0 \\ 0 & 0 & 0 \\ 0 & 0 & \Delta_{0,S} e^{i\phi_R} \end{pmatrix}, \qquad (6)$$

Next, we define the phase difference across the junction as $\phi_R - \phi_L = \phi$. Thus, the Hamiltonian for the full SNS junction reads in Nambu space [31,37]

$$H_{\rm SNS} = \begin{pmatrix} h_{\rm SNS} & \Delta_{\rm SNS} \\ \Delta^{\dagger}_{\rm SNS} & -h^{*}_{\rm SNS} \end{pmatrix}. \qquad (7)$$

In what follows, we discuss short ($L_N \ll \xi$) and long ($L_N \gg \xi$) SNS junctions, where L_N is the length of the normal region and $\xi = \hbar v_F / \Delta$ is the superconducting coherence length [52]. The previous Hamiltonian is diagonalized numerically and in our calculations we consider realistic system parameters for InSb as described previously.

Low-energy Andreev spectrum

Now, we are in a position to investigate the low-energy Andreev spectrum in short and long SNS junctions. In particular, we discuss the formation of Andreev bound states and their evolution from the trivial ($B < B_c$) into the topological phases ($B > B_c$). For this purpose we focus on the phase and the Zeeman-dependent low-energy spectrum in short and long junctions, presented in Figure 4 and Figure 5 for $L_S \leq 2\xi_M$. For completeness we also present the case of $L_S \gg 2\xi_M$ in Figure 6 and Figure 7.

We first discuss short junctions with $L_S \leq 2\xi_M$. In this regime, at $B = 0$ two degenerate ABSs appear within Δ as solutions to the BdG equations described by Equation 7, see Figure 4a. It is interesting to point out that within standard theory for a transparent channel the ABS energies reach zero at $\phi = \pi$ in the Andreev approximation $\mu_S \gg \Delta$ [54]. Figure 4a, however, shows that in general the ABS energies do not reach zero at $\phi = \pi$. The dense amount of levels above $|\varepsilon_p| > \Delta$ represents the quasi-continuum of states, which consists of a discrete set of levels due to the finite length of the N and S regions. Moreover, it is worth to point out that the detachment (the space between the ABSs and quasi-continuum) of the quasi-continuum at $\phi = 0$ and 2π is not zero. It strongly depends on the finite length of the S regions (see Figure 6).

For a non-zero Zeeman field, Figure 4b and Figure 4c, the ABSs split and the two different gaps Δ_1 and Δ_2, discussed in section 'Nanowire model', emerge indicated by the dash-dot red and dashed green lines, respectively. By increasing the Zeeman field, the low-momentum gap Δ_1 gets reduced (dash-dot red line), as expected, while the gap Δ_2 (dashed green line) remains finite although it gets slightly reduced (Figure 4b and Figure 4c). For stronger, but unrealistic values of SOC we have checked that Δ_2 is indeed constant. The two lowest levels in this regime, within Δ_1 (dash-dot red line), develop a loop with two crossings that are independent of the length of the S region but exhibit a strong dependence on SOC, Zeeman field and chemical potential. We have checked that they appear due to the interplay of SOC and Zeeman field and disappear when μ acquires very large values, namely, in the Andreev approximation.

At $B = B_c$, the energy spectrum exhibits the closing of the low-momentum gap Δ_1, as indicated by red dash-dot line in Figure 4d. This indicates the topological phase transition, since two gapped topologically different phases can only be connected through a closing gap. By further increasing the Zeeman field, Figure 4e,f, $B > B_c$, the inner gap Δ_1 acquires a finite value again. This reopening of Δ_1 indicates that the system enters into the topological phase and the superconducting regions denoted by $S_{L(R)}$ become topological, while the N

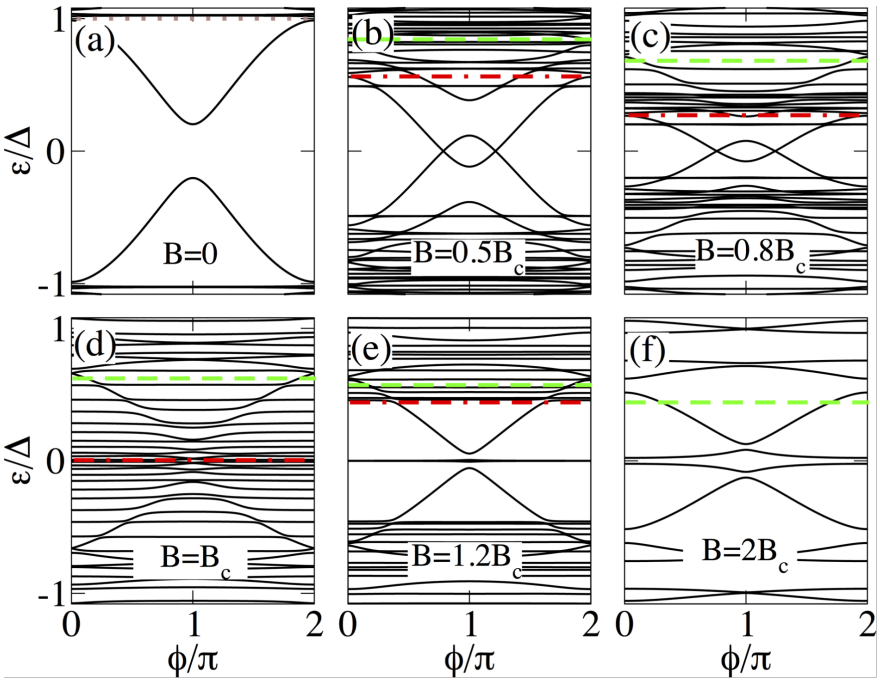

Figure 4: Low-energy Andreev spectrum as a function of the superconducting phase difference ϕ in a short SNS junction with L_N = 20 nm and L_S = 2000 nm. Different panels show the evolution with the Zeeman field: trivial phase for $B < B_c$ (a–c), topological transition at $B = B_c$ (d), and in the topological phase for $B > B_c$ (e,f). The energy spectrum exhibits the two different gaps that appear in the system for finite Zeeman field (marked by red and green dashed horizontal lines). Note that after the gap inversion at $B = B_c$, two MBSs emerge at the ends of the junction as almost dispersionless levels (outer MBSs), while two additional MBSs appear at $\phi = \pi$ (inner MBSs). Parameters: α_R = 20 meV·nm, $\mu_N = \mu_S$ = 0.5 meV and Δ = 0.25 meV.

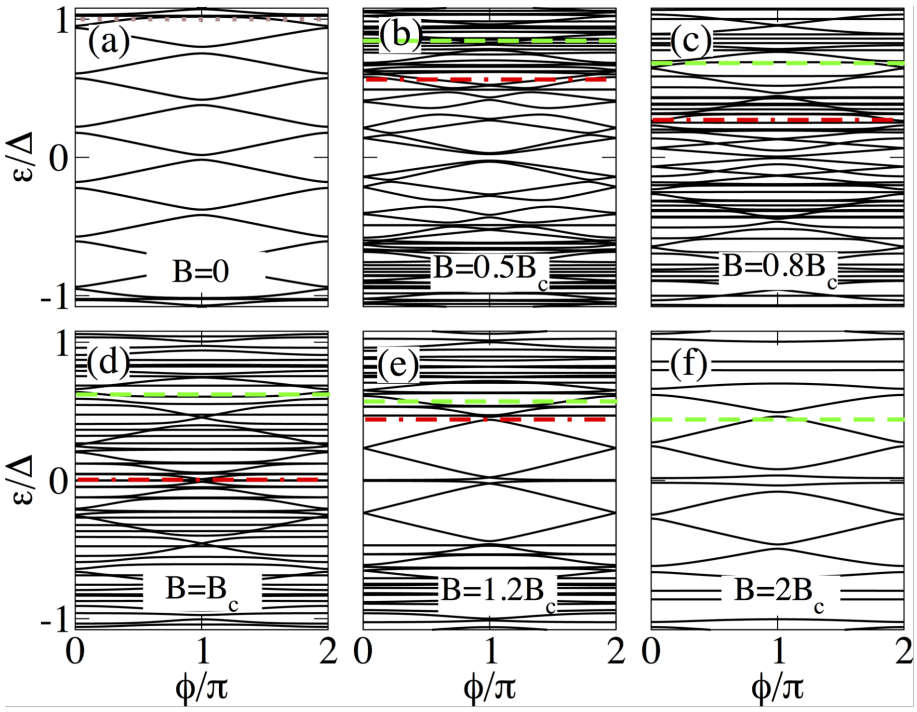

Figure 5: Same as in Figure 4 for a long junction with L_N = 2000 nm and L_S = 2000 nm. Note that, unlike short junctions, in this case the four lowest states for $B > B_c$ coexist with additional levels within the induced gap which arise because L_N is longer.

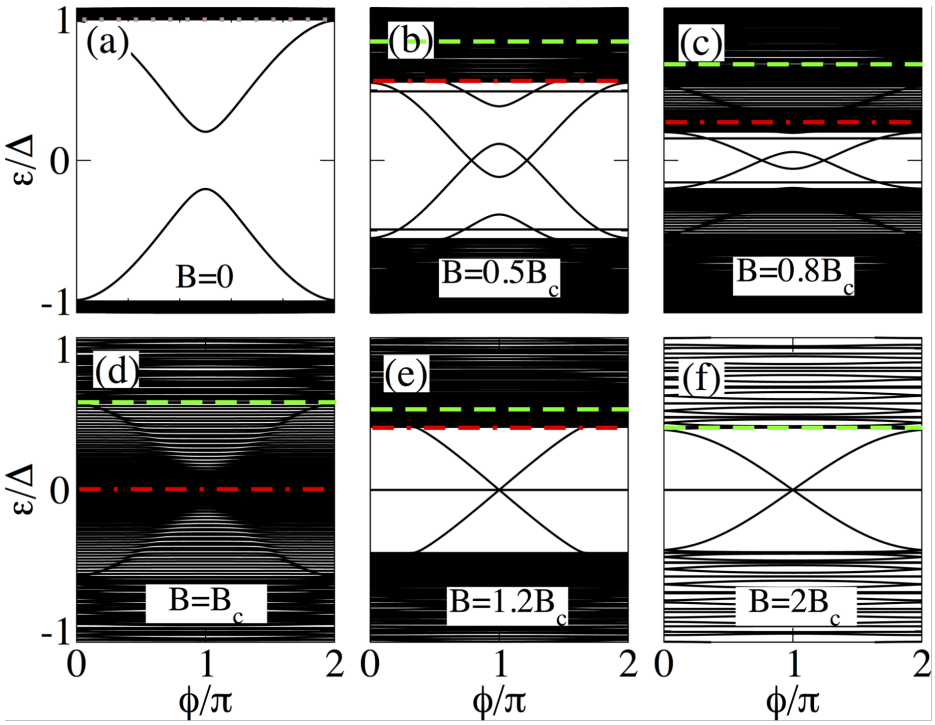

Figure 6: Same as in Figure 4 for a short junction with L_N = 20 nm and L_S = 10000 nm. Note that in this case, the emergent outer MBSs are dispersionless with ϕ, while the inner ones touch zero at $\phi = \pi$ acquiring Majorana character.

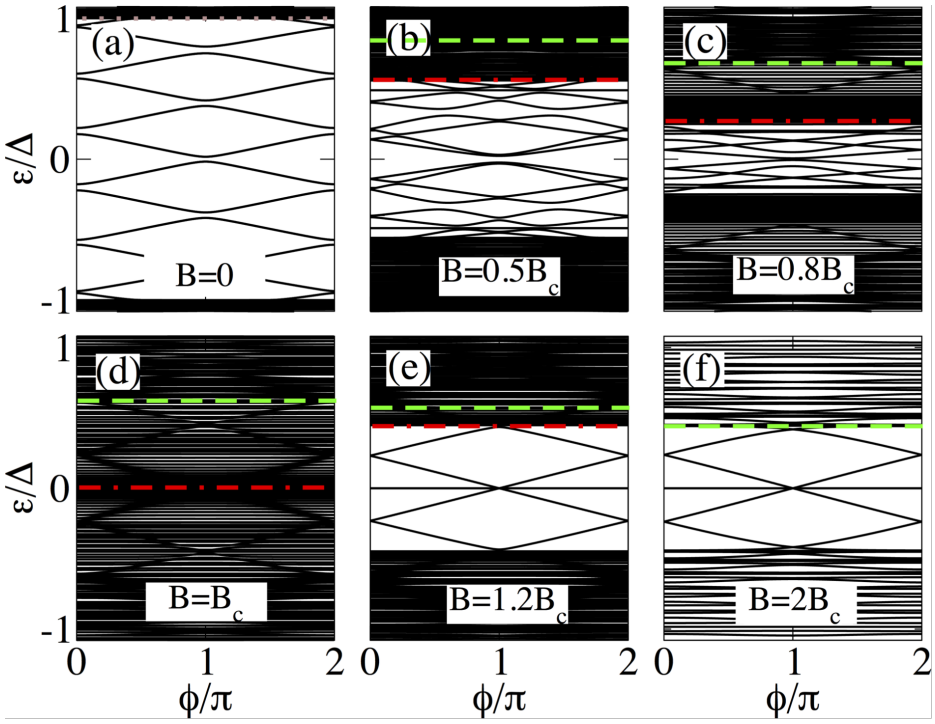

Figure 7: Same as in Figure 4 for a long junction with L_N = 2000 nm and L_S = 10000 nm. The four lowest levels coexist with additional levels. The outer MBSs lie at zero energy and the inner ones reach zero at $\phi = \pi$ acquiring Majorana character.

region remains in the normal state. Thus, MBSs are expected to appear for $B > B_c$ at the ends of the two topological superconducting sectors, since they define interfaces between topologically different regions.

This is what we indeed observe for $B > B_c$ in Figure 4e and Figure 4f, where the low-energy spectrum has Majorana properties. In fact, for $B > B_c$, the topological phase is characterized by the emergence of two (almost) dispersionless levels with ϕ, which represent the outer MBSs $\gamma_{1,4}$ formed at the ends of the junction. Additionally, the next two energy levels strongly depend on ϕ and tend towards zero at $\phi = \pi$, representing the inner MBSs $\gamma_{2,3}$ formed inside the junction. For sufficiently strong fields, $B = 2B_c$, the lowest gap is Δ_2 indicated by the green dashed line, which in principle bounds the MBSs. The quasi-continuum in this case corresponds to the discrete spectrum above and below Δ_2, where Δ_2 is the high-momentum gap marked by the green dashed horizontal line in Figure 4e,f.

The four MBSs develop a large splitting around $\phi = \pi$, which arises when the wave-functions of the MBSs have a finite spatial overlap $L_S \leq 2\xi_M$. Since the avoided crossing between the dispersionless levels (belonging to $\gamma_{1,4}$) and the dispersive levels (belonging to $\gamma_{2,3}$) around $\phi = \pi$ depends on the overlap of MBSs on each topological segment. It can be used to quantify the degree of Majorana non-locality (a variant of this idea using quantum-dot parity crossings has been discussed in [55,56]). This can be explicitly checked by considering SNS junctions with longer superconducting regions, where the condition $L_S \gg 2\xi_M$ is fulfilled such that the energy splitting at $\phi = \pi$ is reduced.

As an example, we present in Figure 6 the energy levels as a function of the phase difference for $L_S \gg 2\xi_M$, where the low-energy spectrum undergoes some important changes. First, we notice in Figure 6 that the energy spectrum at $B = 0$ for $|\varepsilon_p| > \Delta$, exhibits a visibly denser spectrum than that in Figure 4 signaling the quasi-continuum of states. Notice that in the topological phase, $B > B_c$, the lowest two energy levels, associated to the outer MBSs, are insensitive to ϕ remaining at zero energy. Thus, they can be considered as truly zero modes. On the other hand, the inner MBSs are truly bound within Δ_2, unlike in Figure 4, and for $\phi = 0$ and $\phi = 2\pi$ they merge with the quasi-continuum at $\pm\Delta$. Thus, an increase in the length of the superconducting regions favors the reduction of the detachment between the discrete spectrum and the quasi-continuum at 0 and 2π, as it should be for a ballistic junction [23,24]. Moreover, the energy splitting at $\phi = \pi$ is considerably reduced, even negligible. However, it will be always non-zero, though not visible to the naked eye, due to the finite length and, thus, due to the presence of the outer MBSs.

The low-energy spectrum as a function of the superconducting phase difference for different values of the Zeeman field in long SNS junctions is presented in Figure 5 for $L_S \leq 2\xi_M$. Additionally, we show in Figure 7 the case for $L_S \gg 2\xi_M$.

As expected, long junctions contain more levels within the energy gap Δ, see Figure 5a and Figure 7a, than short junctions. As we shall discuss, this eventually affects the signatures of Majorana origin in the supercurrents for $B\ B_c$, namely, the ones corresponding to the lowest four levels.

The above discussion can be clarified by considering the dependence of the low-energy spectrum on the Zeeman field at fixed phase difference $\phi = 0$ and $\phi = \pi$. This is shown in Figure 8 (short junction limit), Figure 9 (intermediate junction limit) and Figure 10 (long junction limit) for $L_S \leq 2\xi_M$ (panels a and c in each figure) and $L_S \gg 2\xi_M$ (panels b and d in each figure). In panels a and b, the gaps Δ_1, Δ_2 and $\min(\Delta_1,\Delta_2)$ are also plotted as solid red, solid green and dashed cyan lines to visualize the gap closing and reopening discussed in the previous section. In all cases, it is clear that MBS smoothly evolve from the lowest ABS either following the closing of the induced gap Δ_1, indicated by the solid red curve, at $\phi = 0$ or evolving from the lowest detached levels at $\phi = \pi$. The latter first cross zero energy, owing to Zeeman splitting, and eventually become four low-energy levels oscillating out of phase around zero energy (Figure 8c). The emergence of these oscillatory low-energy levels, separated by a minigap Δ_2, indicated by the solid green curve, from the quasi-continuum characterizes the topological phase of the SNS junction. As expected, the oscillations become reduced for $L_S \gg 2\xi_M$ and the four levels at $\phi = \pi$ become degenerate at zero energy, see Figure 8b,d.

An increase in the length of the normal section results in an increase of the amount of subgap levels as observed in Figure 9 and Figure 10. In both cases, in the topological phase, $B > B_c$, these additional levels reduce the minigap with respect to short junctions and also slightly reduce the amplitude of the oscillations of the energy levels around zero as seen Figure 9a and Figure 9b as well as Figure 10a and Figure 10b. Also, the minigaps for $\phi = 0$ and $\phi = \pi$ are different, in contrast to short junctions. In fact, the minigap at $\phi = 0$ is almost half of the value at $\phi = \pi$ for the chosen parameters. This can be understood from the phase dispersion of the long junction ABS spectra such as the ones in Figure 5 and Figure 7. For longer N regions, this difference can be even larger.

From the above discussion it is clear that the energy spectrum of SNS nanowire junctions offers the possibility to directly monitor the ABSs that trace the gap inversion and eventually evolve into MBSs.

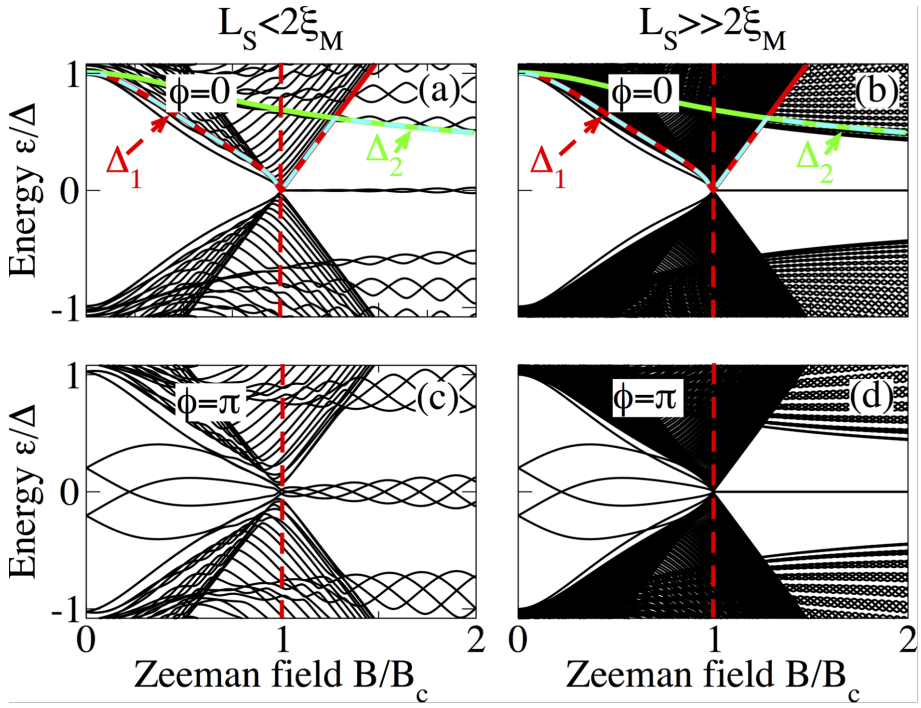

Figure 8: Low-energy Andreev spectrum as a function of the Zeeman field in a short SNS junction at $\phi = 0$ (a,b) and $\phi = \pi$ (c,d) with L_S = 2000 nm (a,c) and L_S = 10000 nm (b,d). The low-energy spectrum traces the gap closing and reopening by the solid red curve that corresponds to Δ_1, while for $B > B_c$ we observe the emergence of two MBSs at $\phi = 0$ (a) and four MBSs at $\phi = \pi$ (c), which oscillate around zero energy with B due to $L_S \leq 2\xi_M$ within a minigap defined by Δ_2 (solid green curve). For $L_S \gg 2\xi_M$ the MBSs are truly zero modes (b,d). Parameters: L_N = 20 nm, α_R = 20 meV·nm, μ = 0.5 meV and Δ = 0.25 meV.

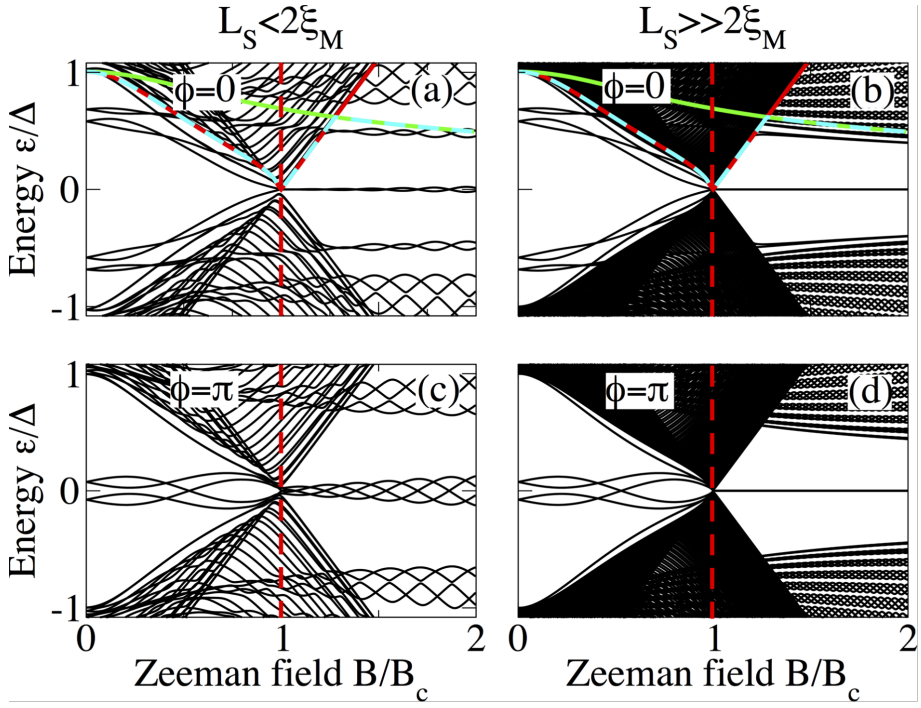

Figure 9: Same as in Figure 8 for an intermediate junction with L_N = 400 nm.

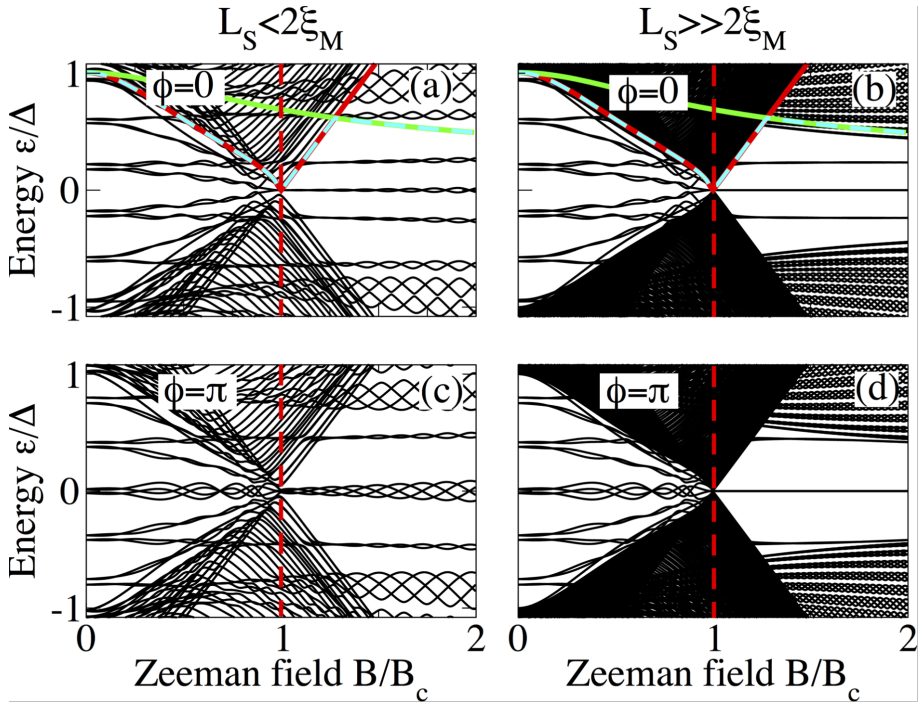

Figure 10: Same as in Figure 8 for a long junction with L_N = 2000 nm.

Supercurrents

After having established in detail the energy spectrum in short and long SNS junctions, we now turn our attention to the corresponding phase-dependent supercurrents. They can be calculated directly from the discrete Andreev spectrum ε_p as [37,54,57]:

$$I(\phi) = -\frac{e}{\hbar}\sum_{p>0}\tanh\left(\frac{\varepsilon_p}{2k_BT}\right)\frac{d\varepsilon_p}{d\phi}, \qquad (8)$$

where k_{rmB} is the Boltzmann constant, T is the temperature and the summation is performed over positive eigenvalues ε_p. By construction, our junctions have finite length, which implies that Equation 8 exactly includes the discrete quasi-continuum contribution.

In Figure 11 and Figure 12 we present supercurrents as a function of the superconducting phase difference $I(\phi)$ for different values of the Zeeman field in short and long SNS junctions, respectively. Panels a and c correspond to $L_S \leq 2\xi_M$, while panels b and d correspond to $L_S \gg 2\xi_M$.

First, we discuss the short junction regime presented in Figure 11. At $B = 0$ the supercurrent $I(\phi)$ has a sine-like dependence on ϕ, with a relative fast change of sign around $\phi = \pi$ that is determined by the derivative of the lowest-energy spectrum profile around $\phi = \pi$. This result is different from usual ballistic full transparent supercurrents in trivial SNS junctions [54], where the supercurrent is proportional to $\sin(\phi/2)$ being maximum at $\phi = \pi$. This difference from the standard ballistic limit can be ascribed to deviations from the ideal Andreev approximation, see also the discussion of Figure 4a, owing to the relatively low chemical potential needed to reach the helical limit and, eventually, the topological regime as the Zeeman field increases. At finite values of the Zeeman field B, but still in the trivial phase $B < B_c$ (dashed and dash-dot curves), $I(\phi)$ undergoes changes. First, the maximum value of $I(\phi)$ is reduced due to the reduction of the induced gap that is caused by the Zeeman effect. Second, $I(\phi)$ develops a zig-zag profile (just before and after $\phi = \pi$) signalling a 0–π transition in the supercurrent. This transition arises from the zero-energy crossings in the low-energy spectrum, see Figure 4b,c. As discussed above, these level crossings result from the combined action of both SOC and Zeeman field at low μ, and introduce discontinuities in the derivatives with respect to ϕ. Besides these features, all the supercurrent curves for $B < B_c$, for both $L_S \leq 2\xi_M$ and $L_S \gg 2\xi_M$, exhibit a similar behavior, see Figure 11. Interestingly, the system is gapless at the topological transition, $B = B_c$, but the supercurrent remains finite, see red curve in Figure 11c.

For $B > B_c$, the S regions of the SNS junction become topological and MBSs emerge at their ends, as described in the previous subsection. Despite the presence of MBSs, the super-

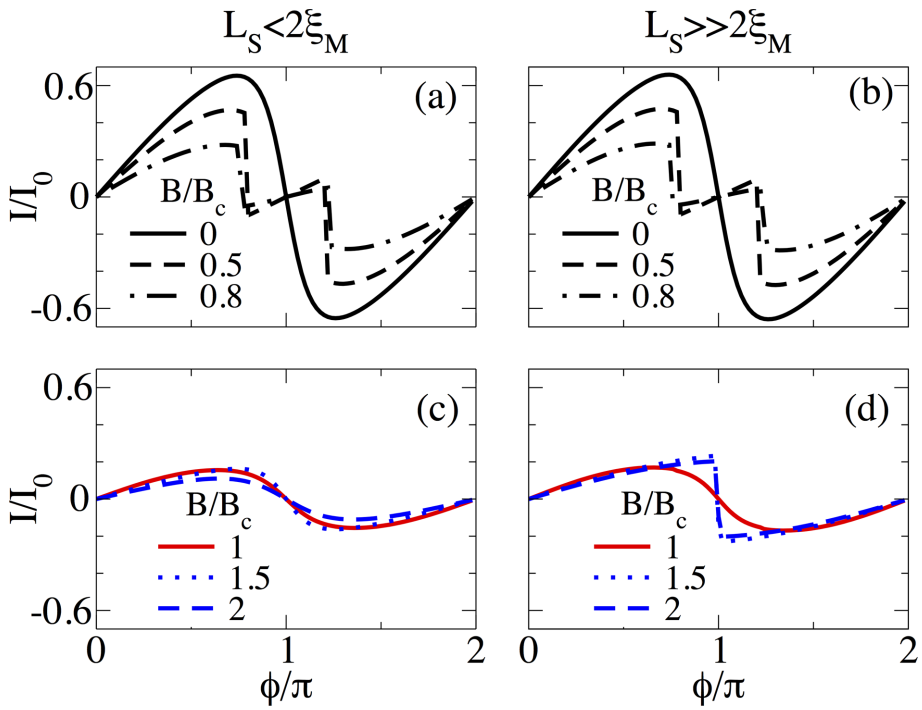

Figure 11: Supercurrent as a function of the superconducting phase difference in a short SNS junction, $I(\phi)$, for L_S = 2000 nm ≤ $2\xi_M$ (a,c) and L_S = 10000 nm ≫ $2\xi_M$ (b,d). Panels a and b show the Josephson current in the trivial phase for different values of the Zeeman field, $B < B_c$, while panels c and d correspond to different values of the Zeeman field in the topological phase, $B \geq B_c$. Note the sawtooth feature at $\phi = \pi$ for $L_S \gg 2\xi_M$. Parameters: α_R=20 meV·nm, μ = 0.5 meV, Δ = 0.25 meV and $I_0 = e\Delta/\hbar$.

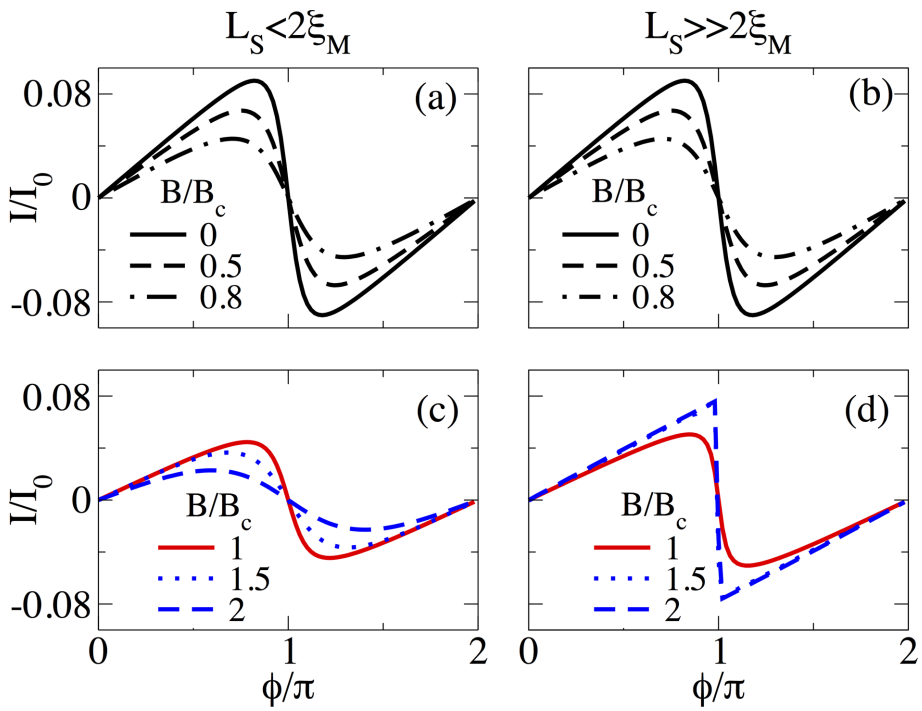

Figure 12: Supercurrent as a function of the superconducting phase difference in a long SNS junction with L_N = 2000 nm, for L_S = 2000 nm ≤ $2\xi_M$ (a,c) and L_S = 10000 nm ≫ $2\xi_M$ (b,d). Panels a and b show the Josephson current in the trivial phase for different values of the Zeeman field, $B < B_c$, while panels c and d correspond to different values of the Zeeman field in the topological phase, $B \geq B_c$. In this case the magnitude of the supercurrent is reduced, an effect caused by the length of the normal section.

current $I(\phi)$ remains 2π-periodic, i.e., $I(\phi) = I(\phi + 2\pi)$. This results from the fact that we sum up positive levels only, as we deal with an equilibrium situation. Since the supercurrent is a ground state property, transitions between the negative and positive energies are not allowed, because of an energy gap originating from Majorana overlaps. Strategies to detect the presence of MBSs beyond the equilibrium supercurrents described here include the ac Josephson effect, noise measurements, switching-current measurements, microwave spectroscopy and dynamical susceptibility measurements [25-30].

As the Zeeman field is further increased in the topological phase, $B > B_c$, the supercurrent tends to decrease due to the finite Majorana overlaps when $L_S \leq 2\xi_M$, see dotted and dashed blue curves in Figure 11d. On the other hand, as the length of S becomes larger such that $L_S \gg 2\xi_M$ the overlap is reduced, which is reflected in a clear sawtooth profile at $\phi = \pi$, see dotted and dashed blue curves in Figure 11d. This discontinuity in $I(\phi)$ depends on L_S and results from the profile of the lowest-energy spectrum at $\phi = \pi$, as shown in Figure 6d. The sawtooth profile thus indicates the emergence of well-localized MBSs at the ends of S and represents one of our main findings.

As discussed above, the supercurrent for $B < B_c$, Figure 11a and Figure 11b, does not depend on L_S. In contrast, supercurrents in the topological phase, Figure 11c and Figure 11d, do strongly depend on L_S owing to the emergence of MBSs.

In Figure 12 we present $I(\phi)$ for long junctions $L_N \gg \xi$ at different values of the Zeeman field. Panels a and c correspond to $L_S \leq 2\xi_M$ and panels b and d correspond to $L_S \gg 2\xi_M$. Even though the maximum value of the current is reduced in this regime, the overall behavior is very similar to the short-junction regime for both $B < B_c$ and $B > B_c$. The only important difference with respect to the short junction case is that $I(\phi)$ in the long-junction regime does not exhibit the zig-zag profile due to 0–π transitions.

As the system enters into the topological phase for $B > B_c$ and $L_S \leq 2\xi_M$, Figure 12c, the maximum supercurrent decreases, indicating the non-zero splitting at $\phi = \pi$ in the low-energy spectrum. Deep in the topological phase, the supercurrent exhibits a slow (slower than in the trivial phase Figure 12a) sign change around $\phi = \pi$, and its dependence on ϕ tends to approach a sine function. However, for $L_S \gg 2\xi_M$, shown in Figure 12d, the supercurrent acquires an almost constant value as B increases and develops a clear sawtooth profile at $\phi = \pi$ due to the zero energy splitting in the low-energy spectrum at $\phi = \pi$, similarly to the short-junction case. It is worth to point out that, although the maximum supercurrent is slightly reduced, deep in the topological phase (dashed and dotted blue curves) its maximum value is approximately close to the maximum value in the trivial phase, which is different from what we found in the short-junction case. This is a clear consequence of the emergence of additional levels within the induced gap due to the increase of L_N. These additional levels exhibit a strong dependence on the superconducting phase, very similar to the inner MBSs as one can see in Figure 5e,f.

In order analyze the individual contribution of outer and inner MBSs with respect to the quasi-continuum we calculate and identify supercurrents for such situations. This is presented in Figure 13 for short junctions (Figure 13a,b) and for long junctions (Figure 13c,d). In this regime the lowest gap is the high-momentum gap Δ_2, and the levels outside this gap constitute the quasi-continuum.

Firstly, we discuss short junctions. The supercurrent due to outer MBSs for $L_S \leq 2\xi_M$ is finite only around $\phi = \pi$, exhibiting an odd dependence on ϕ around π. However, away from this point it is approximately zero and independent of ϕ (see blue curve in Figure 13a). When $L_S \gg 2\xi_M$, the outer MBSs are very far apart and their contribution to $I(\phi)$ is zero (see blue curve in Figure 13b). On the other hand, the contribution of the inner MBSs to $I(\phi)$ is enormous and the outer part only slightly changes the shape of the maximum supercurrent when $L_S \leq 2\xi_M$, while for $L_S \gg 2\xi_M$ the outer MBSs do not contribute, as shown by the dashed brown curve in Figure 13a,b. Moreover, the inner contribution exhibits roughly the same dependence on ϕ as the contribution of the whole energy spectrum shown by the black curve in Figure 13a,b. As described in the previous subsection, the quasi-continuum is considered to be the discrete energy spectrum above $|\varepsilon_p| > \Delta_2$. The quasi-continuum contribution to $I(\phi)$ is finite and odd in ϕ around π, as shown by green curves in Figure 13a,b. The quasi-continuum contribution to the total supercurrent $I(\phi)$ far away from $\phi = \pi$ is appreciable mainly when the MBSs exhibit a finite energy splitting as seen in Figure 13a. Interestingly, the outer and in particular the inner MBSs (levels within Δ_2) are the main source when such overlap is completely reduced and determine the profile of $I(\phi)$, as shown in Figure 13b.

In long junctions the situation is different, mainly because more levels emerge within Δ in the trivial phase. For $B > B_c$ within Δ_2 these additional levels coexist with the inner and outer MBSs, see Figure 13c,d. The contribution of the outer MBSs to $I(\phi)$ exhibits roughly similar behaviour as for short junctions although smoother around $\phi = \pi$, shown by the blue curve in Figure 13c,d. The inner MBSs, however, have a strong dependence on ϕ and develop their maximum value close to $\phi = 2\pi n$ with $n = 0,1,\ldots$ (see red curve). The outer MBSs almost do not affect the overall shape of the $I(\phi)$ curve (see dashed brown

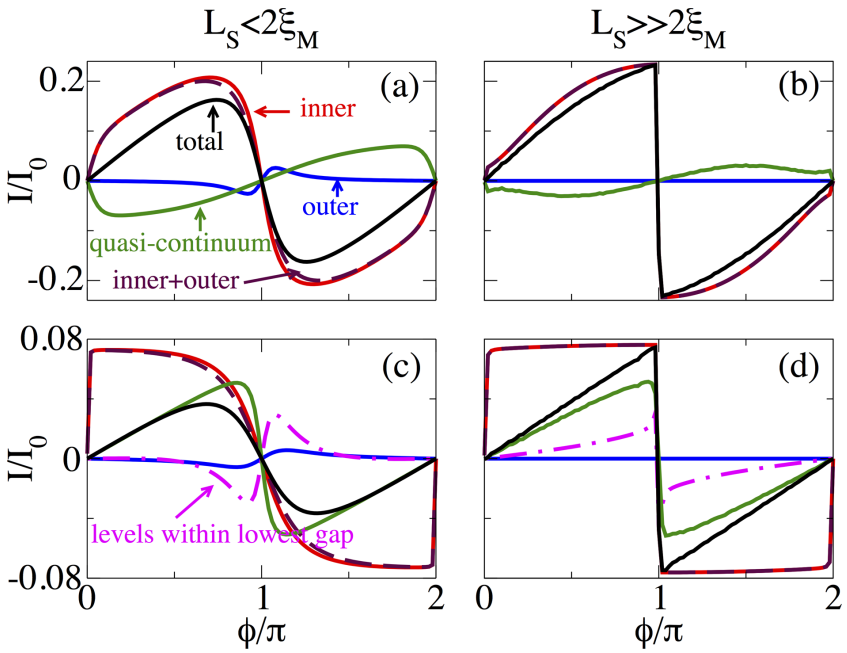

Figure 13: Supercurrent as a function of ϕ at $B = 1.5B_c$. Contributions to the supercurrent for (a,b) short and (c,d) long junctions. (a,c) $L_S \leq 2\xi_M$ and (b,d) $L_S \gg 2\xi_M$. The different curves in (a,b) correspond to individual contributions to $I(\phi)$ from outer, inner, and outer + inner (levels within the lowest induced gap Δ_2), quasi-continuum (levels above the lowest gap Δ_2) and total levels. In (c,d), the additional magenta curve corresponds to all levels within Δ_2. In long junctions the number of levels within Δ_2 exceeds the number of MBSs. MBSs coexist with additional levels within Δ_2. Parameters: α_R = 20 meV·nm, μ = 0.5 meV, Δ = 0.25 meV and $I_0 = e\Delta/\hbar$.

curve). Since a long junction hosts more levels, we also show by the dash-dot magenta curve the contribution of all the levels within Δ_2, including also the four MBSs. This contribution is considerably large only close to $\phi = \pi$, with a minimum and maximum value before and after $\phi = \pi$ for $L_S \leq 2\xi_M$, respectively. This is indeed the reason why the supercurrent is reduced as B increases in the topological phase for $L_S \leq 2\xi_M$, see dotted and dashed blue curves in Figure 12c. For $L_S \gg 2\xi_M$ the contribution of all the levels within Δ_2 exhibits a sawtooth profile at $\phi = \pi$, which, instead of reducing the quasi-continuum contribution (green curve), increases the maximum value of $I(\phi)$ at $\phi = \pi$ resulting in the solid black curve. Importantly, unlike in short junctions, in long junctions the quasi-continuum modifies $I(\phi)$ around $\phi = \pi$. Thus, a zero-temperature current-phase measurement in an SNS junction setup could indeed reveal the presence of MBSs by observing the reduction of the maximum supercurrent. In particular, well-localized MBSs are revealed in the sawtooth profile of $I(\phi)$ at $\phi = \pi$. In what follows we analyze the effect of temperature, variation of normal transmission and random disorder on the sawtooth profile at $\phi = \pi$ of the supercurrent.

Temperature effects

In this part, we analyze the effect of temperature on supercurrents in the topological phase. In Figure 14 we present the supercurrent as a function of the superconducting phase difference, $I(\phi)$, in the topological phase $B = 1.5B_c$ at different temperature values for $L_S \leq 2\xi_M$ (Figure 14a) and $L_S \gg 2\xi_M$ (Figure 14b). At zero temperature, for $L_S \leq 2\xi_M$, shown by the black solid curve in Figure 14a, the dependence of the supercurrent on ϕ approximately corresponds to a sine-like function. A small increase in temperature $k_BT = 0.01$ meV (magenta dashed curve) slightly modifies the profile of the maximum supercurrent. However, for $L_S \gg 2\xi_M$ (Figure 14b), the same temperature (dashed curve) value has a detrimental effect on the sawtooth profile of $I(\phi)$ at $\phi = \pi$, which reduces the maximum value and smooths the curve out due to the thermal population of ABSs. We have checked that smaller temperature values than the ones presented in Figure 14 also smooth out the sawtooth profile but the fast sign change around $\phi = \pi$ is still visible. This effect remains as long as $k_BT \ll \Delta$. As the temperature increases, $I(\phi)$ smoothly acquires a true sine shape, as seen in Figure 14a. Although the sawtooth profile might be hard to observe in real experiments, the maximum value of $I(\phi)$, which is finite in the topological phase and almost halved with respect to the trivial phase in short junctions [37], still provides a measure to distinguish it from $I(\phi)$ in trivial junctions.

Normal transmission effects

The assumption of perfect coupling between N and S regions in previous calculations is indeed a good approximation because of the enormous advances in fabrication of hybrid systems.

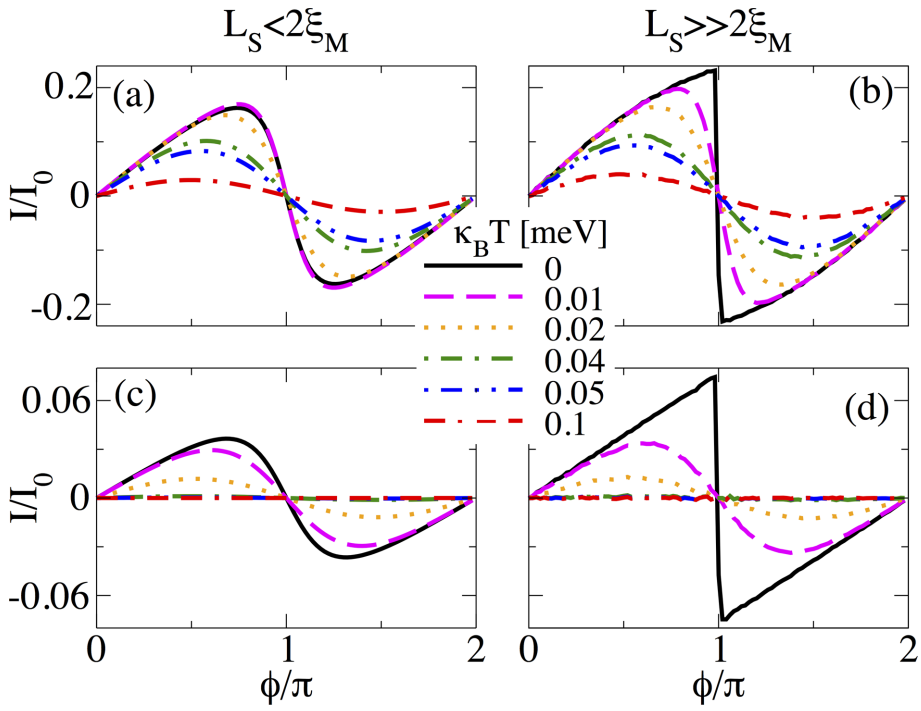

Figure 14: Finite temperature effect on the supercurrent, $I(\phi)$, in (a,b) a short and (c,d) a long junction. (a,c) L_S = 2000 nm ≤ $2\xi_M$ and (b,d) L_S = 10000 nm ≫ $2\xi_M$. Different curves correspond to different values of k_BT. The sawtooth profile smooths out at finite temperature. Parameters: L_N = 20 nm for short and L_N = 2000 nm for long junctions, α_R = 20 meV·nm, μ = 0.5 meV, Δ = 0.25 meV and $I_0 = e\Delta/\hbar$.

However, it is also relevant to study whether the sawtooth profile of $I(\phi)$ is preserved or not when the normal transmission T_N, described by τ, is varied.

Figure 15 shows the supercurrent $I(\phi)$ in short junctions at $B = 1.5B_c$ for different values of τ for $L_S \leq 2\xi_M$ (Figure 15a) and $L_S \gg 2\xi_M$ (Figure 15b). When τ is reduced, the supercurrent $I(\phi)$ is also reduced. However, for $L_S \leq 2\xi_M$, there is a transition from a sudden sign change around $\phi = \pi$ to a true sine function with reducing τ, very similar to the effect of temperature discussed above. Notice that in the tunnel regime, τ = 0.6, $I(\phi)$ is approximately zero. For $L_S \gg 2\xi_M$ the sawtooth profile at $\phi = \pi$ is preserved and robust when τ is reduced from the fully transparent to the tunnel regime, as seen in Figure 15b. Quite remarkably, in the tunneling regime, $I(\phi)$ is finite away from $n\pi$ for $n = 0,1,\ldots$. The finite value of the supercurrent could serve as another indicator of the non-trivial topology and, thus, of the emergence of MBSs in the junction.

Disorder effects

Now we analyze the sawtooth profile of $I(\phi)$ for $B > B_c$ in the presence of disorder. Disorder is introduced as a random on-site potential V_i in the tight-binding Hamiltonian given by Equation 4. The values of V_i lie within $[-w, w]$, with w being the disorder strength. When considering this kind of disorder, the chemical potential undergoes random fluctuations. Hence, values of w do not include $w \gg \mu$.

In Figure 16(a,b) we present $I(\phi)$ in short junctions at $B = 1.5B_c$ for 20 disorder realizations and different values of the disorder strength w. Disorder of the order of the chemical potential μ has little effect on $I(\phi)$ as shown by dashed curves in Figure 16a,b. The behavior of $I(\phi)$ is approximately the same as without disorder. This reflects the robustness of the topological phase, and thus of MBSs, against fluctuations in the chemical potential [58,59]. Stronger disorder (dotted and dash-dot curves) reduce the maximum value of $I(\phi)$ although its general behavior is preserved. The sawtooth profile at $\phi = \pi$ in Figure 16b is robust against moderate values of disorder strength. We have confirmed that these conclusions are still valid even when we consider disorder of the order of 5μ (not shown).

Conclusion

In this numerical work we have performed a detailed investigation of the low-energy spectrum and supercurrents in short ($L_N \ll \xi$) and long ($L_N \gg \xi$) SNS junctions based on nanowires with Rashba SOC and in the presence of a Zeeman field.

In the first part, we have studied the evolution of the low-energy Andreev spectrum from the trivial phase into the topological

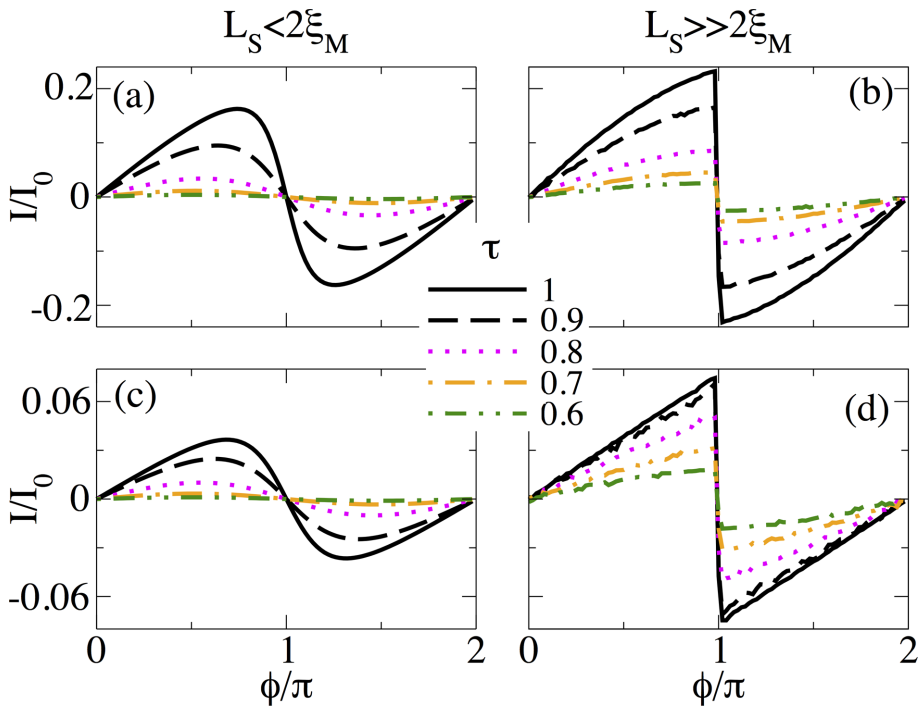

Figure 15: Effect of normal transmission through the coupling parameter τ on the supercurrent, $I(\phi)$, in (a,b) a short and (c,d) a long SNS junction. (a,c) $L_S = 2000$ nm ≤ $2\xi_M$ and (b,d) $L_S = 10000$ nm ≫ $2\xi_M$. Although after decreasing τ the magnitude of the supercurrent at $\phi = \pi$ decreases, the sawtooth profile is preserved. Parameters: $L_N = 20$ nm for short and $L_N = 2000$ nm for long junctions, $\alpha_R = 20$meV·nm, $\mu = 0.5$ meV, $\Delta = 0.25$ meV and $I_0 = e\Delta/\hbar$.

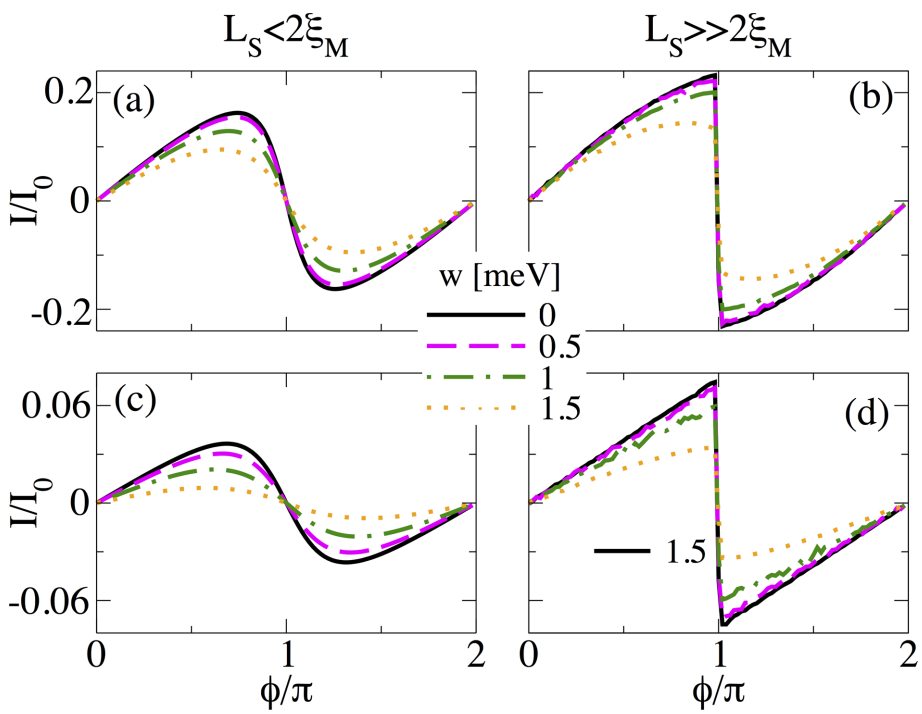

Figure 16: Effect of random on-site scalar disorder on the supercurrent $I(\phi)$ in (a,b) a short and (c,d) a long SNS junction at $B = 1.5B_c$. (a,c) $L_S = 2000$ nm ≤ $2\xi_M$ and (b,d) $L_S = 10000$ nm ≫ $2\xi_M$. Each curve corresponds to 20 realizations of disorder, where w is the disorder strength. For small values of w of the order of the chemical potential, the sawtooth profile at $\phi = \pi$ is preserved (see right panel). Parameters: $L_N = 20$ nm for short and $L_N = 2000$ nm for long junctions, $\alpha_R = 20$ meV·nm, $\mu = 0.5$ meV, $\Delta = 0.25$ meV and $I_0 = e\Delta/\hbar$.

phase and the emergence of MBSs in short and long SNS junctions. We have shown that the topological phase is characterized by the emergence of four MBSs in the junction (two at the outer part of the junction and two at the inner part) with important consequences to the equilibrium supercurrent. In fact, the outer MBSs are almost dispersionless with respect to superconducting phase ϕ, while the inner ones disperse and tend to reach zero at $\phi = \pi$. A finite energy splitting at $\phi = \pi$ occurs when the length of the superconducting nanowire regions, L_S, is comparable to or less than $2\xi_M$. Although in principle such energy splitting can be reduced by making the S regions longer, we conclude that in a system of finite length the current–phase curves are 2π-periodic and the splitting always spoils the so-called 4π-periodic fractional Josephson effect in an equilibrium situation.

In short junctions the four MBSs are truly bound within Δ only when $L_S \gg 2\xi_M$, while in long junctions the four MBSs coexist with additional levels, which profoundly affects phase-biased transport. As the Zeeman field increases in the trivial phase $B < B_c$, the supercurrent $I(\phi)$ is reduced due to the reduction of the induced gap. In this case, the supercurrents $I(\phi)$ are independent of the length of the superconducting regions, L_S, an effect preserved in both short and long junctions.

In short junctions in the topological phase with $B > B_c$ the contribution of the four MBSs levels within the gap determines the shape of the current–phase curve $I(\phi)$ with only little contribution from the quasi-continuum. For $L_S < 2\xi_M$, the overlap of MBS wavefunctions at each S region is finite, and the quasi-continuum contribution is appreciable and of the opposite sign than the contribution of the bound states. This induces a reduction of the maximum supercurrent in the topological phase. For $L_S \gg 2\xi_M$, when both the spatial overlap between MBSs and the splitting at $\phi = \pi$ are negligible, the quasi-continuum contribution is very small and the supercurrent $I(\phi)$ is dominated by the inner MBSs. Remarkably, we have demonstrated that the current–phase curve $I(\phi)$ develops a clear sawtooth profile at $\phi = \pi$, which is independent of the quasi-continuum contribution and represents a robust signature of MBSs.

In the case of long junctions we have found that the additional levels that emerge within the gap affect the contribution of the individual MBSs. Here, it is the combined contribution of the levels within the gap and the quasi-continuum that determine the full current–phase curve $I(\phi)$, unlike in short junctions. The maximum supercurrent in long junctions is reduced in comparison to short junctions, as expected. Our results also show that the maximum value of the supercurrent in the topological phase depends on L_S, acquiring larger values for $L_S \gg 2\xi_M$ than for $L_S \leq 2\xi_M$.

Finally, we have analyzed the robustness of the characteristic sawtooth profile in the topological phase against temperature, changes in transmission across the junction and random on-site scalar disorder. We found that a small finite temperature smooths it out due to thermal population of ABSs. We demonstrated that, although this might be a fragile indicator of MBSs, the fast sign change around $\phi = \pi$ could help to distinguish the emergence of MBSs from trivial ABSs. Remarkably, the sawtooth profile is preserved against changes in transmission, i.e., it is preserved even in the tunneling regime. And finally, we showed that reasonable fluctuations in the chemical potential μ (up to 5μ) do not affect the sawtooth profile of $I(\phi)$ at $\phi = \pi$.

Our main contribution are summarized as follows. In short and long SNS junctions of finite length four MBSs emerge, two at the inner part of junction and two at the outer ends. The unavoidable overlap of the four MBSs gives rise to a finite energy splitting at $\phi = \pi$, thus rendering the equilibrium Josephson effect 2π-periodic in both short and long junctions. Current–phase curves of short and long junctions exhibit a clear sawtooth profile when the energy splitting near $\phi = \pi$ is small, which indicates the presence of weakly overlapping MBSs. Remarkably, the current–phase curves do not depend on L_S in the trivial phase for both short and long junctions, while they strongly depend on L_S in the topological phase. This effect is solely connected to the splitting of MBSs at $\phi = \pi$, indicating a unique feature of the topological phase and therefore of the presence of MBSs in the junction.

Supporting Information

Supporting Information File 1

Majorana wavefunction and charge density in SNS junctions.
[https://www.beilstein-journals.org/bjnano/content/supplementary/2190-4286-9-127-S1.pdf]

Acknowledgements

J.C. thanks O. A. Awoga, K. Björnson, M. Benito and S. Pradhan for motivating and helpful discussions. J.C. and A.B.S. acknowledge financial support from the Swedish Research Council (Vetenskapsrådet), the Göran Gustafsson Foundation, the Swedish Foundation for Strategic Research (SSF), and the Knut and Alice Wallenberg Foundation through the Wallenberg Academy Fellows program. We also acknowledge financial support from the Spanish Ministry of Economy and Competitiveness through Grant No. FIS2015-64654-P (R. A.), FIS2016-80434-P (AEI/FEDER, EU) (E. P.) and the Ramón y Cajal programme through grant No. RYC-2011-09345 (E. P).

ORCID® iDs

Ramón Aguado - https://orcid.org/0000-0002-7464-7363

References

1. Lutchyn, R. M.; Sau, J. D.; Das Sarma, S. *Phys. Rev. Lett.* **2010,** *105,* 077001. doi:10.1103/PhysRevLett.105.077001
2. Oreg, Y.; Refael, G.; von Oppen, F. *Phys. Rev. Lett.* **2010,** *105,* 177002. doi:10.1103/PhysRevLett.105.177002
3. Alicea, J. *Phys. Rev. B* **2010,** *81,* 125318. doi:10.1103/PhysRevB.81.125318
4. Kitaev, A. Yu. *Phys.-Usp.* **2001,** *44,* 131–136. doi:10.1070/1063-7869/44/10S/S29
5. Nayak, C.; Simon, S. H.; Stern, A.; Freedman, M.; Das Sarma, S. *Rev. Mod. Phys.* **2008,** *80,* 1083–1159. doi:10.1103/RevModPhys.80.1083
6. Sarma, S. D.; Freedman, M.; Nayak, C. *npj Quantum Inf.* **2015,** *1,* 15001. doi:10.1038/npjqi.2015.1
7. Law, K. T.; Lee, P. A.; Ng, T. K. *Phys. Rev. Lett.* **2009,** *103,* 237001. doi:10.1103/PhysRevLett.103.237001
8. Mourik, V.; Zuo, K.; Frolov, S. M.; Plissard, S. R.; Bakkers, E. P. A. M.; Kouwenhoven, L. P. *Science* **2012,** *336,* 1003–1007. doi:10.1126/science.1222360
9. Deng, M. T.; Yu, C. L.; Huang, G. Y.; Larsson, M.; Caroff, P.; Xu, H. Q. *Nano Lett.* **2012,** *12,* 6414–6419. doi:10.1021/nl303758w
10. Das, A.; Ronen, Y.; Most, Y.; Oreg, Y.; Heiblum, M.; Shtrikman, H. *Nat. Phys.* **2012,** *8,* 887–895. doi:10.1038/nphys2479
11. Finck, A. D. K.; Van Harlingen, D. J.; Mohseni, P. K.; Jung, K.; Li, X. *Phys. Rev. Lett.* **2013,** *110,* 126406. doi:10.1103/PhysRevLett.110.126406
12. Churchill, H. O. H.; Fatemi, V.; Grove-Rasmussen, K.; Deng, M. T.; Caroff, P.; Xu, H. Q.; Marcus, C. M. *Phys. Rev. B* **2013,** *87,* 241401. doi:10.1103/PhysRevB.87.241401
13. Chang, W.; Albrecht, S. M.; Jespersen, T. S.; Kuemmeth, F.; Krogstrup, P.; Nygård, J.; Marcus, C. M. *Nat. Nanotechnol.* **2015,** *10,* 232–236. doi:10.1038/nnano.2014.306
14. Higginbotham, A. P.; Albrecht, S. M.; Kiršanskas, G.; Chang, W.; Kuemmeth, F.; Krogstrup, P.; Nygård, T. S. J. J.; Flensberg, K.; Marcus, C. M. *Nat. Phys.* **2015,** *11,* 1017–1021. doi:10.1038/nphys3461
15. Krogstrup, P.; Ziino, N. L. B.; Chang, W.; Albrecht, S. M.; Madsen, M. H.; Johnson, E.; Nygård, J.; Marcus, C. M.; Jespersen, T. S. *Nat. Mater.* **2015,** *14,* 400–406. doi:10.1038/nmat4176
16. Zhang, H.; Gül, Ö.; Conesa-Boj, S.; Zuo, K.; Mourik, V.; de Vries, F. K.; van Veen, J.; van Woerkom, D. J.; Nowak, M. P.; Wimmer, M.; Car, D.; Plissard, S.; Bakkers, E. P. A. M.; Quintero-Pérez, M.; Goswami, S.; Watanabe, K.; Taniguchi, T.; Kouwenhoven, L. P. *Nat. Commun.* **2017,** *8,* 16025. doi:10.1038/ncomms16025
17. Albrecht, S. M.; Higginbotham, A. P.; Madsen, M.; Kuemmeth, F.; Jespersen, T. S.; Nygård, J.; Krogstrup, P.; Marcus, C. M. *Nature* **2016,** *531,* 206–209. doi:10.1038/nature17162
18. Deng, M. T.; Vaitiekėnas, S.; Hansen, E. B.; Danon, J.; Leijnse, M.; Flensberg, K.; Nygård, J.; Krogstrup, P.; Marcus, C. M. *Science* **2016,** *354,* 1557–1562. doi:10.1126/science.aaf3961
19. Nichele, F.; Drachmann, A. C. C.; Whiticar, A. M.; O'Farrell, E. C. T.; Suominen, H. J.; Fornieri, A.; Wang, T.; Gardner, G. C.; Thomas, C.; Hatke, A. T.; Krogstrup, P.; Manfra, M. J.; Flensberg, K.; Marcus, C. M. *Phys. Rev. Lett.* **2017,** *119,* 136803. doi:10.1103/PhysRevLett.119.136803
20. Suominen, H. J.; Kjaergaard, M.; Hamilton, A. R.; Shabani, J.; Palmstrøm, C. J.; Marcus, C. M.; Nichele, F. *Phys. Rev. Lett.* **2017,** *119,* 176805. doi:10.1103/PhysRevLett.119.176805
21. Zhang, H.; Liu, C.-X.; Gazibegovic, S.; Xu, D.; Logan, J. A.; Wang, G.; van Loo, N.; Bommer, J. D. S.; de Moor, M. W. A.; Car, D.; Op het Veld, R. L. M.; van Veldhoven, P. J.; Koelling, S.; Verheijen, M. A.; Pendharkar, M.; Pennachio, D. J.; Shojaei, B.; Lee, J. S.; Palmstrøm, C. J.; Bakkers, E. P. A. M.; Das Sarma, S.; Kouwenhoven, L. P. *Nature* **2018,** *556,* 74–79. doi:10.1038/nature26142
22. Aguado, R. *Riv. Nuovo Cimento Soc. Ital. Fis.* **2017,** *40,* 523. doi:10.1393/ncr/i2017-10141-9
23. Fu, L.; Kane, C. L. *Phys. Rev. B* **2009,** *79,* 161408. doi:10.1103/PhysRevB.79.161408
24. Kwon, H.-J.; Sengupta, K.; Yakovenko, V. M. *Eur. Phys. J. B* **2003,** *37,* 349–361. doi:10.1140/epjb/e2004-00066-4
25. Badiane, D. M.; Houzet, M.; Meyer, J. S. *Phys. Rev. Lett.* **2011,** *107,* 177002. doi:10.1103/PhysRevLett.107.177002
26. San-Jose, P.; Prada, E.; Aguado, R. *Phys. Rev. Lett.* **2012,** *108,* 257001. doi:10.1103/PhysRevLett.108.257001
27. Pikulin, D. I.; Nazarov, Y. V. *Phys. Rev. B* **2012,** *86,* 140504. doi:10.1103/PhysRevB.86.140504
28. Peng, Y.; Pientka, F.; Berg, E.; Oreg, Y.; von Oppen, F. *Phys. Rev. B* **2016,** *94,* 085409. doi:10.1103/PhysRevB.94.085409
29. Väyrynen, J. I.; Rastelli, G.; Belzig, W.; Glazman, L. I. *Phys. Rev. B* **2015,** *92,* 134508. doi:10.1103/PhysRevB.92.134508
30. Trif, M.; Dmytruk, O.; Bouchiat, H.; Aguado, R.; Simon, P. *Phys. Rev. B* **2018,** *97,* 041415. doi:10.1103/PhysRevB.97.041415
31. Cayao, J.; Prada, E.; San-José, P.; Aguado, R. *Phys. Rev. B* **2015,** *91,* 024514. doi:10.1103/PhysRevB.91.024514
32. Hansen, E. B.; Danon, J.; Flensberg, K. *Phys. Rev. B* **2016,** *93,* 094501. doi:10.1103/PhysRevB.93.094501
33. van Woerkom, D. J.; Proutski, A.; van Heck, B.; Bouman, D.; Väyrynen, J. I.; Glazman, L. I.; Krogstrup, P.; Nygård, J.; Kouwenhoven, L. P.; Geresdi, A. *Nat. Phys.* **2017,** *13,* 876–881. doi:10.1038/nphys4150
34. Kjaergaard, M.; Suominen, H. J.; Nowak, M. P.; Akhmerov, A. R.; Shabani, J.; Palmstrøm, C. J.; Nichele, F.; Marcus, C. M. *Phys. Rev. Appl.* **2017,** *7,* 034029. doi:10.1103/PhysRevApplied.7.034029
35. Goffman, M. F.; Urbina, C.; Pothier, H.; Nygård, J.; Marcus, C. M.; Krogstrup, P. *New J. Phys.* **2017,** *19,* 092002. doi:10.1088/1367-2630/aa7641
36. San-José, P.; Cayao, J.; Prada, E.; Aguado, R. *New J. Phys.* **2013,** *15,* 075019. doi:10.1088/1367-2630/15/7/075019
37. Cayao, J.; San-José, P.; Black-Schaffer, A. M.; Aguado, R.; Prada, E. *Phys. Rev. B* **2017,** *96,* 205425. doi:10.1103/PhysRevB.96.205425
38. Bychkov, Y. A.; Rashba, E. I. *Sov. Phys. - JETP* **1984,** *39,* 78.
39. Bychkov, Yu. A.; Rashba, E. I. *J. Phys. C: Solid State Phys.* **1984,** *17,* 6039–6045. doi:10.1088/0022-3719/17/33/015
40. Governale, M.; Zülicke, U. *Phys. Rev. B* **2002,** *66,* 073311. doi:10.1103/PhysRevB.66.073311
41. Středa, P.; Šeba, P. *Phys. Rev. Lett.* **2003,** *90,* 256601. doi:10.1103/PhysRevLett.90.256601
42. Quay, C. H. L.; Hughes, T. L.; Sulpizio, J. A.; Pfeiffer, L. N.; Baldwin, K. W.; West, K. W.; Goldhaber-Gordon, D.; de Picciotto, R. *Nat. Phys.* **2010,** *6,* 336–339. doi:10.1038/nphys1626
43. Porta, S.; Gambetta, F. M.; Traverso Ziani, N.; Kennes, D. M.; Sassetti, M.; Cavaliere, F. *Phys. Rev. B* **2018,** *97,* 035433. doi:10.1103/PhysRevB.97.035433

44. de Gennes, P. G. *Rev. Mod. Phys.* **1964,** *36,* 225–237. doi:10.1103/RevModPhys.36.225
45. Doh, Y.-J.; van Dam, J. A.; Roest, A. L.; Bakkers, E. P. A. M.; Kouwenhoven, L. P.; De Franceschi, S. *Science* **2005,** *309,* 272–275. doi:10.1126/science.1113523
46. Alicea, J. *Rep. Prog. Phys.* **2012,** *75,* 076501. doi:10.1088/0034-4885/75/7/076501
47. Anderson, P. W. *J. Phys. Chem. Solids* **1959,** *11,* 26. doi:10.1016/0022-3697(59)90036-8
48. Prada, E.; San-José, P.; Aguado, R. *Phys. Rev. B* **2012,** *86,* 180503. doi:10.1103/PhysRevB.86.180503
49. Das Sarma, S.; Sau, J. D.; Stanescu, T. D. *Phys. Rev. B* **2012,** *86,* 220506. doi:10.1103/PhysRevB.86.220506
50. Klinovaja, J.; Loss, D. *Phys. Rev. B* **2012,** *86,* 085408. doi:10.1103/PhysRevB.86.085408
51. Rainis, D.; Trifunovic, L.; Klinovaja, J.; Loss, D. *Phys. Rev. B* **2013,** *87,* 024515. doi:10.1103/PhysRevB.87.024515
52. Likharev, K. K. *Rev. Mod. Phys.* **1979,** *51,* 101–159. doi:10.1103/RevModPhys.51.101
53. Fleckenstein, C.; Domínguez, F.; Ziani, N. T.; Trauzettel, B. *Phys. Rev. B* **2018,** *97,* 155425. doi:10.1103/PhysRevB.97.155425
54. Beenakker, C. W. J. Three ”Universal” Mesoscopic Josephson Effects. In *Transport phenomena in mesoscopic systems: Proceedings of the 14th Taniguchi symposium,* Springer: Berlin, Germany, 1992; p 235.
55. Prada, E.; Aguado, R.; San-Jose, P. *Phys. Rev. B* **2017,** *96,* 085418. doi:10.1103/PhysRevB.96.085418
56. Deng, M. T.; Vaitiekénas, S.; Prada, E.; San-Jose, P.; Nygård, J.; Krogstrup, P.; Aguado, R.; Marcus, C. M. *arXiv* **2017,** No. 1712.03536.
57. Zagoskin, A. *Quantum Theory of Many-Body Systems: Techniques and Applications;* Springer: Berlin, Germany, 2014.
58. Awoga, O. A.; Björnson, K.; Black-Schaffer, A. M. *Phys. Rev. B* **2017,** *95,* 184511. doi:10.1103/PhysRevB.95.184511
59. Murani, A.; Chepelianskii, A.; Guéron, S.; Bouchiat, H. *Phys. Rev. B* **2017,** *96,* 165415. doi:10.1103/PhysRevB.96.165415

License and Terms

BEILSTEIN JOURNAL OF NANOTECHNOLOGY

Disorder-induced suppression of the zero-bias conductance peak splitting in topological superconducting nanowires

Jun-Tong Ren[1], Hai-Feng Lü[*1,2], Sha-Sha Ke[1], Yong Guo[2] and Huai-Wu Zhang[1]

Full Research Paper

Open Access

Address:
[1]State Key Laboratory of Electronic Thin Films and Integrated Devices and School of Physical Electronics, University of Electronic Science and Technology of China, Chengdu 610054, China and [2]Department of Physics and State Key Laboratory of Low-Dimensional Quantum Physics, Tsinghua University, Beijing 100084, China

Email:
Hai-Feng Lü[*] - lvhf04@uestc.edu.cn

* Corresponding author

Keywords:
conductance peak spacing; disorder; Majorana energy splitting; shot noise; zero-bias conductance

Beilstein J. Nanotechnol. **2018,** *9,* 1358–1369.
doi:10.3762/bjnano.9.128

Received: 16 November 2017
Accepted: 27 March 2018
Published: 04 May 2018

This article is part of the Thematic Series "Topological materials".

Guest Editor: J. J. Palacios

Abstract

We investigate the effect of three types of intrinsic disorder, including that in pairing energy, chemical potential, and hopping amplitude, on the transport properties through the superconducting nanowires with Majorana bound states (MBSs). The conductance and the noise Fano factor are calculated based on a tight-binding model by adopting a non-equilibrium Green's function method. It is found that the disorder can effectively lead to a reduction in the conductance peak spacings and significantly suppress the peak height. Remarkably, for a longer nanowire, the zero-bias peak could be reproduced by weak disorder for a finite Majorana energy splitting. It is interesting that the shot noise provides a signature to discriminate whether the zero-bias peak is induced by Majorana zero mode or disorder. For Majorana zero mode, the noise Fano factor approaches zero in the low bias voltage limit due to the resonant Andreev tunneling. However, the Fano factor is finite in the case of a disorder-induced zero-bias peak.

Introduction

Searching for Majorana bound states (MBSs) have recently received widespread attention due to their potential applications in topologically-protected quantum computing [1-9]. In the past two decades, the realizations of MBSs has been predicted in many condensed-matter systems, including *p*-wave superconductors [10,11], topological insulator-superconductor hybrid structures [12,13], artificially engineered Kitaev chains [14,15], semiconductor-superconductor hybrid nanowire systems [16-21]. Very recently, the one-dimensional Majorana mode running along the sample edge was shown in the heterostructure consisted of a quantum anomalous Hall insulator bar contacted by a superconductor [22]. Among all these proposals, the semiconductor-superconductor hybrid Majorana systems have attracted particular attention and have been demonstrated in several experiments since 2012 [23-30]. As an important signature of MBSs in the semiconductor nanowires which are

proximity-coupled to *s*-wave superconductors, the zero-bias conductance peak has been observed in the tunneling spectra in the presence of a finite magnetic field [23-28]. However, it is suggested that such zero-bias features could also be induced by non-topological physics such as Kondo effect [31], smooth confinement [32], or strong disorder [33-35].

In one-dimensional case, the hybridization of the pair of MBSs localized at the wire ends produces a finite Majorana energy splitting and zero-bias peak splitting [36-38] due to the finite size effects. In a recent experiment [39], the energy splitting of Majorana zero mode has been observed in InAs nanowire segments with epitaxial aluminium, which forms a proximity-induced superconducting Coulomb island. It is illustrated that the energy splitting is exponentially suppressed with increasing wire length. For short wires with a typical length of a few hundred nanometers, the Majorana energies oscillate as the magnetic field varies. These observations are consistent with previous theoretical predictions [36,37]. However, there still exist some critical discrepancies between the theories and experimental results of the evidences for the MBSs. Firstly, it is easy to note that the zero-bias peak is significantly lower than the predicated value of $2e^2/h$, whereas the MBSs are expected to give exactly $2e^2/h$ [40-43]. Secondly, theory predicts an increasing oscillation magnitude of Majorana energy splitting with the increase of magnetic field [36,44], while the experiment indicates the damped oscillation with increasing field. Similar discrepancy was also shown in the Majorana-quantum dot hybrid devices in the subsequent experiments [45-47]. It is important to know what physical mechanism leads to the damped oscillation of Majorana energy splitting.

Up to now, several theoretical studies have been devoted to explain these discrepancies [48-61], among which some possible reasons have been proposed, such as the combining effect of high temperature and multisubband occupancy in a Coulomb-blocked nanowire where the non-topological low-energy Andreev bound states and MBSs simultaneously exist [53], the zero-energy pinning effect induced by the interactions between the bound charges in the dielectric surroundings and the free charges in the nanowire [55], a finite leakage out of the Majorana modes due to the presence the normal drain [59], a finite coherence length in the induced superconducting pairing [60], and the orbital magnetic effects [61]. Although it is noticed that the trivial Andreev bound states are non-negligible in the experiments, the enhanced Majorana energy oscillation for increasing Zeeman field is robust and unaffected when various mechanisms are taken into account.

Here we investigate the effect of different types of disorder on the transport properties of a topological superconducting wire hosting a pair of MBSs. Although the disorder-modulated phase transition in this system has been widely discussed [43,62-74], we focus on the transport properties, especially the splitting of zero-bias conductance peak in presence of disorder. We adopt the non-equilibrium Green's function (NEGF) method for a tight-binding model of the nanowire. Three different types of disorder are separately considered, including the disorder in the site-dependent chemical potential, the spatial deformations of the superconducting gap, and hopping disorder between the nearest neighbors. The results reveal that the disorder could significantly suppress the conductance magnitude. More importantly, the splitting of the conductance peak is removed by the disorder and a zero-bias peak is reformed with an increasing disorder strength. This paper is organized as follows. In section 'The model' we present a tight-binding model for the one-dimensional superconducting nanowire and the theoretical framework based on NEGF. In section 'Numerical results' we give the numerical results of the conductance and the noise Fano factor for different wire lengths and discuss different types of disorder-induced effect on these transport properties respectively. Finally, we conclude our results in section 'Conclusion'.

Results and Discussion

The model

The schematic representation of our one-dimensional Majorana system is shown in Figure 1. We consider a setup of two normal metal leads sandwiching a spin-orbit coupled semiconductor nanowire, which is covered by a parent *s*-wave superconductor to induce the proximity effect. The Zeeman field is realized by applying a magnetic field perpendicular to the spin-orbit coupling direction and the wire. It is proposed that such a hybrid system can hold a pair of MBSs at the two wire ends by tuning the Zeeman field or chemical potential to satisfy $V_Z > \sqrt{\Delta^2 + \mu^2}$ [16-21], for which the nanowire will be driven into the topolog-

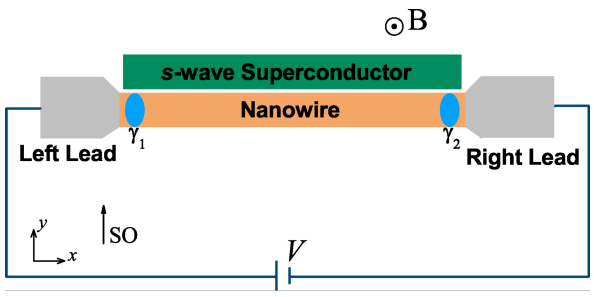

Figure 1: Scheme of our one-dimensional Majorana system. A semiconductor nanowire with spin-orbit interaction sandwiched by two normal leads (L, R) is proximity-coupled to an *s*-wave superconductor. The nanowire is driven into the topological phase and a pair of MBSs (γ_1, γ_2) emerge at the two wire ends with suitable parameters. A bias voltage *V* is applied across the device. The nanowire is arranged along the *x*-axis and the magnetic field (*B*) is applied along the *z*-axis, perpendicular to the spin-orbit coupling field (SO) in the *y*-direction.

ical phase. Here V_Z, Δ and μ are the Zeeman splitting energy, proximity-induced superconducting pairing and the chemical potential, respectively. Although this work is motivated by the experiment by Albrecht et al. [39], our model does not take the Coulomb blockade effects into account. The reason is that the physics of disorder-induced suppression of the conductance peak spacings and reformation of the zero-bias peak, which we discuss below, is independent of Coulomb blockade physics. In the presence of a charging energy in the nanowire, it was shown that the zero-bias conductance values are considerably suppressed by the Coulomb energy [75]. The situation of interest to us is how intrinsic disorder in the nanowire affect the Majorana energy E_M and the splitted zero-bias conductance peak induced by E_M. In situations like this, the intrawire charging energy could modulate the actual conductance value, but the main physics induced by the disorder is captured even though the charging energy is not taken into account.

The generic form of the Hamiltonian that models this Majorana hybrid structure reads as

$$H = H_{\rm nw} + H_{\rm L} + H_{\rm R} + H_{\rm T} \tag{1}$$

where the term $H_{\rm nw}$, $H_{\rm L(R)}$, and $H_{\rm T}$ account for the superconducting nanowire, the left (right) normal metal lead, and the tunnel coupling between the leads and the wire, respectively. Following the Bogoliubov–de Gennes formalism the Hamiltonian describing the low-energy physics for our one-dimensional superconducting wire is given by

$$H_{\rm nw} = \frac{1}{2}\int \Psi^{\dagger}(x) H_{\rm BdG} \Psi(x)\,{\rm d}x, \tag{2}$$

where $\Psi(x) = [c_{\uparrow}(x), c_{\downarrow}^{\dagger}(x), c_{\downarrow}(x), c_{\uparrow}^{\dagger}(x)]^T$ is the Nambu spinor for which $c_\sigma(x)$ ($c_\sigma^{\dagger}(x)$) annihilates (creates) electrons with spin σ at position x. For numerical calculations, we invoke a lattice tight-binding model to discretize the BdG Hamiltonian and the Hamiltonian for the nanowire can then be written as [16-19]

$$\begin{aligned} H_{\rm nw} = &\sum_{i=1}^{N-1}\left[-\frac{t_i}{2}\mathbf{c}_i^{\dagger}\mathbf{c}_{i+1} + \frac{i\alpha}{2}\mathbf{c}_i^{\dagger}\sigma_y\mathbf{c}_{i+1} + {\rm h.c.}\right] \\ &+\sum_{i=1}^{N}\left[(t_i-\mu_i)\mathbf{c}_i^{\dagger}\mathbf{c}_i + \Delta_i\left(c_{i\uparrow}c_{i\downarrow} + {\rm h.c.}\right) + V_Z\mathbf{c}_i^{\dagger}\sigma_z\mathbf{c}_i\right], \end{aligned} \tag{3}$$

where t_i characterizes the nearest-neighbor hopping between site i and $i+1$, μ_i and Δ_i represent the on-site chemical potential and pairing, α is the spin-orbit coupling constant, $\mathbf{c}_i = [c_{i\uparrow}, c_{i\downarrow}]^T$ ($\mathbf{c}_i^{\dagger} = [c_{i\uparrow}^{\dagger}, c_{i\downarrow}^{\dagger}]$) is the spinor form of electron annihilation (creation) operator on the ith site, and σ_i, $i = 0, x, y, z$, are Pauli matrices acting on the spin space. The wire length is $L = Na$ where a is the lattice constant and N is the total number of sites. In this work, three different types of intrinsic disorder in the nanowire are considered: the fluctuations of the site-dependent chemical potential, the nonlinear tunneling between neighboring sites, and the disorder arising in the pairing as a result of inhomogeneous superconductor–semiconductor coupling. In the case of a clean wire, we set $\mu_i = \mu_0$, $\Delta_i = \Delta_0$, and $t_i = t_0$ for all sites. For each single disordered configuration of the system, the on-site disorder are modeled by the white noise and their strength is assumed to be randomly distributed in the range $[-\delta W, +\delta W]$, where the $W = t$, μ, Δ denotes the strength for different types of disorder.

The Hamiltonian describing the normal metallic leads is given by

$$H_{\alpha} = \sum_{k,\sigma}\varepsilon_{\alpha k\sigma}c_{\alpha k\sigma}^{\dagger}c_{\alpha k\sigma}, \tag{4}$$

where $\varepsilon_{\alpha k\sigma}$ (α = L, R) represents the single-particle energy in the lead α and $c_{\alpha k\sigma}$ ($c_{\alpha k\sigma}^{\dagger}$) is the annihilation (creation) operator for the lead α. The sum is over momentum k and the spin σ. The last term in the total Hamiltonian, $H_{\rm T}$, characterizes the coupling between the wire and the two leads, which is given by

$$H_{\rm T} = \sum_{k,\sigma} t_{\rm L}\left(c_{{\rm L}k\sigma}^{\dagger}c_{1\sigma} + {\rm h.c.}\right) + t_{\rm R}\left(c_{{\rm R}k\sigma}^{\dagger}c_{N\sigma} + {\rm h.c.}\right), \tag{5}$$

where $t_{\rm L(R)}$ denotes the hopping strength through left (right) lead and the wire. The operators $c_{1\sigma}$ and $c_{N\sigma}$ correspond to the annihilation operators on the first and last site at opposite ends of the wire. Taking all lattice sites into account, we can now write out the Hamiltonian for the nanowire as a $4N \times 4N$ matrix of which the submatrix entry $H_{i,j}$ fully characterizes the coupling between site i and site j. The nonzero off-diagonal entries read as

$$H_{i,i} = (t_i - \mu_i)\sigma_0 \otimes \tau_z + V_{\rm Z}\sigma_z \otimes \tau_0 + \Delta_i\sigma_z \otimes \tau_x, \tag{6}$$

$$H_{i,i+1} = -\frac{t_i}{2}\sigma_0 \otimes \tau_z - \frac{i\alpha}{2}\sigma_y \otimes \tau_0. \tag{7}$$

and the subdiagonals are related to the superdiagonals by $H_{i+1,i} = H_{i,i+1}^{\dagger}$. Here τ_i, $i = 0, x, y, z$, are the Pauli matrices acting on the Nambu space.

The operator of tunneling current from the lead α to the central region is defined as

$$\mathbf{I}_\alpha(t)\equiv -e\frac{\mathrm{d}\hat{N}_\alpha}{\mathrm{d}t}$$

and then one can obtain [76-79]

$$\begin{aligned}\mathbf{I}_\mathrm{L}&=\frac{ie}{\hbar}\left[\hat{N}_\mathrm{L},\hat{H}\right]=\frac{ie}{}t_\mathrm{L}\sum_{k\sigma}\left(c^\dagger_{\mathrm{L}k\sigma}c_{1\sigma}-c^\dagger_{1\sigma}c_{\mathrm{L}k\sigma}\right),\\ \mathbf{I}_\mathrm{R}&=\frac{ie}{\hbar}\left[\hat{N}_\mathrm{R},\hat{H}\right]=\frac{ie}{}t_\mathrm{R}\sum_{k\sigma}\left(c^\dagger_{\mathrm{R}k\sigma}c_{N\sigma}-c^\dagger_{N\sigma}c_{\mathrm{R}k\sigma}\right).\end{aligned}\tag{8}$$

The current noise correlations are defined as

$$S_{\alpha\beta}(t-t')=\left\langle I_\alpha(t)I_\beta(t')+I_\beta(t')I_\alpha(t)\right\rangle-2\left\langle I_\alpha\right\rangle\left\langle I_\beta\right\rangle.\tag{9}$$

$S_{\alpha\beta}$ is referred to as the noise auto- or cross-correlation between the currents flowing through the lead α and lead β. To evaluate the current and noise within the framework of Keldysh NEGF formalism, we need to derive the retarded (advanced) Green's function $G^{r(a)}$ and the lesser (greater) Green's function $G^{<(>)}$ from the contour-ordered Green function $\mathbf{G}(t,t')=-i\left\langle\Psi(t)\Psi^\dagger(t')\right\rangle$ in the Nambu space spanned by the spinor $\Psi=[\mathbf{c}_\mathrm{L},\mathbf{c}_\mathrm{R},\mathbf{c}^\dagger_\mathrm{L},\mathbf{c}^\dagger_\mathrm{R},\mathbf{c}_1,...,\mathbf{c}_N,\mathbf{c}^\dagger_1,...,\mathbf{c}^\dagger_N]^T$, where $\mathbf{c}_{\mathrm{L(R)}}$ is the electron annihilation operator in the left (right) lead. In this Nambu space, we define the matrix of the lesser Green's function $\mathbf{G}^<$ [78,79]

$$\mathbf{G}^<(t-t')=\left\langle\left\langle\Psi(t)\,|\,\Psi^\dagger(t')\right\rangle\right\rangle^<=i\left\langle\Psi^\dagger(t')\Psi(t)\right\rangle.\tag{10}$$

In this representation, the currents are given by

$$I_\alpha=\mathbf{Tr}\left[\hat{\mathbf{I}}_\alpha\mathbf{G}^<\right],\tag{11}$$

and the noise spectrum $S_{\alpha\beta}(\omega)$ is given by:

$$\begin{aligned}S_{\alpha\beta}(\omega)&=S^{\mathrm{Sch}}_\alpha\delta_{\alpha\beta}\\&+2\int d\omega'\mathbf{Tr}\left[\hat{\mathbf{I}}_\alpha\mathbf{G}^<_{\omega'}\hat{\mathbf{I}}_\beta\mathbf{G}^>_{\omega'+\omega}+\hat{\mathbf{I}}_\beta\mathbf{G}^>_{\omega'}\hat{\mathbf{I}}_\alpha\mathbf{G}^<_{\omega'+\omega}\right],\end{aligned}\tag{12}$$

where S^{Sch}_α is the frequency-independent Schottky noise originating from the self-correlation of a given tunneling event with itself, which the double-time correlation function can not contain, and $\mathbf{G}^{<(>)}_\omega=\int\mathrm{d}t\mathbf{G}^{<(>)}(t)e^{i\omega t}$ denotes the lesser (greater) green functions in the frequency space. The matrices of the current operators are given by

$$\begin{aligned}\hat{\mathbf{I}}_\mathrm{L}&=\frac{e}{2\hbar}t_\mathrm{L}\mathbf{M}^\mathrm{L}\otimes\sigma_0,\\ \hat{\mathbf{I}}_\mathrm{R}&=\frac{e}{2\hbar}t_\mathrm{R}\mathbf{M}^\mathrm{R}\otimes\sigma_0,\end{aligned}\tag{13}$$

where $\mathbf{M}^\mathrm{L}$ and $\mathbf{M}^\mathrm{R}$ are the block $(2N+4)\times(2N+4)$ matrices with nonzero elements

$$\begin{aligned}\mathbf{M}^\mathrm{L}_{5,1}=\mathbf{M}^\mathrm{L}_{N+5,3}&=-\mathbf{M}^\mathrm{L}_{1,5}=-\mathbf{M}^\mathrm{L}_{3,N+5}=1,\\ \mathbf{M}^\mathrm{L}_{6,1}=\mathbf{M}^\mathrm{L}_{N+6,4}&=-\mathbf{M}^\mathrm{L}_{2,6}=-\mathbf{M}^\mathrm{L}_{4,N+6}=1,\end{aligned}\tag{14}$$

respectively. From the standard equation of motion for the central region, we can write the retarded Green's function $\mathbf{G}^\mathrm{r}$ in terms of the Dyson equation $\mathbf{G}^\mathrm{r}=\mathbf{g}^\mathrm{r}+\mathbf{g}^\mathrm{r}\Sigma^\mathrm{r}\mathbf{G}^\mathrm{r}$, which gives

$$\mathbf{G}^\mathrm{r}=\left(1-\mathbf{g}^\mathrm{r}\Sigma^\mathrm{r}\right)^{-1}\mathbf{g}^\mathrm{r}.\tag{15}$$

Here $\mathbf{g}^\mathrm{r}$ is the bare Green's function of the central region without coupling to the leads ($t_\mathrm{L}=t_\mathrm{R}=0$),

$$\mathbf{g}^\mathrm{r}(\omega)^{-1}=\left(\frac{i}{\pi\rho}\mathbf{I}_{8\times8}\right)\otimes\left(\omega\mathbf{I}_{4N\times4N}-\mathbf{H}_\mathrm{nw}\right),\tag{16}$$

where $\mathbf{I}_{n\times n}$ is the $n\times n$ identity matrix. Since $\mathbf{G}^\mathrm{r}$ is already given and the advanced Green's function $\mathbf{G}^\mathrm{a}$ can be obtained from $\mathbf{G}^\mathrm{r}=(\mathbf{G}^\mathrm{a})^\dagger$, it is now straightforward to obtain the lesser Green's function from the standard Keldysh equation,

$$\begin{aligned}\mathbf{G}^<&=\left(1+\mathbf{G}^\mathrm{r}\Sigma^\mathrm{r}\right)\mathbf{g}^<\left(1+\Sigma^a\mathbf{G}^a\right)+\mathbf{G}^\mathrm{r}\Sigma^<\mathbf{G}^\mathrm{a}\\&=\mathbf{G}^\mathrm{r}\mathbf{g}^{\mathrm{r}-1}\mathbf{g}^<\mathbf{g}^{a-1}\mathbf{G}^a+\mathbf{G}^\mathrm{r}\Sigma^<\mathbf{G}^a.\end{aligned}\tag{17}$$

In the present case, $\Sigma^<=0$ and

$$\mathbf{g}^{\mathrm{r}-1}\mathbf{g}^<\mathbf{g}^{a-1}=\begin{pmatrix}\Lambda_e&0\\0&\Lambda_h\end{pmatrix}\otimes\mathbf{O}_{4N\times4N},\tag{18}$$

with

$$\Lambda_{e(h)}=\frac{2i}{\pi\rho}\begin{pmatrix}f(\omega\mp\mu_\mathrm{L})&0\\0&f(\omega\mp\mu_\mathrm{R})\end{pmatrix}\otimes\sigma_0,\tag{19}$$

where $\mathbf{O}_{4N\times4N}$ is the $4N\times4N$ zero matrix, $f(\omega)=[1+e^{\omega/k_\mathrm{B}T}]^{-1}$ is the Fermi–Dirac distribution function and $k_\mathrm{B}T$ is the temperature. In the calculation of the noise spectrum $S_{\alpha\beta}(\omega)$, the greater

Green's function $\mathbf{G}^{>}$ can be readily obtained since the relation $\mathbf{G}^{<} - \mathbf{G}^{>} = \mathbf{G}^{a} - \mathbf{G}^{r}$ holds. Finally, we define the noise Fano factor $F = S_L(\omega = 0)/2eI_L$ to measure the deviation from the uncorrelated Poissonian noise for which $F = 1$, with respect to which the shot noise can be enhanced or suppressed because the current fluctuations in the device are highly susceptible to different interactions in the system.

Numerical results

In this section we present the numerical results of the transport properties for the disordered Majorana nanowire. Here we mainly discuss the disorder-induced effects on the differential conductance, especially on the conductance peak spacing and its relation with the Majorana energy oscillation. To exclude thermal fluctuations, we restrict our discussion to the zero temperature $k_BT = 0$. The lattice constant is set to $a = 10$ nm throughout the paper. For the disorder-free situation, we choose $t_0 = 12$ meV, $\mu_0 = 2.0$ meV, $\Delta_0 = 0.9$ meV, $\alpha = 2.4$ meV, and the symmetric lead-wire coupling strength $\Gamma_L = \Gamma_R = 0.3$ meV. The bias voltage V across the whole device will shift the chemical potential $\mu_L(\mu_R)$ in the leads to $\pm V/2$. In modeling the disorder effect on the quantum transport in mesoscopic devices, the numerical results need to be averaged over enough random configurations. In our calculation, the conductance and the noise Fano factor is averaged over 400 random configurations for each data point.

In previous work [35], it was found that the disorder could induce a nonquantized zero-bias peak at finite temperature even when the nanowire is in a topologically trivial regime. In their work, a single disorder realization is considered for their 3-dimensional multiband Majorana wire. The consideration of the multiband wire model leads to the weaker sample–sample fluctuations than the single channel model. Although a single disorder configuration is considered, their results are obtained at a finite temperature, which implies that thermal averaging is done. With the increase of temperature, the sample-to-sample fluctuations are suppressed [80]. It is thus reasonable for them to consider a single disorder configuration.

Here we study the effect of three types of disorder on the transport in a Majorana device. To exclude the thermal effect, we restrict our discussion to the zero temperature case. The large sample-to-sample fluctuations is thus unavoidable. In principle, several similar samples are also needed in experiments to confirm the existence of related physical mechanisms. In a previous experiment [39], only one sample is reported for each wire length. It is indicated that a damped oscillation magnitude of the Majorana energy splitting occurs with the increase of magnetic field, which contradicts the theoretical result. Our calculation suggests that the discrepancy may arise from the intrinsic disorder. To confirm this, more experiments are expected to be performed in the future for similar samples.

Majorana energy oscillation

We firstly present the lowest energy E_M as a function of the magnetic field in the presence of different kinds of disorder. Considering the finite-size effects on the coupling between the two MBSs and the recently reported suppression of the energy splitting due to the increase in wire length [39], we consider wires of two typical lengths in particular: a shorter one with $L = 0.60$ μm and a longer one with $L = 0.95$ μm. In Figure 2, when V_Z is relatively small, the system stays in the topologically trivial phase, and the lowest energy is linearly suppressed as the magnetic field strength increases. Without disorder in the system, the nanowire is driven into a topological superconducting phase when we tune V_Z to exceed the phase transition point $V_{ZC} = \sqrt{\Delta_0^2 + \mu_0^2}$, and E_M begins to oscillate near the zero value. This behavior, originating from the finite-size effects, is absent in a long enough wire, where the field-independent exact Majorana zero mode emerges with its energy pinned to zero.

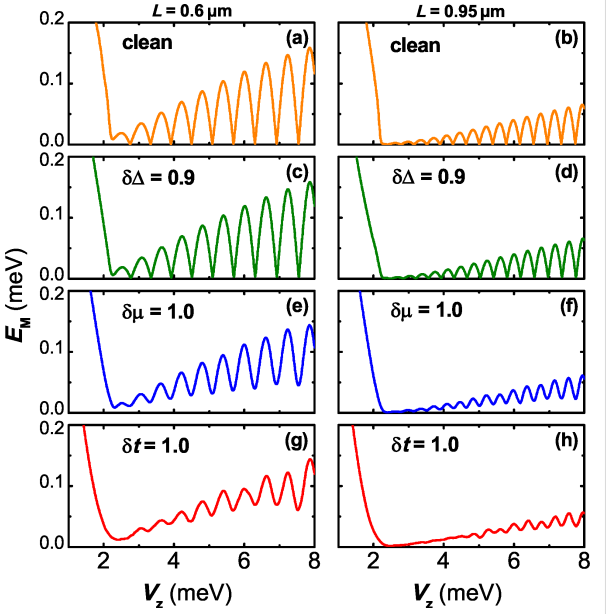

Figure 2: The Majorana energy E_M as a function of the Zeeman splitting V_Z for different types of disorder. (a,b) The clean cases; (c,d) disorder in pairing energy $\delta\Delta = 0.9$ meV; (e,f) disorder in the chemical potential $\delta\mu = 1.0$ meV; (g,h) disorder in the nearest hopping $\delta t = 1.0$ meV. For comparison, two different wire lengths $L = 0.6$ μm (left panels) and $L = 0.95$ μm (right panels) are separately considered. Other parameters are taken as $t_0 = 12.0$ meV, $\Delta_0 = 0.9$ meV, $\mu_0 = 2.0$ meV, $\alpha = 2.4$ meV, and $\Gamma_L = \Gamma_R = 0.3$ meV. The MBSs appears at the wire ends for $V_Z > V_{ZC}$.

For disordered wires, we find that the exact Majorana zero mode gradually vanishes in the presence of disorder in hopping or chemical potential. In particular, as shown in Figure 2, a δt

with strength 1.0 meV, which is comparable to the strength of Zeeman splitting, can remarkably flatten the energy oscillation. On the contrary, the strong disorder in the pairing energy leaves the Majorana energy oscillation almost unaffected. In the topological phase and in the strong Zeeman field regime, the spins are nearly polarized and one can project the original Hamiltonian onto a simpler one-band problem [7]. To leading order, one obtains an effective p-wave-like Hamiltonian with the effective chemical potential $\mu_{\text{eff}} = \mu + V_Z/2$ and the effective pairing energy $\Delta_{\text{eff}} = \alpha\Delta/2V_Z$. Because small spin-orbit coupling is considered, the effect of the disorder $\delta\Delta$ in the pairing energy is considerably suppressed with increasing V_Z due to the multiplication factor $\alpha/2V_Z$. However, there is no multiplication factor for μ, hence the disorder $\delta\mu$ has a stronger influence on the Majorana energy oscillation. The hopping disorder and chemical potential disorder can both considerably destroy the Majorana zero modes, leading to increased Majorana energy splitting and enhancement of the MBSs hybridization.

To get a closer look into the effects of disorder on the Majorana energy splitting, it is beneficial to investigate the localization length that characterizes the hybridization between the pair of MBSs. In weak spin-orbit coupling regime, the localization length increases gradually as $\propto B$ [36,38]. Therefore, the strength of the Zeeman splitting V_Z should be chosen as the energy scale to determine whether the disorder strength is strong or not. Meanwhile, the disorder strength that can remove the energy splitting signature is also determined by the wire length. For a longer wire, a disorder of the same strength could lead to a more evident suppression of the energy splitting signature.

In Figure 3, without loss of generality, we focus on the evolution of the MBS probability density on the left wire end in the presence of disorder in chemical potential, of which the influence is more evident compared with the limited effects induced by the pairing disorder. Here we choose a rather long wire of length $L = 2.0$ μm, where the two spatially separated MBSs are well localized at each end of the wire, thus the hybridization between the pair of MBSs is negligibly small. In our case where $V_Z \gg m(\alpha a)^2/\hbar$ the system is in a weak spin-orbit interaction regime, and the approximate value of the localization length for a discretized tight-binding model is analytically given by

$$\xi^{-1} \approx \frac{2\alpha\Delta}{aV_Z t},$$

with which the MBS probability density has an exponentially decaying envelope of the form $|\Psi|^2_{\text{env}} \propto e^{-x/\xi}$ [81]. As shown in Figure 3, the numerically fitted decaying envelope of the disorder-free probability density gives $\xi \approx 0.0727$ μm, compared to the approximate analytical results of $\xi \approx 0.0775$ μm the difference is below a lattice constant. With the disorder strength increasing, the probability density at the end is suppressed and the localization length ξ of the fitted envelope becomes larger. This can also be directly identified from the noticeable deformations of the tail part of the probability density, which implies an enhanced hybridization between the two MBSs with an increasing disorder strength. In a shorter wire where the overlap between the two MBSs is stronger, it is reasonable to expect a more evident disorder-induced increment in the MBSs hybridization, which agrees with the results shown in Figure 2.

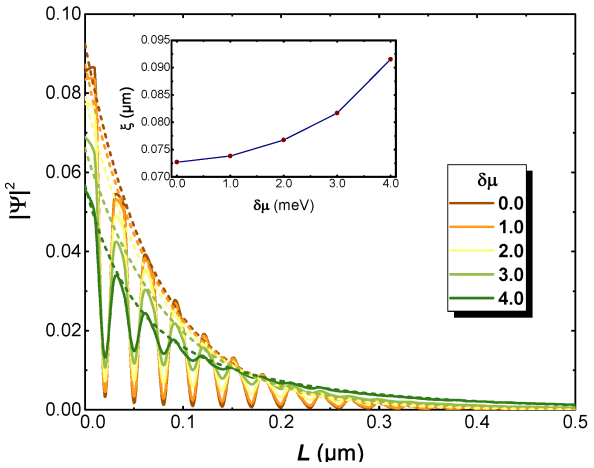

Figure 3: The spatial distribution of probability density $|\Psi|^2$ (solid lines) and their fitted envelopes $|\Psi|^2_{\text{env}}$ (dashed lines) in the presence of different strengths of chemical potential disorder $\delta\mu$; the inset shows the localization length ξ of the fitted envelope varies with different values of $\delta\mu$. Here we choose $L = 2.0$ μm, $\mu = 0$, $\Delta = 2.0$ meV, $V_Z = 6.1$ meV and other parameters are taken as those used in Figure 2.

Conductance peak spacings

In Figure 4, we demonstrate the effects of three types of disorder on the conductance peak spacings for different wire lengths. In a disorder-free case, the Majorana energy splitting of the system can be reflected by the conductance peak spacing. We take a Zeeman field $V_Z = 6.6$ meV that is associated with clear energy splittings and conductance peak spacings.

For a shorter nanowire $L = 0.6$ μm, it is found that all three types of disorder can suppress the amplitude of the conductance peak and broaden the peak width to some different extent. The presence of disorder in the system leads to a similar result induced by dissipation or finite temperature, both of which can lower the peak and broaden its width [57]. What makes a difference here is that one can additionally observe a suppression, which is pronounced especially in the cases of hopping or chemical potential, of the conductance peak spacings due to the effect of disorder.

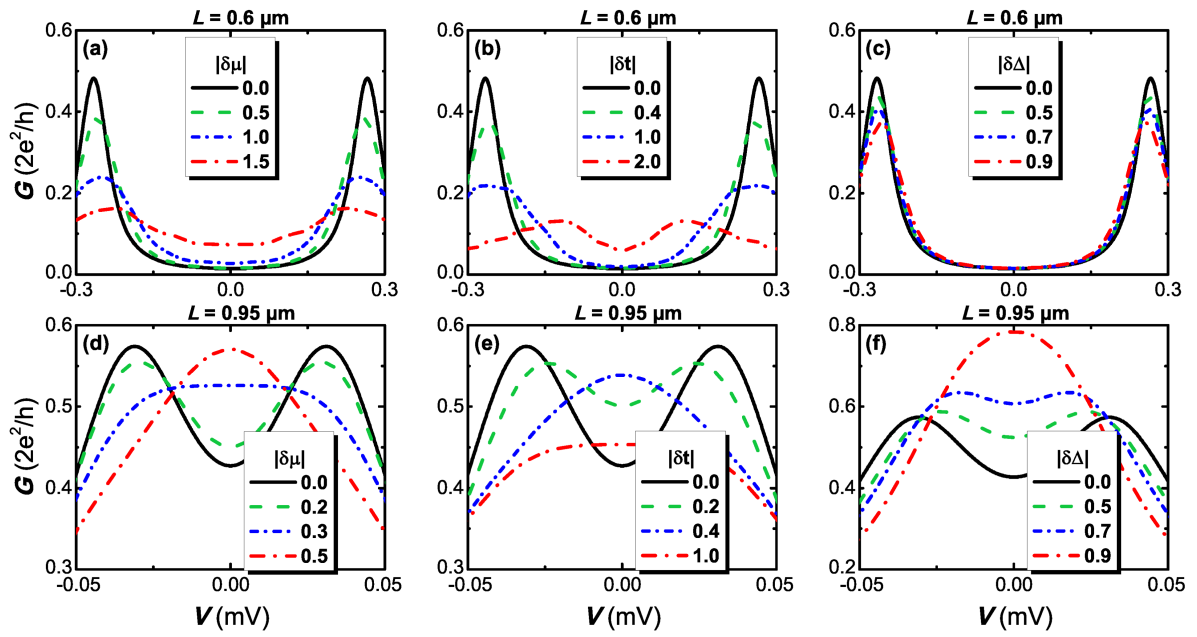

Figure 4: The differential conductance $G = dI/dV$ as a function of the bias voltage V under the influence of different types of disorder. (a,d) disorder δμ in the chemical potential; (b,e) disorder δt in the nearest hopping; (c,f) disorder δΔ in pairing energy. The upper panels corresponds to the shorter wire case L = 0.6 μm and the lower panels represents the case of L = 0.95 μm. Other parameters are taken as those used in Figure 2.

When the device becomes longer (L = 0.95 μm), the Majorana energy splitting is exponentially suppressed, thus the conductance peak spacing in a clean system becomes much narrower. As illustrated in the lower panels of Figure 4, smaller disorder than that in the shorter wire can lead to notable suppressions on the conductance peak spacings, and as the disorder strength eventually exceeds some certain value, a zero-bias peak is formed from the two spaced peaks. It is interesting that a strong disorder in pairing could even elevate the induced zero-bias conductance peak. These numerical results, together with that revealed in Figure 2, suggest that we can not simply neglect the role played by disorder in detecting Majorana energy oscillation experimentally through transport measurements since for some values of Zeeman field the disorder-induced effects can broaden the Majorana energy splitting of the low-energy states while simultaneously narrows the conductance peak spacing. This means that the Majorana energy splitting can not be genuinely characterized by the conductance signature. One possible reason is that the Majorana energy splitting is not robust. When the energy splitting of the Majorana modes is negligible compared to the magnitude of disorder, the conductance signature associated with the Majorana energy splitting could be annihilated by the noise arising in the system, which is equivalent to raising the temperature. Different from the thermal fluctuations that could be excluded by lowering the temperature, the three types of intrinsic disorder discussed here are hard to avoid in a realistic experiment.

Above we consider the case that the critical Zeeman field V_{ZC} is much stronger than the disorder strength δW. Now we turn to discuss the more experimentally relevant case where $\delta W \approx V_{ZC}$. Figure 5 demonstrates the effect of three types of disorder on the conductance for a small V_{ZC}. The chemical potential in the wire is tuned as $\mu_0 = 0$, while the other parameters are taken as the same as that for the lower panels in Figure 4. It is shown in

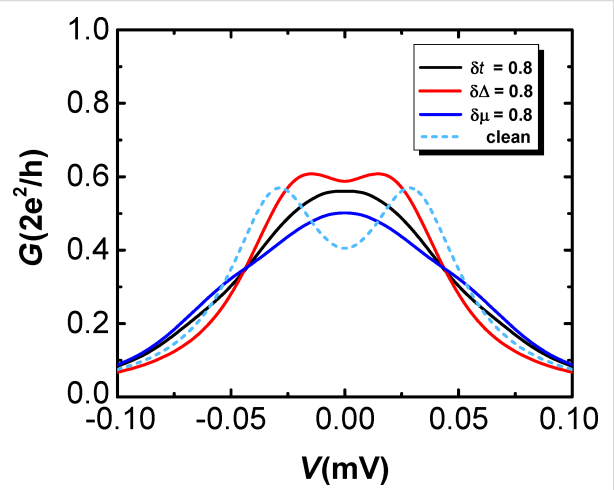

Figure 5: The differential conductance $G = dI/dV$ in the longer wire (L = 0.95 μm) as a function of the bias voltage V with δμ = δΔ = δt = 0.8 meV approaching the critical Zeeman splitting V_{ZC} = 0.9 meV. Here we have $\mu_0 = 0$, V_Z = 6.0 meV and other parameters are taken as those used in Figure 4.

Figure 5 that for $\delta W \approx V_{ZC}$, the disorder can suppress the peak spacing and a single zero-bias peak is produced. Similar to the large V_{ZC} case, the main conclusion is qualitatively consistent with the results in Figure 4.

In previous experiments [39,46,47], the Majorana energy splitting for a nanowire with Coulomb interactions was represented by the even–odd peak spacing differences. However, the expected field-dependent decay behavior of Majorana energy oscillations is not observed in the experiments. On the contrary, the detected conductance peak differences tend to decay sharply as the magnetic field increases, which contradicts the theoretical predictions. Although here we consider an interaction-free scenario, our results indicate that the disorder can partially reduce the splitting of the conductance peak. In addition, for a shorter wire, the hybridization of the MBSs at two ends can generate a relatively large splitting in the conductance peak, which is consistent with the result of the previous experiments. The magnetic field could suppress the superconducting pairing energy, which leads to the enhancement of disorder strength in some sense.

Zero-bias conductance as a function of Zeeman field

In superconducting nanowire systems, a quantized zero-bias conductance peak is considered as direct evidence for the presence of MBSs, and its emergence is often associated with the resonant Andreev reflection [41]. However, for realistic Majorana nanowires, the observed conductance peaks are often much smaller than $2e^2/h$. In Figure 6, we show the disorder-induced effects on the zero-bias conductance oscillation as a function of the Zeeman splitting V_Z. For the clean wire, the zero-bias conductance has a clear oscillating behavior in the topological phase ($V_Z > V_{ZC}$), and its peak value is quantized to $2e^2/h$. These quantized peaks of the conductance emerge from the exact zero-energy modes, while the valley of the conductance corresponds to the peak value of Majorana energy splitting. With an increasing magnetic field, the valley of the conductance gradually decays, corresponding to an enhancement of the Majorana energy splitting through the magnetic field. When the magnetic field is strong enough, the transport channel of the resonant Andreev reflection is almost closed and the valley of conductance approaches zero.

In the presence of disorder, the most notable difference is that the conductance oscillation peaks do not become more quantized. In Figure 2, it is shown that the disorder could destroy the exact Majorana zero mode and produce a finite energy splitting. Correspondingly, the quantized zero-bias conductance peak is suppressed by the disorder, as a manifestation of the induced finite energy splitting. This phenomenon is particularly evident for the cases where the disorder in the hopping or in chemical potential exists. As shown in Figure 6b and Figure 6f, the conductance peaks stay almost quantized even in the presence of a relatively strong pairing disorder. Additionally, one can find that the valleys of the conductance oscillation are almost unaffected by all kinds of disorder, which also agrees with the result of Figure 2. These observations suggest that the intrinsic disorder in the nanowire could strongly reduce the zero-bias conductance oscillation associated with the Majorana energy

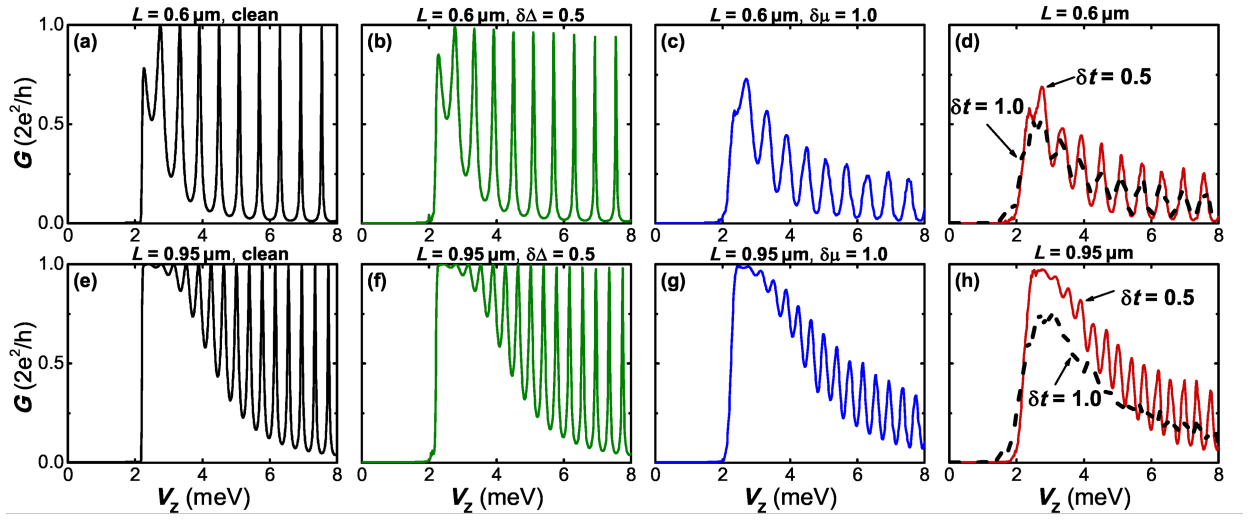

Figure 6: The zero-bias conductance G as a function of the Zeeman splitting V_Z for different types of disorder. (a,e) The clean case; (b,f)disorder in pairing energy $\delta\Delta$ = 0.5 meV; (c,g) disorder in the chemical potential $\delta\mu$ = 1.0 meV; (d,h) disorder in the nearest hopping δt = 0.5 meV and 1.0 meV. The upper panels correspond to the shorter wire case L = 0.6 μm and the lower panels represent the case of L = 0.95 μm. In panel (h), we show that a disorder of δt = 1.0 meV could remove the conductance oscillation as V_Z increases. Other parameters are taken as those used in Figure 2.

splitting. However, although the disorder significantly suppresses the oscillation, it does not eliminate the zero-bias conductance peak.

Shot noise

We now turn to investigate the shot noise properties of the Majorana system. For a long nanowire, the Majorana energy splitting is negligible, and the noise Fano factor is suppressed at zero voltage due to the resonant Andreev tunneling in an isolated MBS. In the clean case, a large Majorana energy splitting could strongly suppress the resonant Andreev tunneling, leading to the increase of the noise Fano factor and splitting of the conductance peak. It is shown in Figure 4 that the split conductance peaks are reformed to one zero-bias peak by the disorder. However, the zero-bias conductance peak can also arise due to the exact Majorana zero mode in the clean case. It is expected that the shot noise may provide the signature to distinguish the zero-bias conductance peak in a clean system from that which arises in a disordered one. This can be verified by the results given in Figure 7.

Here we present the Majorana energy splitting E_M, the conductance G and the noise Fano factor $F = S/2eI$ in the clean and disordered cases, in which three different types of disorder are taken into account. In the clean case, we separately choose point A and B which represents the zero energy mode and a finite splitting case, respectively. For a Majorana zero mode, a quantized zero-bias conductance peak could be induced and the noise Fano factor approaches zero due to the resonant Andreev tunneling. While for the case of finite energy splitting, the zero-bias conductance peak is split and the shot noise is enhanced due to the crossed Andreev reflection (CAR) which, contrasting with the local Andreev reflection that injects a Cooper pair in a single lead, would split a Cooper pair over two leads. The CAR processes will induce a current noise cross-correlation between two normal leads and predominate over the local Andreev reflection with the presence of a MBSs pair [77-79]. For short wires, the Fano factor at zero bias is close to unity for a strongly coupled MBS pair between two leads. As the wire length increases, the coupling between the MBSs at the two ends decreases, leading to the suppression of CAR process and a reduction of Fano factor.

For comparison we also choose a point C for the disordered case. The points C correspond to MBSs with a finite energy splitting in the disordered case, where V_Z at point C is equal to

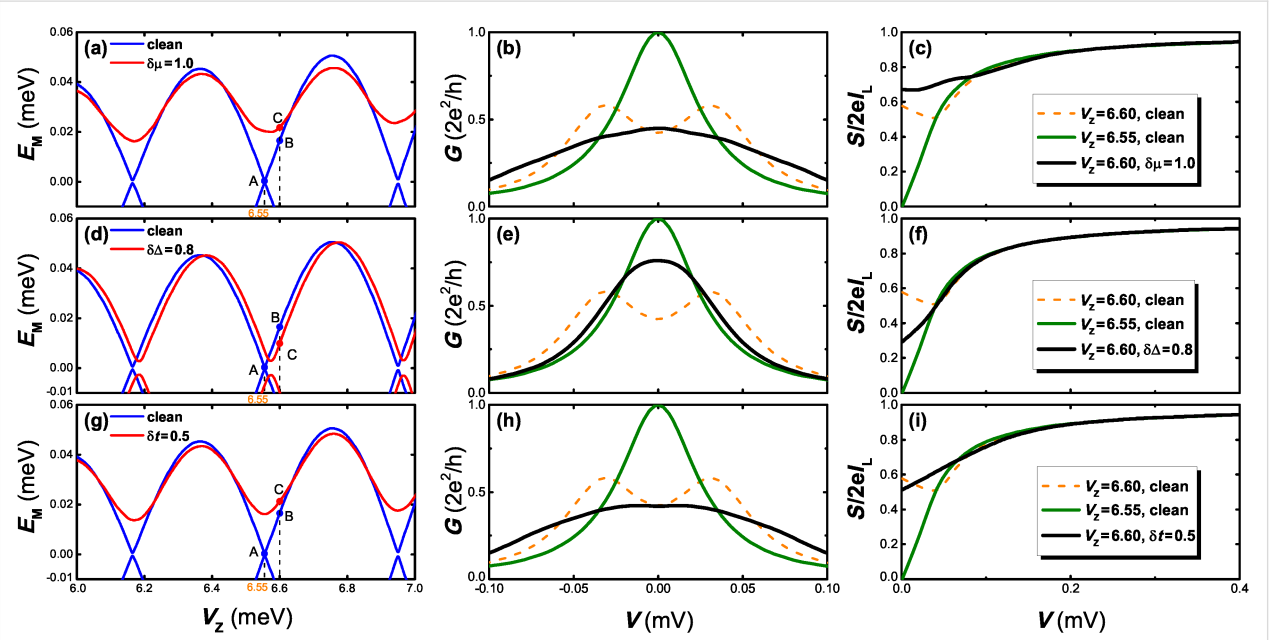

Figure 7: Comparison of the noise Fano factor F between the cases of Majorana zero mode and disorder-induced zero-bias conductance peaks. The upper, middle, and lower panels represent the effect of disorder in chemical potential δμ, superconducting pairing δΔ, and the hopping amplitude δt, respectively. (a), (d) and (g): Majorana energy E_M as a function of V_Z. The points A and B denote the MBSs with zero energy and a finite energy in the disorder-free case, respectively. The points C corresponds to the MBSs with a finite energy splitting in the disordered cases, where V_Z at point C equals to that at point B. (b), (e) and (h): The differential conductance G as a function of the bias voltage V. In the clean case, the quantized zero-bias peak is formed for Majorana zero mode (green lines). Disorder-induced zero-bias peaks (black lines) are formed from the spaced conductance peaks (orange, dotted line). (c), (f) and (i): The noise Fano factor F as a function of the bias voltage V. In the clean case, F in the low bias limit approaches zero for Majorana zero mode (green line), and F is finite for a finite energy splitting (orange, dotted line). For the disordered case, F in the low bias limit is finite (black line) although a zero-bias peak emerges in this case. The disorder strengths are δμ = 1.0 meV, δΔ = 0.8 meV, and δt = 0.5 meV. The wire length is taken as L = 0.95 μm and other parameters are taken as those in Figure 2.

the Zeeman field at point B. As shown in Figure 7 the Majorana energy splitting in point C has a non-zero value, and its value is slightly enhanced or weakened with respect to the Zeeman field strength. For the conductance, the peak splitting at point B is reformed to a single zero-bias peak induced by three types of disorder. Differently, in the low-bias voltage regime, the noise Fano factor F deviates from zero in the presence of disorder, indicating a stronger coupling between the two separated MBS. This result is a clear manifestation of the Majorana-assisted CAR process. This means that although the zero-bias conductance peak could originate from an exact zero mode or intrinsic disorder in the nanowire, one can discriminate these two different mechanisms from the shot noise properties. In a clean nanowire, the zero-bias peak is induced by the Majorana zero mode. In this case, the appearance of the zero-bias peak is always accompanied by the zero noise Fano factor, i.e., $F = 0$. However, in the disordered case, the zero-bias conductance peak could also be induced for a finite energy splitting, while the noise Fano factor F has a finite value. Thus, whether the Fano factor F at the low-bias limit equals to zero or a finite value provides a signature to distinguish the zero-bias peak induced by Majorana zero mode from that by disorder.

Conclusion

To conclude, we investigated the effect of intrinsic disorder on the transport properties of a Majorana nanowire by adopting a one-dimensional tight-binding model. We introduce three types of disorder into the system, including random fluctuations in the chemical potential, spatially changing in the superconducting pair potential, and the anisotropy of the nearest-neighbor hopping strength through lattice sites. We demonstrated that the disorder could remove the peak spacing in the differential conductance and induce a zero-bias peak for a finite Majorana energy splitting. For a shorter nanowire, the magnitude of the conductance peaks and the peak spacings are considerably suppressed as the disorder is taken into account. Such a disorder-induced suppression of conductance peaks and peak spacings provides a simple but interesting scenario to explain the absence of Majorana energy oscillation observed in previous experiments. Especially for a longer nanowire ($L \approx 1$ μm), the Majorana energy splitting is exponentially small, and the spaced conductance peaks are facilitated to form a zero-bias peak by the disorder. However, the presence of disorder does not suppress the Majorana energy splitting. On the contrary, the disorder in hopping and chemical potential destroys the localization of MBSs and thus enhance their hybridization, leading to an increase in the Majorana energy splitting. This phenomenon can be further identified with the disorder-induced increment in the localization length. The exact Majorana zero modes in the clean case gradually vanish with increasing disorder strength. As a function of Zeeman field, the quantized zero-bias conductance peaks by the exact zero mode are shown to be strongly suppressed due to the presence of disorder. In particular, for an increase in hopping disorder, the oscillation behavior in the zero-bias conductance spectra vanishes in the longer wire case.

In the presence of disorder, the Majorana energy splitting is not suppressed and zero modes are removed, while the zero-bias conductance peaks are induced for a finite energy splitting. To distinguish whether the zero-bias conductance peak is induced by a Majorana zero mode or by the disorder, we further investigate the shot noise properties of the device. For a clean nanowire, we show that the appearance of the zero-bias peak is always accompanied by a zero-noise Fano factor ($F = 0$) in the low-bias voltage limit. In contrast, the Fano factor F in the disordered case has a finite value at the low-bias limit. In this case, the finite Majorana energy splitting induces a crossed Andreev reflection and the resonant Andreev tunneling is suppressed, resulting in the deviation of the Fano factor from zero. Therefore, the shot noise provides a clear signature to discriminate between the two different mechanisms that lead to the formation of the zero-bias conductance peak.

Acknowledgements

We thank J. Liu and J. T. Song for helpful discussions. This work was supported by the Natural Science Foundation of China under Grant No. 61474018 and No. 11574173, the Fundamental Research Funds for the Central Universities (No. ZYGX2016J064) and the Open Project of State Key Laboratory of Low-Dimensional Quantum Physics (Grant No. KF201709).

References

1. Ivanov, D. A. *Phys. Rev. Lett.* **2001,** *86,* 268–271. doi:10.1103/PhysRevLett.86.268
2. Kitaev, A. Yu. *Ann. Phys.* **2003,** *303,* 2–30. doi:10.1016/S0003-4916(02)00018-0
3. Nayak, C.; Simon, S. H.; Stern, A.; Freedman, M.; Das Sarma, S. *Rev. Mod. Phys.* **2008,** *80,* 1083–1159. doi:10.1103/RevModPhys.80.1083
4. Sau, J. D.; Lutchyn, R. M.; Tewari, S.; Das Sarma, S. *Phys. Rev. Lett.* **2010,** *104,* 040502. doi:10.1103/PhysRevLett.104.040502
5. Stern, A. *Nature* **2010,** *464,* 187–193. doi:10.1038/nature08915
6. Flensberg, K. *Phys. Rev. Lett.* **2011,** *106,* 090503. doi:10.1103/PhysRevLett.106.090503
7. Alicea, J.; Oreg, Y.; Refael, G.; von Oppen, F.; Fisher, M. P. A. *Nat. Phys.* **2011,** *7,* 412–417. doi:10.1038/nphys1915
8. Leijnse, M.; Flensberg, K. *Semicond. Sci. Technol.* **2012,** *27,* 124003. doi:10.1088/0268-1242/27/12/124003
9. Sarma, S. D.; Freedman, M.; Nayak, C. *npj Quantum Inf.* **2015,** *1,* 15001. doi:10.1038/npjqi.2015.1
10. Read, N.; Green, D. *Phys. Rev. B* **2000,** *61,* 10267–10297. doi:10.1103/physrevb.61.10267
11. Kitaev, A. Yu. *Phys.-Usp.* **2001,** *44,* 131. doi:10.1070/1063-7869/44/10S/S29

12. Fu, L.; Kane, C. L. *Phys. Rev. Lett.* **2008,** *100,* 096407. doi:10.1103/PhysRevLett.100.096407
13. Fu, L.; Kane, C. L. *Phys. Rev. B* **2009,** *79,* 161408. doi:10.1103/PhysRevB.79.161408
14. Nadj-Perge, S.; Drozdov, I. K.; Bernevig, B. A.; Yazdani, A. *Phys. Rev. B* **2013,** *88,* 020407. doi:10.1103/PhysRevB.88.020407
15. Nadj-Perge, S.; Drozdov, I. K.; Li, J.; Chen, H.; Jeon, S.; Seo, J.; MacDonald, A. H.; Bernevig, B. A.; Yazdani, A. *Science* **2014,** *346,* 602–607. doi:10.1126/science.1259327
16. Oreg, Y.; Refael, G.; Von Oppen, F. *Phys. Rev. Lett.* **2010,** *105,* 177002. doi:10.1103/PhysRevLett.105.177002
17. Lutchyn, R. M.; Sau, J. D.; Das Sarma, S. *Phys. Rev. Lett.* **2010,** *105,* 077001. doi:10.1103/PhysRevLett.105.077001
18. Sau, J. D.; Tewari, S.; Lutchyn, R. M.; Stanescu, T. D.; Das Sarma, S. *Phys. Rev. B* **2010,** *82,* 214509. doi:10.1103/PhysRevB.82.214509
19. Alicea, J. *Phys. Rev. B* **2010,** *81,* 125318. doi:10.1103/PhysRevB.81.125318
20. Stanescu, T.; Lutchyn, R. M.; Sarma, S. D. *Phys. Rev. B* **2011,** *84,* 144522. doi:10.1103/PhysRevB.84.144522
21. Alicea, J. *Rep. Prog. Phys.* **2012,** *75,* 076501. doi:10.1088/0034-4885/75/7/076501
22. He, Q. L.; Pan, L.; Stern, A. L.; Burks, E. C.; Che, X.; Yin, G.; Wang, J.; Lian, B.; Zhou, Q.; Choi, E. S.; Murata, K.; Kou, X.; Chen, Z.; Nie, T.; Shao, Q.; Fan, Y.; Zhang, S.-C.; Liu, K.; Xia, J.; Wang, K. L. *Science* **2017,** *357,* 294–299. doi:10.1126/science.aag2792
23. Mourik, V.; Zuo, K.; Frolov, S. M.; Plissard, S. R.; Bakkers, E. P. A. M.; Kouwenhoven, L. P. *Science* **2012,** *336,* 1003–1007. doi:10.1126/science.1222360
24. Das, A.; Ronen, Y.; Most, Y.; Oreg, Y.; Heiblum, M.; Shtrikman, H. *Nat. Phys.* **2012,** *8,* 887–895. doi:10.1038/nphys2479
25. Rokhinson, L. P.; Liu, X.; Furdyna, J. K. *Nat. Phys.* **2012,** *8,* 795–799. doi:10.1038/nphys2429
26. Deng, M. T.; Yu, C. L.; Huang, G. Y.; Larsson, M.; Caroff, P.; Xu, H. Q. *Nano Lett.* **2012,** *12,* 6414–6419. doi:10.1021/nl303758w
27. Churchill, H. O. H.; Fatemi, V.; Grove-Rasmussen, K.; Deng, M. T.; Caroff, P.; Xu, H. Q.; Marcus, C. M. *Phys. Rev. B* **2013,** *87,* 241401. doi:10.1103/PhysRevB.87.241401
28. Finck, A. D. K.; Van Harlingen, D. J.; Mohseni, P. K.; Jung, K.; Li, X. *Phys. Rev. Lett.* **2013,** *110,* 126406. doi:10.1103/PhysRevLett.110.126406
29. Lee, E. J. H.; Jiang, X.; Houzet, M.; Aguado, R.; Lieber, C. M.; De Franceschi, S. *Nat. Nanotechnol.* **2014,** *9,* 79–84. doi:10.1038/nnano.2013.267
30. Deng, M. T.; Yu, C. L.; Huang, G. Y.; Larsson, M.; Caroff, P.; Xu, H. Q. *Sci. Rep.* **2014,** *4,* 7261. doi:10.1038/srep07261
31. Lee, E. J. H.; Jiang, X.; Aguado, R.; Katsaros, G.; Lieber, C. M.; De Franceschi, S. *Phys. Rev. Lett.* **2012,** *109,* 186802. doi:10.1103/PhysRevLett.109.186802
32. Kells, G.; Meidan, D.; Brouwer, P. W. *Phys. Rev. B* **2012,** *86,* 100503. doi:10.1103/PhysRevB.86.100503
33. Pikulin, D. I.; Dahlhaus, J. P.; Wimmer, M.; Schomerus, H.; Beenakker, C. W. J. *New J. Phys.* **2012,** *14,* 125011. doi:10.1088/1367-2630/14/12/125011
34. Bagrets, D.; Altland, A. *Phys. Rev. Lett.* **2012,** *109,* 227005. doi:10.1103/PhysRevLett.109.227005
35. Liu, J.; Potter, A. C.; Law, K. T.; Lee, P. A. *Phys. Rev. Lett.* **2012,** *109,* 267002. doi:10.1103/PhysRevLett.109.267002
36. Das Sarma, S.; Sau, J. D.; Stanescu, T. D. *Phys. Rev. B* **2012,** *86,* 220506. doi:10.1103/PhysRevB.86.220506
37. Stanescu, T. D.; Lutchyn, R. M.; Das Sarma, S. *Phys. Rev. B* **2013,** *87,* 094518. doi:10.1103/PhysRevB.87.094518
38. Rainis, D.; Trifunovic, L.; Klinovaja, J.; Loss, D. *Phys. Rev. B* **2013,** *87,* 024515. doi:10.1103/PhysRevB.87.024515
39. Albrecht, S. M.; Higginbotham, A. P.; Madsen, M.; Kuemmeth, F.; Jespersen, T. S.; Nygård, J.; Krogstrup, P.; Marcus, C. M. *Nature* **2016,** *531,* 206–209. doi:10.1038/nature17162
40. Sengupta, K.; Žutić, I.; Kwon, H.-J.; Yakovenko, V. M.; Das Sarma, S. *Phys. Rev. B* **2001,** *63,* 144531. doi:10.1103/PhysRevB.63.144531
41. Law, K. T.; Lee, P. A.; Ng, T. K. *Phys. Rev. Lett.* **2009,** *103,* 237001. doi:10.1103/PhysRevLett.103.237001
42. Flensberg, K. *Phys. Rev. B* **2010,** *82,* 180516. doi:10.1103/PhysRevB.82.180516
43. Akhmerov, A. R.; Dahlhaus, J. P.; Hassler, F.; Wimmer, M.; Beenakker, C. W. J. *Phys. Rev. Lett.* **2011,** *106,* 057001. doi:10.1103/PhysRevLett.106.057001
44. Lin, C.-H.; Sau, J. D.; Das Sarma, S. *Phys. Rev. B* **2012,** *86,* 224511. doi:10.1103/PhysRevB.86.224511
45. Sherman, D.; Yodh, J. S.; Albrecht, S. M.; Nygård, J.; Krogstrup, P.; Marcus, C. M. *Nat. Nanotechnol.* **2017,** *12,* 212–217. doi:10.1038/nnano.2016.227
46. Deng, M. T.; Vaitiekenas, S.; Hansen, E. B.; Danon, J.; Leijnse, M.; Flensberg, K.; Nygård, J.; Krogstrup, P.; Marcus, C. M. *Science* **2016,** *354,* 1557. doi:10.1126/science.aaf3961
47. Albrecht, S. M.; Hansen, E. B.; Higginbotham, A. P.; Kuemmeth, F.; Jespersen, T. S.; Nygård, J.; Krogstrup, P.; Danon, J.; Flensberg, K.; Marcus, C. M. *Phys. Rev. Lett.* **2017,** *118,* 137701. doi:10.1103/PhysRevLett.118.137701
48. Van Heck, B.; Lutchyn, R. M.; Glazman, L. I. *Phys. Rev. B* **2016,** *93,* 235431. doi:10.1103/PhysRevB.93.235431
49. Zazunov, A.; Egger, R.; Levy Yeyati, A. *Phys. Rev. B* **2016,** *94,* 014502. doi:10.1103/PhysRevB.94.014502
50. Chiu, C.-K.; Cole, W. S.; Das Sarma, S. *Phys. Rev. B* **2016,** *94,* 125304. doi:10.1103/PhysRevB.94.125304
51. Sticlet, D.; Nijholt, B.; Akhmerov, A. *Phys. Rev. B* **2017,** *95,* 115421. doi:10.1103/PhysRevB.95.115421
52. Reeg, C.; Maslov, D. L. *Phys. Rev. B* **2017,** *95,* 205439. doi:10.1103/PhysRevB.95.205439
53. Chiu, C.-K.; Sau, J. D.; Das Sarma, S. *Phys. Rev. B* **2017,** *96,* 054504. doi:10.1103/PhysRevB.96.054504
54. Liu, C.-X.; Sau, J. D.; Stanescu, T. D.; Sarma, S. D. *Phys. Rev. B* **2017,** *96,* 075161. doi:10.1103/PhysRevB.96.075161
55. Domínguez, F.; Cayao, J.; San-Jose, P.; Aguado, R.; Yeyati, A. L.; Prada, E. *npj Quantum Mater.* **2017,** *2,* 13. doi:10.1038/s41535-017-0012-0
56. Stenger, J.; Stanescu, T. D. *arXiv* **2017,** 1703.02543.
57. Liu, C.-X.; Sau, J. D.; Das Sarma, S. *Phys. Rev. B* **2017,** *95,* 054502. doi:10.1103/PhysRevB.95.054502
58. Liu, C.-X.; Setiawan, F.; Sau, J. D.; Sarma, S. D. *Phys. Rev. B* **2017,** *96,* 054520. doi:10.1103/PhysRevB.96.054520
59. Danon, J.; Hansen, E. B.; Flensberg, K. *Phys. Rev. B* **2017,** *96,* 125420. doi:10.1103/PhysRevB.96.125420
60. Fleckenstein, C.; Domínguez, F.; Ziani, N. T.; Trauzettel, B. *arXiv* **2017,** No. 1710.08866.
61. Dmytruk, O.; Klinovaja, J. *arXiv* **2017,** No. 1710.01671.
62. Brouwer, P. W.; Duckheim, M.; Romito, A.; von Oppen, F. *Phys. Rev. B* **2011,** *84,* 144526. doi:10.1103/PhysRevB.84.144526
63. Brouwer, P. W.; Duckheim, M.; Romito, A.; Von Oppen, F. *Phys. Rev. Lett.* **2011,** *107,* 196804. doi:10.1103/PhysRevLett.107.196804

64. Lobos, A. M.; Lutchyn, R. M.; Das Sarma, S. *Phys. Rev. Lett.* **2012,** *109,* 146403. doi:10.1103/PhysRevLett.109.146403
65. Sau, J. D.; Tewari, S.; Das Sarma, S. *Phys. Rev. B* **2012,** *85,* 064512. doi:10.1103/PhysRevB.85.064512
66. Lutchyn, R. M.; Stanescu, T. D.; Das Sarma, S. *Phys. Rev. B* **2012,** *85,* 140513. doi:10.1103/PhysRevB.85.140513
67. Pientka, F.; Kells, G.; Romito, A.; Brouwer, P. W.; Von Oppen, F. *Phys. Rev. Lett.* **2012,** *109,* 227006. doi:10.1103/PhysRevLett.109.227006
68. Sau, J. D.; Das Sarma, S. *Phys. Rev. B* **2013,** *88,* 064506. doi:10.1103/PhysRevB.88.064506
69. Takei, S.; Fregoso, B. M.; Hui, H.-Y.; Lobos, A. M.; Das Sarma, S. *Phys. Rev. Lett.* **2013,** *110,* 186803. doi:10.1103/PhysRevLett.110.186803
70. Adagideli, I.; Wimmer, M.; Teker, A. *Phys. Rev. B* **2014,** *89,* 144506. doi:10.1103/PhysRevB.89.144506
71. Hui, H. Y.; Sau, J. D.; Das Sarma, S. *Phys. Rev. B* **2015,** *92,* 174512. doi:10.1103/PhysRevB.92.174512
72. Cole, W. S.; Sau, J. D.; Das Sarma, S. *Phys. Rev. B* **2016,** *94,* 140505. doi:10.1103/PhysRevB.94.140505
73. Maśka, M. M.; Gorczyca-Goraj, A.; Tworzydło, J.; Domański, T. *Phys. Rev. B* **2017,** *95,* 045429. doi:10.1103/PhysRevB.95.045429
74. Awoga, O. A.; Björnson, K.; Black-Schaffer, A. M. *Phys. Rev. B* **2017,** *95,* 184511. doi:10.1103/PhysRevB.95.184511
75. Hützen, R.; Zazunov, A.; Braunecker, B.; Yeyati, A. L.; Egger, R. *Phys. Rev. Lett.* **2012,** *109,* 166403. doi:10.1103/PhysRevLett.109.166403
76. Sun, Q.-f.; Wang, J.; Guo, H. *Phys. Rev. B* **2005,** *71,* 165310. doi:10.1103/PhysRevB.71.165310
77. Wu, B. H.; Cao, J. C. *Phys. Rev. B* **2012,** *85,* 085415. doi:10.1103/PhysRevB.85.085415
78. Lü, H.-F.; Lu, H.-Z.; Shen, S.-Q. *Phys. Rev. B* **2014,** *90,* 195404. doi:10.1103/PhysRevB.90.195404
79. Lü, H.-F.; Lu, H.-Z.; Shen, S.-Q. *Phys. Rev. B* **2016,** *93,* 245418. doi:10.1103/PhysRevB.93.245418
80. Lee, P. A.; Stone, A. D. *Phys. Rev. Lett.* **1985,** *55,* 1622–1625. doi:10.1103/PhysRevLett.55.1622
81. Klinovaja, J.; Loss, D. *Phys. Rev. B* **2012,** *86,* 085408. doi:10.1103/PhysRevB.86.085408

License and Terms

BEILSTEIN JOURNAL OF NANOTECHNOLOGY

Interplay between pairing and correlations in spin-polarized bound states

Szczepan Głodzik[1], Aksel Kobiałka[1], Anna Gorczyca-Goraj[2], Andrzej Ptok[3], Grzegorz Górski[4], Maciej M. Maśka[2] and Tadeusz Domański[*1]

Full Research Paper

Open Access

Address:
[1]Institute of Physics, M. Curie-Skłodowska University, 20-031 Lublin, Poland, [2]Institute of Physics, University of Silesia, 41-500 Chorzów, Poland, [3]Institute of Nuclear Physics, Polish Academy of Sciences, 31-342 Kraków, Poland and [4]Faculty of Mathematics and Natural Sciences, University of Rzeszów, 35-310 Rzeszów, Poland

Email:
Tadeusz Domański[*] - doman@kft.umcs.lublin.pl

* Corresponding author

Keywords:
bound states in superconductors; Majorana quasiparticles; subgap Kondo effect

Beilstein J. Nanotechnol. **2018,** *9,* 1370–1380.
doi:10.3762/bjnano.9.129

Received: 15 December 2017
Accepted: 09 April 2018
Published: 07 May 2018

This article is part of the Thematic Series "Topological materials".

Guest Editor: J. J. Palacios

Abstract

We investigate single and multiple defects embedded in a superconducting host, studying the interplay between the proximity-induced pairing and interactions. We explore the influence of the spin–orbit coupling on energies, polarization and spatial patterns of the bound (Yu–Shiba–Rusinov) states of magnetic impurities in a two-dimensional square lattice. We also address the peculiar bound states in the proximitized Rashba chain, resembling the Majorana quasiparticles, focusing on their magnetic polarization that has been recently reported by S. Jeon et al. (*Science* **2017,** *358,* 772). Finally, we study leakage of these polarized Majorana quasiparticles into side-attached nanoscopic regions and confront them with the subgap Kondo effect near to the singlet–doublet phase transition.

Introduction

Magnetism is usually detrimental to superconductivity because it breaks the Cooper pairs (at the critical field strength H_{c2}). There are, however, a few exceptions in which these phenomena coexist, e.g., in iron pnictides [1], $CeCoIn_5$ [2]. Also, sometimes magnetic fields induce superconductivity [3]. Plenty of other interesting examples can be found in nanoscopic systems, where magnetic impurities (dots) exhibit a more subtle relationship with the electron pairing driven by the proximity effect [4,5]. Cooper pairs easily penetrate the nanoscopic impurities, inducing the bound (Yu–Shiba–Rusinov) states that manifest the local pairing in coexistence with magnetic polarization. Such bound states have been observed in various systems [6-14]. In-gap states (appearing in pairs symmetrically around the Fermi level) can be nowadays controlled electrostatically or magnetically [12] whereas their topography, spatial extent and polarization can be precisely inspected by the state-of-art tunneling measurements [15,16].

It has been reported that adatoms deposited on a two-dimensional (2D) superconducting surface develop

Yu–Shiba–Rusinov (YSR) states, extending to a dozen of intersite distances and they reveal particle–hole oscillations [11]. Bound states of these magnetic impurities in superconducting $NbSe_2$ are characterized by the star shape [17] typical for the rotational symmetry of its triangular lattice. More complex objects, such as dimers, reveal other spatial features, showing the bonding and antibonding states [18]. In a somewhat different context it has been pointed out [19] that exchange coupling between numerous quantum defects involving their intrinsic spins can couple them ferromagnetically. This can be used (e.g., in metallic carbon nanotubes) for a robust transmission of magnetic information over large distances.

In all cases the bound YSR states are also sensitive to interactions. One of them is the spin–orbit coupling (usually meaningful at boundaries, e.g., surfaces) [20-22]. Such interaction in one-dimensional magnetic nanowires can induce the topologically nontrivial superconducting phase, in which the YSR states undergo mutation to Majorana (zero-energy) quasiparticles. Coulomb repulsion between the opposite spin electrons can bring additional important effects. In the proximitized quantum dots it can lead to a parity change (quantum phase transition) with further influence on the subgap Kondo effect (driven by effective spin-exchange coupling with mobile electrons). Furthermore, such spin exchange can be amplified by the induced electron pairing, and can have constructive influence on the Kondo effect [23,24].

We study here the polarized bound states, taking into account the spin–orbit and/or Coulomb interactions. In particular, we consider: (i) a single magnetic impurity in a 2D square lattice of a superconducting host, (ii) a nanoscopic chain of magnetic impurities on the classical superconductor (i.e., proximitized Rashba nanowire) in its topologically trivial/nontrivial superconducting phase, and (iii) a strongly correlated quantum dot side-attached to the Rashba chain, where the Kondo and the leaking Majorana quasiparticle can be confronted with each other. These magnetically polarized YSR and Majorana quasiparticles as well as the subgap Kondo effect can be experimentally verified using tunneling heterostructures with ferromagnetic lead (STM tip).

Results and Discussion

Single magnetic impurity

Let us start by considering a single magnetic impurity on the surface of an *s*-wave superconductor in presence of spin–orbit interactions. This situation can be modeled by the Anderson-type Hamiltonian

$$\widehat{\mathcal{H}} = \widehat{\mathcal{H}}_{\rm sc} + \widehat{\mathcal{H}}_{\rm imp} + \widehat{\mathcal{H}}_{\rm SOC}. \qquad (1)$$

We describe the superconducting substrate by

$$\widehat{\mathcal{H}}_{\rm sc} = -t\sum_{\langle i,j\rangle\sigma}\hat{c}^{\dagger}_{i\sigma}\hat{c}_{j\sigma} + U\sum_{i}\hat{n}_{i\uparrow}\hat{n}_{i\downarrow} - \mu\sum_{i\sigma}\hat{n}_{i\sigma}, \qquad (2)$$

where $\hat{c}^{\dagger}_{i\sigma}$ ($\hat{c}_{i\sigma}$) denotes creation (annihilation) of an electron with spin σ at the *i*-th site, *t* is a hopping integral between the nearest neighbors, μ is the chemical potential, and $\hat{n}_{i\sigma} = \hat{c}^{\dagger}_{i\sigma}\hat{c}_{i\sigma}$ is the number operator. For simplicity, we assume a weak attractive potential $U < 0$ between itinerant electrons and treat it within the mean-field decoupling

$$\hat{c}^{\dagger}_{i\uparrow}\hat{c}_{i\uparrow}\hat{c}^{\dagger}_{i\downarrow}\hat{c}_{i\downarrow} \approx \chi_i\hat{c}^{\dagger}_{i\uparrow}\hat{c}^{\dagger}_{i\downarrow} + \chi^{*}_i\hat{c}_{i\downarrow}\hat{c}_{i\uparrow} - |\chi_i|^2 + n_{i\uparrow}\hat{c}^{\dagger}_{i\downarrow}\hat{c}_{i\downarrow} + n_{i\downarrow}\hat{c}^{\dagger}_{i\uparrow}\hat{c}_{i\uparrow} - n_{i\uparrow}n_{i\downarrow},$$

where $\chi_i = \langle\hat{c}_{i\downarrow}\hat{c}_{i\uparrow}\rangle$ is the local superconducting order parameter and $n_{i\sigma} = \langle\hat{n}_{i\sigma}\rangle$. The Hartree term can be incorporated into the local (spin-dependent) chemical potential $\mu \to \tilde{\mu}_{i\sigma} \equiv \mu - Un_{i\bar{\sigma}}$. The second term in Equation 1 refers to the local impurity

$$\widehat{\mathcal{H}}_{\rm imp} = -J\left(\hat{c}^{\dagger}_{0\uparrow}\hat{c}_{0\uparrow} - \hat{c}^{\dagger}_{0\downarrow}\hat{c}_{0\downarrow}\right) + K\left(\hat{c}^{\dagger}_{0\uparrow}\hat{c}_{0\uparrow} + \hat{c}^{\dagger}_{0\downarrow}\hat{c}_{0\downarrow}\right), \qquad (3)$$

which affects the order parameter χ_i near the impurity site $i = 0$, inducing the YSR states [25,26]. In this work we focus on the magnetic term *J* [4,27], disregarding the potential scattering *K*.

The spin–orbit coupling (SOC) can be expressed by

$$\widehat{\mathcal{H}}_{\rm SOC} = -{\rm i}\lambda\sum_{ij\sigma\sigma'}\hat{c}^{\dagger}_{i+\mathbf{d}_j\sigma}\left(\mathbf{d}_j\times\hat{\boldsymbol{\sigma}}^{\sigma\sigma'}\right)\cdot\widehat{\mathbf{w}}\,\hat{c}_{i\sigma'}, \qquad (4)$$

where the vector $\mathbf{d}_j = (d^x_j, d^y_j, 0)$ refers to positions of the nearest neighbors of the *i*-th site, and $\hat{\boldsymbol{\sigma}} = (\sigma_x, \sigma_y, \sigma_z)$ stands for the Pauli matrices. The unit vector $\widehat{\mathbf{w}}$ shows the direction of the spin–orbit field, which can be arbitrary. Here we restrict our considerations to the in-plane $\widehat{\mathbf{w}} \equiv \hat{x} = (1, 0, 0)$ polarization, which will be important for nontrivial superconductivity in nanowires discussed in the subsection 'Magnetically polarized Majorana quasiparticles'. The other (out-of-plane) component could eventually mix ↑ and ↓ spins [22].

Impurities break the translational invariance, therefore the pairing amplitude χ_i and occupancy $n_{i\sigma}$ have to be determined for each lattice site individually. We can diagonalize the Hamiltonian (Equation 1) by the unitary transformation

$$\hat{c}_{i\sigma} = \sum_n \left(u_{in\sigma}\hat{\gamma}_n - \sigma v^*_{in\sigma}\hat{\gamma}^\dagger_n \right), \tag{5}$$

where $\hat{\gamma}^{(\dagger)}_n$ are quasiparticle fermionic operators with eigenvectors $u_{in\sigma}$ and $v_{in\sigma}$. This leads to the Bogoliubov–de Gennes (BdG) equations

$$\mathcal{E}_n \begin{pmatrix} u_{in\uparrow} \\ v_{in\downarrow} \\ u_{in\downarrow} \\ v_{in\uparrow} \end{pmatrix} = \sum_j \begin{pmatrix} H_{ij\uparrow} & D_{ij} & S^{\uparrow\downarrow}_{ij} & 0 \\ D^*_{ij} & -H^*_{ij\downarrow} & 0 & S^{\downarrow\uparrow}_{ij} \\ S^{\downarrow\uparrow}_{ij} & 0 & H_{ij\downarrow} & D_{ij} \\ 0 & S^{\uparrow\downarrow}_{ij} & D^*_{ij} & -H^*_{ij\uparrow} \end{pmatrix} \begin{pmatrix} u_{jn\uparrow} \\ v_{jn\downarrow} \\ u_{jn\downarrow} \\ v_{jn\uparrow} \end{pmatrix}, \tag{6}$$

where $D_{ij} = \delta_{ij} U \chi_i$, and the single-particle term is given by

$$H_{ij\sigma} = -t\delta_{\langle i,j\rangle} - \left(\tilde{\mu}_{i\sigma} - \sigma J \delta_{i0}\right)\delta_{ij} + S^{\sigma\sigma}_{ij}$$

with the spin–orbit coupling term

$$S^{\sigma\sigma'}_{ij} = -\mathrm{i}\lambda \sum_l \left(\mathbf{d}_l \times \hat{\boldsymbol{\sigma}}^{\sigma\sigma'} \right) \cdot \hat{\mathbf{w}}\, \delta_{j,i+\mathbf{d}_l}.$$

Here, $S^{\sigma\sigma}_{ij}$ and $S^{\sigma\bar{\sigma}}_{ij}$ (where $\bar{\sigma}$ is opposite to σ) correspond to in-plane and out-of-plane spin–orbit field, respectively, and satisfy $S^{\sigma\sigma'}_{ij} = (S^{\sigma'\sigma}_{ji})*$.

Solving numerically the BdG equations (Equation 6) we can determine the local order parameter χ_i and occupancy $n_{i\sigma}$

$$\chi_i = \sum_n \left[u_{in\downarrow} v^*_{in\uparrow} f\left(\mathcal{E}_n\right) - u_{in\uparrow} v^*_{in\downarrow} f\left(-\mathcal{E}_n\right) \right], \tag{7}$$

$$n_{i\sigma} = \sum_n \left[\left|u_{in\sigma}\right|^2 f\left(\mathcal{E}_n\right) + \left|v_{in\bar{\sigma}}\right|^2 f\left(-\mathcal{E}_n\right) \right], \tag{8}$$

where $f(\omega) = [1 + \exp(\omega/k_B T)]^{-1}$. In what follows, we shall inspect the spin-resolved local density of states

$$\rho_{i\sigma}(\omega) = \sum_n \left[\left|u_{in\sigma}\right|^2 \delta\left(\omega - \mathcal{E}_n\right) + \left|v_{in\sigma}\right|^2 \delta\left(\omega + \mathcal{E}_n\right) \right].$$

For its numerical computation we replace the Dirac delta function with the Lorentzian function $\delta(\omega) = \zeta/[\pi(\omega^2 + \zeta^2)]$ with a small broadening $\zeta = 0.01$ t. We have solved the BdG equations, considering a single magnetic impurity in a square lattice, comprising $N_a \times N_b = 41 \times 41$ sites. We assumed $U/t = -3$, $\mu/t = 0$, and determined the bound states for two representative values of the spin–orbit coupling λ upon varying J.

The magnetic potential has substantial influence on the local order parameter χ_0. In particular, at some critical value J_c this quantity discontinuously changes its magnitude and sign (see the upper panel in Figure 1), signaling a first-order phase transition [28-30]. This quantum phase transition at J_c is an artifact of the classical spin approximation. When spin fluctuations are allowed, a Kondo-like crossover is obtained instead of a first-order phase transition [31,32]. In general, the quasiparticle spectrum at the impurity site is characterized by two bound states $\pm E_{YSR}$ inside the gap Δ of the superconducting host (displayed in the bottom panel of Figure 1). These energies $\pm E_{YSR}$ and the related spectral weights depend on J. At $J = J_c$ the YSR bound states cross each other $E_{YSR}(J_c) = 0$ and their crossing signifies the ground-state parity change [33] from BCS-type (spinless) to the singly occupied (spinful) configurations [8,15,21,34]. Let us remark that this quantum phase transition is also accompanied with a reversal of the YSR polarization (see bottom panel in Figure 1). A similar behavior can be observed also for multiple impurities, at several critical values of J [35].

Within the BdG approach we can inspect spatial profiles of the YSR states by integrating the spectral weights

$$\rho^{\pm}_{i\sigma} = \int_{\omega_1}^{\omega_2} \rho_{i\sigma}(\omega)\mathrm{d}\omega$$

in the interval $\omega \in (\omega_1, \omega_2)$ capturing the quasiparticles at negative/positive energies $\pm E_{YSR}$ [36]. Figure 2 illustrates the results obtained for $\lambda = 0$ (left panel) and $\lambda = t$ (right panel). We clearly notice a fourfold rotational symmetry (typical for the square lattice) and the spatial extent of YSR states reaching several sites away from the magnetic impurity. The non-vanishing difference of the spectral weight $|u_{in\uparrow}|^2 - |u_{in\downarrow}|^2$ at the positive energy $\omega = +E_{YSR}$ and of $|v_{in\uparrow}|^2 - |v_{in\downarrow}|^2$ at the negative energy $\omega = -E_{YSR}$ implies the effective spin-polarization of the bound states (their polarization is illustrated in the bottom panel of Figure 1).

For a quantitative estimation of the spatially varying magnetization (driven by the particle–hole asymmetry) we have computed the displaced moving average $\bar{\rho}^{\pm}(r)$, which corresponds to an averaged spectral weight contained in a ring of the radius r and a small half-width δr. This quantity is sensitive only to the radial distance r from the magnetic impurity, averaging the angular anisotropy. Our results, presented in Figure 3, clearly indicate the spatial particle–hole oscillations $\bar{\rho}^{\pm}(r)$ of the YSR states (compare the blue and red lines). Such particle–hole oscillations decay exponentially with r in agreement with previous studies [11,37,38]. The dominant (particle or hole) contributions to the YSR bound states are displayed by the

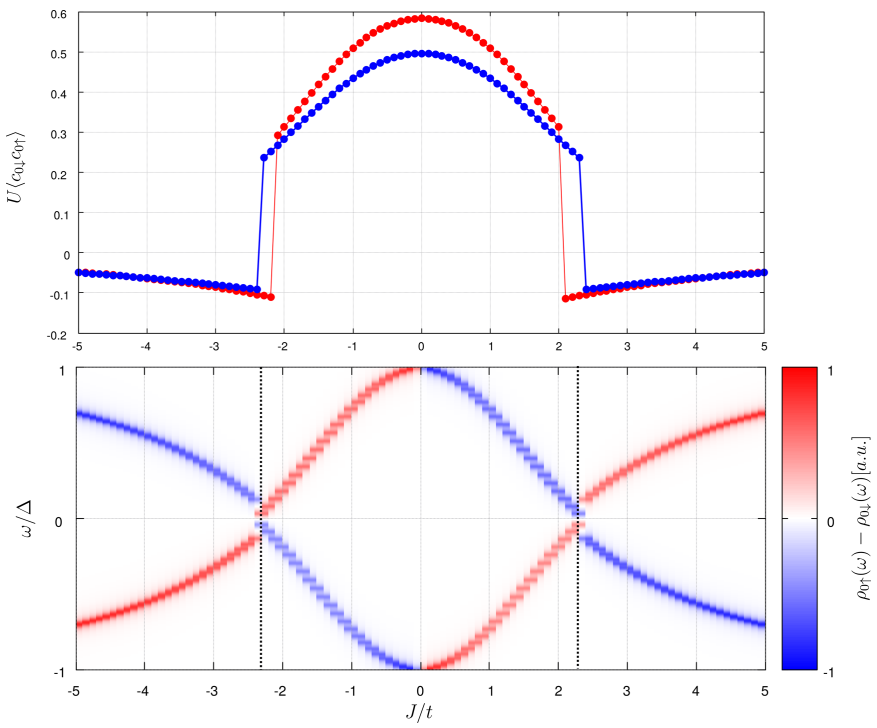

Figure 1: The local order parameter obtained at zero temperature for weak $\lambda/t = 0.1$ (red line) and strong spin–orbit coupling $\lambda/t = 1$ (blue line). The bottom panel shows the energies and magnetic polarization $\rho_{0\uparrow}(\omega) - \rho_{0\downarrow}(\omega)$ of YSR states obtained in the weak-coupling limit $\lambda/t = 0.1$.

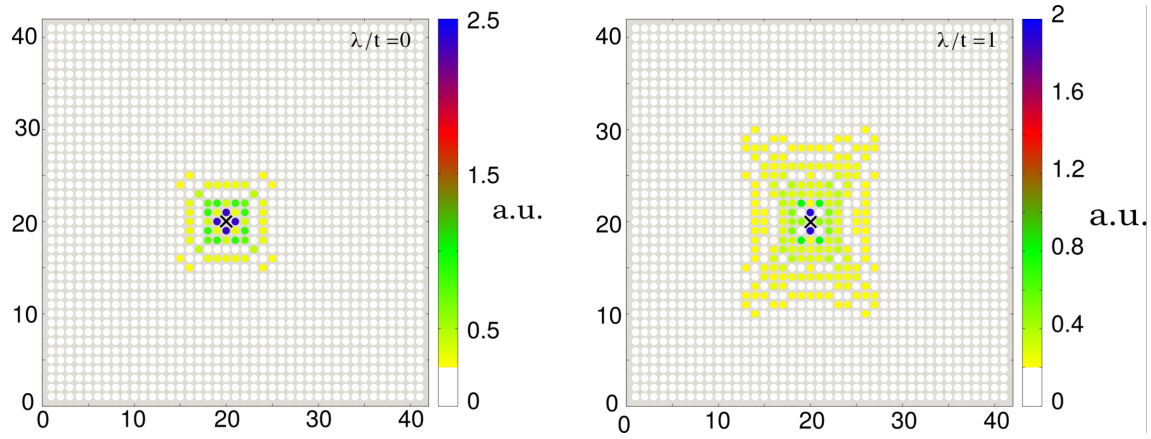

Figure 2: Spatial profiles of the YSR states $\sum_\sigma \rho^+_{i\sigma}$ obtained for $|J| < J_c$ in the absence of spin–orbit coupling (left panel) and for strong in-plane coupling $\lambda = t$ (right panel). The spin–orbit field is chosen along the *x*-axis and leads to an additional imaginary hopping term along the *y*-axis, which elongates the YSR states in the *y*-direction. The impurity spin is oriented along the (0, 0, 1) direction.

alternating color of the background in Figure 3. We notice that the spin–orbit coupling seems to suppress these particle–hole oscillations.

Summarizing this section, we point out that the quantum phase transition at J_c depends on the spin–orbit coupling λ and it has experimentally observable consequences in the magnetization induced near the impurity site. For weak magnetic scattering $|J| < J_c$ the impurity is partly screened, whereas for stronger couplings $|J| > J_c$ the impurity polarizes its neighborhood in the direction of its own magnetic moment. Similar effects have been previously discussed in [21], but here we additionally consider the role of spin–orbit coupling. First of all, such interaction shifts the quantum phase transition (to larger values of *J*) and secondly it enhances the spatial extent of YSR states and gradually smoothes the particle–hole oscillations.

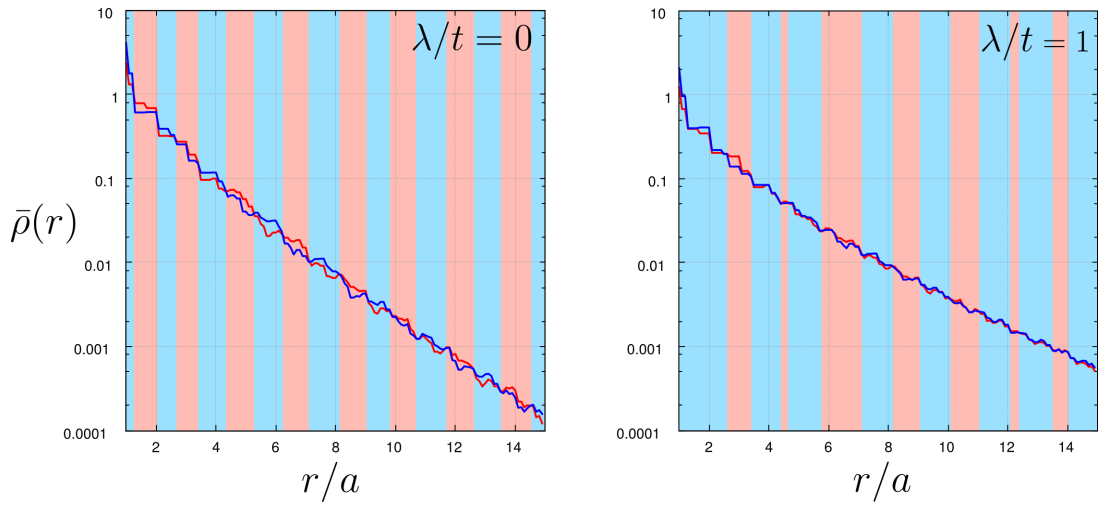

Figure 3: Hole-like (blue line) and electron-like (red line) displaced moving average $\bar{\rho}^{\pm}(r)$ as a function of the radial distance r from the impurity site obtained for $|J| < J_c$ using $\delta r = 0.5a$. The blue and red background color indicates the dominant type (hole or particle) of the YSR states at a given distance r. The left and right panels correspond to $\lambda = 0$ and $\lambda = t$, respectively.

Magnetically polarized Majorana quasiparticles

In this section we increase the number of impurities. Let us now imagine a nanoscopic chain of magnetic impurities (for instance Fe atoms) deposited on the surface of a conventional *s*-wave superconductor. We study the magnetically polarized bound states, focusing on the proximity-induced nontrivial superconducting phase. In practice, the quasiparticle spectrum can be probed within STM-type setups, by attaching a conducting [39,40], superconducting [41], or a magnetically polarized tip [42]. We assume the spin–orbit interaction aligned perpendicularly to the wire and the magnetic field parallel to it, leading to the effective intersite pairing of identical spins and (under specific conditions) inducing zero-energy end modes resembling Majorana quasiparticles. This issue has been recently studied very intensively but here we simply focus on the spin-polarized aspects of this problem.

Due to the spin–orbit interaction, momentum and spin are no longer "good" quantum numbers. By solving the problem numerically, however, we can estimate the percentage with which the true quasiparticles are represented by the initial spin. We have recently emphasized [43], that the amplitude of intersite pairing (between identical spin electrons) differs several times for ↑ and ↓ sectors. This leads to an obvious polarization of the YSR and Majorana quasiparticles (the latter appearing near the nanochain edges).

Let us consider the STM-type geometry relevant to the recent experimental situation addressed by A. Yazdani and co-workers [42], which can be described by the following Hamiltonian

$$\widehat{\mathcal{H}} = \widehat{\mathcal{H}}_{\text{tip}} + \widehat{\mathcal{H}}^{\text{prox}}_{\text{chain}} + \widehat{\mathcal{H}}_{\text{tip-chain}}. \tag{9}$$

We assume here that the STM tip describes a polarized fermion gas

$$\widehat{\mathcal{H}}_{\text{N}} = \sum_{\mathbf{k},\sigma} \xi^{\sigma}_{\mathbf{k}\text{N}} \hat{c}^{\dagger}_{\mathbf{k}\sigma\text{N}} \hat{c}_{\mathbf{k}\sigma\text{N}}$$

where the energy $\xi^{\sigma}_{\mathbf{k}\text{N}} = \varepsilon_{\mathbf{k}} - \mu_{\text{N}\sigma}$ can be controlled by some finite detuning of the chemical potentials $\mu_{\text{N}\uparrow} - \mu_{\text{N}\downarrow}$. Individual atoms of the nanochain are coupled with such STM tip through

$$\widehat{\mathcal{H}}_{\text{tip-chain}} = \sum_{\mathbf{k},\sigma} \left(V_{i,\mathbf{k}\text{N}}\, \hat{d}^{\dagger}_{i,\sigma} \hat{c}_{\mathbf{k}\sigma\text{N}} + V^{*}_{i,\mathbf{k}\beta} \hat{c}^{\dagger}_{\mathbf{k}\sigma\text{N}} \hat{d}_{i,\sigma} \right).$$

For simplicity, we assume constant couplings

$$\Gamma_{\beta} = 2\pi \sum_{\mathbf{k}} \left| V_{i,\mathbf{k}\beta} \right|^2 \delta\left(\omega - \xi_{\mathbf{k}\beta}\right).$$

The low-energy physics of such proximitized Rashba nanowire can be described by [44]

$$\widehat{\mathcal{H}}^{\text{prox}}_{\text{chain}} = \sum_{i,j,\sigma} \left(t_{ij} - \delta_{ij}\mu \right) \hat{d}^{\dagger}_{i,\sigma} \hat{d}_{j,\sigma} + \widehat{\mathcal{H}}_{\text{Rashba}} + \widehat{\mathcal{H}}_{\text{Zeeman}} + \widehat{\mathcal{H}}_{\text{prox}}, \tag{10}$$

where $\hat{d}^{(\dagger)}_{i,\sigma}$ annihilates (creates) an electron of spin σ at site i with energy ε_i, and t_{ij} is the hopping integral. The effective intersite (*p*-wave) pairing is induced through a combined effect of the Rashba and the Zeeman terms

$$\widehat{\mathcal{H}}_{\text{Rashba}} = -\alpha \sum_{i,\sigma,\sigma'} \left[\hat{d}^{\dagger}_{i+1,\sigma} \left(i\sigma^{y} \right)_{\sigma\sigma'} \hat{d}_{i,\sigma'} + \text{H.c.} \right], \quad (11)$$

$$\widehat{\mathcal{H}}_{\text{Zeeman}} = \frac{g\mu_{\text{B}}B}{2} \sum_{i,\sigma,\sigma'} \hat{d}^{\dagger}_{i,\sigma} \left(\sigma^{z} \right)_{\sigma\sigma'} \hat{d}_{i,\sigma'}. \quad (12)$$

The proximity effect, which induces the on-site (trivial) pairing, can be modelled as [45]

$$\widehat{\mathcal{H}}_{\text{prox}} = \Delta_i \left(\hat{d}^{\dagger}_{i,\uparrow} \hat{d}^{\dagger}_{i,\downarrow} + \hat{d}_{i,\downarrow} \hat{d}_{i,\uparrow} \right) \quad (13)$$

with the local pairing potential $\Delta_i = \Gamma_S/2$.

Figure 4 shows evolution of the spin-dependent spectrum $\rho_{i\sigma}(\omega)$ as a function of a varying magnetic field. At a critical value ($B \approx 0.2$) we observe the emergence of zero-energy quasiparticles, whose spectral weights strongly depend on the spin σ.

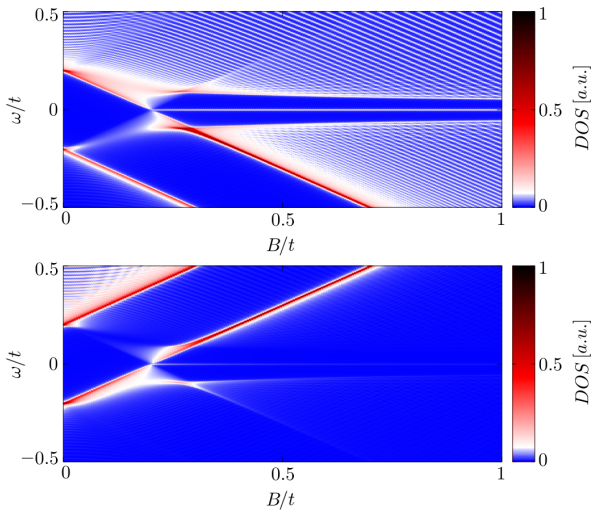

Figure 4: The effective quasiparticle spectrum $\rho_{i\sigma}(\omega)$ as a function of a magnetic field B aligned along the nanochain obtained for σ = ↑ (upper panel) and σ = ↓ (bottom panel). The magnetic field B is expressed in units of $t/(g\mu_B/2)$.

For a better understanding of the polarized zero-energy quasiparticles, we present in Figure 5 the spatial profiles of the zero-energy (Majorana) quasiparticles. As usually such quasiparticles emerge near the edges of a nanoscopic chain, practically over 10 to 15 sites (see inset). Note the substantial quantitative difference between these zero-energy quasiparticles appearing in ↑ and ↓ spin sectors. This "intrinsic polarization" of the Majorana modes has been previously suggested in [46], and recently we have proposed [47] their empirical detection by means of selective equal-spin Andreev reflection (SESAR) spectroscopy.

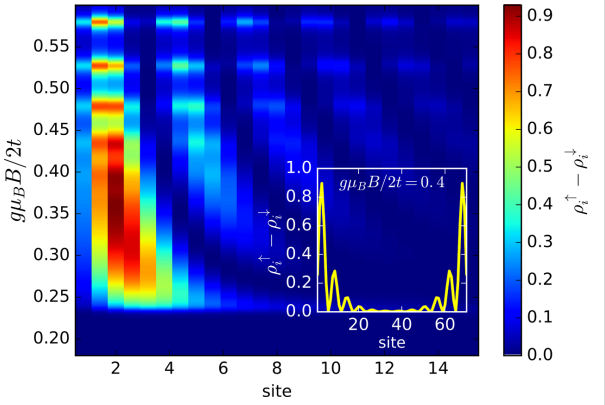

Figure 5: Magnetically polarized spectrum $\rho_{i,\uparrow}(\omega) - \rho_{i,\downarrow}(\omega)$ obtained at ω = 0 for peripheral sites of the Rashba chain.

The main idea is to apply a bias voltage V between the STM tip and the superconducting substrate, inducing a charge transport that, in a subgap regime ($|V| \ll \Delta/|e|$) originates from the Andreev (particle to hole) scattering mechanism. The polarized Andreev current can be expressed by the Landauer–Büttiker formula

$$I_i^{\sigma}(V) = \frac{e}{h} \int \mathrm{d}\omega \, T_i^{\sigma}(\omega) \left[f(\omega - eV) - f(\omega + eV) \right], \quad (14)$$

where transmittance is defined as

$$T_i^{\sigma}(\omega) = \Gamma_{\text{N}}^2 \left| \langle\langle \hat{d}_{i\sigma} \hat{d}_{i+1\sigma} \rangle\rangle \right|^2 + \Gamma_{\text{N}}^2 \left| \langle\langle \hat{d}_{i\sigma} \hat{d}_{i-1\sigma} \rangle\rangle \right|^2$$

and

$$T_1^{\sigma}(\omega) = \Gamma_{\text{N}}^2 \left| \langle\langle \hat{d}_{1\sigma} \hat{d}_{2\sigma} \rangle\rangle \right|^2,$$

$$T_{\text{N}}^{\sigma}(\omega) = \Gamma_{\text{N}}^2 \left| \langle\langle \hat{d}_{N\sigma} \hat{d}_{N-1\sigma} \rangle\rangle \right|^2.$$

The anomalous Green's functions can be computed numerically from the solution of the Bogoliubov–de Gennes equations of this model (Equation 10). The net spin current $I_i^{\text{spin}}(V) = I_i^{\uparrow}(V) - I_i^{\downarrow}(V)$ turns out to be predominantly sensitive to the Majorana end-modes. Its differential conductance $G_i^{\text{spin}}(V) = (\partial / \partial V) I_i^{\text{spin}}(V)$ can thus distinguish the polarized Majorana quasiparticle (near $V = 0$) from the YSR states (appearing at finite voltage).

Bound states can leak to other side-attached nanoscopic objects. This proximity effect has been also predicted for the Majorana quasiparticles by E. Vernek et al. [48] and it has been indeed observed experimentally by M. T. Deng and co-authors [49]. Inspired by this achievement, extensive studies have been carried out regarding the YSR states coalescencing into the zero-energy Majorana states in side-coupled quantum dots driven by electrostatic or magnetic fields [50-52]. This issue would be particularly important when attempting to braid the Majorana end modes, e.g., in T-shape nanowires upon turning on and off the topological superconducting phase in its segments. We briefly analyse here the polarized zero-energy Majorana modes leaking into the multi-site quantum dot (comprising ten lattice sites) side-attached to the proximitized Rashba chain discussed above.

Figure 6 displays the spatial profile of the polarized spectrum obtained at $\omega = 0$ as a function of the gate voltage V_g, which detunes the energies $V_g = \varepsilon_i - \mu$ of the multi-site ($1 \leq i \leq 10$) quantum dot. For numerical calculations we used the model parameters $\lambda = 0.15t$, $\mu = -2t$, $\Delta_i = 0.2t$ and $B > B_c$, which guarantee the Rashba chain to be in its topologically nontrivial superconducting phase, hosting the zero-energy Majorana quasiparticles (intensive black or red regions). We clearly observe that for some values of V_g these Majorana modes spread over the entire quantum dot region. By inspecting Figure 6 we furthermore notice the pronounced spatial oscillations of these zero-energy modes. In our opinion, this is a signature of a partial delocalization of the polarized Majorana quasiparticles. Surprisingly, this process seems to be less efficient in the minor spin ($\sigma = \downarrow$) section. This effect has to be taken into account, when designing nanostructures for a controllable spatial displacement of the Majorana modes (criticial for the realization of quantum computations with use of the Majorana-based qubits) either by electrostatic or magnetic means. Some proposals for such nanodevices have been recently discussed by several authors [52,53].

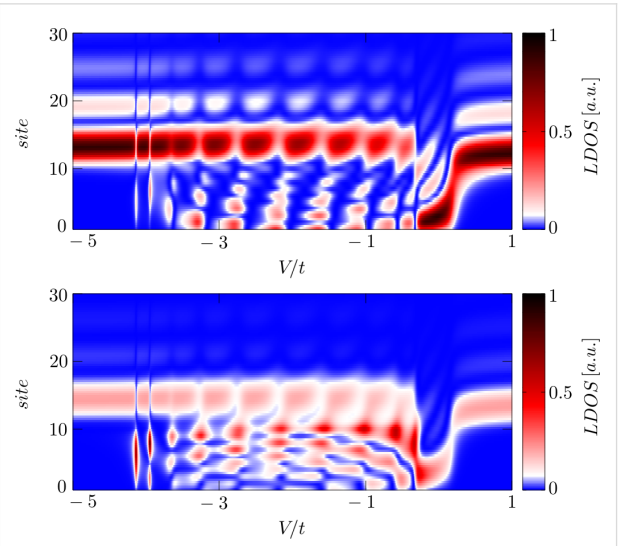

Figure 6: Leakage of the spin-polarized Majorana quasiparticles from the topological superconducting phase of the Rashba chain ($i \geq 10$) onto the side-attached multi-site ($i \in \langle 1;10 \rangle$) quantum dot. The upper and bottom panel show $\rho_{io}(\omega)$ at $\omega = 0$ for $\uparrow$ and $\downarrow$ spin, respectively.

In summary of this section, we emphasize that the Majorana modes coalescing from the YSR states in the proximitized Rashba nanowire are characterized by their magnetic polarization. Indeed, such a feature has been recently observed by STM spectroscopy with use of a polarized tip [42]. We have studied here the evolution of the polarized quasiparticle states with respect to the magnetic field (Figure 4) and investigated the spatial oscillations of the Majorana zero-energy modes near the chain edges (Figure 5). Finally, we analyzed leakage of the polarized Majorana modes on the multi-site quantum dots, revealing their partial delocalization (Figure 6).

Majorana vs Kondo effect

In previous section we have discussed the polarized Majorana modes leaking into side-attached objects, such as single impurities or segments of normal nanowires. In this section we shall focus on the correlation effects [54-56], confronting the Majorana quasiparticle with the Kondo effect (both manifested at zero energy). This can be practically achieved using STM-type configurations sketched in Figure 7. In particular, we consider the subgap Kondo effect, effectively driven by the Coulomb repulsion U and coupling of the quantum dot (QD) with the normal lead Γ_N in presence of electron pairing (induced via Γ_S), which has a significant influence on the spin-polarized bound states of the QD. The basic mechanism of this subgap Kondo effect showing up near the quantum phase transition has been earlier considered by us in absence of the Rashba nanowire

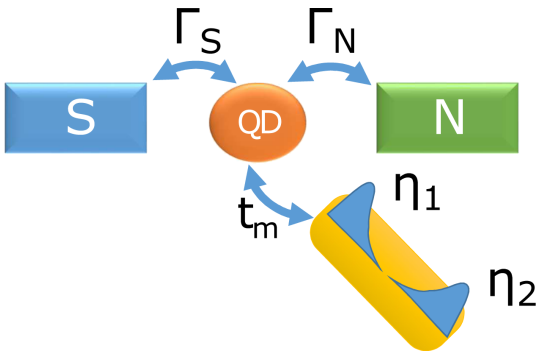

Figure 7: Schematic illustration of the quantum dot (QD) coupled between the metallic (N) and superconducting (S) leads and hybridized with the Rashba nanowire, hosting the Majorana quasiparticles η_1 and η_2 at its edges.

[24,57]. Our considerations can be practically verified within STM geometry [39,40] using magnetic atoms (e.g., Fe) and side-coupled nonmagnetic atoms (for instance Ag or Au) deposited on the superconducting substrate (such as Pb or Al) probed with a conducting STM tip [42].

The topological superconducting phase, hosting the Majorana modes, can be driven in semiconducting wires [58,59] or in nanochains of magnetic atoms [39-42] through nearest-neighbor equal-spin pairing. The efficiency of such *p*-wave pairing differs for each spin [47], giving rise to polarization of the Majorana quasiparticles, with noticeable preference for the ↑ sector (see Figure 4). In order to study the correlation effects we shall assume here a complete polarization of the Majorana quasiparticles. We thus focus, for simplicity, on the topological state originating from intersite pairing of only ↑ electrons and consider its interplay with the correlations. Let us remark, however, that the superconducting lead mixes both the QD spins with the side-attached Majorana quasiparticle [60]. In consequence we shall observe an interesting and spin-dependent relationship between the Majorana and Kondo states that could be probed by the polarized Andreev (particle-to-hole conversion) mechanism.

Our setup (Figure 7) can be described by the following Anderson-type Hamiltonian

$$\widehat{\mathcal{H}} = \sum_{\beta=\mathrm{S,N}} \left(\widehat{\mathcal{H}}_{\beta} + \widehat{\mathcal{H}}_{\beta-\mathrm{QD}} \right) + \widehat{\mathcal{H}}_{\mathrm{QD}} + \widehat{\mathcal{H}}_{\mathrm{MQD}}, \qquad (15)$$

where $\widehat{\mathcal{H}}_{\mathrm{N}}$ corresponds to the metallic electrode, $\widehat{\mathcal{H}}_{\mathrm{S}}$ refers to the *s*-wave superconducting substrate and the correlated QD is modeled by $\widehat{\mathcal{H}}_{\mathrm{QD}} = \sum_{\sigma} \varepsilon \hat{d}_{\sigma}^{\dagger} \hat{d}_{\sigma} + U \hat{n}_{\downarrow} \hat{n}_{\uparrow}$, where ε denotes the energy level and *U* stands for the repulsive interaction between opposite spin electrons. The QD is coupled to both β = N,S reservoirs through $\widehat{\mathcal{H}}_{\beta-\mathrm{QD}} = \sum_{\mathbf{k},\sigma} (V_{\mathbf{k}\beta} \hat{d}_{\sigma}^{\dagger} \hat{c}_{\mathbf{k}\sigma\beta} + \mathrm{H.c.})$ and we assume a wide bandwidth limit, using the constant couplings Γ_{β}. It can be shown [61-64] that for energies $|\omega| \ll \Delta$ the superconducting electrode induces the static on-dot pairing

$$\widehat{\mathcal{H}}_{\mathrm{S}} + \widehat{\mathcal{H}}_{\mathrm{S\text{-}QD}} \approx \mathcal{H}_{\mathrm{prox}} = \sum_{\sigma} \varepsilon \hat{d}_{\sigma}^{\dagger} \hat{d}_{\sigma} + U \hat{n}_{\downarrow} \hat{n}_{\uparrow} - \frac{\Gamma_{\mathrm{S}}}{2} \left(\hat{d}_{\uparrow} \hat{d}_{\downarrow} + \hat{d}_{\downarrow}^{\dagger} \hat{d}_{\uparrow}^{\dagger} \right).$$

Taking into account the finite magnitude of superconducting gap [50] does not affect the main conclusions of our study.

The effective Majorana modes of the nanowire can be modeled by [65]

$$\widehat{\mathcal{H}}_{\mathrm{MQD}} = \mathrm{i}\varepsilon_m \hat{\eta}_1 \hat{\eta}_2 + \lambda \left(\hat{d}_{\uparrow} \hat{\eta}_1 + \hat{\eta}_1 \hat{d}_{\uparrow}^{\dagger} \right),$$

where $\hat{\eta}_i = \hat{\eta}_i^{\dagger}$ are Hermitian operators and ε_m corresponds to an overlap between Majoranas. We recast these operators by the standard fermionic ones [66] $\hat{\eta}_1 = (1/\sqrt{2})(\hat{f} + \hat{f}^{\dagger})$ and $\hat{\eta}_2 = (-\mathrm{i}/\sqrt{2})(\hat{f} - \hat{f}^{\dagger})$. Finally, the Hamiltonian of Equation 15 simplifies to

$$\widehat{\mathcal{H}} = \widehat{\mathcal{H}}_{\mathrm{N}} + \widehat{\mathcal{H}}_{\mathrm{N\text{-}QD}} + \sum_{\sigma} \varepsilon \hat{d}_{\sigma}^{\dagger} \hat{d}_{\sigma} + U \hat{n}_{\downarrow} \hat{n}_{\uparrow} - \frac{\Gamma_S}{2} \left(\hat{d}_{\uparrow} \hat{d}_{\downarrow} + \hat{d}_{\downarrow}^{\dagger} \hat{d}_{\uparrow}^{\dagger} \right) + \varepsilon_m \hat{f}^{\dagger} \hat{f} + t_m \left(\hat{d}_{\uparrow}^{\dagger} - \hat{d}_{\uparrow} \right) \left(\hat{f} + \hat{f}^{\dagger} \right) - \frac{\varepsilon_m}{2}, \qquad (16)$$

with the auxiliary coupling $t_m = \lambda/\sqrt{2}$. The subgap Kondo physics originates in this model from the Coulomb term $U\hat{n}_{\downarrow}\hat{n}_{\uparrow}$ and the effective spin-exchange interactions due to $\widehat{\mathcal{H}}_{\mathrm{N\text{-}QD}}$. It has been shown [23,24] that under specific conditions the on-dot pairing can cooperate with the subgap Kondo effect. This particular situation occurs only near the quantum phase transition.

Let us examine how the subgap Kondo effect gets along with the Majorana mode. Earlier studies of the correlated quantum dot coupled to both normal (conducting) electrodes indicated that the side-attached Rashba chain leads to a competition between the Kondo and Majorana states [67-72]. For a sufficiently long wire ($\varepsilon_m = 0$) the Kondo effect persists only in the spin-channel ↓, whereas for ↑ electrons there appears a dip in the spectral density at ω = 0. The resulting tunneling conductance is then partly reduced (from the perfect value $2e^2/h$) to the fractional value $3e^2/2h$ [67,68,71-73]. In contrast, for the short Rashba wires (with $\varepsilon_m \neq 0$) the Kondo physics persists in both spin channels.

In our present setup (Figure 7) the correlated quantum dot is between the metallic and superconducting reservoirs, therefore the Kondo effect is additionally affected by on-dot pairing. Its influence is mainly controlled by the ratio U/Γ_{S} and partly by the level ε, determining whether the QD ground state is in the spinful or spinless configuration [23,24,62,64,74]. Obviously the latter one cannot be screened. For instance, for the half-filled QD ($\varepsilon = -U/2$) the spinful (doublet) configuration occurs in the regime $U \geq \Gamma_{\mathrm{S}}$.

For studying the correlations we adopt perturbative treatment of the Coulomb potential, treating it self-consistently to the second order in the normal and anomalous channels [62,75]. Specific expressions have been provided by us in [24]. Figure 8 shows the spectral function $\rho_{\sigma}(\omega)$ for both spins obtained at zero temperature for the Coulomb potential *U*, covering the (spinless)

singlet and (spinful) doublet configurations. In the weak interaction regime we observe appearance of two YSR states. For $U \approx \Gamma_S$ these peaks merge, signaling the quantum phase transition. The Kondo effect shows up only in the correlated limit ($U > \Gamma_S$), but its spectroscopic signatures are qualitatively different for each of the spins. Leakage of the Majorana quasiparticle suppresses the low-energy states of ↑ electrons. We notice that the initial density (for $t_m = 0$) is reduced by half, whereas we observe a constructive influence of the Majorana quasiparticle on opposite-spin ↓ electrons.

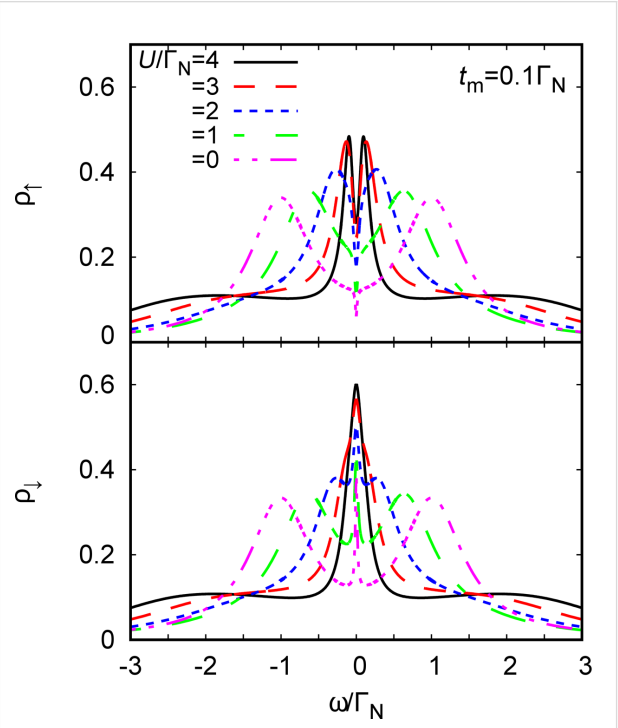

Figure 8: The polarized spectral function $\rho_\sigma(\omega)$ obtained at zero temperature for the half-filled QD ($\varepsilon = -U/2$), $\Gamma_S = 2\Gamma_N$, $t_m = 0.1\Gamma_N$ and several values of the Coulomb potential U (as indicated). Energies are expressed in units of Γ_N.

Figure 9 shows evolution of the spectral function $\rho_\uparrow(\omega)$ for various couplings t_m. In the weak-coupling limit we clearly observe a reduction (by half) of the initial density of states. With increasing t_m the spectrum develops the three-peak structure that is typical for the "molecular" limit. This behavior indicates that the Majorana and Kondo states have rather a complicated relation, which is neither competitive nor cooperative. In fact, some novel scaling laws have been recently reported by several authors [69,70,76-79] also considering the correlation effects directly in the Rashba nanowire.

Conclusion

We have studied the polarized bound states of magnetic impurities embedded in an *s*-wave superconducting material, taking

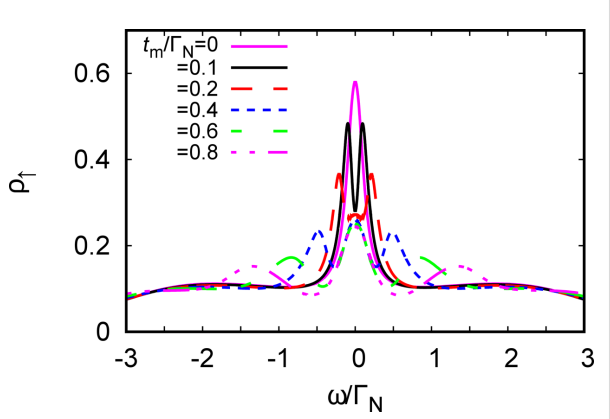

Figure 9: The spectral function $\rho_\uparrow(\omega)$ of the half-filled quantum dot ($\varepsilon = -U/2$) obtained at $T = 0$ for $\Gamma_S/\Gamma_N = 2$, $U/\Gamma_N = 4$ and several values of t_m (as indicated).

into account the spin–orbit and/or Coulomb interactions. We have shown that spin–orbit coupling strongly affects the subgap states, both of the single impurities and their conglomerate arranged into a nanoscopic chain. For the case of single magnetic impurity the spin–orbit interaction (i) shifts the quantum phase transition towards higher magnetic coupling J_c, (ii) enhances the spatial size of the YSR states, and (iii) smoothes the particle–hole oscillations. For the magnetic chain spin–orbit coupling combined with the Zeeman term induce the topologically nontrivial superconducting state and indirectly give rise to substantial polarization of the Majorana modes (Figure 4), the oscillations of which show up near the chain edges (Figure 5). The polarized Majorana quasiparticles can also leak into other side-coupled objects, such as single or multiple quantum impurities (Figure 6). These polarized Majorana quasiparticles can be controlled by a magnetic field or by an electrostatic potential. This would be important for future quantum computers using qubits based on topologically protected Majorana states. Finally, we have also confronted the Majorana quasiparticles with the subgap Kondo effect, revealing their complex relationship that can be hardly regarded as competitive or collaborative in some analogy to the Kondo effect originating from multiple degrees of freedom [80]. The aforementioned spin-polarized effects can be experimentally verified by polarized ballistic tunneling or by using STM spectroscopy, relying on the selective equal-spin Andreev reflections.

Acknowledgements

We thank for instructive remarks from R. Aguado, J. Klinovaja, R. Lutchyn, P. Simon, and R. Žitko on different parts of our study. This work was supported by the National Science Centre (Poland) under grants DEC-2014/13/B/ST3/04451 (AK, SG, TD) and DEC-2013/11/B/ST3/00824 (MMM) UMO-2017/25/

B/ST3/02586 (AP) and by the Faculty of Mathematics and Natural Sciences of the University of Rzeszów through the project WMP/GD-06/2017 (GG).

ORCID® iDs

Andrzej Ptok - https://orcid.org/0000-0002-5566-2656
Maciej M. Maśka - https://orcid.org/0000-0003-2214-3283

References

1. Choi, S.; Choi, H. J.; Ok, J. M.; Lee, Y.; Jang, W.-J.; Lee, A. T.; Kuk, Y.; Lee, S.; Heinrich, A. J.; Cheong, S.-W.; Bang, Y.; Johnston, S.; Kim, J. S.; Lee, J. *Phys. Rev. Lett.* **2017,** *119,* 227001. doi:10.1103/PhysRevLett.119.227001
2. Kenzelmann, M.; Strässle, T.; Niedermayer, C.; Sigrist, M.; Padmanabhan, B.; Zolliker, M.; Bianchi, A. D.; Movshovich, R.; Bauer, E. D.; Sarrao, J. L.; Thompson, J. D. *Science* **2008,** *321,* 1652. doi:10.1126/science.1161818
3. Meul, H. W.; Rossel, C.; Decroux, M.; Fischer, Ø.; Remenyi, G.; Briggs, A. *Phys. Rev. Lett.* **1984,** *53,* 497. doi:10.1103/PhysRevLett.53.497
4. Balatsky, A. V.; Vekhter, I.; Zhu, J.-X. *Rev. Mod. Phys.* **2006,** *78,* 373. doi:10.1103/RevModPhys.78.373
5. Heinrich, B. W.; Pascual, J. I.; Franke, K. J. *Prog. Surf. Sci.* **2018,** *93,* 1. doi:10.1016/j.progsurf.2018.01.001
6. Yazdani, A.; Jones, B. A.; Lutz, C. P.; Crommie, M. F.; Eigler, D. M. *Science* **1997,** *275,* 1767. doi:10.1126/science.275.5307.1767
7. Ji, S.-H.; Zhang, T.; Fu, Y.-S.; Chen, X.; Ma, X.-C.; Li, J.; Duan, W.-H.; Jia, J.-F.; Xue, Q.-K. *Phys. Rev. Lett.* **2008,** *100,* 226801. doi:10.1103/PhysRevLett.100.226801
8. Franke, K. J.; Schulze, G.; Pascual, J. I. *Science* **2011,** *332,* 940. doi:10.1126/science.1202204
9. Ruby, M.; Pientka, F.; Peng, Y.; von Oppen, F.; Heinrich, B. W.; Franke, K. J. *Phys. Rev. Lett.* **2015,** *115,* 087001. doi:10.1103/PhysRevLett.115.087001
10. Hatter, N.; Heinrich, B. W.; Ruby, M.; Pascual, J. I.; Franke, K. J. *Nat. Commun.* **2015,** *6,* 8988. doi:10.1038/ncomms9988
11. Ménard, G. C.; Guissart, S.; Brun, C.; Pons, S.; Stolyarov, V. S.; Debontridder, F.; Leclerc, M. V.; Janod, E.; Cario, L.; Roditchev, D.; Simon, P.; Cren, T. *Nat. Phys.* **2015,** *11,* 1013. doi:10.1038/nphys3508
12. Jellinggaard, A.; Grove-Rasmussen, K.; Madsen, M. H.; Nygård, J. *Phys. Rev. B* **2016,** *94,* 064520. doi:10.1103/PhysRevB.94.064520
13. Choi, D.-J.; Rubio-Verdú, C.; de Bruijckere, J.; Ugeda, M. M.; Lorente, N.; Pascual, J. I. *Nat. Commun.* **2017,** *8,* 15175. doi:10.1038/ncomms15175
14. Assouline, A.; Feuillet-Palma, C.; Zimmers, A.; Aubin, H.; Aprili, M.; Harmand, J.-C. *Phys. Rev. Lett.* **2017,** *119,* 097701. doi:10.1103/PhysRevLett.119.097701
15. Salkola, M. I.; Balatsky, A. V.; Schrieffer, J. R. *Phys. Rev. B* **1997,** *55,* 12648. doi:10.1103/PhysRevB.55.12648
16. Flatté, M. E.; Byers, J. M. *Phys. Rev. Lett.* **1997,** *78,* 3761. doi:10.1103/PhysRevLett.78.3761
17. Ugeda, M. M.; Bradley, A. J.; Zhang, Y.; Onishi, S.; Chen, Y.; Ruan, W.; Ojeda-Aristizabal, C.; Ryu, H.; Edmonds, M. T.; Tsai, H.-Z.; Riss, A.; Mo, S.-K.; Lee, D.; Zettl, A.; Hussain, Z.; Shen, Z.-X.; Crommie, M. F. *Nat. Phys.* **2016,** *12,* 92. doi:10.1038/nphys3527
18. Kezilebieke, S.; Dvorak, M.; Ojanen, T.; Liljeroth, P. *Nano Lett.* **2018,** *18,* 2311. doi:10.1021/acs.nanolett.7b05050
19. Santos, H.; Soriano, D.; Palacios, J. J. *Phys. Rev. B* **2014,** *89,* 195416. doi:10.1103/PhysRevB.89.195416
20. Kim, Y.; Zhang, J.; Rossi, E.; Lutchyn, R. M. *Phys. Rev. Lett.* **2015,** *114,* 236804. doi:10.1103/PhysRevLett.114.236804
21. Kaladzhyan, V.; Bena, C.; Simon, P. *Phys. Rev. B* **2016,** *93,* 214514. doi:10.1103/PhysRevB.93.214514
22. Ptok, A.; Głodzik, S.; Domański, T. *Phys. Rev. B* **2017,** *96,* 184425. doi:10.1103/PhysRevB.96.184425
23. Žitko, R.; Lim, J. S.; López, R.; Aguado, R. *Phys. Rev. B* **2015,** *91,* 045441. doi:10.1103/PhysRevB.91.045441
24. Domański, T.; Weymann, I.; Barańska, M.; Górski, G. *Sci. Rep.* **2016,** *6,* 23336. doi:10.1038/srep23336
25. Smith, E. D. B.; Tanaka, K.; Nagai, Y. *Phys. Rev. B* **2016,** *94,* 064515. doi:10.1103/PhysRevB.94.064515
26. Goertzen, S. L.; Tanaka, K.; Nagai, Y. *Phys. Rev. B* **2017,** *95,* 064509. doi:10.1103/PhysRevB.95.064509
27. Koerting, V.; Andersen, B. M.; Flensberg, K.; Paaske, J. *Phys. Rev. B* **2010,** *82,* 245108. doi:10.1103/PhysRevB.82.245108
28. Pershoguba, S. S.; Björnson, K.; Black-Schaffer, A. M.; Balatsky, A. V. *Phys. Rev. Lett.* **2015,** *115,* 116602. doi:10.1103/PhysRevLett.115.116602
29. Głodzik, S.; Ptok, A. *J. Supercond. Novel Magn.* **2018,** *31,* 647. doi:10.1007/s10948-017-4360-6
30. Mashkoori, M.; Björnson, K.; Black-Schaffer, A. M. *Sci. Rep.* **2017,** *7,* 44107. doi:10.1038/srep44107
31. Satori, K.; Shiba, H.; Sakai, O.; Shimizu, Y. *J. Phys. Soc. Jpn.* **1992,** *61,* 3239–3254. doi:10.1143/JPSJ.61.3239
32. Sakai, O.; Shimizu, Y.; Shiba, H.; Satori, K. *J. Phys. Soc. Jpn.* **1993,** *62,* 3181–3197. doi:10.1143/JPSJ.62.3181
33. Sakurai, A. *Prog. Theor. Phys.* **1970,** *44,* 1472. doi:10.1143/PTP.44.1472
34. van Gerven Oei, W.-V.; Tanasković, D.; Žitko, R. *Phys. Rev. B* **2017,** *95,* 085115. doi:10.1103/PhysRevB.95.085115
35. Morr, D. K.; Yoon, J. *Phys. Rev. B* **2006,** *73,* 224511. doi:10.1103/PhysRevB.73.224511
36. Röntynen, J.; Ojanen, T. *Phys. Rev. Lett.* **2015,** *114,* 236803. doi:10.1103/PhysRevLett.114.236803
37. Morr, D. K.; Stavropoulos, N. A. *Phys. Rev. B* **2003,** *67,* 020502. doi:10.1103/PhysRevB.67.020502
38. Kawakami, T.; Hu, X. *Phys. Rev. Lett.* **2015,** *115,* 177001. doi:10.1103/PhysRevLett.115.177001
39. Nadj-Perge, S.; Drozdov, I. K.; Li, J.; Chen, H.; Jeon, S.; Seo, J.; MacDonald, A. H.; Bernevig, B. A.; Yazdani, A. *Science* **2014,** *346,* 602. doi:10.1126/science.1259327
40. Pawlak, R.; Kisiel, M.; Klinovaja, J.; Maier, T.; Kawai, S.; Glatzel, T.; Loss, D.; Meyer, E. *npj Quantum Inf.* **2016,** *2,* 16035. doi:10.1038/npjqi.2016.35
41. Ruby, M.; Pientka, F.; Peng, Y.; von Oppen, F.; Heinrich, B. W.; Franke, K. J. *Phys. Rev. Lett.* **2015,** *115,* 197204. doi:10.1103/PhysRevLett.115.197204
42. Jeon, S.; Xie, Y.; Li, J.; Wang, Z.; Bernevig, B. A.; Yazdani, A. *Science* **2017,** *358,* 772. doi:10.1126/science.aan3670
43. Maśka, M. M.; Gorczyca-Goraj, A.; Tworzydło, J.; Domański, T. *Phys. Rev. B* **2017,** *95,* 045429. doi:10.1103/PhysRevB.95.045429
44. Liu, X.; Li, X.; Deng, D.-L.; Liu, X.-J.; Das Sarma, S. *Phys. Rev. B* **2016,** *94,* 014511. doi:10.1103/PhysRevB.94.014511
45. Stanescu, T. D.; Tewari, S. *J. Phys.: Condens. Matter* **2013,** *25,* 233201. doi:10.1088/0953-8984/25/23/233201
46. Sticlet, D.; Bena, C.; Simon, P. *Phys. Rev. Lett.* **2012,** *108,* 096802. doi:10.1103/PhysRevLett.108.096802

47. Maśka, M. M.; Domański, T. *Sci. Rep.* **2017,** *7,* 16193. doi:10.1038/s41598-017-16323-3
48. Vernek, E.; Penteado, P. H.; Seridonio, A. C.; Egues, J. C. *Phys. Rev. B* **2014,** *89,* 165314. doi:10.1103/PhysRevB.89.165314
49. Deng, M. T.; Vaitiekenas, S.; Hansen, E. B.; Danon, J.; Leijnse, M.; Flensberg, K.; Nygård, J.; Krogstrup, P.; Marcus, C. M. *Science* **2016,** *354,* 1557. doi:10.1126/science.aaf3961
50. Liu, C.-X.; Sau, J. D.; Stanescu, T. D.; Das Sarma, S. *Phys. Rev. B* **2017,** *96,* 075161. doi:10.1103/PhysRevB.96.075161
51. Hoffman, S.; Chevallier, D.; Loss, D.; Klinovaja, J. *Phys. Rev. B* **2017,** *96,* 045440. doi:10.1103/PhysRevB.96.045440
52. Ptok, A.; Kobiałka, A.; Domański, T. *Phys. Rev. B* **2017,** *96,* 195430. doi:10.1103/PhysRevB.96.195430
53. Chevallier, D.; Szumniak, P.; Hoffman, S.; Loss, D.; Klinovaja, J. *Phys. Rev. B* **2018,** *97,* 045404. doi:10.1103/PhysRevB.97.045404
54. Chirla, R.; Moca, C. P. *Phys. Rev. B* **2016,** *94,* 045405. doi:10.1103/PhysRevB.94.045405
55. Prada, E.; Aguado, R.; San-Jose, P. *Phys. Rev. B* **2017,** *96,* 085418. doi:10.1103/PhysRevB.96.085418
56. Barański, J.; Kobiałka, A.; Domański, T. *J. Phys.: Condens. Matter* **2017,** *29,* 075603. doi:10.1088/1361-648X/aa5214
57. Domański, T.; Žonda, M.; Pokorný, V.; Górski, G.; Janiš, V.; Novotný, T. *Phys. Rev. B* **2017,** *95,* 045104. doi:10.1103/PhysRevB.95.045104
58. Mourik, V.; Zuo, K.; Frolov, S. M.; Plissard, S. R.; Bakkers, E. P. A. M.; Kouwenhoven, L. P. *Science* **2012,** *336,* 1003. doi:10.1126/science.1222360
59. Gül, Ö.; Zhang, H.; Bommer, J. D. S.; de Moor, M. W. A.; Car, D.; Plissard, S. R.; Bakkers, E. P. A. M.; Geresdi, A.; Watanabe, K.; Taniguchi, T.; Kouwenhoven, L. P. *Nat. Nanotechnol.* **2018,** *13,* 192. doi:10.1038/s41565-017-0032-8
60. Golub, A. *Phys. Rev. B* **2015,** *91,* 205105. doi:10.1103/PhysRevB.91.205105
61. Bauer, J.; Oguri, A.; Hewson, A. C. *J. Phys.: Condens. Matter* **2007,** *19,* 486211. doi:10.1088/0953-8984/19/48/486211
62. Yamada, Y.; Tanaka, Y.; Kawakami, N. *Phys. Rev. B* **2011,** *84,* 075484. doi:10.1103/PhysRevB.84.075484
63. Martín-Rodero, A.; Levy Yeyati, A. *Adv. Phys.* **2011,** *60,* 899. doi:10.1080/00018732.2011.624266
64. Barański, J.; Domański, T. *J. Phys.: Condens. Matter* **2013,** *25,* 435305. doi:10.1088/0953-8984/25/43/435305
65. Liu, D. E.; Cheng, M.; Lutchyn, R. M. *Phys. Rev. B* **2015,** *91,* 081405. doi:10.1103/PhysRevB.91.081405
66. Elliott, S. R.; Franz, M. *Rev. Mod. Phys.* **2015,** *87,* 137. doi:10.1103/RevModPhys.87.137
67. Ruiz-Tijerina, D. A.; Vernek, E.; Dias da Silva, L. G. G. V.; Egues, J. C. *Phys. Rev. B* **2015,** *91,* 115435. doi:10.1103/PhysRevB.91.115435
68. Lee, M.; Lim, J. S.; López, R. *Phys. Rev. B* **2013,** *87,* 241402. doi:10.1103/PhysRevB.87.241402
69. Cheng, M.; Becker, M.; Bauer, B.; Lutchyn, R. M. *Phys. Rev. X* **2014,** *4,* 031051. doi:10.1103/PhysRevX.4.031051
70. van Beek, I. J.; Braunecker, B. *Phys. Rev. B* **2016,** *94,* 115416. doi:10.1103/PhysRevB.94.115416
71. Weymann, I. *J. Phys.: Condens. Matter* **2017,** *29,* 095301. doi:10.1088/1361-648X/aa5526
72. Weymann, I.; Wójcik, K. P. *Phys. Rev. B* **2017,** *95,* 155427. doi:10.1103/PhysRevB.95.155427
73. López, R.; Lee, M.; Serra, L.; Lim, J. S. *Phys. Rev. B* **2014,** *89,* 205418. doi:10.1103/PhysRevB.89.205418
74. Tanaka, Y.; Kawakami, N.; Oguri, A. *J. Phys. Soc. Jpn.* **2007,** *76,* 074701. doi:10.1143/JPSJ.76.074701
75. Vecino, E.; Martín-Rodero, A.; Levy Yeyati, A. *Phys. Rev. B* **2003,** *68,* 035105. doi:10.1103/PhysRevB.68.035105
76. Béri, B.; Cooper, N. R. *Phys. Rev. Lett.* **2012,** *109,* 156803. doi:10.1103/PhysRevLett.109.156803
77. Galpin, M. R.; Mitchell, A. K.; Temaismithi, J.; Logan, D. E.; Béri, B.; Cooper, N. R. *Phys. Rev. B* **2014,** *89,* 045143. doi:10.1103/PhysRevB.89.045143
78. Plugge, S.; Zazunov, A.; Eriksson, E.; Tsvelik, A. M.; Egger, R. *Phys. Rev. B* **2016,** *93,* 104524. doi:10.1103/PhysRevB.93.104524
79. Béri, B. *Phys. Rev. Lett.* **2017,** *119,* 027701. doi:10.1103/PhysRevLett.119.027701
80. Jacob, D.; Soriano, M.; Palacios, J. J. *Phys. Rev. B* **2013,** *88,* 134417. doi:10.1103/PhysRevB.88.134417

License and Terms

BEILSTEIN JOURNAL OF NANOTECHNOLOGY

Predicting the strain-mediated topological phase transition in 3D cubic $ThTaN_3$

Chunmei Zhang and Aijun Du*

Full Research Paper

Open Access

Address:
School of Chemistry, Physics and Mechanical Engineering, Queensland University of Technology, Gardens Point Campus, QLD 4001, Brisbane, Australia

Email:
Aijun Du* - aijun.du@qut.edu.au

* Corresponding author

Keywords:
Dirac cone; strain; $ThTaN_3$; topological insulator

Beilstein J. Nanotechnol. **2018,** *9,* 1399–1404.
doi:10.3762/bjnano.9.132

Received: 01 December 2017
Accepted: 25 April 2018
Published: 11 May 2018

This article is part of the Thematic Series "Topological materials".

Guest Editor: J. J. Palacios

Abstract

The cubic $ThTaN_3$ compound has long been known as a semiconductor with a band gap of approximately 1 eV, but its electronic properties remain largely unexplored. By using density functional theory, we find that the band gap of $ThTaN_3$ is very sensitive to the hydrostatic pressure/strain. A Dirac cone can emerge around the Γ point with an ultrahigh Fermi velocity at a compressive strain of 8%. Interestingly, the effect of spin–orbital coupling (SOC) is significant, leading to a band gap reduction of 0.26 eV in the $ThTaN_3$ compound. Moreover, the strong SOC can turn $ThTaN_3$ into a topological insulator with a large inverted gap up to 0.25 eV, which can be primarily attributed to the inversion between the d-orbital of the heavy element Ta and the p-orbital of N. Our results highlight a new 3D topological insulator with strain-mediated topological transition for potential applications in future spintronics.

Introduction

The $ThTaN_3$ compound generally presents three structural phases in cubic perovskite (c-PV), hypothetic orthorhombic perovskite (o-PV $GdFeO_3$-type), and post-perovskite (PPV) forms [1]. Among them, c-PV $ThTaN_3$ was first synthesized in early 1995 [2] and is known to crystallize in the space group *Pm*3*m* with a band gap of approximately 1 eV [1]. Pressure can induce a phase transition from c-PV to o-PV and PPV accompanied by the transition from a moderate band gap semiconductor (≈1 eV band gap in c-PV) to a small band gap semiconductor (PPV) in $ThTaN_3$ [1]. c-PV $ThTaN_3$ has also been proposed as a potential ground for studying nonlinear optical response [2] due to its large band gap and non-centrosymmetry. As protons are found to be significantly stable in nitrides, c-PV $ThTaN_3$ is also evaluated as an ideal proton-conducting ceramic [1]. Nevertheless, theoretical understanding of the electronic properties of $ThTaN_3$ is so far very limited and mainly focused on pressure-induced phase transition [3]. Therefore, a systematic study of the electron structure of $ThTaN_3$ in a certain phase is highly desired.

Topological insulators (TIs) have attracted much attention due to their distinct quantum mechanical properties, which makes

them important in the fields of physics [4,5], chemistry, and materials science [6]. TIs are materials with a bulk band gap generated by strong spin–orbit coupling (SOC) that have topologically protected metallic surface states. Although many materials are theoretically predicted to be TIs [7-11], the experimental realization of TIs is very limited. Therefore, the search for experimentally synthesized large band gap TIs is of paramount importance for their practical application. Theoretically, the transition from the trival insulator to the topological insulator can be achieved by increasing the SOC or by altering the lattice parameters [12,13]. A number of compounds [14-25], such as LaPtBi, LuPtSb, YPdBi [15-18], and HgTe [19,20], have been studied using a first-principles approach, showing that they can be turned into TIs under external strain. All these materials possess heavy elements and the strong SOC can induce a band inversion, which is a typical mechanism for TIs [26,27].

The experimentally observed pressure-induced phase transition in $ThTaN_3$ indicates that the electronic structure of 3D $ThTaN_3$ is likely very sensitive to the external strain. In particular, c-PV $ThTaN_3$ can crystallize in the tetragonal shape with C_4 rotational symmetry, which is an ideal platform to study its topological properties [28]. The combination of such C_4 rotational and time-reversal symmetry and the heavy elements (Th, Ta) in $ThTaN_3$ are expected to substantially alter the electronic band structure and thus achieve an exotic topological property [26].

By using first-principles calculations, we demonstrate here, for the first time, that the cubic perovskite $ThTaN_3$, a relatively large band gap semiconductor, can turn into a TI under moderate pressure/strain. A Dirac cone can emerge in the $ThTaN_3$ compound with an ultrahigh Fermi velocity under an 8% compressive strain. The band gap opening, induced by SOC, can be as high as 0.25 eV, which is large enough for the realization of the quantum spin Hall (QSH) states at room temperature. In addition, by tuning the SOC strength, we predict that the topological feature actually starts to show up at a 5% compressive strain. The strain-mediated topological phase transition in the perovskite $ThTaN_3$ compound is attributed to band inversion between the d-orbital of the heavy elements and the p-orbital of the N atom [12,29,30].

Computational Methods

First-principles calculations were performed based on density functional theory (DFT) as implemented in the plane wave basis VASP code [31-33]. A generalized gradient approximation (GGA) in the Perdew, Burke, and Ernzerhof (PBE) form exchange–correlation functional was used. The hybrid Heyd–Scuseria–Ernzerhof (HSE06) functional [34,35] was adopted for the accurate calculation of band structures of 3D $ThTaN_3$. A plane-wave basis set with an energy cut-off of 500 eV was employed and long range van der Waals dispersion [36] was incorporated to correct the total energy. The geometry structures were fully optimized until the maximum energy and force were less than 10^{-6} eV and 0.01 eV/Å, respectively. A Monkhorst–Pack *k*-point mesh of 7 × 7 × 7 was used for geometry optimization. The SOC effect was also considered in the calculation. The electron effective mass (m^*) of $ThTaN_3$ at the conduction band minimum (CBM) is estimated from the curvature of the electronic band dispersion, that is, the formula

$$m^* = \hbar \left(\frac{\partial E^2}{\partial k^2} \right)^{-1},$$

where E and k are the band energy and reciprocal lattice vector. For anisotropic materials, $m^* = \sqrt{m_i^* m_j^* m_k^*}$, where i, j and k label the transport direction along the x, y and z-axis.

Results and Discussion

The geometry structure of cubic perovskite $ThTaN_3$ was first fully relaxed as shown in Figure 1a. It crystallizes in the space group $Pm3m$ with C_4 rotational symmetry. The lattice parame-

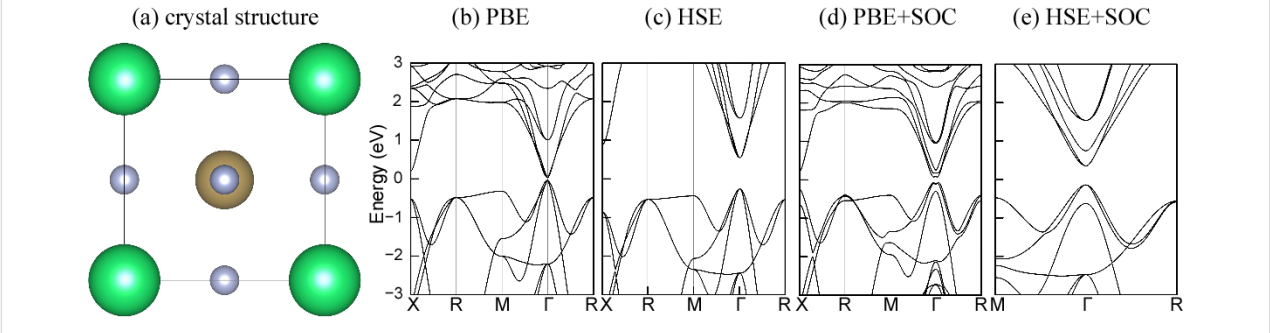

Figure 1: (a) Top view of $ThTaN_3$ with green, grey, and brown spheres representing Th, N, and Ta atoms, respectively. (b–e) The band structures of 3D cubic $ThTaN_3$ calculated by PBE, HSE, PBE+SOC, and HSE+SOC methods, respectively.

ters of c-PV $ThTaN_3$ were then calculated by using the PBE functional and the hybrid HSE06 functional methods, respectively. It was found that the PBE functional overestimates the experimental lattice constants by 1%, whereas the HSE06 can successfully reproduce the experimentally reported lattice parameters (4.02 Å) [2].

Figure 1 presents the detailed electronic band structure of 3D $ThTaN_3$ for the PBE exchange correlation (Figure 1b) and HSE hybrid functional (Figure 1c). A small direct band gap of 0.07 eV at the Γ point is predicted by the PBE functional and the HSE functional produced a large band gap of 0.76 eV, which is very close to the experimental measurement (1.0 eV) [1]. The band gap should exhibit substantial differences depending on the relative weights of the Hartree–Fock and traditional LDA or GGA exchange energies in the hybrid functional as well as those of the long range van der Waals interactions. However, we found that the impact of van der Waals interaction on the band gap of $ThTaN_3$ is negligible. Figure 1d and Figure 1e present band structures in the presence of the effect of SOC. Clearly, an energy gap of 0.15 eV and 0.49 eV were opened by the SOC for the PBE and the HSE functional methods, respectively. Compared to the HSE result without SOC (Figure 1c), the band gap reduction is significantly high (0.26 eV) after the incorporation of SOC.

Then we turned to study the effect of strain [37] on the electronic structure of c-PV $ThTaN_3$ by applying a hydrostatic strain ranging from −10% (compressive strain) to +15% (tensile strain) on 3D $ThTaN_3$. As shown in Figure 2d–g, the size of the direct gap continued to increase as the positive strain was increased. At a strain of 3%, the direct band gap turned to an indirect one and the band gap slightly decreased with further increasing strain. When a compressive strain was exerted into 3D $ThTaN_3$, the band gap could be significantly reduced. As shown in Figure 2a, the energy gap was reduced to 0 eV at a compressive strain of −8%. A Dirac-cone-like band structure [38] emerged with an ultrahigh Fermi velocity 6.33×10^5 m/s that is comparable to that of graphene (1.1×10^6 m/s) [39]. It is very important to note that the conduction band (CB) of $ThTaN_3$ is very dispersive around the Γ point, signifying a very low electron effective mass. The effective mass of the electron at the Γ point is calculated to be 0.395 m_e. Such a small electron mass will greatly improve charge carrier mobility, suggesting great potential for application of $ThTaN_3$ in electronics.

As eluded to above, the effect of SOC on the band gap of $ThTaN_3$ is significant. It is therefore important to further study the effect of strain on the electronic structure of $ThTaN_3$ in the presence of SOC (Figure 3). For strain-free $ThTaN_3$, the band gap is 0.49 eV as calculated by the HSE+SOC method. The band gap is reduced approximately 0.26 eV compared to the HSE result (0.76 eV) without SOC. When an 8% compressive strain is exerted on the $ThTaN_3$ compound, SOC opens a large band gap (approximately 0.25 eV) for the Dirac cone as shown in Figure 3d. It can be seen that under compressive strain, the SOC gap of $ThTaN_3$ can be closed and reopened. In addition, the shape of the band structure is changed correspondingly, indicating a topological phase transition [40-42]. In order to determine topological features, we calculated the Z2 topological index [19,27]. The topological invariant Z_2 is 1;(0,0,0) for $ThTaN_3$ under 8% compressive strain, which indicates the strong topological property (more details including methods and parities of the relevant bands can be found in Supporting Information File 1). We further scrutinized the SOC band structure of $ThTaN_3$ (Figure 3c) and find that the band inversion actually occurred at a 5% compressive strain. The above results clearly indicated that we can turn $ThTaN_3$ into a TI by applying an external hydrostatic pressure in the presence of SOC.

We further analyzed the orbital-resolved band structure of $ThTaN_3$ at a lower compressive strain (5%) as shown in Figure 4. The conduction band (CB) state mainly consisted of p_x, p_y and p_z orbitals of the N atom, while the valence band

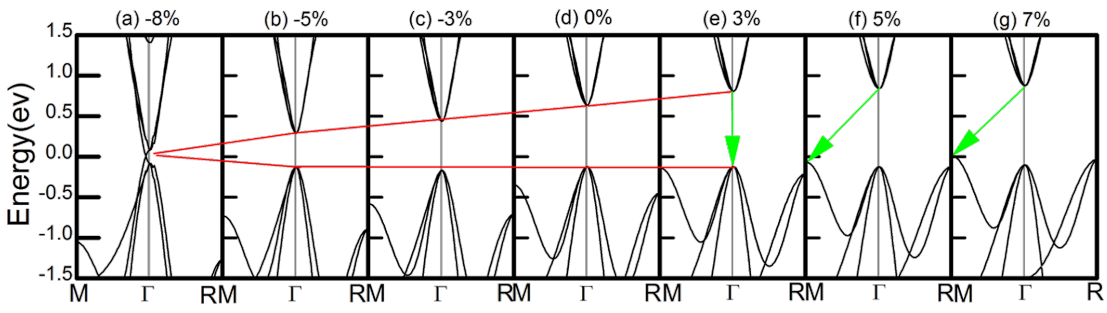

Figure 2: The modulation of band gap (red line) by hydrostatic and tensile strain (−8% to +7%) in $ThTaN_3$ by using the HSE method. A Dirac cone emerges when a −8% strain is added to the $ThTaN_3$ compound. And the green arrow shows that the change from a direct band gap to an indirect band gap with strain is increased from 3% to 7%. The Fermi level is set at an energy of zero.

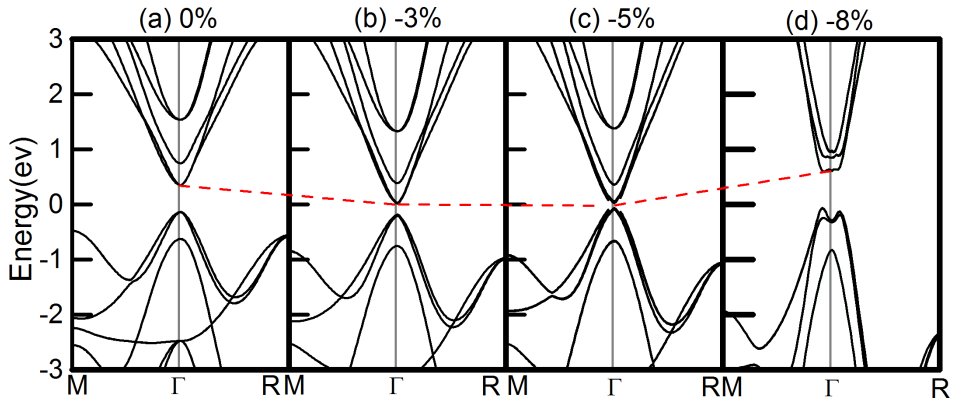

Figure 3: Band structures of $ThTaN_3$ calculated by the HSE+SOC method under a strain of −8% to 0%. The Fermi level is set to zero.

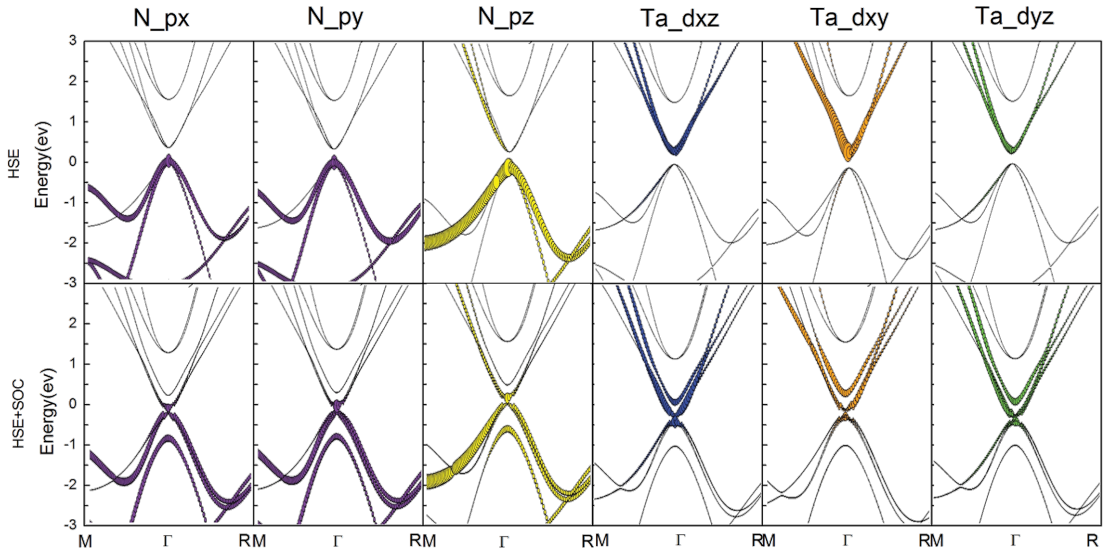

Figure 4: Orbital-resolved band structures for $ThTaN_3$ under 5% compressive strain as calculated by the HSE (top panel) and HSE+SOC methods (bottom panel). The contributions are mainly from p_x, p_y, p_z of N atoms and d_{xz}, d_{xy}, d_{yz} of Ta atoms. The thicker and thinner lines account for large and low orbital contributions, respectively.

(VB) state is comprised of the hybridization d_{xy}, d_{xz}, d_{yz} orbitals of the Ta atom. When the SOC effect was incorporated, a p–d-type band inversion took place with the reduction of the band gap, manifesting a topological phase transition due to the synergistic effects of SOC and lattice strain.

Generally, the topological phase transition can be also directly observed by modifying the SOC strength [29,30]. To provide a clear picture of the band inversion or topological phase transition in $ThTaN_3$ under a 5% compressive strain, we then studied the electronic structure of 3D cubic perovskite $ThTaN_3$ at various SOC strengths as shown in Figure 5a–e. With increasing SOC, the VBM and CBM gradually become closer (see Figure 5a–e), and then the gap closed and reopened with a large portion of band inversion, which can be clearly seen from the enormous change of the CBM and VBM band shape into Mexican-hat-like band dispersion, a typical indication of topological phase transition (see Figure 5e).

Conclusion

In summary, we have systematically studied the electronic structure in the 3D perovskite $ThTaN_3$ compound. We find the band gap of $ThTaN_3$ is very sensitive to the lattice strain. A Dirac-cone-like band with an ultrahigh Fermi velocity can emerge at a compressive strain of 8%. The topological phase transition can be realized with a large gap (≈0.25 eV) opened in the presence of SOC. Further analysis of orbital contribution indicates p–d band inversion in 3D $ThTaN_3$. Our results highlight a new, interesting, 3D, topological insulator material with great potential for future application in spintronics.

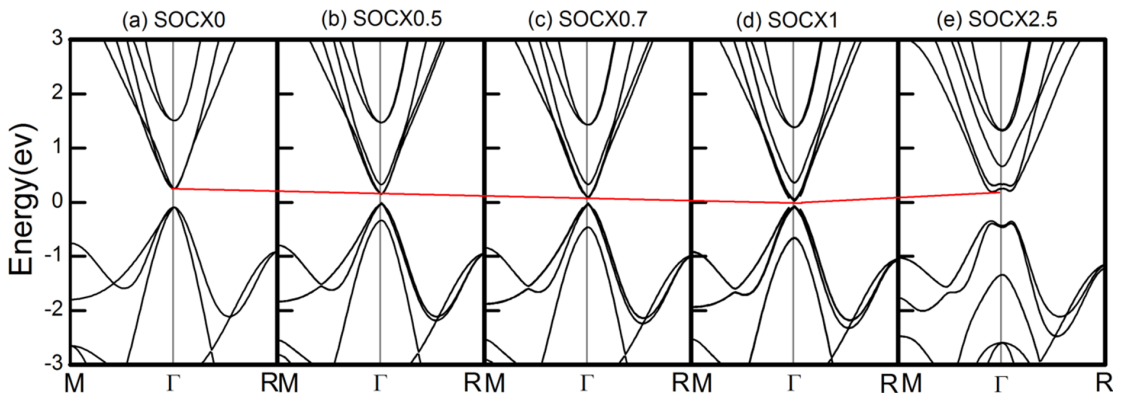

Figure 5: Band structures for 3D cubic $ThTaN_3$ with a 5% compressive strain as calculated by the HSE+SOC method at different SOC strengths (0–2.5 times). The Fermi energy level is set to zero.

Supporting Information

Supporting Information File 1

Additional calculations.

The lattice parameters of $ThTaN_3$ under strain, the surface state of $ThTaN_3$, and the calculation of the topological invariant number Z2.

[https://www.beilstein-journals.org/bjnano/content/supplementary/2190-4286-9-132-S1.pdf]

Acknowledgements

We acknowledge generous grants of high-performance computer time from the computing facility at the Queensland University of Technology, The Pawsey Supercomputing Centre and Australian National Facility. A.D. greatly appreciates the Australian Research Council QEII Fellowship (DP110101239) and financial support of Australian Research Council under Discovery Project (DP130102420 and DP170103598).

References

1. Matar, S. F.; Demazeau, G. *J. Solid State Chem.* **2010,** *183,* 994–999. doi:10.1016/j.jssc.2010.03.002
2. Brese, N. E.; DiSalvo, F. J. *J. Solid State Chem.* **1995,** *120,* 378–380. doi:10.1006/jssc.1995.1423
3. Polfus, J. M.; Haugsrud, R. *Solid State Commun.* **2012,** *152,* 1921–1923. doi:10.1016/j.ssc.2012.07.010
4. Bernevig, B. A.; Zhang, S.-C. *Phys. Rev. Lett.* **2006,** *96,* 106802. doi:10.1103/PhysRevLett.96.106802
5. Huang, C.; Zhou, J.; Wu, H.; Deng, K.; Jena, P.; Kan, E. *Phys. Rev. B* **2017,** *95,* 045113. doi:10.1103/PhysRevB.95.045113
6. Kong, D.; Cui, Y. *Nat. Chem.* **2011,** *3,* 845–849. doi:10.1038/nchem.1171
7. Zhou, L.; Shao, B.; Shi, W.; Sun, Y.; Felser, C.; Yan, B.; Frauenheim, T. *2D Mater.* **2016,** *3,* 035022. doi:10.1088/2053-1583/3/3/035022
8. Zhou, L.; Shi, W.; Sun, Y.; Shao, B.; Felser, C.; Yan, B.; Frauenheim, T. *2D Mater.* **2016,** *3,* 035018. doi:10.1088/2053-1583/3/3/035018
9. Zhou, L.; Kou, L.; Sun, Y.; Felser, C.; Hu, F.; Shan, G.; Smith, S. C.; Yan, B.; Frauenheim, T. *Nano Lett.* **2015,** *15,* 7867–7872. doi:10.1021/acs.nanolett.5b02617
10. Ma, Y.; Kou, L.; Dai, Y.; Heine, T. *Phys. Rev. B* **2016,** *94,* 201104. doi:10.1103/PhysRevB.94.201104
11. Ma, Y.; Kou, L.; Li, X.; Dai, Y.; Heine, T. *NPG Asia Mater.* **2016,** *8,* e264. doi:10.1038/am.2016.51
12. Xu, S.-Y.; Xia, Y.; Wray, L. A.; Jia, S.; Meier, F.; Dil, J. H.; Osterwalder, J.; Slomski, B.; Bansil, A.; Lin, H.; Cava, R. J.; Hasan, M. Z. *Science* **2011,** *332,* 560–564. doi:10.1126/science.1201607
13. Huang, C.; Zhou, J.; Wu, H.; Deng, K.; Jena, P.; Kan, E. *J. Phys. Chem. Lett.* **2016,** *7,* 1919–1924. doi:10.1021/acs.jpclett.6b00651
14. Zhou, D.; Li, Q.; Ma, Y.; Cui, Q.; Chen, C. *J. Phys. Chem. C* **2013,** *117,* 8437–8442. doi:10.1021/jp401928j
15. Xiao, D.; Yao, Y.; Feng, W.; Wen, J.; Zhu, W.; Chen, X.-Q.; Stocks, G. M.; Zhang, Z. *Phys. Rev. Lett.* **2010,** *105,* 096404. doi:10.1103/PhysRevLett.105.096404
16. Feng, W.; Xiao, D.; Zhang, Y.; Yao, Y. *Phys. Rev. B* **2010,** *82,* 235121. doi:10.1103/PhysRevB.82.235121
17. Chadov, S.; Qi, X.; Kübler, J.; Fecher, G. H.; Felser, C.; Zhang, S. C. *Nat. Mater.* **2010,** *9,* 541–545. doi:10.1038/nmat2770
18. Lin, H.; Wray, L. A.; Xia, Y.; Xu, S.; Jia, S.; Cava, R. J.; Bansil, A.; Hasan, M. Z. *Nat. Mater.* **2010,** *9,* 546–549. doi:10.1038/nmat2771
19. Fu, L.; Kane, C. L. *Phys. Rev. B* **2007,** *76,* 045302. doi:10.1103/PhysRevB.76.045302
20. Brüne, C.; Liu, C. X.; Novik, E. G.; Hankiewicz, E. M.; Buhmann, H.; Chen, Y. L.; Qi, X. L.; Shen, Z. X.; Zhang, S. C.; Molenkamp, L. W. *Phys. Rev. Lett.* **2011,** *106,* 126803. doi:10.1103/PhysRevLett.106.126803
21. Zhang, H.; Ma, Y.; Chen, Z. *Nanoscale* **2015,** *7,* 19152–19159. doi:10.1039/C5NR05006E
22. Zhang, S.; Xie, M.; Cai, B.; Zhang, H.; Ma, Y.; Chen, Z.; Zhu, Z.; Hu, Z.; Zeng, H. *Phys. Rev. B* **2016,** *93,* 245303. doi:10.1103/PhysRevB.93.245303
23. Ma, Y.; Kou, L.; Li, X.; Dai, Y.; Smith, S. C.; Heine, T. *Phys. Rev. B* **2015,** *92,* 085427. doi:10.1103/PhysRevB.92.085427

24. Zhao, M.; Chen, X.; Li, L.; Zhang, X. *Sci. Rep.* **2015,** *5,* 8441. doi:10.1038/srep08441
25. Zhao, M.; Zhang, X.; Li, L. *Sci. Rep.* **2015,** *5,* 16108. doi:10.1038/srep16108
26. Bernevig, B. A.; Hughes, T. L.; Zhang, S.-C. *Science* **2006,** *314,* 1757–1761. doi:10.1126/science.1133734
27. Fu, L.; Kane, C. L.; Mele, E. J. *Phys. Rev. Lett.* **2007,** *98,* 106803. doi:10.1103/PhysRevLett.98.106803
28. Fu, L. *Phys. Rev. Lett.* **2011,** *106,* 106802. doi:10.1103/PhysRevLett.106.106802
29. Zhang, W.; Yu, R.; Zhang, H.-J.; Dai, X.; Fang, Z. *New J. Phys.* **2010,** *12,* 065013. doi:10.1088/1367-2630/12/6/065013
30. Murakami, S. *Prog. Theor. Phys. Suppl.* **2008,** *176,* 279–301. doi:10.1143/PTPS.176.279
31. Kresse, G.; Furthmüller, J. *Comput. Mater. Sci.* **1996,** *6,* 15–50. doi:10.1016/0927-0256(96)00008-0
32. Kresse, G.; Furthmüller, J. *Phys. Rev. B* **1996,** *54,* 11169. doi:10.1103/PhysRevB.54.11169
33. Blöchl, P. E. *Phys. Rev. B* **1994,** *50,* 17953. doi:10.1103/PhysRevB.50.17953
34. Heyd, J.; Scuseria, G. E.; Ernzerhof, M. *J. Chem. Phys.* **2003,** *118,* 8207–8215. doi:10.1063/1.1564060
35. Perdew, J. P.; Burke, K.; Ernzerhof, M. *Phys. Rev. Lett.* **1996,** *77,* 3865. doi:10.1103/PhysRevLett.77.3865
36. Grimme, S. *J. Comput. Chem.* **2006,** *27,* 1787–1799. doi:10.1002/jcc.20495
37. Zhang, C.; Kou, L.; He, T.; Jiao, Y.; Liao, T.; Bottle, S.; Du, A. *Comput. Mater. Sci.* **2018,** *149,* 158–161. doi:10.1016/j.commatsci.2018.03.027
38. Zhang, C.; Jiao, Y.; Ma, F.; Bottle, S.; Zhao, M.; Chen, Z.; Du, A. *Phys. Chem. Chem. Phys.* **2017,** *19,* 5449–5453. doi:10.1039/C7CP00157F
39. Trevisanutto, P. E.; Giorgetti, C.; Reining, L.; Ladisa, M.; Olevano, V. *Phys. Rev. Lett.* **2008,** *101,* 226405. doi:10.1103/PhysRevLett.101.226405
40. Zhang, H.; Liu, C.-X.; Qi, X.-L.; Dai, X.; Fang, Z.; Zhang, S.-C. *Nat. Phys.* **2009,** *5,* 438–442. doi:10.1038/nphys1270
41. Xu, Y.; Yan, B.; Zhang, H.-J.; Wang, J.; Xu, G.; Tang, P.; Duan, W.; Zhang, S.-C. *Phys. Rev. Lett.* **2013,** *111,* 136804. doi:10.1103/PhysRevLett.111.136804
42. Si, C.; Liu, J.; Xu, Y.; Wu, J.; Gu, B.-L.; Duan, W. *Phys. Rev. B* **2014,** *89,* 115429. doi:10.1103/PhysRevB.89.115429

License and Terms

BEILSTEIN JOURNAL OF NANOTECHNOLOGY

Robust midgap states in band-inverted junctions under electric and magnetic fields

Álvaro Díaz-Fernández*, Natalia del Valle and Francisco Domínguez-Adame

Full Research Paper

Open Access

Address:
GISC, Departamento de Física de Materiales, Universidad Complutense, E-28040 Madrid, Spain

Email:
Álvaro Díaz-Fernández* - alvaro.diaz@ucm.es

* Corresponding author

Keywords:
crystalline topological insulators; electric and magnetic fields; Landau levels; midgap states

Beilstein J. Nanotechnol. **2018,** *9,* 1405–1413.
doi:10.3762/bjnano.9.133

Received: 22 September 2017
Accepted: 16 April 2018
Published: 14 May 2018

This article is part of the Thematic Series "Topological materials".

Guest Editor: J. J. Palacios

Abstract

Several IV–VI semiconductor compounds made of heavy atoms, such as $Pb_{1-x}Sn_xTe$, may undergo band-inversion at the L point of the Brillouin zone upon variation of their chemical composition. This inversion gives rise to topologically distinct phases, characterized by a change in a topological invariant. In the framework of the $\mathbf{k}\cdot\mathbf{p}$ theory, band-inversion can be viewed as a change of sign of the fundamental gap. A two-band model within the envelope-function approximation predicts the appearance of midgap interface states with Dirac cone dispersions in band-inverted junctions, namely, when the gap changes sign along the growth direction. We present a thorough study of these interface electron states in the presence of crossed electric and magnetic fields, the electric field being applied along the growth direction of a band-inverted junction. We show that the Dirac cone is robust and persists even if the fields are strong. In addition, we point out that Landau levels of electron states lying in the semiconductor bands can be tailored by the electric field. Tunable devices are thus likely to be realizable, exploiting the properties studied herein.

Introduction

In 1982, Thouless et al. [1] made a connection between the quantum Hall effect and a topological invariant, the so-called first Chern number [2]. The fact that a quantum Hall system was insulating in the bulk but had a quantized conductivity on the edge could be related to the non-trivial topology of the band structure. In 2006, topology came up to stage once again with the theoretical prediction by Bernevig et al. [3] of a topological insulating behaviour in a HgTe/CdTe quantum well. The difference between the latter and the quantum Hall system lies in the fact that the quantum well required no magnetic field at all, but just relativistic corrections (Darwin and mass–velocity interactions) large enough so as to invert the Γ_6 and Γ_8 bands [4]. The HgTe/CdTe quantum well possesses non-trivial edge states when a certain width is exceeded. In 2007, experiments verified this remarkable result and established the existence of the quantum spin Hall effect [5]. However, no clear signatures of conductance quantization have been observed yet [6,7].

Besides II–VI compound semiconductors, such as HgTe, IV–VI semiconductors support non-trivial edges states as well [8]. In this regard, Dziawa et al. reported evidence of topological crystalline insulator states in $Pb_{1-x}Sn_xSe$ [9]. High-resolution scanning tunneling microscopy studies of these topological crystalline insulators provided strong evidence of the coexistence of massless Dirac fermions, protected by crystal symmetry, with massive Dirac fermions consistent with crystal-symmetry breaking [10]. Recently, these results have received further support with the aid of Dirac Landau level spectroscopy [11,12].

Band-inverted structures were already studied back in the 1980's and 1990's under the name of band-inverted junctions, in which the fundamental gap has opposite sign on each semiconductor. A salient feature is the existence of interface states lying within the gap, provided that the two gaps overlap [13-17]. These states are protected by symmetry, and are responsible for the conducting properties of the surface. In IV–VI heterojunctions, such as PbTe/SnTe, interface states are accurately described by means of a two-band model using the effective $\mathbf{k}\cdot\mathbf{p}$ approximation [18,19]. The equation governing the conduction- and valence-band envelope functions reduces to a Dirac-like equation after neglecting far-band corrections. In view of this analogy, exact solutions can be then straightforwardly found by means of supersymmetric [16] or Green's function approaches [20]. In the context of symmetry-protected topological phases, our model can be applied not only to topological crystalline insulators, like the ones mentioned above [8], but also to more general three-dimensional topological insulators, such as Bi_2Se_3, in contact with a trivial insulator [21,22]. In the former case, mirror symmetry makes it possible to define mirror Chern numbers, which determine the topological crystalline phase [8]. In the latter, time-reversal symmetry, parity and particle–hole symmetry allow us to define a topological index given by the sign of the Dirac mass [21].

In 1994, Agassi studied the case of a band-inverted junction with a magnetic field applied parallel to the junction [23]. This author showed that the Dirac point remains robust upon the application of a magnetic field of arbitrary strengths and that the Landau levels in the continuum split for non-zero values of the in-plane momentum in the direction perpendicular to the magnetic field. By means of the modern theory of symmetry-protected topological phases, the protection of the Dirac point can be understood in the case of topological crystalline insulators from the fact that a magnetic field perpendicular to a mirror plane renders a system that is still symmetric about that plane [8]. This is not the case in a magnetic field parallel to the mirror plane, where the Dirac cone turns into the usual relativistic Landau levels [13,15,24]. Going back to the parallel magnetic field, Agassi demonstrated that for large values of this in-plane momentum, the states evolve to the bulk Landau states and the midgap state becomes the zero Landau level, usual of these Dirac systems. The reason is that the in-plane momentum perpendicular to the magnetic field is proportional to the position of the Landau orbits. If it becomes very large and the magnetic length is at the same time small, which happens for large magnetic fields, then the orbits do not intersect the junction and they might not notice that boundary. Hence, the case of most interest is in the vicinity of low in-plane momentum perpendicular to the field, where the states differ the most from the Landau levels of the bulk and we can see the effects of the interface.

In this same topic of external fields applied to band-inverted junctions, we have recently studied band-inverted junctions based on IV–VI compounds using a two-band model when an electric field is applied along the growth direction [25]. We have demonstrated that the Dirac cone of midgap states is robust against moderate values of the electric field but Fermi's velocity decreases quadratically with the applied field. The aim of this paper is to characterize electron states in band-inverted junctions using a two-band model in the presence of crossed magnetic and electric fields, the former parallel to the junction, the latter perpendicular to it. We show that the Dirac cone of midgap states arising in the single-junction configuration is robust against crossed electric and magnetic fields. In addition, Landau levels of electron states lying in the semiconductor bands can be tailored by the electric field. Finally, the electronic structure of band-inverted junctions when the magnetic field is applied along the growth direction, parallel to the electric field, will also be briefly discussed for comparison.

Theoretical model

We consider heterojunctions of IV–VI compound semiconductors, such as $Pb_{1-x}Sn_xTe$ and $Pb_{1-x}Sn_xSe$. The latter are known to shift from being semiconductors to topological crystalline insulators due to the band inversion at the L points of the Brillouin zone as the Sn fraction increases [8,26,27]. In order to keep the algebra as simple as possible, we restrict ourselves to the symmetric heterojunction with same-sized and aligned gaps, as depicted in Figure 1a. This assumption simplifies the calculations while keeping the underlying physics [28]. Thus, a single and abrupt interface presents the following profile for the magnitude of the gap

$$E_{\mathrm{G}}(z) = 2\Delta\,\mathrm{sgn}(z), \tag{1}$$

where $\mathrm{sgn}(z) = |z|/z$ is the sign function. Here the Z-axis is parallel to the growth direction [111].

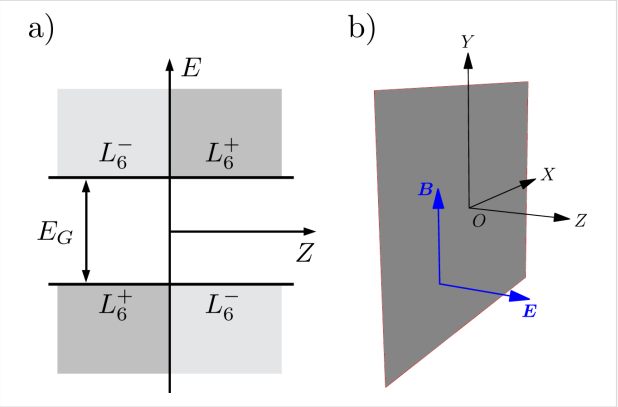

Figure 1: (a) L_6^+ and L_6^- band-edge profile of an abrupt band-inverted junction with aligned and same-sized gaps, located at the *XY*-plane, and b) schematic view of the applied electric and magnetic fields.

The envelope functions of the electron states near the band extrema L_6^+ and L_6^- in IV–VI compounds are determined from the following Dirac-like Hamiltonian [15,16,19]

$$\mathcal{H}_0 = v\boldsymbol{\alpha}\cdot\mathbf{p} + \frac{1}{2}E_{\mathrm{G}}(z)\beta\,. \tag{2}$$

Here $\boldsymbol{\alpha} = (\alpha_x, \alpha_y, \alpha_z)$ and β denote the usual 4×4 Dirac matrices, $\alpha_i = \sigma_x \otimes \sigma_i$ and $\beta = \sigma_z \otimes \mathbb{1}_2$, σ_i and $\mathbb{1}_n$ being the Pauli matrices and $n \times n$ identity matrix, respectively. Moreover, v is an interband matrix element having dimensions of velocity and it is assumed scalar, corresponding to isotropic bands around the L point. It is worth mentioning that the bands of IV–VI compounds around the L points are actually anisotropic. Nevertheless, this anisotropy can be absorbed in the definition of the dimensionless parameters defined below. That is, it is possible to consider a direction-dependent velocity, but it will not change the results shown below, except for a proportionality constant in the definition of the dimensionless in-plane momenta (see [19,28] for further details). In addition, we focus on states close to one of the L points of the Brillouin zone [8] and neglect other valleys in what follows since midgap states are stable against gap opening by valley mixing. Also notice that only linear momentum terms are taken into account in Equation 2 but quadratic momentum terms could have an impact of the electronic levels [29,30]. However, the two-band model Hamiltonian (Equation 2) successfully describes the hybridization of interface states in band-inverted quantum wells [31], in perfect agreement with more elaborated models including quadratic momentum terms [30]. The Hamiltonian (Equation 2) acts upon the envelope function $\boldsymbol{\chi}(\mathbf{r})$, which is a four-component vector composed of the two-component spinors $\boldsymbol{\chi}_+(\mathbf{r})$ and $\boldsymbol{\chi}_-(\mathbf{r})$ belonging to the L_6^+ and L_6^- bands. The interface momentum is conserved and the envelope function can be expressed as $\boldsymbol{\chi}(\mathbf{r}) = \tilde{\boldsymbol{\chi}}(z)\exp(\mathrm{i}\mathbf{r}_\perp\cdot\mathbf{k}_\perp)$, where it is understood that the subscript "$\perp$" in a vector indicates the nullification of its z-component. In the case of aligned and same-sized gaps, it is found that $\tilde{\boldsymbol{\chi}}(z) \sim \exp(-|z|/d)$, with $d = \hbar v/\Delta$ and the interface dispersion relation is a single Dirac cone $E(\mathbf{k}_\perp) = \pm\hbar v|\mathbf{k}_\perp|$, where the origin of energy is taken at the center of the gaps [20]. v is the group velocity at the Fermi level in undoped samples and it will be referred to as Fermi velocity hereafter.

Electron states under crossed electric and magnetic fields

We now turn to the electronic states of a single band-inverted junction exposed to a perpendicular electric field $\mathbf{F} = F\hat{\mathbf{z}}$ and a parallel magnetic field $\mathbf{B} = B\hat{\mathbf{y}}$, as shown schematically in Figure 1b. By choosing the Landau gauge, the vector potential is given as $\mathbf{A}(z) = Bz\hat{\mathbf{x}}$.

The electrostatic potential eFz and the vector potential $\mathbf{A}(z)$ only depend on the z-coordinate. Therefore, $\mathbf{p}_\perp = \hbar\mathbf{k}_\perp$ is a constant of motion and the envelope function can still be factorized to the form $\boldsymbol{\chi}(\mathbf{r}) = \tilde{\boldsymbol{\chi}}(z)\exp(\mathrm{i}\mathbf{r}_\perp\cdot\mathbf{k}_\perp)$. Now the longitudinal envelope function $\tilde{\boldsymbol{\chi}}(z)$ satisfies the following Dirac equation:

$$\left[\mathcal{H}_0 + ev\boldsymbol{\alpha}\cdot\mathbf{A}(z) + eFz - E\right]\tilde{\boldsymbol{\chi}}(z) = 0\,, \tag{3}$$

where $\mathcal{H}_0$ is given by Equation 2. To address this problem we shall follow the Feynman–Gell-Mann ansatz [32] and define a new four-component vector $\boldsymbol{\psi}(z)$ as

$$\tilde{\boldsymbol{\chi}}(z) = \left[\mathcal{H}_0 + ev\boldsymbol{\alpha}\cdot\mathbf{A}(z) - eFz + E\right]\boldsymbol{\psi}(z). \tag{4}$$

It is convenient to introduce the following dimensionless quantities $\boldsymbol{\kappa}_\perp = \mathbf{k}_\perp d$, $\xi = z/d$, $\varepsilon = E/\Delta$, $f = eFd/\Delta$, and $b = eBd^2/\hbar$. Notice that $f/2$ is the ratio between the electric potential drop across the spatial extent of the midgap states $d = \hbar v/\Delta$ in the absence of fields and the magnitude of the fundamental gap 2Δ. Similarly, b is the square of the ratio between d and the magnetic length $\ell = \sqrt{\hbar/eB}$. Hereafter we shall consider $b > f \geq 0$ for reasons that will become clear shortly. Let us define

$$\begin{aligned} p &= \frac{1}{2\mu^2}\left(\varepsilon^2 - \boldsymbol{\kappa}_\perp^2 - 1 + \frac{\left(\kappa_x b - \varepsilon f\right)^2}{\mu^4}\right), \\ s &= -\sqrt{2}\mu\left(\xi - \frac{\kappa_x b - \varepsilon f}{\mu^4}\right), \end{aligned} \tag{5}$$

where $\mu = (b^2 - f^2)^{1/4}$ is real. Then, inserting the ansatz (Equation 4) in Equation 3 and taking into account Equation 5, we get

$$\left[-\frac{d^2}{ds^2}+\frac{s^2}{4}-p+\mathcal{M}\right]\boldsymbol{\psi}(s)=\delta(s-s_0)\mathcal{N}\boldsymbol{\psi}(s), \quad (6)$$

where $s_0 \equiv s(\xi = 0)$. Here $\mathcal{M}$ and $\mathcal{N}$ are 4 × 4 matrices given by

$$\mathcal{M}=-\frac{\mathrm{i}}{2\mu^2}(b\alpha_x-f)\alpha_z, \qquad \mathcal{N}=\mathrm{i}\frac{\sqrt{2}}{\mu}\alpha_z\beta. \quad (7)$$

Let us diagonalize the left-hand side of the equation by introducing a unitary matrix U such that $\mathcal{M}=U(\beta/2)U^{-1}$. Doing so and defining $\mathcal{W}=U^{-1}\mathcal{N}U$ and $\boldsymbol{\phi}(s)=U^{-1}\boldsymbol{\psi}(s)$ we obtain

$$\left[-\frac{d^2}{ds^2}+\frac{s^2}{4}-p+\frac{1}{2}\beta\right]\boldsymbol{\phi}(s)=\delta(s-s_0)\mathcal{W}\boldsymbol{\phi}(s). \quad (8)$$

In order to solve Equation 8 we shall use the Green's function method. The solution to Equation 8 will be given by

$$\begin{aligned}\boldsymbol{\phi}(s)&=\int_{-\infty}^{\infty}ds'\,G(s,s')\delta(s'-s_0)\mathcal{W}\boldsymbol{\phi}(s')\\&=G(s,s_0)\mathcal{W}\boldsymbol{\phi}(s_0),\end{aligned} \quad (9)$$

where the retarded Green's function $G(s,s')$ satisfies

$$\left[-\frac{\partial^2}{\partial s^2}+\frac{s^2}{4}-p+\frac{1}{2}\beta\right]G(s,s')=\delta(s-s')\,\mathbb{1}_4, \quad (10)$$

and $G(s,s')\to 0$ as $|s|,|s|'\to\infty$. Note that $G(s,s')$ is continuous on the line $s = s'$. Equation 9 can be particularized for $s = s_0$, leading to a homogeneous system of equations with non-trivial solutions existing for energies satisfying the vanishing of the determinant

$$\det\left[\mathbb{1}_4-G(s_0,s_0)\mathcal{W}\right]=0. \quad (11)$$

Since $G(s,s')$ can be considered as the inverse of the operator that acts upon it and the latter is diagonal, we may consider $G(s,s')$ to be block diagonal. Hence,

$$G(s,s')=\begin{pmatrix}g_+(s,s')\,\mathbb{1}_2 & \mathbb{0}_2\\ \mathbb{0}_2 & g_-(s,s')\,\mathbb{1}_2\end{pmatrix}, \quad (12)$$

where $\mathbb{0}_2$ is the 2 × 2 null matrix and the scalar functions $g_\pm(s,s')$ satisfy

$$\left[-\frac{\partial^2}{\partial s^2}+\frac{s^2}{4}-p_\pm\right]g_\pm(s,s')=\delta(s-s'), \quad (13)$$

with $p_\pm = p \mp 1/2$. Since s is real because we have chosen μ to be so, then $s^2 > 0$ and this equation corresponds to a harmonic oscillator. Notice that this would not be the case if μ were imaginary as in that case $s^2 < 0$ and we would not have the positive parabola required for a harmonic oscillator. The solution to this problem is known to be [33,34]

$$g_\pm(s,s')=\frac{1}{\sqrt{2\pi}}\Gamma\left(\frac{1}{2}-p_\pm\right)D_{p_\pm-1/2}(s_>)D_{p_\pm-1/2}(-s_<), \quad (14)$$

where $\Gamma(z)$ is the Gamma function, $D_\gamma(z)$ is the parabolic-cylinder function, $s_> = \max(s,s')$ and $s_< = \min(s,s')$. Now that we have $G(s,s')$, it is straightforward to obtain from Equation 11 that $g_+(s_0,s_0)g_-(s_0,s_0) = \mu^2/2$. Equivalently

$$D_p(s_0)D_p(-s_0)D_{p-1}(s_0)D_{p-1}(-s_0)+\frac{\pi\mu^2}{p\Gamma^2(-p)}=0. \quad (15)$$

Equation 15 determines the dispersion relation $\varepsilon(\boldsymbol{\kappa})$ of midgap interface states as well as Landau levels lying in the semiconductor bands. It reduces to the result found by Agassi when the electric field vanishes [23].

Results and Discussion

Energy levels in the absence of electric field

This section is added for completeness and essentially reproduces the results found by Agassi [23] for small values of κ_x. However, we will be able to give approximate dispersion relations for the midgap state and the Landau levels that will provide us with a clearer view of the effect of the magnetic field in our case of interest. This section then corresponds to the $f = 0$ case, where approximate results can be obtained. In fact, these results are exact when $\kappa_x = 0$, where $s_0 = 0$. Let us explore this last case. Using $\Gamma(1+z) = z\Gamma(z)$ and the Legendre duplication formula $\Gamma(2z)=2^{2z-1}\Gamma(z)\Gamma(z+1/2)/\sqrt{\pi}$, it is straightforward to obtain from Equation 15

$$\frac{1+2p\mu^2}{p^2\Gamma^2(-p)}=0. \quad (16)$$

There are now two possibilities, either the numerator goes to zero or the denominator goes to infinity. If $p < 0$, it is neces-

sary to have a numerator equal to zero, which amounts to having,

$$\varepsilon = \pm\kappa_y \ . \tag{17}$$

This is nothing but a Dirac linear dispersion in the *y*-direction. It is remarkable that the Dirac point remains robust for any strength of *b*. Taking into account the definition of *p*, the case where $p < 0$ corresponds to $|\varepsilon| < 1$ at $\kappa_x = \kappa_y = 0$, meaning that these states lie within the gap.

Let us explore other possibilities. If $p = 0$, then both the numerator and the denominator are finite, which implies that $p = 0$ is not a solution. The other option where $p > 0$ is only achieved if the denominator goes to infinity because the numerator is always positive in this case. For this to happen, *p* must be a positive integer. The corresponding energies are the usual Landau levels of a relativistic particle

$$\varepsilon = \pm\sqrt{1+2nb+\kappa_y^2}\ , \qquad n = 1,2,\ldots \tag{18}$$

There is no zero Landau level because the requirement of $p > 0$ implies $|\varepsilon| > 1$ at $\kappa_x = \kappa_y = 0$, that is, Landau levels exist outside the gap. With this results in mind, we can now turn to the case where $\kappa_x \neq 0$, but $s_0 \to 0$. After some tedious algebra we arrive at the following expression:

$$\frac{1}{p^2\Gamma^2(-p)}\left\{1+2p\mu^2-s_0^2 p\left[\eta(p)+\frac{1}{\eta(p)}\right]\right\}=0\,, \tag{19}$$

where

$$\eta(p)=\frac{p}{2}\left[\frac{\Gamma(-p/2)}{\Gamma(1/2-p/2)}\right]^2 . \tag{20}$$

If $s_0 = 0$ we obtain again Equation 16, corresponding to $\kappa_x = 0$. Now if $\kappa_x \neq 0$, then either the term in curly brackets is zero or the prefactor multiplying this term is zero. As before, if the prefactor is zero then *p* is a positive integer. However, that would imply two possible energies for each integer, but numerically we will show briefly that this is not the case. Thus, we must consider the term in curly brackets to be equal to zero. If we consider $b \to 0$, but at the same time $\kappa_x \to 0$ sufficiently fast so that $s_0 \to 0$, then it is not difficult to obtain for the states inside the gap

$$\varepsilon = \pm\sqrt{\left(1-\frac{5b^2}{4}\right)\kappa_x^2+\kappa_y^2}\ , \tag{21}$$

whereas for the Landau levels we obtain to lowest order in κ_x

$$\varepsilon = \pm\sqrt{1+2nb+\kappa_y^2 \pm\sqrt{\frac{8nbc(n)}{1+2nb}}\kappa_x}\ , \tag{22}$$

where $c(n)$ results from the expansion around integer values of *p* of $\eta(p) + \eta^{-1}(p) + 2 \approx c(n)(p-n)^{-2}$. For instance, $c(1) = 2/\pi$, $c(2) = 1/\pi$, $c(3) = 3/2\pi$,… Before we consider each case, it is important to mention that the approximation of low *b* corresponds to the range of interest in experiments since typically *d* ≈ 4.5 nm and as a result $b = 0.5$ corresponds to a very large magnetic field of about 16 T.

Let us now consider each case separately. On the one hand, Equation 21 corresponds to an elliptic cone and for $b = 0$ we recover the original Dirac cone. It is not only remarkable, as we mentioned above, that the Dirac point is robust, but also that the shape of the dispersion relation remains a cone but slightly widened in the *x*-direction, as shown in Figure 2. Hence, the Fermi velocity becomes anisotropic and can actually be modulated with the magnetic field. It is expected that the application of an electric field will lead to further reduction of the Fermi velocity [25]. We will prove later that this is actually the case.

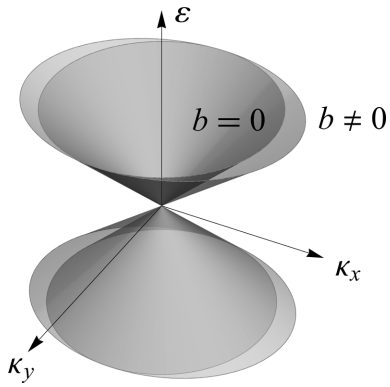

Figure 2: Dirac cones with, $b \neq 0$, and without, $b = 0$, a magnetic field applied. The original cone is distorted along the *x*-direction and the Fermi velocity, i.e., the slope, becomes anisotropic.

In Figure 3a we show a comparison between the Fermi velocity in the *x*-direction (recall that it does not change in the *y*-direction) given by the numerical evaluation of Equation 15 and the approximation in Equation 21. The agreement is noteworthy for low values of *b*.

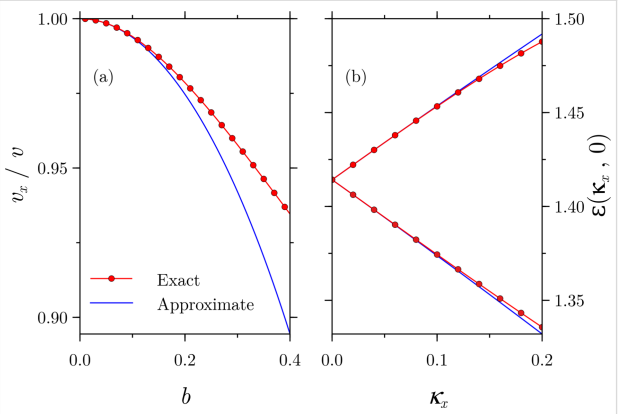

Figure 3: Comparison between exact and approximate results given by (a) Equation 21 and (b) Equation 22. In panel (a) the Fermi velocity along the *x*-direction, calculated as the slope of the dispersion relation, is substantially reduced and the agreement between the exact and approximate results is noteworthy up to $b \leq 0.2$. In panel (b), the Landau level splitting in the *x*-direction is very well predicted even for $b = 0.5$, as shown for the first level.

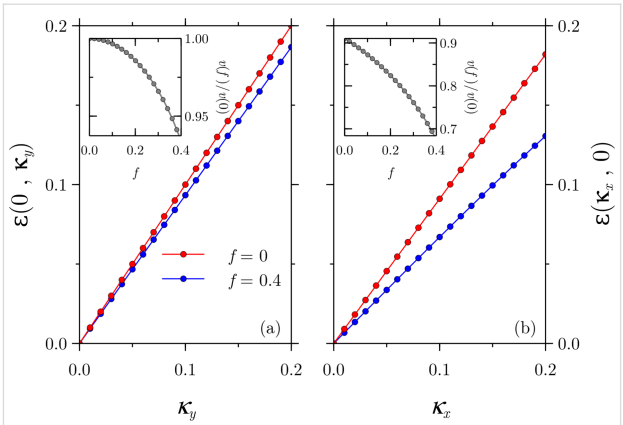

Figure 4: The additional effect of the electric field leads to a further reduction of the Fermi velocity in the *x*-direction and to a reduction along the *y*-direction as well. The Dirac point, however, remains robust. The insets show the Fermi velocity reduction as a function the electric field for a fixed magnetic field of $b = 0.5$.

We can now focus on the Landau levels given by Equation 22. As it can be seen, for non-zero values of κ_x, each Landau level at $\kappa_x = 0$ splits into two Landau levels at $\kappa_x \neq 0$ due to the occurrence of a "±"-sign inside the square root. The comparison for the first Landau level, $n = 1$, between the approximate result and the numerical calculations from Equation 15 are shown in Figure 3b. In contrast to Figure 3a, there is still agreement between both approaches for a large field of $b = 0.5$.

Energy levels at finite electric field

Let us now bring our attention to the case of $f \neq 0$. In contrast to the case of $f = 0$, we have been unable to obtain explicit expressions of the dispersion relation, but the numerics shows remarkable results. Let us focus first on the midgap states. Since the magnetic field did not erase the Dirac point and based on known results of a band-inverted junction under an electric field [25,28], it seems plausible to argue that the effect of the electric field will be to enhance the reduction of the Fermi velocity in the *x*-direction and to introduce a reduction in the *y*-direction as well, leaving however the Dirac point untouched. This is indeed what we observe and we show our results in Figure 4. The insets show the Fermi velocity reduction as a function of the electric field for a fixed value of $b = 0.5$. It is remarkable how the Fermi velocity along the *x*-direction is substantially decreased in band-inverted junctions subject to crossed magnetic and electric fields.

We may now turn to the evolution of the Landau levels as a function of the electric field. For simplicity, we shall consider only the first Landau level. It is illustrative to consider first the evolution of the lowest point of the Landau bands, that is, $\boldsymbol{\kappa}_\perp = 0$. If the electric field is zero, we already know what the energy will be from the discussion above. However, as we turn on the electric field, a splitting similar to the one we had with κ_x begins to develop. This splitting increases with electric field, up to a point where it starts decreasing again as *f* approaches *b*. In the limiting case where $f \to b$, the splitting goes to zero, as we show in Figure 5 for $b = 0.5$.

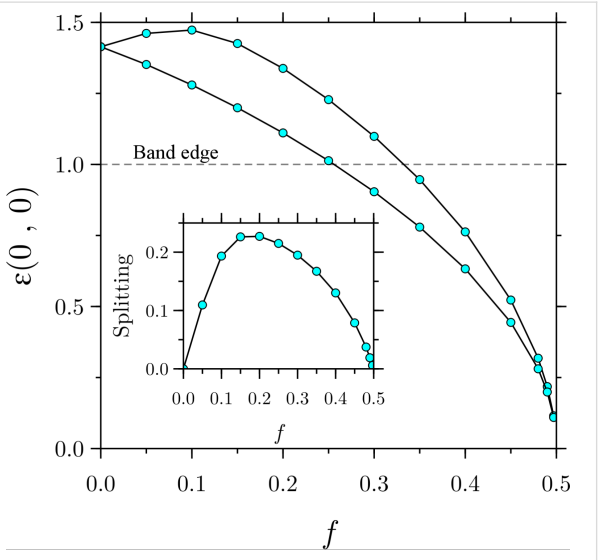

Figure 5: Splitting of the Landau levels at $\mathbf{k}_\perp = 0$ and $b = 0.5$ as a function of the electric field. It is important to note that the Landau levels move below the band edge due to the bending by the electric field (see main text for details).

In Figure 5 it may be surprising to see that the Landau bands shift below the band edge, leading to the apparent and erroneous belief that the latter enter the band gap. The effect of the electric field is to bend the constant band edges shown in Figure 1a upwards due to the presence of the electrostatic

potential eFz, and so the Landau levels of the conduction band can move towards lower energies as long as the corresponding wave functions are not inside the band gap in position space.

Finally, it deserves consideration the previous discussion for low values of $\boldsymbol{\kappa}_\perp$. As we can see in Figure 6, the parabolic dispersion that we obtained in the y-direction in the absence of an electric field splits into two parabolic bands. However, it is more remarkable to see that, instead of obtaining a splitting similar to that in Figure 3b, the dispersion goes downwards.

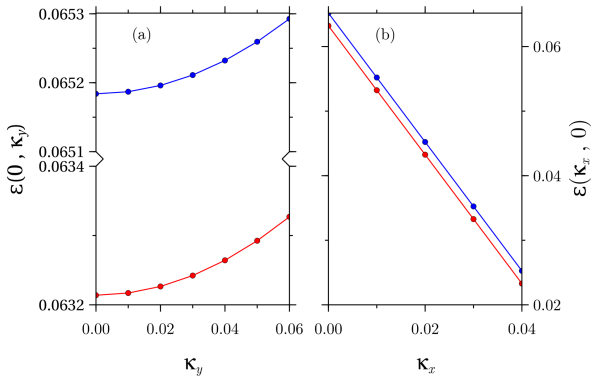

Figure 6: First Landau level dispersions for b = 0.5 and f =0.499. In panel (a), the original parabolic dispersion along the y-direction splits into two parabolic dispersions with energies below the band edge for the chosen fields, whereas in panel (b), the previously obtained splitting in the x-direction is now exclusively downwards.

Electron states under perpendicular electric and magnetic fields

In the previous sections we considered electron states when the magnetic field is parallel to the band-inverted junction, as depicted in Figure 1. For completeness, we now briefly discuss the salient features of the energy spectrum when the electric and magnetic fields are both perpendicular to the junction. The vector potential is then given as $\mathbf{A}(x) = Bx\hat{\mathbf{y}}$ in the Landau gauge and thus $\mathbf{B} = B\hat{\mathbf{z}}$. Starting from the Dirac Equation 3 with this vector potential and using the Feynman–Gell-Mann ansatz (Equation 4), one is led to a two-dimensional Schrödinger equation in the XZ plane. The resulting equation turns out to be separable in the x and z coordinates and can be straightforwardly solved by Green's function techniques. At low or moderate electric and magnetic fields ($f < b < 1$), the energy levels within the gap are found to be

$$\varepsilon = \pm\sqrt{2nb}\left(1-\frac{5}{8}f^2\right), \tag{23}$$

where n = 0, 1,… The above expression resembles the Landau levels of relativistic particles for an effective dimensionless magnetic field $b_{\text{eff}} \equiv b(1 - 5f/8)^2 \approx b(1 - 5f/4)$. Therefore, the electric field decreases the Landau level spacing as in the previous field configuration. There is yet another way of interpreting this result. If we undo the change of variables, we obtain for the energy the usual expression for the Landau levels that develop from a Dirac cone, the same as in graphene,

$$E = \pm v_{\text{F}}(F)\sqrt{2eB\hbar n}\,, \tag{24}$$

but with a renormalized Fermi velocity,

$$v_{\text{F}}(F) \equiv v\left(1-\frac{5F^2}{8F_{\text{C}}^2}\right), \tag{25}$$

where $F_{\text{C}} = \Delta/ed$. In [25], it was anticipated that this renormalization of the Fermi velocity in a band-inverted junction with a perpendicular electric field could be measured by means of magnetotransport experiments, a prediction that is confirmed here.

Conclusion

We have studied band-inverted junctions under crossed electric and magnetic fields, the electric field being applied along the growth direction. Electron states are described by a spinful two-band model that is equivalent to the Dirac model for relativistic electrons. The mass term is half the bandgap and changes its sign across the junction. For the sake of algebraic simplicity, we assumed same-sized and aligned gaps, although this is not a serious limitation to the validity of the results [28].

In the absence of external fields, it is well known that band-inverted junctions support topologically protected states located at the interface. Their energy lies within the common gap of the two semiconductors and the dispersion relation is a Dirac cone [13,15,16,20]. The Dirac cone remains even if an electric field perpendicular to the junction is applied, but it widens and the Fermi velocity is quadratically reduced with the electric field [25,28]. In this paper we have proved that electrons with energy within the gap still behave as massless fermions when an additional magnetic field parallel to the band-inverted junction is applied. The original Dirac cone widens only in the direction perpendicular to the magnetic field but remarkably the dispersion relation remains gapless. Hence, the Fermi velocity becomes anisotropic and the combination of both electric and magnetic fields allows the Fermi velocity to be finely tuned. In addition, states lying within the semiconductor bands display relativistic-like Landau levels that split upon the application of the magnetic and electric fields. Interestingly, if both fields are parallel to the growth direction, the Landau level spacing can be

further reduced by the electric field. We expect that the control of the Fermi velocity of topologically protected states will have applications for the design of novel electronic devices based on topological materials.

Acknowledgements

The authors thank L. Chico and J. W. González for helpful discussions. This work was supported by the Spanish MINECO under grant MAT2016-75955.

ORCID® iDs

Álvaro Díaz-Fernández - https://orcid.org/0000-0001-9432-7845
Natalia del Valle - https://orcid.org/0000-0001-7751-5422
Francisco Domínguez-Adame - https://orcid.org/0000-0002-5256-4196

References

1. Thouless, D. J.; Kohmoto, M.; Nightingale, M. P.; den Nijs, M. *Phys. Rev. Lett.* **1982,** *49,* 405. doi:10.1103/PhysRevLett.49.405
2. Kane, C. L.; Mele, E. J. *Phys. Rev. Lett.* **2005,** *95,* 146802. doi:10.1103/PhysRevLett.95.146802
3. Bernevig, B. A.; Hughes, T. L.; Zhang, S.-C. *Science* **2006,** *314,* 1757. doi:10.1126/science.1133734
4. Chu, J.; Sher, A. *Physics and Properties of Narrow Gap Semiconductors;* Springer: Berlin, Germany, 2008; p 157.
5. König, M.; Wiedmann, S.; Brüne, C.; Roth, A.; Buhmann, H.; Molenkamp, L. W.; Qi, X.-L.; Zhang, S.-C. *Science* **2007,** *318,* 766. doi:10.1126/science.1148047
6. Gusev, G. M.; Kvon, Z. D.; Shegai, O. A.; Mikhailov, N. N.; Dvoretsky, S. A.; Portal, J. C. *Phys. Rev. B* **2011,** *84,* 121302. doi:10.1103/PhysRevB.84.121302
7. Grabecki, G.; Wróbel, J.; Czapkiewicz, M.; Cywiński, Ł.; Gierałtowska, S.; Guziewicz, E.; Zholudev, M.; Gavrilenko, V.; Mikhailov, N. N.; Dvoretski, S. A.; Teppe, F.; Knap, W.; Dietl, T. *Phys. Rev. B* **2013,** *88,* 165309. doi:10.1103/PhysRevB.88.165309
8. Hsieh, T. H.; Lin, H.; Li, J.; Duan, W.; Bansil, A.; Fu, L. *Nat. Commun.* **2012,** *3,* 982. doi:10.1038/ncomms1969
9. Dziawa, P.; Kowalski, B. J.; Dybko, K.; Buczko, R.; Szczerbakow, A.; Szot, M.; Łusakowska, E.; Balasubramanian, T.; Wojek, B. M.; Berntsen, M. H.; Tjernberg, O.; Story, T. *Nat. Mater.* **2012,** *11,* 1023. doi:10.1038/nmat3449
10. Okada, Y.; Serbyn, M.; Lin, H.; Walkup, D.; Zhou, W.; Dhital, C.; Neupane, M.; Xu, S.; Wang, Y. J.; Sankar, R.; Chou, F.; Bansil, A.; Hasan, M. Z.; Wilson, S. D.; Fu, L.; Madhavan, V. *Science* **2013,** *341,* 1496. doi:10.1126/science.1239451
11. Serbyn, M.; Fu, L. *Phys. Rev. B* **2014,** *90,* 035402. doi:10.1103/PhysRevB.90.035402
12. Phuphachong, T.; Assaf, B. A.; Volobuev, V. V.; Bauer, G.; Springholz, G.; de Vaulchier, L.-A.; Guldner, Y. *Crystals* **2017,** *7,* 29. doi:10.3390/cryst7010029
13. Volkov, B. A.; Pankratov, O. A. *Sov. Phys. - JETP* **1985,** *42,* 178.
14. Korenman, V.; Drew, H. D. *Phys. Rev. B* **1987,** *35,* 6446. doi:10.1103/PhysRevB.35.6446
15. Agassi, D.; Korenman, V. *Phys. Rev. B* **1988,** *37,* 10095. doi:10.1103/PhysRevB.37.10095
16. Pankratov, O. A. *Semicond. Sci. Technol.* **1990,** *5,* S204. doi:10.1088/0268-1242/5/3S/045
17. Kolesnikov, A. V.; Silin, A. P. *J. Phys.: Condens. Matter* **1997,** *9,* 10929. doi:10.1088/0953-8984/9/49/012
18. Kriechbaum, M. Envelope Function Calculations for Superlattices. In *Two-Dimensional Systems: Physics and New Devices;* Bauer, G.; Kuchar, F.; Heinrich, H., Eds.; Springer: Berlin, Germany, 1986; pp 120–129.
19. Ando, Y.; Fu, L. *Annu. Rev. Condens. Matter Phys.* **2015,** *6,* 361. doi:10.1146/annurev-conmatphys-031214-014501
20. Domínguez-Adame, F. *Phys. Status Solidi B* **1994,** *186,* K49. doi:10.1002/pssb.2221860231
21. Zhang, F.; Kane, C. L.; Mele, E. J. *Phys. Rev. B* **2012,** *86,* 081303. doi:10.1103/PhysRevB.86.081303
22. Tchoumakov, S.; Jouffrey, V.; Inhofer, A.; Bocquillon, E.; Plaçais, B.; Carpentier, D.; Goerbig, M. O. *Phys. Rev. B* **2017,** *96,* 201302. doi:10.1103/PhysRevB.96.201302
23. Agassi, D. *Phys. Rev. B* **1994,** *49,* 10393. doi:10.1103/PhysRevB.49.10393
24. Pankratov, O. A.; Pakhomov, S. V.; Volkov, B. A. *Solid State Commun.* **1987,** *61,* 93. doi:10.1016/0038-1098(87)90934-3
25. Díaz-Fernández, A.; Chico, L.; González, J. W.; Domínguez-Adame, F. *Sci. Rep.* **2017,** *8,* 8058. doi:10.1038/s41598-017-08188-3
26. Assaf, B. A.; Phuphachong, T.; Volobuev, V. V.; Inhofer, A.; Bauer, G.; Springholz, G.; de Vaulchier, L. A.; Guldner, Y. *Sci. Rep.* **2016,** *6,* 20323. doi:10.1038/srep20323
27. Xu, S.-Y.; Liu, C.; Alidoust, N.; Neupane, M.; Qian, D.; Belopolski, I.; Denlinger, J. D.; Wang, Y. J.; Lin, H.; Wray, L. A.; Landolt, G.; Slomski, B.; Dil, J. H.; Marcinkova, A.; Morosan, E.; Gibson, Q.; Sankar, R.; Chou, F. C.; Cava, R. J.; Bansil, A.; Hasan, M. Z. *Nat. Commun.* **2016,** *7,* 12505. doi:10.1038/ncomms12505
28. Díaz-Fernández, A.; Domínguez-Adame, F. *Phys. E (Amsterdam, Neth.)* **2017,** *93,* 230. doi:10.1016/j.physe.2017.06.026
29. Kriechbaum, M.; Ambrosch, K. E.; Fantner, E. J.; Clemens, H.; Bauer, G. *Phys. Rev. B* **1984,** *30,* 3394. doi:10.1103/PhysRevB.30.3394
30. Buczko, R.; Cywiński, Ł. *Phys. Rev. B* **2012,** *85,* 205319. doi:10.1103/PhysRevB.85.205319
31. Díaz-Fernández, A.; Chico, L.; Domínguez-Adame, F. *J. Phys.: Condens. Matter* **2017,** *29,* 475301. doi:10.1088/1361-648X/aa91a6
32. Feynman, R. P.; Gell-Mann, M. *Phys. Rev.* **1958,** *109,* 193. doi:10.1103/PhysRev.109.193
33. Domínguez-Adame, F. *Europhys. Lett.* **1991,** *15,* 569. doi:10.1209/0295-5075/15/6/001
34. Glasser, M. L.; Nieto, L. M. *Can. J. Phys.* **2015,** *93,* 1588. doi:10.1139/cjp-2015-0356

BEILSTEIN JOURNAL OF NANOTECHNOLOGY

Robust topological phase in proximitized core–shell nanowires coupled to multiple superconductors

Tudor D. Stanescu[1], Anna Sitek[2,3] and Andrei Manolescu[*3]

Full Research Paper

Open Access

Address:
[1]Department of Physics and Astronomy, West Virginia University, Morgantown, WV 26506, USA, [2]Department of Theoretical Physics, Faculty of Fundamental Problems of Technology, Wroclaw University of Science and Technology, Wroclaw, 50-370, Poland and [3]School of Science and Engineering, Reykjavik University, Menntavegur 1, IS-101 Reykjavik, Iceland

Email:
Andrei Manolescu[*] - manoles@ru.is

* Corresponding author

Keywords:
core–shell nanowires; Majorana states; multiple 1D chains; prismatic geometry; topological superconducting phase

Beilstein J. Nanotechnol. **2018,** *9,* 1512–1526.
doi:10.3762/bjnano.9.142

Received: 03 December 2017
Accepted: 13 April 2018
Published: 22 May 2018

This article is part of the Thematic Series "Topological materials".

Guest Editor: J. J. Palacios

Abstract

We consider core–shell nanowires with prismatic geometry contacted with two or more superconductors in the presence of a magnetic field applied parallel to the wire. In this geometry, the lowest energy states are localized on the outer edges of the shell, which strongly inhibits the orbital effects of the longitudinal magnetic field that are detrimental to Majorana physics. Using a tight-binding model of coupled parallel chains, we calculate the topological phase diagram of the hybrid system in the presence of non-vanishing transverse potentials and finite relative phases between the parent superconductors. We show that having finite relative phases strongly enhances the stability of the induced topological superconductivity over a significant range of chemical potentials and reduces the value of the critical field associated with the topological quantum phase transition.

Introduction

The intense ongoing search for Majorana zero modes (MZMs) in solid states systems is motivated, in part, by the perspective of using them as a platform for fault-tolerant topological quantum computation [1-4]. Several practical realizations of "synthetic" topological superconductors that host zero-energy Majorana modes have been proposed in the past few years, the most promising involving semiconductor-superconductor hybrid systems [5-9]. The basic idea [10-13] is to proximity-couple a semiconductor nanowire with strong Rashba-type spin-orbit coupling (e.g., InSb or InAs) to a standard s-type superconductor (e.g., NbTiN or Al) in the presence of a longitudinal magnetic field. The system is predicted to host zero-energy Majorana modes localized at the two ends of the nanowire [5,7,8]. These zero-energy states combine equal proportions of electrons and holes and are created by second quantized operators satisfying the "Majorana condition" $\gamma^{\dagger} = \gamma$. The topological character of these modes endows them with robustness against perturbations that do not close the superconductor gap, e.g.,

weak interactions, wire bending, a certain amount of disorder, etc.

The most straightforward experimental signature of a Majorana mode is a zero-bias conductance peak that is produced in a charge transport measurement by tunneling electrons between the semiconductor wire and external electrodes attached to its ends [14-24]. These experiments have provided strong indications regarding the presence of Majorana bound states at the end of the wire, but no clear evidence of a phase transition to the topological phase, as revealed by the closing of the bulk quasiparticle gap [10-13], or evidence of correlated features at the opposite ends of the wire [25].

Ideally, the MZMs are hosted by a one-dimensional (1D) p-wave superconductor. However, the experimental realization and detection of these modes involve 3D nanowires [26]. The most common materials are InSb and InAs due to their large g-factor and strong SOC. The wires are grown by bottom-up methods and have usually a prismatic shape with a hexagonal cross section, as determined by the crystal structure [27]. The finite cross section of the wires used in the experiments may generate additional phenomena, which are not captured by ideal 1D models. In particular, the orbital effects of the magnetic field, which is oriented parallel to the nanowire, may reduce or even destroy the stability of the Majorana modes [28].

Proximitized core–shell nanowires are slightly more complex systems recently shown [29] to have interesting Majorana physics that is practically immune to orbital effects. With a conductive shell and an insulating core, such heterostructures become tubular conductors. The prismatic shape of the core–shell wires implies that the cross section of the shell can be seen as a polygonal ring. This is an interesting geometry because the corners of the polygon act like quantum wells where the states with the lowest energies are localized. Furthermore, a group of states with higher energies is localized on the sides of the polygon [30]. Although most of the core–shell nanowires have a hexagonal profile, square [31] or triangular [32-36] cross sections can also be obtained. The core diameter is typically between 50–500 nm and the shell thickness is between 1–20 nm. For all these geometries, the edge states corresponding to corner localization represent better approximations of the ideal 1D limit than the states hosted by a full wire. Remarkably, the energy separation between the corner states and the side states increases when the shell thickness is narrow compared to the radius of the wire, and when the corners are sharp. This means that the triangular shell would be the best choice for the realization of 1D edge channels. For example, with a shell thickens of 8–10 nm and a radius of 50 nm the energy separation between corner and side states can be between 50–100 meV [29,37]. In this case the corner states are extremely robust to orbital effects of the magnetic field and the low-energy subspace is well separated from higher-energy states. Another interesting aspect of a prismatic shell is that it can host several Majorana states at each end of the wire. One can actually view the wire as a set of n coupled chains, each having a pair of Majorana modes at its ends. On the one hand, this results in a rich phase diagram [29], which means that core–shell nanowires provide an interesting playground for studying topological quantum phase transitions. On the other hand, this richness is associated with rather fragile topological phases [29]. In practice, it would be extremely useful to have a knob enabling one to control the robustness of topological superconducting phase.

In this work we show that coupling a core–shell nanowire to two or more parent superconductors with non-vanishing relative phases enhances the stability of the topological phase and lowers the critical magnetic field associated with the (lowest field) topological quantum phase transition. In principle the phase difference between superconductors can be achieved either by applying an additional magnetic field, i.e., other than the longitudinal field needed for the Zeeman energy, or by driving a supercurrent through the superconductors. Hence, by controlling the relative phases of the parent superconductors coupled to the wire one can stabilize the topological superconducting phase that hosts the zero-energy Majorana modes and one can obtain an additional experimental knob for exploring a rich phase diagram and observing potentially interesting low-energy physics.

The rest of this article is organized as follows. We first describe the coupled-chains tight binding model that we use in our numerical analysis. Then, using this simple model, we study the topological phase diagram of (infinite) core–shell wires with triangular and square cross section coupled to superconductors having the same superconducting phase. Next, we show that a finite phase difference can stabilize the topological phase in both triangular and square geometries. In addition, we show that the critical field associated with the (low-field) topological quantum phase transition can be made arbitrarily low. The implications of these findings for the stability of the Majorana modes emerging in finite wires is discussed in the subsequent section. Next, we corroborate our results for the topological phase diagram using an alternative "geometric" model. Finally, we summarize our findings and present our main conclusions.

The Coupled-chains Tight-binding Model

We start by formulating the effective thigh-binding model that describes the low-energy physics of a core–shell nanowire with

n edges. The model has already been introduced for triangular core–shell nanowires in [29] (Appendix), and also previously considered by other authors, in different forms, for ladder systems [38,39]. A "coarse-grained" shell is modeled by one chain associated with each vertex and one or more chains corresponding to each side, as shown in Figure 1. Note that the minimal model for a nanowire with n edges consists of $2n$ coupled chains (n for vertexes and n for sides), but more detailed representations can be obtained by increasing the number of chains associated with the sides. A model that takes into account the details of the internal geometry of the wire [29] will be used later in the paper to corroborate the results obtained with this simple tight-binding model. In the numerical calculations we use minimal tight-binding models consisting of 6 (for triangular wires) or 8 (for square wires) parallel chains. Note that the odd chains, $\ell = 1,3,\ldots$, correspond to the corners, while the even chains, $\ell = 2,4,\ldots$, represent the sides.

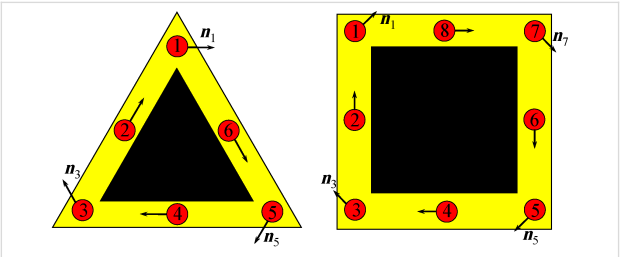

Figure 1: Schematic representation of the chain model for triangular (left) and square (right) core–shell nanowires. The shell (yellow) is coarse-grained so that the vertices and the sides are represented by 1D chains (red circles). The arrows indicate the direction of the effective spin-orbit field $\boldsymbol{n}_\ell$ associated with the (longitudinal) Rashba spin-orbit coupling. In a minimal model each side is represented by one chain (left); a more detailed representation can be obtained by adding more chains associated with the sides (right).

Consider now $2n$ 1D coupled chains proximity-coupled to one or more s-wave superconductors. The superconducting proximity effect is incorporated through the pairing potential Δ_ℓ, $1 \le \ell \le 2n$ associated with each chain. Note that, in principle, the induced pairing potential may be chain-dependent. The low-energy physics of the hybrid structure is described by the following Bogoliubov–de Gennes (BdG) Hamiltonian:

$$
\begin{aligned}
H = & -t\sum_{i,\ell,\sigma}\left(c^{\dagger}_{i+1\ell\sigma}c_{i\ell\sigma}+h.c.\right)-t'\sum_{i,\ell,\sigma}\left(c^{\dagger}_{i\ell+1\sigma}c_{i\ell\sigma}+h.c.\right)\\
& +\sum_{i,\ell,\sigma}\left[V_{\mathrm{eff}}\left(\ell\right)-\mu\right]c^{\dagger}_{i\ell\sigma}c_{i\ell\sigma}+\varepsilon_0\sum_{i,\sigma}\sum_{\ell}^{(\mathrm{even})}c^{\dagger}_{i\ell\sigma}c_{i\ell\sigma}\\
& +\frac{i}{2}\sum_{i,\ell}\left[\alpha c^{\dagger}_{i+1\ell}\left(\hat{\boldsymbol{\sigma}}\cdot\boldsymbol{n}_\ell\right)c_{i\ell}+\alpha' c^{\dagger}_{i\ell+1}\hat{\sigma}_z c_{i\ell}+h.c.\right]\\
& +\Gamma_B\sum_{i,\ell}c^{\dagger}_{i\ell}\hat{\sigma}_z c_{i\ell}+\sum_{i,\ell}\left(\Delta_\ell c^{\dagger}_{i\ell\uparrow}c^{\dagger}_{i\ell\downarrow}+\Delta^{*}_{\ell}c_{i\ell\downarrow}c_{i\ell\uparrow}\right),
\end{aligned}
\tag{1}
$$

where $c_{i\ell\sigma}$ is the annihilation operator for an electron with spin projection σ localized on the lattice site i of the chain ℓ and $c_{i\ell}=\left(c_{i\ell\uparrow},c_{i\ell\downarrow}\right)^T$ is the corresponding spinor operator. The first two terms in Equation 1 represent the nearest-neighbor hopping along the chains, with characteristic energy t, and the inter-chain coupling, with characteristic energy t'. In the summations over the chain index ℓ we use the convention $2n + 1 \equiv 1$. The third term of the Hamiltonian (Equation 1) contains a chain-dependent effective potential $V_{\mathrm{eff}}(\ell)$ that incorporates the presence of various external electrostatic fields (e.g., gate potentials) and the chemical potential μ. Note that, in general, $V_{\mathrm{eff}}(\ell)$ breaks the n-fold rotation symmetry of the original nanowire. The term proportional to ε_0 accounts for the fact that the side states have higher energies than the corner states and the parameter $\varepsilon_0 > 0$ controls the energy gap between the two types of states. The next term represents the Rashba type spin-orbit coupling (SOC), with longitudinal and transverse components proportional to α and α′, respectively. The underlying assumption is that the spin-orbit coupling is generated by an effective potential in the shell region due to the presence of the core [29]. The corresponding direction of the spin-orbit field $\boldsymbol{n}_\ell$ for electrons moving along the wire is shown in Figure 1. The next term in Equation 1, $\Gamma_B = g\mu_b B$, corresponds to the Zeeman spin splitting generated by an external magnetic field applied parallel to the wire (e.g., along the z-axis). The last term describes the proximity-induced pairing and takes into account the possibility that pairing potential Δ_ℓ be chain-dependent. We assume that the vertex regions are covered by n different superconductors separated by gaps over the side regions. The corresponding proximity-induced pairing potentials are

$$
\Delta_\ell = \begin{cases} 0 & \text{if } \ell \text{ is even,} \\ \Delta e^{i\phi_\ell} & \text{if } \ell \text{ is odd,} \end{cases} \tag{2}
$$

where ϕ_ℓ, the phase of the superconductor coupled to the vertex ℓ, is an experimentally-controllable quantity. In the numerical calculations presented below we use the following values for the model parameters: t = 5.64 meV, t' = 1.41 meV (or t' = 2.25 meV, when explicitly specified), α = 2.0 meV, α′ = 0.5 meV, ε_0 = 15.0 meV, and Δ = 0.3 meV.

To determine whether a given superconducting phase is topologically trivial or not, we calculate the $\mathbb{Z}_2$ topological index $\mathcal{M}$, i.e., the Majorana number [1],

$$
\mathcal{M} = \mathrm{sign}\left[\mathrm{Pf}\,B(0)\right]\mathrm{sign}\left[\mathrm{Pf}\,B(\pi)\right]. \tag{3}
$$

The trivial and topological superconducting phases are characterized by $\mathcal{M} = +1$ and $\mathcal{M} = -1$, respectively. In Equation 3

Pf[…] represents the Pfaffian [40], while the antisymmetric matrix $B(k)$ is the Fourier transform of the Hamiltonian (Equation 1) in the Majorana basis. The matrix $B(k)$ can be constructed using the particle–hole symmetry of the BdG Hamiltonian [8,41],

$$\mathcal{T}\,\mathcal{H}(k)\,\mathcal{T}^{-1} = \mathcal{H}(-k), \tag{4}$$

where $\mathcal{H}(k)$ is the Fourier transform of the (single particle) Hamiltonian corresponding to Equation 1 and $\mathcal{T} = U_t K$ is the antiunitary time-reversal operator, with U_t a unitary operator and K the complex conjugation. Explicitly, we have

$$B(\Lambda) = \mathcal{H}(\Lambda)U_t\,, \tag{5}$$

where $\Lambda = 0, \pi/a$ are the time-reversal invariant points characterized by the property $\mathcal{H}(-\Lambda) = \mathcal{H}(\Lambda)$. The antisymmetry of $B(k)$ at the time-reversal invariant points, $B^T(\Lambda) = -B(\Lambda)$, is a direct consequence of Equation 4 and Equation 5. Considering that for typical parameter values the Pfaffian is always positive at the boundary of the Brillouin zone, sign[Pf$B(\pi)$] = +1, we conclude that the topological phase boundary is determined by a sign change of Pf$B(0)$. Finally, using the general relation between the Pfaffian of a skew matrix A and its determinant, $[\mathrm{Pf}(A)]^2 = \mathrm{Det}(A)$, we have $\mathrm{Det}\,\mathcal{H}(0) = [\mathrm{Pf}B(0)]^2$. Note that $\mathrm{Det}\,\mathcal{H}(0) = 0$ signals the presence of gapless states. Thus, the phase boundary, which corresponds to a sign change of the Pfaffian, is accompanied by the closing of the quasiparticle gap at $k = 0$.

Results and Discussion

Nanowire coupled to superconductors with no relative phase difference

The emergence of topological superconductivity and zero-energy Majorana bound states in core–shell nanowires coupled to a single superconductor (i.e., in the absence of superconducting phase differences) was discussed in [29]. Here, we summarize the main results, as revealed by the simplified tight-binding model given by Equation 1. First, we consider a triangular system without a symmetry-breaking potential, $V_{\mathrm{eff}}(\ell) = 0$, and no superconducting phase difference, $\phi_\ell = 0$. The corresponding topological phase diagram (as function of the chemical potential and the applied Zeeman field) is shown in panel (A) of Figure 2. The white regions correspond to $\mathcal{M} = +1$ (i.e., topologically trivial phases), while the orange areas represent topologically nontrivial phases with $\mathcal{M} = -1$. The effect of a symmetry-breaking potential is illustrated in panel (B) of Figure 2. While the topology of the phase diagram is the same, the phase boundaries are modified significantly with respect to panel (A). We note that this result was obtained by applying a rather modest symmetry breaking potential with values V_{eff} = (0.67, 0.17, −0.33, −0.33, −0.33, 0.17) meV on the six chains.

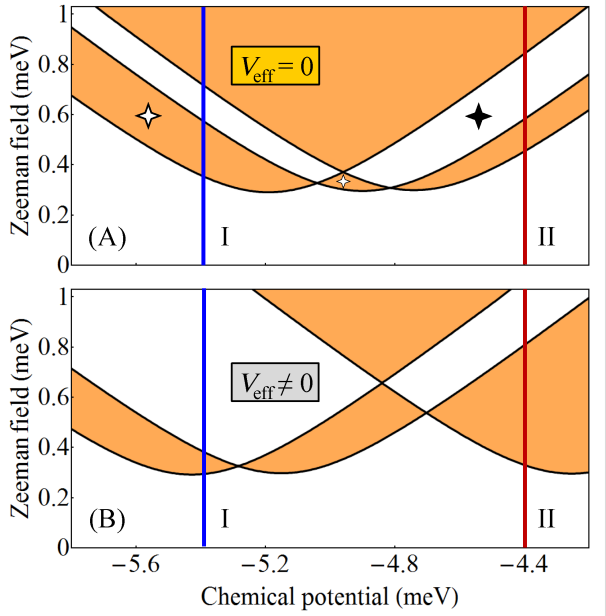

Figure 2: (A) Topological phase diagram for a triangular wire with $V_{\mathrm{eff}}(\ell) = 0$ and $\phi_\ell = 0$. The white areas are topologically trivial and the orange regions are nontrivial. The 4-star symbols indicate gapless superconducting phases. (B) Topological phase diagram for a triangular wire with $V_{\mathrm{eff}}(\ell) \neq 0$ and $\phi_\ell = 0$. The values of the effective potential on the 6 chains are (0.67, 0.17, −0.33, −0.33, −0.33, 0.17) meV. The evolution of the (minimum) quasiparticle gap along the cuts I (blue lines) corresponding to μ = −5.4 meV and II (red lines) corresponding to μ = −4.4 meV are shown in Figure 3 and Figure 4, respectively. See also [29].

To get further insight into the nature of the phases shown in Figure 2, we calculate the minimum quasiparticle energy $E_{\mathrm{min}}(\mu,\Gamma_B)$ along the constant chemical potential cuts I (blue) and II (dark red) marked on the phase diagrams. This energy (which corresponds to the minimum quasiparticle gap) is defined as

$$E_{\mathrm{min}}(\mu,\Gamma_B) = \pm \min_{n,k} |E_n(k)|, \tag{6}$$

where $E_n(k)$ are the eigenvalues of the BdG Hamiltonian from Equation 1. The dependence of E_{min} on the Zeeman field for μ = −5.4 meV (i.e., the blue cuts I in Figure 2) is shown in Figure 3, while the evolution of the minimum gap along the cuts II (dark red) corresponding to μ = −4.4 meV is shown in Figure 4.

At zero Zeeman field, $\Gamma_B = 0$, the system is in a trivial superconducting phase characterized by a quasiparticle gap

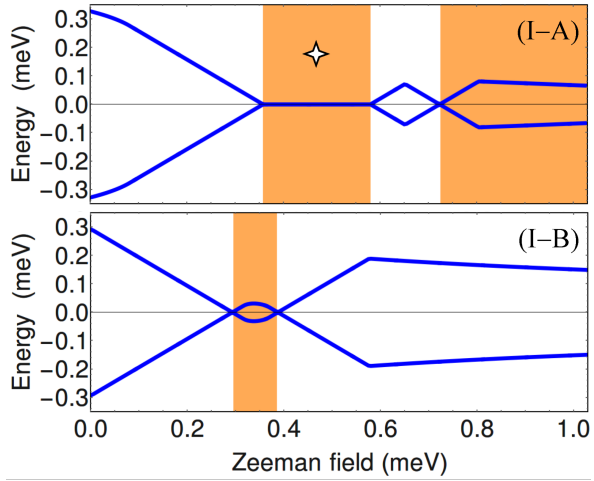

Figure 3: Dependence of the minimum quasiparticle gap on the Zeeman field along the blue cuts (I) corresponding to μ = −5.4 meV in Figure Figure 2. Top: $V_{\text{eff}}(\ell) = 0$, see Figure 2A. Bottom: $V_{\text{eff}}(\ell) \neq 0$, see Figure 2B. The white/orange regions correspond to the trivial/nontrivial phases shown in Figure 2. Note the gapless superconducting phase marked be the 4-star symbol (top panel). See also [29].

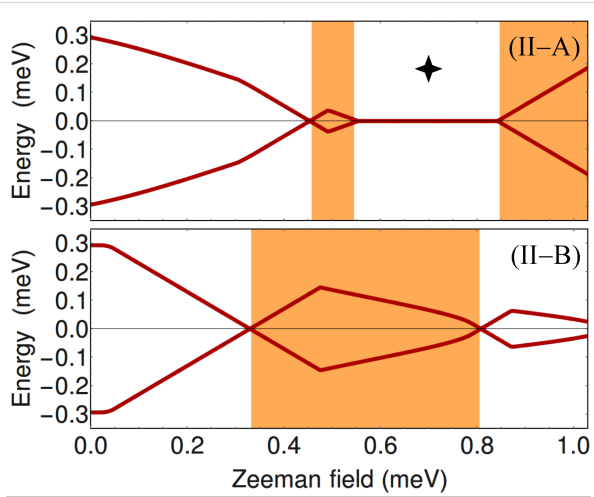

Figure 4: Dependence of the minimum quasiparticle gap on the Zeeman field along the dark red cuts (II) corresponding to μ = −4.4 meV in Figure 2. Top: $V_{\text{eff}}(\ell) = 0$, see Figure 2A. Bottom: $V_{\text{eff}}(\ell) \neq 0$, see Figure 2B. The white/orange regions correspond to the trivial/nontrivial phases shown in Figure 2. Note the gapless superconducting phase marked be the 4-star symbol (top panel). See also [29].

Δ = 0.3 meV (see Figure 3 and Figure 4) given by the value of the induced pairing potential. With increasing Γ_B, the quasiparticle gap reduces and eventually closes at a certain critical Zeeman energy. In the absence of a symmetry breaking potential, the system with μ = −5.4 meV (see cut (I-A) in Figure 2) remains gapless throughout the first (i.e., low-field) orange region, which means that the system becomes a gapless superconductor. Another gapless superconducting phase corresponds to the intermediate white region in panel (II-A) of Figure 4, i.e., for Zeeman fields between approximately 0.55 meV and 0.85 meV. These gapless phases are marked by a 4-star symbol in the phase diagram (see Figure 2A) and in Figure 3(I-A) and Figure 4(II-A). We note that inside the gapless superconducting phases the gap closes at $k \neq 0$. Of course, at the phase boundaries the gap always closes at $k = 0$. Furthermore, by increasing the Zeeman energy above 0.7 meV in panel (I-A) of Figure 3 or above 0.85 meV in panel (II-A) of Figure 4, the system evolves into topological phase with a finite gap.

Upon breaking the three-fold rotation symmetry of the original triangular wire, the gapless superconducting phases become gapped. Also notice in panel (II-B) that the low-field topological phase corresponding to μ = −4.4 meV is now characterized by a sizable quasiparticle gap, indicating a regime which may be more favorable for robust zero-energy Majorana modes. We note that the robust low-field topological phase in panel (II-B) corresponds to a single pair of Majorana modes (i.e., one MZM at each end of the wire) hosted by chain 1 (with the highest value of V_{eff}, while the narrow low-field topological phase in panel (I-B) corresponds to a pair of Majorana modes shared by chains 2 and 3 (the chains with the lowest value of the potential). Note that the expression “hosted by chain 1” (or chains 2 and 3) actually means that most of spectral weight associated with the Majorana wave function is localized on the corresponding chain(s) (also see below, Figure 11 and Figure 13). The wide trivial region above $\Gamma_B \approx 0.4$ meV in panel (I-B) corresponds to a finite system with two pairs of Majorana bound states (on chains 2 and 3). We also note that the low-field phase boundaries converge to a single boundary in the limit of isolated chains, i.e., when the inter-chain hopping energy is much smaller than the hopping along the chains, $t'/t \to 0$. In this case three Majorana pairs would form independently at the ends of each chain, and coexist at zero energy, without “talking” to each other. Physically, the limit $t'/t \to 0$ corresponds an infinitely-thin shell. For finite values of t'/t (corresponding to finite shell thicknesses), the coupling between chains lifts the degeneracy, such that at most one Majorana state can have zero energy, while the other two will acquire finite energy.

The existence of gapless superconducting phases in systems with rotation symmetry is generic, i.e., it holds for $n > 3$. We emphasize that gapless phases cannot host stable Majorana modes and, therefore, they are not suitable for studying Majorana physics. Applying a symmetry-braking potential $V_{\text{eff}}(\ell) \neq 0$ opens a finite gap throughout the entire phase diagram, except, of course, the phase boundaries, where the quasiparticle gap vanishes at $k = 0$. To better illustrate this point, we calculate the topological phase diagram for a square wire with $V_{\text{eff}}(\ell) \neq 0$ and the minimum gap along a representative cut through the phase diagram. The results are shown in

Figure 5. Note that all topologically trivial and nontrivial phases are gapped. However, the gaps are rather small indicating the fact that topological superconductivity (and the corresponding Majorana modes) are not very robust.

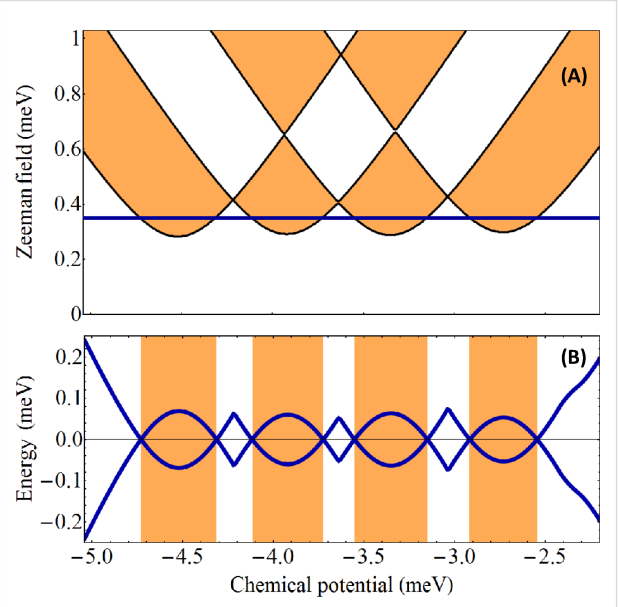

Figure 5: (A) Topological phase diagram for a square wire with $V_{\text{eff}}(\ell) \neq 0$ and $\phi_\ell = 0$. The white areas are topologically trivial and the orange regions are nontrivial. The values of the effective potential on the 8 chains are (0.5, 0, −0.5, −0.5, −0.5, 0, 0.5, 0.5) meV and the inter-chain hopping is $t' = 2.25$ meV. (B) Evolution of the minimum quasiparticle gap along the horizontal cut $\Gamma = 0.35$ meV shown in the top panel.

An important difference between the phase diagram shown in Figure 5 and that in Figure 2 is that for the square wire we have used a larger value of the inter-chain hopping, $t' = 2.25$ meV. Enhancing the coupling between chains widens the low-field topological regions (which would practically vanish in the limit $t'/t \to 0$). Finally, we emphasize that although a finite system with parameters corresponding to a topologically nontrivial phase will support one pair of MZMs (i.e., one Majorana mode at each end of the wire), generically each Majorana mode is hosted by multiple chains (rather than a single chain). For example, in a configuration corresponding to Figure 5, the low-field topological phases with $\mu < 3.7$ meV can support MZMs hosted by chains 3 and 5 (with minimum values of $V_{\text{eff}}(\ell)$), while for $\mu > 3.7$ meV the MZMs are hosted by chains 1 and 7 (corresponding to the maximum values of $V_{\text{eff}}(\ell)$).

Wires coupled with multiple superconductors: the stabilizing role of the phase difference

A critical question that we want to investigate concerns the effect of a nonzero superconducting phase difference in a wire coupled to multiple parent superconductors. A non-zero phase difference was shown to stabilize the topological phase in a Josephson junction across a 2D electron gas with Rashba spin-orbit coupling and in-plane magnetic field [42] and in a topological insulator nanoribbon coupled with two superconductors [43]. Here, for concreteness, we consider a triangular core–shell nanowire modeled by six chains, as described above, which are coupled to three separate superconductors that induce pairing potentials characterized by $\phi_1 = 0$, $\phi_3 = \pi/2$, and $\phi_5 = -\pi/2$. The other parameters are the same as in Figure 2B, i.e., the case $V_{\text{eff}} \neq 0$ discussed above. The corresponding phase diagram is shown in Figure 6. Remarkably, the "crossing points" that characterize the phase diagram in Figure 2 disappear and, upon increasing the Zeeman field, we have an alternance of trivial and nontrivial phases for all values of the chemical potential. More importantly, the low-field topological phase becomes stable for a wide range of chemical potentials, i.e., it is characterized by a

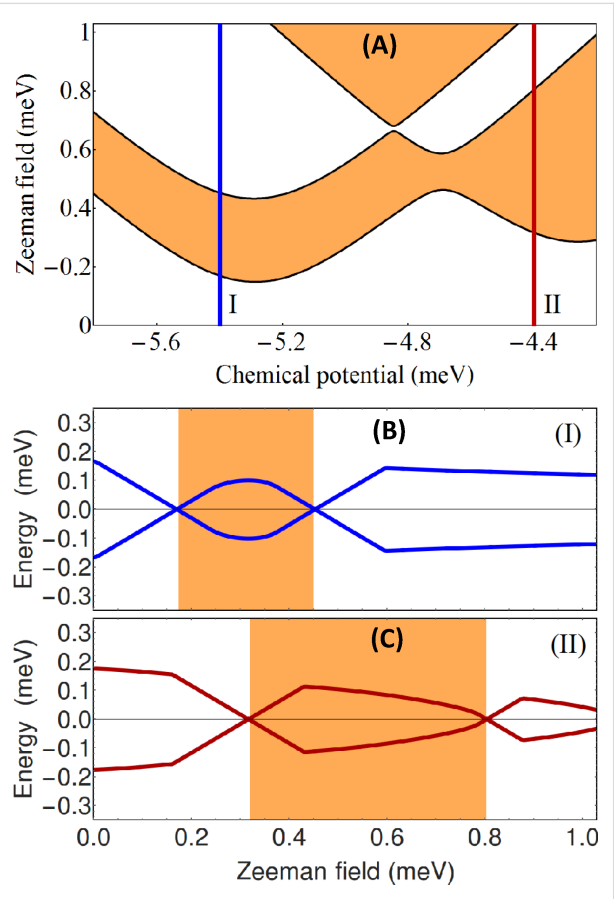

Figure 6: (A) Topological phase diagram for a triangular wire with $V_{\text{eff}}(\ell) \neq 0$ and $\phi_1 = 0$, $\phi_3 = \pi/2$, $\phi_5 = -\pi/2$. The white and orange phases are topologically trivial and nontrivial, respectively. The effective potential is the same as in Figure 2B. (B) Dependence of the minimum quasiparticle gap on the Zeeman field along the blue cut (I) in panel (A). (C) Dependence of the minimum quasiparticle gap on the Zeeman field along the dark red cut (II) in panel (A). Note the increased stability of the low-field topological phase (see for comparison Figure 2B) and the fact that the minimum critical field $\Gamma_B^c \approx 0.15$ meV is lower than the pairing potential for corner chains, $\Delta = 0.3$ meV.

significant quasiparticle gap, as shown in panels (B) and (C). In addition, the lowest critical field $\Gamma_B^c \approx 0.15$ meV is about half the value of the pairing potential (i.e., $\Delta/2$). This is in sharp contrast with the case of hybrid systems involving a single superconductor, or multiple superconductors having the same phase, ϕ_ℓ = const., where the minimum critical field is $\Gamma_B^c = \Delta$.

A comparison between the results in Figure 2 and those in Figure 6 suggests that the superconducting phase could be used as a knob for tuning the system across a topological quantum phase transition. For example, if $\mu = -5.4$ meV and $\Gamma_B = 0.25$ meV the system evolves as a function of the superconducting phase differences from a topologically-trivial state when $\phi_\ell = 0$ to a topological superconductor when $\phi_1 = 0$ and $\phi_3 = -\phi_5 = \pi/2$. We emphasize that the simplified tight-binding model can only provide a qualitative picture of the low-energy physics of proximitized core–shell wires. For quantitative predictions regarding the dependence of the low-energy physics on the effective bias potential V_{eff} and the superconducting phases ϕ_ℓ a more detailed modeling of the hybrid structure (possibly, at the microscopic level) is necessary.

To corroborate our findings regarding the effect of a phase difference, we consider the square wire corresponding to the phase diagram shown in Figure 5 coupled to four separate superconductors that induce pairing potentials characterized by $\phi_1 = \pi/2$, $\phi_3 = -\pi/2$, $\phi_5 = \pi/2$, and $\phi_7 = -\pi/2$. The corresponding phase diagram is shown in Figure 7. The qualitative effect of having finite phase differences is the same as in the case of the triangular wire, while quantitatively it is more significant as a results of a stronger inter-chain coupling t'. The topology of the phase diagram is similar to that shown in Figure 6. However, the low-field topological phase now occupies a significant region of the parameter space and the minimum critical field Γ_B^c is practically zero. Furthermore, the topological gap is substantial, as shown in the lower panel of Figure 7, indicating a robust topological superconducting phase.

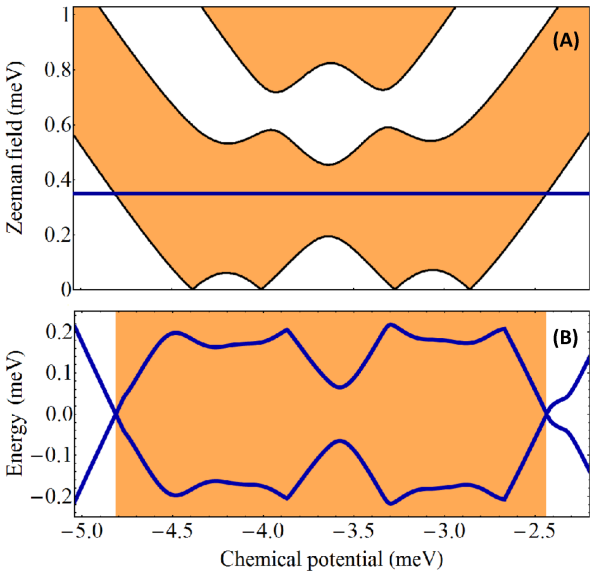

Figure 7: (A) Topological phase diagram for a square wire with $V_{\text{eff}}(\ell) \neq 0$ and $\phi_1 = \pi/2$, $\phi_3 = -\pi/2$, $\phi_5 = \pi/2$, and $\phi_7 = -\pi/2$. The white areas are topologically trivial and the orange regions are nontrivial. The values of $V_{\text{eff}}(\ell)$ and the inter-chain hopping t' are the same as in Figure 5. (B) Evolution of the minimum quasiparticle gap along the horizontal cut $\Gamma = 0.35$ meV shown in the top panel. Note the significant expansion of the low-field topological phase (see for comparison Figure 5), the large topological gap, and the low values of the critical field.

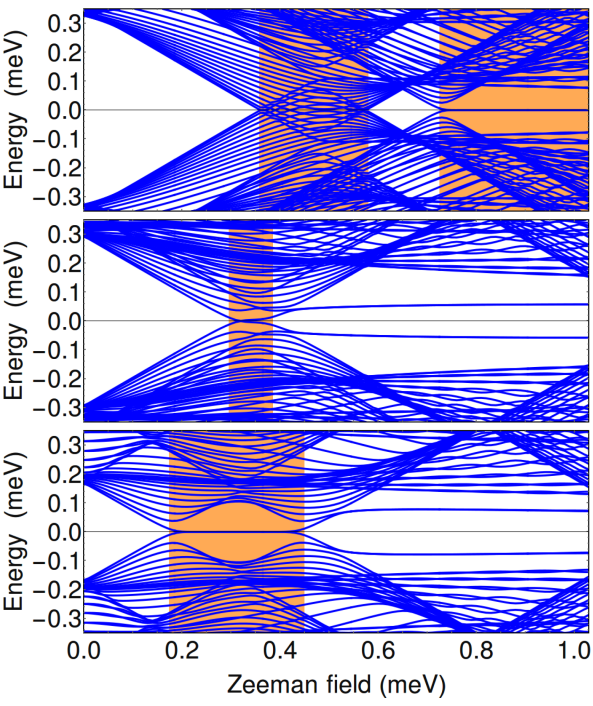

Figure 8: Dependence of the low-energy spectrum on the Zeeman field for a finite triangular wire of length $L = 2.25$ μm and chemical potential $\mu = -5.4$ meV. The parameters used in the top, middle, and bottom panels correspond to Figure 3(I-A), Figure 3(I-B), and Figure 6B, respectively.

Majorana modes in finite core–shell nanowires

As a consistency check for the results discussed above, which are based on a translation-invariant model (i.e., infinite wire), and to gain further insight into the low-energy physics of the hybrid structure, we continue now with the case of wires of finite length. For concreteness, we consider a triangular wire of length $L = 2.25$ μm in the parameter regimes corresponding to the panels labeled by "I" and "II" in Figure 3, Figure 4, and Figure 6. The dependence of the low-energy spectrum on the Zeeman field for $\mu = -5.4$ meV, i.e., corresponding to the (I) panels, is shown in Figure 8. Note that when $V_{\text{eff}} = 0$ and $\phi_\ell = 0$ (top panel) the first transition is from a topologically-trivial

phase to a gapless superconductor, as already discussed in the context of Figure 3. The high-field topological phase ($\Gamma_B > 0.7$ meV) is characterized by a zero-energy Majorana mode separated by a finite gap from finite energy excitations. Applying a symmetry-breaking potential V_{eff} (middle panel) generates a low-field topological phase characterized by a small bulk gap and a weakly stable, energy-split Majorana mode. However, the stability of this topological phase can be significantly enhanced by creating phase differences between the parent superconductors (bottom panel). Note that in the middle and bottom panels the second trivial phase (Γ_B larger than about 0.35 meV and 0.45 meV, respectively) is characterized by sub-gap states that can be viewed as pairs of overlapping, energy split Majorana bound states (at each end of the wire). This result suggests that coupling the nanowire to multiple parent superconductors and controlling their relative phases represents a powerful scheme for enhancing the robustness of the topological phase and tuning the system across a topological quantum phase transition.

The low-energy spectra for μ = −4.4 meV, i.e., those corresponding to the (II) panels in Figure 4 and Figure 6, are shown in Figure 9. In the top panel, note the presence of a gapless superconducting phase, which is consistent with our conclusions based on the results shown in Figure 4. Also note that the high-field topological phase ($\Gamma_B > 0.85$ meV) supports two finite energy sub-gap modes, in addition to the zero-energy Majorana mode. Again, we can interpret these modes as pairs of overlapping Majoranas. We conclude that in this phase the hybrid system has three Majorana bound states at each end of the wire, two Majorana modes acquiring finite energy and one remaining gapless, consistent with a $\mathbb{Z}_2$ topological classification. Applying a symmetry-breaking potential (middle panel) enhances significantly the stability of the low-field topological phase and generates a second trivial phase ($\Gamma_B > 0.9$ meV) that is gapped in the bulk, consistent with Figure 4. Remarkably, this trivial phase supports a pair of zero-energy Majorana modes at each end of the wire, which correspond to the mid-gap states visible in the middle panel of Figure 9. This indicates the presence of an additional "hidden" symmetry in the system, which makes it an element of the BDI symmetry class [44]. This symmetry is broken in the presence of a superconducting phase difference (bottom panel), when the sub-gap modes acquire finite energy.

Symmetry and gapless superconducting phases

The existence of the gapless superconducting phases (indicated by the star in the top panels of Figure 2 and Figure 3) is a consequence of the threefold rotation symmetry of the triangular wire with $V_{\text{eff}}(\ell) = 0$ and identical superconductors.

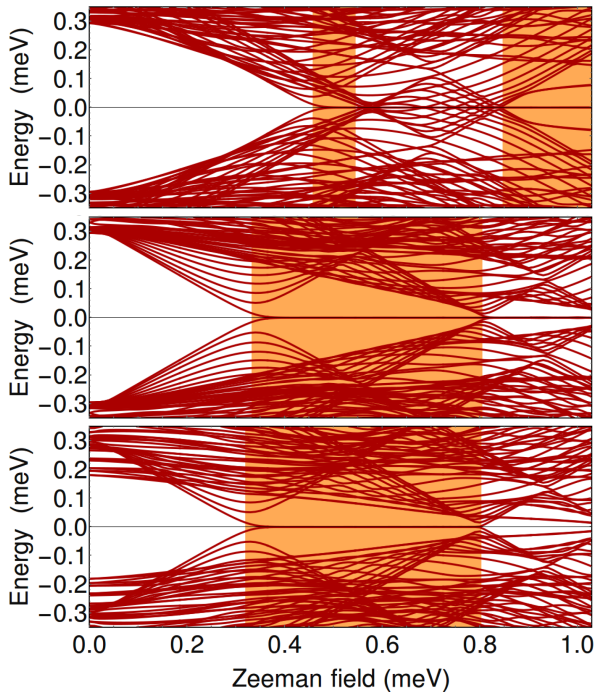

Figure 9: Dependence of the low-energy spectrum on the Zeeman field for a finite triangular wire of length L = 2.25 μm and chemical potential μ = −4.4 meV. The parameters used in the top, middle, and bottom panels correspond to Figure 4(II-A), Figure 4(II-B), and Figure 6C, respectively.

Breaking this symmetry automatically opens a (bulk) gap in the spectrum. To illustrate this property we consider the system of finite length L = 2.25 nm, with the other parameters corresponding to Figure 2A, with chemical potential μ = −5.4 meV (i.e., the blue vertical line there), and $V_{\text{eff}}(\ell) = 0$, and we focus on the gapless phase $0.36 < \Gamma_B < 0.58$ meV. The low-energy spectrum is shown in Figure 10A, which is in fact a zoom into the top panel of Figure 8. We consider now a small symmetry-breaking potential, with the same proportions as in Figure 2B, Figure 3(I-B), and middle panel of Figure 8, but now ten times weaker, i.e., $V_{\text{eff}} = V_0(2, 0.5, -1, -1, -1, 0.5)$ with V_0 = 33.3 μeV. The potential opens a bulk gap that hosts a mid-gap Majorana mode, as shown in Figure 10B. To emphasize that the opening of a bulk gap is the result of breaking the threefold rotation symmetry, we also consider a system with vanishing effective potential, $V_{\text{eff}}(\ell) = 0$, in which we break the symmetry by coupling the wire to parent superconductors having different bulk gaps, so that the proximity-induced pairing potentials for the edges are Δ_1 = 0.375 meV, Δ_3 = 0.300 meV, and Δ_5 = 0.300 meV. Here we do not consider any relative phase between the superconductors. Again, a small bulk gap opens in the (bulk) spectrum and a (nearly-zero) Majorana mode emerges as a mid-gap state, as can be seen Figure 10C.

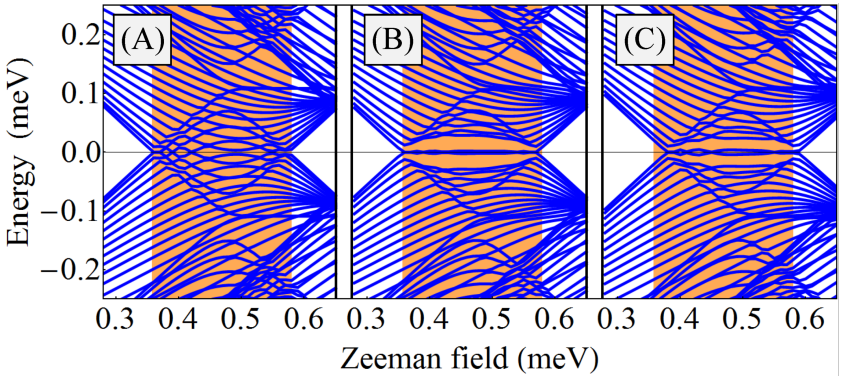

Figure 10: Low-energy spectra as a function of the Zeeman field for a finite triangular wire of length L = 2.25 μm and chemical potential μ = −5.4 meV. (A) Gapless superconducting phase in a system with threefold rotation symmetry, like in Figure 2A and Figure 3(I-A). (B) Applying a symmetry-breaking V_{eff}, ten times waker than in Figure 2B, a small bulk gap develops, like in Figure 3(I-B), that hosts a mid-gap Majorana mode. (C) Symmetry broken by coupling the wire to different superconductors inducing edge pairing potentials Δ_1 = 0.375 meV, Δ_3 = 0.3 meV, and Δ_5 = 0.3 meV. The filled (orange) region $0.36 < \Gamma_B < 0.58$ meV represents the topological superconducting phase (of an infinite wire) in the presence of an infinitesimally-small symmetry-breaking perturbation.

Another important general property of the Majorana modes illustrated in Figure 10, panels (B) and (C), is the presence of energy splitting oscillations [25,45]. In general, the energy splitting is caused by a finite overlap of the Majorana modes localized at the opposite ends of the wire. The amplitude of the oscillations depends on the Majorana localization length ξ [25], which increases as the topological gap decreases, diverging in the gapless limit. This behavior is illustrated in Figure 11. The top panel represents the lowest-energy state corresponding to a gapless system with threefold rotation symmetry (i.e., $V_{\text{eff}} = 0$), which could be seen as a linear combination of Majorana modes with an infinite characteristic lenghscale, $\xi \to \infty$. Introducing a symmetry-breaking perturbation ($V_{\text{eff}} \neq 0$) opens a (bulk) topological gap that increases with increasing the effective potential. In addition, in a finite system a midgap state emerges, consisting of two (partially) overlapping Majorana modes localized at the opposite ends of the wire. As clearly shown in Figure 11, the characteristic length scale ξ of the Majorana modes decreases as the amplitude V_0 of the symmetry-breaking potential increases (i.e., as the topological gap increases).

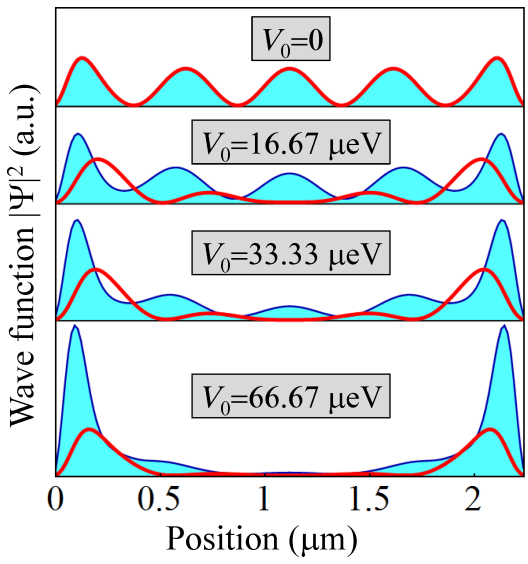

Figure 11: Position dependence of the lowest energy wave function corresponding to a finite triangular wire of length L = 2.25 μm, chemical potential μ = −5.4 meV, Zeeman field Γ_B = 0.45 meV, and symmetry-breaking effective potential with amplitude V_0 (see Figure 10B). The thick (red) line represents the probability distribution $|\Psi_1(x)|^2$ along the edge ℓ = 1, while the filled (blue) line represents the probability distribution along the edges ℓ = 3,5. With increasing the amplitude of the symmetry-breaking potential the (bulk) topological gap increases, which leads to the reduction of the characteristic length ξ of the Majorana modes localized at the opposite ends of the wire.

We note that, from the perspective of quantum computation, the zero-energy Majorana modes have to be i) well separated spatially (to minimize the overlap and, consequently, the energy splitting δE) and ii) well separated in energy from all other low-energy states (by a certain minimum quasiparticle gap ΔE). The first condition ensures that the Majorana modes have non-Abelian properties, while the second guarantees that the parity of the low-energy Majorana sub-space is fixed (the presence of other low-energy states would allow excitations from the Majorana sub-space, which would change its parity and destroy any quantum information stored in the Majorana system). If these conditions are satisfied, the Majorana modes span a nearly-zero energy subspace that can be used for storing and processing quantum information. The characteristic timescale τ for quantum operations has to satisfy the condition $\delta E \ll \hbar/\tau \ll \Delta E$. Of course, the impossibility of satisfying this condition is manifest in regimes characterized by small topological gaps, as δE and ΔE become comparable in the gapless superconductor limit.

Effects of disorder

Another element that can compromise the topological protection of the Majorana subspace is the presence of disorder. Generically, disorder induces low-energy sub-gap states, thus reducing ΔE[46-50]. The effect of potential disorder on a topological phase realized in a triangular wire is illustrated in Figure 12. Panel (A) shows the position dependence (along the wire) of a typical disorder potential $V_{\rm dis}(x)$ considered in the calculation. Next, we calculate the low-energy spectrum in the presence of a disorder potential with a fixed profile but a varying amplitude $V_{\rm max}$ (see Figure 12B). As the disorder strength increases, several low-energy states converge toward zero-energy, so that the quasiparticle gap ΔE practically collapses when the amplitude of the effective disorder potential is larger than $V_{\rm max}\approx$ 1 meV. To demonstrate that this is not an accidental property of a specific disorder realization, we also calculated the spectrum averaged over multiple disorder realizations (see Figure 12C). The qualitative features discussed above are manifestly present. We note that "critical" disorder strength associated with the collapse of the quasiparticle gap depends on the characteristic length scale of the disorder potential, as well as the topological gap of the clean system, larger gaps implying an increased robustness against disorder.

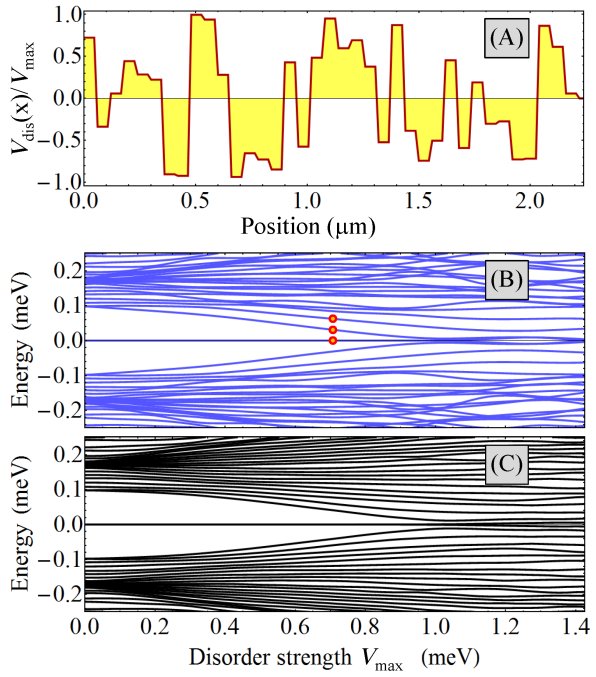

Figure 12: (A) Position dependence of the normalized disorder potential along the edge ℓ = 3 of a triangular wire for a specific disorder realization. The disorder profiles along the edges ℓ = 1,5 (not shown) are different, but characterized by similar qualitative features. In particular, the characteristic length scale for the potential variations is δ_d = 60 nm. (B) Dependence of the low-energy spectrum on the amplitude $V_{\rm max}$ of the disorder potential for the disorder realization shown in panel (A). (C) Low-energy spectrum averaged over 50 different disorder realizations as a function of $V_{\rm max}$. The parameters of the system are: wire length L = 2.25 μm, chemical potential μ = −5.4 meV, effective potential $V_{\rm eff}$ = (0.67, 0.17, −0.33, −0.33, −0.33, 0.17) meV, superconducting phases $\phi_1 = 0$, $\phi_3 = \pi/2$, $\phi_5 = -\pi/2$ and Zeeman field Γ_B = 0.35 meV.

The final point that we want to address concerns the structure of the disorder-induced low-energy states. Specifically, we calculate the spatial profiles of the three lowest-energy states marked by red dots in Figure 12B. The results are shown in Figure 13. We note that the Majorana modes (n = 1) are well localized near the opposite ends of the wire and have most of the spectral weight on the edges ℓ = 3,5 as a result of applying a bias potential $V_{\rm eff}(\ell)$. The disorder-induced states (n = 2,3) are localized inside the wire and have most of their spectral weight on the same edges, ℓ = 3,5. We conclude that the presence of disorder induces low-energy localized states than can destroy the topological protection of the Majorana subspace. We note that within a topological quantum computation scheme based on qubits characterized by a finite charging energy [51,52], interaction-mediated transitions between the Majorana modes and disorder-induced localized states are possible even when the spatial overlap of the two types of states is exponentially small. Such transitions, which create low-energy quasiparticles, could completely compromise the topological protection of the quantum computation scheme.

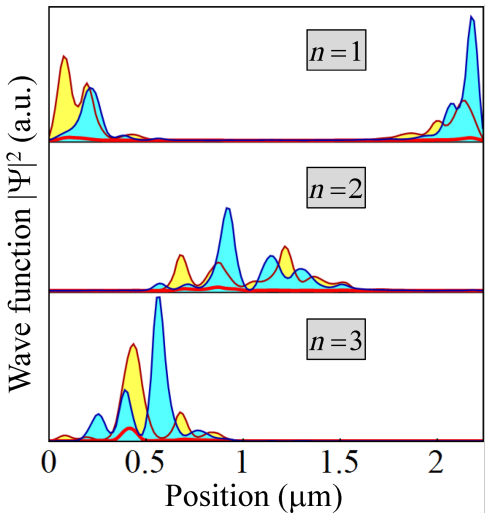

Figure 13: Spatial profiles of the three lowest energy states corresponding to the red dots in Figure 12B. The thick (red) line represents the profile along the edge ℓ = 1, while the filled lines represent the profiles along the edge ℓ = 3 (blue/light blue filling) and ℓ = 5 (dark red/yellow filling).

Geometrical model of a prismatic shell

In this section we analyze the results of a finer-grained model of triangular and square prismatic shells, based on a geometrical

description [29]. First the two-dimensional Hamiltonian of a single electron confined on the polygonal cross section is discretized on a grid defined in polar coordinates and diagonalized numerically [37,53]. The resulting low-energy eigenstates, corresponding to corner localization, are further used as a basis to find the eigenstates of the BdG Hamiltonian, assuming plane waves in direction longitudinal to the prism. The basis includes the spin and the isospin. The variable Zeeman energy is generated by a uniform magnetic field B longitudinal to the wire. In addition we consider a relatively weak electric field E transverse to the wire as a technical tool to break the symmetry of the polygon, indicated by the red arrows in Figure 14. This field is equivalent with the chain dependent potential $V_{\text{eff}}(\ell)$ introduced before. First, a perfectly symmetric shell is experimentally unrealistic from fabrication. Second, as already mentioned, in a regular experimental setup external gates and other contacts may affect the wire symmetries. Third, a generic electric field can be seen as a tunable parameter that can change the topological phase diagram.

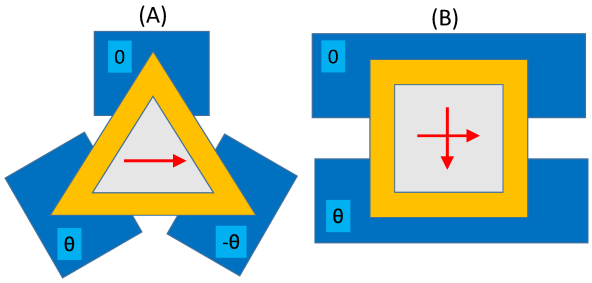

Figure 14: A schematic cross section of the hybrid semiconductor-superconductor experimental device incorporating a core–shell wire. The core is shown in grey and the shell in yellow. The blue blocks represent the superconductor metals attached to the wire. The lower superconductors can have phases ±θ relatively to the upper one considered with zero phase. The red arrows indicate the electric field included in our geometrical model. (A) In the triangular case it is parallel to one side of the triangle. (B) In the square case it can be either perpendicular or parallel to the superconductors.

We characterize the lateral size of the wire with the radius R of a circle surrounding the shell, and with the shell thickness d. In the present calculations we use R = 50 nm for both geometries, but d = 12.5 nm for the triangular shell and d = 8 nm for the square shell. These values are comparable to the dimensions of the realistic core–shell nanowires mentioned in the experimental papers [32-36]. The material parameters of the shell are chosen as for InSb. For these geometric parameters and with m_{eff} = 0.014 the energy separation between the corner and side states is about 41 and 38 meV for the triangular and square case, respectively, meaning that for these parameters the low energy physics can be very well described by the corner states. Therefore we can use a Rashba SOC model similar to that of the planar electron gas, but on a cylindrical surface of radius R, i.e., transformed from Cartesian to polar coordinates [54]. Since the sides of the triangular shell are unpopulated this model is qualitatively reasonable, and can lead to Majorana states. As mentioned before a more elaborated microscopic description of the SOC is beyond the scope of the present paper, and here we simply adopt in the numerical calculations the coupling constant of bulk InSb, of 50 meV/nm.

For a symmetric triangle the corner states have equal probability distribution at each corner [37], whereas in the presence of a weak electric field E, here corresponding to 0.22 mV across the radius R, they separate. The wave functions still have some exponential tails along the sides of the polygon, which are equivalent to the inter-chain hopping introduced earlier. The phase diagram shown in Figure 15A is obtained with a real valued superconductor gap Δ = 0.5 meV, and can be compared with Figure 2B (where all ϕ_ℓ = 0). The fragmentation of the phase boundaries in three dark lines reflects the presence of the three corners (edges) of the prismatic wire. The boundaries approach each other when the aspect ratio of the triangle (d/R) decreases, which results in reduced overlap of the wave functions of the corner states [29].

The colors used indicate the minimum gap of the BdG spectrum at any wave vector k, on a logarithmic scale, so the representation is complementary to the two-color scheme of Figure 2B (or A). Here the topological phases can be identified by the number of crossings of the dark lines. Along these lines the gap closes at k = 0. Starting from any point outside the boundaries one enters into a topological Majorana phase after the first intercept of a dark line, then into the trivial phase after the second intercept, and again into the topological phase after the third intercept.

Next, in Figure 15B, we show the phase diagram obtained with a complex valued superconductor gap, of constant modulus and variable phases, which are zero at one corner and $\pm\pi/6$ at the other corners (i.e., $\theta = \pi/6$ in Figure 14A). We obtain a splitting (or anticrossing) of the phase boundaries at the former crossing point, similar to that shown in Figure 6A, although now more pronounced than in the chain model.

By further increasing the relative (angular) phase θ to $\pm\pi/2$ the boundaries of the quantum phase transitions become nearly parallel, Figure 15C. This result can be interpreted as an increased interaction between the corner states in the presence of the phase shift θ of the superconductors. Another consequence of this phase shift is that the absolute gap of the BdG spectrum decreases in some topological regions, as indicated by the diffuse reddish regions, suggesting that some topological states

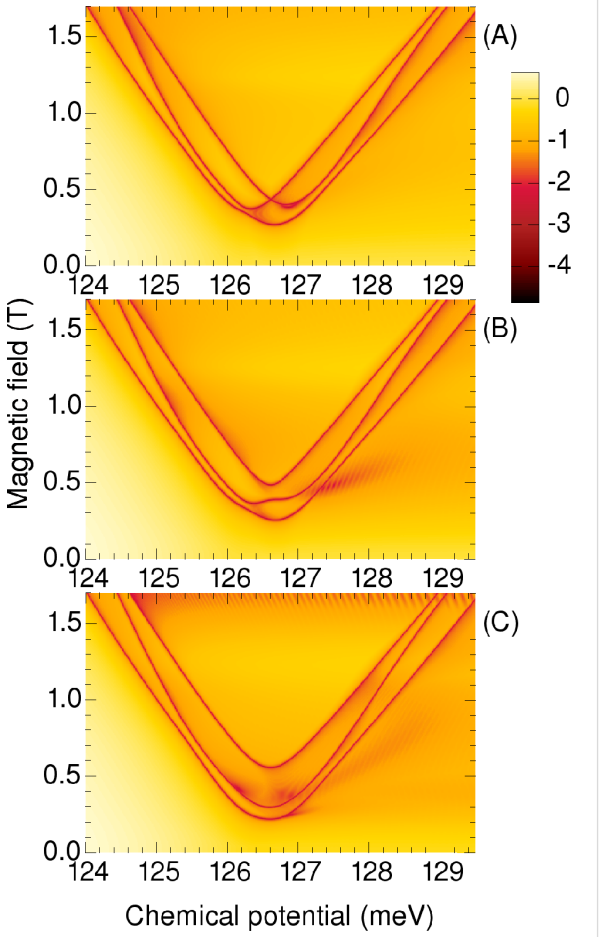

Figure 15: Phase boundaries for the triangular wire in the corner-state domain. The color code describes the minimum gap of the BdG spectra for all wave vectors. The character of each phase can be identified by counting the boundary crossings along a vertical line, starting at zero magnetic field, i.e., topological or trivial for an odd or an even number of crossings, respectively. Along these boundaries the gap closes at $k = 0$. Starting from any point outside the (A) All superconductor phases are equal to zero. (B) Phases are: 0 at one corner and $\pm\pi/6$ at the other corners, i.e., $\theta = \pi/6$ in Figure 14A. (C) The same phase distribution, with $\theta = \pi/2$.

may become gapless. This tendency is consistent with the results of the multiple chain model, compare Figure 4B with Figure 6C.

As with the coupled-chains model, we also tested the effect of using two superconductors with different gaps, for example by reducing the gap parameter Δ of one or two superconductors by one half, and using no relative phase, $\theta = 0$. The resulting phase diagrams were qualitatively like those shown in Figure 15B,C, although with lower energy gaps in the topological phases. This indicates no particular gain by creating an asymmetry in this way, compared to using the superconductors with the large gap and creating the asymmetry via the relative phase θ.

Finally, in Figure 16 we show the phase diagrams obtained with the geometric model for the square shell profile. Here, in the geometrical model, we use a particular setup for the square geometry, with only two superconductors. Unlike in the coupled-chains model, in this case the superconductors are also connected to the states localized on the sides of the polygon, if those states would be populated, but this is not the case for the chemical potentials used for Figure 16. First we note that we obtain four phase boundaries, according to the presence of four corner states. As for the triangular geometry the trivial or topological character of the phases is associated with odd or even number of boundary crossings, respectively, when starting from the outer regions. Therefore the central zone of the phase diagrams is now topologically trivial. In Figure 16A we show

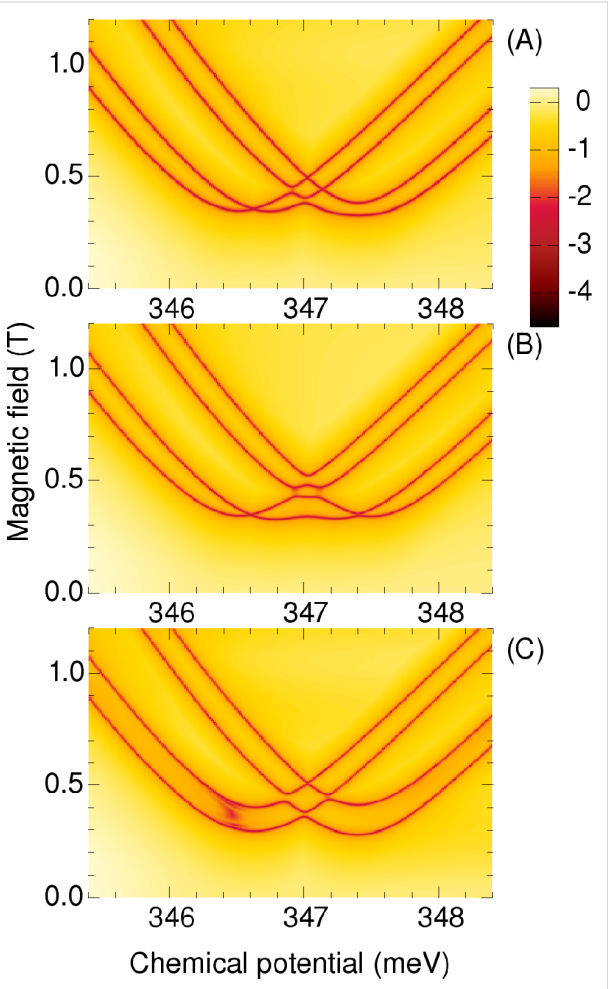

Figure 16: Phase boundaries for the square wire in the corner-state domain. The color code describes the minimum gap of the BdG spectra for all wave vectors. The topological or trivial character of the phases can be identified by the number of boundary crossings, as described in the caption of Figure 15. (A) The superconductor phases equal to zero. (B) The superconductor phases are zero and $\theta = \pi/2$, and the electric field perpendicular to the superconductors, see Figure 14B. (C) Again $\theta = \pi/2$, but with the electric field parallel to the superconductors.

the results with θ = 0, i.e., no phase shift between the superconductors (Figure 14B). The electric field corresponds now to 60 mV per radius, and obviously the results do not depend on the two orientation considered here if θ = 0.

Remarkably, with a finite phase shift, here θ = π/2, the phase diagrams are different when the electric field is perpendicular, Figure 16B, or parallel to the superconductors, Figure 16C, respectively. In the perpendicular case the phase frontiers are mostly changed in the central region, whereas in the parallel case they are more affected in the low field part. In the first case the corner states with phase θ are separated energetically from those with zero phase, but they still interact when they are all grouped within or close to the superconductor gap. In the second case the states with the same superconductivity phase are separated, and the frontiers tend to become parallel.

Conclusion

In this work we have studied the phase diagram of core–shell nanowires coupled with multiple parent superconductors using a simplified tight-binding parallel-chain model. We found that applying a potential that breaks the (intrinsic) rotation symmetry of the wire does not modify the topology of the phase diagram, but removes the gapless superconducting phases that populate certain regions of the phase diagram and partially stabilizes the topological superconducting phase. Remarkably, finite phase differences between the parent superconductors have dramatic effects. First, the topology of the phase diagram is modified. In particular the "crossing points" that characterize the phase diagram in the presence of a uniform superconducting phase disappear and, upon increasing the Zeeman field, we have an alternance of trivial and nontrivial phases for all values of the chemical potential. More importantly, the low-field topological phase becomes stable for a wide range of chemical potentials and the minimum critical field Γ_B^c can have arbitrarily low values. We conclude that by controlling the relative phases of the parent superconductors coupled to the wire one can stabilize the topological superconducting phase that hosts the zero-energy Majorana modes and one can obtain a powerful additional experimental knob for exploring a rich phase diagram and observing potentially interesting low-energy physics. Given the potential experimental significance of these conclusions, we believe that a more detailed and systematic investigation of these effects, which is beyond the goal of the present work, would be warranted.

In particular, the effect of electrostatic interactions on the properties of the normal electronic states in core–shell nanowires can be important. The effect of interactions should be calculated using a Schrödinger–Poisson scheme, e.g., like in [55], to take into account both the interface potential between the core and the shell, and the presence of the carrier density in the shell. In addition, for Majorana devices, one should incorporate the effects due to the presence of a parent superconductor, including the work function difference between the superconductor and the semiconductor, as well as the effects generated by gate-induced electric fields. An efficient method for implementing the Schrödinger–Poisson scheme in calculations using realistic three-dimensional models of hybrid devices has been recently proposed in [56]. We emphasize that, due to the corner and side localization, the electron–electron interactions have nontrivial effects [57], which can modify the proximity-induced superconductor gap and the phase diagram of the Majorana states [58-65]. The calculation of the effective potential profile is also essential for estimating the SOC in the nanowire. Therefore, accounting for the electrostatic effects represents a key step toward a quantitative theory of Majorana physics in core–shell nanowires.

Acknowledgements

This work was partially financed by the research funds of Reykjavik University and by the Icelandic Research Fund. TDS was supported in part by NSF DMR-1414683.

ORCID® iDs

Andrei Manolescu - https://orcid.org/0000-0002-0713-4664

References

1. Kitaev, A. Yu. *Phys.-Usp.* **2001,** *44,* 131. doi:10.1070/1063-7869/44/10S/S29
2. Kitaev, A. Yu. *Ann. Phys.* **2003,** *303,* 2. doi:10.1016/S0003-4916(02)00018-0
3. Wilczek, F. *Nat. Phys.* **2009,** *5,* 614. doi:10.1038/nphys1380
4. Stanescu, T. D. *Introduction to topological quantum matter and quantum computation;* CRC Press: Boca Raton, FL, U.S.A., 2017.
5. Sau, J. D.; Lutchyn, R. M.; Tewari, S.; Das Sarma, S. *Phys. Rev. Lett.* **2010,** *104,* 040502. doi:10.1103/PhysRevLett.104.040502
6. Alicea, J. *Phys. Rev. B* **2010,** *81,* 125318. doi:10.1103/physrevb.81.125318
7. Oreg, Y.; Refael, G.; von Oppen, F. *Phys. Rev. Lett.* **2010,** *105,* 177002. doi:10.1103/PhysRevLett.105.177002
8. Lutchyn, R. M.; Sau, J. D.; Das Sarma, S. *Phys. Rev. Lett.* **2010,** *105,* 077001. doi:10.1103/PhysRevLett.105.077001
9. Sau, J. D.; Tewari, S.; Lutchyn, R. M.; Stanescu, T. D.; Das Sarma, S. *Phys. Rev. B* **2010,** *82,* 214509. doi:10.1103/PhysRevB.82.214509
10. Alicea, J. *Rep. Prog. Phys.* **2012,** *75,* 076501. doi:10.1088/0034-4885/75/7/076501
11. Stanescu, T. D.; Tewari, S. *J. Phys.: Condens. Matter* **2013,** *25,* 233201. doi:10.1088/0953-8984/25/23/233201
12. Beenakker, C. W. J. *Annu. Rev. Condens. Matter Phys.* **2013,** *4,* 113. doi:10.1146/annurev-conmatphys-030212-184337
13. Franz, M. *Nat. Nanotechnol.* **2013,** *8,* 149. doi:10.1038/nnano.2013.33
14. Mourik, V.; Zuo, K.; Frolov, S. M.; Plissard, S. R.; Bakkers, E. P. A. M.; Kouwenhoven, L. P. *Science* **2012,** *336,* 1003. doi:10.1126/science.1222360

15. Deng, M. T.; Yu, C. L.; Huang, G. Y.; Larsson, M.; Caroff, P.; Xu, H. Q. *Nano Lett.* **2012,** *12,* 6414. doi:10.1021/nl303758w
16. Das, A.; Ronen, Y.; Most, Y.; Oreg, Y.; Heiblum, M.; Shtrikman, H. *Nat. Phys.* **2012,** *8,* 887. doi:10.1038/nphys2479
17. Finck, A. D. K.; Van Harlingen, D. J.; Mohseni, P. K.; Jung, K.; Li, X. *Phys. Rev. Lett.* **2013,** *110,* 126406. doi:10.1103/PhysRevLett.110.126406
18. Churchill, H. O. H.; Fatemi, V.; Grove-Rasmussen, K.; Deng, M. T.; Caroff, P.; Xu, H. Q.; Marcus, C. M. *Phys. Rev. B* **2013,** *87,* 241401. doi:10.1103/PhysRevB.87.241401
19. Albrecht, S. M.; Higginbotham, A. P.; Madsen, M.; Kuemmeth, F.; Jespersen, T. S.; Nygård, J.; Krogstrup, P.; Marcus, C. M. *Nature* **2016,** *531,* 206. doi:10.1038/nature17162
20. Deng, M. T.; Vaitiekėnas, S.; Hansen, E. B.; Danon, J.; Leijnse, M.; Flensberg, K.; Nygård, J.; Krogstrup, P.; Marcus, C. M. *Science* **2016,** *354,* 1557. doi:10.1126/science.aaf3961
21. Chen, J.; Yu, P.; Stenger, J.; Hocevar, M.; Car, D.; Plissard, S. R.; Bakkers, E. P. A. M.; Stanescu, T. D.; Frolov, S. M. *Sci. Adv.* **2017,** *3,* e1701476. doi:10.1126/sciadv.1701476
22. Zhang, H.; Gül, O.; Conesa-Boj, S.; Nowak, M. P.; Wimmer, M.; Zuo, K.; Mourik, V.; de Vries, F. K.; van Veen, J.; de Moor, M. W.; Bommer, J. D.; van Woerkom, D. J.; Car, D.; Plissard, S. R.; Bakkers, E. P.; Quintero-Perez, M.; Cassidy, M. C.; Koelling, S.; Goswami, S.; Watanabe, K.; Taniguchi, T.; Kouwenhoven, L. P. *Nat. Commun.* **2017,** *8,* 16025. doi:10.1038/ncomms16025
23. Nichele, F.; Drachmann, A. C. C.; Whiticar, A. M.; O'Farrell, E. C. T.; Suominen, H. J.; Fornieri, A.; Wang, T.; Gardner, G. C.; Thomas, C.; Hatke, A. T.; Krogstrup, P.; Manfra, M. J.; Flensberg, K.; Marcus, C. M. *Phys. Rev. Lett.* **2017,** *119,* 136803. doi:10.1103/PhysRevLett.119.136803
24. Zhang, H.; Liu, C.-X.; Gazibegovic, S.; Xu, D.; Logan, J. A.; Wang, G.; van Loo, N.; Bommer, J. D.; de Moor, M. W.; Car, D.; het Veld, R. L. M. O.; van Veldhoven, P. J.; Koelling, S.; Verheijen, M. A.; Pendharkar, M.; Pennachio, D. J.; Shojaei, B.; Lee, J. S.; Palmstrom, C. J.; Bakkers, E. P.; Sarma, S. D.; Kouwenhoven, L. P. *arXiv* **2017,** No. 1712.08459.
25. Das Sarma, S.; Sau, J. D.; Stanescu, T. D. *Phys. Rev. B* **2012,** *86,* 220506. doi:10.1103/PhysRevB.86.220506
26. Lutchyn, R. M.; Bakkers, E. P. A. M.; Kouwenhoven, L. P.; Krogstrup, P.; Marcus, C. M.; Oreg, Y. *arXiv* **2017,** No. 1707.04899. And references therein.
27. Ihn, T. *Semiconductor Nanostructures: Quantum states and electronic transport;* Oxford Scholarship Online: Oxford, United Kingdom, 2010.
28. Nijholt, B.; Akhmerov, A. R. *Phys. Rev. B* **2016,** *93,* 235434. doi:10.1103/PhysRevB.93.235434
29. Manolescu, A.; Sitek, A.; Osca, J.; Serra, L.; Gudmundsson, V.; Stanescu, T. D. *Phys. Rev. B* **2017,** *96,* 125435. doi:10.1103/PhysRevB.96.125435
30. Bertoni, A.; Royo, M.; Mahawish, F.; Goldoni, G. *Phys. Rev. B* **2011,** *84,* 205323. doi:10.1103/PhysRevB.84.205323
31. Hu, M.; Zhang, X.; Giapis, K. P.; Poulikakos, D. *Phys. Rev. B* **2011,** *84,* 085442. doi:10.1103/PhysRevB.84.085442
32. Wong, B. M.; Léonard, F.; Li, Q.; Wang, G. T. *Nano Lett.* **2011,** *11,* 3074. doi:10.1021/nl200981x
33. Blömers, C.; Rieger, T.; Zellekens, P.; Haas, F.; Lepsa, M. I.; Hardtdegen, H.; Gül, Ö.; Demarina, N.; Grützmacher, D.; Lüth, H.; Schäpers, T. *Nanotechnology* **2013,** *24,* 035203. doi:10.1088/0957-4484/24/3/035203
34. Qian, F.; Brewster, M.; Lim, S. K.; Ling, Y.; Greene, C.; Laboutin, O.; Johnson, J. W.; Gradečak, S.; Cao, Y.; Li, Y. *Nano Lett.* **2012,** *12,* 3344. doi:10.1021/nl301690e
35. Heurlin, M.; Stankevič, T.; Mickevičius, S.; Yngman, S.; Lindgren, D.; Mikkelsen, A.; Feidenhans, R.; Borgström, M. T.; Samuelson, L. *Nano Lett.* **2015,** *15,* 2462. doi:10.1021/nl5049127
36. Yuan, X.; Caroff, P.; Wang, F.; Guo, Y.; Wang, Y.; Jackson, H. E.; Smith, L. M.; Tan, H. H.; Jagadish, C. *Adv. Funct. Mater.* **2015,** *25,* 5300. doi:10.1002/adfm.201501467
37. Sitek, A.; Serra, L.; Gudmundsson, V.; Manolescu, A. *Phys. Rev. B* **2015,** *91,* 235429. doi:10.1103/PhysRevB.91.235429
38. Pöyhönen, K.; Westström, A.; Röntynen, J.; Ojanen, T. *Phys. Rev. B* **2014,** *89,* 115109. doi:10.1103/PhysRevB.89.115109
39. Wakatsuki, R.; Ezawa, M.; Nagaosa, N. *Phys. Rev. B* **2014,** *89,* 174514. doi:10.1103/PhysRevB.89.174514
40. Wimmer, M. *ACM Trans. Math. Softw.* **2012,** *38,* 30. doi:10.1145/2331130.2331138
41. Ghosh, P.; Sau, J. D.; Tewari, S.; Das Sarma, S. *Phys. Rev. B* **2010,** *82,* 184525. doi:10.1103/PhysRevB.82.184525
42. Pientka, F.; Keselman, A.; Berg, E.; Yacoby, A.; Stern, A.; Halperin, B. I. *Phys. Rev. X* **2017,** *7,* 021032. doi:10.1103/PhysRevX.7.021032
43. Sitthison, P.; Stanescu, T. D. *Phys. Rev. B* **2014,** *90,* 035313. doi:10.1103/PhysRevB.90.035313
44. Dumitrescu, E.; Stanescu, T. D.; Tewari, S. *Phys. Rev. B* **2015,** *91,* 121413. doi:10.1103/PhysRevB.91.121413
45. Cheng, M.; Lutchyn, R. M.; Galitski, V.; Das Sarma, S. *Phys. Rev. Lett.* **2009,** *103,* 107001. doi:10.1103/PhysRevLett.103.107001
46. Bagrets, D.; Altland, A. *Phys. Rev. Lett.* **2012,** *109,* 227005. doi:10.1103/PhysRevLett.109.227005
47. Liu, J.; Potter, A. C.; Law, K. T.; Lee, P. A. *Phys. Rev. Lett.* **2012,** *109,* 267002. doi:10.1103/PhysRevLett.109.267002
48. DeGottardi, W.; Sen, D.; Vishveshwara, S. *Phys. Rev. Lett.* **2013,** *110,* 146404. doi:10.1103/PhysRevLett.110.146404
49. Rainis, D.; Trifunovic, L.; Klinovaja, J.; Loss, D. *Phys. Rev. B* **2013,** *87,* 024515. doi:10.1103/PhysRevB.87.024515
50. Adagideli, I.; Wimmer, M.; Teker, A. *Phys. Rev. B* **2014,** *89,* 144506. doi:10.1103/PhysRevB.89.144506
51. Aasen, D.; Hell, M.; Mishmash, R. V.; Higginbotham, A.; Danon, J.; Leijnse, M.; Jespersen, T. S.; Folk, J. A.; Marcus, C. M.; Flensberg, K.; Alicea, J. *Phys. Rev. X* **2016,** *6,* 031016. doi:10.1103/physrevx.6.031016
52. Karzig, T.; Knapp, C.; Lutchyn, R. M.; Bonderson, P.; Hastings, M. B.; Nayak, C.; Alicea, J.; Flensberg, K.; Plugge, S.; Oreg, Y.; Marcus, C. M.; Freedman, M. H. *Phys. Rev. B* **2017,** *95,* 235305. doi:10.1103/PhysRevB.95.235305
53. Sitek, A.; Thorgilsson, G.; Gudmundsson, V.; Manolescu, A. *Nanotechnology* **2016,** *27,* 225202. doi:10.1088/0957-4484/27/22/225202
54. Bringer, A.; Schäpers, T. *Phys. Rev. B* **2011,** *83,* 115305. doi:10.1103/PhysRevB.83.115305
55. Buscemi, F.; Royo, M.; Bertoni, A.; Goldoni, G. *Phys. Rev. B* **2015,** *92,* 165302. doi:10.1103/PhysRevB.92.165302
56. Woods, B. D.; Stanescu, T. D.; Das Sarma, S. *arXiv* **2018,** 1801.02630.
57. Sitek, A.; Ţolea, M.; Niţă, M.; Serra, L.; Gudmundsson, V.; Manolescu, A. *Sci. Rep.* **2017,** *7,* 40197. doi:10.1038/srep40197
58. Gangadharaiah, S.; Braunecker, B.; Simon, P.; Loss, D. *Phys. Rev. Lett.* **2011,** *107,* 036811. doi:10.1103/PhysRevLett.107.036801

59. Sela, E.; Altland, A.; Rosch, A. *Phys. Rev. B* **2011,** *84,* 085114. doi:10.1103/PhysRevB.84.085114
60. Lutchyn, R. M.; Fisher, M. P. A. *Phys. Rev. B* **2011,** *84,* 214528. doi:10.1103/PhysRevB.84.214528
61. Stoudenmire, E. M.; Alicea, J.; Starykh, O. A.; Fisher, M. P. A. *Phys. Rev. B* **2011,** *84,* 014503. doi:10.1103/PhysRevB.84.014503
62. Lobos, A. M.; Lutchyn, R. M.; Das Sarma, S. *Phys. Rev. Lett.* **2012,** *109,* 146403. doi:10.1103/PhysRevLett.109.146403
63. Hassler, F.; Schuricht, D. *New J. Phys.* **2012,** *14,* 125018. doi:10.1088/1367-2630/14/12/125018
64. Thomale, R.; Rachel, S.; Schmitteckert, P. *Phys. Rev. B* **2013,** *88,* 161103. doi:10.1103/PhysRevB.88.161103
65. Manolescu, A.; Marinescu, D. C.; Stanescu, T. D. *J. Phys.: Condens. Matter* **2014,** *26,* 172203. doi:10.1088/0953-8984/26/17/172203

License and Terms

BEILSTEIN JOURNAL OF NANOTECHNOLOGY

Spatial Rabi oscillations between Majorana bound states and quantum dots

Jun-Hui Zheng, Dao-Xin Yao and Zhi Wang*

Full Research Paper

Open Access

Address:
School of Physics, Sun Yat-sen University, Guangzhou 510275, China

Email:
Zhi Wang* - wangzh356@mail.sysu.edu.cn

* Corresponding author

Keywords:
Andreev bound state; Majorana bound state; nonlocal quantum correlation; quantum dot; spatial Rabi oscillation

Beilstein J. Nanotechnol. **2018,** *9,* 1527–1535.
doi:10.3762/bjnano.9.143

Received: 30 December 2017
Accepted: 18 April 2018
Published: 22 May 2018

This article is part of the Thematic Series "Topological materials".

Guest Editor: J. J. Palacios

Abstract

Background: A Majorana bound state is a superconducting quasiparticle that is the superposition of particle and hole with equal amplitude. We propose a verification of this amplitude equality by analyzing the spatial Rabi oscillations of the quantum states of a quantum dot that is tunneling-coupled to the Majorana bound states.

Results: We find two resonant Rabi driving energies that correspond to the energy splitting due to the coupling of two spatially separated Majorana bound states. The resulting Rabi oscillating frequencies from these two different resonant driving energies are identical for the Majorana bound states, while different for ordinary Andreev bound states. We further study a double-quantum-dot setup and find a nonlocal quantum correlation between them that is mediated by two Majorana bound states. This nonlocal correlation has the signature of additional resonant driving energies.

Conclusion: Our method can be used to distinguish between Majorana bound states and Andreev bound states. It also gives a precise measurement of the energy splitting between two Majorana bound states.

Introduction

Majorana bound states are exotic non-Abelian quasiparticles in topological superconductors [1-26]. The study of Majorana bound states has attracted tremendous interest recently because they constitute topological parity qubits. These qubits are defined by the degenerate ground states of topological superconductors, and therefore are protected by the superconducting energy gap [4,15]. They have a long coherence time and are resistant to local decoherence sources [2,15,18,19]. Most importantly, the topological qubits can be topologically manipulated by braiding the Majorana bound states [4,15,17]. These topological braiding operations set the foundation for topological quantum computation [4,15], despite the fact that they are insuf-

ficient to construct universal quantum gates for the topological qubit [15,17,19,20].

A unique feature of the Majorana bound states is the self-conjugateness. In the language of second quantization, a self-conjugate quasiparticle means that the superposition of the electron creation operators and electron annihilation operators are equal [2,15,16]. This equality is the essential difference between the Majorana bound states and the ordinary Andreev bound states. Another unique feature of Majorana bound states is the exponential protection [17-19], which states that the splitting energy between two Majorana bound states exponentially decays as the distance between them increases. The experimental verification of these two properties helps the identification of Majorana bound states in real systems.

Majorana bound states have been theoretically proposed in several systems [5,6,9,13,20], while the experiments concentrate on semiconductors with spin–orbit coupling and the superconducting gap that is induced by the superconducting proximity effect [19,21,24,25]. One promising candidate is the hybrid system of a spin–orbit-coupling nanowire and a conventional superconductor. Robust zero-bias conductance peak was first reported in this system, which originates from the self-conjugate nature of Majorana bound states and therefore was wildly recognized as a signature. An exotic fractional Josephson effect was also studied in the nanowire Josephson junctions, where novel Shapiro steps and Josephson radiations have been reported. Recently, the Coulomb blockade spectroscopy was exploited on finite-size nanowire segments that form nanowire islands with two Majorana bound states possibly existing at the two ends of the island. The splitting energy between two Majorana bound states is found to be decreasing exponentially when the length of the island increases [24]. This exponential protection of zero-energy Majorana bound states stirs new excitement in pursuing Majorana bound states.

Quantum dot has been proved to be a good probe to study the Majorana bound states [3,7,27-38]. The quantum dots are zero-dimensional systems that have controllable discrete energy levels. The Rabi oscillation, a fundamental quantum phenomenon in two-level quantum systems, may occur between the states of the quantum dot when the quantum dot is periodically modulated. In particular, the spatial Rabi oscillation between two quantum dots has been proven to be useful for single-electron pumping. An attractive idea is to exploit the spatial Rabi oscillation between the quantum dots and the Majorana bound states [29] and to investigate the self-conjugateness and exponential protection of Majorana bound states. In recent experiments, a hybrid structure of a quantum dot and a one-dimensional topological superconductor nanowire has been realized [36]. This system attracts theoretical interest [7,37]. In this context, it is interesting to study the spatial Rabi oscillation between the quantum dot and the topological nanowire.

In this work, we study the spatial Rabi oscillations between quantum dots and a Majorana island. This system involves two Majorana bound states that have an exponentially protected small splitting energy. As shown in Figure 1a, one of the Majorana bound states is coupled to the quantum dot with a single electron tunneling through a potential barrier. The barrier is produced by a voltage gate, which is implemented between the quantum dot and the Majorana island. If an ac voltage is applied to the gate, the tunneling strength between the quantum dot and the Majorana bound states will be driven periodically [39]. We show that there are two resonant driving energies that induce coherent spatial Rabi oscillations between the quantum dot and the island. The difference between the two driving energies is proportional to the exponentially protected splitting energy between two Majorana bound states. More importantly, the Rabi frequencies connected to the two different resonant driving energies are identical, which is a result of the self-conjugateness of the Majorana bound states. For comparison, we show the results when the Majorana bound state is replaced by an Andreev bound state as shown in Figure 1b. We find that the two Rabi frequencies at the different resonant driving energies are now different. We also investigate the setup with two quantum dots at each side of the island and calculate the resonant driving energies for spatial Rabi oscillation. We show that the two quantum dots exhibit nonlocal correlations when coupled with Majorana bound states while the two dots have no correlation when coupled with Andreev bound states, since two Majorana bound states can form one single fermionic level while two Andreev bound states are two distinct fermionic levels.

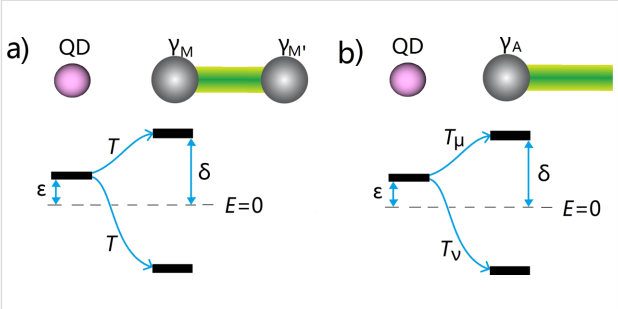

Figure 1: Schematics of a quantum dot tunneling-coupled to a nanowire island with (a) Majorana bound states, and (b) an Andreev bound state. The Andreev bound state has a small excitation energy δ, which is similar to the splitting energy between two Majorana bound states. The effective coupling between the quantum dot and the Andreev bound state has different electron and hole components T_μ and T_v, due to the different electron and hole wave functions of the Andreev bound state. In contrary, the effective coupling between the quantum dot and the Majorana bound state has identical electron and hole component T, due to the self-conjugateness of the Majorana bound states.

Results and Discussion

Model

The hybrid system schematically illustrated in Figure 1 consists of two parts, a quantum dot and a nanowire island, where Majorana or Andreev bound states are present at the ends of the island. Let us first consider the model for the quantum dot. Realistic topological superconducting systems usually involve a large Zeeman field, which in principle should break the spin degeneracy and split the two spin-dependent levels with the Zeeman energy. Therefore, it is reasonable to consider only one-spin direction. Meanwhile, we consider a large Coulomb blockade regime for the quantum dot, which corresponds to a large Coulomb interaction. For this regime, additional electron hopping to the quantum dot requires a large Coulomb energy, which effectively reduces the quantum dot to only one relevant energy level. The Hamiltonian of a minimal model for the quantum dot is [3,7,27,38],

$$H_{\mathrm{d}} = \varepsilon d^{\dagger} d, \tag{1}$$

where ε is the excitation energy for the single energy level of the quantum dot and $d^{\dagger}$ represents the creation operator on the energy level.

The Majorana island consists of a one-dimensional topological superconductor such as a nanowire–superconductor hybrid structure and a ferromagnetic chain, with zero-energy Majorana bound states at the ends of the system. The wave functions of the two Majorana bound states overlap with each other, inducing an energy splitting that exponentially decays as the length of the island increases. The low-energy physics of the island can be described by an effective Hamiltonian [2,3],

$$H_{\delta} = -\mathrm{i}\delta\gamma_{\mathrm{M}}\gamma_{\mathrm{M}'}, \tag{2}$$

where and γ_{M} and $\gamma_{\mathrm{M}'}$ represent the two Majorana bound states, and δ represents the exponentially protected splitting energy. The quantum dot is coupled to one of the Majorana bound states by electron tunneling through a potential barrier between the dot and the Majorana island. This coupling can be described by a tunneling Hamiltonian,

$$H_{\mathrm{T}} = T\gamma_{\mathrm{M}}\left(d + d^{\dagger}\right), \tag{3}$$

where T is the tunneling strength that is taken as a real number for simplicity. Here we consider an oscillating tunneling strength $T = T_0 + 2T_1\cos\omega t$, with T_0 being the static tunneling strength, T_1 the oscillating tunneling strength, and ω the oscillating frequency for the tunneling strength. It can be produced by an ac gate voltage controlling the tunneling barrier [39]. When the driving frequency is at resonance, this oscillating tunneling strength can induce a Rabi oscillation on the quantum dot.

We write out the matrix form for the total Hamiltonian $H_{\mathrm{M}} = H_{\mathrm{d}} + H_{\delta} + H_{\mathrm{T}}$. We first define a new fermionic operator $f^{\dagger} = (\gamma_{\mathrm{M}} - \mathrm{i}\gamma_{\mathrm{M}'})/2$, which leads to

$$H_{\mathrm{M}} = \varepsilon d^{\dagger} d + \delta\left(ff^{\dagger} - f^{\dagger} f\right) + T\left(d + d^{\dagger}\right)\left(f + f^{\dagger}\right). \tag{4}$$

Then we take the four eigenstates of the fermionic operators $|0\rangle$, $d^{\dagger}f^{\dagger}|0\rangle$, $f^{\dagger}|0\rangle$, and $d^{\dagger}|0\rangle$ as the basis states of the Hilbert space, and express the Hamiltonian in this basis explicitly,

$$\tilde{H}_{\mathrm{M}} = \begin{pmatrix} \delta & T & 0 & 0 \\ T & \varepsilon - \delta & 0 & 0 \\ 0 & 0 & -\delta & T \\ 0 & 0 & T & \varepsilon + \delta \end{pmatrix}. \tag{5}$$

This matrix is block diagonal due to the parity conservation of the total system. We notice that the upper left and the lower right 2 × 2 blocks have the same off-diagonal elements but different diagonal elements.

Now we consider the scenario that the nanowire island has an Andreev bound state at the end instead of Majorana bound states. From the mean-field Bogoliubov–de Gennes approach, the general form for Andreev bound states is the quantum superposition of electron and hole wave function, which in the second quantization form writes as,

$$\gamma_{\mathrm{A}}^{\dagger} = \int \mathrm{d}r\left[\mu(r)c^{\dagger}(r) + \nu(r)c(r)\right], \tag{6}$$

where $c^{\dagger}(r)$ is the creation operator for the electron, μ and ν are the electron and hole wave functions. For the sake simplicity they are real numbers and the factor of 1/2 for describing superconducting quasiparticles is absorbed into μ and ν. We assume the simplest wave function of delta equations since the Andreev bound state is extremely localized at the end of the wire. Then the Andreev operators can be written as $\gamma_{\mathrm{A}}^{\dagger} = \mu c^{\dagger} + \nu c$. With this in mind, we can now study the Hamiltonian of the system of a quantum dot and an Andreev bound state. It can be written as $H_{\mathrm{A}} = H_{\mathrm{d}} + H_{\mathrm{Ta}} + H_{\mathrm{a}}$ where the Hamiltonian for the Andreev bound state, H_{a}, is

$$\begin{aligned} H_{\mathrm{a}} &= \delta'\gamma_{\mathrm{A}}^{\dagger}\gamma_{\mathrm{A}} \\ &= \delta'\left(|\mu|^2\, c^{\dagger}c + |\nu|^2\, cc^{\dagger} + \mu\nu c^{\dagger}c^{\dagger} + \nu\mu cc\right) \\ &\equiv \delta c^{\dagger}c, \end{aligned} \tag{7}$$

with $\delta = \delta'(|\mu|^2 - |\nu|^2)$. Due to the particle–hole symmetry of the superconducting system, we can always obtain another Andreev bound state by defining a new operator $\gamma_{\mathrm{A}'} = \gamma_{\mathrm{A}}^{\dagger}$. This leads to the excitation energy $-\delta$, which accounts for the negative energy excitations observed in experiments [17,37]. The tunneling Hamiltonian between the Andreev bound state and the quantum dot is,

$$\begin{aligned} H_{\mathrm{Ta}} &= T\left(d^{\dagger}\gamma_{\mathrm{A}} + \gamma_{\mathrm{A}}^{\dagger}d\right) \\ &= T_{\mu}\left(d^{\dagger}c + c^{\dagger}d\right) + T_{\nu}\left(d^{\dagger}c^{\dagger} + cd\right), \end{aligned} \tag{8}$$

where we define $T_{\mu} = \mu T$ and $T_{\nu} = \nu T$. Now we can establish a basis for H_{A} with eigenstates $|0\rangle$, $d^{\dagger}c^{\dagger}|0\rangle$, $c^{\dagger}|0\rangle$ and $d^{\dagger}|0\rangle$, and rewrite in the matrix form,

$$\tilde{H}_{\mathrm{A}} = \begin{pmatrix} 0 & T_{\nu} & 0 & 0 \\ T_{\nu} & \varepsilon+\delta & 0 & 0 \\ 0 & 0 & \delta & T_{\mu} \\ 0 & 0 & T_{\mu} & \varepsilon \end{pmatrix}. \tag{9}$$

It looks similar to Equation 5 but with one critical difference: The off-diagonal terms in the upper left block and the lower right block are now different because they contain electron and hole wave functions, which are different for Andreev bound states. We note that the Andreev bound state may have equivalent particle and hole components ($u_{\uparrow} = v_{\uparrow}$) for some spin directions. For this case, the matrices in Equation 5 and Equation 9 are identical if the energy level of the quantum dot is in the same direction. However, the spin direction of the quantum level on the dot can be reversed by inverting the Zeeman field. Then the matrix for the Andreev bound state contains the electron and hole wave functions in the reverse spin direction and must be different.

Spatial Rabi oscillations

Now we are ready to consider the spacial Rabi oscillations where an electron oscillates between the quantum dot and the bound states. For this purpose we solve the Schrödinger equation $i\hbar d\Psi / dt = \tilde{H}_{\mathrm{M/A}}\Psi$. The Hamiltonian is periodic in time, therefore the equation is not exactly solvable. To obtain the Rabi oscillations, we need to study the transition probability from one state to the other under this time periodic Hamiltonian. We take advantage of the Floquet theory, which states that the solution of the Schrödinger equation for any time-periodic Hamiltonian must satisfy $\Psi(t) = \psi(t)\, e^{-iDt}$, with $\psi(t) = \psi(t + (2\pi/\omega)$ a time-periodic function that has a Fourier transformation $\psi(t) = \sum_n \psi_n e^{in\omega t}$. Let us first consider the scenario of Majorana bound states where we can obtain a series of secular equations by inserting the ansatz solution back into the Schrödinger equation,

$$(D - n\omega)\psi_n = \sum_l H_l \psi_{n-l}, \tag{10}$$

where $l = 0, \pm 1$, and the Fourier transformed components of the Hamiltonian H_l are

$$\begin{aligned} H_0 &= \begin{pmatrix} \delta & T_0 & 0 & 0 \\ T_0 & \varepsilon-\delta & 0 & 0 \\ 0 & 0 & -\delta & T_0 \\ 0 & 0 & T_0 & \varepsilon+\delta \end{pmatrix}, \\ H_{\pm 1} &= \begin{pmatrix} 0 & T_1 & 0 & 0 \\ T_1 & 0 & 0 & 0 \\ 0 & 0 & 0 & T_1 \\ 0 & 0 & T_1 & 0 \end{pmatrix}. \end{aligned} \tag{11}$$

Now the problem of solving a time-dependent Schrödinger equation is transformed to a problem of solving a set of time-independent secular equations [40]. Since ψ_n is a vector with two components, special care is needed when trying to solve the secular equations. They should be rewritten as

$$D\psi_{n,\alpha} = \sum_{l,\beta}\left(H_{n-l,\alpha,\beta} + n\omega I_{\alpha,\beta}\delta_{nl}\right)\psi_{l,\beta},$$

with $\alpha,\beta = 0, 1, 2, 3$. Then, the secular equations can be viewed as the eigenproblem for the infinite dimensional Floquet Hamiltonian [40],

$$H_{\mathrm{F}} = \begin{pmatrix} \ddots & & & \\ & H_0+\omega & H_1 e^{i\omega t} & 0 \\ & H_{-1}e^{-i\omega t} & H_0 & H_1 e^{i\omega t} \\ & 0 & H_{-1}e^{-i\omega t} & H_0-\omega \\ & & & \ddots \end{pmatrix}. \tag{12}$$

In this Floquet formalism, the transition probability between any two states is written as

$$P_{\alpha\to\beta} = \sum_n \left|\langle n,\beta| e^{-iH_{\mathrm{F}}(t-t_0)} |0,\alpha\rangle\right|^2, \tag{13}$$

which could be calculated once we solve the eigenproblem for the Floquet Hamiltonian.

In the Floquet Hamiltonian, the off-diagonal elements are between the nearest blocks. For the zero-order perturbation, we first consider the transition between $|0,\alpha\rangle$ and $|\pm1,\beta\rangle$. Two cases are studied: α = 0 with β = 1 and α = 2 with β = 3. Then we can extract a 4 × 4 matrix,

$$\tilde{H}_{\text{bare}} = \begin{pmatrix} \delta & T_1 & 0 & 0 \\ T_1 & \varepsilon-\delta-\omega & 0 & 0 \\ 0 & 0 & -\delta & T_1 \\ 0 & 0 & T_1 & \varepsilon+\delta-\omega \end{pmatrix}, \tag{14}$$

which of course can be divided into two relevant 2 × 2 matrices,

$$\begin{aligned} \tilde{H}^{\text{U}}_{\text{bare}} &= \begin{pmatrix} \delta & T_1 \\ T_1 & \varepsilon-\delta-\omega \end{pmatrix}, \\ \tilde{H}^{\text{L}}_{\text{bare}} &= \begin{pmatrix} -\delta & T_1 \\ T_1 & \varepsilon+\delta-\omega \end{pmatrix}. \end{aligned} \tag{15}$$

We can also include the second-order perturbation, which slightly alters the diagonal elements of the 2 × 2 matrix,

$$\begin{aligned} \tilde{H}^{\text{U}}_{\text{eff}} &= \begin{pmatrix} \delta+\Delta_{\text{M}} & T_1 \\ T_1 & \varepsilon-\delta-\omega-\Delta_{\text{M}} \end{pmatrix}, \\ \tilde{H}^{\text{L}}_{\text{eff}} &= \begin{pmatrix} -\delta+\Delta_{\text{M}'} & T_1 \\ T_1 & \varepsilon+\delta-\omega-\Delta_{\text{M}'} \end{pmatrix}, \end{aligned} \tag{16}$$

where

$$\Delta_{\text{M}} = \sum_{n,\alpha} \frac{\left|H_{0n,0\alpha}\right|^2}{E_{|0,0\rangle} - E_{|n,\alpha\rangle}} = -\frac{T_0^2 + T_1^2/2}{\varepsilon - 2\delta}$$

and

$$\Delta_{\text{M}'} = -\frac{T_0^2 + T_1^2/2}{\varepsilon + 2\delta}.$$

Now the transition probability is clear. Starting from an initial state

$$\left|\psi(0)\right| = \left[\frac{\sqrt{2}}{2}, 0, \frac{\sqrt{2}}{2}, 0\right]^T,$$

we would have a Rabi oscillation for

$$\begin{aligned} \left|\psi_0(t)\right|^2 &= \frac{1}{2} - \frac{T_0^2}{2\omega_r^2}\sin^2\omega_r t, \\ \left|\psi_1(t)\right|^2 &= \frac{T_0^2}{2\omega_r^2}\sin^2\omega_r t, \end{aligned} \tag{17}$$

with

$$\omega_r^2 = T_1^2 + \left[\frac{\varepsilon}{2} - \delta + \frac{\left(T_0^2 + T_1^2/2\right)}{(\varepsilon - 2\delta)} - \frac{\omega}{2}\right]^2,$$

or for

$$\begin{aligned} \left|\psi_2(t)\right|^2 &= \frac{1}{2} - \frac{T_1^2}{2\omega_{r'}^2}\sin^2\omega_{r'} t, \\ \left|\psi_3(t)\right|^2 &= \frac{T_1^2}{2\omega_{r'}^2}\sin^2\omega_{r'} t, \end{aligned} \tag{18}$$

with

$$\omega_{r'}^2 = T_1^2 + \left[\frac{\varepsilon}{2} + \delta + \frac{\left(T_0^2 + T_1^2/2\right)}{(\varepsilon + 2\delta)} - \frac{\omega}{2}\right]^2.$$

Clearly, there are Rabi oscillations at with two resonant driving energies at

$$\omega = \varepsilon \pm 2\delta + \frac{2T_0^2 + T_1^2}{\varepsilon \pm 2\delta}.$$

However, for both resonant driving energies, the Rabi frequency is the same $\omega_r = \omega_{r'} = T_1$. This is not a coincidence, but is a result of the self-conjugateness of the Majorana bound states.

Now we consider the scenario of Andreev bound states. With the same Floquet approach, we can obtain the effective Floquet Hamiltonians,

$$\begin{aligned} \tilde{H}^{\text{UA}}_{\text{eff}} &= \begin{pmatrix} \Delta_{\text{A}} & \nu T_1 \\ \nu T_1 & \varepsilon+\delta-\omega-\Delta_{\text{A}} \end{pmatrix}, \\ \tilde{H}^{\text{LA}}_{\text{eff}} &= \begin{pmatrix} \delta+\Delta_{\text{A}'} & \mu T_1 \\ \mu T_1 & \varepsilon-\omega-\Delta_{\text{A}'} \end{pmatrix}, \end{aligned} \tag{19}$$

where

$$\Delta_{\mathrm{A}} = \varepsilon + \delta + \frac{(\nu T_1)^2}{\varepsilon + \delta}$$

and

$$\Delta_{\mathrm{A}'} = \varepsilon - \delta + \frac{(\mu T_1)^2}{\varepsilon - \delta}$$

when we set $T_0 = 0$. Clearly, we also have two resonant driving energies. However, now we have different Rabi frequencies for these two resonant driving energies, $\omega_r = \nu T_1$ and $-\omega_{r'} = \mu T_1$, which are given by solving the Floquet Hamiltonians in Equation 19. The difference between the Rabi frequencies comes from different particle and hole wave functions, μ and ν, for the Andreev bound states.

We present numerical simulations for the hybrid system in Figure 2. First, we show the largest oscillation amplitude on the quantum dot as a function of the driving energy ω in Figure 2a, where the scenario for Majorana bound states and for Andreev bound states present the same result. The two peaks represent the two resonant driving energies. For the Majorana bound state, the energy difference between these two peaks is proportional to the splitting energy between the two Majorana bound states at the ends of the island. Since the measurement of Rabi oscillation is much more accurate than transport measurements, the resonant driving energy provides a precise method to measure the exponential decay of the splitting energy. The Rabi oscillations of the occupation state of the quantum dot for Majorana and Andreev bound states are presented in Figure 2b. We find that the Rabi frequencies of the Majorana bound state are identical as predicted by the analytic results based on the Floquet theory. For comparison, we also present the Rabi frequencies for the Andreev bound state. The Rabi frequencies are different, reflecting the inequality of the electron and hole components for the Andreev bound state.

The results presented in Figure 2 are the central results of our work. We emphasize that these theoretical results can be measured with existing experimental techniques. Our calculation gives the Rabi oscillations of the occupation states of the quantum dot, which can be measured by probing the electron occupation on the quantum dot. The measurement of the electron occupation state of the quantum dot has been achieved with the single-electron transistor [27,41], which is a routine technique in the study of charge qubits based on quantum dots [42].

Finally, we note that our results are based on the minimal models for the quantum dot, the Majorana bound state and the Andreev bound state. It is certainly helpful to consider more sophisticated models for the quantum dot by including the Zeeman energy and Coulomb energy explicitly, and more realistic models for the Majorana bound state and Andreev bound state by exploiting the Bogoliubov–de Gennes Hamiltonian. However, these works are beyond the scope of our current work and belong to our plan of future works.

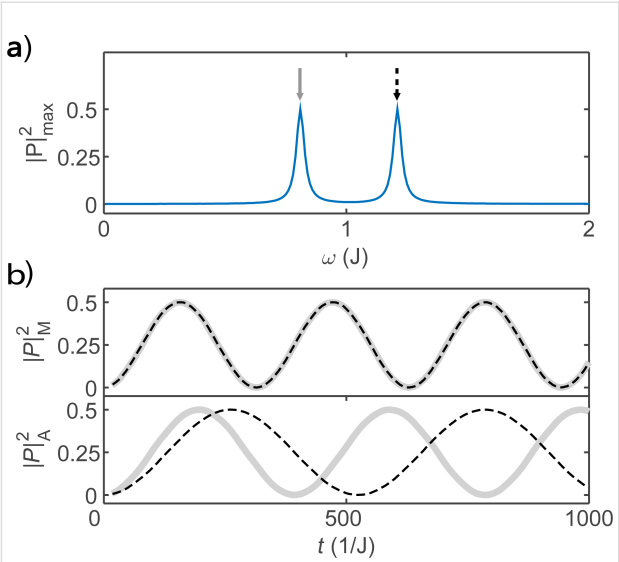

Figure 2: Numerical simulations of the Rabi oscillations. (a) The maximum Rabi oscillation amplitude measured by the occupation probability of the quantum dot, as a function of the driving energy, where the two peaks marks the resonant driving energies. (b) The Rabi oscillation for the two resonant driving energies for the Majorana bound state (upper panel) and the Andreev bound state (lower panel). We see that the Rabi frequencies are identical for the Majorana bound state while they are different for the Andreev bound state. Parameters are taken as $\varepsilon \equiv J$, $T_0 = 0$, $\delta = 0.1J$, $T_1 = 0.01J$, $\delta = 0.2J$, $\mu T_1 = 0.008J$ and $\nu T_1 = 0.006J$ with the initial state $\Psi(0) = [(\sqrt{2}/2), 0, (\sqrt{2}/2), 0]^T$.

Correlation between quantum dots through Majorana islands

Now we investigate the setup with two quantum dots on the two sides of a nanowire island, as shown in Figure 3. In this setup, nonlocal entanglement between quantum dots mediated by Majorana bound states has been discussed [28]. It seems logical to consider how this nonlocal entanglement influences the Rabi oscillations. First, each quantum dot certainly has Rabi oscillations with a Majorana bound state or an Andreev bound state at each end. However, we will show a more interesting correlation between quantum dots mediated by two Majorana bound states. This correlation does not occur for the Andreev bound state. Let us first establish the Hamiltonian for the proposed setup. The two quantum dots have the Hamiltonian

$$H_{2\mathrm{d}} = \varepsilon_1 d_1^\dagger d_1 + \varepsilon_2 d_2^\dagger d_2, \tag{20}$$

where $\varepsilon_{1,2}$ are the energy for quantum dot levels, and $d^{\dagger}_{1,2}$ are the creation operators on the quantum dot levels.

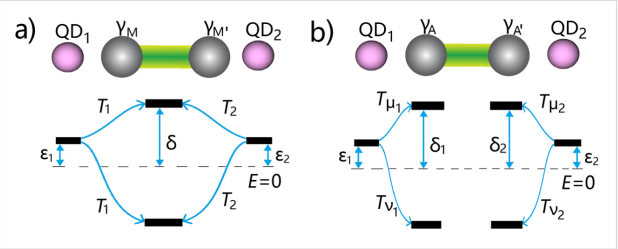

Figure 3: Schematics of two quantum dots coupling with the nanowire island with (a) two Majorana bound states and (b) two Andreev bound states. The two Majorana bound states form a single energy level, while the Andreev bound states form two energy levels.

The Hamiltonian for the Majorana bound states is the same as in the previous section, which could be described by a fermionic operator $f^{\dagger} = (\gamma_M - i\gamma_{M'})/2$. The two quantum dots are coupled with the Majorana bound states through the tunneling Hamiltonian

$$H_{2T} = T_1\gamma_M\left(d_1 + d_1^{\dagger}\right) + T_2\gamma_{M'}\left(d_2 + d_2^{\dagger}\right), \qquad (21)$$

where $T_{1,2}$ are the tunneling strength between the left and the right pair of quantum dot and Majorana bound state in the form of $T_{1,2} = 2T'_{1,2}\cos\omega_{1,2}t$. We can explicitly write down the total Hamiltonian in the matrix form by defining basis functions $f^{\dagger}|0\rangle$, $d_1^{\dagger}|0\rangle$, $d_1^{\dagger}d_2^{\dagger}f^{\dagger}|0\rangle$, $d_2^{\dagger}|0\rangle$, $|0\rangle$, $d_1^{\dagger}f^{\dagger}|0\rangle$, $d_1^{\dagger}d_2^{\dagger}|0\rangle$ and $d_2^{\dagger}f^{\dagger}|0\rangle$, where $|0\rangle$ is the vacuum state. We arrive at an 8 × 8 matrix that is block diagonal because the total fermionic parity of the system is conserved. For simplify, we take the even total parity, and get a 4 × 4 matrix,

$$H_{M'} = \begin{pmatrix} \delta & T_1 & 0 & -iT_2 \\ T_1 & \varepsilon_1 - \delta & iT_2 & 0 \\ 0 & -iT_2 & \varepsilon_1 + \varepsilon_2 + \delta & T_1 \\ iT_2 & 0 & T_1 & \varepsilon_2 - \delta \end{pmatrix}. \qquad (22)$$

Now let us look at the quantum dots coupling with two Andreev bound states at the end of the nanowire island. Since Andreev bound states are eigenstates of superconductors, there are, in principle, four energy levels in the entire system. The Hamiltonian of the system cam be written as

$$H'_A = \sum_{i=1,2} \varepsilon_i d_i^{\dagger}d_i + \delta_i c_i^{\dagger}c_i + T_{i\mu}\left(d_i^{\dagger}c_i + c_i^{\dagger}d_i\right) + T_{i\nu}\left(d_i^{\dagger}c_i^{\dagger} + c_i d_i\right), \qquad (23)$$

where i represents the left/right side of each operator with $T_{i\mu} = \mu T_i$, $T_{iv} = \nu T_i$. For this case, the system can be divided into left and right segments, which are uncoupled from each other. For simplicity, we take the even parity of both sides, where the basis states are chosen as $|0\rangle$, $d_1^{\dagger}c_1^{\dagger}|0\rangle$, $d_1^{\dagger}d_2^{\dagger}c_1^{\dagger}c_2^{\dagger}|0\rangle$ and $d_2^{\dagger}c_2^{\dagger}|0\rangle$. Then the Hamiltonian can be reformed to a four by four matrix:

$$H'_{A_1} = \begin{pmatrix} 0 & T_{1v} & 0 & T_{2v} \\ T_{1v} & \varepsilon_1 + \delta_1 & T_{2v} & 0 \\ 0 & T_{2v} & \varepsilon_1 + \varepsilon_2 + \delta_1 + \delta_2 & T_{1v} \\ T_{2v} & 0 & T_{1v} & \varepsilon_2 + \delta_2 \end{pmatrix}. \qquad (24)$$

We find that this matrix is very similar to the matrix of quantum dots and Majorana bound states. However, there is the key distinction that the left quantum dot and the right quantum dot should be entirely uncoupled. We note that this matrix is different from the one shown in Equation 22 even if μ = ν, since the two Andreev bound states correspond to two superconducting quasiparticles with a 4 × 4 Hilbert subspace, while the two Majorana bound states gives a single superconducting quasiparticle with a 2 × 2 Hilbert subspace.

We numerically simulate the oscillations for the Majorana bound states scenario and illustrate the maximum oscillation amplitude for the occupation state of the left quantum dot in Figure 4a. We find three lines of resonant driving energy. The two vertical lines represent the resonant Rabi oscillation at $\omega_1 = \varepsilon_1 \pm 2\delta$, with a typical result shown in Figure 4c. They are identical to the case of the single quantum dot and represents the Rabi oscillation between the left quantum dot and the two Majorana bound states, while leaving the right quantum dot

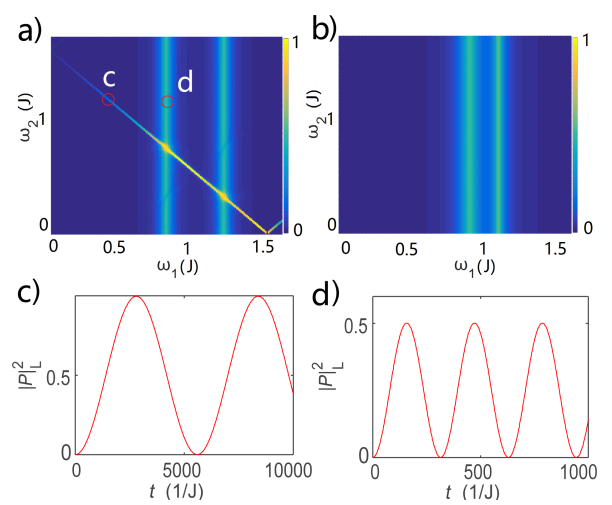

Figure 4: The maximum occupation probability of the left quantum dot for (a) Majorana bound states and (b) Andreev bound states. Panels (c) and (d) give the detailed oscillation as a function of the time at two specific parameters marked as circles on (a).

uninvolved. There is one extra line that represents the resonant Rabi driving energy at $\omega_1 + \omega_2 = \varepsilon_1 + \varepsilon_2$. This resonant energy involves both quantum dots, and therefore would be coming from the nonlocal entanglement of the quantum dots. We present a typical Rabi oscillation in Figure 4d. It is the higher-order oscillations between the states $|00\rangle$ and $|11\rangle$, namely a charge oscillation between the left and right quantum dots. This is a nonlocal coherent charge transfer process between the quantum dots mediated by the two Majorana bound states. For comparison, we illustrate the results for quantum dot occupation mediated through Andreev bound states. We find that the Rabi oscillations at $\omega_1 \approx \varepsilon_1 \pm \delta$ still exist, however, the higher-order oscillations disappear. This can be explained by the fact that left and the right part of the setup are uncoupled. The extra resonant driving energy for Majorana bound states is a result of the nonlocal quantum dot correlation and can be used as a signature for Majorana bound states.

Conclusion

We studied the spatial Rabi oscillation between quantum dots and Majorana bound states in a topological superconducting island. We demonstrate that the coupling energy between Majorana bound states can be detected by investigating the resonant driving energy for the Rabi oscillation. We also show that the Rabi oscillating frequency carries the information of the electron and hole components, therefore can be used to differentiate Majorana bound states and Andreev bound states. At the two resonant driving energies, we find identical Rabi frequencies for Majorana bound states and different Rabi frequencies for Andreev bound states. We further study the case of two quantum dots coupled through the island and show that the Majorana bound states are able to create correlated higher-order Rabi oscillations on the quantum dots.

Acknowledgements

This work was supported by the National Natural Science Foundation of China under Grants No. 11774435 and No. 61471401, and China Scholarship Council under Grants No. 201706385057.

ORCID® iDs

Zhi Wang - https://orcid.org/0000-0003-4788-6737

References

1. Read, N.; Green, D. *Phys. Rev. B* **2000,** *61,* 10267–10297. doi:10.1103/PhysRevB.61.10267
2. Kitaev, A. Yu. *Phys.-Usp.* **2000,** *44,* 131–136. doi:10.1070/1063-7869/44/10S/S29
3. Liu, D. E.; Baranger, H. U. *Phys. Rev. B* **2011,** *84,* 201308. doi:10.1103/PhysRevB.84.201308
4. Ivanov, D. A. *Phys. Rev. Lett.* **2001,** *86,* 268–271. doi:10.1103/PhysRevLett.86.268
5. Lutchyn, R. M.; Sau, J. D.; Das Sarma, S. *Phys. Rev. Lett.* **2010,** *105,* 077001. doi:10.1103/PhysRevLett.105.077001
6. Sau, J. D.; Lutchyn, R. M.; Tewari, S.; Das Sarma, S. *Phys. Rev. Lett.* **2010,** *104,* 040502. doi:10.1103/PhysRevLett.104.040502
7. Prada, E.; Aguado, R.; San-Jose, P. *Phys. Rev. B* **2017,** *96,* 085418. doi:10.1103/PhysRevB.96.085418
8. Liu, C.-X.; Sau, J. D.; Stanescu, T. D.; Das Sarma, S. *Phys. Rev. B* **2017,** *96,* 075161. doi:10.1103/PhysRevB.96.075161
9. Oreg, Y.; Refael, G.; von Oppen, F. *Phys. Rev. Lett.* **2010,** *105,* 177002. doi:10.1103/PhysRevLett.105.177002
10. Huang, Z.; Shimasaki, S.; Nitta, M. *Phys. Rev. B* **2017,** *96,* 220504. doi:10.1103/PhysRevB.96.220504
11. Ptok, A.; Kobiałka, A.; Domański, T. *Phys. Rev. B* **2017,** *96,* 195430. doi:10.1103/PhysRevB.96.195430
12. Sticlet, D.; Nijholt, B.; Akhmerov, A. *Phys. Rev. B* **2017,** *95,* 115421. doi:10.1103/PhysRevB.95.115421
13. Fu, L.; Kane, C. L. *Phys. Rev. Lett.* **2008,** *100,* 096407. doi:10.1103/PhysRevLett.100.096407
14. Landau, L. A.; Sela, E. *Phys. Rev. B* **2017,** *95,* 035135. doi:10.1103/PhysRevB.95.035135
15. Hasan, M. Z.; Kane, C. L. *Rev. Mod. Phys.* **2010,** *82,* 3045–3067. doi:10.1103/RevModPhys.82.3045
16. Qi, X.-L.; Zhang, S.-C. *Rev. Mod. Phys.* **2011,** *83,* 1057–1110. doi:10.1103/RevModPhys.83.1057
17. Alicea, J. *Rep. Prog. Phys.* **2012,** *75,* 076501. doi:10.1088/0034-4885/75/7/076501
18. Beenakker, C. W. J. *Annu. Rev. Condens. Matter Phys.* **2013,** *4,* 113–136. doi:10.1146/annurev-conmatphys-030212-184337
19. Stanescu, T. D.; Tewari, S. *J. Phys.: Condens. Matter* **2013,** *25,* 233201. doi:10.1088/0953-8984/25/23/233201
20. Elliott, S. R.; Franz, M. *Rev. Mod. Phys.* **2015,** *87,* 137–163. doi:10.1103/RevModPhys.87.137
21. Mourik, V.; Zuo, K.; Frolov, S. M.; Plissard, S. R.; Bakkers, E. P. A. M.; Kouwenhoven, L. P. *Science* **2012,** *336,* 1003. doi:10.1126/science.1222360
22. Deng, M. T.; Yu, C. L.; Huang, G. Y.; Larsson, M.; Caroff, P.; Xu, H. Q. *Nano Lett.* **2012,** *12,* 6414–6419. doi:10.1021/nl303758w
23. San-Jose, P.; Prada, E.; Aguado, R. *Phys. Rev. Lett.* **2012,** *108,* 257001. doi:10.1103/PhysRevLett.108.257001
24. Albrecht, S. M.; Higginbotham, A. P.; Madsen, M.; Kuemmeth, F.; Jespersen, T. S.; Nygård, J.; Krogstrup, P.; Marcus, C. M. *Nature* **2016,** *531,* 206–209. doi:10.1038/nature17162
25. Deng, M.; Vaitiekénas, S.; Prada, E.; San-Jose, P.; Nygård, J.; Krogstrup, P.; Aguado, R.; Marcus, C. *arXiv* **2017,** No. 1712.03536.
26. Escribano, S. D.; Yeyati, A. L.; Prada, E. *arXiv* **2017,** No. 1712.07625.
27. Flensberg, K. *Phys. Rev. Lett.* **2011,** *106,* 090503. doi:10.1103/PhysRevLett.106.090503
28. Wang, Z.; Hu, X.-Y.; Liang, Q.-F.; Hu, X. *Phys. Rev. B* **2013,** *87,* 214513. doi:10.1103/PhysRevB.87.214513
29. Wang, Z.; Liang, Q.-F.; Yao, D.-X.; Hu, X. *Sci. Rep.* **2015,** *5,* 11686. doi:10.1038/srep11686
30. Cheng, M.; Becker, M.; Bauer, B.; Lutchyn, R. M. *Phys. Rev. X* **2014,** *4,* 031051. doi:10.1103/PhysRevX.4.031051
31. Lü, H.-F.; Lu, H.-Z.; Shen, S.-Q. *Phys. Rev. B* **2014,** *90,* 195404. doi:10.1103/PhysRevB.90.195404
32. Li, D.; Kuo, W.; Chung, M.-C. *Sci. Rep.* **2015,** *5,* 11188. doi:10.1038/srep11188
33. Li, Y.-X.; Bai, Z.-M. *J. Appl. Phys.* **2013,** *114,* 033703. doi:10.1063/1.4813229

34. Gong, W.-J.; Gao, Z.; Shan, W.-F.; Yi, G.-Y. *Sci. Rep.* **2016,** *6,* 23033. doi:10.1038/srep23033
35. Jiang, Z. T.; Li, S. *AIP Adv.* **2016,** *6,* 125122. doi:10.1063/1.4973565
36. Deng, M. T.; Vaitiekėnas, S.; Hansen, E. B.; Danon, J.; Leijnse, M.; Flensberg, K.; Nygård, J.; Krogstrup, P.; Marcus, C. M. *Science* **2016,** *354,* 1557. doi:10.1126/science.aaf3961
37. Liu, C.-X.; Sau, J. D.; Stanescu, T. D.; Das Sarma, S. *Phys. Rev. B* **2017,** *96,* 075161. doi:10.1103/PhysRevB.96.075161
38. Schuray, A.; Weithofer, L.; Recher, P. *Phys. Rev. B* **2017,** *96,* 085417. doi:10.1103/PhysRevB.96.085417
39. Kaestner, B.; Kashcheyevs, V. *Rep. Prog. Phys.* **2015,** *78,* 103901. doi:10.1088/0034-4885/78/10/103901
40. Shirley, J. H. *Phys. Rev.* **1965,** *138,* B979–B987. doi:10.1103/PhysRev.138.B979
41. Hützen, R.; Zazunov, A.; Braunecker, B.; Yeyati, A. L.; Egger, R. *Phys. Rev. Lett.* **2012,** *109,* 166403. doi:10.1103/PhysRevLett.109.166403
42. Harvey-Collard, P.; Jacobson, N. T.; Rudolph, M.; Dominguez, J.; Ten Eyck, G. A.; Wendt, J. R.; Pluym, T.; Gamble, J. K.; Lilly, M. P.; Pioro-Ladrière, M.; Carroll, M. S. *Nat. Commun.* **2017,** *8,* 1029. doi:10.1038/s41467-017-01113-2

License and Terms

BEILSTEIN JOURNAL OF NANOTECHNOLOGY

Solid-state Stern–Gerlach spin splitter for magnetic field sensing, spintronics, and quantum computing

Kristofer Björnson*[1,2] and Annica M. Black-Schaffer[1]

Full Research Paper

Open Access

Address:
[1]Department of Physics and Astronomy, Uppsala University, Box 516, S-751 20 Uppsala, Sweden and [2]Niels Bohr Institute, University of Copenhagen, Juliane Maries Vej 30, DK-2100 Copenhagen, Denmark

Email:
Kristofer Björnson* - kristofer.bjornson@physics.uu.se

* Corresponding author

Keywords:
Aharanov–Bohm; quantum computing; spintronics; Stern–Gerlach; SU(2); topological insulator

Beilstein J. Nanotechnol. **2018,** *9,* 1558–1563.
doi:10.3762/bjnano.9.147

Received: 22 November 2017
Accepted: 24 April 2018
Published: 25 May 2018

This article is part of the Thematic Series "Topological materials".

Guest Editor: J. J. Palacios

Abstract

We show conceptually that the edge of a two-dimensional topological insulator can be used to construct a solid-state Stern–Gerlach spin splitter. By threading such a Stern–Gerlach apparatus with a magnetic flux, Aharanov–Bohm-like interference effects are introduced. Using ferromagnetic leads, the setup can be used to both measure magnetic flux and as a spintronics switch. With normal metallic leads a switchable spintronics NOT-gate can be implemented. Furthermore, we show that a sequence of such devices can be used to construct a single-qubit SU(2)-gate, one of the two gates required for a universal quantum computer. The field sensitivity, or switching field, b, is related to the characteristic size of the device, r, through $b = h/(2\pi q r^2)$, with q being the unit of electric charge.

Introduction

Two famous examples of the fundamental difference between quantum mechanical and classical particles are provided through the Stern–Gerlach (SG) experiment [1] and the Aharanov–Bohm (AB) effect [2]. The SG experiment demonstrates the peculiar behavior of the quantum mechanical spin, teaching us that for any chosen axis the spin can be pointing either up or down. Even more nonintuitive, the spin can also be in a superposition of these two states, and thereby split in a SG apparatus to travel along different paths [1]. The AB effect, on the other hand, shows that the introduction of a magnetic vector potential has important effects on the phase of the wave function. This is not merely a mathematical formality, but has measurable consequences in interference measurements. When a particle travels along two different paths that enclose a magnetic flux, it picks up different phases along the two paths, even though the paths do not pass through the magnetic flux [2].

A topological insulator is a material with insulating bulk, but with topologically protected helical edge states. Here we show that it is possible to construct a solid state SG apparatus, or spin

splitter, using the edge states in a two-dimensional topological insulator (2D TI) [3-13]. The device consists of a small hole drilled in the 2D TI, contacted by two leads. By threading a magnetic flux through the hole an AB-like effect gives rise to important interference effects, which allows for precise manipulation of spin currents, as has already been noted in [14]. While the ordinary AB effect arises because of interference in a single complex number, the effects achieved here relies on modifying the relative phase between the up and down components of the spin. Thus, the effects we describe here can be classified as a SU(2)-AB effects, while the ordinary situation corresponds to a U(1)-AB effect.

While the AB effect recently has attracted some attention in 3D TI [15-19], we here outline the concept for several concrete and different applications of the SU(2)-AB effect in a 2D TI. More specifically, we find that if using ferromagnetic leads, the device can be used for sensitive measurements of magnetic field strengths. The same setup can also be used to implement a spintronic switch. Instead using normal metallic leads, we show that a switchable spintronics NOT-gate can be constructed. Finally, we also demonstrate how a sequential setup of normal-lead solid-state SG spin splitters can be used to construct a single-qubit SU(2)-gate, one of two gates required to construct a universal quantum computer [20]. This also demonstrates the full extent to which the effect is best thought of as a generalization of the AB effect from U(1)-AB to SU(2)-AB.

Results

Setup

Consider the conceptual setup in Figure 1. The circular channel around the hole forms an edge of the 2D TI and therefore hosts helical edge states. We assume for simplicity that the spin-polarization axis is perpendicular to the plane of the TI. The Hamiltonian describing the two counter-propagating edge channels is then simply given by

$$H_{\uparrow} = -\frac{\mathrm{i}\hbar}{r}\partial_{\theta},$$
$$H_{\downarrow} = \frac{\mathrm{i}\hbar}{r}\partial_{\theta},$$

where arrows indicate the spin direction. In the ground state no net current is carried from one side to the other. Since the system is symmetric under a rotation of π around the z-axis orthogonal to the TI, even persistent currents are prevented. However, if a voltage is applied across the circuit, electrons can start to flow from one side to the other, say from the left to the right. This current will be proportional to the transfer matrix of the states that are occupied at the left side, but unoccupied on the right. We therefore begin by calculating this transfer matrix.

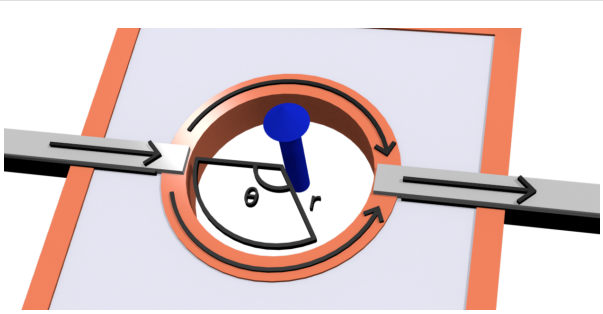

Figure 1: A hole drilled in a 2D TI creates two edge channels (orange). Leads (grey) are attached on each side of the hole, and a bias voltage is applied across the circuit. The transport properties of the device can be altered by threading a magnetic flux (blue arrow) through the hole, as well as by choosing either ferromagnetic or normal leads. The circular shape is not essential, but is used to simplify calculations.

When considering processes that transfers electrons from the left to the right, we can, because of the helicity of the edge states, restrict ourselves to up-spins along the upper edge, and down-spins along the lower edge. Further, we introduce the coordinate $x_1 = r(2\pi - \theta)$ and $x_2 = r\theta$ along the upper and lower edges, respectively. The eigenvalue equations along the two edges are then

$$H_{\uparrow}\Psi_{\uparrow p} = \mathrm{i}\hbar\partial_{x_1}\Psi_{\uparrow p} = E\Psi_{\uparrow p},$$
$$H_{\downarrow}\Psi_{\downarrow p} = \mathrm{i}\hbar\partial_{x_2}\Psi_{\downarrow p} = E\Psi_{\downarrow p},$$

and the corresponding eigenstates can be written as

$$\left|\Psi_{\uparrow p}\right\rangle = \begin{bmatrix}1\\0\end{bmatrix} e^{-\mathrm{i}px_1/\hbar},$$
$$\left|\Psi_{\downarrow p}\right\rangle = \begin{bmatrix}0\\1\end{bmatrix} e^{-\mathrm{i}px_2/\hbar}.$$

We now thread a magnetic flux of magnetic field strength B through the hole. To describe this we choose the vector potential $A = (B/2)r\hat{\theta}$, which translates into $-(B/2)r\hat{x}_1$ and $(B/2)r\hat{x}_2$ in the new (x_1, x_2)-coordinates. The addition of this vector potential acts on the phase of the eigenstates according to

$$\left|\Psi_{\uparrow p}\right\rangle = \begin{bmatrix}1\\0\end{bmatrix} e^{-\mathrm{i}(p+qBr/2)x_1/\hbar},$$
$$\left|\Psi_{\downarrow p}\right\rangle = \begin{bmatrix}0\\1\end{bmatrix} e^{-\mathrm{i}(p-qBr/2)x_2/\hbar},$$

where q is the unit of electric charge. It is therefore clear that the transfer matrix that describes the transport of spins from

the left side, $x_1 = x_2 = 0$, to the right side, $x_1 = x_2 = r\pi$, is given by

$$O = e^{-\mathrm{i}pr\pi/\hbar}\begin{bmatrix} e^{-\mathrm{i}qBr^2\pi/2\hbar} & 0 \\ 0 & e^{\mathrm{i}qBr^2\pi/2\hbar} \end{bmatrix}. \qquad (1)$$

We here note that under a gauge transformation $A \to A + A'$, where A' satisfies $\int_0^{2\pi} A'(\theta)\mathrm{d}\theta = 0$, the transfer matrix transforms as

$$O \to Oe^{\left(\mathrm{i}\frac{q}{\hbar}\int_0^{\pi} A'(\theta)\mathrm{d}\theta\right)}.$$

We have confirmed that this additional phase drops out of all physical quantities below, proving the gauge invariance of our results, and we can therefore set $A' = 0$. Similarly, the overall phase in the above equation will drop out of all physical quantities. This also justifies us in not having specified the chemical potential. Because, as long as the spectrum is described by the same edge Hamiltonian, the only role of the chemical potential is to determine around which momentum p_f the relevant excitations are located.

Transfer between lead and edge channels

The total transfer matrix for the system will not only depend on the transfer matrix that describes the motion around the hole, but also on the matrices that describe the transfer processes between the leads and the circular edge. We will here assume that this process preserves phase coherence between the states in the leads and the TI edge states, and that it is described by a single tunneling parameter t, which we for now set to $t = 1$ to indicate perfect transmission between lead and edge. That is, the transmission is described by the identity matrix, and therefore contributes trivially to the total transfer matrix. However, we will in what follows be interested in tilting the TI by an angle φ relative to the quantization axis of the leads. It is therefore necessary to also let the total transfer matrix encode a change of basis between the leads and the TI. For this purpose we define two sets of coordinate axes, the laboratory axes x,y,z, and the TI axes x',y',z'. We choose to describe the electrons in the leads with the coordinates in the laboratory frame, while the edge states in the TI are described by the primed coordinates. It is clear that Equation 1 refers to the transfer of states in the primed basis. In particular, we choose the x,x'-axes along the direction of motion of the electrons through the circuit, while the z,z'-axes are chosen such that they coincide when $\varphi = 0$ and z' is always perpendicular to the TI. Explicitly, the x,y,z- and x',y',z'-coordinates are related through

$$\begin{aligned} x' &= x, \\ y' &= y\cos(\varphi) - z\sin(\varphi), \\ z' &= y\sin(\varphi) + z\cos(\varphi). \end{aligned}$$

Using that spins transform according to

$$U = \begin{bmatrix} \cos\left(\frac{\varphi}{2}\right) & \sin\left(\frac{\varphi}{2}\right)e^{\mathrm{i}\theta} \\ -\sin\left(\frac{\varphi}{2}\right)e^{-\mathrm{i}\theta} & \cos\left(\frac{\varphi}{2}\right) \end{bmatrix},$$

and simultaneously performing a gauge transformation $G = \mathrm{diag}(1, \mathrm{i})$ to simplify the expressions below, the change of basis from the x,y,z-basis to the x',y',z'-basis for the spins is given by

$$L \equiv R^{\dagger} \equiv \begin{bmatrix} \cos\left(\frac{\varphi}{2}\right) & -\mathrm{i}\sin\left(\frac{\varphi}{2}\right) \\ \sin\left(\frac{\varphi}{2}\right) & \mathrm{i}\cos\left(\frac{\varphi}{2}\right) \end{bmatrix}. \qquad (2)$$

We have here used L and R to denote the transformations from the unprimed to the primed coordinates, and the primed to the unprimed coordinates, respectively. The symbols L and R are chosen since they are applied at the left and right end of the system, respectively. With these definitions we are now ready to write down the complete transfer matrix for the system

$$T(B, r, \varphi) = ROL.$$

Here we have made explicit the dependence of T on the parameters B and r on Equation 1, and of φ on Equation 2. The main advantage of introducing the L and R matrices is that they allow us to work in the laboratory frame alone. To calculate the probability that an incoming spin σ in the left lead is transferred to a spin λ in the right lead, we now simply need to calculate the square of the corresponding matrix element

$$\left|T_{\lambda\sigma}\right|^2 = \left|\langle\lambda|T(B, r, \varphi)|\sigma\rangle\right|^2.$$

Measuring magnetic flux

As a first example of a concrete application, we consider a system with fully spin-polarized ferromagnetic leads only containing electrons with spin-up. Further, the SG spin splitter is assumed to be oriented at an angle $\varphi = \pi/2$, which forces the incoming spins to split equally into both channels. Because the leads only conduct spin-up electrons, the only relevant matrix

element for the scattering matrix is

$$T_{\uparrow\uparrow} = \langle\uparrow|T\left(B, r, \frac{\pi}{2}\right)|\uparrow\rangle = \cos\left(\frac{qBr^2\pi}{2\hbar}\right)e^{-\mathrm{i}pr\pi/\hbar}.$$

The conductance is therefore given by

$$G = \frac{e^2}{\hbar}\left|T_{\uparrow\uparrow}\right|^2 = \frac{e^2}{\hbar}\cos^2\left(\frac{qBr^2\pi}{2\hbar}\right). \tag{3}$$

It is clear that the very strong dependence of the current on the magnetic flux $Br^2\pi$ makes this setup ideal for measuring magnetic field strength, as a potential alternative to superconducting quantum interference devices (SQUIDs). The measurement resolution is directly set by the radius of the hole in the TI. This is of special interest because it provides a potential route for high-resolution magnetic field measurements even at room temperatures [21,22].

Logic spintronics gates

Next we note that the configuration in the previous section can also be used as a spintronics switch, with voltage used to encode 0 and 1. The two leads can be used as source and drain, while the magnetic field is used as the gate. From Equation 3 it is clear that a magnetic field strength $B = (\hbar n)/(qr^2)$ corresponds to "on" and "off" states for n even and odd, respectively, and we therefore define the magnetic switching quantum

$$b = \frac{\hbar}{qr^2}. \tag{4}$$

An alternative way to encode 1 and 0 is to use the currents of up- and down-spins, respectively. This requires normal leads through which both up- and down-spins can be transported. We therefore consider the same configuration, but now evaluate all four components of the transfer matrix $T(B, r, \pi/2)$:

$$T_{\uparrow\uparrow} = T_{\downarrow\downarrow} = \cos\left(\frac{qBr^2\pi}{2\hbar}\right)e^{-\mathrm{i}pr\pi/\hbar},$$

$$T_{\downarrow\uparrow} = -T_{\uparrow\downarrow} = \sin\left(\frac{qBr^2\pi}{2\hbar}\right)e^{-\mathrm{i}pr\pi/\hbar}.$$

Similarly to the expressions above, the square of the transfer matrices gives the transfer probability of the spin-polarized currents. In particular, the off-diagonal matrix elements $T_{\downarrow\uparrow} = -T_{\uparrow\downarrow}$ converts between up and down spin currents. Therefore, the device relates the ingoing and outgoing spin currents to each other through

$$I_{\uparrow}^{\mathrm{out}} = \left|T_{\uparrow\uparrow}\right|^2 I_{\uparrow}^{\mathrm{in}} + \left|T_{\uparrow\downarrow}\right|^2 I_{\downarrow}^{\mathrm{in}},$$

$$I_{\downarrow}^{\mathrm{out}} = \left|T_{\downarrow\uparrow}\right|^2 I_{\uparrow}^{\mathrm{in}} + \left|T_{\downarrow\downarrow}\right|^2 I_{\downarrow}^{\mathrm{in}}.$$

Considering once again the special case $B = (\hbar n)/(qr^2)$, with n being an integer, the currents transforms according to

$$I_{\uparrow}^{\mathrm{out}}, I_{\downarrow}^{\mathrm{out}} = \begin{cases} I_{\uparrow}^{\mathrm{in}}, I_{\downarrow}^{\mathrm{in}} & \text{even } n, \\ I_{\downarrow}^{\mathrm{in}}, I_{\uparrow}^{\mathrm{in}} & \text{odd } n. \end{cases}$$

This means that the device can be switched between a normal lead and a NOT-gate, simply by changing B by the switching quantum in Equation 4.

Quantum computer gate

Having seen how a TI SG apparatus can be used to construct classical logic gates for spintronics, we finally turn to possible applications in quantum computing. It has been shown that a universal quantum computer can be built using only two-qubit CNOT-gates and single-qubit SU(2)-gates [20]. We here show

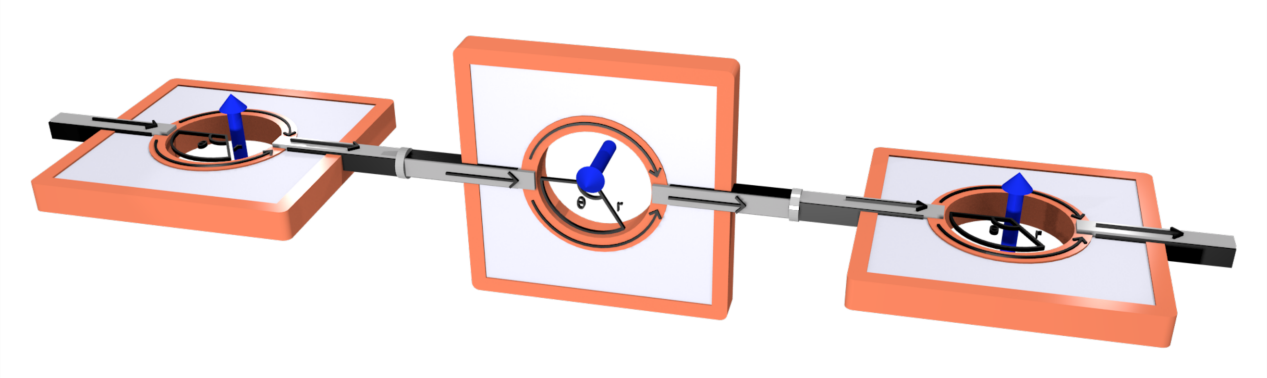

Figure 2: Three solid-state SG spin splitters in series, with the middle device at an angle π/2 relative to the other two.

that a SG TI spin-splitter provides a route for implementing the latter of these two gates.

For this purpose we consider three sequential spin-splitters connected by normal leads. The three devices are oriented as in Figure 2, with the middle device oriented at an angle $\varphi_2 = \pi/2$, while the first and the last spin splitter are at an angle $\varphi_1 = \varphi_3 = 0$. The total transfer matrix for the complete system is then given by

$$T_{\mathrm{U}(2)} = T\left(B_3, r_3, 0\right) T\left(B_2, r_2, \frac{\pi}{2}\right) T\left(B_1, r_1, 0\right).$$

When evaluated, this expression can be written as

$$T_{\mathrm{U}(2)} = \begin{bmatrix} e^{\mathrm{i}\alpha} & 0 \\ 0 & e^{\mathrm{i}\alpha} \end{bmatrix} \begin{bmatrix} e^{\mathrm{i}\beta_3/2} & 0 \\ 0 & e^{-\mathrm{i}\beta_3/2} \end{bmatrix} \begin{bmatrix} \cos\left(\frac{\beta_2}{2}\right) & \sin\left(\frac{\beta_2}{2}\right) \\ -\sin\left(\frac{\beta_2}{2}\right) & \cos\left(\frac{\beta_2}{2}\right) \end{bmatrix} \begin{bmatrix} e^{\mathrm{i}\beta_1/2} & 0 \\ 0 & e^{-\mathrm{i}\beta_1/2} \end{bmatrix}, \quad (5)$$

where

$$\alpha = -\frac{p\left(r_1 + r_2 + r_3\right)\pi}{\hbar},$$

$$\beta_i = -\frac{qB_i r_i^2 \pi}{\hbar}.$$

The six physical parameters B_i, r_i are more than sufficient to make the four parameters α, β_1, β_2 and β_3 independent of each other. Moreover, when all these four parameters can be chosen independently, it is possible to express any U(2)-matrix using Equation 5 [20]. Thus, it is possible to implement any unitary single-qubit gate, and in particular any SU(2)-gate, through the use of three sequential solid-state SG spin splitters. In fact, the overall U(1)-phase provided by the parameter α can be ignored for reasons similar to those for which the U(1)-phase provided by the gauge transformation $A \rightarrow A + A'$ can be ignored. This phase would only be relevant if the incoming electron is further split up into one part passing through the device, and one part moving through another path joining only at the far right outgoing lead.

In light of these results it is useful to think of the devices discussed here as exhibiting an SU(2)-AB effect. While the ordinary AB effect arises as a consequence of interference in a single U(1)-phase, these devices rely on a generalized SU(2)-interference effect in the relative phase and amplitude of the up- and down-components of the spin. To be able to create an arbitrary SU(2)-transformation, a sequence of three devices is needed, while an individual spin splitter gives rise to a subset of such SU(2)-transformations. Finally, we note that in this calculation we have omitted transfer matrices describing the propagation through the leads. We are justified in doing so because these would be proportional to the identity matrix and therefore only contribute to the irrelevant α phase.

Discussion

We would like to end with a few comments on some of the assumptions made when deriving the above results. First of all, the tunneling parameter t, which otherwise would have multiplied the L and R matrices was set to $t = 1$. It is clear that the zero-th order correction to deviations from $t = 1$ is to include the factor t^2 in front of all transmission coefficients, which shows up as t^4 in the conductivity. The higher-order corrections would come from particles that are reflected and travel an additional time around the loop. While such terms can introduce corrections to the interference pattern for intermediate field strengths, they would not affect the result at multiples of the switching quantum in Equation 4. The reason for this is that additional circuits around the loop will only affect the relative phase between the up- and down-spins by multiples of 2π. Such interference effect could also play a role for $t = 1$ when ferromagnetic leads are used, because the down spins at the right edge will be completely reflected. In a standard Landauer treatment such reflected terms would have been taken into account through reflection matrices in addition to the transmission matrix we have derived, as was for example done in [14]. However, a 2D TI is very special in this regard, because the reflected spins travel back along the opposite edge from which it traveled toward the exit lead. Since we are only interested in forward propagation of up spins along one edge, and down spins along the other, it is possible to add additional floating ferromagnetic leads with opposite spin polarization to the forward propagating modes to the two edges. This allows for reflected spins to escape without affecting the forward propagating spins and thereby we can suppress higher-order corrections.

We also mention that although the setup in Figure 2 might seem difficult to realize in practice, the focus of this work is to provide a conceptual setup and an explanation of the phenomenon itself. In fact, the only reason the middle spin splitter is tilted at an angle π/2 is to make its edge states have their spin-polarization perpendicular to those of the other two. In practice it would therefore be possible to have all three devices in the same plane, if it is constructed out of two different types of 2D TIs with perpendicular spin-polarization axes.

Conclusion

We have shown that the helical edge states of a 2D TI can be utilized to construct a solid-state SG spin splitter that when threaded by a magnetic flux gives rise to a generalized SU(2)-

AB interference effect. With two ferromagnetic leads, the device can be used to accurately measure magnetic flux, as well as be used as a magnetic field gated spintronics switch. Instead by using normal leads, a switchable spintronics NOT-gate can be implemented, or when using three devices connected in sequence, a SU(2)-gate for quantum computing is achieved.

Acknowledgements

We are grateful to J. Bardarson, J. Fransson, and E. Sjöqvist for useful discussions and the Swedish Research Council (Vetenskapsrådet), the Göran Gustafsson Foundation, and the Swedish Foundation for Strategic Research (SSF) for financial support.

ORCID® iDs

Kristofer Björnson - https://orcid.org/0000-0003-0918-0469

References

1. Sakurai, J. J. *Modern Quantum Mechanics (Revised Edition);* Addison-Wesley: New York, NY, U.S.A., 1994.
2. Aharonov, Y.; Bohm, D. *Phys. Rev.* **1959,** *115,* 485–491. doi:10.1103/PhysRev.115.485
3. Kane, C. L.; Mele, E. J. *Phys. Rev. Lett.* **2005,** *95,* 226801. doi:10.1103/PhysRevLett.95.226801
4. Kane, C. L.; Mele, E. J. *Phys. Rev. Lett.* **2005,** *95,* 146802. doi:10.1103/PhysRevLett.95.146802
5. Bernevig, B. A.; Zhang, S.-C. *Phys. Rev. Lett.* **2006,** *96,* 106802. doi:10.1103/PhysRevLett.96.106802
6. Kane, C. L.; Mele, E. J. *Science* **2006,** *314,* 1692–1693. doi:10.1126/science.1136573
7. Bernevig, B. A.; Hughes, T. L.; Zhang, S.-C. *Science* **2006,** *314,* 1757–1761. doi:10.1126/science.1133734
8. König, M.; Wiedmann, S.; Brüne, C.; Roth, A.; Buhmann, H.; Molenkamp, L. W.; Qi, X.-L.; Zhang, S.-C. *Science* **2007,** *318,* 766–770. doi:10.1126/science.1148047
9. Liu, C.; Hughes, T. L.; Qi, X.-L.; Wang, K.; Zhang, S.-C. *Phys. Rev. Lett.* **2008,** *100,* 236601. doi:10.1103/PhysRevLett.100.236601
10. Liu, C.-C.; Feng, W.; Yao, Y. *Phys. Rev. Lett.* **2011,** *107,* 076802. doi:10.1103/PhysRevLett.107.076802
11. Knez, I.; Du, R.-R.; Sullivan, G. *Phys. Rev. Lett.* **2011,** *107,* 136603. doi:10.1103/PhysRevLett.107.136603
12. Hasan, M. Z.; Kane, C. L. *Rev. Mod. Phys.* **2010,** *82,* 3045–3067. doi:10.1103/RevModPhys.82.3045
13. Qi, X.-L.; Zhang, S.-C. *Rev. Mod. Phys.* **2011,** *83,* 1057–1110. doi:10.1103/RevModPhys.83.1057
14. Maciejko, J.; Kim, E.-A.; Qi, X.-L. *Phys. Rev. B* **2010,** *82,* 195409. doi:10.1103/PhysRevB.82.195409
15. Zhang, Y.; Vishwanath, A. *Phys. Rev. Lett.* **2010,** *105,* 206601. doi:10.1103/PhysRevLett.105.206601
16. Bardarson, J. H.; Brouwer, P. W.; Moore, J. E. *Phys. Rev. Lett.* **2010,** *105,* 156803. doi:10.1103/PhysRevLett.105.156803
17. Peng, H.; Lai, K.; Kong, D.; Meister, S.; Chen, Y.; Qi, X.-L.; Zhang, S.-C.; Shen, Z.-X.; Cui, Y. *Nat. Mater.* **2010,** *9,* 225. doi:10.1038/nmat2609
18. Cho, S.; Dellabetta, B.; Zhong, R.; Schneeloch, J.; Liu, T.; Gu, G.; Gilbert, M. J.; Mason, N. *Nat. Commun.* **2015,** *6,* 7634. doi:10.1038/ncomms8634
19. Ilan, R.; de Juan, F.; Moore, J. E. *Phys. Rev. Lett.* **2015,** *115,* 096802. doi:10.1103/PhysRevLett.115.096802
20. Barenco, A.; Bennett, C. H.; Cleve, R.; DiVincenzo, D. P.; Margolus, N.; Shor, P.; Sleator, T.; Smolin, J. A.; Weinfurter, H. *Phys. Rev. A* **1995,** *52,* 3457–3467. doi:10.1103/PhysRevA.52.3457
21. Xu, Y.; Yan, B.; Zhang, H.-J.; Wang, J.; Xu, G.; Tang, P.; Duan, W.; Zhang, S.-C. *Phys. Rev. Lett.* **2013,** *111,* 136804. doi:10.1103/PhysRevLett.111.136804
22. Zhu, F.-f.; Chen, W.-j.; Xu, Y.; Gao, C.-l.; Guan, D.-d.; Liu, C.-h.; Qian, D.; Zhang, S.-C.; Jia, J.-f. *Nat. Mater.* **2015,** *14,* 1020. doi:10.1038/nmat4384

License and Terms

BEILSTEIN JOURNAL OF NANOTECHNOLOGY

Josephson effect in junctions of conventional and topological superconductors

Alex Zazunov[1], Albert Iks[1], Miguel Alvarado[2], Alfredo Levy Yeyati[2] and Reinhold Egger[*1]

Full Research Paper

Open Access

Address:
[1]Institut für Theoretische Physik, Heinrich-Heine-Universität, D-40225 Düsseldorf, Germany and [2]Departamento de Física Teórica de la Materia Condensada C-V, Condensed Matter Physics Center (IFIMAC) and Instituto Nicolás Cabrera, Universidad Autónoma de Madrid, E-28049 Madrid, Spain

Email:
Reinhold Egger[*] - egger@hhu.de

* Corresponding author

Keywords:
Andreev bound states; Josephson current–phase relation; Majorana zero modes; topological superconductivity

Beilstein J. Nanotechnol. **2018,** *9,* 1659–1676.
doi:10.3762/bjnano.9.158

Received: 30 January 2018
Accepted: 27 April 2018
Published: 06 June 2018

This article is part of the Thematic Series "Topological materials".

Associate Editor: J. M. van Ruitenbeek

Abstract

We present a theoretical analysis of the equilibrium Josephson current-phase relation in hybrid devices made of conventional *s*-wave spin-singlet superconductors (S) and topological superconductor (TS) wires featuring Majorana end states. Using Green's function techniques, the topological superconductor is alternatively described by the low-energy continuum limit of a Kitaev chain or by a more microscopic spinful nanowire model. We show that for the simplest S–TS tunnel junction, only the *s*-wave pairing correlations in a spinful TS nanowire model can generate a Josephson effect. The critical current is much smaller in the topological regime and exhibits a kink-like dependence on the Zeeman field along the wire. When a correlated quantum dot (QD) in the magnetic regime is present in the junction region, however, the Josephson current becomes finite also in the deep topological phase as shown for the cotunneling regime and by a mean-field analysis. Remarkably, we find that the S–QD–TS setup can support φ_0-junction behavior, where a finite supercurrent flows at vanishing phase difference. Finally, we also address a multi-terminal S–TS–S geometry, where the TS wire acts as tunable parity switch on the Andreev bound states in a superconducting atomic contact.

Introduction

The physics of topological superconductors (TSs) is being vigorously explored at present. After Kitaev [1] showed that a one-dimensional (1D) spinless fermionic lattice model with nearest-neighbor *p*-wave pairing ('Kitaev chain') features a topologically nontrivial phase with Majorana bound states (MBSs) at open boundaries, references [2,3] have pointed out that the physics of the Kitaev chain could be realized in spin–orbit coupled nanowires with a magnetic Zeeman field and in the proximity to a nearby *s*-wave superconductor. The spinful nanowire model of references [2,3] indeed features *p*-wave pairing correlations for appropriately chosen model parameters. In addition, it also contains *s*-wave pairing correlations which become gradually smaller as one moves into the deep topological regime. Topologically nontrivial hybrid semiconductor

nanowire devices are of considerable interest in the context of quantum information processing [4-12], and they may also be designed in two-dimensional layouts by means of gate lithography techniques. Over the last few years, several experiments employing such platforms have provided mounting evidence for MBSs, e.g., from zero-bias conductance peaks in N–TS junctions (where N stands for a normal-conducting lead) and via signatures of the 4π-periodic Josephson effect in TS–TS junctions [13-25]. Related MBS phenomena have been reported for other material platforms as well [26-30], and most of the results reported below also apply to those settings. Available materials are often of sufficiently high quality to meet the conditions for ballistic transport, and we will therefore neglect disorder effects.

In view of the large amount of published theoretical works on the Josephson effect in such systems, let us first motivate the present study. (For a more detailed discussion and references, see below.) Our manuscript addresses the supercurrent flowing in Josephson junctions with a magnetic impurity. By considering Josephson junctions between a topological superconductor and a non-topological superconductor, we naturally extend previous works on Josephson junctions with a magnetic impurity between two conventional superconductors, as well as other works on Josephson junctions between topological and non-topological superconductors but without a magnetic impurity. In the simplest description, Josephson junctions between topological and non-topological supeconductors carry no supercurrent. Instead, a supercurrent can flow only with certain deviations from the idealized model description. The presence of a magnetic impurity in the junction is one of these deviations, and this effect allows for novel signatures for the topological transition via the so-called φ_0-behavior and/or through the kink-like dependence of the critical current on a Zeeman field driving the transition. We consider two different geometries in various regimes, e.g., the cotunneling regime where a controlled perturbation theory is possible, and a mean-field description of the stronger-coupling regime. We study both idealized Hamiltonians (allowing for analytical progress) as well as more realistic models for the superconductors.

To be more specific, we address the equilibrium current–phase relation (CPR) in different setups involving both conventional *s*-wave BCS superconductors ('S' leads) and TS wires, see Figure 1 for a schematic illustration. In general, the CPR is closely related to the Andreev bound state (ABS) spectrum of the system. For S–TS junctions with the TS wire deep in the topological phase such that it can be modeled by a Kitaev chain, the supercurrent vanishes identically [31]. This supercurrent blockade can be traced back to the different (*s*/*p*-wave) pairing symmetries for the S/TS leads, together with the fact that MBSs have a definite spin polarization. For an early study of Josephson currents between superconductors with different (*p*/*d*) pairing symmetries, see also [32]. A related phenomenon concerns Multiple Andreev Reflection (MAR) features in nonequilibrium superconducting quantum transport at subgap voltages [33-36]. Indeed, it has been established that MAR processes are absent in S–TS junctions (with the TS wire in the deep topological regime) such that only quasiparticle transport above the gap is possible [37-44].

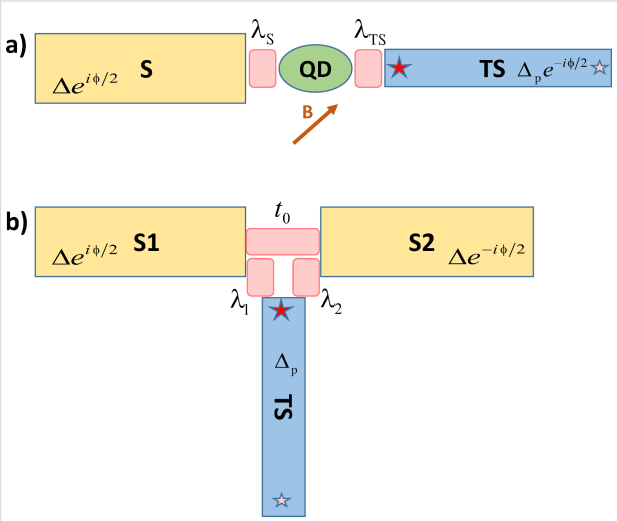

Figure 1: Schematic setups studied in this paper. a) S–QD–TS geometry: S denotes a conventional *s*-wave BCS superconductor with order parameter $\Delta e^{i\phi/2}$, and TS represents a topologically nontrivial superconducting wire with MBSs (shown as stars) and proximity-induced order parameter $\Delta_p e^{-i\phi/2}$. The interface contains a quantum dot (QD) corresponding to an Anderson impurity, connected to the S/TS leads by tunnel amplitudes $\lambda_{S/TS}$ (light red). The QD is also exposed to a local Zeeman field **B**. b) S–TS–S geometry: Two conventional superconductors (S1 and S2) with the same gap Δ and a TS wire with proximity gap Δ_p form a trijunction. The order parameter phase of S1 (S2), $\phi_1 = \phi/2$ ($\phi_2 = -\phi/2$), is taken relative to the phase of the TS wire, and tunnel couplings $\lambda_{1/2}$ connect S1/S2 to the TS wire. When the TS wire is decoupled ($\lambda_{1,2} = 0$), the S–S junction becomes a standard SAC with transparency $\mathcal{T}$ determined by the tunnel amplitude t_0, see Equation 42.

There are several ways to circumvent this supercurrent blockade in S–TS junctions. (i) One possibility has been described in [43]. For a trijunction formed by two TS wires and one S lead, crossed Andreev reflections allow for the nonlocal splitting of Cooper pairs in the S electrode involving both TS wires (or the reverse process). In this way, an equilibrium supercurrent will be generated unless the MBS spin polarization axes of both TS wires are precisely aligned. (ii) Even for a simple S–TS junction, a finite Josephson current is expected when the TS wire is modeled as spinful nanowire. This effect is due to the residual *s*-wave pairing character of the spinful TS model [2,3]. Interestingly, upon changing a control parameter, e.g., the bulk Zeeman field, which drives the TS wire across the topological phase

transition, we find that the critical current exhibits a kink-like feature that is mainly caused by a suppression of the Andreev state contribution in the topological phase. (iii) Yet another possibility is offered by junctions containing a magnetic impurity in a local magnetic field. We here analyze the S–QD–TS setup in Figure 1a in some detail, where a quantum dot (QD) is present within the S–TS junction region. The QD is modeled as an Anderson impurity [36], which is equivalent to a spin-1/2 quantum impurity over a wide parameter regime. Once spin mixing is induced by the magnetic impurity and the local magnetic field, we predict that a finite Josephson current flows even in the deep topological limit. In particular, in the cotunneling regime, we find an anomalous Josephson effect with finite supercurrent at vanishing phase difference (φ_0-junction behavior) [45-47], see also [48-51]. The 2π-periodic CPR found in S–QD–TS junctions could thereby provide independent evidence for MBSs via the anomalous Josephson effect. In addition, we compute the CPR within the mean-field approximation in order to go beyond perturbation theory in the tunnel couplings connecting the QD to the superconducting leads. Our mean-field analysis shows that the φ_0-junction behavior is a generic feature for S–QD–TS devices in the topological regime which is not limited to the cotunneling regime.

In the final part of the paper, we turn to the three-terminal S–TS–S setup shown in Figure 1b, where the S–S junction by itself (with the TS wire decoupled) represents a standard superconducting atomic contact (SAC) with variable transparency of the weak link. Recent experiments have demonstrated that the many-body ABS configurations of a SAC can be probed and manipulated to high accuracy by microwave spectroscopy [52-54]. When the TS wire is coupled to the S–S junction, see Figure 1b, the Majorana end state acts as a parity switch on the ABS system of the SAC. This effect allows for additional functionalities in Andreev spectroscopy. We note that similar ideas have also been explored for TS–N–TS systems [55].

Results and Discussion

S–QD–TS junction

Model

Let us start with the case of an S–QD–TS junction, where an interacting spin-degenerate single-level quantum dot (QD) is sandwiched between a conventional *s*-wave superconductor (S) and a topological superconductor (TS). This geometry is shown in Figure 1a. The corresponding topologically trivial S–QD–S problem has been studied in great detail over the past decades both theoretically [56-63] and experimentally [64-69]. A main motivation for those studies came from the fact that the QD can be driven into the magnetic regime where it represents a spin-1/2 impurity subject to Kondo screening by the leads. The Kondo effect then competes against the superconducting bulk gap and one encounters local quantum phase transitions. By now, good agreement between experiment and theory has been established. Rather than studying the fate of the Kondo effect in the S–QD–TS setting of Figure 1a, we here pursue two more modest goals. First, we shall discuss the cotunneling regime in detail, where one can employ perturbation theory in the dot–lead couplings. This regime exhibits π-junction behavior in the S–QD–S case [56]. Second, in order to go beyond the cotunneling regime, we have performed a mean-field analysis similar in spirit to earlier work for S–QD–S devices [57,58].

The Hamiltonian for the setup in Figure 1a is given by

$$H = H_{\mathrm{S}} + H_{\mathrm{TS}} + H_{\mathrm{QD}} + H_{\mathrm{tun}}\,, \tag{1}$$

where $H_{\mathrm{S/TS}}$ and H_{QD} describe the semi-infinite S/TS leads and the isolated dot in between, respectively, and H_{tun} refers to the tunnel contacts. We often use units with $e = \hbar = k_{\mathrm{B}} = 1$, and $\beta = 1/T$ denotes inverse temperature. The QD is modeled as an Anderson impurity [36], i.e., a single spin-degenerate level of energy ε_0 with repulsive on-site interaction energy $U > 0$,

$$H_{\mathrm{QD}} = \sum_{\sigma=\uparrow,\downarrow} \varepsilon_0\left(n_\sigma - \frac{1}{2}\right) + U n_\uparrow n_\downarrow - \mathbf{B}\cdot\mathbf{S}\,, \tag{2}$$

where the QD occupation numbers are $n_\sigma = d_\sigma^\dagger d_\sigma = 0,1$, with dot fermion operators d_σ and $d_\sigma^\dagger$ for spin σ. Using standard Pauli matrices $\sigma_{x,y,z}$, we define

$$\mathbf{S}_{i=x,y,z} = \sum_{\sigma,\sigma'} d_\sigma^\dagger \left(\sigma_i\right)_{\sigma\sigma'} d_{\sigma'}\,, \tag{3}$$

such that $\mathbf{S}/2$ is a spin-1/2 operator. In the setup of Figure 1a, we also take into account an external Zeeman field $\mathbf{B} = (B_x, B_y, B_z)$ acting on the QD spin, where the units in Equation 2 include gyromagnetic and Bohr magneton factors. The spinful nanowire proposal for TS wires [2,3] also requires a sufficiently strong bulk Zeeman field oriented along the wire in order to realize the topologically nontrivial phase, but for concreteness, we here imagine the field $\mathbf{B}$ as independent local field coupled only to the QD spin. One could use, e.g., a ferromagnetic grain near the QD to generate it. This field here plays a crucial role because for $\mathbf{B} = 0$, the S+QD part is spin rotation [SU(2)] invariant and the arguments of [31] then rule out a supercurrent for TS wires in the deep topological regime. We show below that unless $\mathbf{B}$ is inadvertently aligned with the MBS spin polarization axis, spin mixing will indeed generate a supercurrent.

The S/TS leads are coupled to the QD via a tunneling Hamiltonian [70],

$$H_{\rm tun} = \lambda_{\rm S} \sum_{\sigma=\uparrow,\downarrow} \Psi_\sigma^\dagger d_\sigma + \lambda_{\rm TS} e^{-i\phi/2} \Psi^\dagger d_\uparrow + \text{h.c.}, \tag{4}$$

where ψ_σ and ψ are boundary fermion fields representing the S lead and the effectively spinless TS lead, respectively. For the S lead, we assume the usual BCS model [62], where the operator ψ_σ annihilates an electron with spin σ at the junction. The TS wire will, for the moment, be described by the low-energy Hamiltonian of a Kitaev chain in the deep topological phase with chemical potential $\mu = 0$ [1,5]. The corresponding fermion operator ψ at the junction includes both the MBS contribution and above-gap quasiparticles [40]. Without loss of generality, we choose the unit vector $\hat{e}_z$ as the MBS spin polarization direction and take real-valued tunnel amplitudes $\lambda_{\rm S/TS}$, see Figure 1a, using a gauge where the superconducting phase difference ϕ appears via the QD–TS tunneling term. These tunnel amplitudes contain density-of-states factors for the respective leads. The operator expression for the current flowing through the system is then given by

$$\hat{I} = \frac{2e}{\hbar} \partial_\phi H_{\rm tun}\,. \tag{5}$$

We do not specify $H_{\rm S/TS}$ in Equation 1 explicitly since within the imaginary-time (τ) boundary Green's function (bGF) formalism [40] employed here, we only need to know the bGFs. For the S lead with gap value Δ, the bGF has the Nambu matrix form [40]

$$\begin{aligned} g(\tau) &= -\left\langle \mathcal{T}_\tau \Psi_{\rm S}(\tau) \Psi_{\rm S}^\dagger(0) \right\rangle_0 = \beta^{-1} \sum_\omega e^{-i\omega\tau} g(\omega), \\ \Psi_{\rm S} &= \begin{pmatrix} \Psi_\uparrow \\ \Psi_\downarrow^\dagger \end{pmatrix}, \qquad g(\omega) = -\frac{i\omega\tau_0 + \Delta\tau_x}{\sqrt{\omega^2+\Delta^2}}, \end{aligned} \tag{6}$$

where the expectation value $\langle ... \rangle_0$ refers to an isolated S lead, $\mathcal{T}$ denotes time ordering, ω runs over fermionic Matsubara frequencies, i.e., $\omega = 2\pi(n + 1/2)/\beta$ with integer n, and we define Pauli (unity) matrices $\tau_{x,y,z}$ (τ_0) in particle–hole space corresponding to the Nambu spinor $\Psi_{\rm S}$. Similarly, for a TS lead with proximity-induced gap $\Delta_{\rm p}$, the low-energy limit of a Kitaev chain yields the bGF [40]

$$\begin{aligned} G(\tau) &= -\left\langle \mathcal{T}_\tau \Psi_{\rm TS}(\tau) \Psi_{\rm TS}^\dagger(0) \right\rangle_0, \quad \Psi_{\rm TS} = \begin{pmatrix} \Psi \\ \Psi^\dagger \end{pmatrix}, \\ G(\omega) &= \frac{1}{i\omega} \left(\sqrt{\omega^2 + \Delta_{\rm p}^2}\, \tau_0 + \Delta_{\rm p} \tau_x \right). \end{aligned} \tag{7}$$

The matrices $\tau_{0,x}$ here act in the Nambu space defined by the spinor $\Psi_{\rm TS}$. Later on we will address how our results change when the TS wire is modeled as spinful nanowire [2,3], where the corresponding bGF has been specified in [43]. We emphasize that the bGF (Equation 7) captures the effects of both the MBS (via the $1/\omega$ term) and of the above-gap continuum quasiparticles (via the square root) [40,71].

In most of the following discussion, we will assume that U is the dominant energy scale, with the single-particle level located at $\varepsilon_0 \approx -U/2$. In that case, low-energy states with energy well below U are restricted to the single occupancy sector,

$$n_\uparrow + n_\downarrow = 1, \tag{8}$$

and the QD degrees of freedom become equivalent to the spin-1/2 operator $\mathbf{S}/2$ in Equation 3. In this regime, the QD acts like a magnetic impurity embedded in the S–TS junction. Using a Schrieffer–Wolff transformation to project the full Hamiltonian to the Hilbert subspace satisfying Equation 8, $H \to H_{\rm eff}$, one arrives at the effective low-energy Hamiltonian

$$H_{\rm eff} = H_0 + H_{\rm int}, \quad H_0 = H_{\rm S} + H_{\rm TS} - \mathbf{B}\cdot\mathbf{S}, \tag{9}$$

with the interaction term

$$\begin{aligned} H_{\rm int} = & -\frac{2}{U} \sum_{\sigma,\sigma'} \left(\eta_\sigma^\dagger d_\sigma d_{\sigma'}^\dagger \eta_{\sigma'} + \text{h.c.} \right) \\ = & \frac{2}{U} \sum_{\sigma=\uparrow/\downarrow=\pm} \left(\sigma S_z \eta_\sigma^\dagger \eta_\sigma + S_\sigma \eta_{-\sigma}^\dagger \eta_\sigma \right) \\ & + \frac{2}{U} \delta n \sum_\sigma \eta_\sigma^\dagger \eta_\sigma - \frac{2\Lambda}{U} (\delta n + 1), \end{aligned} \tag{10}$$

where $S_\pm = S_x \pm i S_y$ and $\delta n = \sum_\sigma n_\sigma - 1$. Moreover, $\Lambda = \left[\eta_\sigma, \eta_\sigma^\dagger \right]_+$ is the anticommutator of the composite boundary fields

$$\eta_\sigma = \lambda_{\rm S} \Psi_\sigma + \delta_{\sigma,\uparrow} \lambda_{\rm TS} e^{i\phi/2} \Psi. \tag{11}$$

We note that Λ is real-valued and does not depend on ϕ. Due to the constraint (Equation 8) on the dot occupation, the last two terms in Equation 10 do not contribute to the system dynamics and we obtain

$$\begin{aligned} H_{\rm int} &= \frac{4}{U} \sum_{\sigma,\sigma'} \mathcal{Q}_{\sigma\sigma'} \eta_\sigma^\dagger \eta_{\sigma'}, \\ \mathcal{Q}_{\sigma\sigma} &= \frac{\sigma}{2} S_z, \quad \mathcal{Q}_{\sigma,-\sigma} = \frac{1}{2} S_{-\sigma}. \end{aligned} \tag{12}$$

A formally exact expression for the partition function is then given by

$$Z = \mathrm{Tr}\big|_{\delta n=0}\left(e^{-\beta H_0}\mathcal{T}_\tau e^{-\int_0^\beta \mathrm{d}\tau H_{\mathrm{int}}(\tau)}\right), \tag{13}$$

where $H_{\mathrm{int}}(\tau) = e^{\tau H_0}H_{\mathrm{int}}e^{-\tau H_0}$ with H_0 in Equation 9 and the trace extends only over the Hilbert subspace corresponding to Equation 8. We can equivalently write Equation 13 in the form

$$\begin{aligned} Z &= Z_0\left\langle T_\tau e^{-\beta\hat{W}}\right\rangle_0 = e^{-\beta F},\\ \hat{W} &= \beta^{-1}\int_0^\beta \mathrm{d}\tau H_{\mathrm{int}}(\tau),\\ Z_0 &= \mathrm{Tr}\big|_{\delta n=0}\, e^{-\beta H_0} = e^{-\beta F_0}, \end{aligned} \tag{14}$$

where F is the free energy. The Josephson current then follows as $I = (2e/\hbar)\,\partial_\phi F$, see Equation 5.

Cotunneling regime

We now address the CPR in the elastic cotunneling regime,

$$\lambda_S\lambda_{TS} \ll \min\{\Delta, \Delta_p, U\}, \tag{15}$$

where perturbation theory in H_{int} is justified. We thus wish to compute the free energy $F(\phi)$ from Equation 14 to lowest nontrivial order. With $W_0 = \langle\hat{W}\rangle_0$, the standard cumulant expansion gives

$$F - F_0 = W_0 - \frac{\beta}{2}\left(\left\langle\hat{W}^2\right\rangle_0 - W_0^2\right) + \mathcal{O}(W)^2. \tag{16}$$

By virtue of Wick's theorem, time-ordered correlation functions of the boundary operators (Equation 11) are now expressed in terms of S/TS bGF matrix elements, see Equation 6 and Equation 7,

$$\left\langle\mathcal{T}_\tau\eta_\sigma(\tau)\eta^\dagger_{\sigma'}(0)\right\rangle_0 = \delta_{\sigma\sigma'}\begin{bmatrix}\lambda_S^2\left\langle\mathcal{T}_\tau\Psi_\sigma(\tau)\Psi^\dagger_\sigma(0)\right\rangle_0\\ +\delta_{\sigma,\uparrow}\lambda_{TS}^2\left\langle\mathcal{T}_\tau\Psi(\tau)\Psi^\dagger(0)\right\rangle_0\end{bmatrix} \tag{17}$$

and similarly

$$\begin{aligned}\left\langle\mathcal{T}_\tau\eta_\sigma(\tau)\eta_{\sigma'}(0)\right\rangle_0 = {}& \delta_{\sigma,-\sigma'}\lambda_S^2\left\langle\mathcal{T}_\tau\Psi_\sigma(\tau)\Psi_{-\sigma}(0)\right\rangle_0\\ &+ e^{i\phi}\delta_{\sigma\sigma'}\delta_{\sigma,\uparrow}\lambda_{TS}^2\left\langle\mathcal{T}_\tau\Psi(\tau)\Psi(0)\right\rangle_0.\end{aligned} \tag{18}$$

Next we observe that $\partial_\phi\langle H_{\mathrm{int}}\rangle_0 = 0$. As a consequence, the ϕ-independent terms W_0 and W_0^2 in Equation 16 do not contribute to the Josephson current. The leading contribution is then of second order in H_{int},

$$\begin{aligned} I(\phi) &= -\beta^{-1}\partial_\phi\int_0^\beta \mathrm{d}\tau_1\mathrm{d}\tau_2\left\langle\mathcal{T}_\tau H_{\mathrm{int}}(\tau_1)H_{\mathrm{int}}(\tau_2)\right\rangle_0\\ &= -\frac{\kappa^2}{\beta}\int_0^\beta \mathrm{d}\tau_1\mathrm{d}\tau_2 g_{12}(\tau_1-\tau_2)G_{12}(\tau_1-\tau_2)\\ &\quad\times ie^{i\phi}\sum_\sigma\sigma\left\langle\mathcal{T}_\tau\mathcal{Q}_{\sigma,\uparrow}(\tau_1)\mathcal{Q}_{-\sigma,\uparrow}(\tau_2)\right\rangle_0 + \mathrm{h.c.}, \end{aligned} \tag{19}$$

with $\mathcal{Q}_{\sigma,\sigma'}$ in Equation 12 and the small dimensionless parameter

$$\kappa = \frac{4\lambda_S\lambda_{TS}}{U} \ll 1. \tag{20}$$

From Equation 6 and Equation 7, the bGF matrix elements needed in Equation 19 follow as

$$\begin{aligned} g_{12}(\tau) &= -\frac{\Delta}{\beta}\sum_\omega\frac{\cos(\omega\tau)}{\sqrt{\omega^2+\Delta^2}},\\ G_{12}(\tau) &= -\frac{\Delta_p}{\beta}\sum_\omega\frac{\sin(\omega\tau)}{\omega} \simeq -\frac{\Delta_p}{2}\mathrm{sgn}(\tau). \end{aligned} \tag{21}$$

Now $|g_{12}(\tau)|$ is exponentially small unless $\Delta|\tau| < 1$. In particular, $g_{12}(\tau) \to -\delta(\tau)$ for $\Delta \to \infty$. Moreover, for $B \ll \Delta$ with $B \equiv |\mathbf{B}|$, the magnetic impurity (**S**) dynamics will be slow on time scales of the order of $1/\Delta$. We may therefore approximate the spin–spin correlators in Equation 19 by their respective equal-time expressions,

$$\lim_{\tau_1\to\tau_2}\left\langle\mathcal{T}_\tau\mathcal{Q}_{\sigma,\uparrow}(\tau_1)\mathcal{Q}_{-\sigma,\uparrow}(\tau_2)\right\rangle_0 = \frac{\sigma}{4}\mathrm{sgn}(\tau_1-\tau_2)\langle S_+\tau_1\rangle_0\,. \tag{22}$$

Inserting Equation 21 and Equation 22 into the expression for the supercurrent in Equation 19, the time integrations can be carried out analytically.

We obtain the CPR in the cotunneling regime as

$$\begin{aligned} I(\phi) &= I_x\sin\phi + I_y\cos\phi,\\ I_{x,y} &= \frac{e\kappa^2\Delta_p}{2\hbar}\frac{B_{x,y}}{B}\tanh(\beta B), \end{aligned} \tag{23}$$

with κ in Equation 20. We note that while $I(\phi)$ is formally independent of Δ, the value of Δ must be sufficiently large to justify the steps leading to Equation 23. Remarkably, Equation 23 predicts anomalous supercurrents for the S–QD–TS setup, i.e., a finite Josephson current for vanishing phase difference ($\phi = 0$) [45,46,72]. One can equivalently view this effect as a φ_0-shift in the CPR, $I(\phi) = I_c \sin(\phi + \varphi_0)$. An observation of this φ_0-junction behavior could then provide additional evidence for MBSs (see also [47]), where Equation 23 shows that the local magnetic field is required to have a finite B_y-component with $\hat{e}_z$ defining the MBS spin polarization direction. In particular, if **B** is aligned with $\hat{e}_z$, the supercurrent in Equation 23 vanishes identically since *s*-wave Cooper pairs cannot tunnel from the S lead into the TS wire in the absence of spin flips [31]. Otherwise, the CPR is 2π-periodic and sensitive to the MBS through the peculiar dependence on the relative orientation between the MBS spin polarization ($\hat{e}_z$) and the local Zeeman field **B** on the QD. The fact that $B_y \neq 0$ (rather than $B_x \neq 0$) is necessary to have $\varphi_0 \neq 0$ can be traced back to our choice of real-valued tunnel couplings. For tunable tunnel phases, also the field direction where one has $\varphi_0 = 0$ will vary accordingly.

Noting that the anomalous Josephson effect has recently been observed in S–QD–S devices [73], we expect that similar experimental techniques will allow to access the CPR (Equation 23). We mention in passing that previous work has also pointed out that experiments employing QDs between N (instead of S) leads and TS wires can probe nonlocal effects due to MBSs [12,16,74-78]. In our case, e.g., by variation of the field direction in the *xy*-plane, Equation 23 predicts a tunable anomalous supercurrent. We conclude that in the cotunneling regime, the π-junction behavior of S–QD–S devices is replaced by the more exotic physics of φ_0-junctions in the S–QD–TS setting.

Mean-field approximation

Next we present a mean-field analysis of the Hamiltonian (Equation 1) which allows us to go beyond the perturbative cotunneling regime. For the corresponding S–QD–S case, see [58,79]. We note that a full solution of this interacting many-body problem requires a detailed numerical analysis using, e.g., the numerical renormalization group [60,61] or quantum Monte Carlo simulations [59,63], which is beyond the scope of the present work. We start by defining the GF of the QD,

$$G_d(\tau) = -\left\langle \mathcal{T}_\tau \Psi_d(\tau) \Psi_d^\dagger(0) \right\rangle, \quad \Psi_d^\dagger = \left(d_\uparrow^\dagger, d_\downarrow, d_\downarrow^\dagger, -d_\uparrow\right)^T. \tag{24}$$

Note that this notation introduces double counting, which implies that only half of the levels are physically independent. Of course, the results below take this issue into account.

With the above Nambu bi-spinor basis, the mean-field Hamiltonian has the 4 × 4 matrix representation

$$\mathcal{H}_{\rm MF} = \begin{pmatrix} \varepsilon_\uparrow & \Delta_d & \alpha_d & 0 \\ \Delta_d^* & -\varepsilon_\downarrow & 0 & \alpha_d \\ \alpha_d^* & 0 & \varepsilon_\downarrow & \Delta_d \\ 0 & \alpha_d^* & \Delta_d^* & -\varepsilon_\uparrow \end{pmatrix}, \tag{25}$$
$$\varepsilon_\uparrow = \varepsilon_0 - B_z + U\left\langle n_\downarrow \right\rangle, \ \varepsilon_\downarrow = \varepsilon_0 + B_z + U\left\langle n_\uparrow \right\rangle,$$
$$\alpha_d = B_x + iB_y - U\left\langle d_\downarrow^\dagger d_\uparrow \right\rangle, \quad \Delta_d = U\left\langle d_\downarrow d_\uparrow \right\rangle.$$

The mean-field parameters appearing in Equation 25 follow by solving the self-consistency equations

$$\left\langle n_\uparrow \right\rangle = \frac{1}{\beta}\sum_\omega G_{d,11}(\omega), \quad \left\langle n_\downarrow \right\rangle = \frac{1}{\beta}\sum_\omega G_{d,33}(\omega),$$
$$\left\langle d_\downarrow^\dagger d_\uparrow \right\rangle = \frac{1}{\beta}\sum_\omega G_{d,13}(\omega), \ \left\langle d_\downarrow d_\uparrow \right\rangle = \frac{1}{\beta}\sum_\omega G_{d,21}(\omega), \tag{26}$$

where the mean-field approximation readily yields

$$G_d(\omega) = \left[i\omega - \mathcal{H}_{\rm MF} - \Sigma_{\rm S}(\omega) - \Sigma_{\rm TS}(\omega) \right]^{-1}. \tag{27}$$

The self-energies $\Sigma_{\rm S/TS}(\omega)$ due to the coupling of the QD to the S/TS leads have the matrix representation

$$\Sigma_{\rm S} = \Gamma_{\rm S} \begin{pmatrix} g_{11} & -g_{12} & 0 & 0 \\ -g_{21} & g_{22} & 0 & 0 \\ 0 & 0 & g_{11} & -g_{12} \\ 0 & 0 & -g_{21} & g_{22} \end{pmatrix} \tag{28}$$

and

$$\Sigma_{\rm TS} = \Gamma_{\rm TS} \begin{pmatrix} G_{11} & 0 & 0 & -G_{12}e^{i\phi} \\ 0 & 0 & 0 & 0 \\ 0 & 0 & 0 & 0 \\ -G_{21}e^{i\phi} & 0 & 0 & G_{22} \end{pmatrix} \tag{29}$$

with the hybridization parameters $\Gamma_{\rm S/TS} = \lambda_{\rm S/TS}^2$. The bGFs $g(\omega)$ and $G(\omega)$ have been defined in Equation 6 and Equation 7, respectively. Once a self-consistent solution to Equation 26 has been determined, which in general requires numerics, the Josephson current is obtained from Equation 5 as

$$I(\phi) = -\frac{e}{\hbar\beta}\sum_{\omega}\frac{\partial_\phi \det\left[G_d^{-1}(\omega)\right]}{\det\left[G_d^{-1}(\omega)\right]}. \tag{30}$$

In what follows, we study a setup with $\Delta_p = \Delta$ and consider the zero-temperature limit.

In order to compare our self-consistent mean-field results to the noninteracting case, let us briefly summarize analytical expressions for the $U = 0$ ABS spectrum in the atomic limit defined by $\Gamma_{S,TS} \ll \Delta$. First we notice that at low energy scales, the self-energy $\Sigma = \Sigma_S + \Sigma_{TS}$, see Equation 28 and Equation 29, simplifies to

$$\Sigma \simeq \begin{pmatrix} \frac{2\Delta}{i\omega}\Gamma_{TS} & -\Gamma_S & 0 & -\frac{2\Delta}{i\omega}\Gamma_{TS}e^{i\phi} \\ -\Gamma_S & 0 & 0 & 0 \\ 0 & 0 & 0 & -\Gamma_S \\ -\frac{2\Delta}{i\omega}\Gamma_{TS}e^{i\phi} & 0 & -\Gamma_S & \frac{2\Delta}{i\omega}\Gamma_{TS} \end{pmatrix} \tag{31}$$

The ABS spectrum of the S–QD–TS junction then follows by solving a determinantal equation, $\det\left[G_d^{-1}(\omega)\right] = 0$. One finds a zero-energy pole which is related to the MBS and results from the $1/\omega$ dependence of $\Sigma_{TS}(\omega)$. In addition, we get finite-energy subgap poles for

$$i\omega \equiv E_A^{(\sigma_1=\pm,\sigma_2=\pm)} = \sigma_1\sqrt{\frac{b_0 + \sigma_2\sqrt{b_0^2 + 4c_0}}{2}}, \tag{32}$$

with the notation

$$\begin{aligned} b_0 &= \varepsilon_\downarrow^2 + \varepsilon_\uparrow^2 + 4\Gamma_{TS}\Delta + 2\Gamma_S^2 + 2|\alpha_d|^2, \\ c_0 &= -4\Gamma_{TS}\Delta\left(\varepsilon_\downarrow^2 + \Gamma_S^2 + |\alpha_d|^2\right) - \varepsilon_\uparrow^2\varepsilon_\downarrow^2 \\ &\quad -\left(|\alpha_d|^2 - \Gamma_S^2\right)\left(|\alpha_d|^2 - \Gamma_S^2 - \varepsilon_\uparrow\omega_\downarrow\right) \\ &\quad +8\Delta\Gamma_S\Gamma_{TS}\,\mathrm{Re}\left(\alpha_d e^{i\phi}\right). \end{aligned} \tag{33}$$

In Figure 2, numerically exact results for the $U = 0$ ABS spectrum are compared to the analytical prediction (Equation 32). We first notice that, as expected, Equation 32 accurately fits the numerical results in the atomic limit, see the left panel in Figure 2. Deviations can be observed for larger values of $\Gamma_{S,TS}/\Delta$. However, as shown in the right panel of Figure 2, rather good agreement is again obtained by rescaling Equation 32 with a constant factor of the order of $(1 + \Gamma_{S,TS}/\Delta)$. For finite B_y, we find (data not shown) that the phase-dependent ABS spectrum is shifted with respect to $\phi = 0$. In fact, since the phase dependence of the subgap states comes from the term $\mathrm{Re}\left(\alpha_d e^{i\phi}\right)$ in the atomic limit, see Equation 25 and Equation 33, B_y can be fully accounted for in this limit by simply shifting $\phi \to \phi + \varphi_0$. We thereby recover the φ_0-junction behavior discussed before for the cotunneling regime, see Equation 23.

We next turn to self-consistent mean-field results for the phase-dependent ABS spectrum at finite U. Figure 3 shows the spectrum for the electron–hole symmetric case $\varepsilon_0 = -U/2$, with other parameters as in the right panel of Figure 2. For moderate interaction strength, e.g., taking $U = \Delta$ (left panel), we find that com-

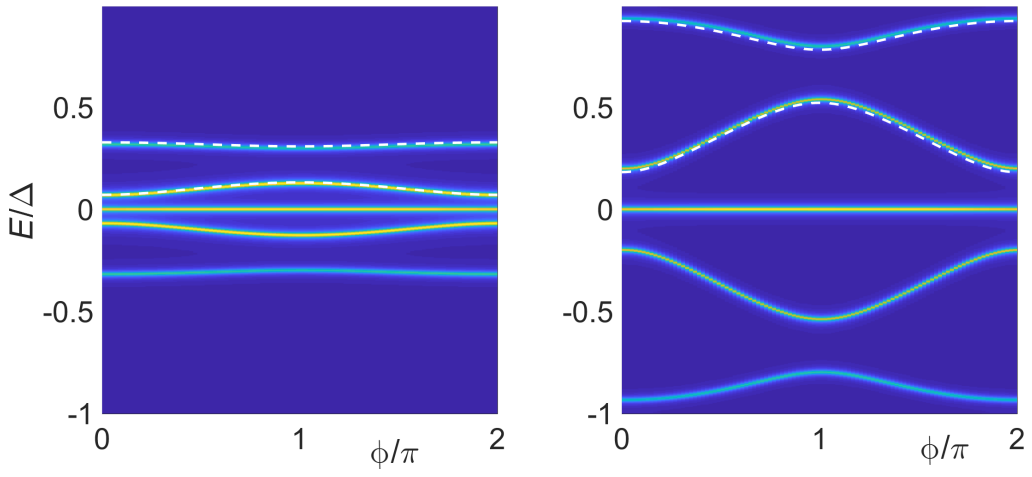

Figure 2: Phase dependence of the subgap spectrum of an S–QD–TS junction in the noninteracting case, $U = 0$. The TS wire is modeled from the low-energy limit of a Kitaev chain, and we use the parameters $B_y = 0$, $B_x = B_z = B/\sqrt{2}$, $\varepsilon_0 = 0$, $\Delta_p = \Delta$, and $\Gamma_S = \Gamma_{TS} = \Gamma$. From blue to yellow, the color code indicates increasing values of the spectral density. The left (right) panel is for $\Gamma = 0.045\Delta$ and $B = 0.1\Delta$ ($\Gamma = B = 0.5\Delta$). Solid curves were obtained by numerical evaluation of Equation 30. Dashed curves give the analytical prediction (Equation 32). In the right panel, the energies resulting from Equation 32 have been rescaled by the factor $1 + \Gamma/\Delta$.

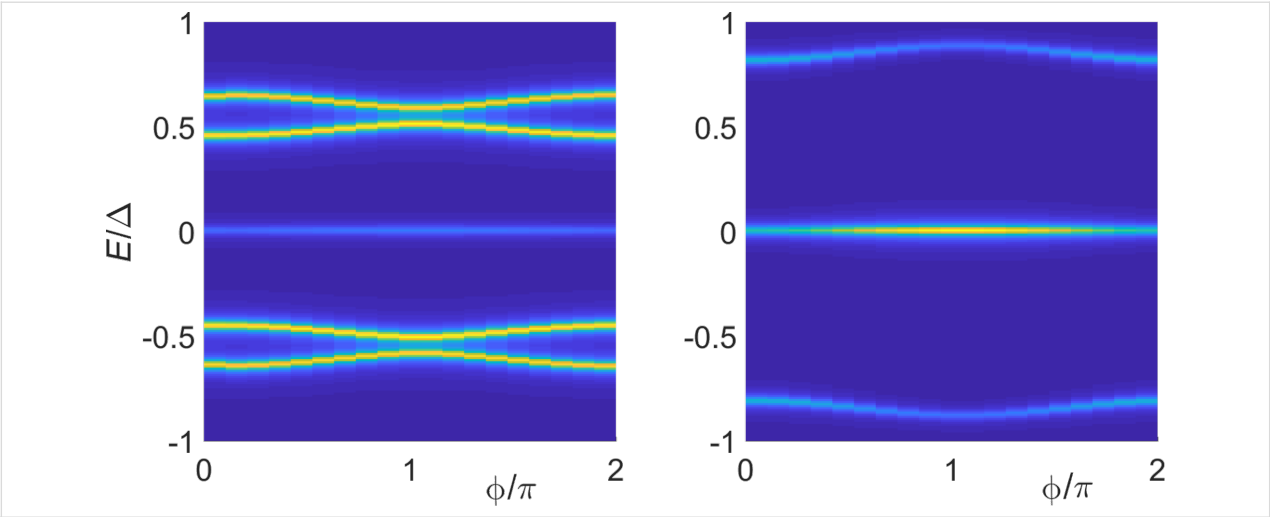

Figure 3: Phase-dependent ABS spectrum from mean-field theory for S–QD–TS junctions as in Figure 2 but with $U > 0$ and $\varepsilon_0 = -U/2$. We put $\Delta_p = \Delta$, $B_y = 0$, and $\Gamma_S = \Gamma_{TS} = \Gamma$. The color code is as in Figure 2. The left panel is for $U = \Delta$, $\Gamma = 0.5\Delta$, and $B_x = B_z = B/\sqrt{2}$ with $B = 0.5\Delta$ [cf. the right panel of Figure 2]. The right panel is for $U = 10\Delta$, $\Gamma = 4.5\Delta$, $B_x = 15\Delta$, and $B_z = 0$.

pared to the $U = 0$ case in Figure 2, interactions push together pairs of Andreev bands, e.g., the pair corresponding to $E_A^{(+,\pm)}$ in Equation 30. On the other hand, for stronger interactions, e.g., $U = 10\Delta$ (right panel), the outer ABSs leak into the continuum spectrum and only the inner Andreev states remain inside the superconducting gap. The ABS spectrum shown in Figure 3 is similar to what is observed in mean-field calculations for S–QD–S systems with broken spin symmetry and in the magnetic regime of the QD, where one finds up to four ABSs for $U < \Delta$ while the outer ABSs merge with the continuum for $U > \Delta$ [79]. Interestingly, the inner ABS contribution to the free energy for $U = 10\Delta$ is minimal for $\phi = \pi$, see right panel of Figure 3, and we therefore expect π-junction behavior for $B_y = 0$ also in the regime with $U \gg \Delta$ and $B \gg \Delta$. We notice, however, that changing the sign of B_x would result in zero junction behavior. We interpret the inner ABSs for $U \gg \Delta$ as Shiba states with the phase dependence generated by the coupling to the MBS. Without the latter coupling, the Shiba state has ϕ-independent energy slightly below Δ determined by the scattering phase shift difference between both spin polarizations [80].

As illustrated in Figure 4, the CPR computed numerically from Equation 30 for different values of $\Gamma_{S,TS}/\Delta$, where B_x has been inverted with respect to its value in Figure 3, results in zero junction behavior. This behavior is expected from Equation 23 in the cotunneling regime, and Figure 4 shows that it also persists for $\Gamma_{S,TS} \gg \Delta$. In contrast to Equation 23, however, the CPR for $\Gamma_{S,TS} \gg \Delta$ differs from a purely sinusoidal behavior, see Figure 4. Moreover, for $B_y \neq 0$, we again encounter φ_0-junction behavior, cf. the inset of Figure 4, in accordance with the perturbative result in Equation 23. Our mean-field results suggest that φ_0-junction behavior is very robust and extends also into other parameter regimes as long as the condition $B_y \neq 0$ is met.

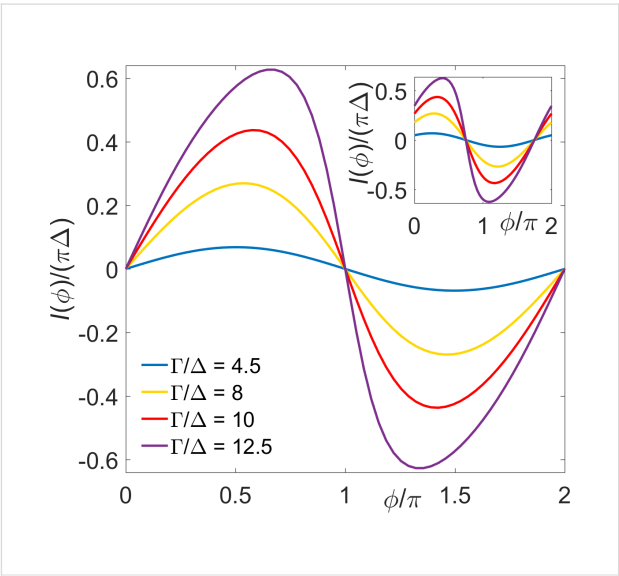

Figure 4: Main panel: Mean-field results for the CPR of S–QD–TS junctions with different Γ/Δ values, where we assume $\Delta_p = \Delta$, $U = 10\Delta$, $\varepsilon_0 = -U/2$, $\Gamma_S = \Gamma_{TS} = \Gamma$, $B = 15\Delta$, and $B_z = 0$. Main panel: For $B_x = -B$ and $B_y = 0$. Inset: Same but for $B_y = -B_x = B/\sqrt{2}$, where φ_0-junction behavior occurs.

Next, Figure 5 shows mean-field results for the critical current, $I_c = \max_\phi |I(\phi)|$, as function of the local magnetic field B_x and otherwise the same parameters as in Figure 4. The main panel in Figure 5 shows that I_c increases linearly with B_x for small $B_x < \Delta$, then exhibits a maximum around $B_x \approx \Gamma$, and subsequently decreases again to small values for $B_x \gg \max\{\Gamma_{S,TS}, \Delta\}$. On the other hand, for a fixed absolute

value B of the magnetic field and $B_y = 0$, the critical current also exhibits a maximum as a function of the angle θ_B between **B** and the MBS spin polarization axis ($\hat{e}_z$). This effect is illustrated in the inset of Figure 5. As expected, the Josephson current vanishes for $\theta_B \to 0$, where the supercurrent blockade argument of [31] implies $I_c = 0$, and reaches its maximal value for $\theta_B = \pi/2$.

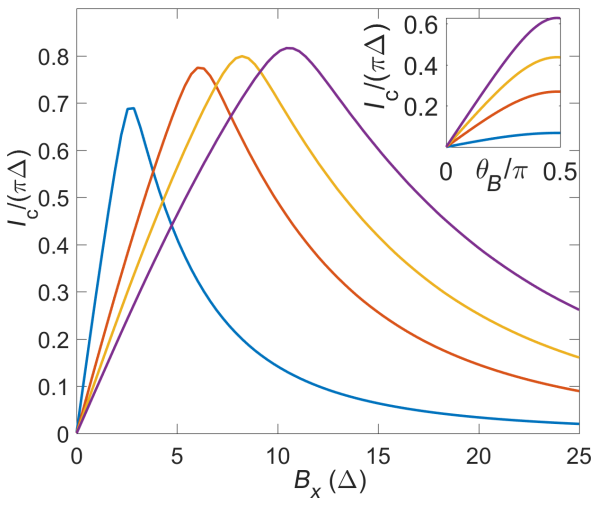

Figure 5: Main panel: Mean-field results for the critical current I_c vs local magnetic field scale B_x in S–QD–TS junctions. Parameters are as in the main panel of Figure 4, i.e., $U = 10\Delta$, $\varepsilon_0 = -U/2$, and $B_{y,z} = 0$. From left to right, different curves are for $\Gamma/\Delta = 4.5$, 8, 10 and 12.5. Inset: I_c vs angle θ_B, where $\mathbf{B} = B\,(\sin\theta_B, 0, \cos\theta_B)$ with $B = 15\Delta$.

Spinful nanowire model for the TS

Model

Before turning to the S–TS–S setup in Figure 1b, we address the question of how the above results for S–QD–TS junctions change when using the spinful nanowire model of [2,3] instead of the low-energy limit of a Kitaev chain, see Equation 7. In fact, we will first describe the Josephson current for the elementary case of an S–TS junction using the spinful nanowire model. Surprisingly, to the best of our knowledge, this case has not yet been addressed in the literature.

In spatially discretized form, the spinful nanowire model for TS wires reads [2,3,43]

$$\begin{aligned} H_{\mathrm{TS}} &= \frac{1}{2}\sum_j \left[\Psi_j^\dagger \hat{h} \Psi_j + \left(\Psi_j^\dagger \hat{t} \Psi_{j+1} + \mathrm{h.c.} \right) \right], \\ \hat{h} &= \left(2t - \mu\right)\tau_z\sigma_0 + V_x\tau_0\sigma_x + \Delta_{\mathrm{p}}\tau_x\sigma_0\,, \\ \hat{t} &= -t\tau_z\sigma_0 + i\alpha\tau_z\sigma_z\,, \end{aligned} \tag{34}$$

where the lattice fermion operators $c_{j\sigma}$ for given site j with spin polarizations $\sigma = \uparrow,\downarrow$ are combined to the four-spinor operator

$$\Psi_j = \left(c_{j\uparrow}, c_{j\downarrow}, c_{j\downarrow}^\dagger, -c_{j\uparrow}^\dagger \right)^T .$$

The Pauli matrices $\tau_{x,y,z}$ (and unity τ_0) again act in Nambu space, while Pauli matrices $\sigma_{x,y,z}$ and σ_0 refer to spin. In the figures shown below, we choose the model parameters in Equation 34 as discussed in [43]. The lattice spacing is set to a = 10 nm, which results in a nearest-neighbor hopping $t = \hbar^2/(2m^*a^2) = 20$ meV and the spin–orbit coupling strength $\alpha = 4$ meV for InAs nanowires. The proximity-induced pairing gap is again denoted by Δ_{p}, the chemical potential is μ, and the bulk Zeeman energy scale V_x is determined by a magnetic field applied along the wire. Under the condition

$$V_x > V_x^c = \sqrt{\mu^2 + \Delta_{\mathrm{p}}^2}, \tag{35}$$

the topologically nontrivial phase is realized [2,3]. As we discuss below, the physics of the S–QD–TS junction sensitively depends on both the bulk Zeeman field V_x and on the local magnetic field **B** acting on the QD, where one can either identify both magnetic fields or treat **B** as independent field. In any case, the bGF $\tilde{G}(\omega)$ for the model in Equation 34, which now replaces the Kitaev chain result $G(\omega)$ in Equation 7, needs to be computed numerically. The bGF $\tilde{G}$ has been described in detail in [43], where also a straightforward numerical scheme for calculating $\tilde{G}(\omega)$ has been devised. With the replacement $G \to \tilde{G}$, we can then take over the expressions for the Josephson current discussed before. Below we study these expressions in the zero-temperature limit.

S–TS junction

Let us first address the CPR for the S–TS junction case. The Josephson current can be computed using the bGF expression for tunnel junctions in [40], which is a simplified version of the above expressions for the S–QD–TS case. The spin-conserving tunnel coupling λ defines a transmission probability (transparency) $\mathcal{T}$ of the normal junction [40,43]. Close to the topological transition, the transparency is well approximated by

$$\mathcal{T} = \frac{4\left(\lambda/t\right)^2}{\left[1 + \left(\lambda/t\right)^2\right]^2}, \tag{36}$$

where $t = 20$ meV is the hopping parameter in Equation 34. We then study the CPR and the resulting critical current I_c as a function of $\mathcal{T}$ for both the topologically trivial ($V_x < V_x^c$) and the nontrivial ($V_x > V_x^c$) regime, see Equation 35.

In Figure 6, we show the V_x dependence of the critical current I_c for the symmetric case $\Delta = \Delta_p$. In particular, it is of interest to determine how I_c changes as one moves through the phase transition in Equation 35. First, we observe that I_c is strongly suppressed in the topological phase in comparison to the topologically trivial phase. In fact, I_c slowly decreases as one moves into the deep topological phase by increasing V_x. This observation is in accordance with the expected supercurrent blockade in the deep topological limit [31]: $I_c = 0$ for the corresponding Kitaev chain case since *p*-wave pairing correlations on the TS side are incompatible with *s*-wave correlations on the S side. However, a residual finite supercurrent can be observed even for rather large values of V_x. We attribute this effect to the remaining *s*-wave pairing correlations contained in the spinful nanowire model (Equation 34). Second, Figure 6 shows kink-like features in the $I_c(V_x)$ curve near the topological transition, $V_x \approx V_x^c$. The inset of Figure 6 demonstrates that this feature comes from a rapid decrease of the ABS contribution while the continuum contribution remains smooth. This observation suggests that continuum contributions in this setup mainly originate from *s*-wave pairing correlations which are not particularly sensitive to the topological transition.

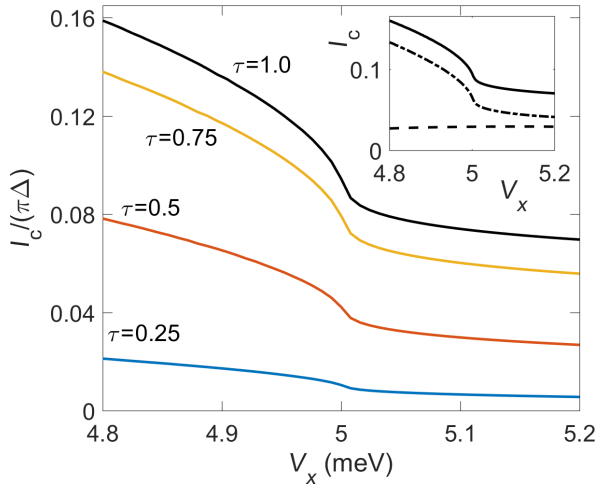

Figure 6: Main panel: Critical current I_c vs Zeeman energy V_x for an S–TS junction using the spinful TS nanowire model (Equation 34) for $\Delta_p = \Delta = 0.2$ meV, $\mu = 5$ meV, and different transparencies $\mathcal{T}$ calculated from Equation 36. All other parameters are specified in the main text. Inset: Decomposition of I_c for $\mathcal{T} = 1$ into ABS (dotted-dashed) and continuum (dashed) contributions.

In Figure 7, we show the CPR for the S–TS junction with $\mathcal{T} = 1$ in Figure 6, where different curves correspond to different Zeeman couplings V_x near the critical value. We find that in many parameter regions, in particular for $\mathcal{T} < 1$, the CPR is to high accuracy given by a conventional 2π-periodic Josephson relation, $I(\phi) = I_c \sin\phi$. In the topologically trivial phase, small deviations from the sinusoidal law can be detected, but once one enters the topological phase, these deviations become extremely small.

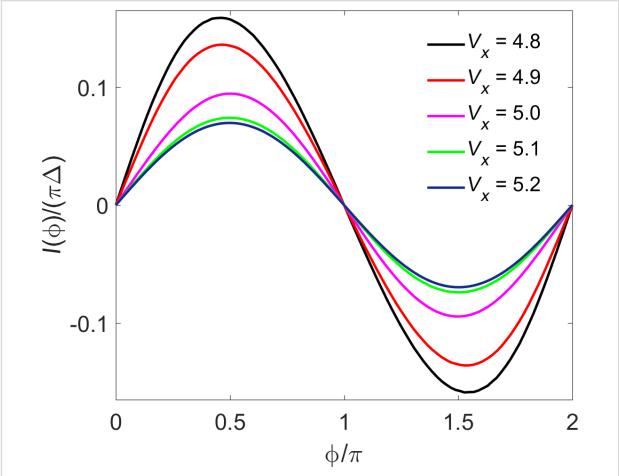

Figure 7: CPR for the S–TS junction with $\mathcal{T} = 1$ in Figure 6, for different bulk Zeeman fields V_x (in meV) near the critical value $V_x^c = 5.004$ meV.

S–QD–TS junction with spinful TS wire: Mean-field theory

Apart from providing a direct link to experimental control parameters, another advantage of using the spinful nanowire model of [2,3] for modeling the TS wire is that the angle between the local Zeeman field **B** and the MBS spin polarization does not have to be introduced as phenomenological parameter but instead results from the calculation [43]. It is thus interesting to study the Josephson current in S–QD–TS junctions where the TS wire is described by the spinful nanowire model. For this purpose, we now revisit the mean-field scheme for S–QD–TS junctions using the bGF $\tilde{G}(\omega)$ for the spinful nanowire model (Equation 34). In particular, with the replacement $G \to \tilde{G}$, we solve the self-consistency equations (Equation 26) and thereby obtain the mean-field parameters in Equation 25. The resulting QD GF, $G_d(\omega)$ in Equation 27, then determines the Josephson current in Equation 30. Below we present self-consistent mean-field results obtained from this scheme. In view of the huge parameter space of this problem, we here only discuss a few key observations. A full discussion of the phase diagram and the corresponding physics will be given elsewhere.

The main panel of Figure 8 shows the critical current I_c vs the bulk Zeeman energy V_x for several values of the chemical potential μ, where the respective critical value V_x^c in

Equation 35 for the topological phase transition also changes with μ. The results in Figure 8 assume that the local magnetic field **B** acting on the QD coincides with the bulk Zeeman field V_x in the TS wire, i.e., **B** = (V_x,0,0). For the rather large values of $\Gamma_{S,TS}$ taken in Figure 8, the I_c vs V_x curves again exhibit a kink-like feature near the topological transition, $V_x \approx V_x^c$. This behavior is very similar to what happens in S–TS junctions with large transparency $\mathcal{T}$, cf. Figure 6. As demonstrated in the inset of Figure 8, the physical reason for the kink feature can be traced back to a sudden drop of the ABS contribution to I_c when entering the topological phase $V_x > V_x^c$. In the latter phase, I_c becomes strongly suppressed in close analogy to the S–TS junction case shown in Figure 6.

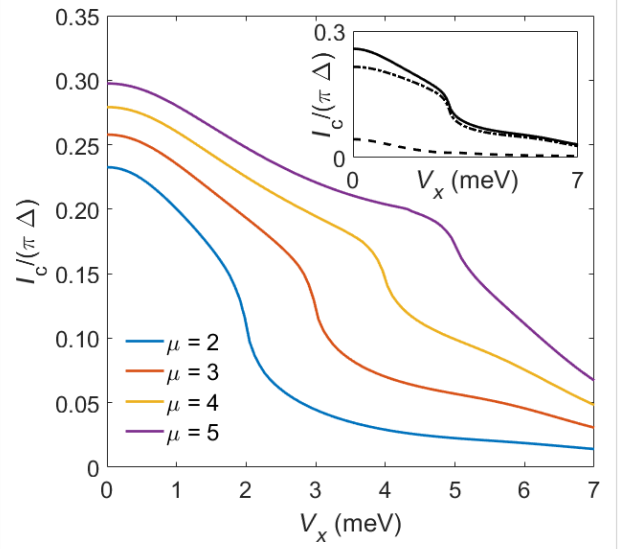

Figure 8: Main panel: Critical current I_c vs Zeeman energy V_x for S–QD–TS junctions from mean-field theory using the spinful TS nanowire model (Equation 34). Results are shown for several values of the chemical potential μ (in meV), where we assume $U = 10\Delta$, $\varepsilon_0 = -U/2$, $\Delta_p = \Delta = 0.2$ meV, $\Gamma_S = 2\Gamma_{TS} = 9\Delta$, and **B** = ($V_x$,0,0). Inset: Detailed view of the transition region $V_x \approx V_x^c$ for μ = 4 meV, including a decomposition of I_c into the ABS (dotted-dashed) and the continuum (dashed) contribution.

In Figure 8, both the QD and the TS wire were subject to the same magnetic Zeeman field. If the direction and/or the size of the local magnetic field **B** applied to the QD can be varied independently from the bulk magnetic field $V_x\hat{e}_x$ applied to the TS wire, one can arrive at rather different conclusions. To illustrate this statement, Figure 9 shows the I_c vs B_z dependence for **B** = (0,0,B_z) perpendicular to the bulk field, with $V_x > V_x^c$ such that the TS wire is in the topological phase. In this case, Figure 9 shows that I_c exhibits a maximum close to $B_z \sim \Gamma$. This behavior is reminiscent of what we observed above in Figure 5, using the low-energy limit of a Kitaev chain for the bGF of the TS wire. Remarkably, the critical current can here reach values close to the unitary limit, $I_c \sim e\Delta/\hbar$. We note that since B_z does not drive a phase transition, no kink-like features appear for the $I_c(B_z)$ curves shown in Figure 9. Finally, the inset of Figure 9 shows that for **B** perpendicular to $V_x\hat{e}_x$, where $V_x > V_x^c$ for the parameters chosen in Figure 9, the ABSs provide the dominant contribution to the current in this regime.

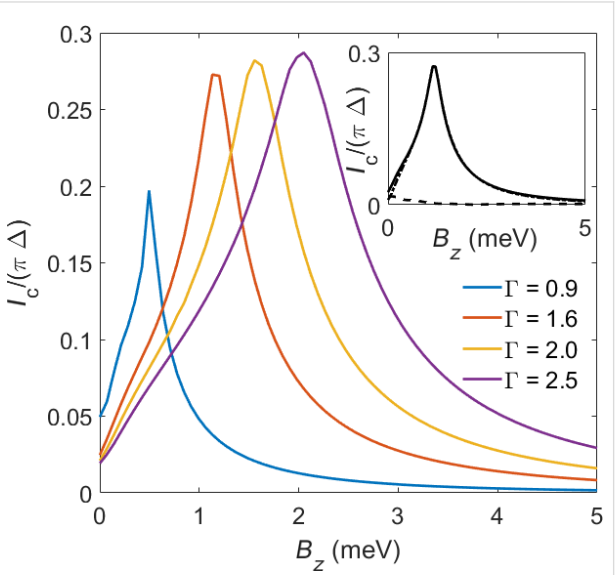

Figure 9: Main panel: Mean-field results for I_c vs B_z in S–QD–TS junctions for several values of $\Gamma_S = \Gamma_{TS} = \Gamma$ (in meV) and μ = 4 meV. The bulk Zeeman field V_x = 5 meV along $\hat{e}_x$ (where $V_x > V_x^c$ for our parameters) is applied to the spinful TS wire, while the QD is subject to the local magnetic field **B** = $B_z\hat{e}_z$. All other parameters are as in Figure 8. Inset: Decomposition of I_c into ABS (dotted-dashed) and continuum (dashed) contributions for Γ = 1.6 meV.

S–TS–S junctions: Switching the parity of a superconducting atomic contact

Model

We now proceed to the three-terminal S–TS–S setup shown in Figure 1b. The CPR found in the related TS–S–TS trijunction case has been discussed in detail in [43], see also [44]. Among other findings, a main conclusion of [43] for the TS–S–TS geometry was that the CPR can reveal information about the spin canting angle between the MBS spin polarization axes in both TS wires. In what follows, we study the superficially similar yet rather different case of an S–TS–S junction. Throughout this section, we model the TS wire via the low-energy theory of a spinless Kitaev chain, where the bGF $G(\omega)$ in Equation 7 applies.

One can view the setup in Figure 1b as a conventional superconducting atomic contact (SAC) with a TS wire tunnel-coupled to the S–S junction. Over the past few years, impressive experimental progress [52-54] has demonstrated that the ABS level system in a SAC [81] can be accurately probed and

manipulated by coherent or incoherent microwave spectroscopy techniques. We show below that an additional TS wire, cf. Figure 1b, acts as tunable parity switch on the many-body ABS levels of the SAC. As we have discussed above, the supercurrent flowing directly between a given S lead and the TS wire is expected to be strongly suppressed. However, through the hybridization with the MBS, Andreev level configurations with even and odd fermion parity are connected. This effect has profound and potentially useful consequences for Andreev spectroscopy.

An alternative view of the setup in Figure 1b is to imagine an S–TS junction, where S1 plays the role of the S lead and the spinful TS wire is effectively composed from a spinless (Kitaev) TS wire and the S2 superconductor. The *p*- and *s*-wave pairing correlations in the spinful TS wire are thereby spatially separated. Since the *s*- and *p*-wave bands represent normal modes, they are not directly coupled to each other in this scenario, i.e., we have to put $\lambda_2 = 0$. We discuss this analogy in more detail later on.

We consider a conventional single-channel SAC (gap Δ) coupled via a point contact to a TS wire (gap Δ_p), cf. Figure 1b. The superconducting phase difference across the SAC is denoted by $\phi = \phi_1 - \phi_2$, where ϕ_j is the phase difference between the respective S arm (j = 1,2) and the TS wire. In practice, the SAC can be embedded into a superconducting ring for magnetic flux tuning of ϕ. To allow for analytical progress, we here assume that Δ_p is so large that continuum quasiparticle excitations in the TS wire can be neglected. In that case, only the MBS at the junction has to be kept when modeling the TS wire. However, we will also hint at how one can treat the general case.

For the two S leads, boundary fermion fields are contained in Nambu spinors as in Equation 6,

$$\Psi_{\mathrm{S},j=1,2} = \begin{pmatrix} \Psi_{j,\uparrow} \\ \Psi^\dagger_{j,\downarrow} \end{pmatrix}, \tag{37}$$

where their bGF follows with the Nambu matrix $g(\omega)$ in Equation 6 as

$$g_j^{-1}(\omega) = g^{-1}(\omega) + b_j\tau_0\,. \tag{38}$$

We again use Pauli matrices $\tau_{x,y,z}$ and unity τ_0 in Nambu space. The dimensionless parameters $b_{1,2}$ describe the Zeeman field component along the MBS spin polarization axis, see below. Since above-gap quasiparticles in the TS wire are neglected here, the TS wire is represented by the Majorana operator $\gamma = \gamma^\dagger$, with $\gamma^2 = 1/2$, which anticommutes with all other fermions. We may represent γ by an auxiliary fermion $f_\uparrow$, where the index reminds us that the MBS spin polarization points along $\hat{e}_z$,

$$\gamma = \left(f_\uparrow + f_\uparrow^\dagger\right)\Big/\sqrt{2}\,. \tag{39}$$

The other Majorana mode $\gamma' = -i\left(f_\uparrow - f_\uparrow^\dagger\right)\Big/\sqrt{2}$, which is localized at the opposite end of the TS wire, is assumed to have negligible hybridization with the $\Psi_{\mathrm{S},j}$ spinors and with γ. Writing the Euclidean action as $S = S_0 + S_{\mathrm{tun}}$, we have an uncoupled action contribution,

$$\begin{aligned} S_0 = &\sum_{j=1,2}\int_0^\beta \mathrm{d}\tau\mathrm{d}\tau'\bar{\Psi}_{\mathrm{S},j}(\tau)g_j^{-1}(\tau-\tau')\Psi_{\mathrm{S},j}(\tau') \\ &+\frac{1}{2}\int_0^\beta \mathrm{d}\tau\,\gamma(\tau)\partial_\tau\gamma(\tau)\,. \end{aligned} \tag{40}$$

The leads are connected by a time-local tunnel action corresponding to the tunnel Hamiltonian

$$\begin{aligned} H_{\mathrm{tun}} = &t_0\left(\Psi^\dagger_{\mathrm{S},1}\tau_z e^{i\tau_z\phi/2}\Psi_{\mathrm{S},2} + \mathrm{h.c.}\right) \\ &+\sum_{j=1,2}\frac{\lambda_j}{\sqrt{2}}\left(\Psi^\dagger_{j,\uparrow}e^{i\phi_j/2} - \mathrm{h.c.}\right)\gamma. \end{aligned} \tag{41}$$

Without loss of generality, we assume that the tunnel amplitudes t_0 and $\lambda_{1,2}$, see Figure 1b, are real-valued and that they include density-of-state factors again. The parameter t_0 (with $0 \le t_0 \le 1$) determines the transparency $\mathcal{T}$ of the SAC in the normal-conducting state [36], cf. Equation 36,

$$\mathcal{T} = \frac{4t_0^2}{\left(1+t_0^2\right)^2}. \tag{42}$$

Note that in Equation 41 we have again assumed spin-conserving tunneling, where only spin-↑ fermions in the SAC are tunnel-coupled to the Majorana fermion γ, cf. Equation 4.

At this stage, it is convenient to trace out the $\Psi_{\mathrm{S},2}$ spinor field. As a result, the SAC is described in terms of only one spinor field, $\Psi \equiv \Psi_{\mathrm{S},1}$, which however is still coupled to the Majorana field γ. After some algebra, we obtain the effective action

$$S_{\rm eff}=\int_0^\beta {\rm d}\tau{\rm d}\tau'\left\{\begin{array}{l}\bar{\Psi}(\tau)K^{-1}(\tau-\tau')\Psi(\tau')\\ +\Phi^T(\tau)\left[\begin{array}{l}\frac{1}{2}\delta(\tau-\tau')\partial_{\tau'}\\ -\lambda_2^2P_\downarrow g_2(\tau-\tau')P_\uparrow\end{array}\right]\Phi(\tau')\\ +\left[\bar{\Psi}(\tau)\left(\begin{array}{l}\lambda_1 e^{i\phi_1/2}\delta(\tau-\tau')\\ -\lambda_2 e^{i\phi_2/2}t_0\tau_z e^{i\tau_z\phi/2}g_2(\tau-\tau')\end{array}\right)\right]\\ \left[P_\uparrow\Phi(\tau')+{\rm h.c.}\right]\end{array}\right\}, \quad (43)$$

where the operator $P_\uparrow = (\tau_0 + \tau_z)/2$ projects a Nambu spinor to its spin-↑ component. Moreover, we have defined an effective GF in Nambu space with frequency components

$$K^{-1}(\omega)=g_1^{-1}(\omega)-t_0^2\tau_z e^{i\tau_z\phi/2}g_2(\omega)e^{-i\tau_z\phi/2}\tau_z\,, \quad (44)$$

and the TS lead has been represented by the Majorana–Nambu spinor

$$\Phi(\tau)=\frac{1}{\sqrt{2}}\begin{pmatrix}1\\1\end{pmatrix}\gamma(\tau)=\tau_x\Phi^*(\tau). \quad (45)$$

We note in passing that Equation 43 could at this point be generalized to include continuum states in the TS wire. To that end, one has to (i) replace $\Phi \to (\psi, \psi^\dagger)^T$, where ψ is the boundary fermion of the effectively spinless TS wire, and (ii) replace $\delta(\tau - \tau')\partial_{\tau'} \to G^{-1}(\tau - \tau')$ with G in Equation 7. Including bulk TS quasiparticles becomes necessary for small values of the proximity gap, $\Delta_p \ll \Delta$, and/or when studying nonequilibrium applications within a Keldysh version of our formalism.

In any case, after neglecting the above-gap TS continuum quasiparticles, the partition function follows with $S_{\rm eff}$ in Equation 43 in the functional integral representation

$$Z=\int\mathcal{D}\left[\bar{\Psi},\Psi,\gamma\right]e^{-S_{\rm eff}}\equiv e^{-\beta F(\phi_1,\phi_2)}. \quad (46)$$

As before, the Josephson current through S lead no. j then follows from the free energy via

$$I_j=(2e/\mathsf{h})\partial_{\phi_j}F.$$

The supercurrent flowing through the TS wire is then given by

$$I_{\rm TS}=-(I_1+I_2), \quad (47)$$

as dictated by current conservation.

Atomic limit

In order to get insight into the basic physics, we now analyze in detail the atomic limit, where Δ represents the largest energy scale of interest and hence the dynamics is confined to the subgap region. In this case, we can approximate $\sqrt{\Delta^2+\omega^2}\approx\Delta$. After the rescaling

$$\Psi\to\sqrt{\Delta/\left(1+t_0^2\right)}\Psi$$

in Equation 43, we arrive at an effective action, $S_{\rm eff} \to S_{\rm at}$, valid in the atomic limit,

$$S_{\rm at}=\int_0^\beta {\rm d}\tau\left\{\begin{array}{l}\frac{1}{2}\gamma\partial_\tau\gamma+\bar{\Psi}\left[\begin{array}{l}\partial_\tau+\Delta\cos(\phi/2)\tau_x\\ +r\Delta\sin(\phi/2)\tau_y+B_z\tau_0\end{array}\right]\Psi\\ +\frac{1}{\sqrt{2}}\sum\limits_{\sigma=\uparrow,\downarrow}\left(\lambda_\sigma\Psi_\sigma^\dagger-{\rm h.c.}\right)\gamma\end{array}\right\}, \quad (48)$$

where $r=\sqrt{1-T}$ is the reflection amplitude of the SAC, see Equation 42. We recall that $\Psi=\left(\psi_\uparrow,\psi_\downarrow^\dagger\right)^T$, see Equation 37. Moreover, we define the auxiliary parameters

$$\begin{aligned}\lambda_\uparrow&=\lambda_1\sqrt{(1+r)\Delta/2}e^{i\phi_1/2},\\ \lambda_\downarrow&=-\lambda_2\sqrt{(1-r)\Delta/2}e^{-i\phi_2/2},\\ B_z&=\left(\frac{1+r}{2}b_1+\frac{1-r}{2}b_2\right)\Delta\,.\end{aligned} \quad (49)$$

The parameters $b_{1,2}$ in Equation 38 thus effectively generate the Zeeman scale B_z in Equation 49.

As a consequence of the atomic limit approximation, the action $S_{\rm at}$ in Equation 48 is equivalently expressed in terms of the effective Hamiltonian

$$\begin{aligned}H_{\rm at}=&\sum_{\sigma=\uparrow,\downarrow=\pm}\sigma B_z\Psi_\sigma^\dagger\Psi_\sigma+\left(\delta_A\Psi_\uparrow^\dagger\Psi_\downarrow^\dagger+{\rm h.c.}\right)\\ &+\frac{1}{\sqrt{2}}\sum_\sigma\left(\lambda_\sigma\Psi_\sigma^\dagger-{\rm h.c.}\right)\gamma\,,\end{aligned} \quad (50)$$

where we define

$$\delta_A(\phi)=\Delta\left[\cos(\phi/2)-ir\sin(\phi/2)\right]. \quad (51)$$

For a SAC decoupled from the TS wire and taken at zero field ($B_z = 0$), the ABS energy follows from Equation 50 in the standard form [62]

$$E_A(\phi) = |\delta_A| = \Delta\sqrt{1-\mathcal{T}\sin^2(\phi/2)}\,. \tag{52}$$

We emphasize that $H_{\rm at}$ neglects TS continuum quasiparticles as well as all types of quasiparticle poisoning processes. Let us briefly pause in order to make two remarks. First, we note that the Majorana field

$$\gamma = \left(f_\uparrow + f_\uparrow^\dagger\right)\!/\sqrt{2}\,,$$

see Equation 39, couples to both spin modes ψ_σ in Equation 50. The coupling $\lambda_\downarrow$ between γ and the spin-$\downarrow$ field in the SAC, $\psi_\downarrow$, is generated by crossed Andreev reflection processes, where a Cooper pair in lead S2 splits according to $\psi_{2,\uparrow}^\dagger\psi_{2,\downarrow}^\dagger \to f_\uparrow^\dagger\psi_{1,\downarrow}^\dagger$, plus the conjugate process. Second, we observe that $H_{\rm at}$ is invariant under a particle–hole transformation, amounting to the replacements $\psi_\sigma \to \psi_\sigma^\dagger$ and $f_\uparrow \to f_\uparrow^\dagger$, along with $B_z \to -B_z$ and $\phi_j \to 2\pi - \phi_j$.

We next notice that with $n_\sigma = \psi_\sigma^\dagger\psi_\sigma = 0,1$ and $n_f = f_\uparrow^\dagger f_\uparrow = 0,1$, the total fermion parity of the junction,

$$\mathcal{P}_{\rm tot} = (-1)^{n_f + n_\uparrow + n_\downarrow} = \pm 1\,, \tag{53}$$

is a conserved quantity, $[\mathcal{P}_{\rm tot}, H_{\rm at}]_- = 0$. Below we restrict our analysis to the even-parity sector $\mathcal{P}_{\rm tot} = +1$, but analogous results hold for the odd-parity case. The corresponding Hilbert subspace is spanned by four states,

$$\left|n_\uparrow, n_\downarrow, n_f\right\rangle = \left(\Psi_\uparrow^\dagger\right)^{n_\uparrow}\left(\Psi_\downarrow^\dagger\right)^{n_\downarrow}\left(f_\uparrow^\dagger\right)^{n_f}|0\rangle, \tag{54}$$

where $(n_\uparrow, n_\downarrow, n_f) \in \{(0,0,0), (1,1,0), (1,0,1), (0,1,1)\}$ and $|0\rangle$ is the vacuum state. In this basis, the Hamiltonian (Equation 50) has the matrix representation

$$\mathcal{H}_{\rm at}(\phi_1,\phi_2) = \begin{pmatrix} 0 & \delta_A^* & \lambda_\uparrow^*/2 & \lambda_\downarrow^*/2 \\ \delta_A & 0 & \lambda_\downarrow/2 & -\lambda_\uparrow/2 \\ \lambda_\uparrow/2 & \lambda_\downarrow^*/2 & B_z & 0 \\ \lambda_\downarrow/2 & -\lambda_\uparrow^*/2 & 0 & -B_z \end{pmatrix}. \tag{55}$$

The even-parity ground state energy, $E_G^{(e)} = \min(\varepsilon)$, follows as the smallest root of the quartic equation

$$\det\left(\mathcal{H}_{\rm at} - \varepsilon\right) = 0. \tag{56}$$

In order to obtain simple results, let us now consider the special case $\lambda_2 = 0$, where the TS wire is directly coupled to lead S1 only, see Figure 1b. In that case, we also have $\lambda_\downarrow = 0$, see Equation 49, and Equation 56 implies the four eigenenergies $\pm\varepsilon_\pm$ with

$$\varepsilon_\pm = \frac{1}{\sqrt{2}}\left(E_A^2 + B_z^2 + \frac{1}{2}|\lambda_\uparrow|^2 \pm\sqrt{\left(E_A^2 - B_z^2\right) + |\lambda_\uparrow|^2\left(E_A^2 + B_z^2\right)}\right)^{1/2}, \tag{57}$$

with $|\lambda_\uparrow|^2 = \lambda_1^2(1+r)\Delta/2$, see Equation 49. The ground-state energy is thus given by $E_G^{(e)} = -\varepsilon_+$. Since E_G depends on the phases $\phi_{1,2}$ only via the Andreev level energy $E_A(\phi)$ in Equation 52, the Josephson current through the SAC is given by

$$I_1 = -I_2 = \frac{2e}{\hbar}\partial_\phi E_G^{(e)} = -\frac{2e}{\hbar}\partial_\phi\varepsilon_+\,. \tag{58}$$

Note that Equation 47 then implies that no supercurrent flows into the TS wire.

Next we observe that in the absence of the TS probe ($\lambda_1 = 0$), the even and odd fermion parity sectors of the SAC, $\mathcal{P}_{\rm SAC} = (-1)^{n_\uparrow + n_\downarrow} = \pm 1$, are decoupled, see Equation 55, and Equation 57 yields $E_G^{(e)} = -\max(E_A, |B_z|)$. Importantly, the Josephson current is therefore fully blocked if the ground state is in the $\mathcal{P}_{\rm SAC} = -1$ sector, i.e., for $|B_z| > E_A(\phi)$. For $\lambda_1 \neq 0$, however, $\mathcal{P}_{\rm SAC}$ is not conserved anymore. This implies that the MBS can act as parity switch between the two Andreev sectors with parity $\mathcal{P}_{\rm SAC} = \pm 1$. Near the level crossing point at $E_A \approx |B_z|$, i.e., assuming $\left|E_A^2 - B_z^2\right| \ll |\lambda_\uparrow|^2 \ll E_A^2 + B_z^2$, we obtain

$$\varepsilon_\pm \simeq \frac{1}{\sqrt{2}}\left(E_A^2 + B_z^2 \pm \lambda_1\sqrt{2(1+r)\Delta\left(E_A^2 + B_z^2\right)}\right)^{1/2}, \tag{59}$$

which implies a nonvanishing supercurrent through the SAC even in the field-dominated regime, $|B_z| > E_A$. The MBS therefore acts as a parity switch and leaves a trace in the CPR by lifting the supercurrent blockade.

Another interpretation

Interestingly, for $\lambda_2 = \phi_2 = 0$, the S–TS–S setup in Figure 1b could also be viewed as a toy model for an S–TS junction, where the TS part corresponds to a spinful model. In that analogy, the Nambu spinor $\Psi_{S,1}$ stands for the S lead while the spinful TS wire is represented by (i) the Nambu spinor $\Psi_{S,2}$ which is responsible for the residual *s*-wave pairing correlations, and (ii) by the MF γ (or, more generally, by the Kitaev-chain spinless boundary fermion ψ) which encodes *p*-wave pairing correlations. Moreover, t_0 and λ_1 should now be understood as spin-conserving phenomenological tunnel couplings acting in the *s*–*s* and *s*–*p* wave channels, respectively. The phase difference across this effective S–TS junction is $\phi = \phi_1$ and the net S–TS tunnel coupling is given by $\lambda = \sqrt{t_0^2 + \lambda_1^2}$. Putting $\lambda_1 = 0$ in the topologically trivial phase of the TS wire, the Josephson current carried by Andreev states in the *s*–*s* channel is blocked when the ground state is in the odd parity sector of the SAC. For $\lambda_1 \neq 0$, the MBS-mediated switching between odd and even parity sectors will now be activated and thereby lift the supercurrent blockade.

Conventional midgap level

A similar behavior as predicted above for the MBS-induced parity switch between $\mathcal{P}_{\mathrm{SAC}} = \pm 1$ sectors could also be expected from a conventional fermionic subgap state tunnel-coupled to the SAC. Such a subgap state may be represented, e.g., by a single-level quantum dot in the Coulomb blockade regime. In particular, for a midgap (zero-energy) level with the fermion operator d, the Hamiltonian H_{at} in Equation 50 has to be replaced with

$$\tilde{H}_{\mathrm{at}} = \sum_{\sigma=\uparrow,\downarrow=\pm} \sigma B_z \Psi_\sigma^\dagger \Psi_\sigma + \left(\delta_A \Psi_\uparrow^\dagger \Psi_\downarrow^\dagger + \mathrm{h.c.}\right) + \sum_\sigma \left(\lambda_\sigma \Psi_\sigma^\dagger d + \mathrm{h.c.}\right). \tag{60}$$

In the even total parity basis (Equation 54), the matrix representation of the Hamiltonian is then instead of Equation 55 given by

$$\mathcal{H}_{\mathrm{at}}(\phi_1, \phi_2) = \begin{pmatrix} 0 & \delta_A^* & 0 & 0 \\ \delta_A & 0 & \lambda_\downarrow & -\lambda_\uparrow \\ 0 & \lambda_\downarrow^* & B_z & 0 \\ 0 & -\lambda_\uparrow^* & 0 & -B_z \end{pmatrix}. \tag{61}$$

Assuming $|\lambda_\uparrow| = |\lambda_\downarrow| \equiv \lambda$, Equation 56 then yields the eigenenergies $\pm\varepsilon_\pm$ with

$$\varepsilon_\pm = \frac{1}{\sqrt{2}} \left(E_A^2 + B_z^2 + 2\lambda^2 \pm \sqrt{\left(E_A^2 - B_z^2\right) + 4\lambda^2 \left(E_A^2 + B_z^2 + \lambda^2\right)} \right)^{1/2}. \tag{62}$$

Remarkably, the ABS spectra in Equation 62 and Equation 57 are rather similar for $\lambda^2 = \max\left(E_A^2, B_z^2\right)$. However, the MBS will automatically be located at zero energy and thus represents a generic situation.

Conclusion

We close this paper by summarizing our main findings. We have studied the Josephson effect in different setups involving both conventional *s*-wave BCS superconductors (S leads) and topologically nontrivial 1D *p*-wave superconductors (TS leads) with Majorana end states. The TS wires have been described either by a spinless theory applicable in the deep topological regime, which has the advantage of allowing for analytical progress but makes it difficult to establish contact to experimental control parameters, or by a spinful nanowire model as suggested in [2,3]. We have employed a unified imaginary-time Green's function approach to analyze the equilibrium properties of such devices, but a Keldysh generalization is straightforward and allows one to study also nonequilibrium applications.

For S–TS tunnel junctions, we find that in the topological phase of the TS wire, the supercurrent is mainly carried by above-gap continuum contributions. We confirm the expected supercurrent blockade [31] in the deep topological regime (where the spinless theory is fully valid and thus no residual *s*-wave pairing exists), while for realistic parameters, a small but finite critical current is found. To good approximation, the Josephson current obeys the usual 2π-periodic sinusoidal current–phase relation. The dependence of the critical current on the bulk Zeeman field driving the TS wire through the topological phase transition shows a kink-like feature at the critical value, which is caused by a sudden drop of the Andreev state contribution.

The supercurrent blockade in the deep topological phase could be lifted by adding a magnetic impurity to the junction, also allowing for the presence of a local magnetic field **B**. Such a magnetic impurity arises from a spin-degenerate quantum dot (QD), and we have studied the corresponding S–QD–TS problem for both the spinless and the spinful TS wire model. Based on analytical results valid in the cotunneling regime as well as numerical results within the mean-field approximation, we predict φ_0-junction behavior (anomalous Josephson effect) for the current–phase relation when the TS wire is in the topological phase.

As a final example for devices combining conventional and topological superconductors, we have shown that S–TS–S devices allow for a Majorana-induced parity switch between Andreev state sectors with different parity in a superconducting atomic contact. This observation could be useful for future microwave spectroscopy experiments of Andreev qubits in such contacts.

Acknowledgements

We acknowledge funding by the Deutsche Forschungsgemeinschaft (Grant No. EG 96/11-1) and by the Spanish MINECO through Grant No. FIS2014-55486-P and through the "María de Maeztu" Programme for Units of Excellence in R&D (MDM-2014-0377).

References

1. Kitaev, A. Yu. *Phys.-Usp.* **2001,** *44,* 131. doi:10.1070/1063-7869/44/10S/S29
2. Lutchyn, R. M.; Sau, J. D.; Das Sarma, S. *Phys. Rev. Lett.* **2010,** *105,* 077001. doi:10.1103/physrevlett.105.077001
3. Oreg, Y.; Refael, G.; von Oppen, F. *Phys. Rev. Lett.* **2010,** *105,* 177002. doi:10.1103/physrevlett.105.177002
4. Alicea, J.; Oreg, Y.; Refael, G.; von Oppen, F.; Fisher, M. P. A. *Nat. Phys.* **2011,** *7,* 412. doi:10.1038/nphys1915
5. Alicea, J. *Rep. Prog. Phys.* **2012,** *75,* 076501. doi:10.1088/0034-4885/75/7/076501
6. Leijnse, M.; Flensberg, K. *Semicond. Sci. Technol.* **2012,** *27,* 124003. doi:10.1088/0268-1242/27/12/124003
7. Beenakker, C. W. J. *Annu. Rev. Condens. Matter Phys.* **2013,** *4,* 113. doi:10.1146/annurev-conmatphys-030212-184337
8. Aasen, D.; Hell, M.; Mishmash, R. V.; Higginbotham, A.; Danon, J.; Leijnse, M.; Jespersen, T. S.; Folk, J. A.; Marcus, C. M.; Flensberg, K.; Alicea, J. *Phys. Rev. X* **2016,** *6,* 031016. doi:10.1103/physrevx.6.031016
9. Landau, L. A.; Plugge, S.; Sela, E.; Altland, A.; Albrecht, S. M.; Egger, R. *Phys. Rev. Lett.* **2016,** *116,* 050501. doi:10.1103/physrevlett.116.050501
10. Plugge, S.; Landau, L. A.; Sela, E.; Altland, A.; Flensberg, K.; Egger, R. *Phys. Rev. B* **2016,** *94,* 174514. doi:10.1103/physrevb.94.174514
11. Plugge, S.; Rasmussen, A.; Egger, R.; Flensberg, K. *New J. Phys.* **2017,** *19,* 012001. doi:10.1088/1367-2630/aa54e1
12. Aguado, R. *Riv. Nuovo Cimento Soc. Ital. Fis.* **2017,** *40,* 523. doi:10.1393/ncr/i2017-10141-9
13. Mourik, V.; Zuo, K.; Frolov, S. M.; Plissard, S. R.; Bakkers, E. P. A. M.; Kouwenhoven, L. P. *Science* **2012,** *336,* 1003. doi:10.1126/science.1222360
14. Das, A.; Ronen, Y.; Most, Y.; Oreg, Y.; Heiblum, M.; Shtrikman, H. *Nat. Phys.* **2012,** *8,* 887. doi:10.1038/nphys2479
15. Albrecht, S. M.; Higginbotham, A. P.; Madsen, M.; Kuemmeth, F.; Jespersen, T. S.; Nygård, J.; Krogstrup, P.; Marcus, C. M. *Nature* **2016,** *531,* 206. doi:10.1038/nature17162
16. Deng, M. T.; Vaitiekenas, S.; Hansen, E. B.; Danon, J.; Leijnse, M.; Flensberg, K.; Nygård, J.; Krogstrup, P.; Marcus, C. M. *Science* **2016,** *354,* 1557. doi:10.1126/science.aaf3961
17. Gül, Ö.; Zhang, H.; de Vries, F. K.; van Veen, J.; Zuo, K.; Mourik, V.; Conesa-Boj, S.; Nowak, M. P.; van Woerkom, D. J.; Quintero-Pérez, M.; Cassidy, M. C.; Geresdi, A.; Koelling, S.; Car, D.; Plissard, S. R.; Bakkers, E. P. A. M.; Kouwenhoven, L. P. *Nano Lett.* **2017,** *17,* 2690. doi:10.1021/acs.nanolett.7b00540
18. Albrecht, S. M.; Hansen, E. B.; Higginbotham, A. P.; Kuemmeth, F.; Jespersen, T. S.; Nygård, J.; Krogstrup, P.; Danon, J.; Flensberg, K.; Marcus, C. M. *Phys. Rev. Lett.* **2017,** *118,* 137701. doi:10.1103/physrevlett.118.137701
19. Zhang, H.; Gül, Ö.; Conesa-Boj, S.; Nowak, M. P.; Wimmer, M.; Zuo, K.; Mourik, V.; de Vries, F. K.; van Veen, J.; de Moor, M. W. A.; Bommer, J. D. S.; van Woerkom, D.; Car, D.; Plissard, S. R.; Bakkers, E. P. A. M.; Quintero-Pérez, M.; Cassidy, M. C.; Koelling, S.; Goswami, S.; Watanabe, K.; Taniguchi, T.; Kouwenhoven, L. P. *Nat. Commun.* **2017,** *8,* 16025. doi:10.1038/ncomms16025
20. Nichele, F.; Drachmann, A. C. C.; Whiticar, A. M.; O'Farrell, E. C. T.; Suominen, H. J.; Fornieri, A.; Wang, T.; Gardner, G. C.; Thomas, C.; Hatke, A. T.; Krogstrup, P.; Manfra, M. J.; Flensberg, K.; Marcus, C. M. *Phys. Rev. Lett.* **2017,** *119,* 136803. doi:10.1103/physrevlett.119.136803
21. Suominen, H. J.; Kjaergaard, M.; Hamilton, A. R.; Shabani, J.; Palmstrøm, C. J.; Marcus, C. M.; Nichele, F. *Phys. Rev. Lett.* **2017,** *119,* 176805. doi:10.1103/physrevlett.119.176805
22. Gazibegovich, S.; Car, D.; Zhang, H.; Balk, S. C.; Logan, J. A.; de Moor, M. W. A.; Cassidy, M. C.; Schmits, R.; Xu, D.; Wang, G.; Krogstrup, P.; Op het Veld, R. L. M.; Shen, J.; Bouman, D.; Shojaei, B.; Pennachio, D.; Lee, J. S.; van Veldhoven, P. J.; Koelling, S.; Verheijen, M. A.; Kouwenhoven, L. P.; Palmstrøm, C. J.; Bakkers, E. P. A. M. *Nature* **2017,** *548,* 434. doi:10.1038/nature23468
23. Zhang, H.; Liu, C.-X.; Gazibegovic, S.; Xu, D.; Logan, J. A.; Wang, G.; van Loo, N.; Bommer, J. D. S.; de Moor, M. W. A.; Car, D.; Op het Veld, R. L. M.; van Veldhoven, P. J.; Koelling, S.; Verheijen, M. A.; Pendharkar, M.; Pennachio, D. J.; Shojaei, B.; Lee, J. S.; Palmstrom, C. J.; Bakkers, E. P. A. M.; Das Sarma, S.; Kouwenhoven, L. P. *Nature* **2018,** *556,* 74–79. doi:10.1038/nature26142
24. Deng, M. T.; Vaitiekénas, S.; Prada, E.; San-José, P.; Nygård, J.; Krogstrup, P.; Aguado, R.; Marcus, C. M. *arXiv* **2017,** No. 1712.03536.
25. Laroche, D.; Bouman, D.; van Woerkom, D. J.; Proutski, A.; Murthy, C.; Pikulin, D. I.; Nayak, C.; van Gulik, R. J. J.; Nygård, J.; Krogstrup, P.; Kouwenhoven, L. P.; Geresdi, A. *arXiv* **2017,** No. 1712.08459.
26. Nadj-Perge, S.; Drozdov, I. K.; Li, J.; Chen, H.; Jeon, S.; Seo, J.; MacDonald, A. H.; Bernevig, B. A.; Yazdani, A. *Science* **2014,** *346,* 602. doi:10.1126/science.1259327
27. Ruby, M.; Pientka, F.; Peng, Y.; von Oppen, F.; Heinrich, B. W.; Franke, K. J. *Phys. Rev. Lett.* **2015,** *115,* 197204. doi:10.1103/physrevlett.115.197204
28. Sun, H.-H.; Zhang, K.-W.; Hu, L.-H.; Li, C.; Wang, G.-Y.; Ma, H.-Y.; Xu, Z.-A.; Gao, C.-L.; Guan, D.-D.; Li, Y.-Y.; Liu, C.; Qian, D.; Zhou, Y.; Fu, L.; Li, S.-C.; Zhang, F.-C.; Jia, J.-F. *Phys. Rev. Lett.* **2016,** *116,* 257003. doi:10.1103/physrevlett.116.257003
29. Feldman, B. E.; Randeria, M. T.; Li, J.; Jeon, S.; Xie, Y.; Wang, Z.; Drozdov, I. K.; Andrei Bernevig, B.; Yazdani, A. *Nat. Phys.* **2017,** *13,* 286. doi:10.1038/nphys3947
30. Deacon, R. S.; Wiedenmann, J.; Bocquillon, E.; Domínguez, F.; Klapwijk, T. M.; Leubner, P.; Brüne, C.; Hankiewicz, E. M.; Tarucha, S.; Ishibashi, K.; Buhmann, H.; Molenkamp, L. W. *Phys. Rev. X* **2017,** *7,* 021011. doi:10.1103/physrevx.7.021011
31. Zazunov, A.; Egger, R. *Phys. Rev. B* **2012,** *85,* 104514. doi:10.1103/physrevb.85.104514

32. Kwon, H.-J.; Sengupta, K.; Yakovenko, V. M. *Eur. Phys. J. B* **2004,** *37,* 349. doi:10.1140/epjb/e2004-00066-4
33. Bratus, E. N.; Shumeiko, V. S.; Wendin, G. *Phys. Rev. Lett.* **1995,** *74,* 2110. doi:10.1103/physrevlett.74.2110
34. Averin, D.; Bardas, A. *Phys. Rev. Lett.* **1995,** *75,* 1831. doi:10.1103/physrevlett.75.1831
35. Cuevas, J. C.; Martín-Rodero, A.; Levy Yeyati, A. *Phys. Rev. B* **1996,** *54,* 7366. doi:10.1103/physrevb.54.7366
36. Nazarov, Y.; Blanter, Y. *Quantum Transport: Introduction to Nanoscience;* Cambridge University Press: Cambridge, United Kingdom, 2010.
37. Peng, Y.; Pientka, F.; Vinkler-Aviv, Y.; Glazman, L. I.; von Oppen, F. *Phys. Rev. Lett.* **2015,** *115,* 266804. doi:10.1103/physrevlett.115.266804
38. Ioselevich, P. A.; Ostrovsky, P. M.; Feigel'man, M. V. *Phys. Rev. B* **2016,** *93,* 125435. doi:10.1103/physrevb.93.125435
39. Sharma, G.; Tewari, S. *Phys. Rev. B* **2016,** *93,* 195161. doi:10.1103/physrevb.93.195161
40. Zazunov, A.; Egger, R.; Levy Yeyati, A. *Phys. Rev. B* **2016,** *94,* 014502. doi:10.1103/physrevb.94.014502
41. Setiawan, F.; Cole, W. S.; Sau, J. D.; Das Sarma, S. *Phys. Rev. B* **2017,** *95,* 174515. doi:10.1103/PhysRevB.95.174515
42. Setiawan, F.; Cole, W. S.; Sau, J. D.; Das Sarma, S. *Phys. Rev. B* **2017,** *95,* 020501. doi:10.1103/physrevb.95.020501
43. Zazunov, A.; Egger, R.; Alvarado, M.; Levy Yeyati, A. *Phys. Rev. B* **2017,** *96,* 024516. doi:10.1103/physrevb.96.024516
44. Deb, O.; Sengupta, K.; Sen, D. *arXiv* **2017,** No. 1712.03726.
45. Buzdin, A. *Phys. Rev. Lett.* **2008,** *101,* 107005. doi:10.1103/physrevlett.101.107005
46. Zazunov, A.; Egger, R.; Jonckheere, T.; Martin, T. *Phys. Rev. Lett.* **2009,** *103,* 147004. doi:10.1103/physrevlett.103.147004
47. Schrade, C.; Hoffman, S.; Loss, D. *Phys. Rev. B* **2017,** *95,* 195421. doi:10.1103/physrevb.95.195421
48. Yokoyama, T.; Eto, M.; Nazarov, Y. V. *Phys. Rev. B* **2014,** *89,* 195407. doi:10.1103/physrevb.89.195407
49. Camjayi, A.; Arrachea, L.; Aligia, A.; von Oppen, F. *Phys. Rev. Lett.* **2017,** *119,* 046801. doi:10.1103/physrevlett.119.046801
50. Cayao, J.; San-José, P.; Black-Schaffer, A. M.; Aguado, R.; Prada, E. *Phys. Rev. B* **2017,** *96,* 205425. doi:10.1103/physrevb.96.205425
51. Cayao, J.; San-José, P.; Black-Schaffer, A. M.; Prada, E.; Aguado, R. *arXiv* **2017,** No. 1712.08127.
52. Bretheau, L.; Girit, Ç. Ö.; Pothier, H.; Esteve, D.; Urbina, C. *Nature* **2013,** *499,* 312. doi:10.1038/nature12315
53. Bretheau, L.; Girit, Ç. Ö.; Urbina, C.; Esteve, D.; Pothier, H. *Phys. Rev. X* **2013,** *3,* 041034. doi:10.1103/physrevx.3.041034
54. Janvier, C.; Tosi, L.; Bretheau, L.; Girit, Ç. Ö.; Stern, M.; Bertet, P.; Joyez, P.; Vion, D.; Esteve, D.; Goffman, M. F.; Pothier, H.; Urbina, C. *Science* **2015,** *349,* 1199. doi:10.1126/science.aab2179
55. Tarasinski, B.; Chevallier, D.; Hutasoit, J. A.; Baxevanis, B.; Beenakker, C. W. J. *Phys. Rev. B* **2015,** *92,* 144306. doi:10.1103/physrevb.92.144306
56. Glazman, L. I.; Matveev, K. A. *JETP Lett.* **1989,** *49,* 659.
57. Rozhkov, A. V.; Arovas, D. P. *Phys. Rev. Lett.* **1999,** *82,* 2788. doi:10.1103/physrevlett.82.2788
58. Vecino, E.; Martín-Rodero, A.; Levy Yeyati, A. *Phys. Rev. B* **2003,** *68,* 035105. doi:10.1103/physrevb.68.035105
59. Siano, F.; Egger, R. *Phys. Rev. Lett.* **2004,** *93,* 047002. doi:10.1103/physrevlett.93.047002
60. Choi, M.-S.; Lee, M.; Kang, K.; Belzig, W. *Phys. Rev. B* **2004,** *70,* 020502. doi:10.1103/physrevb.70.020502
61. Karrasch, C.; Oguri, A.; Meden, V. *Phys. Rev. B* **2008,** *77,* 024517. doi:10.1103/physrevb.77.024517
62. Martín-Rodero, A.; Levi Yeyati, A. *Adv. Phys.* **2011,** *60,* 899. doi:10.1080/00018732.2011.624266
63. Luitz, D. J.; Assaad, F. F.; Novotný, T.; Karrasch, C.; Meden, V. *Phys. Rev. Lett.* **2012,** *108,* 227001. doi:10.1103/physrevlett.108.227001
64. Kasumov, A. Yu.; Deblock, R.; Kociak, M.; Reulet, B.; Bouchiat, H.; Khodos, I. I.; Gorbatov, Yu. B.; Volkov, V. T.; Journet, C.; Burghard, M. *Science* **1999,** *284,* 1508. doi:10.1126/science.284.5419.1508
65. van Dam, J. A.; Nazarov, Y. V.; Bakkers, E. P. A. M.; De Franceschi, S.; Kouwenhoven, L. P. *Nature* **2006,** *442,* 667. doi:10.1038/nature05018
66. Cleuziou, J.-P.; Wernsdorfer, W.; Bouchiat, V.; Ondarçuhu, T.; Monthioux, M. *Nat. Nanotechnol.* **2006,** *1,* 53. doi:10.1038/nnano.2006.54
67. Ingerslev Jørgensen, H.; Novotný, T.; Grove-Rasmussen, K.; Flensberg, K.; Lindelof, P. E. *Nano Lett.* **2007,** *7,* 2441. doi:10.1021/nl071152w
68. Eichler, A.; Deblock, R.; Weiss, M.; Karrasch, C.; Meden, V.; Schönenberger, C.; Bouchiat, H. *Phys. Rev. B* **2009,** *79,* 161407. doi:10.1103/physrevb.79.161407
69. Delagrange, R.; Luitz, D. J.; Weil, R.; Kasumov, A.; Meden, V.; Bouchiat, H.; Deblock, R. *Phys. Rev. B* **2015,** *91,* 241401. doi:10.1103/physrevb.91.241401
70. Zazunov, A.; Levy Yeyati, A.; Egger, R. *Phys. Rev. B* **2011,** *84,* 165440. doi:10.1103/physrevb.84.165440
71. Peng, Y.; Bao, Y.; von Oppen, F. *Phys. Rev. B* **2017,** *95,* 235143. doi:10.1103/physrevb.95.235143
72. Brunetti, A.; Zazunov, A.; Kundu, A.; Egger, R. *Phys. Rev. B* **2013,** *88,* 144515. doi:10.1103/physrevb.88.144515
73. Szombati, D. B.; Nadj-Perge, S.; Car, D.; Plissard, S. R.; Bakkers, E. P. A. M.; Kouwenhoven, L. P. *Nat. Phys.* **2016,** *12,* 568. doi:10.1038/nphys3742
74. Leijnse, M.; Flensberg, K. *Phys. Rev. Lett.* **2011,** *107,* 210502. doi:10.1103/physrevlett.107.210502
75. Sticlet, D.; Bena, C.; Simon, P. *Phys. Rev. Lett.* **2012,** *108,* 096802. doi:10.1103/physrevlett.108.096802
76. Prada, E.; San-Jose, P.; Aguado, R. *Phys. Rev. B* **2012,** *86,* 180503. doi:10.1103/physrevb.86.180503
77. Prada, E.; Aguado, R.; San-Jose, P. *Phys. Rev. B* **2017,** *96,* 085418. doi:10.1103/physrevb.96.085418
78. Hoffman, S.; Chevallier, D.; Loss, D.; Klinovaja, J. *Phys. Rev. B* **2017,** *96,* 045440. doi:10.1103/physrevb.96.045440
79. Martin-Rodero, A.; Levy Yeyati, A. *J. Phys.: Condens. Matter* **2012,** *24,* 385303. doi:10.1088/0953-8984/24/38/385303
80. Balatsky, A. V.; Vekhter, I.; Zhu, J.-X. *Rev. Mod. Phys.* **2006,** *78,* 373. doi:10.1103/revmodphys.78.373
81. Zazunov, A.; Shumeiko, V. S.; Bratus', E. N.; Lantz, J.; Wendin, G. *Phys. Rev. Lett.* **2003,** *90,* 087003. doi:10.1103/physrevlett.90.087003

BEILSTEIN JOURNAL OF NANOTECHNOLOGY

A zero-dimensional topologically nontrivial state in a superconducting quantum dot

Pasquale Marra*[1], Alessandro Braggio[2] and Roberta Citro[3]

Full Research Paper

Open Access

Address:
[1]RIKEN Center for Emergent Matter Science, Wakoshi, Saitama 351-0198, Japan, [2]NEST, Istituto Nanoscienze CNR and Scuola Normale Superiore, Piazza San Silvestro 12, 56127 Pisa, Italy and [3]Dipartimento di Fisica "E. R. Caianiello", Università di Salerno and CNR-SPIN, 84084 Fisciano (Salerno), Italy

Email:
Pasquale Marra* - pasquale.marra@riken.jp

* Corresponding author

Keywords:
Josephson effect; Josephson junctions; quantum dots; superconducting quantum dots; topological states; topological superconductors

Beilstein J. Nanotechnol. **2018,** *9,* 1705–1714.
doi:10.3762/bjnano.9.162

Received: 14 February 2018
Accepted: 09 May 2018
Published: 08 June 2018

This article is part of the Thematic Series "Topological materials".

Guest Editor: J. J. Palacios

Abstract

The classification of topological states of matter in terms of unitary symmetries and dimensionality predicts the existence of nontrivial topological states even in zero-dimensional systems, i.e., systems with a discrete energy spectrum. Here, we show that a quantum dot coupled with two superconducting leads can realize a nontrivial zero-dimensional topological superconductor with broken time-reversal symmetry, which corresponds to the finite size limit of the one-dimensional topological superconductor. Topological phase transitions corresponds to a change of the fermion parity, and to the presence of zero-energy modes and discontinuities in the current–phase relation at zero temperature. These fermion parity transitions therefore can be revealed by the current discontinuities or by a measure of the critical current at low temperatures.

Introduction

Since the discovery of the quantum Hall effect [1,2] and the theoretical prediction of Majorana bound states in triplet superconductors [3], a whole new class of novel electronic phases has been theoretically described and experimentally realized, namely, the class of topologically nontrivial states of matter [4-7]. Topological states of matter can be classified in terms of the antiunitary symmetries and dimensionality of the Hamiltonian [7-10]. Analogously to the periodic table of chemical elements in chemistry, this classification has been a general guide to the discovery of novel topological phases in solid-state physics. Moreover, it predicts the existence of nontrivial topological states even in zero dimensions, i.e., in a system with discrete energy spectrum.

A very important class of topological states of matter are topological superconductors: These materials support Majorana

zero-energy modes at the edges of the system [11-13], which have been proposed as the building block of topological quantum devices [14-20]. The simplest realization of a topological superconductor is the well-known Kitaev chain [3], which can be implemented in a one-dimensional system proximized by a conventional superconductor in the presence of a magnetic field and spin–orbit coupling [21-25]. Moreover, topological superconductors exhibit very distinct features in their transport properties and in particular in their Josephson current [26-49].

In a recent work [50], we have studied the short-size limit of a one-dimensional (1D) topological superconductor with broken time-reversal and chiral symmetries. In this limit, the system turns zero-dimensional (0D), i.e., its energy spectrum is a finite set of discrete energy levels. This 0D superconductor exhibits topological phase transitions that correspond to variations of the fermion parity and to the occurrence of zero-energy modes that are a linear combination of particle and hole states [50]. These fermion parity transitions can be revealed by discontinuities in the Josephson current–phase relation (CPR) in the zero-temperature limit.

Here we describe the simplest realization of such a 0D topological superconductor, i.e., a quantum dot [51-54] coupled with two superconducting leads in a magnetic Zeeman field, forming a superconductor–quantum dot–superconductor (SC–QD–SC) Josephson junction. Zero-energy modes and the corresponding CPR discontinuities and ground-state parity crossings [55-61] have been recognized as precursors of Majorana modes in the long-wire limit [27,50], and of Floquet–Majorana modes realized in driven quantum dots [62,63]. We will analytically derive and discuss the spectrum and the Josephson current of the dot, which agrees with the universal prediction for zero-dimensional systems described in our previous work [50]. This allows us to reinterpret in terms of topological states the different regimes of the dot, which are already discussed in the literature [34,64-68]. We will analyze in detail the relation between the topological properties of the groundstate, the zero-energy modes, and the corresponding CPR discontinuities. We will show that, in this system, a topologically nontrivial state can be induced by a finite Zeeman field that breaks the time-reversal symmetry, even without a finite spin–orbit coupling. The resulting topological transitions coincide with a change of the fermion parity (topological invariant) and can be identified by discontinuities in the CPR and by a measure of the critical current at low temperatures.

Results and Discussion

Effective model

We consider a semiconducting quantum dot in a magnetic field B and coupled with two superconducting leads, as shown in Figure 1. We assume that the only effect of the magnetic field is the lifting of the spin degeneracy via the Zeeman effect, and we neglect orbital effects of the field. Moreover, we assume that the level spacing of the dot is larger than the Zeeman energy B and larger than the Coulomb interaction U within the dot. Therefore we neglect the contribution of higher energy levels and take into account only the levels $\varepsilon \pm B$ of the Kramers doublet closest to the Fermi energy. Here, ε is the energy level of the dot in absence of Zeeman field, which can be modified by controlling the gate voltage. This system can be described by a superconducting Anderson impurity model

$$H = H_{\mathrm{QD}} + \sum_{i=L,R} H_i + H_{t_i}, \tag{1}$$

where the dot Hamiltonian is given by

$$H_{\mathrm{QD}} = \varepsilon \begin{bmatrix} d_\uparrow^\dagger & d_\downarrow^\dagger \end{bmatrix} \cdot \begin{bmatrix} d_\uparrow \\ d_\downarrow \end{bmatrix} + B \begin{bmatrix} d_\uparrow^\dagger & d_\downarrow^\dagger \end{bmatrix} \cdot \sigma_z \cdot \begin{bmatrix} d_\uparrow \\ d_\downarrow \end{bmatrix} + U\left(n_\uparrow - \frac{1}{2}\right)\left(n_\downarrow - \frac{1}{2}\right), \tag{2}$$

where $d_\uparrow^\dagger, d_\downarrow^\dagger$ and $d_\uparrow$, $d_\downarrow$ are the creation and annihilation operators of the electrons in the dot, $n_\uparrow = d_\uparrow^\dagger d_\uparrow$ and $n_\downarrow = d_\downarrow^\dagger d_\downarrow$ the number operators, $\varepsilon \pm B$ the two-energy levels of the dot, and U the onsite Coulomb repulsion. We assume hereafter that $e = \hbar = 1$.

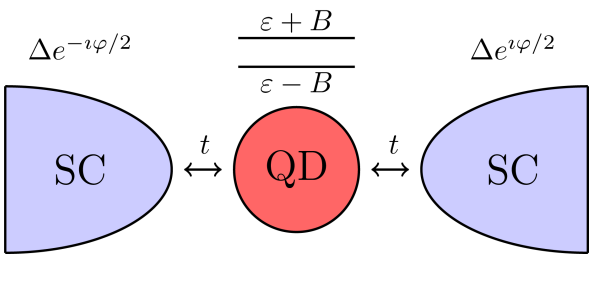

Figure 1: An SC–QD–SC Josephson junction realized by a two-level quantum dot in a magnetic field B and electric gate ε coupled with two superconducting leads. The two energy levels are respectively $\varepsilon \pm B$. The dot is coupled to the superconducting leads via tunneling junctions with transparency t. The Josephson current I_φ through the dot depends on the gauge-invariant phase difference φ between the two superconducting leads.

The Hamiltonians of the two superconducting leads $i = L, R$ are given by

$$H_i = \sum_{\mathbf{k}} \varepsilon_{\mathbf{k}} \begin{bmatrix} c^{\dagger}_{\mathbf{k},i,\uparrow} & c^{\dagger}_{\mathbf{k},i,\downarrow} \end{bmatrix} \cdot \begin{bmatrix} c_{\mathbf{k},i,\uparrow} \\ c_{\mathbf{k},i,\downarrow} \end{bmatrix} + \left(\frac{1}{2} \Delta e^{\imath\varphi_i} \begin{bmatrix} c^{\dagger}_{\mathbf{k},i,\uparrow} & c^{\dagger}_{\mathbf{k},i,\downarrow} \end{bmatrix} \cdot \left(\imath\sigma_y\right) \cdot \begin{bmatrix} c^{\dagger}_{-\mathbf{k},i,\uparrow} \\ c^{\dagger}_{-\mathbf{k},i,\downarrow} \end{bmatrix} + \text{h.c.} \right), \quad (3)$$

where $c^{\dagger}_{\mathbf{k},i,\uparrow}$, $c^{\dagger}_{\mathbf{k},i,\downarrow}$ and $c_{\mathbf{k},i,\uparrow}$,$c_{\mathbf{k},i,\downarrow}$ are the creation and annihilation operators of electrons in the superconducting lead $i = L, R$ and with momentum $\mathbf{k}$, $\varepsilon_{\mathbf{k}}$ is the bare electron dispersion with respect to the Fermi level $\varepsilon_F = 0$, Δ the magnitude of the superconducting gap, and φ_i the phase of the superconducting gap in the two leads, respectively. Here we assumed a standard BCS *s*-wave pairing and the same bare electron dispersion in the two superconducting leads. In the following we furthermore assume that the bare electron dispersion varies in the interval $[-D,D]$ and that the density of states is $\rho_0 = 1/(2D)$ with $2D$ the total bandwidth.

The tunneling between the dot and the leads is described by the tunnel Hamiltonians, which read

$$H_{t_i} = t \sum_{\mathbf{k}} \begin{bmatrix} c^{\dagger}_{\mathbf{k},i,\uparrow} & c^{\dagger}_{\mathbf{k},i,\downarrow} \end{bmatrix} \cdot \begin{bmatrix} d_{\uparrow} \\ d_{\downarrow} \end{bmatrix} + \text{h.c.}, \quad (4)$$

where $t = t_L = t_R$ is the transparency of the dot–lead tunneling. We assume that the junction is symmetric and that the tunneling amplitudes do not depend on the electron momenta (wide band limit approximation).

In the limit of a large superconducting gap, i.e., when the gap is larger than the characteristic frequencies of the quantum dot, the degrees of freedom of the leads can be effectively integrated out [34,64-68]. In absence of interactions ($U = 0$) the system can be described by an effective Hamiltonian that reads [34,64,65,67,68]

$$H_{\text{eff}} = \begin{bmatrix} d^{\dagger}_{\uparrow} & d^{\dagger}_{\downarrow} \end{bmatrix} \cdot \left(\varepsilon + B\sigma_z\right) \cdot \begin{bmatrix} d_{\uparrow} \\ d_{\downarrow} \end{bmatrix} + \Gamma\cos\left(\varphi/2\right) \begin{bmatrix} d^{\dagger}_{\uparrow} & d^{\dagger}_{\downarrow} \end{bmatrix} \cdot \left(\imath\sigma_y\right) \cdot \begin{bmatrix} d^{\dagger}_{\uparrow} \\ d^{\dagger}_{\downarrow} \end{bmatrix} + \text{h.c.}, \quad (5)$$

where $\varphi = \varphi_R - \varphi_L$ is the gauge-invariant phase difference between the two leads, and where

$$\Gamma = 4t^2\rho_0 \arctan\left(\frac{D}{\Delta}\right) \quad (6)$$

is the effective local superconducting pairing induced by the leads on the dot [64,65]. The Hamiltonian (Equation 5) can be written in the Bogoliubov–de Gennes formalism as

$$H_{\text{eff}} = \Psi^{\dagger} \cdot \begin{bmatrix} \varepsilon + B\sigma_z & \Gamma\cos\left(\varphi/2\right)\imath\sigma_y \\ -\Gamma\cos\left(\varphi/2\right)\imath\sigma_y & -\varepsilon - B\sigma_z \end{bmatrix} \cdot \Psi, \quad (7)$$

where $\Psi^{\dagger} = [d^{\dagger}_{\uparrow}, d^{\dagger}_{\downarrow}, d_{\uparrow}, d_{\downarrow}]$ and $\Psi = [d_{\uparrow}, d_{\downarrow}, d^{\dagger}_{\uparrow}, d^{\dagger}_{\downarrow}]^{\mathsf{T}}$ are the Nambu spinors describing the electron–hole pairs in the dot. Notice that our definition of Nambu spinor differs from [64,65], but it will allow us to define the topological invariant using the same formalism used in 1D superconductors.

The spectrum of this effective Hamiltonian is a set of four single-particle states corresponding to two pairs of particle–hole symmetric Andreev levels $\pm E_{\uparrow}$ and $\pm E_{\downarrow}$ with

$$E_{\uparrow} = E_{\varphi} + B, \quad (8)$$

$$E_{\downarrow} = E_{\varphi} - B, \quad (9)$$

with

$$E_{\varphi} = \sqrt{\varepsilon^2 + \Gamma^2\cos^2\left(\varphi/2\right)},$$

which correspond to the eigenstates described by the operators $\bar{d}^{\dagger}_{\uparrow\downarrow}$ defined by the Bogoliubov transformation

$$\bar{d}^{\dagger}_{\uparrow} = u d^{\dagger}_{\uparrow} + v d_{\downarrow}, \quad (10)$$

$$\bar{d}^{\dagger}_{\downarrow} = u d^{\dagger}_{\downarrow} - v d_{\uparrow}, \quad (11)$$

where

$$u = \sqrt{\left(1 + \varepsilon/E_{\varphi}\right)/2}, \quad (12)$$

$$v = \sqrt{\left(1 - \varepsilon/E_{\varphi}\right)/2}, \quad (13)$$

The Bogoliubov factors satisfy the properties $u^2 + v^2 = 1$, $u^2 - v^2 = \varepsilon/E_{\varphi}$, and $uv = \Gamma|\cos(\varphi/2)|/(2E_{\varphi})$.

Now we generalize the Hamiltonian (Equation 7) to the case of finite interaction $U > 0$. A tedious but elementary calculation gives $(n_\uparrow - 1/2)(n_\downarrow - 1/2) = (\bar{n}_\uparrow - 1/2)(\bar{n}_\downarrow - 1/2)$ where $\bar{n}_\uparrow = \bar{d}_\uparrow^\dagger \bar{d}_\uparrow$ and $\bar{n}_\downarrow = \bar{d}_\downarrow^\dagger \bar{d}_\downarrow$ are the number operators corresponding to the eigenstates of the effective Hamiltonian. Therefore the Hamiltonian in the presence of Coulomb interaction $U > 0$ can be written in diagonal form as

$$\bar{H}_{\text{eff}} = \left(E_\varphi - \frac{U}{2}\right)\left(\bar{n}_\uparrow + \bar{n}_\downarrow\right) + B\left(\bar{n}_\uparrow - \bar{n}_\downarrow\right) + U\,\bar{n}_\uparrow \bar{n}_\downarrow, \quad (14)$$

up to a numerical phase-independent constant.

The Hamiltonian eigenstates comprise the vacuum $|00\rangle$, the two single-particle states $|01\rangle$ and $|10\rangle$, and the two-particle state $|11\rangle$ with energies

$$\bar{E}_0 = 0, \quad (15)$$

$$\bar{E}_\downarrow = E_\varphi - U/2 - B, \quad (16)$$

$$\bar{E}_\uparrow = E_\varphi - U/2 + B, \quad (17)$$

$$\bar{E}_{\uparrow\downarrow} = 2E_\varphi. \quad (18)$$

Each of these particle states corresponds to a hole state by particle–hole symmetry. The groundstate energy of the superconducting condensate is given by the sum of the single-particle energy levels [69], which yield in this case

$$E_{\text{GS}}(\varphi) = \left|E_\varphi - U/2 - B\right| + \left|E_\varphi - U/2 + B\right|, \quad (19)$$

whereas the Josephson current at zero temperature is defined as $I_\varphi = -\partial_\varphi E_{\text{GS}}(\varphi)$. Notice that for small couplings $U/2 < |\varepsilon|, |\Gamma|$, the only effect of the interaction is to shift the energy of the single-particle levels. For this reason, if the conductance from the dot to the superconductor is relatively large (high dot–lead transparency) and one can consider the effect of interactions as a small perturbation. Therefore, the ground-state properties, such as the topological invariant and the Josephson current at zero temperature, are not affected in the case where $U/2 < \varepsilon$ and $U/2 < \Gamma$, as long as the particle–hole gap remains open and the Andreev levels do not cross.

In absence of interactions $U = 0$, the only possible ground states are those with energies

$$E_{\text{GS}}(\varphi) = \begin{cases} 2E_\varphi & \text{for } E_\uparrow E_\downarrow > 0, \\ 2B & \text{for } E_\uparrow E_\downarrow < 0, \end{cases} \quad (20)$$

which correspond, respectively, to the cases where the two single-particle levels $E_\uparrow$ and $E_\downarrow$ have the same sign or opposite sign. We will show that the ground state with energy $2E_\varphi$ is topologically trivial and has a finite Josephson current, whereas the ground state with energy $2B$ is topologically nontrivial and has a Josephson current that vanishes at zero temperature.

The phase diagram of this system has been already discussed in the literature [34,64-68]. Since we consider here only the weak interacting case, we will not discuss the 0–π transition driven by the presence of strong interaction. A more thorough discussion of the role of interactions on the 0D topological transition and on the ensuing π-phase will be addressed in a following research paper. Therefore, we will discuss hereafter only quantum phase transition in the regime of weak interactions in systems which can be described by Equation 7 or Equation 14 for $U = 0$. Our findings cannot be applied to 0–π transitions and to other kinds of quantum phase transitions that may be eventually present in this system, beyond the topological one we discussed.

The particle–hole gap and gapless points

The particle–hole gap, i.e., the difference between the particle and hole levels closest to the Fermi level, closes if $|B| = E_\varphi$. If one defines the two threshold fields $B_{\text{min}} = |\varepsilon|$ and $B_{\text{max}} = \sqrt{\varepsilon^2 + \Gamma^2}$, one can verify that the spectrum is gapped for both small $|B| < B_{\text{min}}$ and large $|B| > B_{\text{max}}$ Zeeman fields. For intermediate fields $B_{\text{min}} < |B| < B_{\text{max}}$, the energy gap closes at specific values of the gauge-invariant phase $\varphi = \pm\varphi^*$ where

$$\varphi^* = \arccos(-\lambda) \quad \text{with } \lambda = 1 + \frac{2\left(\varepsilon^2 - B^2\right)}{\Gamma^2}, \quad (21)$$

where $|\lambda| < 1$ if $B_{\text{min}} < |B| < B_{\text{max}}$. We will show that these gapless points define a topological phase transition in the system that corresponds to the appearance of discontinuous drops in the CPR of the junction.

Figure 2 shows the single-particle energy spectrum of the system, i.e., the four particle–hole symmetric Andreev levels $\pm E_\downarrow$ and $\pm E_\uparrow$, as a function of the gauge-invariant phase differ-

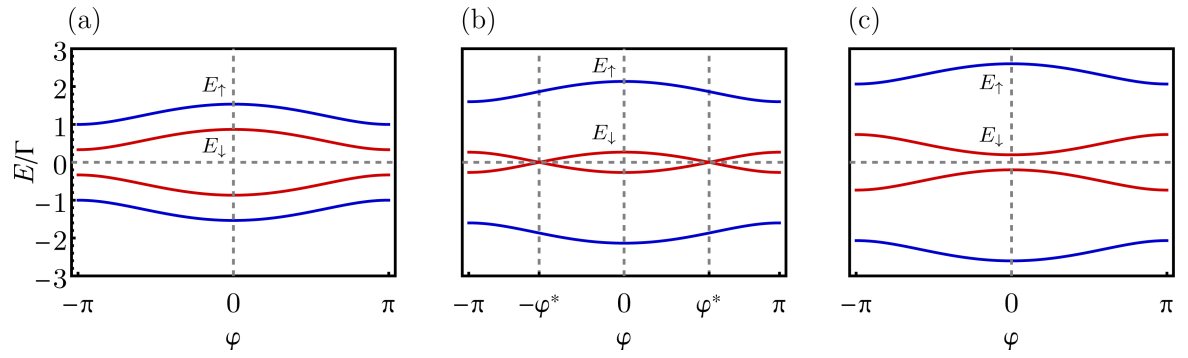

Figure 2: Energy spectrum of a two-level quantum dot coupled with two superconducting leads (SC–QD–SC junction), consisting of a set of four Andreev levels, i.e., two single-particle levels $\pm E_\uparrow$ (blue curves) and $\pm E_\downarrow$ (red curves), as a function of the gauge-invariant phase difference φ between the two superconducting leads. We take $\varepsilon = 2\Gamma/3$ and $U = 0$. The three panels correspond to different values of the Zeeman field: (a) small fields $|B| < B_{\min}$, (b) intermediate fields $B_{\min} < |B| < B_{\max}$, with the particle–hole gap closing at the gapless points $\pm\varphi^*$ (see Equation 21), and (c) large fields $|B| > B_{\max}$.

ence φ. As one can see, the energy spectrum is gapped for small $|B| < B_{\min}$ and large $|B| > B_{\max}$ Zeeman fields, respectively, independently from the phase difference φ. At intermediate fields $B_{\min} < |B| < B_{\max}$, the particle–hole gap closes at the gapless points $\pm\varphi^*$ that satisfy Equation 21. One can verify that the effect of a small Coulomb interaction $U/2 < |\varepsilon|, |\Gamma|$ is a shift of the threshold fields $B_{\min}$ and $B_{\max}$ and of the value of the phases $\pm\varphi^*$ where the gap closes.

Topological invariant

This simple 0D two-level system can realize a topologically nontrivial state that breaks time-reversal symmetry while preserving particle–hole symmetry. This topologically nontrivial state can be seen as the 0D limit of a 1D topological superconductor, and as the minimal model for the system described in [50]. In fact, for finite Zeeman energies ($B \neq 0$) and superconducting pairing ($\Gamma > 0$), the system is in the Altland–Zirnbauer [7-10] symmetry class D (particle–hole symmetry, broken time-reversal and chiral symmetries). This class is characterized in 0D by a $\mathbb{Z}_2$ topological invariant that is defined in the non-interacting case $U = 0$ as the fermion parity of the ground state [50,70] $P = \mathrm{sgn}\,\mathrm{pf}(H_{\mathrm{eff}}\imath\tau_x)$, i.e., as the sign of the Pfaffian of the Hamiltonian in Majorana representation (τ_x is the first Pauli matrix in the particle–hole space). The fermion parity labels the topological inequivalent ground states as a function of the gauge-invariant phase φ, i.e., the trivial state $P = 1$ (even parity) and nontrivial state $P = -1$ (odd parity). The fermion parity of the 0D topological quantum dot described by Hamiltonian (Equation 7) can be evaluated analytically. The square of the Pfaffian of a matrix is equal to the determinant, which is equal to the product of its eigenvalues, and therefore one has $\mathrm{pf}(H_{\mathrm{eff}}\imath\tau_x)^2 = \det(H_{\mathrm{eff}}\imath\tau_x) = \det(H_{\mathrm{eff}}) = E_\uparrow^2 E_\downarrow^2$ due to particle–hole symmetry. A direct calculation of the Pfaffian indeed shows that $\mathrm{pf}(H_{\mathrm{eff}}\imath\tau_x) = E_\uparrow E_\downarrow$ and therefore

$$P_\varphi = \mathrm{sgn}\left(E_\uparrow E_\downarrow\right) = \mathrm{sgn}\left(E_\varphi^2 - B^2\right) = \mathrm{sgn}\left(\lambda + \cos\varphi\right), \quad (22)$$

where we used the definition of λ given in Equation 21. This equation is a special case of Equation 2 of [50]. Notice that if $B = 0$ the time-reversal symmetry is unbroken and the ground state is trivial $P_\varphi = \mathrm{sgn}(E_\varphi^2) = 1$ as expected. As anticipated, the ground state with energy $2E_\varphi$ is topologically trivial, since in this case $E_\uparrow E_\downarrow > 0$, whereas the ground state with energy $2B$ is topologically nontrivial, since in this case one has $E_\uparrow E_\downarrow < 0$. Therefore, the inversion of the lowest-energy Andreev level corresponds to a topological transition to the nontrivial state. The fermion parity defines the topological phase space of the system, and is completely determined by the gauge-invariant phase φ and by the adimensional quantity λ, as shown in Figure 3. Moreover, since $P = \mathrm{sgn}[E_\uparrow E_\downarrow]$, the condition $P_\varphi \equiv 0$ corresponds to the gapless points $\varphi = \pm\varphi^*$ where zero-energy modes occur (solid line in Figure 3).

At small Zeeman fields $|B| < B_{\min}$ (i.e., $\lambda > 1$), the system is in the topologically trivial state with even fermion parity $P = 1$ for any value of the phase φ. At large fields $|B| > B_{\max}$ instead (i.e., $\lambda < -1$), the system realizes the topologically nontrivial state with odd fermion parity $P = -1$ for any value of the phase φ. However, for intermediate $B_{\min} < |B| < B_{\max}$ (i.e., $|\lambda| < 1$) topological transitions occur at the gapless points $\pm\varphi^*$ (see Equation 21). In this case the system realizes the trivial or in the nontrivial state (even or odd parity), respectively, for $|\varphi| < \varphi^*$ and $|\varphi| > \varphi^*$ in the interval $\varphi \in [-\pi, \pi]$, as one can see in Figure 3. The two gapless points $\pm\varphi^*$ therefore correspond to a quantum phase transition where the fermion parity of the ground state changes from trivial to nontrivial. Note that for $|B| = B_{\min}$ and for $|B| = B_{\max}$ (i.e., $|\lambda| = 1$) no topological transition occurs, and the system is, respectively, in the trivial or

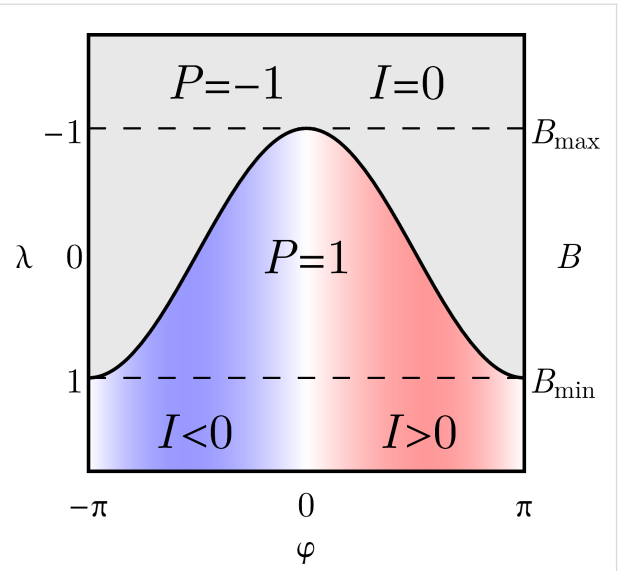

Figure 3: Topological phase space of a 0D topological superconductor realized by a quantum dot coupled with two superconducting leads (SC–QD–SC junction). The system realizes, respectively, a trivial state $P = 1$ for small Zeeman fields $|B| < B_{min}$ (i.e., $\lambda > 1$), and a nontrivial state $P = -1$ for large fields $|B| > B_{max}$ (i.e., $\lambda < -1$). The Josephson current vanishes in the nontrivial state. Topological transitions coincides with the occurrence of zero-energy modes at $\pm\varphi^* = \pm\arccos(-\lambda)$ (solid line) for intermediate fields $B_{min} < |B| < B_{max}$ (i.e., $|\lambda| < 1$). In this case the system is in its trivial $P = 1$ and nontrivial $P = -1$ state respectively for $|\varphi| \lesseqgtr \varphi^*$ within the interval $\varphi \in [-\pi, \pi]$.

nontrivial gapped state with the exceptions of the single gapless point $\varphi^* = \pi$ or $\varphi^* = 0$, respectively.

The particle–hole gap can also close in absence of a Zeeman field if $\varepsilon = 0$. For $B = \varepsilon = 0$ (which gives $\lambda = 1$) the gap closes at $\varphi^* = \pi$. In this case the time-reversal symmetry is unbroken, and the system is gapped and topologically trivial for any value of the phase $\varphi \neq \pi$.

The topological phase space derived in the case of a superconducting quantum dot is universal for the class of zero-dimensional superconductors. It coincides in fact with the topological phase space in Figure 2a of [50], where it was derived in the more general case of a zero-dimensional quantum system (short-size regime) with an arbitrary number of energy modes. The topological phases can be defined also in the case of small Coulomb interactions as long as the particle–hole gap remains open. In this case in fact the topological invariant cannot change, since the phase with small interaction $U > 0$ can be transformed with the non-interacting phase $U = 0$ by a smooth transformation without closing the gap.

It is important to note that in the 0D case (differently from the 1D case) topological states can be realized without spin–orbit coupling. This is because topological states in the symmetry class D are enforced by the presence of the superconducting coupling (particle–hole symmetry) and the Zeeman field (which breaks the time-reversal symmetry). The gap opening, in this case, is guaranteed in general by the gap induced by finite size effects or eventually by interactions.

Josephson current–phase discontinuities

In our previous work [50], we have found the general relation between the topological invariant of a 0D topological superconductor and the discontinuities of the Josephson current–phase relation (CPR). The topological phase transition between the trivial ($P = 1$, even fermion parity) and the nontrivial state ($P = -1$, odd fermion parity) corresponds to the emergence of a discontinuity in the Josephson CPR at zero temperature. In this case, the current is proportional to the phase-derivative of the total energy of the superconducting condensate [69,71], which is given by the sum of the positive energy levels $|E_\uparrow| + |E_\downarrow|$. Hence, the Josephson current is equal to $-2\partial_\varphi E_\varphi$ in the trivial groundstate with energy $E_{GS}(\varphi) = 2E_\varphi$, whereas it vanishes in the nontrivial groundstate with energy $E_{GS}(\varphi) = 2B$ (see Equation 20). The CPR at zero temperature is therefore given by

$$I_\varphi = -\left(1+P_\varphi\right)\partial_\varphi E_\varphi = \left(1+P_\varphi\right)\frac{\Gamma^2 \sin\varphi}{4E_\varphi}. \qquad (23)$$

In the topologically trivial state ($P = 1$) at low fields $|B| < B_{min}$, the two energy levels $E_\uparrow$ and $E_\downarrow$ contribute equally to the Josephson current and one has $I_\varphi = -2\partial_\varphi E_\varphi$. However, when the fermion parity changes, one of the energy level crosses the particle–hole gap, and its contribution to the current changes its sign.

Therefore, in the topologically nontrivial state ($P = -1$) at high fields $|B| > B_{max}$ the Josephson current in Equation 23 vanishes since the contributions from the two energy levels $E_\uparrow$ and $E_\downarrow$ cancel each other. Moreover, as one can see from Equation 23, for intermediate fields $B_{min} < |B| < B_{max}$, (i.e., $|\lambda| < 1$) the CPR exhibits a discontinuity between the trivial state with $I = \pm 2\Gamma^2 \sin\varphi^*/[4E_{\varphi^*}]$ to the nontrivial one with $I = 0$ at the gapless points $\pm\varphi^*$ which is equal to

$$\Delta I = \frac{\Gamma^2\sqrt{1-\lambda^2}}{2|B|}, \qquad (24)$$

which is a special case of Equation 3 of [50]. The discontinuity is a consequence of the crossing at zero-energy of the lowest-energy level with linear phase dispersion. The discontinuity in Equation 24 can be also calculated directly using Equation 3 of [50], which can be rewritten as

$$\Delta I = 2\left.\frac{\left|\partial_\varphi \mathrm{pf}\left(\mathcal{H}_{\mathrm{eff}}\imath\tau_x\right)\right|}{\sqrt{\left|\mathrm{pdet}\left(\mathcal{H}_{\mathrm{eff}}\right)\right|}}\right|_{\varphi=\varphi^*}, \tag{25}$$

where $\mathrm{pdet}(\mathcal{H}_{\mathrm{eff}})$ is the pseudodeterminant of the Hamiltonian (the product of nonzero eigenvalues). The square root of the pseudodeterminant is in this case just the product of the positive eigenvalues (due to particle–hole symmetry). Since the system has only two non-negative single-particle energy levels $|E_\uparrow| = |B + E_{\varphi*}|$ and $|E_\downarrow| = |B - E_{\varphi*}|$, and one of these two energy levels vanishes at gapless points $\pm\varphi^*$ since in this case $|B| = |E_{\varphi*}|$, the denominator of Equation 25 is equal to the nonzero positive energy level given by $|B| + |E_{\varphi*}| = 2|B|$, which yields $\sqrt{|\mathrm{pdet}(\mathcal{H}_{\mathrm{eff}})|} = 2|B|$, which leads via Equation 25 to Equation 24.

Figure 4a shows the CPR of the SC–QD–SC junction for different choices of the Zeeman field B at zero temperature, calculated directly from Equation 23. At low fields $|B| < B_{\mathrm{min}}$ (i.e., $\lambda > 1$) the system is topologically trivial ($P = 1$) and the CPR is smoothly oscillating without any discontinuity. At large fields $|B| > B_{\mathrm{max}}$ (i.e., $\lambda < -1$), the system is topologically nontrivial ($P = -1$) and the Josephson current vanishes due to the opposite contribution of the two Andreev levels. At intermediate fields $B_{\mathrm{min}} < |B| < B_{\mathrm{max}}$ instead (i.e., $|\lambda| < 1$), discontinuities appear at the transition points between the trivial and nontrivial topological states (gapless points $\pm\varphi^*$). The emergence of a discontinuous drop coincides with a change of the fermion parity and to the presence of zero-energy states closing the particle–hole gap. Since the energy levels of the system depends smoothly on the phase φ, gapless points are the only points where the CPR can be discontinuous. At finite temperatures, CPR discontinuities are smoothed out by the effect of thermal fluctuations. However, such discontinuities can be revealed, e.g., by the presence of spikes in the phase-derivative of the CPR at low temperatures [50].

Hence, if time-reversal symmetry is broken ($B \neq 0$), current discontinuities correspond to the presence of zero-energy modes and to a change in the topological invariant. These signatures are topologically robust against small perturbations, such as disorder. This means that these discontinuities and the associated zero-energy modes cannot be removed by the presence of, e.g., disorder or interactions, if these perturbations are small compared to the effective local pairing Γ and Zeeman energy B. The only effect of these small perturbations is in fact to produce a shift of the gapless point $\varphi^* \to \varphi^* + \delta\lambda / \sqrt{1-\lambda^2}$ where the topological transition and zero-energy modes occurs. Discontinuities in the Josephson CPR are still present in the interacting case [65] at zero temperature. As shown in [50], the correspondence between CPR discontinuities and fermion parity transitions relies only on the presence of a broken time-reversal symmetry that removes the spin degeneracy and on the fact that in this case the closing of the particle–hole gap correspond to a change of the topological invariant.

On the other hand, if time-reversal symmetry is unbroken, current discontinuities are still present if $B = \varepsilon = 0$ (where $\lambda = 1$). In this case, the CPR exhibits a single discontinuous drop $\Delta I = \Gamma/2$ at the gapless point $\varphi^* = \pi$, according to Equation 24. This case reproduces the well-known current–phase discontinuity of a

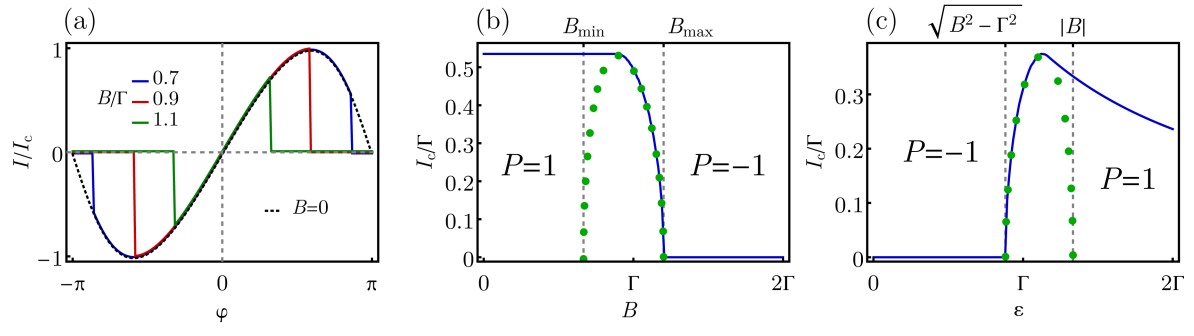

Figure 4: (a) Josephson CPR of the SC–QD–SC junction for different choices of the Zeeman field B in the limit $T \to 0$ (Equation 23) in units of the critical current of the trivial branch. We take $\varepsilon = 2\Gamma/3$. Depending on the Zeeman field, different regimes are realized: At small fields $|B| < B_{\mathrm{min}}$ (i.e, $\lambda > 1$, dotted line) the current is smoothly oscillating as a function of the phase φ and the system is topologically trivial ($P = 1$). At large fields $|B| > B_{\mathrm{max}}$ (i.e., $\lambda < -1$, not shown) the current vanishes and the system is topologically nontrivial ($P = -1$). At intermediate fields $B_{\mathrm{min}} < |B| < B_{\mathrm{max}}$ (i.e., $|\lambda| < 1$, solid lines), discontinuous drops appear at the transition points between the trivial and nontrivial topological states. Current discontinuities correspond to the variations of the fermion parity and to the presence of zero energy modes. (b) Critical current of the SC–QD–SC junction as a function of the Zeeman field at zero temperature (solid line) with $\varepsilon = 2\Gamma/3$. (c) Critical current of the SC–QD–SC junction as a function of the electric gate ε at zero temperature (solid line) with $B = 4\Gamma/3$. In both cases, the critical current drops from a finite value in the trivial state ($P = 1$ and $\lambda > 1$) to zero in the nontrivial state ($P = -1$ and $\lambda < -1$). In the transition regions $B_{\mathrm{min}} < B < B_{\mathrm{max}}$ (b) and $\sqrt{B^2 - \Gamma^2} < |\varepsilon| < |B|$ (c), the trivial and nontrivial states alternate at different phases φ. As one can see, when the system approaches its nontrivial state $P = -1$, the critical current coincides with the magnitude of the discontinuous drop ΔI (green dots) given in Equation 24.

quantum point contact [71]. However, in this case the discontinuity does not correspond to a topological transition.

The presence of a small Coulomb interaction does not affect the Josephson current at zero temperature in the trivial and nontrivial branches of the CPR, since the energy shift $U/2$ of the Andreev levels do not depend on the phase φ.

Critical current

The topological transition can be probed also by a measure of the critical current of the junction. The critical current is defined as the maximum current of the junction up to the phase $I_c = \max I_\varphi$. In the trivial state at low fields $|B| < B_{\min}$ (i.e., $\lambda > 1$) the critical current is finite. Since the CPR is continuous in this case, the maximum of the current coincides with the local maximum of the current where its phase-derivative vanishes $\partial_\varphi I_\varphi = 0$. In the limits $\varepsilon \to 0$ and $\varepsilon \to \pm\Gamma$ for example, the current reaches its maximum at $\tilde{\varphi} = \pi$ or at $\tilde{\varphi} = \pi/2$, which gives critical currents of $I_c = \Gamma/2$ and $I_c = \Gamma^2/(4\sqrt{\varepsilon^2 + \Gamma^2/2})$, respectively. In the nontrivial state at large fields $|B| > B_{\max}$ instead ($\lambda < -1$) the current vanishes and one has $I_c = 0$. However, at intermediate fields $B_{\min} < |B| < B_{\max}$ (i.e., $|\lambda| < 1$) trivial and nontrivial states alternate in the interval $\varphi \in [-\pi, \pi]$, and the CPR has discontinuities. Because the CPR is not continuous, the maximum of the current may coincide either with the local maximum $I_{\tilde{\varphi}}$ of the current where $\partial_\varphi I_\varphi = 0$, or with the current at the discontinuity $I_{\varphi *} = \Delta I$. More precisely, the critical current coincides with the maximum between these two values $I_c = \max(|I_{\tilde{\varphi}}|, |\Delta I|)$. The case $I_c = |\Delta I|$ occurs, for instance, when the system approaches its nontrivial state at large fields $|B| \to B_{\max}$. Therefore for fields $|B| \le B_{\max}$ the critical current coincides with the current discontinuity $I_c = \Delta I$. This regime can be obtained either by a measure of the critical current by varying the magnetic field, or by varying, e.g., the energy level ε in a constant field B.

Figure 4b shows the critical current of the junction as a function of the Zeeman field. As one can see, the critical current is finite in the trivial $P = 1$ state when $|B| < B_{\min}$ (i.e., $\lambda > 1$), and drops to zero in the nontrivial $P = -1$ state when $|B| > B_{\max}$ (i.e., $\lambda < -1$) state. The drop of the critical current is smooth in the intermediate region where $B_{\min} < |B| < B_{\max}$ (i.e., $|\lambda| < 1$). Analogously, Figure 4c shows the critical current of the junction as a function of the electric gate ε at constant field B. The smooth transition is obtained for intermediate values $\sqrt{B^2 - \Gamma^2} < \varepsilon < |B|$ the Zeeman field varies in the range $B_{\min} < |B| < B_{\max}$, where we remind that $B_{\min} = |\varepsilon|$ and $B_{\max} = \sqrt{\varepsilon^2 + \Gamma^2}$. In the intermediate region, when the system approaches its nontrivial state, the critical current coincides with the magnitude of the discontinuous drop $I_c = |\Delta I|$ (dots in the figures). Hence, a measure of the critical current at low temperature can be used to indirectly probe the magnitude of the discontinuous drop and the existence of topological phase transitions and zero-energy modes even when a direct measure of the CPR is not accessible [72]. It is reasonable to speculate that the current discontinuities may indicate a topological transition also in the interacting case.

Conclusion

We have shown that a quantum dot coupled with two superconducting leads can realize a 0D topological superconductor with broken time-reversal symmetry. In this system, topological phase transitions between trivial and nontrivial states correspond to discontinuities in the Josephson CPR at low temperatures and to the presence of zero-energy modes. This simple model, which can be treated analytically, fully confirms the results obtained in a more general model in [50].

The topological phase transitions and the ensuing current discontinuities are robust, in the sense that cannot be removed by small perturbations. A direct measure of the CPR [71,73-75] or of the Josephson radiation [38,76,77] at low temperatures can reveal the presence of such discontinuities. Moreover, the presence of the topological transition can be probed indirectly by a measure of the critical current of the junction as a function of the Zeeman field or gate voltage.

Acknowledgements

P. M. acknowledges financial support from JSPS Kakenhi Grant No. 16H02204. A. B. acknowledges the Italian MIUR-FIRB 2012 via the HybridNanoDev project under Grant no. RBFR1236VV, the European Research Council under the European Union's Seventh Framework Program (FP7/ 2007-2013) ERC Grant No. 615187-COMANCHE for partial financial support, the CNR-CONICET cooperation programme "Energy conversion in quantum nanoscale hybrid devices", and the Royal Society though the International Exchanges between the UK and Italy (grant IES R3 170054).

ORCID® iDs

Pasquale Marra - https://orcid.org/0000-0002-9545-3314
Alessandro Braggio - https://orcid.org/0000-0003-2119-1160
Roberta Citro - https://orcid.org/0000-0002-3896-4759

References

1. v. Klitzing, K.; Dorda, G.; Pepper, M. *Phys. Rev. Lett.* **1980,** *45,* 494–497. doi:10.1103/PhysRevLett.45.494
2. Thouless, D. J.; Kohmoto, M.; Nightingale, M. P.; den Nijs, M. *Phys. Rev. Lett.* **1982,** *49,* 405–408. doi:10.1103/PhysRevLett.49.405
3. Kitaev, A. Yu. *Phys.-Usp.* **2001,** *44,* 131. doi:10.1070/1063-7869/44/10S/S29
4. Hasan, M. Z.; Kane, C. L. *Rev. Mod. Phys.* **2010,** *82,* 3045–3067. doi:10.1103/RevModPhys.82.3045

5. Qi, X.-L.; Zhang, S.-C. *Rev. Mod. Phys.* **2011,** *83,* 1057–1110. doi:10.1103/RevModPhys.83.1057
6. Wehling, T. O.; Black-Schaffer, A. M.; Balatsky, A. V. *Adv. Phys.* **2014,** *63,* 1–76. doi:10.1080/00018732.2014.927109
7. Chiu, C.-K.; Teo, J. C. Y.; Schnyder, A. P.; Ryu, S. *Rev. Mod. Phys.* **2016,** *88,* 035005. doi:10.1103/RevModPhys.88.035005
8. Altland, A.; Zirnbauer, M. R. *Phys. Rev. B* **1997,** *55,* 1142–1161. doi:10.1103/PhysRevB.55.1142
9. Schnyder, A. P.; Ryu, S.; Furusaki, A.; Ludwig, A. W. W. *AIP Conf. Proc.* **2009,** *1134,* 10–21. doi:10.1063/1.3149481
10. Kitaev, A. *AIP Conf. Proc.* **2009,** *1134,* 22–30. doi:10.1063/1.3149495
11. Mourik, V.; Zuo, K.; Frolov, S. M.; Plissard, S. R.; Bakkers, E. P. A. M.; Kouwenhoven, L. P. *Science* **2012,** *336,* 1003–1007. doi:10.1126/science.1222360
12. Nadj-Perge, S.; Drozdov, I. K.; Li, J.; Chen, H.; Jeon, S.; Seo, J.; MacDonald, A. H.; Bernevig, B. A.; Yazdani, A. *Science* **2014,** *346,* 602–607. doi:10.1126/science.1259327
13. Pawlak, R.; Kisiel, M.; Klinovaja, J.; Meier, T.; Kawai, S.; Glatzel, T.; Loss, D.; Meyer, E. *npj Quantum Inf.* **2016,** *2,* 16035. doi:10.1038/npjqi.2016.35
14. Alicea, J. *Rep. Prog. Phys.* **2012,** *75,* 076501. doi:10.1088/0034-4885/75/7/076501
15. Aguado, R. *Riv. Nuovo Cimento Soc. Ital. Fis.* **2017,** *40,* 523. doi:10.1393/ncr/i2017-10141-9
16. Lutchyn, R. M.; Bakkers, E. P. A. M.; Kouwenhoven, L. P.; Krogstrup, P.; Marcus, C. M.; Oreg, Y. *Nat. Rev. Mater.* **2018,** *3,* 52–68. doi:10.1038/s41578-018-0003-1
17. Sato, M.; Ando, Y. *Rep. Prog. Phys.* **2017,** *80,* 076501. doi:10.1088/1361-6633/aa6ac7
18. Leijnse, M.; Flensberg, K. *Semicond. Sci. Technol.* **2012,** *27,* 124003. doi:10.1088/0268-1242/27/12/124003
19. Elliott, S. R.; Franz, M. *Rev. Mod. Phys.* **2015,** *87,* 137–163. doi:10.1103/RevModPhys.87.137
20. Beenakker, C. W. J. *Annu. Rev. Condens. Matter Phys.* **2013,** *4,* 113–136. doi:10.1146/annurev-conmatphys-030212-184337
21. Lutchyn, R. M.; Sau, J. D.; Das Sarma, S. *Phys. Rev. Lett.* **2010,** *105,* 077001. doi:10.1103/PhysRevLett.105.077001
22. Oreg, Y.; Refael, G.; von Oppen, F. *Phys. Rev. Lett.* **2010,** *105,* 177002. doi:10.1103/PhysRevLett.105.177002
23. Gangadharaiah, S.; Braunecker, B.; Simon, P.; Loss, D. *Phys. Rev. Lett.* **2011,** *107,* 036801. doi:10.1103/PhysRevLett.107.036801
24. Klinovaja, J.; Stano, P.; Loss, D. *Phys. Rev. Lett.* **2012,** *109,* 236801. doi:10.1103/PhysRevLett.109.236801
25. Klinovaja, J.; Stano, P.; Yazdani, A.; Loss, D. *Phys. Rev. Lett.* **2013,** *111,* 186805. doi:10.1103/PhysRevLett.111.186805
26. Jiang, L.; Pekker, D.; Alicea, J.; Refael, G.; Oreg, Y.; von Oppen, F. *Phys. Rev. Lett.* **2011,** *107,* 236401. doi:10.1103/PhysRevLett.107.236401
27. San-Jose, P.; Prada, E.; Aguado, R. *Phys. Rev. Lett.* **2012,** *108,* 257001. doi:10.1103/PhysRevLett.108.257001
28. Rokhinson, L. P.; Liu, X.; Furdyna, J. K. *Nat. Phys.* **2012,** *8,* 795–799. doi:10.1038/nphys2429
29. Brunetti, A.; Zazunov, A.; Kundu, A.; Egger, R. *Phys. Rev. B* **2013,** *88,* 144515. doi:10.1103/PhysRevB.88.144515
30. Chang, W.; Manucharyan, V. E.; Jespersen, T. S.; Nygård, J.; Marcus, C. M. *Phys. Rev. Lett.* **2013,** *110,* 217005. doi:10.1103/PhysRevLett.110.217005
31. Dolcini, F.; Houzet, M.; Meyer, J. S. *Phys. Rev. B* **2015,** *92,* 035428. doi:10.1103/PhysRevB.92.035428
32. Khanna, U.; Mukherjee, D. K.; Kundu, A.; Rao, S. *Phys. Rev. B* **2016,** *93,* 121409. doi:10.1103/PhysRevB.93.121409
33. Peng, Y.; Pientka, F.; Berg, E.; Oreg, Y.; von Oppen, F. *Phys. Rev. B* **2016,** *94,* 085409. doi:10.1103/PhysRevB.94.085409
34. Hussein, R.; Jaurigue, L.; Governale, M.; Braggio, A. *Phys. Rev. B* **2016,** *94,* 235134. doi:10.1103/PhysRevB.94.235134
35. Mellars, E.; Béri, B. *Phys. Rev. B* **2016,** *94,* 174508. doi:10.1103/PhysRevB.94.174508
36. Wiedenmann, J.; Bocquillon, E.; Deacon, R. S.; Hartinger, S.; Herrmann, O.; Klapwijk, T. M.; Maier, L.; Ames, C.; Brüne, C.; Gould, C.; Oiwa, A.; Ishibashi, K.; Tarucha, S.; Buhmann, H.; Molenkamp, L. W. *Nat. Commun.* **2016,** *7,* 10303. doi:10.1038/ncomms10303
37. Jellinggaard, A.; Grove-Rasmussen, K.; Madsen, M. H.; Nygård, J. *Phys. Rev. B* **2016,** *94,* 064520. doi:10.1103/PhysRevB.94.064520
38. Deacon, R. S.; Wiedenmann, J.; Bocquillon, E.; Domínguez, F.; Klapwijk, T. M.; Leubner, P.; Brüne, C.; Hankiewicz, E. M.; Tarucha, S.; Ishibashi, K.; Buhmann, H.; Molenkamp, L. W. *Phys. Rev. X* **2017,** *7,* 021011. doi:10.1103/PhysRevX.7.021011
39. Virtanen, P.; Bergeret, F. S.; Strambini, E.; Giazotto, F.; Braggio, A. *arXiv* **2017,** No. 1712.01684.
40. Mukherjee, D. K.; Rao, S.; Kundu, A. *Phys. Rev. B* **2017,** *96,* 161408. doi:10.1103/PhysRevB.96.161408
41. Khanna, U.; Rao, S.; Kundu, A. *Phys. Rev. B* **2017,** *95,* 201115. doi:10.1103/PhysRevB.95.201115
42. Pientka, F.; Keselman, A.; Berg, E.; Yacoby, A.; Stern, A.; Halperin, B. I. *Phys. Rev. X* **2017,** *7,* 021032. doi:10.1103/PhysRevX.7.021032
43. Huang, H.; Liang, Q.-F.; Yao, D.-X.; Wang, Z. *Phys. C (Amsterdam, Neth.)* **2017,** *543,* 22–26. doi:10.1016/j.physc.2017.10.005
44. Lee, E. J. H.; Jiang, X.; Žitko, R.; Aguado, R.; Lieber, C. M.; De Franceschi, S. *Phys. Rev. B* **2017,** *95,* 180502. doi:10.1103/PhysRevB.95.180502
45. Cayao, J.; San-Jose, P.; Black-Schaffer, A. M.; Aguado, R.; Prada, E. *Phys. Rev. B* **2017,** *96,* 205425. doi:10.1103/PhysRevB.96.205425
46. San-Jose, P.; Cayao, J.; Prada, E.; Aguado, R. *New J. Phys.* **2013,** *15,* 075019. doi:10.1088/1367-2630/15/7/075019
47. Cayao, J.; Black-Schaffer, A. M.; Prada, E.; Aguado, R. *Beilstein J. Nanotechnol.* **2018,** *9,* 1339–1357. doi:10.3762/bjnano.9.127
48. Domínguez, F.; Kashuba, O.; Bocquillon, E.; Wiedenmann, J.; Deacon, R. S.; Klapwijk, T. M.; Platero, G.; Molenkamp, L. W.; Trauzettel, B.; Hankiewicz, E. M. *Phys. Rev. B* **2017,** *95,* 195430. doi:10.1103/PhysRevB.95.195430
49. Zyuzin, A.; Alidoust, M.; Loss, D. *Phys. Rev. B* **2016,** *93,* 214502. doi:10.1103/PhysRevB.93.214502
50. Marra, P.; Citro, R.; Braggio, A. *Phys. Rev. B* **2016,** *93,* 220507. doi:10.1103/PhysRevB.93.220507
51. Loss, D.; DiVincenzo, D. P. *Phys. Rev. A* **1998,** *57,* 120–126. doi:10.1103/PhysRevA.57.120
52. Choi, M.-S.; Bruder, C.; Loss, D. *Phys. Rev. B* **2000,** *62,* 13569–13572. doi:10.1103/PhysRevB.62.13569
53. Kouwenhoven, L. P.; Austing, D. G.; Tarucha, S. *Rep. Prog. Phys.* **2001,** *64,* 701. doi:10.1088/0034-4885/64/6/201
54. van der Wiel, W. G.; Fujisawa, T.; Tarucha, S.; Kouwenhoven, L. P. *Jpn. J. Appl. Phys.* **2001,** *40,* 2100. doi:10.1143/JJAP.40.2100
55. Tarasinski, B.; Chevallier, D.; Hutasoit, J. A.; Baxevanis, B.; Beenakker, C. W. J. *Phys. Rev. B* **2015,** *92,* 144306. doi:10.1103/PhysRevB.92.144306

56. Beenakker, C. W. J.; Edge, J. M.; Dahlhaus, J. P.; Pikulin, D. I.; Mi, S.; Wimmer, M. *Phys. Rev. Lett.* **2013,** *111,* 037001. doi:10.1103/PhysRevLett.111.037001
57. Stanescu, T. D.; Lutchyn, R. M.; Das Sarma, S. *Phys. Rev. B* **2013,** *87,* 094518. doi:10.1103/PhysRevB.87.094518
58. Lee, E. J. H.; Jiang, X.; Houzet, M.; Aguado, R.; Lieber, C. M.; De Franceschi, S. *Nat. Nanotechnol.* **2013,** *9,* 79–84. doi:10.1038/nnano.2013.267
59. Yokoyama, T.; Eto, M.; Nazarov, Y. V. *J. Phys. Soc. Jpn.* **2013,** *82,* 054703. doi:10.7566/JPSJ.82.054703
60. Yokoyama, T.; Eto, M.; Nazarov, Y. V. *Phys. Rev. B* **2014,** *89,* 195407. doi:10.1103/PhysRevB.89.195407
61. Klees, R. L.; Rastelli, G.; Belzig, W. *Phys. Rev. B* **2017,** *96,* 144510. doi:10.1103/PhysRevB.96.144510
62. Li, Y.; Kundu, A.; Zhong, F.; Seradjeh, B. *Phys. Rev. B* **2014,** *90,* 121401. doi:10.1103/PhysRevB.90.121401
63. Benito, M.; Platero, G. *Phys. E (Amsterdam, Neth.)* **2015,** *74,* 608–613. doi:10.1016/j.physe.2015.08.030
64. Meng, T.; Florens, S.; Simon, P. *Phys. Rev. B* **2009,** *79,* 224521. doi:10.1103/PhysRevB.79.224521
65. Wentzell, N.; Florens, S.; Meng, T.; Meden, V.; Andergassen, S. *Phys. Rev. B* **2016,** *94,* 085151. doi:10.1103/PhysRevB.94.085151
66. Braggio, A.; Governale, M.; Pala, M. G.; König, J. *Solid State Commun.* **2011,** *151,* 155–158. doi:10.1016/j.ssc.2010.10.043
67. Droste, S.; Andergassen, S.; Splettstoesser, J. *J. Phys.: Condens. Matter* **2012,** *24,* 415301. doi:10.1088/0953-8984/24/41/415301
68. Hussein, R.; Braggio, A.; Governale, M. *Phys. Status Solidi B* **2017,** *254,* 1600603. doi:10.1002/pssb.201600603
69. Nazarov, Y. V.; Blanter, Y. M. *Quantum Transport: Introduction to Nanoscience;* Cambridge University Press, 2009; p 106.
70. Loring, T. A. *Ann. Phys.* **2015,** *356,* 383–416. doi:10.1016/j.aop.2015.02.031
71. Golubov, A. A.; Kupriyanov, M. Y.; Il'ichev, E. *Rev. Mod. Phys.* **2004,** *76,* 411–469. doi:10.1103/RevModPhys.76.411
72. Tiira, J.; Strambini, E.; Amado, M.; Roddaro, S.; San-Jose, P.; Aguado, R.; Bergeret, F. S.; Ercolani, D.; Sorba, L.; Giazotto, F. *Nat. Commun.* **2017,** *8,* 14984. doi:10.1038/ncomms14984
73. Frolov, S. M.; Van Harlingen, D. J.; Oboznov, V. A.; Bolginov, V. V.; Ryazanov, V. V. *Phys. Rev. B* **2004,** *70,* 144505. doi:10.1103/PhysRevB.70.144505
74. Sochnikov, I.; Bestwick, A. J.; Williams, J. R.; Lippman, T. M.; Fisher, I. R.; Goldhaber-Gordon, D.; Kirtley, J. R.; Moler, K. A. *Nano Lett.* **2013,** *13,* 3086–3092. doi:10.1021/nl400997k
75. Szombati, D. B.; Nadj-Perge, S.; Car, D.; Plissard, S. R.; Bakkers, E. P. A. M.; Kouwenhoven, L. P. *Nat. Phys.* **2016,** *12,* 568–572. doi:10.1038/nphys3742
76. Ozyuzer, L.; Koshelev, A. E.; Kurter, C.; Gopalsami, N.; Li, Q.; Tachiki, M.; Kadowaki, K.; Yamamoto, T.; Minami, H.; Yamaguchi, H.; Tachiki, T.; Gray, K. E.; Kwok, W.-K.; Welp, U. *Science* **2007,** *318,* 1291–1293. doi:10.1126/science.1149802
77. Solinas, P.; Gasparinetti, S.; Golubev, D.; Giazotto, F. *Sci. Rep.* **2015,** *5,* 12260. doi:10.1038/srep12260

License and Terms

BEILSTEIN JOURNAL OF NANOTECHNOLOGY

Interaction-induced zero-energy pinning and quantum dot formation in Majorana nanowires

Samuel D. Escribano[1], Alfredo Levy Yeyati[2] and Elsa Prada[*1]

Full Research Paper

Open Access

Address:
[1]Departamento de Física de la Materia Condensada C3, Universidad Autónoma de Madrid, E-28049 Madrid, Spain and [2]Departamento de Física Teórica de la Materia Condensada C5, Condensed Matter Physics Center (IFIMAC) and Instituto Nicolás Cabrera, Universidad Autónoma de Madrid, E-28049 Madrid, Spain

Email:
Elsa Prada[*] - elsa.prada@uam.es

* Corresponding author

Keywords:
hybrid superconductor–semiconductor nanowires; interactions; Majorana bound states; quantum dots

Beilstein J. Nanotechnol. **2018,** *9,* 2171–2180.
doi:10.3762/bjnano.9.203

Received: 21 December 2017
Accepted: 31 July 2018
Published: 15 August 2018

This article is part of the Thematic Series "Topological materials".

Associate Editor: J. M. van Ruitenbeek

Abstract

Majorana modes emerge in non-trivial topological phases at the edges of specific materials such as proximitized semiconducting nanowires under an external magnetic field. Ideally, they are non-local states that are charge-neutral superpositions of electrons and holes. However, in nanowires of realistic length their wave functions overlap and acquire a finite charge that makes them susceptible to interactions, specifically with the image charges that arise in the electrostatic environment. Considering a realistic three-dimensional model of the dielectric surroundings, here we show that, under certain circumstances, these interactions lead to a suppression of the Majorana oscillations predicted by simpler theoretical models, and to the formation of low-energy quantum-dot states that interact with the Majorana modes. Both features are observed in recent experiments on the detection of Majoranas and could thus help to properly characterize them.

Introduction

Semiconducting nanowires with strong spin–orbit interaction, such as InAs or InSb, are becoming ideal systems for the artificial generation of topological superconductivity [1-3]. In addition to its fundamental interest, such nanowires that may host Majorana bound states (MBSs) at their ends or interfaces [4,5] constitute promising platforms for Majorana-based quantum computing devices [6-9]. Progress in fabrication techniques has allowed to induce a hard superconducting gap in InAs [10] or InSb [11] nanowires with epitaxially deposited Al layer. Moreover, last-generation devices exhibit a very low degree of disorder, which allows them to almost reach the ballistic limit [12-14].

In spite of these advances, the experimental signatures of MBSs in the nanowire devices deviate significantly in several aspects from the theoretical predictions of minimal models. This is the case, for instance, regarding the behavior of the subgap conductance through the proximitized nanowire, which has been

addressed in several experiments [10,12-19]. In a long wire (the length of which is much greater than the induced coherence length) the presence of MBSs manifests itself in the appearance of a zero-bias conductance peak the width of which is controlled by the normal-state conductance [20]. However, for typical wire lengths explored in actual experiments, which are of the order of a few micrometers, it is expected that the overlap between MBSs located at both ends of the wire gives rise to conventional Andreev bound states that deviate from zero energy, leading to an oscillatory pattern in the low-bias conductance as a function of Zeeman field, chemical potential or wire length [21-23]. Conspicuously, in most of the available experimental data the emergence of a robust zero-bias conductance peak is observed above some critical Zeeman field without the expected oscillatory pattern [12,19,24,25]. Several mechanisms have been proposed to account for the reduction or lack of oscillations, such as smooth confinement [21,26-28], strong spin–orbit coupling [29], position-dependent pairing [30], orbital magnetic effects [31], Coulomb repulsion among the carriers in the nanowire [22], or the presence of the normal drain lead connected to the hybrid wire [32].

Another source of Majorana oscillation suppression was put forward by some of us in a recent work [33]. The key realization is that MBSs in a finite-length wire posses a finite charge, typically distributed uniformly along the wire [34], which can be susceptible to electrostatic interactions with the surrounding medium. We considered the case of a grounded parent superconductor, thus avoiding the effect of a charging energy associated to the Cooper pairs, and showed that, in such case, a residual effect of interactions may arise from the image charges induced in the electrostatic environment of the nanowire. Using a simple model for the induced potential we concluded that, in typical experimental setups, interactions would lead to pinning of the MBSs to zero energy around parity crossings and, thus, to more robust zero-bias conductance peaks than predicted by the non-interacting models.

The aim of the present work is to test the validity of the predictions of [33] for the case of more realistic calculations of the induced electrostatic potential, taking into account the actual three-dimensional (3D) geometry as well as the effect of nearby metallic leads. We consider the geometry depicted in Figure 1a, where a nanowire of rectangular cross section lies on an insulating substrate (typically SiO_2) and is contacted to a thin superconducting (SC) layer on one of its faces and to two bulk normal leads at both ends, separated by thin insulating barriers. In Figure 1a we indicate the characteristic dielectric constants of each region, which are relevant for the calculation of the induced potential through Poisson's equation (discussed below). Our aim is to solve this equation together with the Bogoliubov–de Gennes equation for determining self-consistently the charge density ρ(x) along the nanowire. For this purpose we derive a generalized method of image charges that allows us to calculate the induced potential under rather general conditions, taking into account a 3D electrostatic environment as the one shown in Figure 1a.

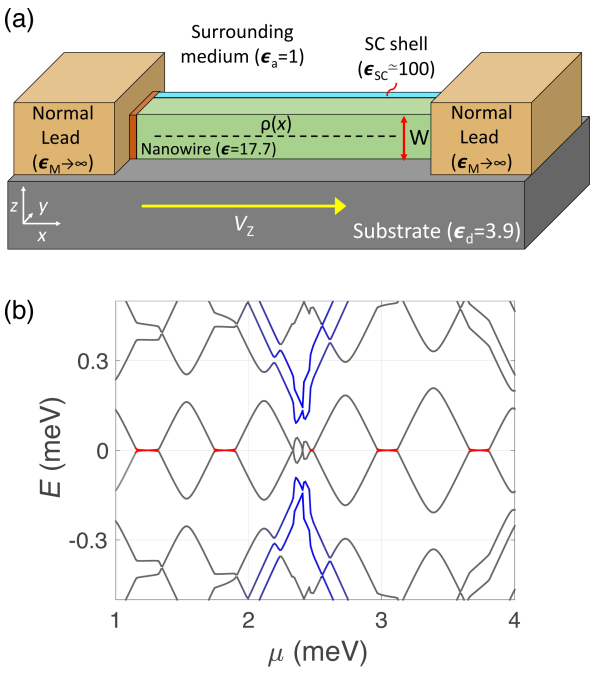

Figure 1: (a) Schematic representation of the setup analyzed in the present work. A nanowire of rectangular cross section (green) lying on an insulating substrate (grey) and in contact to a thin metallic layer in one of its faces (light blue), corresponding to the parent superconductor, and two normal metal leads at its ends (orange) separated by tunnel barriers (brown). Typical values for the dielectric constants for each region are indicated. (b) Low-energy spectrum as a function of the chemical potential μ for a wire of thickness W = 100 nm and length L = 1 μm. Other parameters are the spin–orbit coupling α = 20 nm·meV, the induced pairing energy Δ = 0.3 meV and the Zeeman energy V_Z = 2 meV. Electrostatic environment-induced zero-energy pinned regions between Majorana oscillations are indicated in red. Quantum-dot levels (in blue), occurring at the edges of the wire due to the interaction with the bulk contacts, anticross with Majorana levels and remove their zero-energy pinning.

We find two main effects coming from this interaction, which are exemplified in Figure 1b. One is, as stated before, the suppression of Majorana oscillations around parity crossings (zero-energy crossings where the total fermion parity of the wire changes), both as a function of the Zeeman energy V_Z and the chemical potential μ of the wire. This effect is produced because, at each parity crossing, a finite Majorana charge Q_M enters the wire from the reservoir in an abrupt fashion. If the electrostatic screening is smaller inside the wire than in the reservoirs, a repulsive interaction is produced between the incoming charge and its images, preventing its entrance. This

translates into finite regions in parameter space (in red in Figure 1b) where Majorana modes are pinned to zero energy within a finite range of V_Z or μ proportional to the Majorana charge Q_M and the strength of the interaction. This was already shown in [33] but for a simplified dielectric profile where the presence of the superconducting shell had been ignored. We here include it and find that the size of the pinned regions decreases but the pinning effect is still present under certain conditions that we discuss in detail below. Moreover, we explain the incompressible behavior of the electron liquid within these pinned regions in terms of the Majorana wave functions and their charge.

Another important effect of the electrostatic environment unexplored before is the creation of deep potential wells at the ends of the wire close to the bulk metallic electrodes. These wells, obtained explicitly here through the self-consistent calculation, are similar to the confinement potentials typical of quantum dots. Localized quantum dot-like energy levels in these regions disperse with magnetic field (or chemical potential) and appear below the induced gap in the wire spectrum (in blue in Figure 1b). In the topological regime, dot-like levels interact with Majorana states, anticrossing them when they approach zero energy. Similar phenomena were observed in some experiments [14,19], and have been likely found on other occasions but discarded by experimentalists looking for the simpler picture. Interestingly, it has been shown that the shape of these anticrossings can be used to quantify the degree of non-locality of the Majorana wave functions [35,36], a prediction that has been experimentally demonstrated recently [25]. Here, we show that if the interaction between dots and Majorana levels occurs in a pinning region, Majorana levels are forced to depart from zero energy, revealing the existence of a finite wave function overlap between them in spite of their zero energy. We analyze this behavior again in terms of the wave functions of Majorana state and dot and their charge.

The paper is organized as follows: in the following section we provide insight into the theoretical model used to treat interactions. In the next section we analyze the case in which the influence of the bulk normal leads can be neglected, recovering the pinning effect found in [33] for a repulsive electrostatic environment. However, we focus here on the electrostatic environment effects on the Majorana wave function, rather than on its spectral properties. In the next section we study the effect of including the bulk normal leads of Figure 1a, finding that they give rise to the formation of quantum dot-like bound states. We further analyze the interplay of such states with the MBSs. Finally, we present the conclusions of our work. The robustness of the pinning effect is analyzed in detail in Section 4 of Supporting Information File 1.

Model and Theoretical Approach

We model the electronic states along the proximitized Rashba nanowire of length L using the following single-channel Hamiltonian [4,5]

$$\begin{aligned} H &= \frac{1}{2}\int \mathrm{d}x \Psi^\dagger(x)\mathcal{H}(x)\Psi(x), \\ \mathcal{H} &= \left[-\frac{\hbar^2}{2m^*}\frac{\partial^2}{\partial x^2} - \mu + e\phi(x)\right]\sigma_0\tau_z \\ &\quad -\mathrm{i}\alpha\sigma_y\tau_z\frac{\partial}{\partial x} + V_Z\sigma_x\tau_z + \Delta\sigma_y\tau_y, \end{aligned} \tag{1}$$

where $\Psi^\dagger = (\psi_\uparrow^\dagger, \psi_\downarrow^\dagger, \psi_\uparrow, \psi_\downarrow)$ is a Nambu bi-spinor, $\psi_{\uparrow,\downarrow}(x)$ are electron annihilation operators, and σ and τ are the Pauli matrices in spin and Nambu space, respectively. The model is defined by setting the parameters m^*, μ, α, V_Z and Δ, corresponding to the effective mass, the chemical potential, the spin–orbit coupling, the Zeeman energy caused by an external magnetic field, and the induced SC pairing potential, respectively.

In Equation 1, we also include the electrostatic potential $\phi(x)$ felt by charges in the nanowire, which can be decomposed as $\phi(x) = \phi_{\mathrm{int}}(x) + \phi_{\mathrm{b}}(x)$, where ϕ_{int} is the potential that arises from the free charges inside the nanowire, while ϕ_{b} corresponds to the potential created by bound charges that emerge in the electrostatic environment. We compute the electrostatic potential using Poisson's equation

$$\vec{\nabla}\cdot\left[\varepsilon(\vec{r})\vec{\nabla}\phi(\vec{r})\right] = \left\langle\rho(\vec{r})\right\rangle, \tag{2}$$

where $\varepsilon(\vec{r})$ is the non-homogeneous dielectrical permittivity of the entire system and $\langle\rho(\vec{r})\rangle$ is the quantum and thermal average of the charge density of the nanowire obtained with Equation 1. The intrinsic part $\phi_{\mathrm{int}}(x)$ of the potential satisfies an analogous equation with a uniform ε equal to that of the nanowire. The geometry depicted in Figure 1a is taken into account through a piecewise $\varepsilon(\vec{r})$ function where each material is characterized by a different dielectric constant, so that $\varepsilon(\vec{r})$ changes abruptly at the interfaces. Then, assuming that the charge density in the nanowire is located along its symmetry axis (x-axis), we obtain the electrostatic potential $\phi_{\mathrm{b}}(x)$ using the method of image charges, as explained in detail in Section 1 of Supporting Information File 1. More precisely, ϕ_{b} is given by

$$\phi_{\mathrm{b}}(x) = \int \mathrm{d}x V_{\mathrm{b}}(x,x')\left\langle\hat{\rho}(x')\right\rangle,$$

where $V_{\mathrm{b}}(x,x')$ is a kernel determined in order to satisfy the proper boundary conditions. We find analytical expressions

for $V_b(x,x')$. They are simple but rather lengthy and are given in Supporting Information File 1 for two different cases: neglecting the effect of the bulk normal leads at the wire ends and including it. The results for these two cases are analyzed in the following sections.

The obtained potential $\phi(x)$ on the nanowire axis should be plugged back into Equation 1. The combined Poisson–Schrödinger problem must then be iterated until it achieves self-consistency. As shown in [33], the $\phi_{int}(x)$ part of the electrostatic solution (i.e., the intrinsic electron–electron interaction part of the problem), treated at the Hartree–Fock level, has a negligible effect on the low-energy spectrum in the topological regime. We may therefore concentrate only on the self-consistency with $\phi_b(x)$. In Section 2 of Supporting Information File 1 we explain in detail the self-consistent numerical method used to compute the electrostatic potential profile as well as the eigenvalues and eigenvectors of Equation 1. For completeness, in Section 3 of Supporting Information File 1 we also show the effect of including the intrinsic interaction from $\phi_{int}(x)$, proving that its effect is small and that the main contribution stems from ϕ_b.

In the following calculations, we consider the dielectric constants shown in Figure 1a. For the dielectrics materials, i.e., the wire, the substrate and the surrounding medium, we use typical values [37] of $\varepsilon = 17.7$, $\varepsilon_d = 3.9$ and $\varepsilon_a \approx 1$, respectively. For the metallic leads we assume that, because they are bulky, they screen external electric fields perfectly, i.e., $\varepsilon_M \to \infty$). This may not be the case for the SC shell, the capability of which for screening external electric fields may be weaker due to its small thickness and the unavoidable presence of disorder [38]. If this is the case, it is then characterized by a finite effective dielectric permittivity which depends on the SC shell width as well as its composition, as we show in Section 1 of Supporting Information File 1. Some experiments [39] have reported that for ultrathin metallic layers (ca. 5–10 nm) it is of the order of $\varepsilon_{SC} \approx 100$. For these values, as we show in the next section, we find a repulsive environment, i.e., an environment the effective permittivity of which is smaller than that of the wire so that the bound charges that arise at the interfaces have on average the same sign as the free charges. We consider in Section 4 of Supporting Information File 1 the generality of our results as a function of the dielectric constant of the SC and the location of the charge density within the nanowire section. Below, in Figure 4c we show that, when the charge density is fixed at the center of the wire, as ε_{SC} becomes larger the dielectric environment turns into an attractive one and the pinning effect is eventually lost. This, however, strongly depends on the location of the charge density. If, as pointed out in [40], it happens to be close to the SC shell, the screening effect is larger and the pinning is suppressed. Nevertheless, as we analyze below in Figure 4e, even if $\varepsilon_{SC} \to \infty$, the pinning effect remains when the wave function is located further away from the SC.

Results and Discussion

Results without bulk normal leads

It is convenient to start by analyzing the simpler case in which we neglect the effect of the bulk normal leads in the induced potential ϕ_b. As an example we consider a nanowire of width W = 100 nm, length L = 1 μm and the following choice of realistic parameters: $m^* = 0.015 m_e$, α = 20 nm·meV, Δ = 0.3 meV, μ = 0.5 meV and T = 10 mK. These could correspond, for example, to an InSb nanowire in contact to an Al superconducting shell [14], but similar results are obtained for InAs wire parameters [19]. For an infinite wire, a schematic representation of the energy bands is shown in Figure 2a in the absence and in the presence of a Zeeman field. At zero temperature, the occupied states below the Fermi level are those between the horizontal dashed line and the band bottom. Apart from a small contribution coming from the spin–orbit energy, the position of the band bottom is controlled by the chemical potential of the wire μ, the Zeeman energy V_Z and the induced potential energy $e\phi_b$. The magnetic field lowers the band bottom, charging the wire, whereas the induced potential energy, coming from electrostatic repulsion, tends to compensate that trend. In the finite-

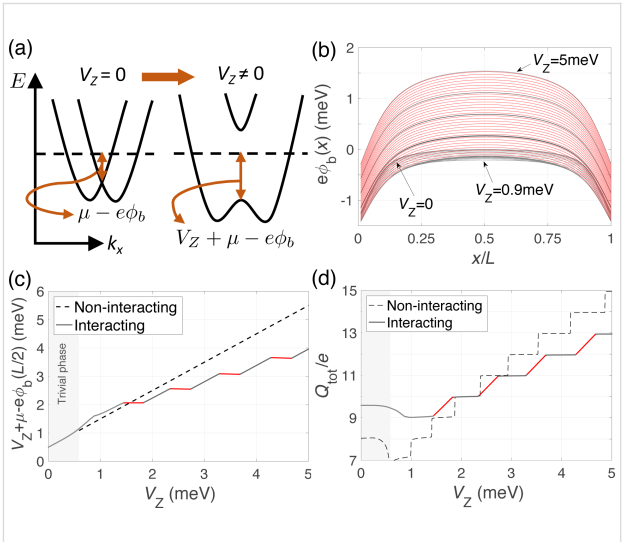

Figure 2: Majorana nanowire subject to interactions from the electrostatic environment (ignoring the influence of the bulk normal leads at its ends). (a) Schematic of the dispersion relation of the nanowire in the absence and in the presence of a Zeeman field. (b) Self-consistent induced potential energy $e\phi_b(x)$ along the length of the wire for increasing values of the Zeeman splitting. Wire parameters as in Figure 1b and with μ = 0.5 meV. (c) Energy difference between the Fermi level and the band bottom at the center of the nanowire, $V_Z + \mu - e\phi_b(L/2)$, and (d) total charge Q_{tot} of the nanowire as a function of V_Z for the non-interacting (dashed) and interacting (solid line) cases. Red curves highlight parameter regions for which there is interaction-induced zero-energy pinning in the spectrum.

length wire, the evolution of the induced potential profile along the nanowire length (x-axis) for different Zeeman fields is shown in Figure 2b. As can be observed, the induced potential tends to expel charge from the center of the wire, where it is positive, while it bends downwards at its ends. On the other hand, the evolution of the potential with Zeeman field exhibits a step-like behavior with regions where it increases linearly with V_Z (red curves), screening the magnetic field effects, and regions where it remains almost constant as V_Z increases (grey curves). This causes the electron fluid to behave in an incompressible or compressible manner, respectively. This different behavior can be clearly seen in Figure 2c where the electrochemical potential at the center of the wire, given by $V_Z + \mu - e\phi_b(L/2)$, is plotted as a function of the Zeeman splitting, both in the presence and absence of interactions.

The effect of this peculiar evolution of the electrostatic potential has direct consequences on the spectral properties of the wire, as we analyze below in Figure 4, but for comparison, let us first see what happens in the non-interacting case. The spectrum of the wire is shown in Figure 3a. There we can observe the emergence of low-energy subgap states for $V_Z > \sqrt{\Delta^2 + \mu^2}$, corresponding roughly to the critical field for the bulk topological transition. We also obtain the typical energy oscillations produced by overlapping Majorana wave functions due to the finite length of the wire [21-23]. More insight can be obtained by analyzing the evolution of the total charge of the wire $Q_{\text{tot}} = \int_0^L \mathrm{d}x \, \langle \rho(x) \rangle$ as well as the Majorana charge Q_M, the absolute value of which is given by

$$|Q_M| = |Q_{+1} - Q_{-1}| = \left| e \int_0^L \mathrm{d}x u_L(x) u_R(x) \right|. \quad (3)$$

Here, $Q_{\pm 1}$ are the charges corresponding to the even/odd lowest-energy eigenstates $\psi_{\pm 1}$, and $u_{L,R}$ are the electron components of the Majorana wave functions $\gamma_L = \psi_{+1} + \psi_{-1}$ and $\gamma_R = -i(\psi_{+1} - \psi_{-1})$. The total charge increases in general with magnetic field but, for finite length wires, it does so by jumping abruptly a quantity equal or smaller than e at each parity crossing (where the Majorana oscillations cross zero energy and the electron parity of the wire changes from even to odd or vice versa), as shown in Figure 2d, dashed curve. This abrupt change in charge is actually injected into the fermion state created by the two overlapping Majoranas and is given by $|Q_M|$ at the parity crossings. The (oscillatory) evolution of $|Q_M|$ with the magnetic field is given in Figure 3b. Strikingly, $|Q_M|$ is maximum at the parity crossing, where the energy is zero, and goes to zero at the oscillation cusps. As the length of the wire approaches to infinity, Q_M approaches zero (not shown). Indeed, the finite value of Q_M at the parity crossings is a direct measurement of the Majorana overlap, as shown in [33]. Note that the Majorana overlap is defined similarly to the right-hand side of Equation 3, but with the absolute value inside the integral.

The behavior of the Majorana wave functions is illustrated in Figure 3c–f. The probability density for the left and right Majorana wave functions exhibits an overall decay towards the

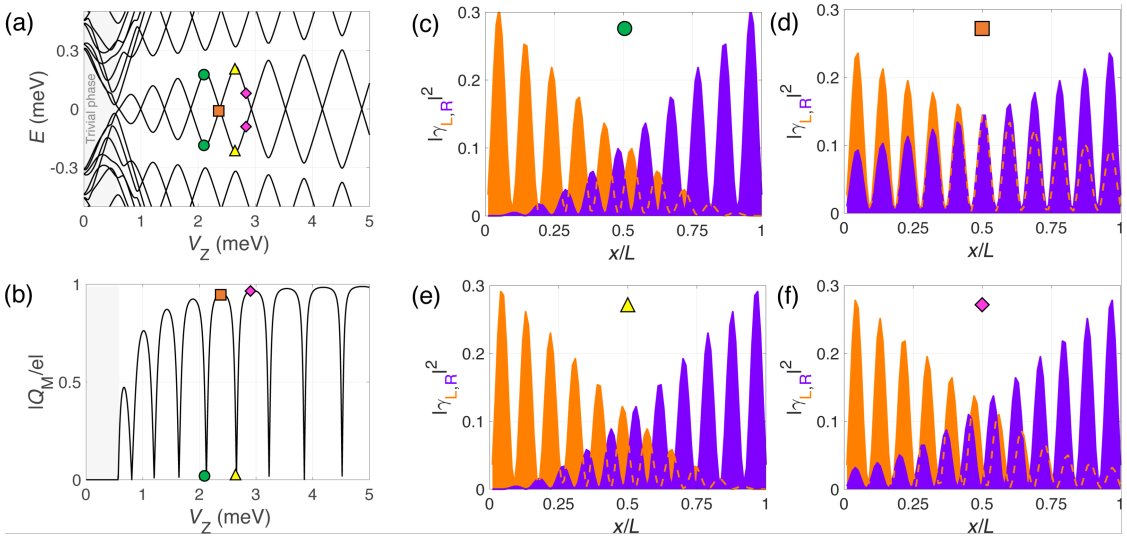

Figure 3: Majorana wave functions in the non-interacting case: Energy levels (a) and the absolute value of the Majorana charge Q_M (b) as functions of the Zeeman energy. Panels (c–f) show the wave-function probability profiles of the two lowest-energy states in the Majorana basis at selected values of the Zeeman field within the topological region. When the splitting is maximum (green circles and yellow triangles) the left and right Majorana wave-function oscillations are out of phase, whereas when the splitting is zero (orange square) they are in phase.

center of the wire controlled by the length $\xi \sim \hbar v_F / \Delta$ and an oscillatory pattern controlled by λ_F[41,42]. Moreover, the number of oscillations that fit in L increases by one with Zeeman field at each parity crossing. Interestingly, we observe that the left–right oscillatory patterns are out of phase for the cases where the splitting of the MBSs is maximum (Figure 3c,e. This minimizes the left–right wave function overlap and the Majorana charge goes to zero. On the other hand, the oscillations are in phase (Figure 3d) when the energy splitting is zero, at the parity crossings, producing a maximum in $|Q_M|$ and overlap. Although the Majorana wave functions are more strongly located at the wire edges, we note that the charge density of this fermionic state is uniform across the wire [34] and, thus, it is uniformly affected by the interaction with the environment when this is present.

When interactions with the image charges occur, the single-point parity crossings as a function of V_Z in the spectrum are replaced by extended regions where the subgap states remain pinned at zero energy, indicated by the red lines in Figure 4a. The abrupt jumps in Q_{tot} in the non-interacting case are replaced by a linear increase with increasing values of V_Z at which zero-energy pinning occurs, see Figure 2d. This is a consequence of the repulsive environment that inhibits the entrance of charge in the wire where the electron liquid behaves in an incompressible manner. On the other hand, the Majorana charge remains basically constant at the pinning plateaus, as shown in Figure 4b. The finite value of Q_M in these regions indicates that zero-energy does not imply absence of overlap between the left and right Majorana states. This is actually a common misconception that we would like to point out here. The Majorana overlap, which is a measurement of the degree of non-locality of the two Majorana wave functions, mostly depends on the length of the nanowire (and to a lesser extent on other parameters, such as the induced superconductor gap and the Rashba coupling), but it is not necessarily correlated to the Majorana energy splitting. Different mechanisms can reduce this splitting, such as interactions with the environment as studied here, smooth potential or gap profiles [21,26-28,30], or orbital magnetic effects [31], and still leave the Majorana overlap unaffected. The behavior of the Majorana wave functions in this case is illustrated in Figure 4c–f. In the pinning regions the Majorana wave functions remain practically frozen and in phase. This in turn explains why $|Q_M|$ is maximum in these regions.

The generality of these results is analyzed in Section 4 of Supporting Information File 1. There we show how the width of the pinning plateau evolves with V_Z when we change the chemical potential, the dielectric permittivity or the width of the SC shell, and the aspect ratio of the nanowire section. We find that pinning remains for any chemical potential, while it vanishes when the attractive contribution of the SC shell becomes dominant over the dielectric repulsion.

Effect of bulk normal leads

In this section we analyze the effect of including the bulk normal leads in the calculation of the induced potential ϕ_b. Figure 5a illustrates the evolution of ϕ_b with increasing Zeeman field for the same set of parameters as in the previous section

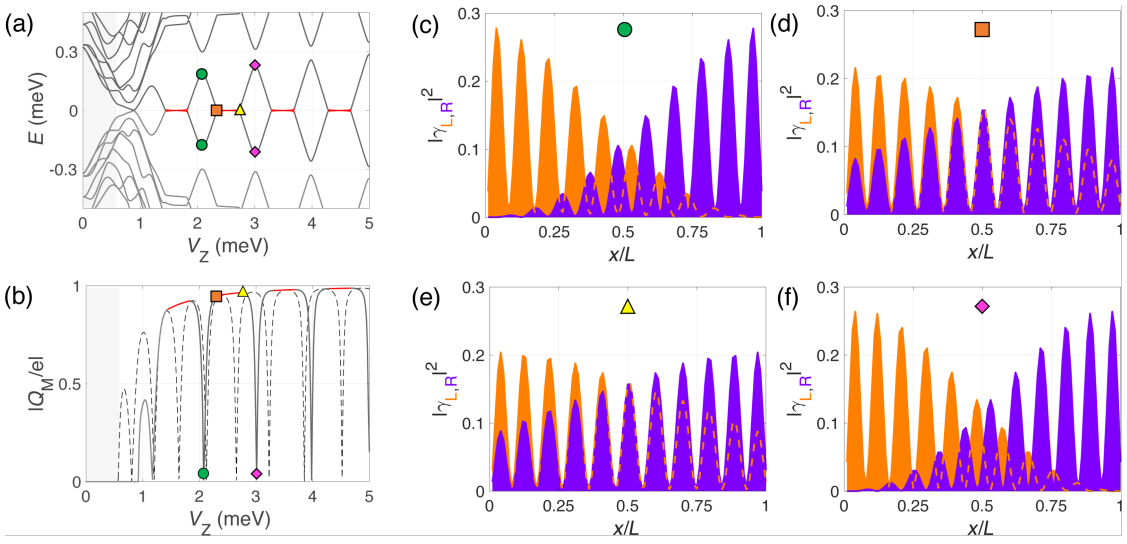

Figure 4: Same as Figure 3 but for the interacting case (without leads). In the pinned regions the Majorana wave functions remain in-phase as a function of the Zeeman field and the Majorana charge (b) freezes at its local maximum value (in red), instead of continuing the oscillation as in the non-interacting case (dashed curve).

but including the normal contacts. While in the central region of the wire a similar repulsive step-like evolution with V_Z is found (corresponding to compressible/incompressible electron fluid behavior), significant attractive regions appear at the wire ends produced by the metallic character ($\varepsilon_M \to \infty$) of the adjacent leads. As we discuss below, these attractive regions give rise to the formation of quantum-dot (QD)-like bound states that may interact with the low energy subgap states of the Majorana wire.

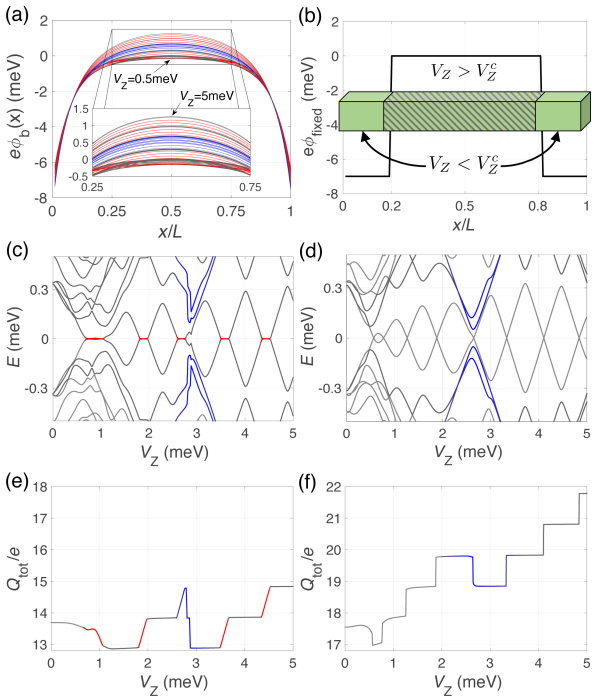

Figure 5: Majorana nanowire subject to interactions from the electrostatic environment (including the influence of the bulk normal leads at its ends). (a) Self-consistent induced potential energy $e\phi_b(x)$ along the length of the wire for increasing values of the Zeeman splitting. The same wire parameters as in Figure 2 were used. Note that the main effect of the bulk normal leads is to create confining potential wells at the wire edges. (b) Barrier-like potential energy profile used to mimic the self-consistent solution. Spectra of the Majorana nanowire as a function of V_Z in the (c) interacting case and in the (d) non-interacting case but using the potential profile model of (b). (e, f) Evolution of the total charge Q_{tot} with Zeeman splitting for the two previous cases, respectively. Red color indicates incompressible electron fluid behavior as before, while blue color indicates QD-like behavior due to the metallic contacts.

The evolution of the spectral properties and of the total charge Q_{tot} in this case are shown in Figure 5c and Figure 5e. On one hand, we observe that the pinning plateaus around each parity crossing (in red) are still present although with a smaller width. On the other hand, the main effect of the presence of the attractive potential regions is the appearance of four additional energy levels (two per contact, in blue) that approach zero energy for a value of V_Z of about 2.5–3.0 meV. At the same time we observe a rather abrupt decrease in the total wire charge (of roughly $2e$), see Figure 5e. We can associate these additional levels with QD-like bound states arising in the attractive regions of the induced potential that anticross with the Majorana levels when their energies are on resonance [35,36,43,44].

To demonstrate the validity of this interpretation we show in Figure 5d and Figure 5f, respectively, the spectral properties and the total charge evolution for an isolated wire with a simple double potential well taken to mimic the effect of the electrostatic environment, shown in Figure 5b. Notice that in this case we do not attempt a self-consistent calculation but rather include the Zeeman field as a rigid shift of the two spin bands (like in the non-interacting case but with an inhomogeneous potential profile). Although the zero-energy pinning is not captured by this model, one can clearly observe the presence of four levels coming down towards zero energy for a value of V_Z of about 2.5–3.0 meV, as in the interacting case. The presence of these states is a consequence of the renormalization of the topological phase transition due to the electrostatic potential (either ϕ_b or ϕ_{fixed}):

$$V_Z^c = \sqrt{\left(\mu - e\phi_{b,fixed}\right)^2 + \Delta^2}, \tag{4}$$

which is not constant along the wire because ϕ_b (or ϕ_{fixed}) depend on x. For the shown values of V_Z, only the central part of the wire is in the topological regime ($V_Z > V_Z^c$), corresponding to an effectively shorter Majorana wire, whereas the outer parts are trivial ($V_Z < V_Z^c$), corresponding to two effective QDs attached to it. Specific details of how QD levels interact with Majorana nanowire ones can be found in [35,36,43-45].

Further information about the nature of the low-energy states at $V_Z \approx 3$ meV is provided in Figure 6 where we plot the wavefunction probability profiles (in the Majorana basis) of the low-energy states around the QD–Majorana levels anticrossing. For simplicity, we consider only the case of the potential barrier model. At the anticrossing, the Majorana and dot states merge and cannot be really told apart, but we will refer to the two lowest in energy as Majorana levels and to the other two as dot levels. As can be observed, at the anticrossing the Majorana levels (green circle) leak into the QD regions leaving the central (topological) part practically void. Conversely, the two dot-like states (immediately above in energy, orange squares) penetrate and delocalize along the wire. When the Zeeman field increases and the QD and Majorana levels are detuned, the dot states depart from low energy (pink rhombus) and from the topological part of the wire, whereas the usual overlapping behavior of the MBSs is recovered but with the Majoranas bound to the effective topological edges (yellow triangle). The absolute value of the Majorana charge as a function of V_Z is shown in

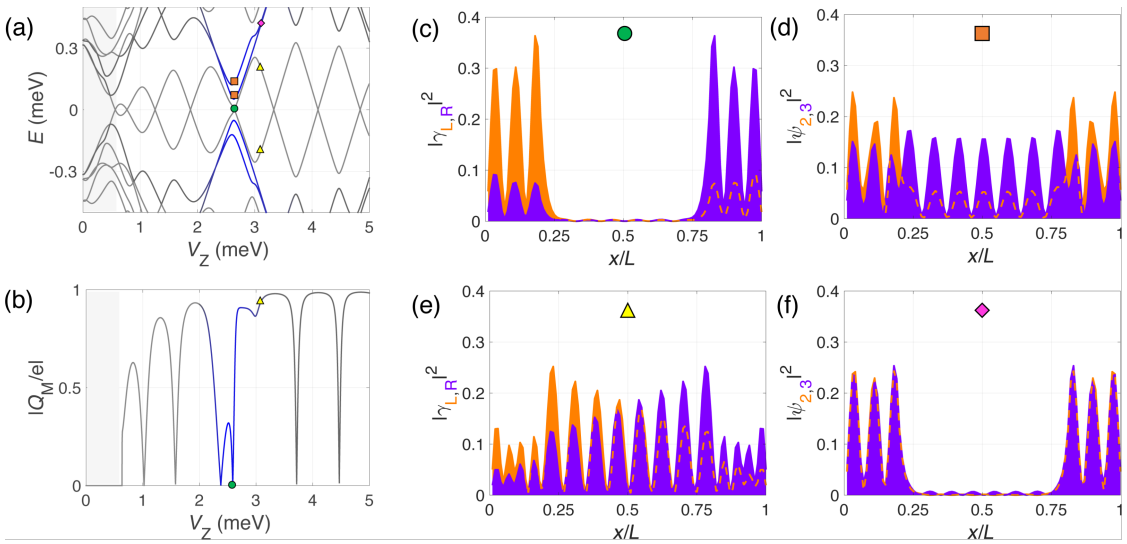

Figure 6: Evolution with Zeeman field of the spectrum (a) and the absolute value of the Majorana charge Q_M (b) for the barrier-like potential model of Figure 5b. Panels (c) and (e) show the wave-function probability profile (in the Majorana basis) of the two lowest-energy states at the V_Z values indicated in (a). Panels (d) and (f) show the same but for the second and third energy states (QD-like states). At the QD–Majorana levels anticrossing, the Majorana wave function leaks into the dot regions leaving the topological region of the wire practically void. This is manifested in $|Q_M|$ by two consecutive zeros, one per dot level (around V_Z = 2.5 meV).

Figure 6b, calculated considering only the two lowest-energy states (as before). At the anticrossing the Majorana charge oscillation is distorted, see blue region, but the area below the curve is conserved. The missing charge in Figure 5b does not come from the Majorana states, but from the dot states. At the anticrossing region, the two QD states (one per potential well) that were occupied (below the Fermi level) move upwards in energy as the Zeeman field increases and cross the Fermi level, emptying themselves. This is why in the blue regions of Figure 5e,f the total charge of the wire does not increase at the corresponding parity crossing, but instead decreases loosing effectively twice the charge of an electron *e*.

Finally, we would like to point out that, when the dot levels anticross the Majorana levels in a pinning region, the Majorana states detach from zero energy. This can be seen in Figure 5c and Figure 1b. The reason is that, although in the pinning regions the Majorana energy is zero, their wave function overlap is not. It is actually maximum, as explained when discussing Figure 4. Each QD acts as a local probe (one couples to the left topological region of the wire, the other to the right). If the length of teh wire were large (much bigger than the coherence length), left and right Majoranas would be disconnected from each other, and a local probe coupled to one of them would not be able to change its energy or perturb it. This is actually the core manifestation of their topological protection. However, when the length of the wire is finite and the Majoranas overlap, each QD couples to both Majoranas at either end and their energies are modified. The typical shapes of the anticrossing were recently analyzed and can be used to quantify the degree of Majorana non-locality [35,36].

Conclusion

In this work we have studied the low-energy characteristics of Majorana nanowires while including their interaction with a realistic 3D electrostatic environment. This is done by solving self-consistently the Bogoliubov–de Gennes equation together with the Poisson's equation. Typically, the total charge of the wire in equilibrium with the reservoirs increases with magnetic field (or the chemical potential of the wire). However, if the electrostatic screening is smaller inside the wire than at the contacts, a repulsive interaction arises that leads to zero-energy pinning around parity crossings in the spectrum of the wire. While the screening due to the parent SC shell tends, in general, to reduce this pinning effect, we find that it still persists depending on the quality of the SC layer and the location of the charge density within the nanowire. The pinning mechanism could help explain the precise shape of the Majorana oscillations (or lack thereof) observed in some dI/dV experiments, which exhibit substantial deviations from the predictions of simple models for finite length wires.

On the other hand, and more importantly, the self-consistent solution of the electrostatic potential varies nonhomogeneously along the wire. It is relatively flat in the central region but, due to the screening from the left/right metallic contacts, it becomes

strongly negative at the edges. This creates potential wells that confine QD-like states at the ends of the wire, which appear in the spectrum as discrete states within the induced gap that disperse with Zeeman energy or chemical potential. These QD levels interact with the Majorana states in a specific way which is strongly dependent on the Majorana wave function, and particularly on its degree of spatial non-locality. The pinning mechanism and the coupling to QD-like states compete against each other, so that the pinned zero-energy plateaus may become lifted at resonance with the dot states, thus revealing their electrostatic origin (as opposed to true wave function non-locality).

Supporting Information

Supporting Information File 1

Calculational details.
[https://www.beilstein-journals.org/bjnano/content/supplementary/2190-4286-9-203-S1.pdf]

Acknowledgements

We thank P. San-Jose and R. Aguado for valuable discussions. Research supported by the Spanish Ministry of Economy and Competitiveness through Grants FIS2014-55486-P, FIS2016-80434-P (AEI/FEDER, EU), the Ramón y Cajal programme Grants RYC-2011-09345 and the María de Maeztu Programme for Units of Excellence in R&D (MDM-2014-0377).

References

1. Alicea, J. *Rep. Prog. Phys.* **2012,** *75,* 076501. doi:10.1088/0034-4885/75/7/076501
2. Beenakker, C. W. J. *Annu. Rev. Condens. Matter Phys.* **2013,** *4,* 113–136. doi:10.1146/annurev-conmatphys-030212-184337
3. Aguado, R. *Riv. Nuovo Cimento Soc. Ital. Fis.* **2017,** *40,* 523–593. doi:10.1393/ncr/i2017-10141-9
4. Oreg, Y.; Refael, G.; von Oppen, F. *Phys. Rev. Lett.* **2010,** *105,* 177002. doi:10.1103/PhysRevLett.105.177002
5. Lutchyn, R. M.; Sau, J. D.; Das Sarma, S. *Phys. Rev. Lett.* **2010,** *105,* 077001. doi:10.1103/PhysRevLett.105.077001
6. Kitaev, A. *Ann. Phys. (Amsterdam, Neth.)* **2003,** *303,* 2–30. doi:10.1016/s0003-4916(02)00018-0
7. Nayak, C.; Simon, S. H.; Stern, A.; Freedman, M.; Das Sarma, S. *Rev. Mod. Phys.* **2008,** *80,* 1083–1159. doi:10.1103/RevModPhys.80.1083
8. Aasen, D.; Hell, M.; Mishmash, R. V.; Higginbotham, A.; Danon, J.; Leijnse, M.; Jespersen, T. S.; Folk, J. A.; Marcus, C. M.; Flensberg, K.; Alicea, J. *Phys. Rev. X* **2016,** *6,* 031016. doi:10.1103/PhysRevX.6.031016
9. Lutchyn, R. M.; Bakkers, E. P. A. M.; Kouwenhoven, L. P.; Krogstrup, P.; Marcus, C. M.; Oreg, Y. *Nat. Rev. Mater.* **2018,** *3,* 52. doi:10.1038/s41578-018-0003-1
10. Albrecht, S. M.; Higginbotham, A. P.; Madsen, M.; Kuemmeth, F.; Jespersen, T. S.; Nygård, J.; Krogstrup, P.; Marcus, C. M. *Nature* **2016,** *531,* 206–209. doi:10.1038/nature17162
11. Gazibegovic, S.; Car, D.; Zhang, H.; Balk, S. C.; Logan, J. A.; de Moor, M. W. A.; Cassidy, M. C.; Schmits, R.; Xu, D.; Wang, G.; Krogstrup, P.; Op het Veld, R. L. M.; Zuo, K.; Vos, Y.; Shen, J.; Bouman, D.; Shojaei, B.; Pennachio, D.; Lee, J. S.; van Veldhoven, P. J.; Koelling, S.; Verheijen, M. A.; Kouwenhoven, L. P.; Palmstrøm, C. J.; Bakkers, E. P. A. M. *Nature* **2017,** *548,* 434–438. doi:10.1038/nature23468
12. Zhang, H.; Gül, Ö.; Conesa-Boj, S.; Nowak, M. P.; Wimmer, M.; Zuo, K.; Mourik, V.; de Vries, F. K.; van Veen, J.; de Moor, M. W. A.; Bommer, J. D. S.; van Woerkom, D. J.; Car, D.; Plissard, S. R.; Bakkers, E. P. A. M.; Quintero-Pérez, M.; Cassidy, M. C.; Koelling, S.; Goswami, S.; Watanabe, K.; Taniguchi, T.; Kouwenhoven, L. P. *Nat. Commun.* **2017,** *8,* 16025. doi:10.1038/ncomms16025
13. Nichele, F.; Drachmann, A. C. C.; Whiticar, A. M.; O'Farrell, E. C. T.; Suominen, H. J.; Fornieri, A.; Wang, T.; Gardner, G. C.; Thomas, C.; Hatke, A. T.; Krogstrup, P.; Manfra, M. J.; Flensberg, K.; Marcus, C. M. *Phys. Rev. Lett.* **2017,** *119,* 136803. doi:10.1103/physrevlett.119.136803
14. Zhang, H.; Liu, C.-X.; Gazibegovic, S.; Xu, D.; Logan, J. A.; Wang, G.; van Loo, N.; Bommer, J. D.; de Moor, M. W.; Car, D.; het Veld, R. L. M. O.; van Veldhoven, P. J.; Koelling, S.; Verheijen, M. A.; Pendharkar, M.; Pennachio, D. J.; Shojaei, B.; Lee, J. S.; Palmstrom, C. J.; Bakkers, E. P.; Sarma, S. D.; Kouwenhoven, L. P. *Nature* **2018,** *556,* 74. doi:10.1038/nature26142
15. Mourik, V.; Zuo, K.; Frolov, S. M.; Plissard, S. R.; Bakkers, E. P. A. M.; Kouwenhoven, L. P. *Science* **2012,** *336,* 1003–1007. doi:10.1126/science.1222360
16. Das, A.; Ronen, Y.; Most, Y.; Oreg, Y.; Heiblum, M.; Shtrikman, H. *Nat. Phys.* **2012,** *8,* 887–895. doi:10.1038/nphys2479
17. Deng, M. T.; Yu, C. L.; Huang, G. Y.; Larsson, M.; Caroff, P.; Xu, H. Q. *Nano Lett.* **2012,** *12,* 6414–6419. doi:10.1021/nl303758w
18. Churchill, H. O. H.; Fatemi, V.; Grove-Rasmussen, K.; Deng, M. T.; Caroff, P.; Xu, H. Q.; Marcus, C. M. *Phys. Rev. B* **2013,** *87,* 241401. doi:10.1103/PhysRevB.87.241401
19. Deng, M. T.; Vaitiekėnas, S.; Hansen, E. B.; Danon, J.; Leijnse, M.; Flensberg, K.; Nygård, J.; Krogstrup, P.; Marcus, C. M. *Science* **2016,** *354,* 1557–1562. doi:10.1126/science.aaf3961
20. Zazunov, A.; Egger, R.; Levy Yeyati, A. *Phys. Rev. B* **2016,** *94,* 014502. doi:10.1103/PhysRevB.94.014502
21. Prada, E.; San-Jose, P.; Aguado, R. *Phys. Rev. B* **2012,** *86,* 180503. doi:10.1103/PhysRevB.86.180503
22. Das Sarma, S.; Sau, J. D.; Stanescu, T. D. *Phys. Rev. B* **2012,** *86,* 220506. doi:10.1103/physrevb.86.220506
23. Rainis, D.; Trifunovic, L.; Klinovaja, J.; Loss, D. *Phys. Rev. B* **2013,** *87,* 024515. doi:10.1103/PhysRevB.87.024515
24. Vaitiekėnas, S.; Deng, M. T.; Nygård, J.; Krogstrup, P.; Marcus, C. M. *Phys. Rev. Lett.* **2018,** *121,* 037703. doi:10.1103/PhysRevLett.121.037703
25. Deng, M. T.; Vaitiekėnas, S.; Prada, E.; San-Jose, P.; Nygård, J.; Krogstrup, P.; Marcus, C. *arXiv* **2017,** 1712.03536.
26. Kells, G.; Meidan, D.; Brouwer, P. W. *Phys. Rev. B* **2012,** *86,* 100503. doi:10.1103/physrevb.86.100503
27. Liu, C.-X.; Sau, J. D.; Stanescu, T. D.; Das Sarma, S. *Phys. Rev. B* **2017,** *96,* 075161. doi:10.1103/physrevb.96.075161
28. Moore, C.; Stanescu, T. D.; Tewari, S. *Phys. Rev. B* **2018,** *97,* 165302. doi:10.1103/PhysRevB.97.165302
29. Liu, C.-X.; Sau, J. D.; Das Sarma, S. *Phys. Rev. B* **2017,** *95,* 054502. doi:10.1103/PhysRevB.95.054502
30. Fleckenstein, C.; Domínguez, F.; Ziani, N. T.; Trauzettel, B. *Phys. Rev. B* **2018,** *97,* 155425. doi:10.1103/PhysRevB.97.155425

31. Dmytruk, O.; Klinovaja, J. *Phys. Rev. B* **2018,** *97,* 155409. doi:10.1103/PhysRevB.97.155409
32. Danon, J.; Hansen, E. B.; Flensberg, K. *Phys. Rev. B* **2017,** *96,* 125420. doi:10.1103/PhysRevB.96.125420
33. Domínguez, F.; Cayao, J.; San-Jose, P.; Aguado, R.; Yeyati, A. L.; Prada, E. *npj Quantum Mater.* **2017,** *2,* 13. doi:10.1038/s41535-017-0012-0
34. Ben-Shach, G.; Haim, A.; Appelbaum, I.; Oreg, Y.; Yacoby, A.; Halperin, B. I. *Phys. Rev. B* **2015,** *91,* 045403. doi:10.1103/PhysRevB.91.045403
35. Prada, E.; Aguado, R.; San-Jose, P. *Phys. Rev. B* **2017,** *96,* 085418. doi:10.1103/physrevb.96.085418
36. Clarke, D. J. *Phys. Rev. B* **2017,** *96,* 201109. doi:10.1103/physrevb.96.201109
37. Prada, D. L. *Handbook of Inorganic Compounds,* 2nd ed.; CRC Press: Boca Raton, FL, U.S.A., 2011. doi:10.1201/b10908
38. Hu, E.-T.; Cai, Q.-Y.; Zhang, R.-J.; Wei, Y.-F.; Zhou, W.-C.; Wang, S.-Y.; Zheng, Y.-X.; Wei, W.; Chen, L.-Y. *Opt. Lett.* **2016,** *41,* 4907–4910. doi:10.1364/ol.41.004907
39. Hövel, M.; Gompf, B.; Dressel, M. *Phys. Rev. B* **2010,** *81,* 035402. doi:10.1103/PhysRevB.81.035402
40. Knapp, C.; Karzig, T.; Lutchyn, R.; Nayak, C. *Phys. Rev. B* **2017,** *97,* 125404. doi:10.1103/PhysRevB.97.125404
41. Kitaev, A. Y. *Phys.-Usp.* **2001,** *44,* 131–136. doi:10.1070/1063-7869/44/10s/s29
42. Klinovaja, J.; Loss, D. *Phys. Rev. B* **2012,** *86,* 085408. doi:10.1103/PhysRevB.86.085408
43. Schuray, A.; Weithofer, L.; Recher, P. *Phys. Rev. B* **2017,** *96,* 085417. doi:10.1103/PhysRevB.96.085417
44. Ptok, A.; Kobiałka, A.; Domański, T. *Phys. Rev. B* **2017,** *96,* 195430. doi:10.1103/PhysRevB.96.195430
45. Chevallier, D.; Szumniak, P.; Hoffman, S.; Loss, D.; Klinovaja, J. *Phys. Rev. B* **2018,** *97,* 045404. doi:10.1103/PhysRevB.97.045404

License and Terms